AFWAL-TR-84-3080
VOLUME III

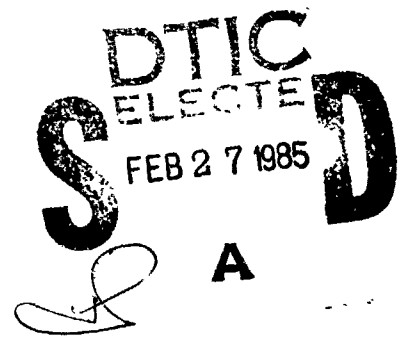# ADVANCED LIFE ANALYSIS

METHODS – Experimental

Evaluation of Crack Growth

Analysis Methods for

Attachment Lugs

AD-A151 058

K. Kathiresan

Lockheed–Georgia Company
Marietta, Georgia 30063

T. R. Brussat

Lockheed–California Company
Burbank, California 91520

September 1984

Flight Dynamics Laboratory
Air Force Wright Aeronautical Laboratories
Air Force Systems Command
Wright-Patterson Air Force Base, Ohio 45433

DTIC
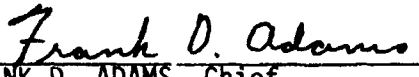ELECTE
FEB 2 7 1985
A

85 02 12 106

NOTICE

When Government drawings, specifications, or other data are used for any purpose other than in connection with a definitely related Government procurement operation, the United States Government thereby incurs no responsibility nor any obligation whatsoever; and the fact that the government may have formulated, furnished, or in any way supplied the said drawings, specifications, or other data, is not to be regarded by implication or otherwise as in any manner licensing the holder or any other person or corporation, or conveying any rights or permission to manufacture use, or sell any patented invention that may in any way be related thereto.
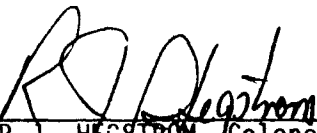
This report has been reviewed by the Office of Public Affairs (ASD/PA) and is releasable to the National Technical Information Service (NTIS). AT NTIS, it will be available to the general public, including foreign nations.

This technical report has been reviewed and is approved for publication.

JAMES L. RUDD
Project Engineer

FRANK D. ADAMS, Chief
Structural Integrity Branch
Structures & Dynamics Division

FOR THE COMMANDER

ROGER J. HEGSTROM, Colonel, USAF
Chief, Structures & Dynamics Division

REPORT DOCUMENTATION PAGE

1a REPORT SECURITY CLASSIFICATION	1b RESTRICTIVE MARKINGS
Unclassified	

2a SECURITY CLASSIFICATION AUTHORITY	3 DISTRIBUTION/AVAILABILITY OF REPORT
	Unclassified/Unlimited
2b DECLASSIFICATION/DOWNGRADING SCHEDULE	

4 PERFORMING ORGANIZATION REPORT NUMBER(S)	5. MONITORING ORGANIZATION REPORT NUMBER(S)
LG82ER 117-III	AFWAL-TR-84-3080, Volume III

6a NAME OF PERFORMING ORGANIZATION	6b. OFFICE SYMBOL (If applicable)	7a NAME OF MONITORING ORGANIZATION
Lockheed-Georgia Company		Air Force Wright Aeronautical Laboratories (AFWAL/FIBEC)

6c ADDRESS (City, State and ZIP Code)	7b ADDRESS (City, State and ZIP Code)
86 South Cobb Drive Marietta, Georgia 30063	Wright-Patterson Air Force Base Ohio 45433

8a NAME OF FUNDING/SPONSORING ORGANIZATION	8b OFFICE SYMBOL (If applicable)	9 PROCUREMENT INSTRUMENT IDENTIFICATION NUMBER
AFWAL/FIBEC		F33615-80-C-3211

8c ADDRESS (City, State and ZIP Code)	10 SOURCE OF FUNDING NOS			
Wright-Patterson Air Force Base Ohio 45433	PROGRAM ELEMENT NO	PROJECT NO	TASK NO.	WORK UNIT NO.
	62201F	2401	01	38

11 TITLE (Include Security Classification)
(See Reverse)

12 PERSONAL AUTHOR(S) Kathiresan, K., Lockheed-Georgia Co., Marietta, Georgia
Brussat, T.R., Lockheed-California Co., Burbank, California

13a. TYPE OF REPORT	13b. TIME COVERED	14 DATE OF REPORT (Yr., Mo., Day)	15 PAGE COUNT
Final Report	FROM Sept.80 TO Sept.84	84-9-17	384

16 SUPPLEMENTARY NOTATION

17 COSATI CODES			18 SUBJECT TERMS (Continue on reverse if necessary and identify by block number)
FIELD	GROUP	SUB GR	Attachment Lugs, Aircraft, Damage Tolerance, Experimental Testing, Crack Initiation, Propagation, Residual Strength, Through-the-Thickness, Corner, Analysis, Correlation
1	3	1	
1	3	3	

19 ABSTRACT (Continue on reverse if necessary and identify by block number)

This report is Vol. III of a 6-part final report on the work conducted under AFWAL Contract No. F33615-80-C-3211. This volume covers the results of experimental evaluation of crack growth analysis methods for attachment lugs which were reported in Vol. II of the final report. These experiments were conducted to assess the damage tolerance of aircraft attachment lugs.

The experimental test program included baseline material characterization, crack initiation, residual strength and crack propagation tests. Several loading and geometric complexities were considered in the test program. The types of loading complexities included were constant-amplitude, block spectrum and flight-by-flight spectrum, symmetric and off-axis loadings. Peak stress levels in the lug which were below and above the yield strength of the materials were also included in the test program. The types of geometric complexities considered were straight, tapered, dogbone, clevis and real aircraft lug

20 DISTRIBUTION/AVAILABILITY OF ABSTRACT	21 ABSTRACT SECURITY CLASSIFICATION
UNCLASSIFIED/UNLIMITED ☒ SAME AS RPT ☐ DTIC USERS ☐	Unclassified

22a NAME OF RESPONSIBLE INDIVIDUAL	22b TELEPHONE NUMBER (Include Area Code)	22c OFFICE SYMBOL
J.L. Rudd	(513) 255-6104	AFWAL/FIBEC

DD FORM 1473, 83 APR EDITION OF 1 JAN 73 IS OBSOLETE

11. TITLE

ADVANCED LIFE ANALYSIS METHODS - Experimental Evaluation of Crack Growth Analysis
Methods for Attachment Lugs   (Unclassified)

18. (Continued)

Constant-Amplitude, Block Spectrum Loading, Flight-by-Flight Spectrum Loading, Symmetric
and Off-Axis Loading, Interference-Fit Bushing, Lower Thickness, Straight Lugs, Tapered
Lugs, Dogbone Lugs, Clevis Lugs, Thick Lugs, Real Lugs

19. (Continued)

configurations. Additional geometric complexities considered include lugs with lower
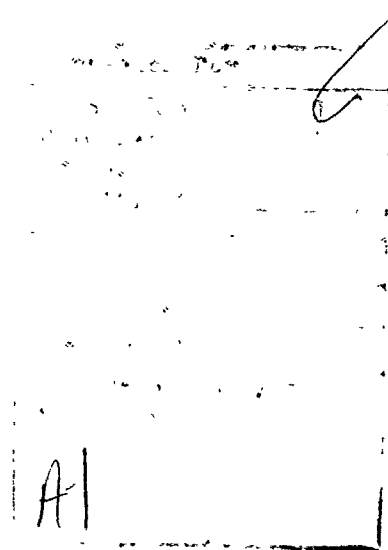thickness and lugs with interference-fit bushings.

The experimental results were correlated with the analytical predictions made using the
methods described in Vol. II of the final report and are presented in this volume.
Excellent correlation results were obtained for most of the test cases. In some cases,
the developed analytical methods needed some improvements or some new solutions had to
be generated. Such efforts were conducted and the refined correlation results are also
included in the present volume.

FOREWORD

This is Volume III of six final report volumes on Contract F33615-80-C-3211, "Advanced Life Analysis Methods." The work reported herein was conducted jointly by Lockheed-Georgia Company and Lockheed-California Company under contract with Air Force Wright Aeronautical Laboratories, Wright-Patterson AFB. J. L. Rudd is the Air Force project leader.

The authors wish to thank T. M. Hsu (presently with Gulf E&P Co.) and H. S. Pearson of Lockheed-Georgia Company and W. P. Renslen, W. F. Bush and P. L. Mohr of Lockheed-California Company for their significant contributions to the experimental testing described in this report.

TABLE OF CONTENTS

TABLE OF CONTENTS (Cont'd)

TABLE OF CONTENTS (Cont'd)

LIST OF FIGURES

LIST OF FIGURES Cont'd

LIST OF FIGURES Cont'd

LIST OF FIGURES Cont'd

LIST OF FIGURES Cont'd

LIST OF TABLES

LIST OF TABLES Cont'd

PROGRAM SUMMARY

The objective of the program is to develop the design criteria and analytical methods necessary to ensure the damage tolerance of aircraft attachment lugs. As planned, the program proceeds logically from an extensive cracking data survey and nondestructive inspection (NDI) assessment, through method development and evaluation, to the preparation of damage tolerance design criteria for aircraft attachment lugs.

The program consists of three phases involving seven tasks. Phase I consists of Tasks I, II and III; Phase II consists of Tasks IV, V and VI; and Phase III consists of Task VII. A roadmap shown in Figure 1-1 summarizes the major activities by task, decision points and their interrelationships.

Task I involves a survey of structural cracking data such as the initial flaw size, shape and location which occur in aircraft attachment lugs. Sources for these data include open literature, available Lockheed data, and visits to the five Air Force Air Logistics Centers (ALCs). The types of aircraft structure used to obtain these data include service aircraft, full scale test articles, component test articles, and coupon specimens.

Task II assesses the current NDI capability to find these flaws or cracks. This assessment is based upon information obtained from the open literature, available Lockheed NDI data and experience, and Air Force ALC data. The NDI techniques capable of finding flaws in attachment lugs and the flaw sizes these techniques are capable of finding are identified. Where possible, the probability of detecting a flaw of a particular size for the NDI technique involved is specified as well as the confidence level assigned to that probability. The results obtained from Tasks I and II are used in the formulation of the initial flaw assumptions developed in Task VII as part of the damage tolerant design criteria for attachment lugs.

Task III involves the development of three different levels of complexity and degrees of sophistication for determining stress intensity factors for single corner cracks and single through-the-thickness cracks in aircraft attachment lugs, and the development of crack growth analyses
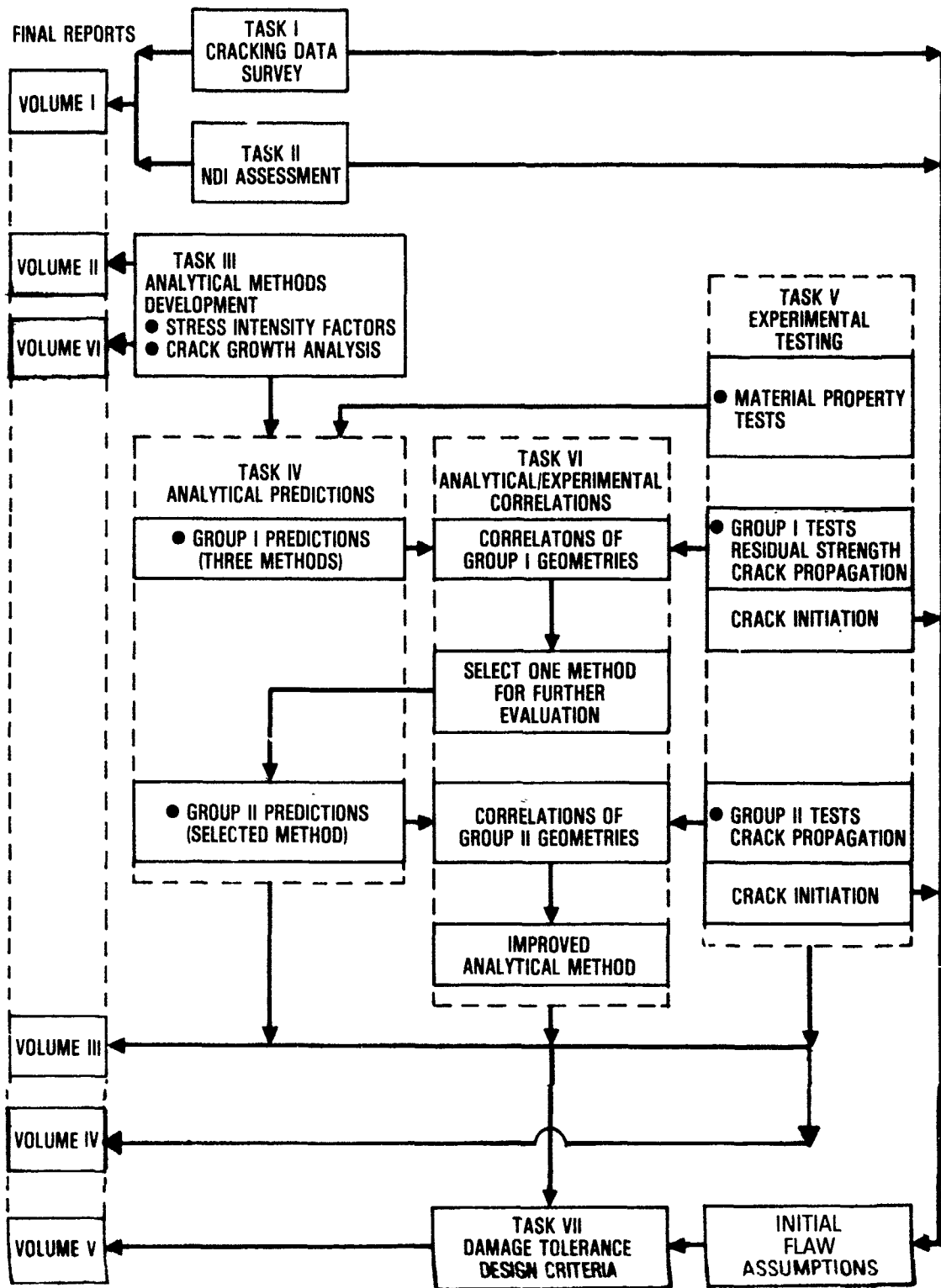
Figure 1-1. Roadmap of the Program

capable of predicting the growth behavior of these cracks and residual strength of these lugs. These stress intensity factors and crack growth analyses are used in Task IV to predict the residual strength and the crack growth behavior for a number of different geometries and test conditions defined in the experimental program. These predictions are made prior to testing. Two groups of attachment lug geometries are tested and experimental test data are generated in Task V. By correlating the analytical predictions made in Task IV with the Group I experimental test data, the analytical methods developed in Task III are evaluated for use in predicting the Group II test results. Further evaluation of the selected method is made by correlating the analytical predictions for the Group II tests (Task IV) with the experimental test results (Task V). These correlations indicate what improvements are necessary for the selected analytical method. The results are presented in parametric format useful to designers and analysts. Damage tolerant design criteria for aircraft attachment lugs are developed in Task VII. These criteria are similar in nature to those of Military Specification MIL-A-83444, and require crack growth analyses by the types of methods developed and verified in Tasks III through VI. The criteria include initial flaw assumptions (e.g., initial flaw type, shape, size, etc.) based upon the cracking data survey of Task I, NDI assessment of Task II, and crack initiation tests of Task V.

As Figure 1-1 shows, the following sequence of final report volumes is planned to cover this project:

Volume I.   Cracking Data Survey and NDI Assessment for Attachment Lugs

Volume II.   Crack Growth Analysis Methods for Attachment Lugs

Volume III. Experimental Evaluation of Crack Growth Analysis Methods for Attachment Lugs

Volume IV.   Tabulated Test Data for Attachment Lugs

Volume V.   Executive Summary and Damage Tolerance Criteria Recommendations for Attachment Lugs

Volume VI.   User's Manual for "LUGRO" Computer Program to Predict Crack Growth in Lugs

This is Volume III on Experimental Evaluation of Crack Growth Analysis Methods for Attachment Lugs which is the result of Tasks IV, V, and VI. This report contains the analytical predictions of crack growth behavior, experimental testing, and the results of analytical/experimental correlations.

INTRODUCTION

In aircraft structures, lug-type joints are frequently used to connect major structural components or in linkage structure. The lug joint is normally connected by a single bolt or pin, creating a simple joint that is easy to assemble and disassemble. Since clamping of the joint is not normally allowed, the lug can act as a pivot. But the elastic gross section stress concentration for lugs is very high which sometimes results in a relatively short crack initiation and crack growth life.

During the past decade, the influence of fracture mechanics on the design, manufacture, and maintenance of aircraft has steadily increased. Also, nondestructive inspection techniques have been improved significantly. However, some cracks still cannot be detected during routine maintenance inspection. Under service loading, such cracks will grow and fracture can occur if the crack length reaches a critical dimension before it can be detected and the part repaired or replaced. To assure aircraft safety, the U.S. Air Force has imposed damage-tolerance requirements (MIL-A-83444)[1] which include the prediction of fatigue crack growth life and residual strength of the structure by assuming that small initial flaws exist at critical locations of new structure due to various material processing and manufacturing operations. Assumptions regarding the initial size, shape, location, multiplicity, etc. for these flaws are specified in MIL-A-83444. However, these assumptions were established primarily with large-area structure in mind, and may not be suitable for attachment lugs.

Attachment lugs are some of the most fracture critical components in aircraft structure, and the consequences of a structural lug failure can be very severe. Therefore, it is necessary to develop damage tolerance design requirements, similar to MIL-A-83444, for attachment lugs to ensure the safety of aircraft. The development of these damage tolerance requirements will be based upon actual cracking data for attachment lugs and current nondestructive inspection capability.

Once the damage tolerance design requirements for aircraft attachment lugs are established, the analytical methods necessary to satisfy the crack

growth and residual strength requirements are needed. In particular, stress intensity factors for cracks in attachment lugs are needed. Such stress intensity factors will depend upon the complexities of structural configuration, crack geometry, applied loads, and the fit between the pin and the lug. Analytical methods for calculating stress intensity factors for cracks in attachment lugs were developed as a part of this program and were reported in Volume II of this report [2].

These analysis procedures can be evaluated and verified through analytical/experimental correlation of test data. Three tasks (IV, V, and VI) were defined in this program for this purpose. These tasks involve the analytical prediction of crack growth behavior, experimental testing of lugs with different geometries and test conditions, and the correlation of analytical and experimental data. This volume of the report describes the results of these three tasks.

Section III describes the details of the experimental program and the test procedures. This includes test specimen descriptions, test matrices, fabrication procedures, test setup and fixtures and other test details. Section IV discusses improvements to the analytical methodologies developed after the writing of Ref. [2]. The experimental program was divided into two major groups, Group I and Group II. The analytical/experimental results and correlations are presented, respectively, in Sections V and VI. Conclusions and recommendations are provided in Section VII.

EXPERIMENTAL PROGRAM

This section describes the experimental program and testing procedures performed under this program. The main objectives of the experimental program are to provide baseline data to evaluate and verify the developed stress intensity factors and crack growth analysis methods, and to assist in the development of the initial flaw assumptions for the damage tolerance design criteria for aircraft attachment lugs.

1.0 SCOPE AND RATIONALE

The experimental program was first divided into two groups, namely Group I and Group II. The main objectives of the Group I tests were to obtain basic data on lugs to evaluate and verify the analysis methods developed in this program. The main objective of the Group II tests was to evaluate the applicability of these methodologies to more complex situations typical of actual aircraft lug design practices.

The two groups of tests were performed sequentially, Group I first at Lockheed-Georgia Company and Group II second at Lockheed-California Company.

1.1 GROUP I TESTS

The Group I tests consisted of a comprehensive study of axially-loaded straight-shank lugs, Figure 3-1. A total of 192 lugs were tested in Group I, as well as 32 material characterization specimens. Crack growth testing covered two different materials (7075-T651 Aluminum and 4340 Steel), three different outer to inner radius ratios (R_o/R_i = 1.50, 2.25 and 3.0), two different positive stress ratios (R = 0.1 and 0.5), two different initial crack geometries (single corner and single through-the-thickness), and two different stress levels (peak notch stress above and below yield), in almost a full 3×2^4 test matrix. Additional Group I crack growth testing considered block and flight simulation spectrum loading, lugs with shrink-fit bushings, and thinner lugs ($2R_i/B$ = 6.0 instead of 3.0). Other Group I

7
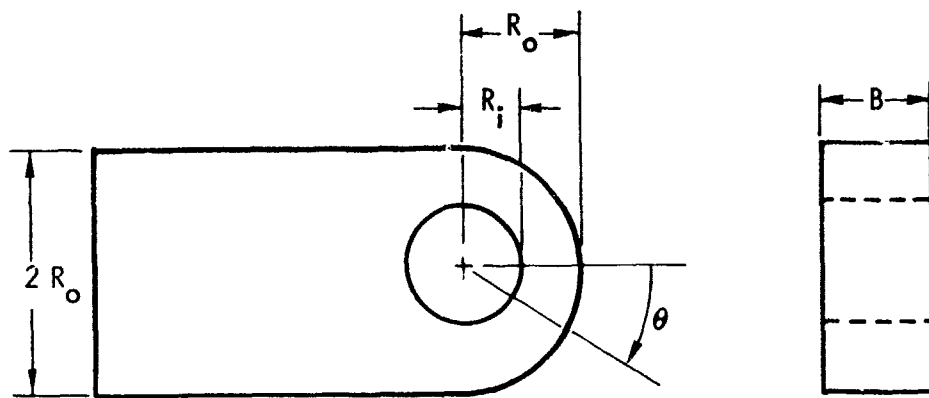
Figure 3-1. Geometry of a Straight Attachment Lug

tests included fatigue tests of uncracked lugs, residual strength tests of lugs, and material characterization tests.

The rationale for selection of each of these test parameters is given in the following paragraphs, in the same order as they are listed above.

Analytical methods of this program were developed to be of a generic nature applicable for different lug materials. Two fundamentally different materials, both commonly used in aircraft applications, were selected.

The three values of R_o/R_i were selected to cover the full range of design usage, based upon a survey of aircraft attachment lugs, discussed more fully in the next subsection.

The critical section of an axially-loaded lug is not put into compression during reversed fatigue loading. Instead, a compressive pin load stretches the critical section in tension, while the equilibrating remote load induces compression. The net result for an applied compressive load is a very small stress, usually tensile. Thus, negative applied load ratios produce positive stress ratios in the critical section of the lug. Consequently, the use of two positive stress ratios in Group I testing was considered ample to cover both positive and negative R values.

The basic stress intensity factors presented in [2] were developed by 2-dimensional analyses of a lug with a through-the-thickness crack. Past data, supplementary analyses and engineering judgement were then used to develop corner crack correction factors. Thus, propagation data for through-the-thickness cracks provide the most basic verification of the 2-dimensional solutions, while the data for corner cracks is used to evaluate the complete analytical solutions, which include the corner crack correction factors.

Similarly, linear elastic fracture mechanics methods are expected to apply when the stresses in the uncracked lug are below the yield strength. Because of the high strength concentration factor however, it can be true of some lugs in service that the peak notch stress exceeds the material yield strength. For these higher stressed lugs a relatively simple elastoplastic analysis method is proposed in [2]. Two stress levels are selected in Group I to evaluate both the basic elastic and the proposed elastoplastic analysis method.

When Group I testing began, the intent was to test both aluminum and steel lugs at peak notch stresses above tensile yield. However, in the

early crack initiation tests of steel at high stress levels, the cracks initiated and grew from the edge of the hole at an angle to the radial direction. No stress intensity factors were developed for a non-radial crack. To circumvent non-radial growth, for which the analysis is inapplicable, flight simulation spectrum tests were conducted in 36 baseline steel lug specimens in place of crack growth testing at the higher stress level. These tests, along with the 36 originally-scheduled block spectrum tests in Group I, provided a broad range of tests of the crack growth retardation models proposed for lugs in [2].

Interference-fit bushings are very commonly used in lug design practice. The installation of an interference-fit bushing introduces a complex stress distribution in the lug. A method of analysis was proposed in [2] to address this problem. A limited number of tests on lugs with bushings were included in Group I to verify the analysis and to assess the effectiveness of using an interference-fit bushing to slow the crack propagation.

In virtually all Group I tests, the selected ratio of pin diameter to lug thickness was $2R_i/B = 3.0$. For lugs with initial corner cracks, reducing the lug thickness could reduce the life, because the corner crack would more quickly become a through-the-thickness crack. A small number of tests of thinner lugs ($2R_i/B = 6.0$) are included in Group I to investigate this effect. (Larger thicknesses than $2R_i/B = 3.0$ are covered in Group II).

To assure a comprehensive study of damage tolerance of lugs, tests were included to investigate fatigue crack initiation and residual strength, as well as crack growth. The initiation tests were to confirm the initial crack conditions in the crack growth tests, while the residual strength tests related to the final crack conditions.

Finally, the analytical methods verification requires that the materials be fully characterized. Thus, material characterization tests were conducted for both materials including tension, compression, fracture toughness and crack growth rate tests.

1.2 GROUP II TESTS

Group II testing employed the lug geometries and loading directions sketched in Figure 3-2. Seventy-six lugs with corner precracks were
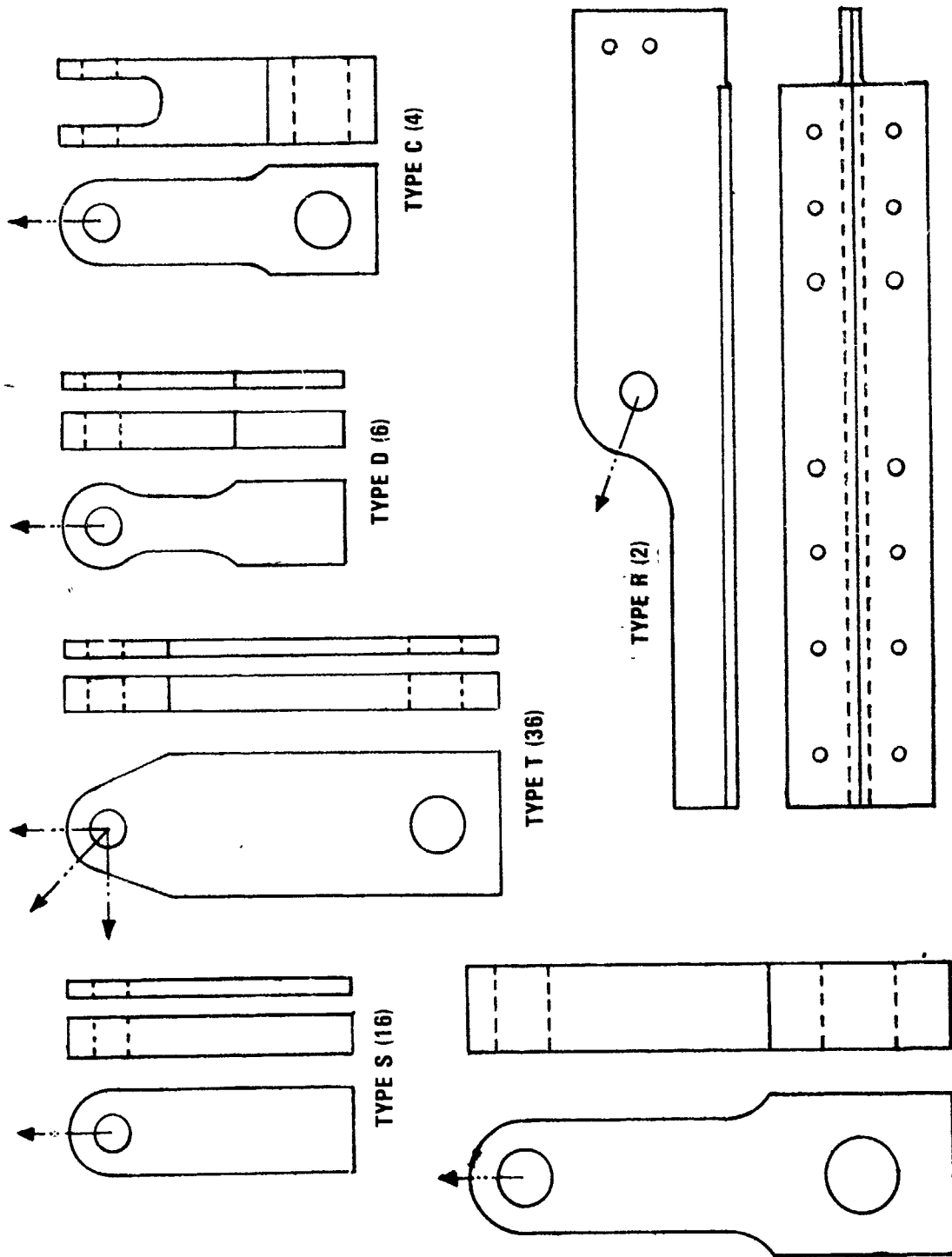
Figure 3-2. Group II Lug Geometries

TYPE C (4)

TYPE D (6)

TYPE T (36)

TYPE S (16)

TYPE R (2)

TYPE S3 (12)
(THREE SIZES)

11

fatigue crack growth tested. In addition, there were 8 crack initiation tests of lugs and 11 compact tension crack growth tests for Group II.

Major variables addressed in the Group II testing include nominal diametrical pin clearances of 0.0005 inch, 0.0015 inch, and 0.0030 inch; pin lubrication (greased or dry); lug shape (straight, tapered, dogbone, clevis); off-axis loading (-45 degrees or -90 degrees to lug axis); initial crack criticality (two angular locations); shrink-fit bushings (bushed or unbushed); and scale-up effects ($2R_i$ = 0.625, 1.0, or 1.5 in.). Also included in Group II were complex redundant structural lugs, load reversals, and flight simulation spectrum loadings. Aluminum was used in 72 of the 84 lugs tested. Finally, in specifying the thickness B, outer radius R_o, and inner radius R_i for the Group II specimens, an effort was made to select values of the ratios R_o/R_i, $2R_i/B$, and $(R_o-R_i)/B$ representing the full range for actual aircraft lugs.

The rationale for selection of each of these test parameters is given in the following paragraphs, in the same order as they are listed above.

The stress intensity factor solution for a cracked lug is very sensitive to the pin load distribution. The load distribution in turn was suspected to be sensitive to pin clearance. Normal tolerances on mating pin and hole diameters allow the pin clearance to vary from 0.0010 inch to 0.0031 inch for the 1.5 inch pins used in Group I testing. Based on Group I test results, this random variation of pin clearance was suspected to be a significant parameter affecting fatigue crack growth.

To minimize wear, the most critical aircraft lugs tend to be lubricated. Like pin clearance, it was suspected that pin lubrication may have a significant effect on the all-important distribution of contact stresses.

Lug shape was not varied at all in the Group I testing; only the straight-shank lug was tested. Aircraft lugs may be tapered wider at the base to provide strength against side loads, or necked down to provide weight savings in the shank where the full width is not needed to carry the load. Furthermore, for every male (single) lug there is a mating female (double) lug, or clevis.

Although off-axis loading is common in many aircraft lugs, axial loading was used exclusively in Group I tests. The straight lug is not

strong enough at the base to withstand the bending stresses induced by off-axis loadings; therefore, a tapered lug is used in practice when off-axis loading occurs. Off-axis loading provides a challange for crack growth analysis of lugs, because the off-axis loaded configuration cannot be likened to a cracked strip. Even crack location and direction are difficult to predict without finite element analysis. Finite element analyses documented in [2] showed two initial crack locations of equal criticality in a tapered lug with a width-to-diameter ratio $R_o/R_i = 2.25$, loaded at -45 degrees to the axis of the lug.

The proposed analysis method for lugs with shrink-fit bushings is valid only if the lug and bushing remain in intimate contact during loading. Intimate contact was assured in Group I testing by the use of unusually high levels of bushing inteference. The residual stresses at these high interference levels were found to drastically change the growth behavior of small fatigue cracks. It was considered essential in Group II testing to re-examine the effects of shrink-fit bushings at the milder levels of interference typical of current design practice, where bushing-lug separation may occur and the residual stresses may or may not be effectual.

Aircraft lugs vary greatly in size, from a small mechanism link to a massive wing-pivot attach lug. Fracture mechanics theory should permit fatigue crack growth test results from small lugs to be applied to larger lugs of proportional dimensions. However, different-sized lugs of identical shape need to be tested to verify the validity of this kind of scaling.

Some aircraft lug shapes do not fit into a neat generic category. For example, one of the wing-to-pylon attachment lugs on some transport aircraft consists basically of a long tee-shaped member, with the lug hole in the flange of the tee. The tee is constructed by bolting two angles together face to face, providing a "fail-safe" redundant feature. The base of the tee is bolted to the wing skin along its entire length with several bolts, and the loading is applied at an odd angle to the longitudinal axis of the tee. The relationship of this complex but fairly common type of lug to the basic test configurations used in this program is not at all obvious, but is certainly an important question.

Although not relevant for axially-loaded lugs, load reversals could affect growth for -90 degree off-axis loading, so limited testing at R = -0.5 was included in Group II.

Because the primary variables in Group II are related to geometry and loading direction, one material (aluminum) and one loading history (constant amplitude with marking cycles) were selected for most tests. However, steel lugs were used in a few selected tests and flight simulation loading in others to assure general applicability of the results.

One goal of the over-all test program was to comprehensively cover the range of geometries of lugs used in aircraft structural design. A survey of lug geometries was conducted covering 78 different lugs from a transport, a trainer and a fighter aircraft. In addition, for 51 different lugs in the cracking data obtained from the Air Force ALCs as part of Task I (Reference [3]), information on lug geometry was available. From these studies, probability plots were developed for ratios of the outer-to-inner radius (R_o/R_i), diameter-to-thickness ($2R_i/B$), and (R_o-R_i)/B, a ratio which reflects the shape of the net section of the lug. Figures 3-3, 3-4, and 3-5 show these probability plots. The staircase-shaped solid line on each figure represents the range of test configurations from the Group I test program. The following are observed:

o   The Group I test matrix covers the range of the most common R_o/R_i ratios (Figure 3-3).

o   Only very high $2R_i/B$ ratios are represented in Group I (Figure 3-4). The median value ($2R_i/B$ of approximately 2) and lower values are not included at all.

o   High values of (R_o-R_i)/B are overrepresented in the Group I test matrix, and very low values are not represented at all (Figure 3-5).

The Group II test specimen dimensions were selected to achieve improvements in the over-all representation of $2R_i/B$ and (R_o/R_i)/B ratios. This improved representation was accomplished by using a larger basic thickness (1.0 inch in Group II compared to .5 inch in Group I), and a smaller hole diameter (1.0 inch in Group II compared to 1.5 inch in Group I), which provided the smaller values of $2R_i/B$ and (R_o-R_i)/B not covered
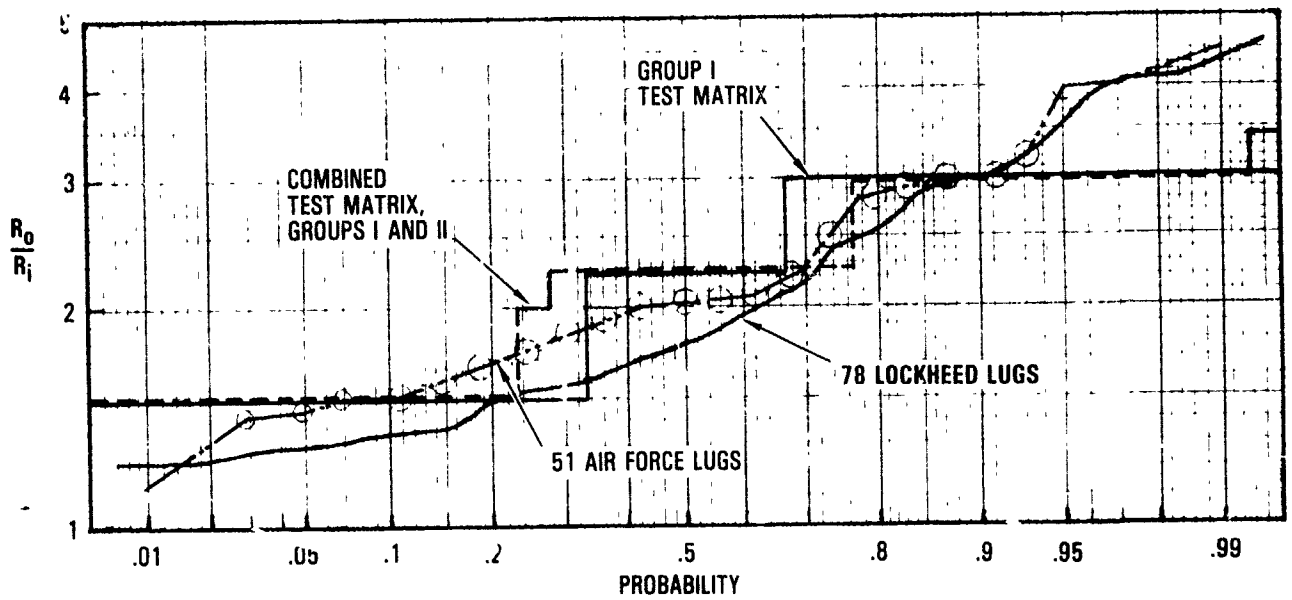
Figure 3-3. Comparison of R_o/R_i Ratios in Test Program and in Structural Lugs
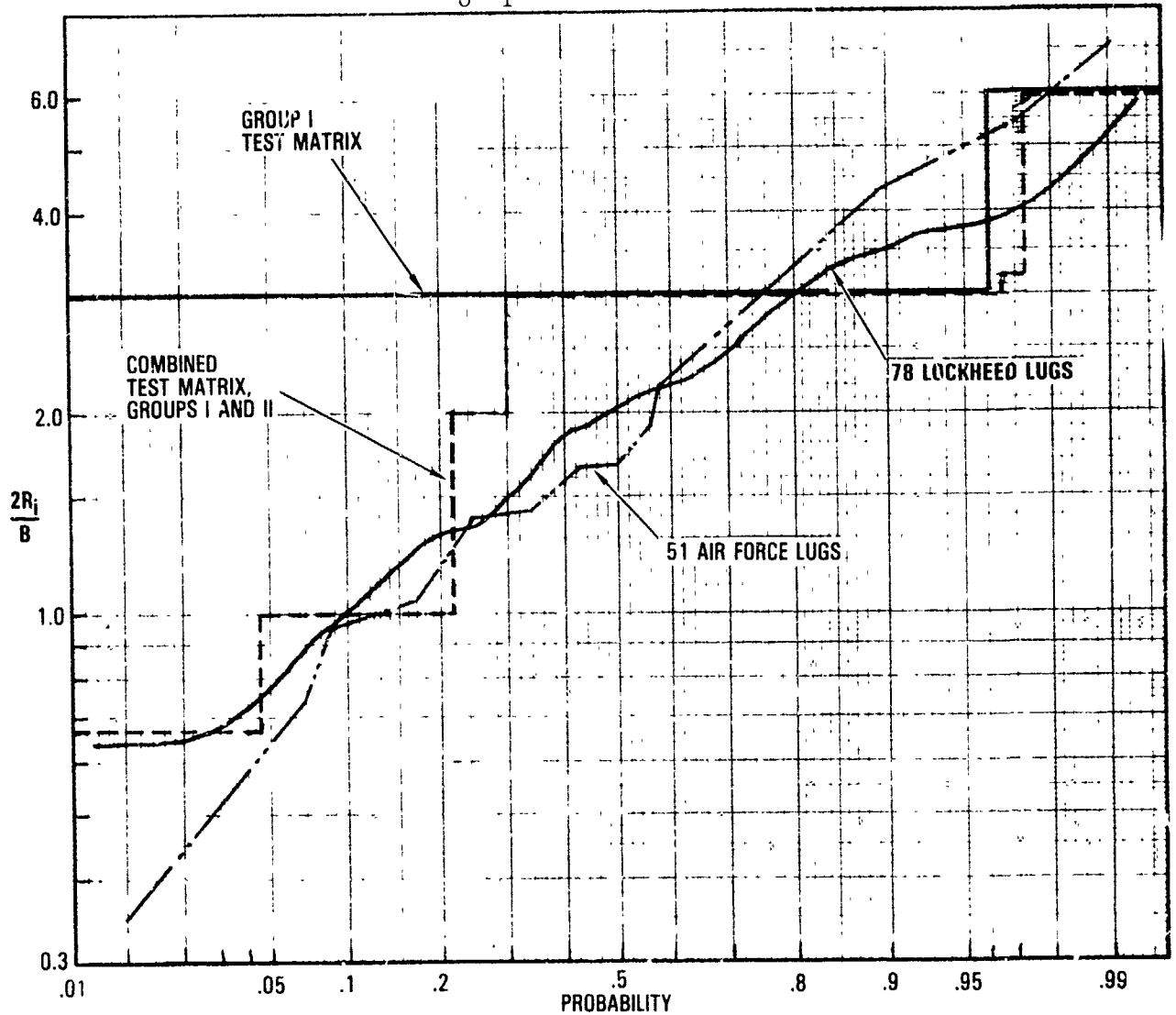
Figure 3-4. Comparison of $2R_i/B$ Ratios in Test Program and in Structural Lugs

15
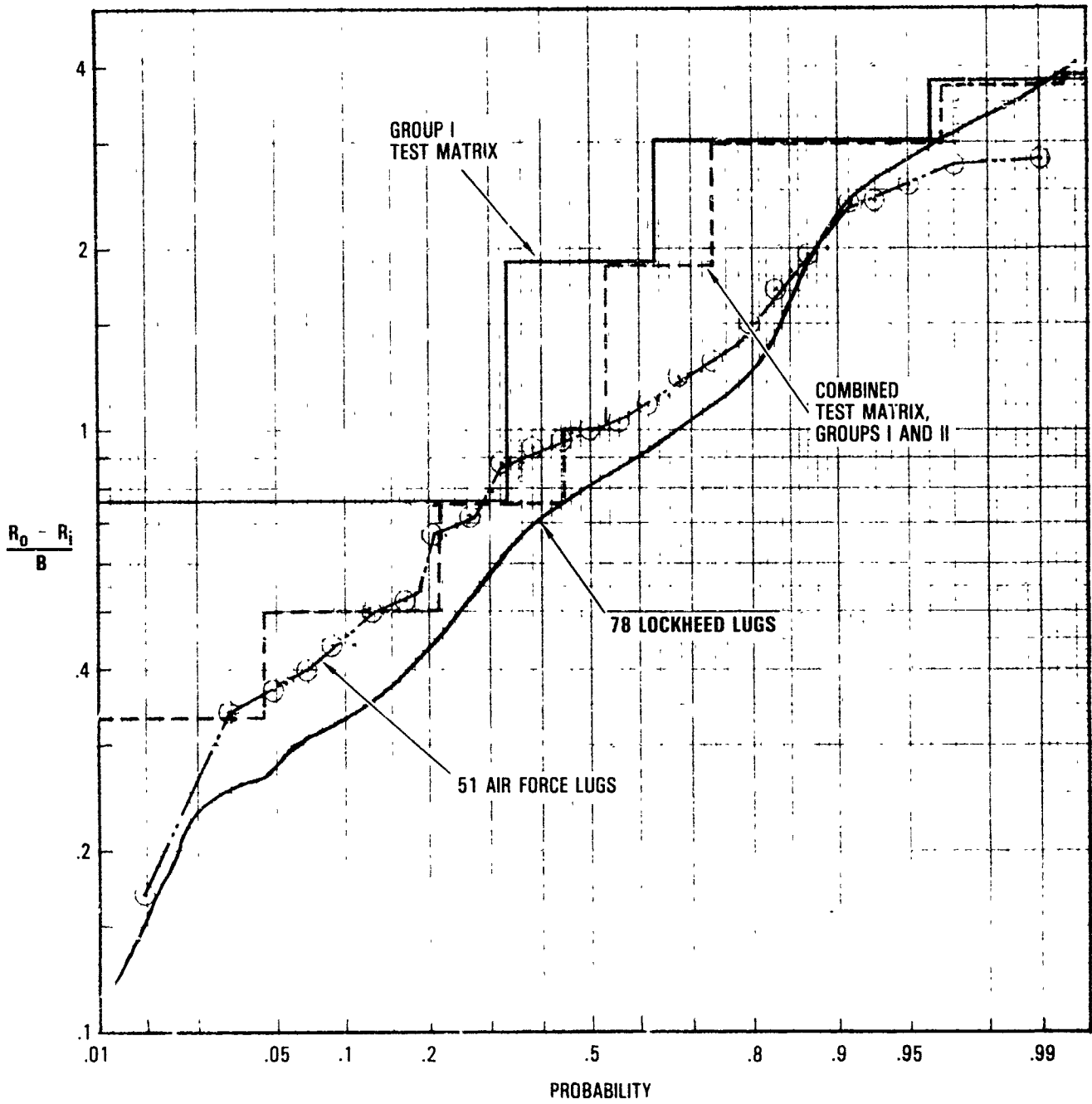
Figure 3-5. Comparison of Net Section Shape in Test Program and in Structural Lugs

16

in Group I. Furthermore the Group II experimental study of scaling effects was done using 12 lugs with even smaller values of these ratios. These thicker lugs, with an initial corner crack, present a more difficult problem for analysis because of their predominantly 3-dimensional nature. When the Group II tests and the Group I tests are considered as a combined package, the R_o/R_i, $2R_i/B$ and $(R_o-R_i)/B$ ratios for the test program are as shown by the dashed-line staircase in Figures 3-3, 3-4, and 3-5, respectively.

2.0 TEST SPECIMEN DESCRIPTIONS

This subsection describes briefly the specimen geometries and materials for the Group I and II tests. The fabrication drawings for all lug specimens tested are given in Appendix A.

2.1 MATERIALS

Based on a survey of actual aircraft attachment lug applications, two different alloys, one aluminum and one steel, in plate form are included in the experimental program. The aluminum alloy is 7075-T651 having either a one-inch or 2.25 inch (for some Group II tests) nominal thickness, and an angle extrusion of 7075-T6511 (for 2 Group II lugs). The steel alloy is 4340 steel, heat-treated to the 180-200 ksi ultimate tensile strength condition. Nominal thickness for the steel alloy is 5/8 inch.

All of the material for Groups I and II testing was purchased together at the start of the program. All of the steel material as received in the annealed condition was from one heat number. The Group I steel specimen material was all heat treated together in a single batch to 180-200 ksi. Likewise, the Group II steel specimen material was heat treated all together in another single batch. The two thicknesses of aluminum plate materials were from the same manufacturer and were purchased from the same supplier at the same time. All of the 2.25-inch thick aluminum plate was from a single heat. All the 1.0-inch thick aluminum plate was also from one heat except the material used for one subset of the Group I specimens, which was from a different heat but the same manufacturer and supplier.

17

The aluminum extrusions were obtained from Lockheed material storage.

2.2 GROUP I SPECIMEN GEOMETRIES

2.2.1 Material Characterization Test Specimens

Specimen configurations used for material characterization are given in Figure 3-6 for tension, compression, fracture toughness and crack growth tests. The fabrication and testing of these material characterization specimens were carried out generally in accordance with applicable ASTM standards.

2.2.2 Attachment Lug Test Specimens

Group I testing consists basically of simple straight male shank lugs, shown schematically in Figure 3-1. The pin radius, R_i = 0.75 inch, was kept constant for all Group I lug tests, which allowed the use of the same clevis fixture for all Group I lug tests. Three outer radii, R_o = 1.125, 1.6875 and 2.25 inches, were considered, as well as two thicknesses, B = 0.25 and 0.5 inches.

When interference-fit bushings were used in Group I, the bushing nominal inner radius was the same as the pin nominal radius, allowing the use of the same clevis fixture and loading pins.

2.3 GROUP II SPECIMEN GEOMETRIES

Figure 3-2 shows the specimen geometries for the Group II testing. Specimen type "S" is the basic straight-shank lug for a pin diameter of 1.0 inch with R_o/R_i = 2.25. Specimen Type "T" is the basic tapered lug with a 45° included taper angle, R_i = 0.5 inch, and R_o/R_i = 2.25, matching the configuration analyzed by the finite element method in Task III. Two thicknesses, 1.0 inch and 0.5 inch, were used for both the basic straight lug and the basic tapered lug.

Specimen Type "S3" was used to examine scaling (size) effects. Three sizes of straight lugs are tested which are different in size but

18
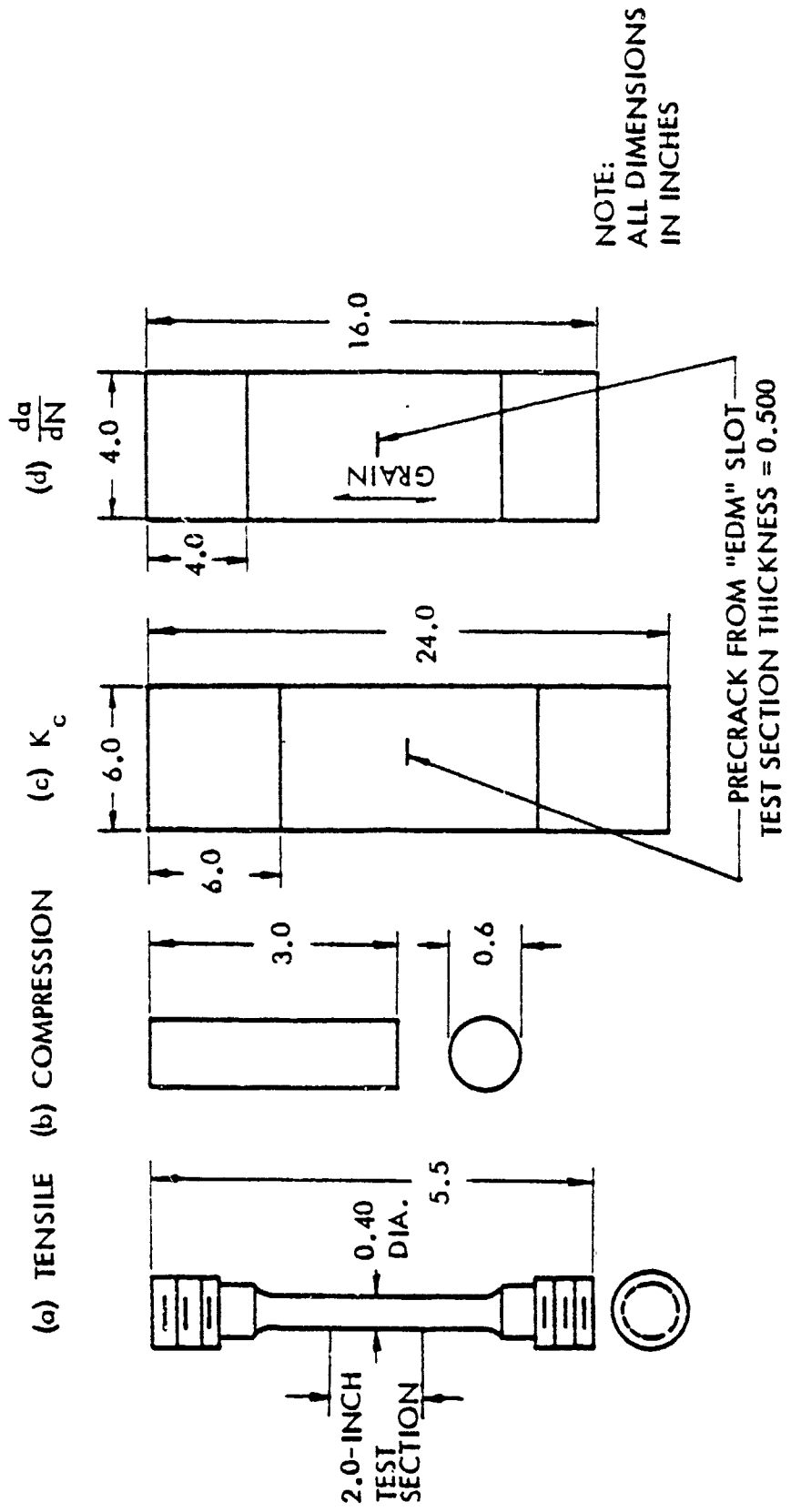
Figure 3-6. Material Characterization Test Specimens

NOTE:
ALL DIMENSIONS
IN INCHES

(a) TENSILE   (b) COMPRESSION   (c) K_c (d) $\frac{da}{dN}$

19

proportional in shape to one another. Each has a R_o/R_i ratio of 2.0, a $2R_i/B$ ratio of 2/3, and a $(R_o-R_i)/B$ ratio of 1/3. Testing these allowed the size effect to be investigated, while at the same time investigating how corner cracks grow in very thick lugs with slim net sections. These were all machined from the 2.25 inch thick aluminum plate stock.

Specimen Type "C" is the clevis lug, and Type "D" is the dogbone-shaped lug. Like the basic straight and tapered lugs, $R_i = 0.5$ inch, $R_o/R_i = 2.25$, and some of the lugs have bushings installed. Also, two thicknesses are included for the dogbone lug, but it was untenable to use a thickness of 1.0 inch for each lug of the clevis, since the basic material stock was only 2.25 inches thick.

Specimen Type "R" is a simulated structural lug. The geometry was selected to represent a typical wing-pylon attach lug for a transport aircraft. The lug consists of a long tee-shaped member, with the hole of the lug in the outstanding flange of the tee. The specimen was affixed to a stationary support frame by 14 bolts in the base of the tee and another 3 bolts at the end of the outstanding flange. The stiffness of the support frame was designed to be representative of the typical stiffnesses of the wing skin and spar cap to which such a lug would typically be attached in an actual aircraft. The tee shape was obtained by bolting two angles together, which potentially gave this lug a special damage tolerant feature. Each angle was machined from a 7075-T6511 extrusion.

The basic configuration and dimensions of this lug were modeled after the rear, outer-wing pylon attach fitting for the C-5 aircraft. It is emphasized, however, that the test of this lug was not a test specifically applicable to evaluating the damage tolerance of C-5 structure, since the test lug was aluminum instead of steel and the test included a number of simplifications and changes in processing and configuration details, support points, loading magnitudes, and loading history.

3.0 TEST MATRICES

This subsection describes the test matrices of both Groups I and II. Group I consisted of 32 material characterization tests, 16 crack initiation tests, 16 residual strength tests and 160 crack propagation

tests. Group II consisted of 8 crack initiation tests and 76 crack propagation tests supported by 11 material crack growth tests using compact tension specimens.

3.1 GROUP I TESTS

3.1.1 Material Characterization Tests

The purpose of material characterization tests is to generate and collect the basic material property data to be used in the residual strength and crack growth predictions for the test specimens of the experimental program. The material characterization tests are summarized in Table 3-1.

Tensile and compressive tests were performed for the long transverse grain direction to characterize mechanical properties and generate stress-strain data to support the analysis of cracked lugs. Fracture toughness (K_c) tests were conducted for each material using the center crack specimen. Crack growth tests were also performed for each material at stress ratios of 0.1 and 0.5 at a test frequency of 10 Hz. Crack growth rate data above 10^{-7} inches per cycle were generated in these tests. Three replicates of each test were conducted. Microstructural analyses were also performed for both materials to chemically characterize them.

3.1.2 Crack Initiation Tests

The main objective of the crack initiation tests was to provide information for determining the location of naturally induced cracks in aircraft attachment lugs and for comparing crack growth behavior and life of an unflawed specimen with that of an identical specimen containing a small intentional initial flaw.

The Group I crack initiation test matrix is summarized in Table 3-2, which includes 16 specimens: 2 materials, 2 outer-to-inner radius ratios, 2 stress levels, and duplicate specimens for each test condition (except steel specimens SBLI9 and SBLI10 which were run at slightly different stress levels when 20 ksi proved to be too low, resulting in too long of a life). The thickness of all 16 lug specimens was 0.50 inch.

21

TABLE 3-1. GROUP I MATERIAL CHARACTERIZATION TESTS

MATERIAL		TENSILE FIG. 3-6 (a)	COMPRESSION FIG. 3-6 (b)	K_c FIG 3-6 (c)	da/dN @ R = FIG. 3-6 (d)		MICRO-STRUCTURE	SPECIMEN ID
7075-T651 ALUMINUM PLATE	4340 STEEL (180-200 KSI)				0.1	0.5		
X		X						AT-1
								AT-2
								AT-3
			X					AC-1
								AC-2
								AC-3
				X				AK-1
								AK-2
								AK-3
					X			ADA-1
								ADA-2
								ADA-3
						X		ADA-4
								ADA-5
								ADA-6
							X	-
	X	X						ST-1
								ST-2
								ST-4
			X					SC-1
								SC-2
								SC-3
				X				SK-1
								SK-2
								SK-3
					X			SDA-1
								SDA-2
								SDA-3
						X		SDA-4
								SDA-5
								SDA-6
							X	-

22

TABLE 3-2. GROUP I CRACK INITIATION TESTS

| MATERIAL | | Ro/Ri | | σ_{MAX}, KSI | SPECIMEN |
7075-T651 ALUMINUM	4340 STEEL (180-200 KSI)	1.5	3.0	R = 0.1	ID
X		X		6	ABLI9 ABLI10
				15	ABLI11 ABLI12
			X	6	ABLI1 ABLI2
				15	ABLI3 ABLI4
	X	X		20 24	SBLI9 SBLI10
				35	SBLI11 SBLI12
			X	24	SBLI1 SBLI2
				35	SBLI3 SBLI4

3.1.3 Residual Strength and Crack Propagation Tests

The main objective of the Group I residual strength and crack propagation tests was to generate data to evaluate and verify the stress intensity factor solutions and crack growth analysis procedures developed under Task III of this program. The scope of the residual strength and crack propagation tests is summarized in Table 3-3.

This test matrix includes baseline tests and variational tests. The baseline tests include 16 static residual strength tests and 144 fatigue crack propagation tests. The 144 crack propagation tests cover three different R_o/R_i ratios and consist of 72 constant amplitude tests (36 each at R = 0.1 and 0.5) and 72 spectrum tests (36 block and 36 flight simulation). The stress levels for constant amplitude tests at R = 0.1 were identical to those used for crack initiation tests, Table 3-2. All baseline specimens were 0.50 inch thick, and each contained either a single quarter-circular corner crack or a single through-the-thickness crack at the edge of the hole perpendicular to the loading direction. The variational tests consist of 8 tests of 0.250 inch thick lug specimens with a single corner precrack, and 8 tests of lug specimens with a single through-the-thickness precrack, having residual stresses in the lug introduced by the installation of an interference-fit bushing.

Tables 3-4 through 3-8 provide details of specimen identifications and test conditions for Group I residual strength and crack propagation testing. Duplicate specimens were employed for each test condition. Loading spectra for Tables 3-6 through 3-8 are described in a later subsection.

3.2 GROUP II TESTS

The fatigue test matrix for Group II consisted of crack growth tests of 76 precracked lugs, supported by 11 material crack growth tests on compact tension specimens and 8 crack initiation tests of uncracked lugs.

3.2.1 Material Crack Growth Tests

The material crack growth tests listed in Table 3-9 cover the four plate and extrusion stocks used in Group II tests. The 1.0-inch 7075-T65

TYPE OF TEST			R_o/R_i 1.5	2.25	3.0	B (INCH) 0.25	0.50	TYPE OF LOADING STATIC	SPECTRUM BLOCK	F-B-F	C.A. @ R = 0.1	0.5	TYPE OF FLAW CORNER	THRU	BUSHING NO	YES	NO. OF TESTS*
BASELINE TESTS — STATIC RESIDUAL STRENGTH			X (8)†				X (R)	X (8)					X (8)		X (8)		8**
BASELINE TESTS — STATIC RESIDUAL STRENGTH					X (8)		X (8)	X (8)						X (8)	X (8)		8**
BASELINE TESTS — PROPAGATION — C.A.	ALU		X (16)	X (16)	X (16)		X (48)				X (24)	X (24)	X (24)	X (24)	X (48)		48***
BASELINE TESTS — PROPAGATION — C.A.	STE		X (8)	X (8)	X (8)		X (24)				X (12)	X (12)	X (12)	X (12)	X (24)		24
BASELINE TESTS — PROPAGATION — BLOCK SPECTRUM	ALU		X (8)	X (8)	X (8)		X (24)		X (24)				X (12)	X (12)	X (24)		24***
BASELINE TESTS — PROPAGATION — BLOCK SPECTRUM	STE		X (4)	X (4)	X (4)		X (12)		X (12)				X (6)	X (6)	X (12)		12
BASELINE TESTS — PROPAGATION — F-B-F SPECTRUM	STEEL		X (12)	X (12)	X (12)		X (36)			X (36)			X (18)	X (18)	X (36)		36++
VARIATIONAL TESTS — C.A. PROPAGATION — 0.25 IN. THICKNESS	ALU			X (4)		X (4)					X (4)		X (4)		X (4)		4***
VARIATIONAL TESTS — C.A. PROPAGATION — 0.25 IN. THICKNESS	STE			X (2)		X (2)					X (2)		X (2)		X (2)		2
VARIATIONAL TESTS — C.A. PROPAGATION — BUSHING	ALU			X (4)			X (4)				X (4)			X (4)		X (4)	4***
VARIATIONAL TESTS — C.A. PROPAGATION — BUSHING	STE			X (2)			X (2)				X (2)			X (2)		X (2)	2
VARIATIONAL TESTS — F-B-F SPECTRUM STEEL — 0.25 THICK				X (2)		X (2)				X (2)			X (2)		X (2)		2+++
VARIATIONAL TESTS — F-B-F SPECTRUM STEEL — BUSHING				X (2)			X (2)			X (2)				X (2)		X (2)	2++
TOTAL			56	64	56	8	168	16	36	40	48	36	88	88	168	8	176

† NUMBER IN THE PARENTHESIS REPRESENTS NUMBER OF TESTS UNDER PARTICULAR COLUMN
* ALL TESTS ARE DUPLICATED
** TESTS INCLUDE 2 CRACK LENGTHS AND 2 MATERIALS
*** TESTS INCLUDE 2 STRESS LEVELS
++ TESTS INCLUDE 3 FLIGHT-BY-FLIGHT SPECTRA (1 CARGO, 1 SEVERE CARGO AND 1 FIGHTER)
+++ SEVERE CARGO SPECTRUM

TABLE 3-4.   GROUP I RESIDUAL STRENGTH TESTS

MATERIAL		Ro/Ri		TYPE OF FLAW		CRACK SIZE (INCH)		
7075-T651 ALUMINUM	4340 STEEL (180-200 KSI)	1.5	3.0	CORNER	THRU	c	a	SPECIMEN ID
X		X		X		0.190	0.240	ABLS13
						0.320	0.400	ABLS14
						0.340	0.390	ABLS15
						0.230	0.300	ABLS16
			X		X	0.408	-	ABLS81
						0.405	-	ABLS83
						0.772	-	ABLS80
						0.792	-	ABLS82
	X	X		X		0.200	0.305	SBLS13
						0.250	0.395	SBLS14
						0.200	0.295	SBLS15
						0.300	0.400	SBLS16
			X		X	0.391	-	SBLS60
						0.399	-	SBLS82
						0.765	-	SBLS57
						0.771	-	SBLS8

26

TABLE 3-5. GROUP 1 BASELINE CONSTANT AMPLITUDE CRACK PROPAGATION TESTS

INITIAL FLAW TYPE		MATERIAL		SPECIMEN ID NO. PREFIX	σ_{omax} (KSI)	R =		R_o/R_i =			SPECIMEN ID NUMBER SUFFIXES	
THRU	CORNER	ALUM.	STEEL			0.1	0.5	1.50	2.25	3.00		
X		X		ABPLC – –	6	X		X			62	63
											46	93
			X	SBPLC – –	14		X		X	X	85	89
											64	68
											47	94
											84	91
		X		ABPLC – –	15	X		X	X	X	62	72
											91	92
											88	90
											63	71
	X	X		ABPLC – –	6		X	X	X	X	47	48
											83	89
											66	72
											48	92
											87	90
											65	110
			X	SBPLC – –	14	X		X	X	X	49	79
											60	86
											17	21
											30	36
											6	56
											18	22
		X		ABPLC – –	15		X	X	X	X	32	34
											5	54
											17	20
											30	32
											55	79
											18	19
											31	34
											5	80
											19	23
											31	33
											8	57
											20	71
											35	37
											55	88

27

TABLE 3-6. GROUP I BASELINE BLOCK SPECTRUM CRACK PROPAGATION TESTS

INITIAL FLAW TYPE		MATERIAL		SPECIMEN ID NO. PREFIX	$\sigma_{o\,max}$ (KSI)	CYCLES PER BLOCK, N_B	$R_o/R_i =$			SPECIMEN ID NUMBER SUFFIXES	
THRU	CORNER	ALUM.	STEEL				1.25	2.25	3.00		
X		X		ABPLS _ _	7.50	2500	X			29	70
								X		75	76
									X	97	101
			X	SBPLS _ _	17.50	2500	X			67	73
								X		75	77
									X	97	98
		X		ABPLS _ _	18.75	100	X			69	105
								X		77*	78
									X	95	96
	X	X		ABPLS _ _	7.50	7500	X			25	27
								X		40	41
									X	58	98
			X	SBPLS _ _	17.50	7500	X			26	28
								X		38	41
									X	58	61**
		X		ABPLS _ _	18.75	300	X			26	28
								X		38	39
									X	59	61

* $\sigma_{o\,max}$ = 21.0 KSI INSTEAD OF 18.75 KSI DUE TO COMPUTER ERROR

** N_B = 2500 CYCLES PER BLOCK INSTEAD OF 7500 CYCLES

TABLE 3-7. GROUP I BASELINE FLIGHT-BY-FLIGHT SPECTRUM
CRACK PROPAGATION TESTS

MATERIAL AND SPECIMEN I.D. NO. PREFIX	SPECIMEN I.D. NUMBER SUFFIXES		INITIAL FLAW TYPE		Ro/Ri	LOADING SPECTRUM	
			CORNER	THRU		DESCRIPTION	TABLES IN APPENDIX B
4340 STEEL (180-200 KSI) SPECIMEN O. SBPLS__	25	22	X		1.50	(1) CARGO SPECTRUM	B-1 AND B-2
	70	65		X	1.50		
	36	35	X		2.25		
	78	94		X	2.25		
	56	54	X		3.0		
	96	95		X	3.0		
	21	99	X		1.50	(2) 1.5 x CARGO SPECTRUM (= SEVERE CARGO SPECTRUM)	B-1 AND P-2
	66	69		X	1.50		
	39	100	X		2.25		
	76	46		X	2.25		
	101	102	X		3.0		
	86	103		X	3.0		
	24	23	X		1.50	(3) FIGHTER SPECTRUM (80-FLIGHT)	B-3 AND B-4
	64	68		X	1.50		
	33	40	X		2.25		
	49	93		X	2.25		
	59	6	X		3.0		
	84	87		X	3.0		

TABLE 3-8. GROUP I VARIATIONAL CRACK PROPAGATION TESTS

| THICKNESS INCH | | BUSHING | | TYPE OF FLAW | | MATERIAL | | σ_{max}, KSI | SPECIMEN |
0.25	0.50	YES	NO	CORNER	THRU	7075-T651 ALUMINUM	4340 STEEL (180-200 KSI)	R = 0.1	I.D.
X			X	X		X		6	AVLT50 AVLT51
						X		15	AVLT52 AVLT53
							X	14	SVLT50 SVLT51
							X	*	SVLT52 SVLT53
	X	X			X	X		6	AVLR44 AVLR45
						X		15	AVLR43 AVLRI03
							X	14	SVLR42 SVLR44
							X	*	SVLR43 SVLR45

* SEVERE CARGO SPECTRUM LOADING, WHICH IS 1.5 TIMES THE CARGO SPECTRUM GIVEN IN TABLES B-1 AND B-2 IN APPENDIX B

TABLE 3-9.   MATERIAL CRACK GROWTH TESTS FOR GROUP II

COMPACT TENSION SPECIMEN		RAW MATERIAL AND SIZE	TEST [1] CONDITION
I.D. NUMBER	W, IN.		
CT-A-1		7075-T651 ALUMINUM 1.0 INCH THICK	A
CT-A-2			A
CT-A-3	5		B
CT-A-4			B
CT-A-5			D
CT-D-1		7075-T651 ALUMINUM 2.25 INCH THICK	C
CT-D-2			SPARE
CT-D-3	5		SPARE
CT-D-4			B
CT-D-5			B,D
CT-S-1		4340 STEEL 180-200 KSI .500 x 6.4 x 6.4 INCH	SPARE
CT-S-2			A
CT-S-3	5		SPARE
CT-S-4			D
CT-S-5			SPARE
CT-E-1		7075-T6511 ALUMINUM EXTRUSION .313 INCH	A
CT-E-2			SPARE
CT-E-3	3.5		SPARE
CT-E-4			SPARE

NOTES: [1] TEST CONDITIONS FOR FATIGUE CRACK GROWTH TESTS ARE AS FOLLOWS:
  A.   CONSTANT AMPLITUDE, $R = 0.1$
  B.   990 CYCLES AT $R = 0.1$ FOLLOWED BY TEN 30% OVERLOADS. SEQUENCE REPEATED UNTIL FAILURE.
  C.   80 FLIGHT FIGHTER WING LOADING SPECTRUM
  D.   1900 CYCLES AT $R = 0.1$ FOLLOWED BY 100 THIRTY PERCENT OVERLOADS. SEQUENCE REPEATED UNTIL FAILURE.

Aluminum plate is from the same heat of material used for Group I testing. Likewise, the 0.625-inch 4340 steel plate (180-200 ksi) is from the same batch of material used for Group I testing, and the heat treatment procedure was identical, although the heat treatment for Group II material was performed at a later time. The 2.25-inch 7075-T651 plate and 7075-T6511 extrusion were not used in Group I testing.

Material crack growth rate tests had already been conducted in the Group I test program for the 1-inch 7075-T651 Aluminum plate and the 0.625-inch 4340 Steel plate (180-200 ksi). Therefore the purpose of the tests listed in Table 3-9 was to supply the supplementary data deemed necessary as a basis for the Group II tests; in particular:

o   To verify the consistency of Group I and II crack growth rate (da/dN) curves for both the steel and 1.0-inch aluminum plate stocks.

o   To verify that the use of periodic 30 percent overloads with constant amplitude loading will produce visible, photographable fracture surface markings in both aluminum and steel, without significantly affecting crack growth rate.

o   To verify that the crack growth rate for the 2.25-inch plate and the extrusion is essentially the same as for the 1.0-inch aluminum plate.

o   To select and verify a crack retardation model by checking it against an experimental crack growth rate per flight (da/dF) curve for the 80-flight fighter wing lower surface spectrum.

The use of constant-amplitude cycling with periodic 30 percent overloads to mark the fracture surface was a key element in the Group II testing. Before any of these compact tension specimens had been tested, it was intended to use 10 thirty-percent overloads each 1000 cycles (Sequence B in Table 3-9). This sequence had been a successful marking sequence in earlier tests conducted at Lockheed-California Company. However, midway through the testing of compact tension specimens it was discovered that better marking was provided using 100 thirty-percent overloads every 2000 cycles (Sequence D). Thus, both sequences are listed in the "Test Conditions" column of Table 3-9.

The specimens were all 5-inch-width (W) compact tension specimens, machined to a thickness (t) of 0.5 inch, except those made from the

extrusion, which had W = 3.5 inch and t = 0.31 inch. Nineteen specimens were fabricated and 11 were tested.

3.2.2 Crack Initiation Tests

Table 3-10 lists eight off-axis fatigue tests of tapered lug specimens conducted in support of Group II testing as part of a Lockheed-funded IR&D program. The data from these tests were used to examine critical crack locations for off-axis loading, as well as check out some of the aspects of the test setup, test procedures, and crack monitoring methods.

3.2.3 Lug Crack Growth Tests

Four separate studies comprise the Group II crack growth test matrix. These are designated as submatrices (a), (b), (c), and (d) in Table 3-11.

The effects of pin clearance, pin lubrication and crack location were systematically studied in submatrix (a). Three levels of nominal pin clearance were selected, corresponding to the midpoint and both extremes of the standard tolerance band for a Class III medium clearance fit. Two different specimens and loading directions are included in submatrix (a). Straight lugs were loaded axially, and tapered lugs were loaded at an angle of -45 degrees to the axis. Half the straight lug tests in this submatrix were conducted with the pins lubricated and half with the pins dry. All tapered lugs were lubricated, and the two potentially critical precrack locations were compared. All lugs were 1.0-inch-thick aluminum, without bushings, and the stress ratio was 0.1 with periodic 30 percent overloads.

The effects of lug configuration and thickness, with and without bushings, were examined in submatrix (b). The basic four lug shapes – straight, tapered, dogbone, and clev s – were tested. All were aluminum lugs, loaded axially at a stress ratio of 0.1 with periodic 30 percent overloads. Test results for the straight, 1.0 inch lugs without bushings were available from submatrix (a), so this case is enclosed in parentheses in submatrix (b), per the explanatory note at the bottom of Table 3-11.

Off-axis loading effects are focused upon in submatrix (c). Data from submatrix (b) for the 0° axial loading case was supplemented by data for

TABLE 3-10. RELATED IRAD TEST PLAN FOR FATIGUE TESTING OF TAPERED LUGS

SPECIMEN CONFIGURATION	MAT'L	THICK. (IN.)	LOADING DIRECTION	R RATIO $\triangle$	PULL PINS TO INSPECT?	LUBE?
Figure A-4 ↑	Aluminum ↑	1.0 ↑	-45^0 ↑	0.1 ↑	No	No
	↕	↕	-45^0 ↕		No	Yes
			-90^0		Yes	No
	Aluminum ↓	1.0 ↓	-90^0 ↓		Yes	Yes
	Steel ↑	0.5 ↑	-45^0 ↑		No	No
	↕	↕	-45^0 ↕		No	Yes
	↓	↓	-90^0	↓	Yes	No
Figure A-4 ↓	Steel	0.5	-90^0	0.1	Yes	Yes

$\triangle$ Loading Sequence:1900 cycles at R = 0 1 one hundred 30% overloads; repeat until failure.

34

TABLE 3-11. PRIMARY SUBMATRICES IN THE GROUP II TEST MATRIX

PIN CLEARANCE, ±.00025 (INCH)	STRAIGHT LUG AXIAL LOADING		TAPERED LUG −45° LOADING LUBRICATED PIN		(a) Pin Clearance and Lubrication and Crack Location
	DRY	LUBED	58° CRACK	227° CRACK.	Loading: R = 0.1
.0005	2	2	2	2	Thickness: 1.0 inch
.0015	2	2	2	2	Material: Aluminum
.0030	2	2	2	2	No bushings

LUG GEOMETRY	B = 1.0 INCH		B = 0.5 INCH		(b) Lug Geometry, Thickness, Bushings
	BUSHING	NO BUSH	BUSHING	NO BUSH	Load Direction: Axial
Straight	2	(2)	2	—	Loading: R = 0.1
Tapered	2	2	2	—	Material: Aluminum
Dogbone	2	2	2	—	Pin Lubricated
Clevis	—	—	2	2	

LOADING		ALUMINUM B = 1.0 INCH		STEEL B = 0.5 INCH		(c) Loading Direction, Material, Bushings, Reversed Loading
DIRECTION	R	BUSHING	NO BUSH	BUSHING	NO BUSH	Geometry: Tapered Lugs
0°	0.1	(2)	(2)	—	—	Pin Lubricated
-45°	0.1	2	(2)	2	2	
-90°	0.1	2	2	2	2	
-90°	-0.5	2	2	—	—	

LUG GEOM.	2Ri (INCH)	R = 0.1 NO BUSH	80 FLT SPECTRUM		(d) Size Effect, Thick Lugs, Spectrum Loading, Wing-Pylon Lug
			NO BUSH	BUSHING	
Straight	.625	2	2	—	Pin Lubricated
2Ri/B = 2/3	1.0	2	2	—	
Axial Load	1.5	2	2	—	
Wing-Pylon 157° Load	1.0	—	—	2	

NOTES: ( ) indicates specimens already included in above submatrix

All specimens contain initial corner cracks

the -45° and -90° loading directions. These off-axis tests of 1.0 inch aluminum tapered lugs were repeated using 0.5 inch 4340 steel specimens. In addition to all these tests at R = 0.1, effects of load reversal were included by testing aluminum lugs at R = -0.5, loaded in the -90° direction. Periodic 30 percent overloads were used in both cases. Half the specimens in submatrix (c) contained shrink-fit bushings and half contained no bushings.

Size effects, very thick lugs, spectrum loading, and a complex structural lug configuration were included in the submatrix (d) tests. Straight-shank aluminum lug specimens with low $2R_i/B$ and $(R_o-R_i)/B$ ratios $(2R_i/B = 2/3$ and $(R_o-R_i)/B = 1/3)$ were tested under both R = 0.1 fatigue loading (with periodic 30 percent overloads) and the 80-flight spectrum. These specimens were identical in shape to one another, differing only in size by ratios of 5:8:12. They did not contain bushings. The final test in submatrix (d) was an 80-flight spectrum test of the simulated wing-pylon attach lug. The lug contained a bushing and was off-axis-loaded at an angle of 157°. The purpose of that test was to provide a very challenging test for the crack growth prediction methodology.

The 76 Group II crack growth tests are listed by specimen identification number summarized in Table 3-12. In the first 3 columns of this table, the figure in Appendix A showing the specimen configuratin is identified along with the individual specimen identification numbers. Duplicate tests were used for every test condition. The nominal pin clearance is listed in Column 4; in one subset of tests pin clearance is closely controlled and systematically varied. In the fifth column of the table it is shown whether or not the pin is lubricated during testing. Loading directions are given in Column 6 in terms of the angle between the applied load and the longitudinal axis of the specimen. In Column 7 the fatigue loading sequence is specified; either constant amplitude cycling at a stress ratio of 0.1 or -0.5 with 100 thirty percent overloads every 2000 cycles; or spectrum loading using the 80-flight spectrum.

Column 8 lists the value of the maximum operating load used. For periodic overload testing, this is the maximum load for the 1900 operating cycles; the overload is 1.3 times the value listed. These load levels were selected by a preliminary analysis to obtain crack growth lives of

TABLE 3-12. GROUP II TEST MATRIX FOR PRECRACKED LUGS

LUG GEOM. FIGURE NO. A-X, APPENDIX A	SPECIMEN ID NUMBERS		NOMINAL PIN CLEARANCE (INCH)	LUBED?	LOADING DIRECTION	R-RATIO OR SPECTRUM	MAXIMUM OPERATING LOAD (KIPS)	PART OF TABLE 3-11 SUBMATRIX:
3	S1-X-1	S1-X-2	.00075	Dry	0°	0.1	15.75	(a)
	S1-X-3	S1-X-4	.00075	Lubed				↕
	S1-Y-1	S1-Y-2	.00175	Dry				(a)
	S1-Y-3	S1-Y-4	.00175	Lubed				(a, b)
	S1-Z-1	S1-Z-2	.00275	Dry				(a)
	S1-Z-3	S1-Z-4	.00275	Lubed			15.75	(a)
	S2-A-1	S2-A-2	.00175				22.50	(b)
3	S2-B-1	S2-B-2	.00175		0°		11.25	(b)
4	T1-X-1	T1-X-2	.00075		-45°		19.30	(a)
	T1-X3	T1-X4	.00075					↕
	T1-Y-1	T1-Y-2	.00175					(a)
	T1-Y-3	T1-Y-4	.00175					(a, b, c)
	T1-Z-1	T1-Z-2	.00275					(a)
	T1-Z-3	T1-Z-4	.00275		-45°		19.30	(a)
	T1-A-1	T1-A-2	.00175		0°		15.75	(b, c)
	T1-A-3	T1-A-4			-90°	0.1	22.00	(c)
	T1-A-5	T1-A-6			-90°	-0.5	22.00	(c)
	T1-S-1	T1-S-2			-45°	0.1	30.00	(c)
	T1-S-3	T1-S-4			-90°		30.00	(c)
	T2-A-1	T2-A-2			0°		22.50	(b, c)
	T2-A-3	T2-A-4			-45°		27.50	(c)
	T2-A-5	T2-A-6			-90°	0.1		↕
	T2-A-7	T2-A-8			-90°	-0.5	27.50	(c)
	T2-B-1	T2-B-2			0°	0.1	11.25	(b)
	T2-S-1	T2-S-2			-45°		30.00	(c)
4	T2-S-3	T2-S-4	.00175		-90°		30.00	(c)
5	S3-A-1	S3-A-2	.00150		0°	0.1	8.20	(d)
5	S3-A-3	S3-A-4	.00150			80 FLT	14.06	
6	S3-B-1	S3-B-2	.00175			0.1	21.00	
6	S3-B-3	S3-B-4	.00175			80 FLT	36.00	
7	S3-C-1	S3-C-2	.00205			0.1	47.20	
7	S3-C-3	S3-C-4	.00205			80 FLT	81.00	(d)
8	C1-A-1	C1-A-2	.00175			0.1	15.75	(b)
9	C2-A-1	C2-A-2					22.50	
10	D1-A-1	D1-A-2					15.75	
11	D2-A-1	D2-A-2					22.50	
11	D2-B-1	D2-B-2			0°	0.1	11.25	(b)
12	R2-E-1	R2-E-2	.00175	Lubed	157°	80 FLT	34.20	(d)

approximately 30,000 to 100,000 cycles. For the 80-flight spectrum the values listed in Column 8 are the once per 80-flight maximum load, selected by preliminary analysis for about 12,000 flights to failure.

Column 9 of Table 3-12 identifies the submatrices (a, b, c or d of Table 3-11) in which each specimen belongs.

4.0 FABRICATION PROCEDURES

The success of the test program required careful attention to detail in the fabrication of test specimens, bushings and loading pins.

4.1 MACHINING OF TEST SPECIMENS

The fabrication drawings for the attachment lug test specimens are given in Appendix A. Detailed fabrication instructions are provided by the notes and dimensional tolerances on these drawings.

The fabrication of steel specimens required an initial step not required for aluminum. After machining the profile (but no thickness reduction and no hole drilling), the steel pieces were heat treated to the 180-200 ksi ultimate tensile strength level and stress relieved.

The rest of the fabrication steps were the same for both materials. First the specimens were final machined, except for the lug hole, the diameter of which was drilled approximately 0.02 inch undersize. In any reduction of thickness during this machining, equal material was removed from both faces to assure flatness. The final lug hole was then bored to final size. Boring was used to achieve the close tolerance required, and the removal of only a small amount of material with this final cut pre-vented the introduction of residual stresses at the hole.

As the final machining step, either a corner or through-the-thickness preflaw was introduced to serve as the origin of the crack, using Electric-Discharge Machining (EDM). The description of EDM flaws is provided in Figure 3-7. Half the preflaws in Group I were corner flaws and half were through-the-thickness, but all were located at $\theta = 90^\circ$ as defined in Figure 3-7. In contrast, although all preflaws in Group II were corner flaws, their locations varied depending upon specimen type and loading direction.

38

EDM FLAW SIZE (TYP):

SECTION AA
- CORNER PREFLAW

VIEW B

VIEW C

SECTION AA
- THROUGH-THE-THICKNESS PREFLAW

VIEW D

DEFINITION OF EDM FLAW LOCATION ANGLE θ:
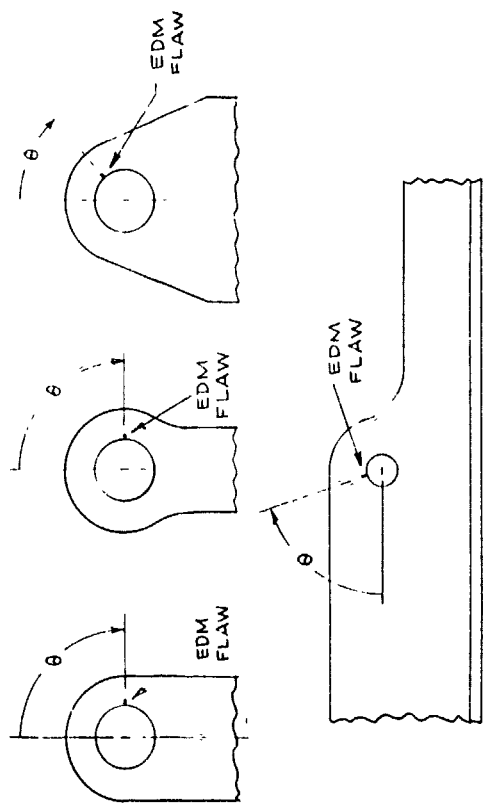
NOTES

1. ANGULAR LOCATIONS (θ) OF EDM NOTCHES ARE 90° EXCEPT AS LISTED IN TABLE 3-13.

2. IF ONE SIDE OF HOLE IS CHAMFERED, THE EDM NOTCH IS ON THE NON-CHAMFERED FACE.
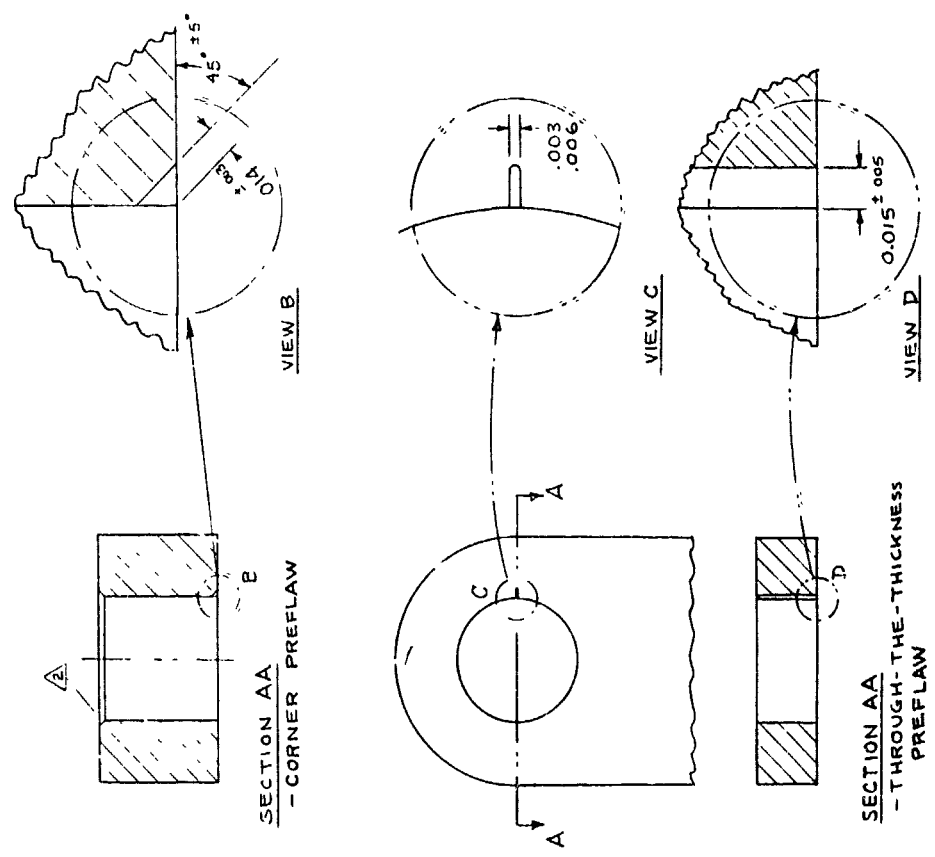
Figure 3-7. Specifications for Machining EDM Notches (Flaws)

39

Table 3-13 lists EDM location by specimen number for the Group II lug specimens.

The objectives of Group II testing introduced the need for a special fabrication requirement not necessary for Group I. The experimental study of effects of pin clearance in Group II required measurement of hole diameter within $\pm$0.0001 inch. Such measurements could be meaningful only if the hole circularity is accurate and the surface finish in the hole is smooth. Ordinary boring on a drill press cannot assure hole circularity within a diameter variation of $\pm$0.0001 inch; therefore the Group II specimens were final bored on a jig bore. It then was possible to achieve the required pin clearance variations by specifying nominal hole diameters that differed by 0.001 inch and nominal pin diameters that differed by 0.0005 inch; measuring both pins and lug holes within $\pm$0.0001 inch; and selectively matching pins and lugs to achieve the precise clearances desired.

One other significant difference between fabrication instructions for Groups I and II was to require on Group II specimens that the edge of the hole be left a sharp edge where the corner EDM flaws were to be introduced. With this sharp edge, the control of EDM size for corner flaws is optimized, as can be concluded by examining View B in Figure 3-7. The note requiring this sharp edge was inadvertantly omitted from Group I specimen drawings, and consequently the size of Group I EDM corner preflaws could not be controlled within the tolerance specified in View B of Figure 3-7.

4.2 BUSHING FABRICATION AND INSTALLATION

Shrink-fit bushings of 4130 steel, 125-145 ksi were used in eight Group I and 26 Group II specimens. In Group I specimens, the maximum interference attainable was selected to assure bushing/lug contact and high residual stress effects, as discussed earlier. Based on thermal coefficients of expansion, diametrical interference levels of 0.007 and 0.008 inches were selected for aluminum and steel lugs, respectively. In Group II specimens, a diametrical interference level of approximately 0.002 inch was used to simulate the typical design usage regime.

The following paragraphs discuss the bushing fabrication and installation procedures used in Group II. The same philosophy was also used in Group I tests, except for higher interference levels.

TABLE 3-13.   ANGULAR LOCATIONS (OTHER THAN θ = 90 DEGREES)
OF EDM PREFLAWS IN GROUP II SPECIMENS

SPECIMEN NO.		θ, DEGREES
T1-X-1	T1-X-2	58
T1-X-3	T1-X-4	228
T1-Y-1	T1-Y-2	58
T1-Y-3	T1-Y-4	228
T1-Z-1	T1-Z-2	58
T1-Z-3	T1-Z-4	228
T1-A-3	T1-A-4	205
T1-A-5	T1-A-6	205
T1-S-1	T1-S-2	58
T1-S-3	T1-S-4	205
T2-A-3	T2-A-4	58
T2-A-5	T2-A-6	205
T2-A-7	T2-A-8	205
T2-S-1	T2-S-2	58
T2-S-3	T2-S-4	205
R2-E-1	R2-E-2	71
SEE FIGURE 3-7 FOR DEFINITIONS OF θ		

The bushing drawing, Figure 3-8, is based on an existing Lockheed standard bushing configuration, except that the tolerance on the outer diameter is tightened to maintain a more limited diametrical interference range of 0.0010 to 0.0023 inch, instead of the standard Class V fit range, 0.0004 to 0.0023 inch. Furthermore, machining variations were more controlled than the drawings required, so that for 24 of the 26 lugs, the interference was 0.0020 ($\pm$0.0003) inch, as shown in Table 3-14.

Table 3-14 lists the measured diameters and net interference levels of the 26 Group Il specimens fitted with shrink-fit bushings. These measurements were very critical because the residual stresses are directly proportional to the interference. Note that the 3 independent measurements of hole diameter varied by as much as $\pm$0.00050 inch for these specimens. Since the average interference for these specimens is 0.00198 inch, an error in measured diameters of 0.00050 inch would cause a 25 percent error in the estimated residual stresses.

The special setup sketched in Figure 3-9 was designed and used for the installation of the shrink-fit bushings. The lug was heated to 200°F (300°F for Group I steel lugs) and placed on parallel blocks on the table of a jig bore machine. One parallel block, the "guide block," was permanently clamped in position below the quill of the jig bore. A hole in the guide block was fitted with a spring-loaded plug. The plug diameter was 0.005 inch less than the lug inner diameter. The height of the plug was the same as the thickness of the parallel blocks. A light spring held the plug in place above the guide block, for use in locating the lug hole on a common centerline with the quill. The bushing was held with a pair of teflon pliers and submerged in a bucket of liquid nitrogen (-320°F) for about 45 seconds, then immediately placed on a locating cylinder on the quill. The quill was rapidly brought down, guiding the bushing into the lug, until the bushing pushed against the plug and the plug bottomed. The bushing was held in place for two or three seconds until it expanded into permanent position in the lug. The entire process was completed within about 10 seconds of the time that the bushing was removed from the liquid nitrogen.

Since the bushing inside diameters were intially undersized, the inner diameters were bored to final size after bushing installation and precision-measured, completing the specimen fabrication process.
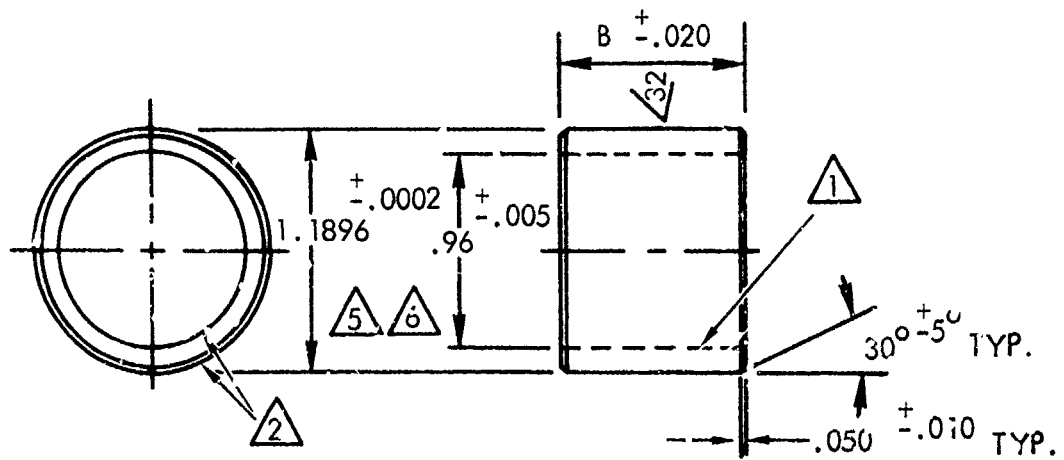
NOTES:

△1 STAMP IDENTIFICATION NO. ON INSIDE SURFACE (SEE NOTE △4)

△2 CONCENTRIC DIAMETERS WITHIN .003 IN. T.I.R.

△3 MATERIAL: 4130 STEEL, 125-145 KSI HEAT TREAT

△4 BUSHING LENGTHS, B, AS FOLLOWS:

BUSHING I.D. NO.	B (INCH)	NUMBER REQD.
1 THRU 13	1.00	13
21 THRU 35	0.50	15
41 THRU 43	0.64	3

△5 MEASURE OUTER DIA. WITHIN $^{+}_{-}.0001$ IN. AT 72°F $^{+}_{-}4$°F AND RECORD ON INSPECTION DATA SHEET

△6 CENTERLESS GRIND OUTER DIAMETER

Figure 3-8.   Bushing Requirements

TABLE 3-14. BUSHING INTERFERENCES FOR GROUP II SPECIMENS

SPECIMEN NO.	LUG INNER DIAMETER			BUSH NO.	BUSHING OUTER DIAMETER		MEDIAN DIAMETRICAL INTERFERENCE
	3 MEASUREMENTS				2 MEASUREMENTS		
	MEDIAN	LARGEST	SMALLEST		MEAN	MAX & MIN	
S2-A-1	1 18780	+.00020	-.00030	13	1.18965	±.00003	0.00185
S2-A-2	83	07	23	12	63	01	180
S2-B-1	77	23	17	23	57	04	180
S2-B-2	73	27	33	30	59	04	186
T2-A-1	70	10	30	7	65	03	195
T2-A-2	70	10	20	1	65	02	195
T2-A-3	67	13	27	8	57	04	190
T2-A-4	70	10	20	2	67	04	197
T2-A-5	70	10	20	3	67	03	197
T2-A-6	53	17	23	6	68	07	215
T2-A-7	63	17	13	14	65	02	202
T2-A-8	70	10	30	9	62	01	192
T2-B-1	43	37	23	25	55	10	212
T2-B-2	30	50	30	28	58	07	228
D2-A-1	70	30	10	10	67	03	197
D2-A-2	60	30	30	5	67	03	207
D2-B-1	80	20	20	34	60	05	180
D2-B-2	83	27	23	29	59	06	176
C2-A-1.							
At Flaw	37	13	07	27	59	06	222
No Flaw	40	10	20	33	52	09	212
C2-A-2							
At Flaw	53	27	23	32	59	06	206
No Flaw	1 18757	+ 00023	-.00017	31	1.18958	±.00003	0 00201
T2-S-1	1.18755	+.00025	-.00035	36	1.18954	±.00009	0.00189
T2-S-2	56	24	46	22	63	02	207
T2-S-3	13	37	23	26	54	08	241
T2-S-4	1.18733	+.00017	-.00033	35	1.18952	±.00009	0.00219
R2-E-1	1.18790	+.00020	-.00040	44	1.18964	±.00001	0.00174
R2-E-2	1.18810	+.00020	-.00040	41	1.18968	±.00003	0.00158

(All dimensions in inches)
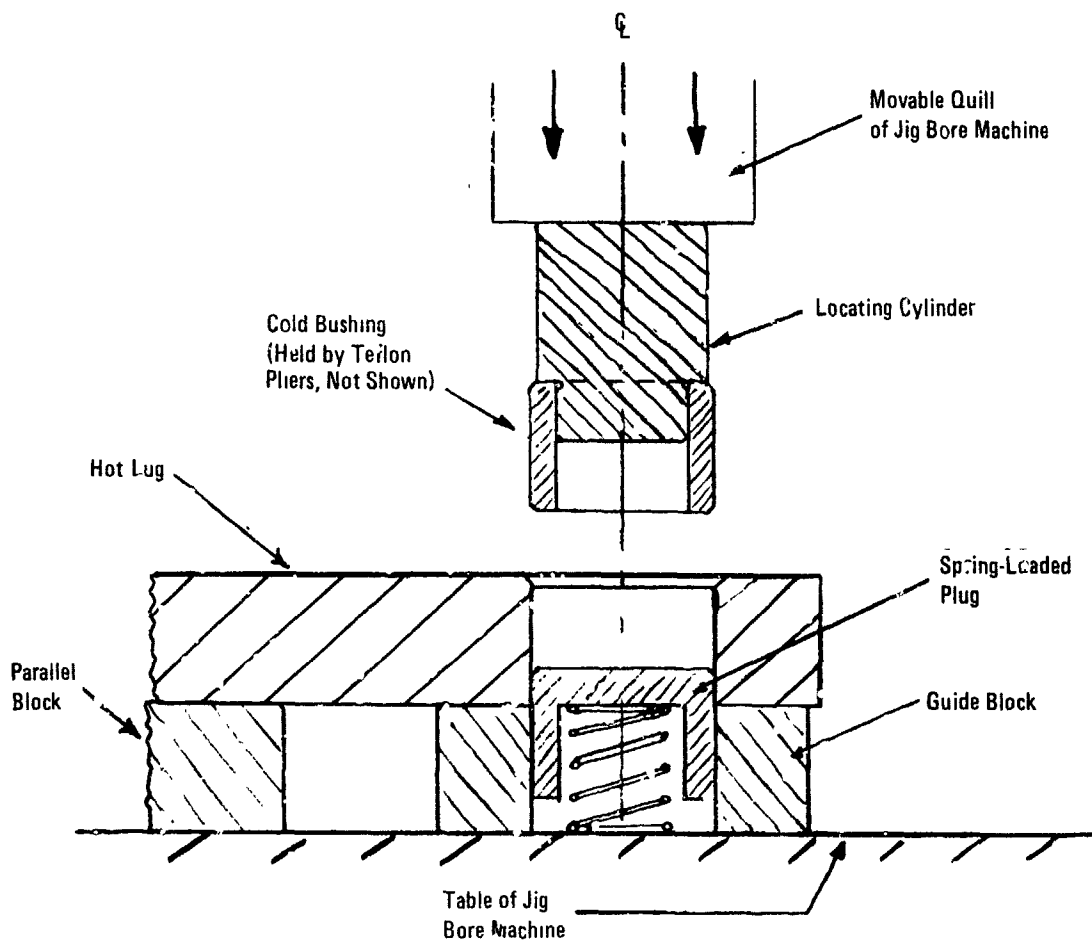
Figure 3-9. Installation Fixturing for Shrink-Fit Bushings

4.3 LOADING PINS

One of the critical dimensions in these tests was the pin-to-lug or pin-to-bushing clearance. These dimensions were held to the standard tolerances given in Table 3-15. Before testing, these mating diameters were precisely measured and recorded at several locations to the nearest 0.0001 inch using an air gage or intramike for inner diameter and high accuracy micrometer for outer diameter. The pins were made from 4340 steel heat treated to 260-280 ksi ultimate strength condition. All the Group I tests needed pins with 1.50 inch nominal diameter and 25 such pins were used for Group I tests. Group II tests warranted additional care due to the study of pin clearance and also required pins with different nominal diameters. Thirty loading pins were ground to the diameters and tolerances listed in Table 3-16. The allowable ranges of diameters for the first 24 pins listed in the table, and the precision measurements of both pin and lug hole diameters, facilitated the pairing of a pin and lug to achieve a required nominal pin diametrical clearance within ± 0.00025 inch. By such pairing, the study of effects of pin clearance was possible.

After each use, the pins were cleaned by mounting in a lathe and lightly touching with a file to remove the fretting residue. Then the diameters were remeasured at several axial and angular locations. If the diameter measurements varied from point to point by more than ± 0.0002, the pin was not reused.

5.0 TEST MACHINES AND FIXTURES

All tests were performed using testing machines that have been calibrated to the National Bureau of Standards. All the Group I tests were conducted at Lockheed-Georgia Company and all the Group II tests were performed at Lockheed-California Company's Kelly Johnson Research and Development Center at Rye Canyon.

Group I tests consisted of only axially-loaded residual strength, crack initiation and crack growth tests. Group II tests consisted of tests with axial and off-axis loading, each requiring special test fixtures as discussed in the following.

46

TABLE 3-15. STANDARD DIAMETRICAL TOLERANCES

TYPE OF FIT AND APPLICATION		NOMINAL DIAMETER D (in.)			
		0.812 ≤ D ≤ 1.0		1.0 < D ≤ 1.5	
		MINIMUM	MAXIMUM	MINIMUM	MAXIMUM
Medium – Clearance Fit (Pin-to-Bushing)	Hole Tolerance	+.0000	+.0009	+.0000	+.0010
	Shaft Tolerance:	-.0008	-.0018	-.0010	-.0021
	Clearance (In.)	+.0008	+.0027	+.0010	+.0031
Interference Fit (Bushing-to-Lug)	Hole Tolerance:	+.0000	+.0009	+.0000	+.0010
	Shaft Tolerance:	+.0020	+.0013	+.0023	+.0015
	Interference (In.)	+.0020	+.0004	+.0023	+.0005

TABLE 3-16. REQUIRED PINS

DIAMETER (INCH)	LENGTH (INCH)	NO. REQ'D	ID NUMBERS*
.9981 – .9985	3.00	5	1 thru 5
.9985 – .9989	3.00	11	6 thru 16
.9989 – .9993	3.00	8	17 thru 24
.6235 – .6244	3.00	2	25 thru 26
.9982 – .9992	5.00	2	27 thru 28
1.4979 – 1.4990	5.75	2	29 thru 30
	TOTAL	30	

* • Number the pins from 1 through 30.

• Measure diameter within ± .0001 inch at a temperature of $72^0F \pm 4^0F$ and record on inspection data sheet.

5.1 AXIAL TEST SETUPS

All the axially loaded crack growth and crack initiation tests were performed in an electrohydraulic servo controlled test system similar to the one shown in Figure 3-10. Each system contains the necessary elements properly integrated to control the servo loop, program loads, monitor loads and perform failsafe functions. A sinewave function generator provides load commands to the servo loop and a calibrated amplitude measurement unit is used to monitor constant amplitude load levels. Each system is interfaced to a digital computer which can be programmed to apply and control the loads for any predetermined fatigue spectrum.

For ease of installation without the need for grip holes, and to provide maximum stability during crack growth in the lug, the plain end of the lug specimen was clamped in a hydraulic grip. The pin load was applied to the lug using a special steel fork fitting. A close-up view of the steel fork fitting is given in Figure 3-11. This fitting design is very similar to the one used by Schijve, et al. [4] with some improvements. It provided visual access to the crack path in the lug specimen by means of machined slots on each side of the loading hole as shown in Figure 3-11. Symmetrical machining on both faces and on each side of the hole was made to ensure uniform load transfer from the pin to the test specimen. The slots eliminated the need for removal of the loading pin to monitor the crack growth, which may influence the crack growth behavior. Two similar fork fittings were also designed and fabricated for Group II testing, one for 1.0-inch thick specimens and one for 0.5-inch thick specimens. The details of these fork fittings are given in Figure 3-12. These fittings were used for both axial and off-axis tests of Group II.

For Group I residual strength tests, however, the slotted fitting was not used, since only the static failure load was sought, and the crack growth was not monitored. A simple pin and clevis fork, as shown in Figure 3-13, was used in the residual strength tests.

Ordinary clevises were also used for the 12 Type "S3" lugs in group II, (see Figure 3-2) because of their odd sizes. Also on the 4 Type "C" clevis specimens, the pin load was applied through a 1 inch steel lug loading fixture. For these 16 specimens the pin was removed periodically

Figure 3-10. Axial Test Setup
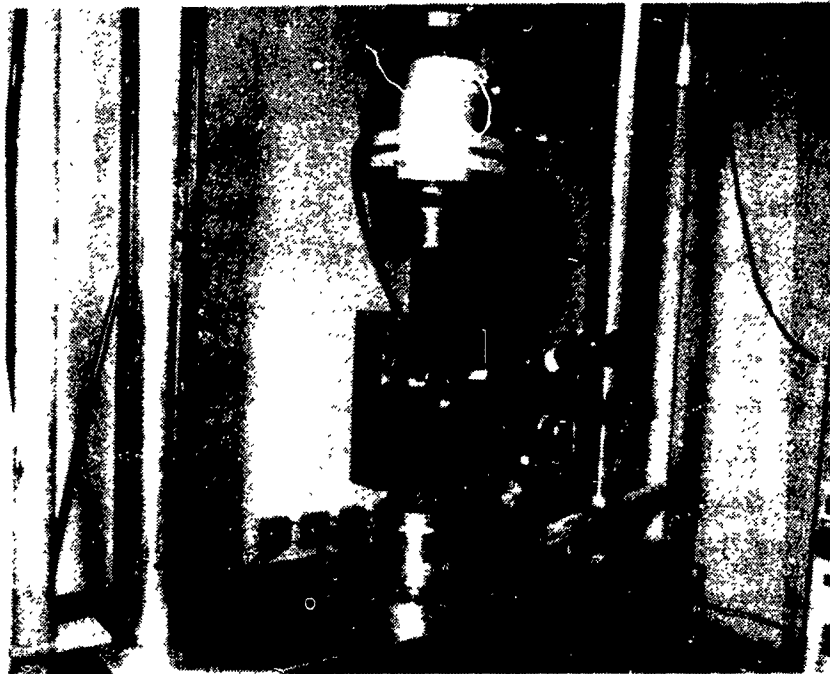
Figure 3-11. Closeup View of Lug and Fork Fitting Arrangement

50

NOTES

$\underline{1}$ CENTERLINE OF 2-IN HOLE TO BE CONCIDENT WITH 1.0-IN. HOLE AND 3.75-IN DEEP SLOT WITHIN .001. MAINTAIN CENTERLINE SYMMETRY OF OUTER DIMENSIONS WITHIN .007 IN TIR

$\underline{2}$ INDICATED CENTERLINES TO BE PERPENDICULAR WITHIN ±0.10°.

$\underline{3}$ MATERIAL IS 4340 STEEL. ROUGH TO OVERSIZED RECTANGLE AND HEAT TREAT 180-200 KSI STRENGTH BEFORE CUTTING ANY HOLES OR SLOTS.

$\underline{4}$ FINISH 40 RHR INSIDE .50 DIA AND 1.0 IN. DIA. HOLES.

$\underline{5}$ CUT 3.75-IN. DEEP SLOT BEFORE BORING 1.0-IN. HOLE. (MAY SPRING OPEN AFTER SLOT IS CUT).

$\underline{6}$ BREAK ALL SHARP CORNERS.

$\underline{7}$ SEE TABLE * FOR "B" DIMENSION AND REQUIRED QUANTITIES
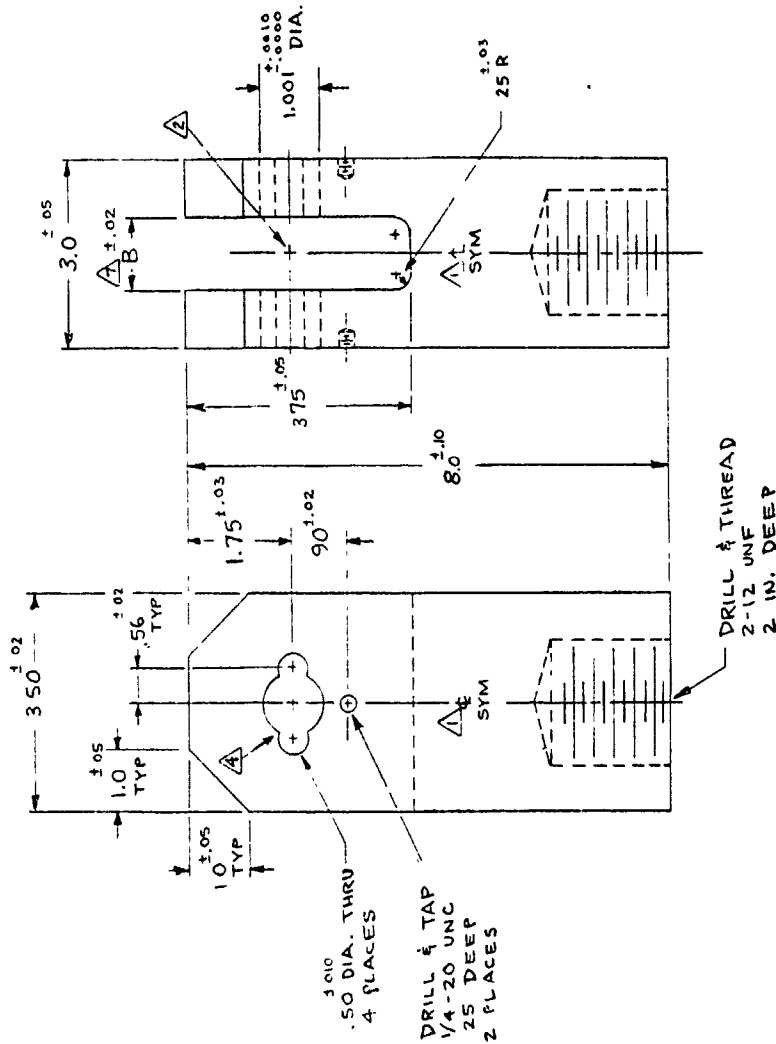
TABLE *
REQUIRED QUANTITIES

B, IN.	NO. REQ'D.
0.55	1
1.08	1

$1.001^{+.0010}_{-.0000}$ DIA.

25 R$^{+.03}$

$3.0 \pm .05$

$B^{+.02}$

$375^{+.05}$

$8.0^{+.10}$

$3.50^{+.02}$

$.56^{+.02}$ TYP

$1.0^{+.05}$ TYP

$1.0^{+.05}$ TYP

$1.75^{+.03}$

$90^{+.02}$

$\frac{\mathlarger{\oplus}}{}$ SYM

DRILL & THREAD
2-12 UNF
2 IN. DEEP

.50 DIA. THRU$^{+.010}$
4 PLACES

DRILL & TAP
1/4-20 UNC
.25 DEEP
2 PLACES

Figure 3-12. Special Test Fixture Clevis for Crack Growth Tests

Figure 3-13. Residual Strength Test Setup

to measure the crack. (This was necessary even on the Type "C" specimens, because the preflaw was placed at the inner face of the clevis where any effects of pin bending would be maximized.)

5.2 TEST SETUP FOR OFF-AXIS LOADING OF TAPERED LUGS

The off-axis tests of tapered lugs, which included 30 precracked lugs and 8 crack initiation tests, were conducted on the special test setup shown in Figures 3-14 and 3-15. Figure 3-14(a) shows the over-all view of the loading jack mounted in a structure of heavy beams and columns termed the "Apartment House" test frame. As shown, the axis of the loading jack forms a 45 degree angle with the horizontal. The lower (fixed) end of the jack is connected in series with a 40-kip load cell to a horizontal beam. The upper end is connected to the clevis. In Figure 3-14(b) the specimen is partially visible, mounted with its axis horizontal in a special holding fixture that is bolted to one of the Apartment House columns. A diagonal brace, mounted parallel to the loading jack as shown in Figure 3-14(a), provided lateral support for the column. For 90-degree loading, the brace was removed and a shorter 40-kir loading jack and load cell was mounted vertically, as shown in Figure 3-15.

A sketch of the holding fixture for the tapered lugs is shown in Figure 3-16. Two steel bars, 8.75 x 2.0 x 1.09 inches, were welded between a pair of 0.75-inch-thick steel angles. The rectangular opening between the angles and between the bars was 1.09 x 4.13 inches. The bottom end of the tapered lug specimen is fitted into that opening and held in place by a 1.5-inch pin and six setscrews. The axial component of the load applied to the tapered lug specimen is reacted at the 1.5-inch pin. The transverse (90-degree) component and the resulting moment are reacted at the 1.5-inch pin and at either Point "B" (indicated in Section A-A of Figure 3-16) for the downward load, or Point "C" for an upward load. (The upward load occurred only upon load reversal in the 4 specimens tested at a negative stress ratio, $R = \pm 0.5$.)
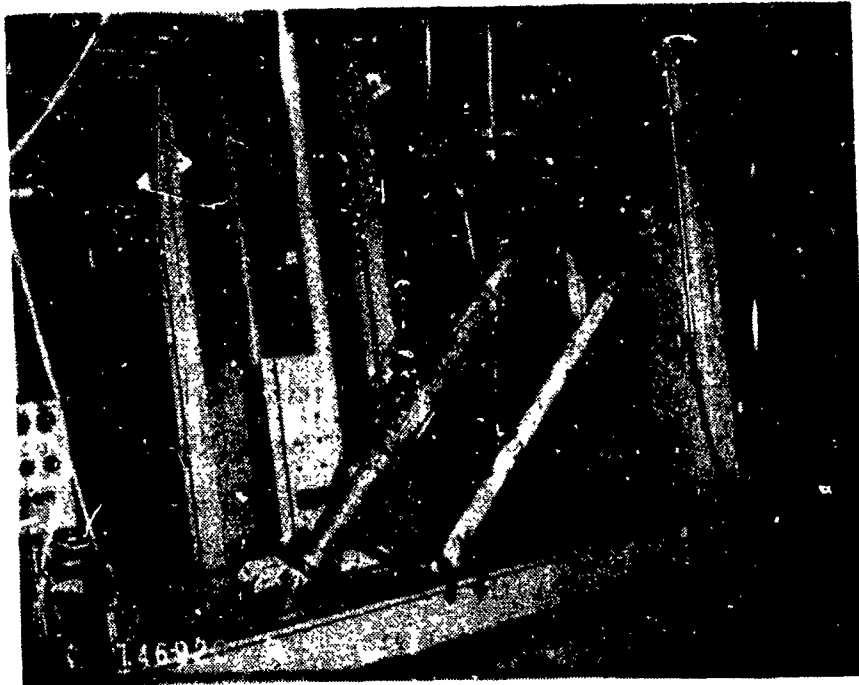
(a) Over-all View of Loading Jack
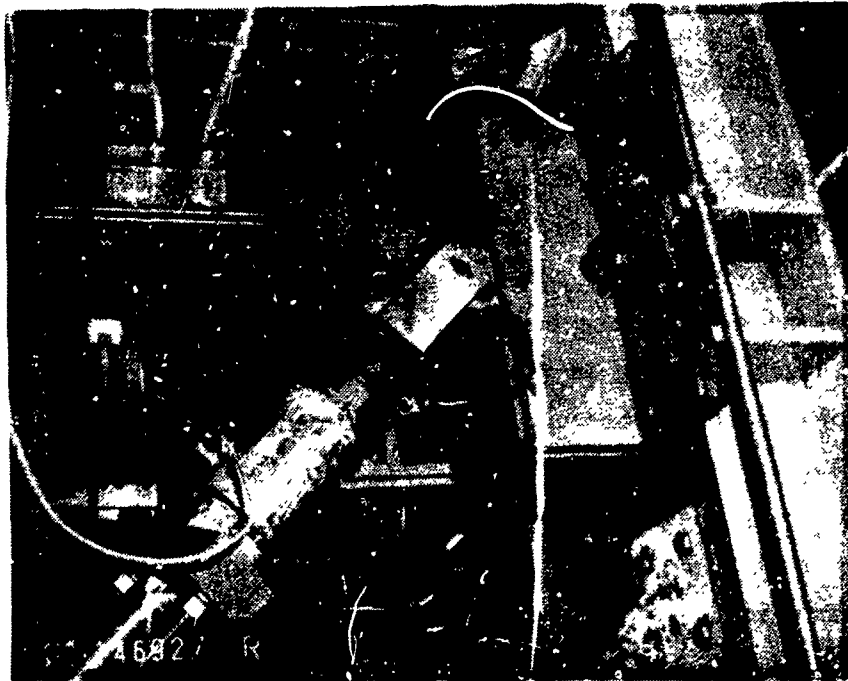
(b) Close-up View of Clevis and Specimen Holding Fixture

Figure 3-14. Test Setup, 45-Degree Off-Axis Fatigue Testing of Tapered Lugs

Figure 3-15. Test Setup, 90-Degree Off-Axis Fatigue Testing of Tapered Lugs

TEN 0.75 DIA BOLTS
MOUNT TO COLUMN
OF "APARTMENT HOUSE"

A

4.13

1.09

A

FRONT VIEW

2 SCREWS TIGHTEN
AGAINST LUG EDGE

TAPERED
LUG
SPECIMEN

© C

1.50 DIA. PIN
THRU LUG AND
BOTH ANGLES

-45°
LOAD

-90°
LOAD

B

4 SCREWS TIGHTEN
AGAINST LUG FACE

2.0 ×1.09 ×8.75
STEEL BAR, WELDED
IN PLACE (2 REQ'D)

SECTION A-A

TAPERED
LUG
SPECIMEN

WELDED-ON
STEEL BARS

8×8×0.75 STEEL ANGLES,
23.0 LONG (2 REQ'D)

18×24×0.625
STEEL PLATE

END VIEW
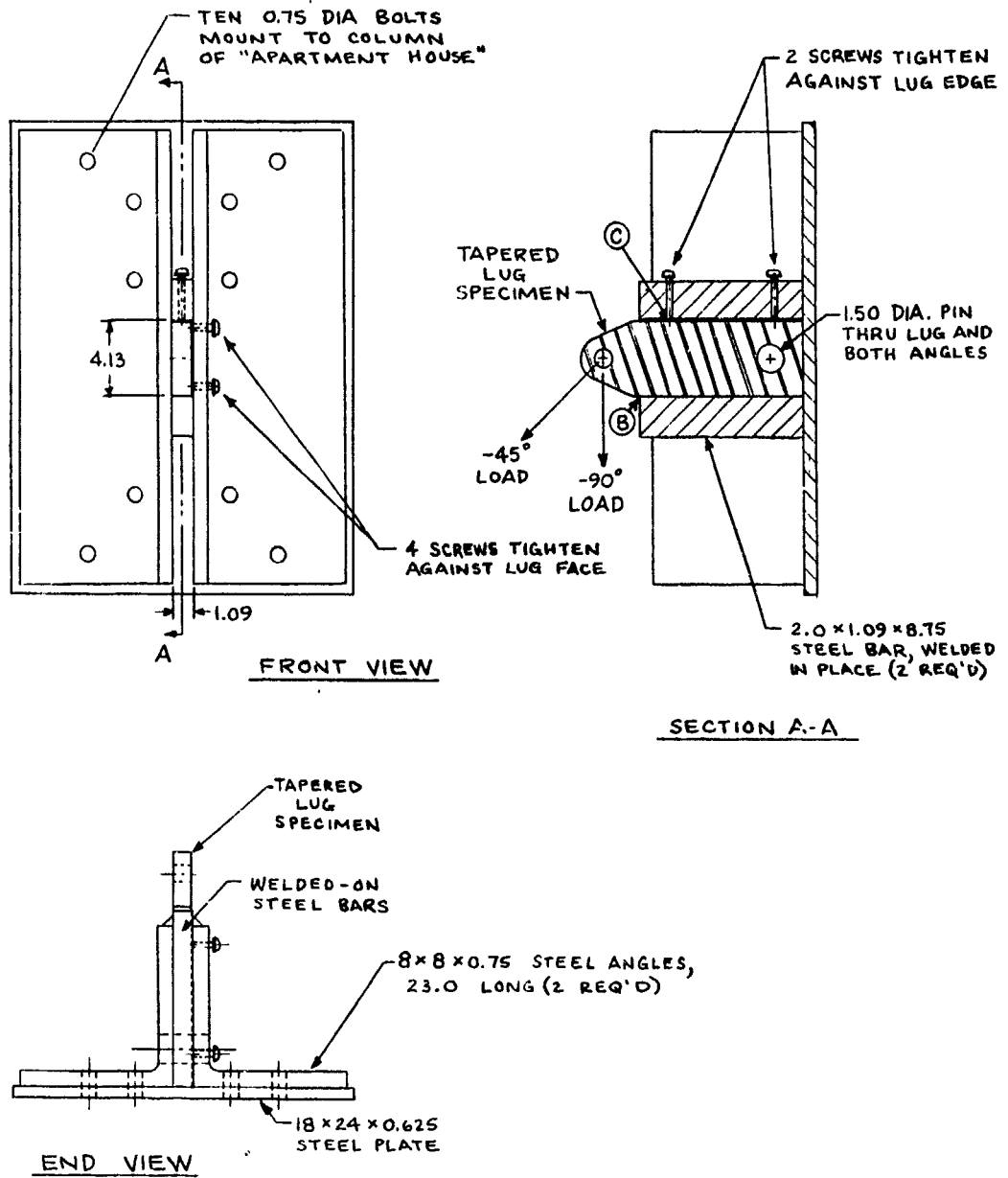
Figure 3-16.   Holding Fixture for Tapered Lugs Subjected to Off-Axis Loading

56

5.3 WING-PYLON LUG TEST SETUP

Like the off-axis tests of tapered lugs, the two simulated wing-pylon attach lugs were tested in the "Apartment House" test frame.

Related experience had indicated that the stress intensity factors for the simulated wing-pylon attach lug would be highly dependent upon the relative stiffnesses of the supporting structure to which the lug is bolted. Therefore, a thorough study was conducted to be certain that the stiffnesses of the supporting structure in the test would be representative of aircraft structure for this type of lug. Since the shape of the test lug was selected based on a particular lug on the C-5 aircraft, the structural supports of that lug on the C-5 were examined in detail.

Based on that study, the test fixture was designed as shown in Figure 3-17. The lug was bolted along its length to a 0.250-inch aluminum plate, and at its end to a 0.75-inch steel angle. The angles and the plate (at its ends) were bolted to the rigid column of the Apartment House test frame, with 3/4-inch diameter bolts. The 0 250-inch plate was unsupported along its length, except for four 7/16-inch fasteners which tied it down to the test frame column, preventing bending deflections at those points.

Figure 3-18 is a photograph showing a simulated wing-pylon lug specimen and baseplate, mounted vertically on a column of the test frame, and the 40-kip loading jack mounted at a 23-degree angle to the vertical.

The thickness of the base plate was selected to simulate the relative axial stiffnesses of the lug and lower wing skin in the C-5. (In the C-5 the lug is steel rather than aluminum and the skin thickness is 0.57 to 0.70 inch.) The 0.75-inch steel angles represented a pair of angles on the C-5 aircraft which tie the flange of the lug to the rear beam web of the wing. The four 7/16-inch fasteners in the test lug were located near the points corresponding to where integral stiffeners of the C-5 wing skin intersect the lug axis, limiting lateral bending deflections.

An advantage of this test fixture system was that it was relatively simple and inexpensive to produce and set up. It was not a goal in these tests to exactly represent the C-5 lug. Nevertheless, it can be stated confidently that the stress distributions in the test lug were typical of this class of aircraft structure and therefore meaningful for methodology assessment.

57
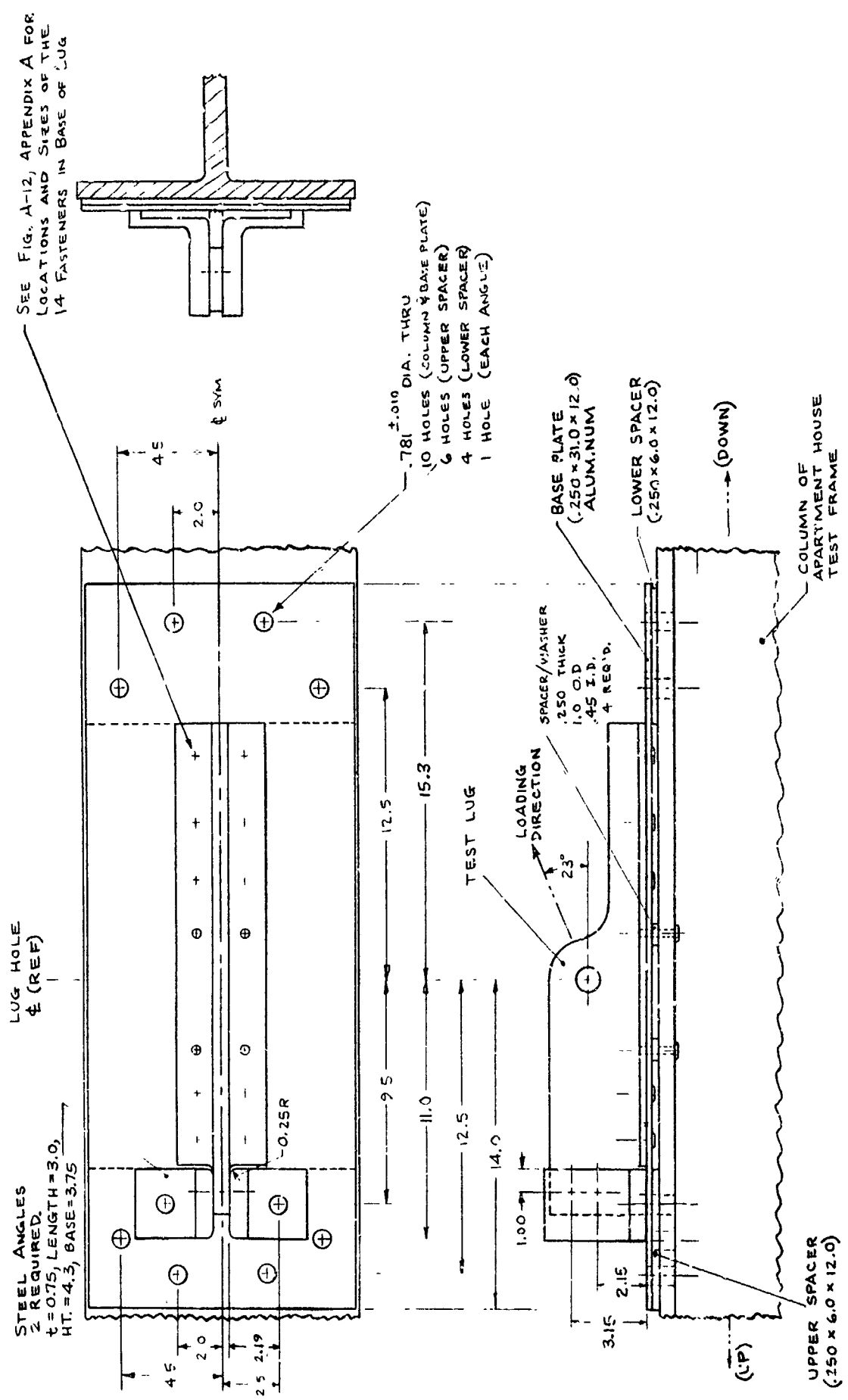
Figure 3.17. Test Setup for Lug Specimens Type R-2 (Typical Wing-Pylon Attach Lug)

58
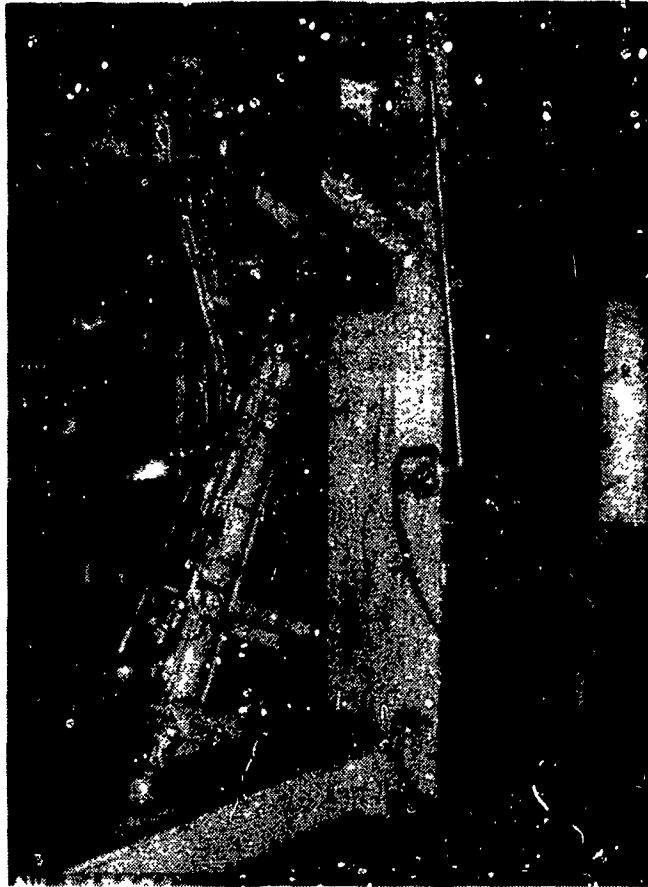
Figure 3-18. Simulated Wing-Pylon Attach Lug Test Setup

59

6.0 TESTING DETAILS AND PROCEDURES

This subsection describes test details and procedures, including test environment, loading spectra, precracking, marker loads, and data acquisition and reduction.

6.1 TEST ENVIRONMENTS AND CYCLIC FREQUENCIES

All tests were conducted in air conditioned laboratory air. The temperature and relative humidity limits for Group I tests were $75^{\circ}F \pm 10^{\circ}F$ and $60\% \pm 20\%$ RH. The corresponsing limits for Group II tests were $72^{\circ}F \pm 5^{\circ}F$ and $40\% \pm 15\%$ RH. The differences in these limits were due to the locations where the tests were conducted; i.e., Group I at Lockheed-Georgia Company and Group II at Lockheed-California Company.

The cyclic frequencies for constant amplitude testing were 10 Hz for Group I and 6 Hz for Group II testing.

6.2 LOADING SPECTRA

The loading sequences used in testing were either constant amplitude with marking cycles or spectrum. The marking cycle loading sequences for constant amplitude tests are discussed in the succeeding subsection on marking cycles. In the paragraphs below, the spectrum loading sequences are discussed. These include both block and flight-by-flight spectrum sequences in Group I, and a flight-by-flight sequence in Group II testing.

The block spectrum used in this program was developed for various types of testing conditions after expending a significant amount of analytical and experimental effort to select the load levels and number of cycles per block. The various types of testing conditions include corner and through-the-thickness cracks, loads above and below the yield of the lug and two materials. The spectrum selection criteria were that the block spectrum have significant retardation effects, load levels compatible with the above constant amplitude tests, and reasonable life in terms of repetition of these blocks (neither too few nor too many from the test duration point of view). Finally, the block spectrum shown in Figure 3-19,

60
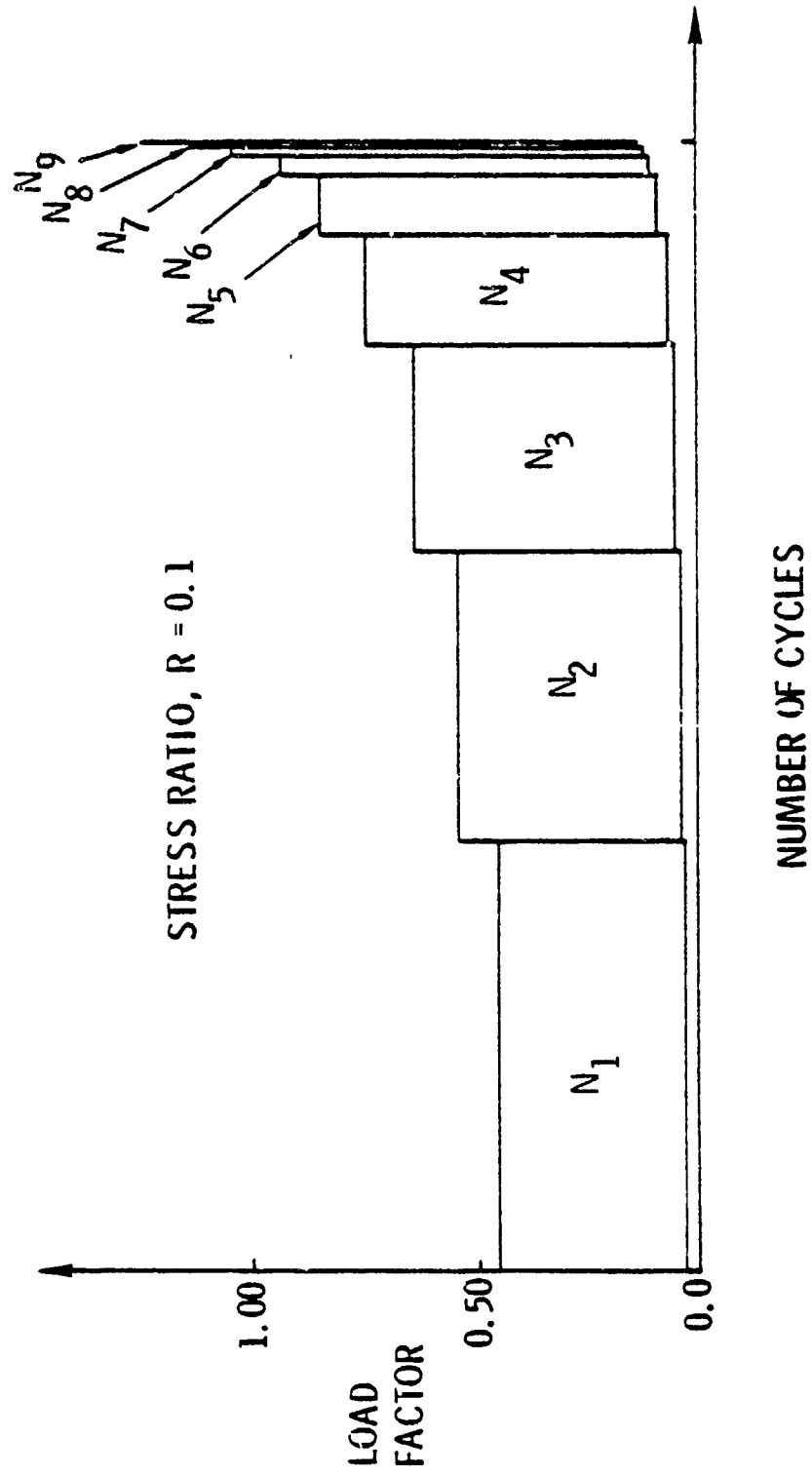
Figure 3-19. Schematic of Block Spectrum Loading

61

which is similar to a simplified version of an A-7 trainer spectrum [5], was selected. This spectrum had 9 load levels, each with different numbers of cycles, N_1 through N_9, as shown. The minimum and maximum load factors were 0.45 and 1.25, respectively, with increments of 0.1. Details of the number of cycles at each load level and corresponding cyclic frequencies for different test conditions are given in Table 3-17. The unit load factor levels and the spectrum maximum loads for both the materials are also provided in the table. As in the case of constant amplitude test conditions, far-field load levels above the yield strength of the lugs were used only for aluminum lugs. Also note that the block spectra for corner crack cases were obtained by multiplying the number of cycles per block for through-the-thickness crack cases by a factor of 3. A study of the block spectrum presented in Figure 3-19 clearly shows that there will be no retardation effect for the first block of loading. When the block spectrum loading is repeated, the spectrum retardation effects begin. During testing, the crack growth data were collected at the end of the first block and at the end of selected subsequent blocks. This provided observations of the crack growth rate behavior with and without spectrum retardation effects.

Three flight-by-flight spectra were selected for Group I testing. The first two are typical for a cargo aircraft (C-5) and the third is typical for a fighter (F-4). These flight-by-flight spectra are tabulated in Appendix B and discussed below.

Spectrum 1, which is a cargo aircraft spectrum, includes thirteen different missions (0, and 1 through 12). The maximum and miminum stress levels and corresponding number of cycles for these thirteen missions are presented in Table B-1 for Appendix B. In this table, a special loading cycle is defined in terms of N/FLT = 0.1, for example in Mission 1. This simply means that particular load is applied once in ten occurances of this mission. When Mission 1 includes this load it is referred to as Mission 1*. The sequence of missions in one pass (mission mix) of the spectrum is given in Table B-2, Appendix B. One pass consists of 120 missions. One mission has the same meaning as a flight. One pass of 120 missions is equivalent to 500 flight hours. After the completion of one pass, the passes are repeated until the specimen fails.

TABLE 3-17. DETAILS OF BLOCK SPECTRUM LOADING OF GROUP 1 TESTS (ONE BLOCK)

LOAD FACTOR			LOW LOAD			HIGH LOAD		
SYMBOL	VALUE	SYMBOL	CORNER CRACK (CYCLES)	THRU CRACK (CYCLES)	FREQUENCY (Hz)	CORNER CRACK (CYCLES)	THRU CRACK (CYCLES)	FREQUENCY (Hz)
σ_1	0.45	N_1	2850	950	20	105	35	10
σ_2	0.55	N_2	1950	650	20	75	25	10
σ_3	0.65	N_3	1350	450	20	45	15	10
σ_4	0.75	N_4	750	250	10	30	10	10
σ_5	0.85	N_5	408	136	10	15	5	10
σ_6	0.95	N_6	132	44	10	12	4	10
σ_7	1.05	N_7	45	15	10	9	3	10
σ_8	1.15	N_8	12	4	10	6	2	10
σ_9	1.25	N_9	3	1	10	3	1	10

NOTE:

UNIT LOAD FACTOR = 6 KSI FOR ALUMINUM LUGS } LOW LOAD
= 14 KSI FOR STEEL LUGS
= 15 KSI FOR ALUMINUM LUGS - HIGH LOAD

SPECTRUM MAX. LOAD = 7.5 KSI FOR ALUMINUM LUGS } LOW LOAD
= 17.5 KSI FOR STEEL LUGS
= 18.75 KSI FOR ALUMINUM LUGS - HIGH LOAD

The second flight-by-flight spectrum is identical to the first spectrum, except that all the loads are multiplied by a factor of 1.5. Though not very realistic, this modification of spectrum 1 was made to provide spectrum data on steel lugs at higher stress levels and examine whether non-radial crack growth occurs.

The third flight-by-flight spectrum selected was the 80-flight spectrum sequence described in detail in Reference [6]. This tension-only sequence included of 40 "severe" flights in random order, simulating the mix of flights in an F-4 pilot training course conducted by the USAF. The load spectrum content for the "typical" flights was the 50 percent probability line taken from results of a literature survey of usage spectra for numerous fighter-attack and trainer aircraft, including the F-104C and D, F-105D, F-4B and F-5A. The "severe" spectrum was selected as the mean of the most severe one-third of the same data. The shapes of the load-exceedance curves for the typical and severe spectra are also similar to some recently-published exceedance spectra for Air Force fighter aircraft (References [7], [8], and [9]). The total number of load cycles in 80 flights is 1080. The maximum and minimum stresses and the number of cycles per 80 flights for this spectrum are tabulated in Table B-3 of Appendix B. From this table, the flights and the load cycles were then selected randomly. First a random selection was made as to whether the flight will be severe or typical. A severe flight consists of 20 load cycles per flight and a typical flight consists of 7 load cycles per flight. Based on the nature of the flight (severe or typical) the loads are then selected, again randomly. For severe flights, the loads are selected from load sequence numbers 1 through 19 (severe loads) and for typical flights, the loads are selected from load sequence numbers 20 through 35 (typical loads). After each flight the load was reduced to zero or nearly zero to represent the GAG cycle. The randomly selected flights and the corresponding loading sequences for the 80 flights are provided in Table B-4, Appendix B.

Eight Group II specimens were tested using a slightly different version of the 80-flight fighter trainer spectrum. In Group I tests after each flight the load was reduced to 1/10 of the in-flight minimum load, held 0.35 seconds, and then reduced to zero load and held another 0.65

64

seconds. In Group II, the excursion to zero load was omitted. As in Group I, the cyclic frequencies varied with load magnitude. The average frequency is 5.6 Hz if the spectrum is applied at 100 percent speed. The simulated wing-pylon lugs were tested at 33 percent speed; all other spectrum tests were run at 100 percent speed.

The maximum spectrum loads used in Group II spectrum tests are listed in Table 3-12. The other loads in the spectrum, listed in Tables B-3 and B-4, can be determined by linear scaling using the ratio of the load in Table 3-12 divided by 20 ksi.

6.3 PRECRACKING, CRACK MONITORING, MARKER LOADS AND FRACTOGRAPHY

As described earlier, EDM was used to produce crack starters for all crack growth specimens. A small triangular edge notch or through-the-thickness notch was machined on the finished hole of the specimen. The precracking was then accomplished at the beginning of each test by subjecting the specimens to fatigue loading using the same test setup. The chosen stress levels for the fatigue loading were either the stress level of the test itself or lower so that no crack retardation effect was introduced. The targeted size of the fatigue crack (including the EDM notch) was 0.025 inch.

Crack measurements were made visually through the viewing window of the clevises (see subsection 5.1 of III), using a traveling microscope setup. These were supplemented by post-test fractographic measurements of marking-cycle striations. Two marking procedures were used in this program for constant amplitude crack growth tests. The first procedure, used exclusively in all Group I constant amplitude crack growth tests, was the application of constant amplitude loading with an increased stress ratio of 0.85 (the test stress ratio was either 0.1 or 0.5) without changing the test maximum stress level. The cycling was continued until an adequate increment of crack growth occurred to cause a visual marking. The advantages of this procedure are that no crack growth retardation effect was introduced during the marker cycles, and that the growth increment due to the marker cycles can be translated into equivalent test cycles during test data correlation. The disadvantage of this procedure is that a large

number of marker load cycles are needed to produce the desired marking. However, the impact of such a disadvantage was minimized by increasing the marker cycle frequency to 30 Hz, when the test frequency was 10 Hz.

The second marking procedure was exclusively used in Group II crack propagation tests. The markings were accomplished in this case by using 100 thirty-percent overload cycles after every block of 1900 operating cycles. The advantage of this procedure is that the marker cycles are an integral part of the programmed sequence of test cycles, thus requiring no special attention from the test engineer for marker cycle loads. Also, only very few cycles are needed for marking. The only disadvantage of this procedure is that it introduces some crack growth retardation effects due to the overload. However, as shown in Section VI, the retardation effect was very small and thus this procedure could be used without significantly affecting the test results.

These marker loads were introduced primarily to enable later measurements of crack lengths on the fracture surface which cannot be visually monitored, such as the crack length along the lug hole wall of a growing corner crack or the length of a crack which has grown beyond the viewing window of the special test clevis. After testing, the failed specimen surfaces with markings were photographed for fractographic examinations. Photographs of fracture surfaces using the above two marking procedures are given in Figure 3-20. The crack lengths along the lug hole wall of Group I corner crack lugs were measured from such photographs. For Group II, fracture surface photographs were taken of the first 12 broken specimens, and measurements were taken from the photographs. It was then decided that better accuracy could be obtained at lower cost using a traveling microscope and measuring directly from the fracture surface without photography. This direct post-failure visual method was used for the remaining sixty-four Group II crack propagation specimens.

In block or flight-by-flight spectra, the marker cycles were not used. In order to obtain maximum information in such tests, the back surface crack lengths, after the corner crack breaks through the thickness, were also monitored.
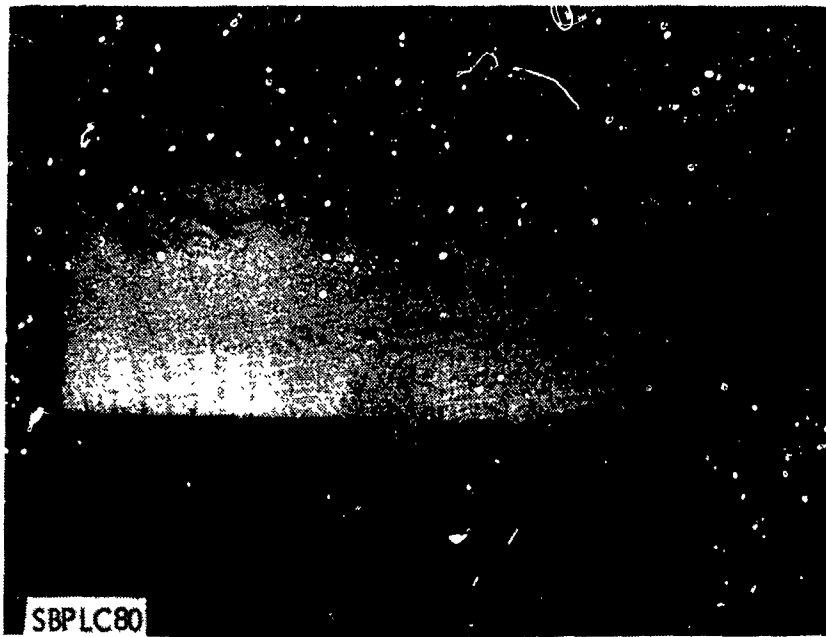
(a) Group I Specimen: Blocks of Marking Cycles at R = 0.85
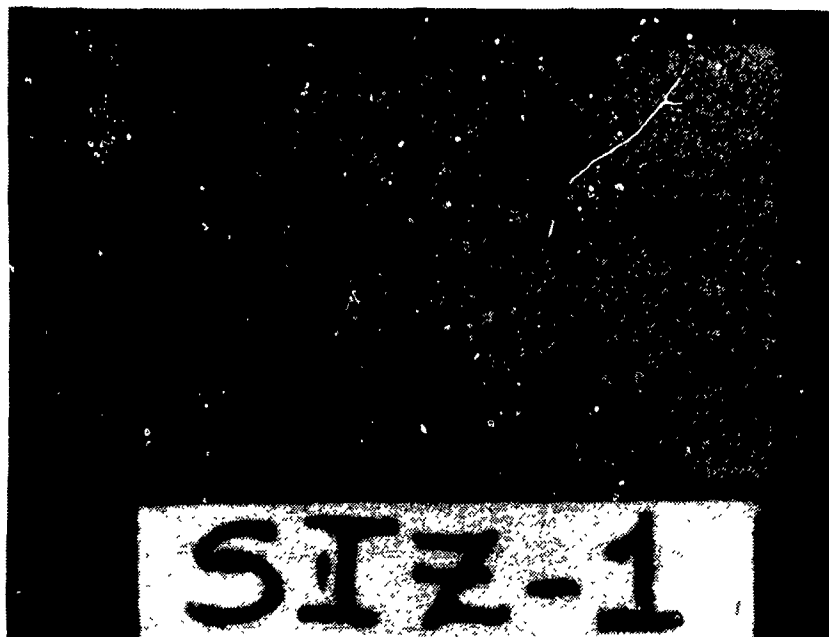
(b) Group II Specimen: Periodic 30 Percent Overloads

Figure 3-20. Typical Fracture Surface Photographs

6.4 DATA REDUCTION

The required crack growth data consisted of measuring through-the-thickness and corner cracks. For through-the-thickness cracks, both the front and back surface crack lengths were measured. For corner cracks, surface and depth lengths and transition behavior to through-the-thickness or across-the-ligament cracks were measured. Critical crack size, and any unusual behavior such as secondary cracking or non-coplanar crack growth were also recorded. For example, a typical Group II corner crack laboratory data sheet is given in Table 3-18. The visual measurements are presented either with no subscripts or with a subscript "visual". The post-failure measurements of markers, with or without photography, are presented with either a subscript "fracto" or "micro". In the case of small differences between the visual and fracture surface measurements, the fracture surface measurements were considered to be more accurate. Such laboratory data sheets were then collected in a consistent and convenient form and are included in Volume IV of this report. Table 3-19 illustrates a sample of the final form of the data given in Table 3-18.

It was intended for all the tests to begin with an initial crack size between 0.02 and 0.03 inch. EDM notching and fatigue precracking were carefully done for this purpose. However, sometimes the initial crack lengths were beyond this limit. Thus, for consistency of data presentation, an extrapolation (or interpolation) method was devised to convert the data to a common initial crack length. An initial crack length 0.025 inch was selected for both Group I and Group II tests. It was observed, in general, that the early crack growth in lugs tended to be approximately linear when plotted as log (c) versus cycles, N. Therefore, extrapolations or (interpolations) to determine the difference in cycles for the above initial crack lengths were made as shown in Figure 3-21. Then, the tables were adjusted accordingly. The number of cycles, ΔN^*, to be added to all raw data cycle counts is given by the equation

$$\Delta N^* = (N_2 - N_1)\ \frac{\log\,(c_2/0.025)}{\log\,(c_2/c_1)} - N_2 \qquad (3\text{-}1)$$

68

TABLE 3-18. EXAMPLE OF TABULATED DATA FROM GROUP II TESTS

SPECIMEN NO. T1-Z-1

Σ CYCLES	c VISUAL	c MICRO	a MICRO	(c_B) MICRO	(a_B) MICRO
(THOUSANDS)	(INCH)	(INCH)	(INCH)	(INCH)	(INCH)
10	0.034				
12	0.043				
14	0.055				
16	0.073				
18	0.097				
20	0.120	0.126	0.154		
22	0.149	0.156	0.203		
24	0.184	0.191	0.255		
26	0.225	0.233	0.318		
28	No Data	0.280	0.385		
30		0.328	0.458		
32		0.38	0.525		
34		0.444	0.605		
36		0.522	0.682		
38	No Data		0.760		0.108
39.908	Failure		0.905		0.485
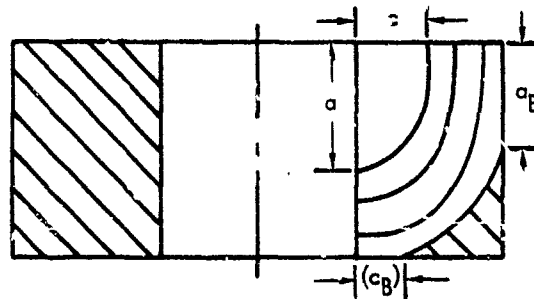
DEFINITION OF CRACK DIMENSIONS

69

TABLE 3-19.   CRACK GROWTH DATA FOR SPECIMEN T1-Z-1

LINE NO.	N	c (IN.)	a (IN.)	cB (IN.)	aB (IN.)	a/c
1	0	0.025	0.025	0.000	0.000	1.000
2	2541	0.034	0.035	0.000	0.000	1.020
3	4541	0.043	0.045	0.000	0.000	1.040
4	6541	0.055	0.059	0.000	0.000	1.066
5	8541	0.073	0.081	0.000	0.000	1.106
6	10540	0.097	0.112	0.000	0.000	1.158
7	12540	0.126	0.154	0.000	0.000	1.222
8	14540	0.156	0.203	0.000	0.000	1.301
9	16540	0.191	0.255	0.000	0.000	1.335
10	18540	0.233	0.318	0.000	0.000	1.365
11	20540	0.280	0.385	0.000	0.000	1.375
12	22540	0.328	0.458	0.000	0.000	1.396
13	24540	0.386	0.525	0.000	0.000	1.360
14	26540	0.444	0.605	0.000	0.000	1.363
15	28540	0.522	0.682	0.000	0.000	1.307
16	30540	−	0.760	0.000	0.108	−
17	32450	−	0.905	0.000	0.485	−

where c_1 and c_2 are the two consecutive crack length measurements which bridge the 0.025 inch length (or the smallest two measured lengths if all measurements exceed 0.025 inch) and N_1 and N_2 are the corresdponding cycle counts.

Generally, the corner crack grows, breaking through either the back surface (a = B) or curved surface (c = $R_o - R_i$) of the lug prior to failure. In such a situation, the crack lengths "c" and "a" are imaginary, but can be computed by using "c_B" and/or "a_B" and assuming that the shape of the crack is an ellipse. For calculating crack depths between the initial size and the first marking or in between markings, the a/c ratio was assumed to vary linearly with "c".

Finally, the following simple procedure was adopted for converting the marker load cycles with increased stress ratio (0.85) to an equivalent number of test cycles. The effects of the marker cycles were included by assuming that the crack growth rate of the marker cycles was the same as the previous constant amplitude loading. On this basis, an equivalent number of constant amplitude load cycles was calculated for the marker load cycles

$$\Delta N_{eq} = \Delta a_m \frac{\Delta N}{\Delta a} \qquad (3-2)$$

where Δa_m is the growth increment due to marker cycles , and Δa and ΔN are the previous constant amplitude crack increment and cycle increment, respectively. These equivalent load cycles were added to the actual constant amplitude load cycles, expressing the test data with a single constant amplitude stress level.

No measurements were made of secondary cracking or crack turning. When these phenomena occurred, appropriate photographs were taken of the specimens to clarify that behavior.
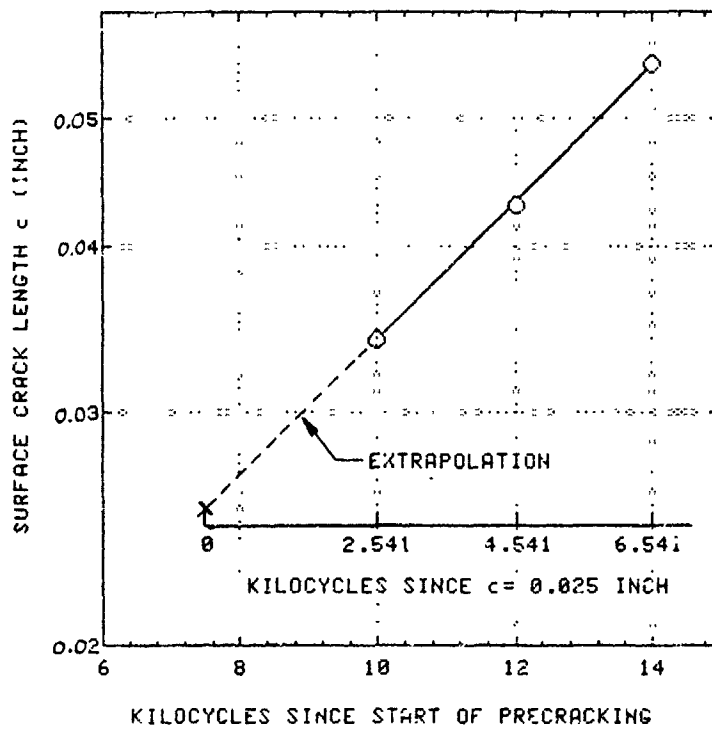
Figure 3-21. Extrapolation to Estimate Cycles to Initiation of a 0.025-inch Crack (Specimen T1-Z-1)

SECTION IV

ANALYTICAL PREDICTION METHODS

Analytical predictions were made before testing for all the Group I and Group II crack propagation tests of lugs. The Group I predictions were made using the stress intensity calculation methods presented in Reference [2], and in general more than one prediction method was used for each test. For Group II, one basic prediction method was selected and employed. However, some improvements to the prediction methods of Reference [2] were developed and used for Group II predictions. A special purpose computer program developed for predicting crack propagation in attachment lugs using all these methods is described in Reference [10], including user's instructions.

This section begins with a synopsis of the prediction methods described in [2] and utilized in the computer program [10]. The prediction schemes used for each specific type of test in Groups I and II are then summarized. Finally, the methodology improvements and new finite element analyses developed after the completion of Reference [2] are described.

1.0 SUMMARY OF ANALYTICAL METHODS

Analytical methods developed in this program for assessment of damage tolerance of attachment lugs were reported in Volume II of this report [2]. An extensive literature survey of analytical and experimental work on attachment lugs can also be found in [2]. A brief summary of the analytical methods developed under this program is presented in the following outline.

Analytical methods were developed to predict:

o   Residual Strength of Cracked Lugs

o   Crack Growth History in Lugs

Each crack growth analysis included the following elements:

- o Stress Intensity Factor Solution

- o Baseline Crack Growth Rate Equation

- o Applied Load Sequence

- o Spectrum Load-Interaction Model

Methods used to calculate the stress intensity factors were:

- o Simple Compounding Solution

- o 2-D Cracked Finite Element Procedure

- o Green's Function Method

- o 3-D Cracked Finite Element Procedure

Parameters and complexities covered in the stress intensity factor solution were:

- o Lug Geometry - Straight and Tapered

- o Crack Geometry - Single Through-the-Thickness and Single Corner

- o Crack Length - Measured on Lug Face and Along Bore of Hole

- o Pin-Bearing Pressure Distribution Change Due to Crack Length Change

- o Outer-to-Inner Radius Ratio - 1.50 to 3.00

- o Relative Rigidity of the Pin and the Lug - 1.00 and 3.00

- o Axial and Off-Axis Loading

- o Interference-Fit Bushings

- o Elastoplastic Analysis When Peak Stress Exceeds Yield Strength

Alternative baseline crack growth rate equations included were:

- o Paris

- o Forman

- o Walker

74

The applied load sequence could be:

- o   Constant Amplitude

- o   Block Spectrum

- o   Flight-by-Flight Spectrum

Alternative spectrum load interactional models were

- o   Wheeler Model

- o   Willenborg Model

- o   Generalized Willenborg Model

- o   Hsu Model

2.0   SELECTED METHODS OF PREDICTING STRESS INTENSITY FACTORS

Four basic methods of stress intensity factor analysis for cracked attachment lugs were developed and presented in Reference [2] and are summarized below:

- o   Compounding Method, where known solutions for single structural geometries are combined.

- o   2-D Crack-Tip Finite Element Method, wherein a two-dimensional finite element analysis is conducted of the cracked lug using a special crack tip element having K_I as its output.

- o   Green's Function Method, wherein the distribution of normal stress in the uncracked lug, taken along the line of cracking, is multiplied by a known Green's function and integrated.

- o   3-D Crack-Front Finite Element Method, wherein a special three-dimensional hybrid displacement finite element is used to calculate the stress intensity factor along the crack front of corner cracks.

Each of the first three methods calculate stress intensity factors for through-the-thickness cracks. Hence, for application to corner cracks, these solutions must be modified with a one-parameter or two-parameter corner-crack factor. In the one-parameter corner crack factor method, it is assumed that the aspect ratio of the crack, a/c, never changes. In the

75

two-parameter corner crack factor method, such an assumption is not made and the stress intensities are calculated using the current value of a/c, which varies during crack growth. Throughout this research program, the one-parameter corner crack factor was used with the compounding method, and the two-parameter corner crack factor was used with the Green's function and 2-D finite element methods.

The fourth method, using the 3-D crack-front finite element, was used to compare and evaluate the stress intensity factor solutions obtained by the other three methods. Since for a corner crack the 3-D special crack finite element method is the most rigorous, mathematically, it can be considered potentially the most accurate among the four methods. As is often the case, it is also the most expensive. Thus, a limited set of corner crack problems were solved using this method, and comparisons were made with the other methods. The results of these comparisons were presented in Reference [2]. Since one of the objectives of this program was to develop simple, accurate and inexpensive methods, only the first three methods were used for crack growth prediction. Thus, in further discussion within this volume of the report, only the first three methods are considered.

Although the 2-dimensional crack tip element was used in developing the Green's functions, the <u>original</u> Green's functions and the crack tip finite element method did not give identical stress intensity factor results. However, as a final step in developing the Green's function method, the original Green's functions were modified so that, at outer to inner radius ratios of 1.50, 2.25 and 3.0, the <u>modified</u> Green's functions and the 2-D crack tip finite element method would compute identical K_I factors. Thereby, the second and third methods above can be thought of as a single method.

A complete computer data management system was set up to make the crack growth predictions for all the tests and compare them with test results. Prediction schemes for the two groups of tests are as follows:

2.1 PREDICTION SCHEMES FOR GROUP I TESTS

<u>Residual strength tests</u> - The fracture toughness and net section yield failure criteria were used for these static tests. 2-D finite element stress intensity factor solutions were used.

76

Constant amplitude tests - Both the compounding and modified Green's function methods were used for these tests. Appropriate stress distributions (linear elastic or elasto-plastic) were used based on the load level (producing peak stress at the hole below or above yield).

Block spectrum tests - The modified Green's function method only was used for these tests, along with several alternative crack growth retardation models. Again, an appropriate stress distribution was used.

Flight-by-flight spectrum tests - The prediction scheme for these tests was the same as that of the block spectrum tests, except that the loading spectrum was much more complex in this case.

Variational tests - These included lower thickness lugs and lugs with shrink-fit bushings. The lower thickness lugs were subjected to constant amplitude and flight-by-flight spectrum loadings. Appropriate methods already described above were used. For lugs with shrink-fit bushings, the original unmodified Green's functions were used as described in [2], in conjunction with residual stresses due to the installation of the bushing and the stresses due to the application of the pin loading.

2.2 PREDICTION SCHEMES FOR GROUP II TESTS

For prediction purposes, the specimen configurations were first grouped as follows:

Straight-type lugs - This includes straight-sided lugs of various sizes, shapes and thicknesses, straight-sided clevises, and dogbone-shaped lugs.

Tapered lugs - This includes axial and off-axis loading.

Simulated wing/pylon-attach lug

Different prediction schemes were required for each configuration group. In addition, the presence of a shrink-fit bushing with standard interference levels introduced further problems. Therefore, five different prediction schemes were employed, as follows:

Straight-type lugs with no bushings – The modified Green's function was used to calculate stress intensity factors, using stress distributions from finite element analyses of uncracked lugs as in the case of Group I tests.

Tapered lugs with no bushings – The stress intensity factors from [2], calculated by the finite element method for 0°, 45° and 90° loadings, were used directly.

Straight-type lugs with steel bushings – The unmodified Green's function was used. The residual stresses and applied stresses were already available as in the case of Group I predictions.

Tapered lugs with steel bushings – The unmodified Green's function for straight lugs was used as an approximation. The distribution of residual stresses was calculated by the closed-form strength of materials equations as described in [2]. The distribution of applied stresses was calculated by modifying and rerunning the finite element models of the uncracked tapered lug to include a neat-fit steel bushing.

Simulated wing/pylon attach lug – The unmodified Green's function for straight lugs was used as an approximation. The distribution of residual stresses was calculated by the closed-form strength of materials equations for circular cylinders. The distribution of applied stresses was calculated by a two-dimensional finite element model.

The application of the Green's functions derived for straight lugs for the analysis of off-axis loading of tapered lugs and the wing-pylon attach lug, was inexact. However, it was deemed to be of value to observe how effective the straight-lug Green's functions would be in estimating K_I for off-axis loading.

3.0 IMPROVEMENTS AND NEW ANALYTICAL SOLUTIONS

Based on analytical comparisons conducted early in the test program, some improvements were made to the crack growth analysis methods described in [2]. Also, some Group II lug configurations warranted generation of some new analytical solutions for analytical/experimental correlations. Such efforts are described in this subsection.

3.1 METHOD IMPROVEMENTS

The attempted method improvements are discussed below. The first is the incorporation of net section yielding as a failure criterion. The other is an unsuccessful attempt to improve the compounding method solution.

3.1.1 Net Section Yielding Criterion for Critical Crack Size

Any structural member containing a crack can fail by either of two residual strength failure criteria. The failure is termed a fracture mechanics failure if the maximum stress intensity factor equals or exceeds the critical value K_c:

$$K_{max} \geq K_c \tag{4-1}$$

The failure is termed a net section tensile yielding failure if the average tension stress across the net section equals o' exceeds the tensile yield strength, σ_{ys}:

$$\sigma_{max} \geq \sigma_{ys} \tag{4-2}$$

79

The smaller the structural member, the more likely it is that Equation (4-2) will be satisfied before Equation (4-1), and the failure will be a net section yielding failure.

In order to apply Equation (4-2) to a lug with a crack on one side of the hole and the other side uncracked, it is necessary to assume what percentage of load is carried on each side. It is generally conservative to assume that half the load is reacted across the cracked section. This is the proposed assumption. Three examples are given below.

Example 1. Axially-Loaded Straight Lug with a Crack at 90 Degrees to the Lug Axis - Consider the lug shown in Figure 4-1(a), containing a quarter-elliptic corner crack on one side of the hole and subjected to an axial load P. It is assumed that half the load will be carried by uniform tensile stress across the net uncracked area A_u. The area of the quarter-elliptic crack is

$$A_c = \pi ac/4 \qquad (4-3)$$

Net section yielding failure will occur at critical load P_c, where from Equation (4-2),

$$P_c = 2\left[(R_o - R_i)B - A_c\right]\sigma_{ys} \qquad (4-4)$$

The following equations can be used when the crack is a transitional crack or a through-the-thickness crack. The area of a through-the-thickness crack is

$$A_c = cB \qquad (4-5)$$

For a transitional crack which has broken through the thickness, the area can be written as

$$A_c = \frac{\pi}{4}\left[\frac{B}{\sqrt{1 - c_B^2/c^2}}(c - c_B) + c_B B\right] \qquad (4-6)$$

where c_B is the back surface crack length.
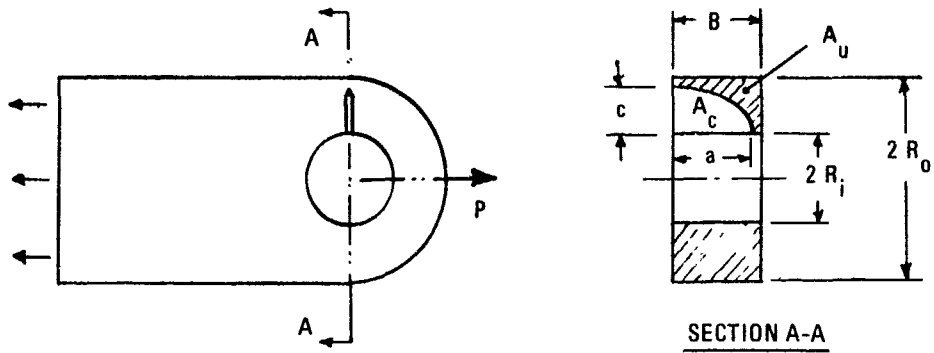
(a) Axially-Loaded Straight Lug, Corner Crack
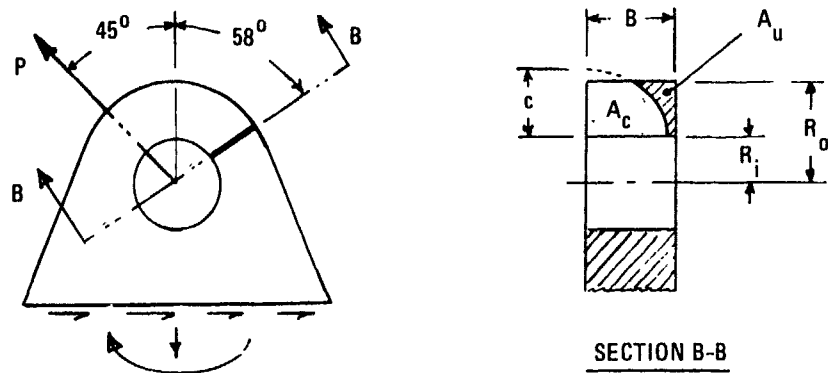
(b) Tapered Lug, -45° Load, 58° Extended Corner Crack
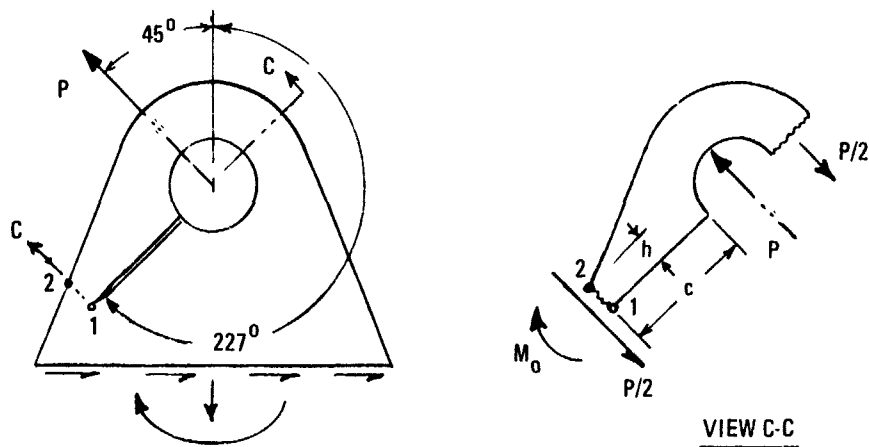
(c) Tapered Lug, -45° Load, -133° Through-Thickness Crack

Figure 4-1. Examples for Application of Net Section Yielding Criterion
for Residual Strength Failure of Lugs

81

The case of a transitional crack breaking through the ligament is considered in the next example. Similar simple equations can be developed when the crack breaks through both the thickness and ligament.

Example 2. Tapered Lug with an Extended Corner Crack at 58 Degrees, Loaded at -45 Degrees - Consider the lug shown in Figure 4-1(b), loaded at -45 degrees to the lug symmetry axis and containing a quarter-elliptic corner crack at the 58 degree location. In this case the surface length, c, of the corner crack is assumed to have grown beyond the outer boundary of the lug. The "extended" corner crack is assumed to be quarter elliptical in shape, intersecting the outer boundary a distance a_B from the front surface, where

$$a_B = a \sqrt{1 - \left(\frac{R_o - R_i}{c}\right)^2} \tag{4-7}$$

The area of the crack is given by

$$A_c = \frac{a}{2c} \left[(R_o - R_i) \sqrt{c^2 - (R_o - R_i)^2} + c^2 \sin^{-1} \left(\frac{R_o - R_i}{c}\right) \right] \tag{4-8}$$

The direction of the load (-45 degrees) is 13 degrees away from the direction of the crack plane (58 degrees). Otherwise, this case is similar to the prior example. Therefore, net section yielding failure will occur at load P_c where

$$P_c = 2 \left[(R_o - R_i)B - A_c \right] \sigma_{ys} / \cos (13^o) \tag{4-9}$$

Example 3. Tapered Lug with a Through-the-Thickness Crack at 227 Degrees, Loaded at -45 Degrees - Consider the 45-degree tapered lug shown in Figure 4-1(c), loaded at -45 degrees and containing a long through-the-thickness crack at the -227 degree location. This case is different from the prior two examples. The extrapolation of the crack plane intersects the nearest free edge of the lug at an angle of 20.5 degrees. Because of this small included angle, the crack is expected to turn suddenly at failure (at Point 1 of Figure 4-1c) and fail across a net section (from

Point 1 to Point 2) in a plane which is parallel to the applied load direction. This net section, which has height h and thickness B, is primarily in a state of beam bending before the crack turns. View C in Figure 4-1(c) is a free-body diagram which resembles that of a cantilever beam, built-in at the lower left-hand (crack-tip) end. Consistent with prior assumptions, half the load P is assumed to be carried at the crack-tip end and half uniformly across the uncracked section above and to the right of the hole. The bending moment reaction at the crack-tip section is found from moment equilibrium to be

$$M_o = (2c + R_i - R_o) \frac{P}{4} \qquad (4-10)$$

Net section yielding in this case is assumed to occur when the crack-tip section bends as a plastic hinge. Assuming perfectly rigid-plastic behavior across this section, the bending moment sustained by this section at the verge of yielding failure is given by

$$M_o = \sigma_{ys} B (h/2)^2 \qquad (4-11)$$

The critical load at yielding failure of this section is estimated by combining Equations (4-10) and (4-11). The result is

$$P_c = \frac{\sigma_{ys} B h^2}{2c + R_i - R_o} \qquad (4-12)$$

3.1.2 Attempts To Improve the Compounding Method Solution

The two-dimensional finite element solutions for stress intensity factor, obtained using the singular crack-tip finite element, are considered to be mathematically exact for a through-the-thickness crack. The compounding method solution for axially-loaded straight lugs was intended to approximate this exact solution. However, as the open symbols

83

in Figure 4-2 show, the compounding method, as developed originally, resulted in some significant errors.

In an attempt to improve the accuracy, the compounding method equations were adjusted to account more exactly for the true distribution of pin pressure in the hole and the true k_t for the uncracked lug. Unfortunately, however, these efforts did not lead to the improvements anticipated. The adjusted compounding solution, shown by the solid points in Figure 4-2, is at best only slightly more accurate than the original compounding solution.

Although this method has been an effective and versatile method for use in large, complex structure (Reference [6]), several shortcomings were encountered in attempting to apply the compounding method to attachment lugs:

    o   For axial loading of straight lugs: Even after special considerations of redistributed pin pressure due to cracking, there are significant errors for the lowest R_o/R_i ratio, 1.5; see Figure 4-2.

    o   For off-axis loading of tapered lugs: A completely new set of compounding method equations would be required to account for width effects and the remotely-applied in-plane bending moment.

    o   For lugs with shrink-fit bushings: There is no known way to account for the residual stresses using the compounding method. On the other hand, the Green's function approach is well-suited for the residual stress problem.

3.2 NEW ANALYTICAL SOLUTIONS

Although the basic methodology framework used in the Group II crack growth predictions was presented in Reference [2], some new analytical details were required. This subsection describes new finite element results for off-axis loaded aluminum lugs with steel bushings and an improved method of accounting for shrink-fit bushings.
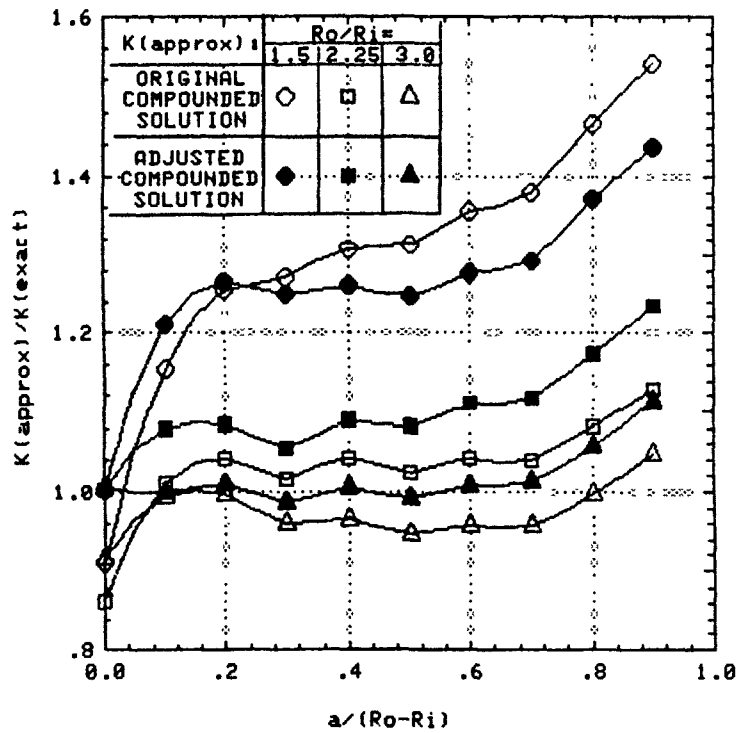
Figure 4-2.   Accuracy of Original and Adjusted Compounding Method
Solution for Axially-Loaded Straight Lugs

85

3.2.1 Finite Element Analyses of Tapered Lugs with Steel Bushings

Application of the Green's Function method for aluminum lugs with shrink-fit steel bushings requires two sets of calculated stresses.

The residual stresses due to bushing interference are calculated using closed-form equations from a strength-of-materials analysis of two concentric elastic circular cylinders. These equations are given in Reference [2].

The applied stresses due to external loading are estimated from a finite element analysis of the uncracked lug. When the lug and bushing are of different materials, the proper material properties of each are included in the finite element model.

The bushing and lug in these finite element models are modeled as being in intimate contact all around the circumference. Thus, the implicit assumption is made that the interference level is sufficiently high and the applied load sufficiently low to maintain that intimate contact. In actual fact, for typical loads and interferences, gapping occurs, which is not properly represented in this analysis, but is discussed in subsection 3.2.3.

The finite element analyses reported in [2] involved axially loaded straight lugs with and without bushings, and tapered lugs without bushings, loaded in various directions. The latter results are applicable to the steel tapered lugs with steel bushings tested in Group II. However, new finite element analyses were needed for aluminum tapered lugs with steel bushings tested in Group II.

Let r_i and r_o denote the inner and outer radii of the bushing, and let R_o denote the outer radius of the lug. Given in Table 4-1 are the tangential normal stresses along a radial line in an uncracked steel tapered lug ($R_o/r_i = 2.25$) containing a steel bushing ($r_o/r_i = =1.1875$), obtained from finite element analyses described in [2].

New finite element analyses were performed for the 45-degree-tapered aluminum lug with a steel bushing, loaded at 0 degrees, -45 degrees and -90 degrees to the symmetry axis of the specimen. The dimensions and material properties in the model were selected to match those in the Group II test matrix. Table 4-2 shows the computed tangential normal stresses along the

86

TABLE 4-1. COMPUTED NORMALIZED TANGENTIAL STRESSES, σ/σ_o, FOR TAPERED STEEL LUG WITH STEEL BUSHING

$\dfrac{c}{(R_o-r_o)}$	-45° LOAD σ/σ_o AT 58°	-90° LOAD σ/σ_o AT 205°
0.000	3.94	3.44
0.118	3.11	2.77
0.235	2.52	2.28
0.353	2.09	1.96
0.471	1.73	1.71
0.588	1.40	1.55
0.706	1.08	1.42
0.823	0.78	1.33
0.941	0.45	1.27

NOTE: $\sigma_o = \dfrac{P}{2R_o B}$

TABLE 4-2. COMPUTED NORMALIZED TANGENTIAL STRESSES, σ/σ_o, FOR TAPERED ALUMINUM LUG WITH STEEL BUSHING

$\dfrac{c}{(R_o-r_o)}$	0° LOAD σ/σ_o AT 90°	-45° LOAD σ/σ_o AT 58°	-90° LOAD σ/σ_o AT 205°
0	3.16	3.29	2.69
.056	2.94	3.02	2.49
.167	2.56	2.57	2.16
.278	2.28	2.21	1.92
.389	2.04	1.91	1.76
.500	1.84	1.64	1.64
.611	1.66	1.36	1.56
.722	1.49	1.08	1.50
.833	1.32	0.80	1.48
.944	1.15	0.49	1.50

direction of expected cracking for each loading direction; that is, 90 degrees for 0 degree loading, 58 degrees for -45 degree loading, and 205 degrees for -90 degree loading. The stresses at these angles were found by curve fitting the computed stresses at the element midpoints. The peak stresses at the edge of the hole were estimated by a polynomial extrapolation.

3.2.2 FEM Solution for Simulated Wing-Pylon Lug

A finite element analysis was also conducted of the simulated wing-pylon attach lug, an aluminum lug with a steel bushing. The specimen and test setup were shown in Figure A-12 (Appendix A) and Figures 3-17 and 3-18 of Section III. The basic finite element model for this specimen is shown in Figure 4-3.

Two-dimentional, quadrilateral membrane elements were used to represent the lug. Two-dimensional triangular elements were used to represent the pin. The inner two rings of quadrilateral membrane elements shown in the enlarged view in Figure 4-3 were used to represent the steel bushing. The 4-inch-wide base of the tee was represented by a line of 40 axial elements, coincident with the bottom edge of the membrane elements shown in Figure 4-3 (See Note 3 in Figure).

The 12-inch-wide base plate was assigned on effective width of 8.0 inches and represented by a line of eight axial elements. The nine model locations at the ends of these eight elements correspond to the two end support points and the seven fastener locations in the base of the tee (See Figure A-10, Appendix A). Axial (spring) elements, with their axes horizontal, connect these base-plate nodes to the corresponding nodes in the lug model. The stiffnesses, K, of these springs were computed from the foundation stiffness k and the thicknesses t_1 and t_2 of the base plate and the tee, using the equation

$$K = \frac{2 \, k t_1 t_2}{t_1 + t_2} \qquad\qquad (4\text{-}13)$$

Figure 4-3. Finite element model for simulated wing-pylon attach lug.
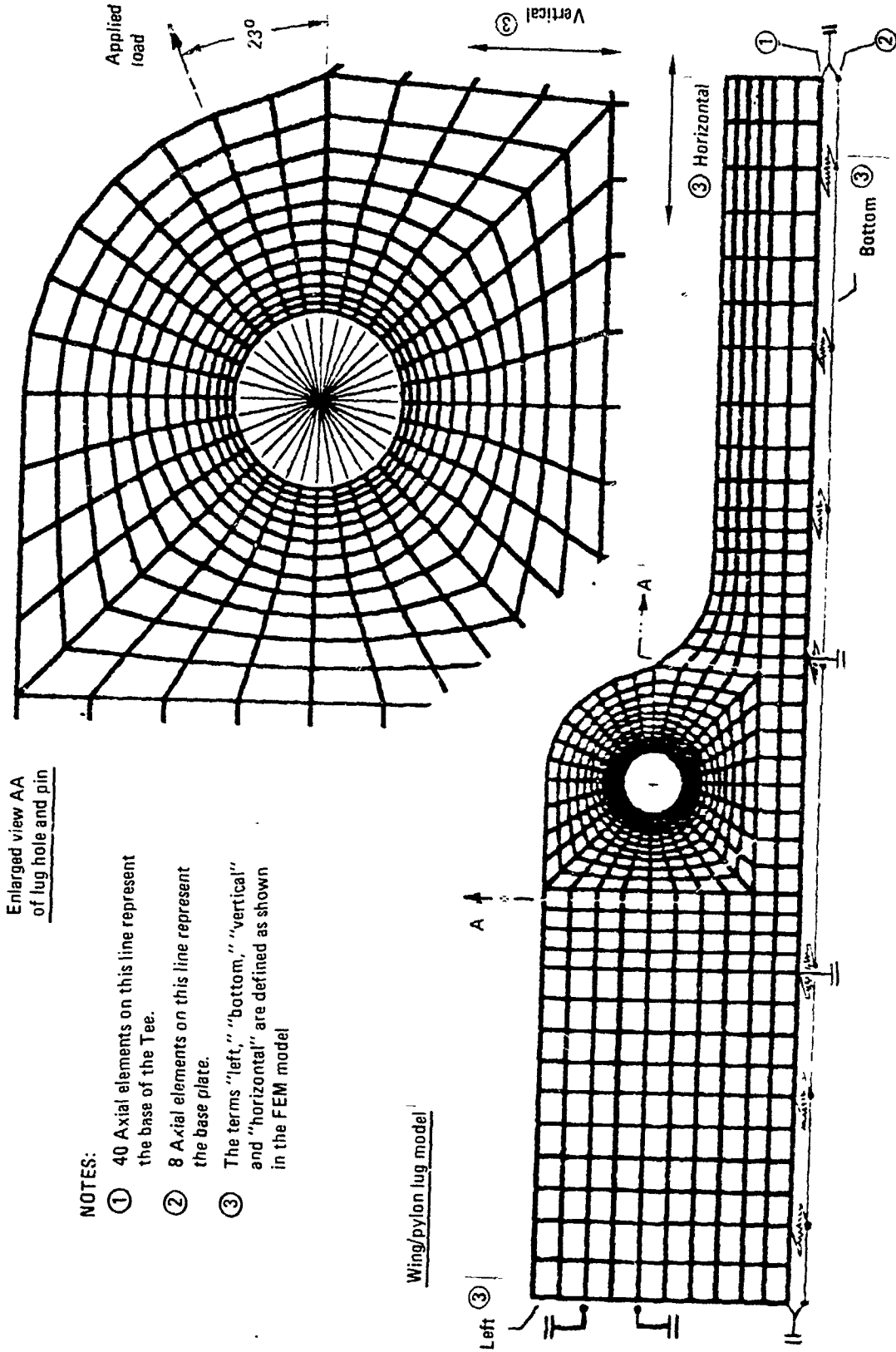
Enlarged view AA
of lug hole and pin

NOTES:

① 40 Axial elements on this line represent the base of the Tee.

② 8 Axial elements on this line represent the base plate.

③ The terms "left," "bottom," "vertical" and "horizontal" are defined as shown in the FEM model

Wing/pylon lug model

89

The factor of 2 is used because each spring must represent two fasteners. A foundation stiffness of K = 4.0 x 10^6 psi for the clearance - fit 0.375-inch diameter fasteners was selected based upon Reference [11]. For the 0.4375-inch diameter fasteners, the foundation stiffness was increased by the ratio of the diameters, to 4.66 x 10^6 psi.

Horizontal displacement constraints were imposed at both ends of the base plate and base of the lug where in the test, 0.75 inch steel bolts clamp both members to a rigid support. Vertical constraints were imposed at the left-hand end of the lug, where the flange of the lug is clamped between two steel angles, and at the two locations where the base of the lug and base plate are clamped down with two pairs of 0.4375-inch diameter bolts.

The radial contact forces at the pin-bushing interface were found iteratively. Axial elements were used to connect the nodes on the surface of the pin to corresponding nodes on the inner wall of the bushing. The cross-sectional area, A, of each of these elements was adjusted in each iteration until the process converged toward a valid solution. Validity of the solution requires that any non-zero contact force must be compressive, and at the location of any non-zero force, the corresponding relative radial displacements of the pin and bushing must equal the initial radial clearance.

The external load was applied at the center of the pin at an angle of 23 degrees above the horizontal (2 o'clock position in Figure 4-3).

The critical results from the finite element analysis were the location of the maximum value of tangential stress, σ_θ, and the distribution of σ_θ along a radial line through that point. The location of maximum stress was used to select the location of the EDM notch in the wing-pylon lug specimens. The stress distribution was used in conjunction with the Green's function to estimate the stress intensity factors for the ensuing crack.

The distribution of tangential stress around the hole in the lug is plotted in Figure 4-4. On the basis of this result, the EDM notch in the simulated wing-pylon lugs was introduced at θ = 109 degrees.

Figure 4-5 shows the distribution of tangential stress along a radial line through the θ = 109 degrees location. This stress distribution is
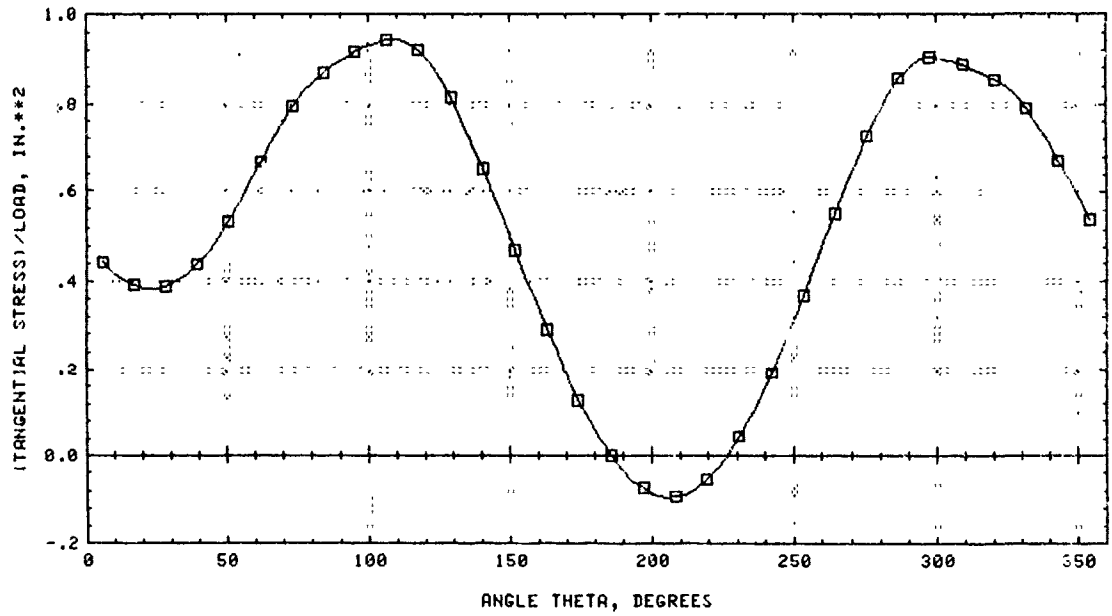
Figure 4-4. Tangential Stress Distribution Around the Edge of the Hole,
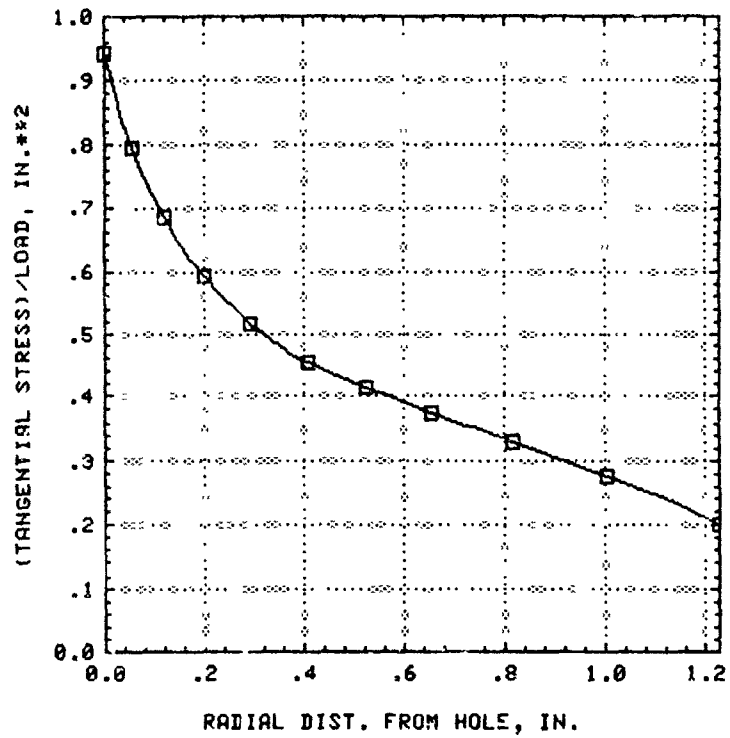Simulated Wing-Pylon Lug (Loaded at 23-Degrees)

Figure 4-5. Distribution of Tangential Stress in Simulated Wing-Pylon
Lug Along a Radial Line Through the Precracking Location, $\theta = 109^{\circ}$

used in conjunction with a calculated distribution of static residual stresses and the Green's Function for a straight-sided lug to estimate the stress intensity factors for various crack lengths. This method of estimating stress intensity factors requires the assumption that the bushing and lug remain in intimate contact. An improved method to account for shrink-fit bushings was also devised, as described in the following subsections.

3.2.3 Improved Prediction Method for Lugs with Bushings

If the applied load is high enough to overcome the effects of the shrink fit of the bushing, the bushing and lug will begin to separate along the interface. Drastic increases in the tangential stresses in the lug may result from the separation.

Two approaches were developed to account for separation between the lug and bushing. First, the finite element model for the wing/pylon lug was revised to model lug-bushing separation. Second, an approximate method was proposed to estimate the stresses by modeling the bushing and pin together as a larger (frictionless) pin.

In the revised finite element model of the wing-pylon lug, the interference of the bushing was simulated by applying a thermal load to the bushing in the form of a uniform temperature increase. The appropriate temperature increase was found from the coefficient of thermal expansion (α) of the bushing and the relative radial interference ($\Delta r/r$) between the bushing and lug, using the equation

$$T = (\Delta r/r)/\alpha \qquad (4-14)$$

The contact problem of the bushing-lug interface was solved iteratively, in a manner analogous to the method used for the pin-bushing interface, which was described in the preceding subsection.

An initial run was made with no externally applied load, to calculate the residual stresses due to the fit of the bushing and the displacements at its inner wall. The finite element results are compared in Figure 4-6 to the approximate residual stresses calculated by the strength-of-materials solution for concentric cylinders discussed in Reference [2].

Also from this initial run, the radial displacements at nodal points around the inner wall of the bushing resulting from the thermal load were determined. The small clearance between the pin and bushing, resulting from these radial displacements, had to be accounted for when the contact problem was formulated. In particular, the compressive displacements of the axial contact elements along the contact region between the pin and bushing due to the external load were set equal to the initial displacements of the bushing inner wall due to the thermal load.

Figure 4-7 compares the finite element solution for bushing-lug separation to the former solution assuming intimate contact. The tangential stresses along the eventual crack path, at $\theta = 109$ degrees, are calculated and compared at several values of x, the radial distance from the edge of the hole. For both models, the stresses at zero load are equal to the residual stresses induced by the shrink fit of the bushing. When intimate contact is assumed at the lug-bushing interface, the stress-load relationships are linear. When the bushing and lug are permitted to separate at points along the interface, the load-stress relationships are approximately bilinear, and the upper lines, if extended back, would all pass through the origin.

The most important observation to be made from Figure 4-7 is that the stresses calculated assuming lug-bushing separation are significantly higher than the corresponding stresses calculated assuming intimate contact. At high loads, the difference is due to the separation. At low stresses, it is because no frictional shearing tractions are permitted at the lug-bushing interface in the separation model, whereas they are permitted when intimate contact is assumed.

No new finite element modeling was carried out for tapered and straight lugs with bushings to account for bushing-lug separation. Instead, a simple approximation was used. In the approximation method, two linear relationships were found relating the tangential stresses, $\sigma_\theta(x)$, to the applied load P.
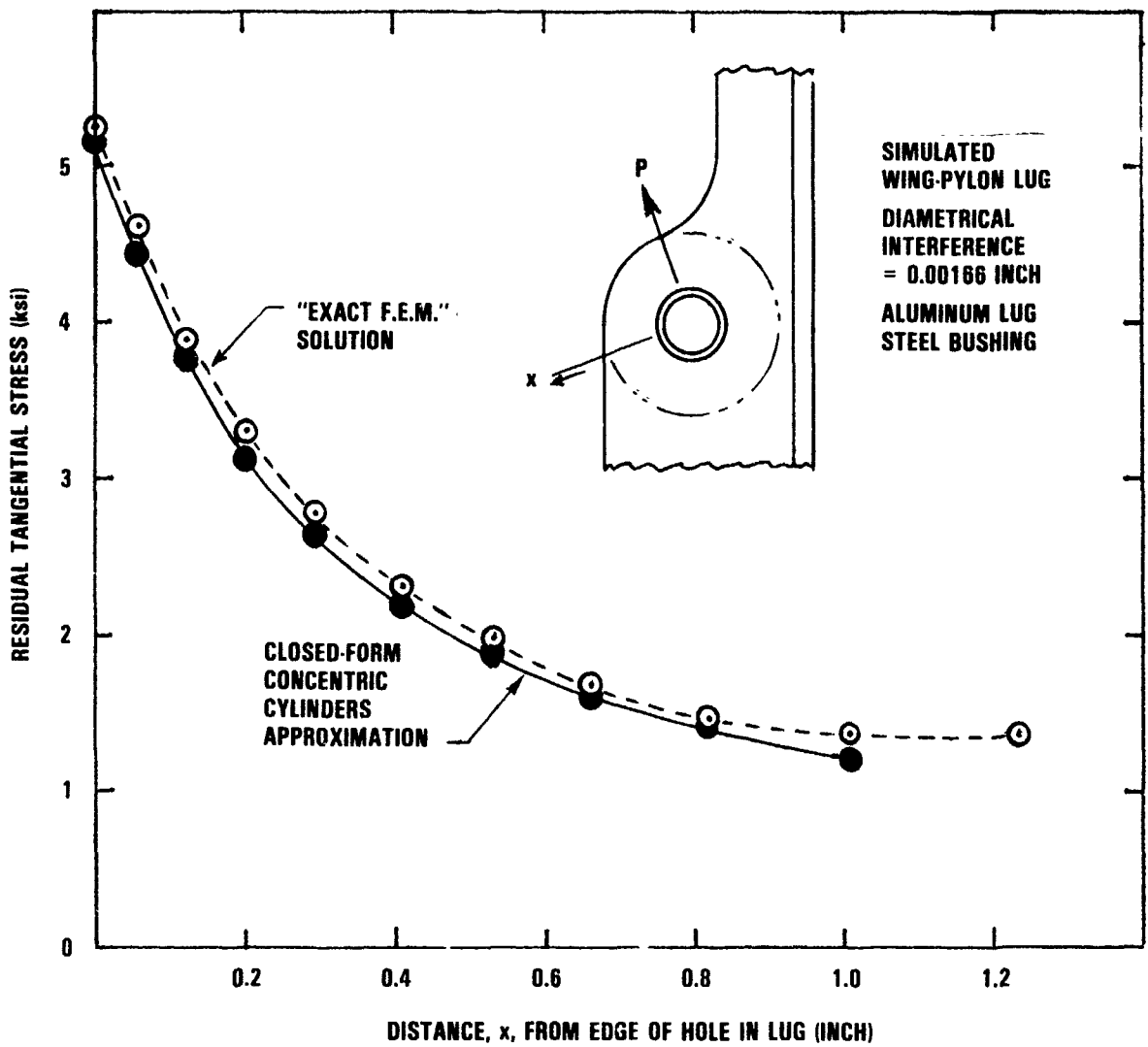
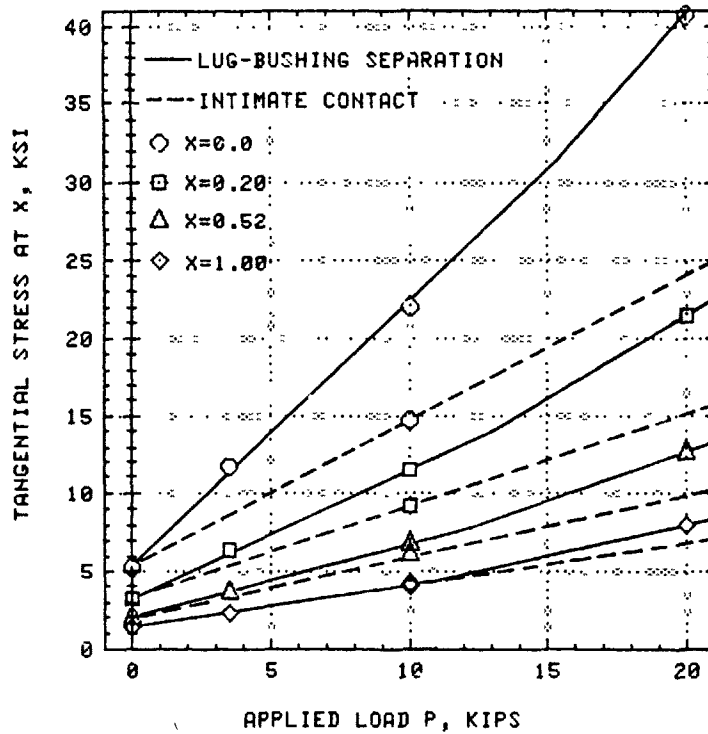Figure 4-6. Accuracy of Closed-Form Approximation of Residual Stress Due to a Shrink-Fit Bushing

Figure 4-7. Comparison of Calculated Tangential Stress on the
Eventual Crack Path in the Simulated Wing-Pylon
Lug, Assuming Lug-Bushing Separation or Intimate Contact

An example of this approximation is showing in Figure 4-8. The example configuraton is a straight aluminum lug with a steel bushing. The outer radius of the lug, and outer and inner radii of the bushing, respectively, are 1.125 inch, 0.594 inch, and 0.500 inch. The radial interference of the bushing is 0.0010 in., and the loading direction is axial.

The bilinear solid curves in Figure 4-8 represent the estimated tangential stresses at selected points along the eventual crack path, plotted as a function of applied gross area stress. Each lower line segment is obtained by assuming intimate contact between the bushing and lug, as in the original method. For each upper line segment, separation is modeled by assuming that the bushing acts like a (frictionless) solid pin with the same outer diameters; consequently σ_θ is directly proportional to P. Darkened symbols have been used in Figure 4-8 to emphasize the points of intersection of these line segments.

The crack growth computer program developed for lugs, Reference [10], requires a linear relationship between load and stress. Therefore, a straight line was fitted to each bilinear curve shown in Figure 4-8. The periodic overload sequence was used in the test, consisting of 1900 cycles between P_{min} and P_{max}, followed by 100 consecutive 30-percent overload cycles between P_{min} and P_{OL}. Therefore, a straight line intersecting the exact curve at P_{min} and P_{max} was judged to be the best straight-line approximation to use in the crack growth computer program. These linear approximations are shown as dashed lines in Figure 4-8.
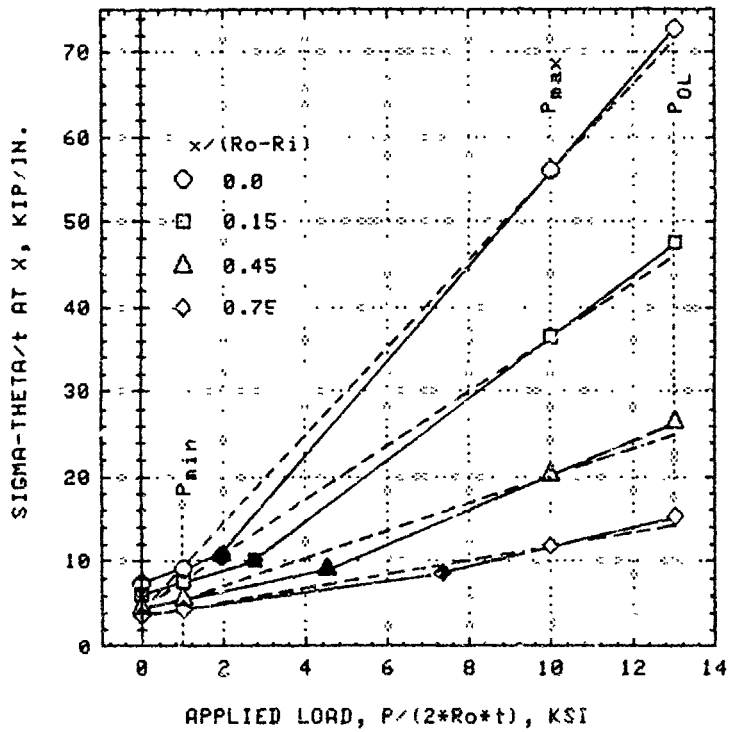
Figure 4-8. Tangential Stress in an Axially-Loaded
Straight Aluminum Lug with a Steel Bushing

GROUP I TEST RESULTS AND CORRELATIONS

This section presents the Group I test results and compares them to the analytical predictions. The Group II results are presented in the next section. All tests were conducted generally in accordance with applicable ASTM and/or other standards. Crack growth predictions were made prior to each test, by the methods discussed in Reference [2] and in Section IV. The Group I test matrix consisted of 224 tests, including material characterization, crack initiation, residual strength and crack propagation tests.

Results of baseline material characterization tests are presented in subsection 1.0. The next two subsections describe the results of crack initiation and residual strength tests of lugs, respectively. The last subsection enumerates the results of the crack propagation tests by subdividing them into the following categories:

(a) Baseline constant amplitude crack propagation tests

(b) Baseline block spectrum crack propagation tests

(c) Baseline flight-by-flight crack propagation tests

(d) Variational crack propagation tests

1.0 MATERIAL CHARACTERIZATION TESTS

Two different materials, 7075-T651 aluminum and 4340 steel (H.T. 180-200 ksi), were employed in the present experimental program. These materials were fully characterized to obtain all the necessary baseline material properties. The scope of the material characterization tests was described in Section III, which included chemical analysis, tensile, compressive, fracture toughness and crack growth rate tests for each material. The results of the material characterization tests are presented in this subsection.

1.1 CHEMICAL ANALYSIS

A standard chemical analysis was performed on samples of the two materials and the results are presented in Table 5-1. Analysis was conducted by x-ray fluorescence and combustion methods using applicable NBS and Alcoa Aluminum standards. Typical photomicrographs characterizing the microstructure of each material are shown in Figure 5-1.

1.2 TENSILE AND COMPRESSIVE TESTS

Using applicable ASTM standards, tensile and compressive tests were conducted for the two materials. Tests were performed using a calibrated universal testing machine and the load versus deformation curves were recorded. From these tests tensile and compressive yield strengths (F_{ty} and F_{cy}), tensile ultimate strength (F_{tu}), percent elongation and percent reduction in area were determined and are tabulated in Table 5-2. Triplicate tests were performed for each material.

1.3 FRACTURE TOUGHNESS TESTS

Fracture toughness tests were conducted using the center cracked tension (CCT) specimens for both the materials. Nominal thicknesses of 0.5 inch and 0.45 inch were used for aluminum and steel, respectively. An electric discharge machine (EDM) was used to produce a central through-the-thickness slot in the specimens. These specimens were then fatigue-loaded to introduce a center crack with sharp notches. Triplicate tests were performed to obtain the fracture toughness values using a universal testing machine and a clip gage was used to record the crack opening displacements. Using the test results and the stress intensity factor solution for a finite plate containing a center crack, fracture toughness (K_c) and apparent fracture toughness (K_{app}) values were calculated and are presented in Table 5-3. The ratio of net section stress to yield strength of the material is also included in the table for validation of the tests.

Though not planned originally, further fracture toughness tests were conducted using compact tension (CT) specimens, and the results are also

TARLE 5-1. CHEMICAL COMPOSITION OF TEST MATERIALS

MATERIAL	Si	Fe	Cu	Mn	Mg	Cr	Zn	Ti	P	S	Ni	Mo	Al
7075-T651 ALUMINUM ALLOY	0.67	0.25	1.38	0.04	2.46	0.19	5.60	0.02	-	-	-	-	REM
4340 STEEL H.T. 180-200 KSI	0.20	REM	-	0.79	-	0.90	-	-	0.019	0.003	1.78	0.26	-

MEASURED PERCENT VALUES

101

/0/
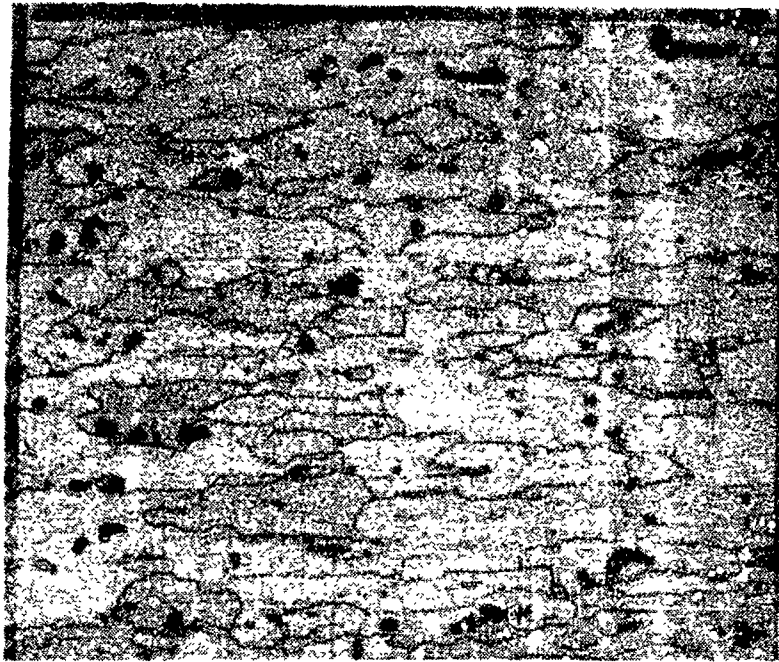
200X   Keller's Reagent – 7075-T651 Aluminum
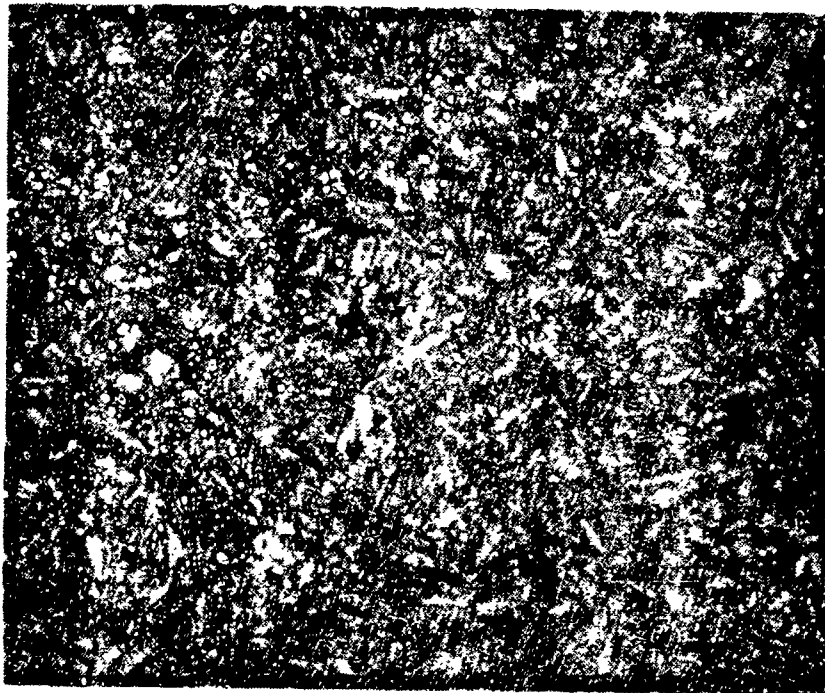
750X   3% Nitol – 4340 Steel (H.T. 180-200 KSI)

Figure 5-1.   Photomicrograph of Test Materials

TABLE 5-2. MECHANICAL PROPERTIES OF MATERIALS

(a) TENSILE TESTS

MATERIAL	SPECIMEN NO.	DIAMETER (IN)	F_{TU} (KSI)	0.2% OFFSET F_{TY} (KSI)	ELONGA-TION IN 2 IN (%)	REDUC-TION IN AREA (%)
7075-T651	AT-1	0.4004	74.7	74.5	10	19
ALUMINUM	AT-2	0.4006	75.5	75.5	10	26
(1 IN THICK PLATE)	AT-3	0.4010	75.2	74.8	12	28
		AVERAGE	75.1	74.9	10.7	24.3
4340 STEEL	ST-1	0.4021	193.0	179.0	12	44
H.T. 180 – 200 KSI	ST-2	0.4005	194.0	179.0	12	46
(0.625 IN THICK PLATE)	ST-4	0.4012	195.0	181.0	13	47
		AVERAGE	194.0	179.7	12.3	45.7

(b) COMPRESSION TESTS

MATERIAL	SPECIMEN NO.	DIAMETER (IN)	0.2% OFFSET F_{CY} (KSI)
7075-T651 ALUMINUM	AC-1	0.6010	75.8
(1.0 IN THICK PLATE)	AC-2	0.6011	76.1
	AC-3	0.6019	74.9
	AVERAGE		75.6
4340 STEEL	SC-1	0.6003	187
H.T. 180 – 200 KSI	SC-2	0.5994	190
(0.625 IN THICK PLATE)	SC-3	0.6004	187
	AVERAGE		188

TABLE 5-3. FRACTURE TOUGHNESSES OF TEST MATERIALS

(a) CENTER CRACKED TENSION SPECIMENS (CCT)

SPECIMEN NO.	DIRECTION	WIDTH W (IN)	THICK-NESS t (IN)	TOTAL CRACK LENGTH $2a_{cr}$ (IN)	PHYSICAL CRACK LENGTH $2a_o$ (IN)	GROSS STRESS σ_o (KSI)	NET SECTION STRESS σ_n (KSI)	σ_n/σ_y	K_C KSI$\sqrt{IN}$	K_{app} KSI$\sqrt{IN}$
7075-T651 ALUMINUM										
AK1	L-T	6.000	0.5018	3.180	2.3015	26.239	42.567	0.568	71.5	60.8
AK2	L-T	6.000	0.5000	2.868	2.0692	29.000	44.266	0.591	72.0	61.2
AK3	L-T	6.001	0.4986	2.826	1.9312	30.079	44.352	0.592	73.6	60.8
								AVERAGE	72.4	60.9
4340 STEEL H.T. 180-200 KSI										
SK1*	L-T	6.005	0.4534	5.284	5.0823	24.608	160.152	0.891	164.0	160.8
SK2	L-T	6.002	0.4534	4.417	3.5448	61.000	145.000	0.807	253.0	226.6
SK3	L-T	6.003	0.4638	4.370	3.5255	61.059	147.946	0.823	248.0	222.8
								AVERAGE	250.5	224.7

(b) COMPACT-TYPE SPECIMENS (CT)**

SPECIMEN NO.	DIRECTION	WIDTH W (IN)	THICK-NESS t (IN)	TOTAL CRACK LENGTH a_{cr} (IN)	PHYSICAL CRACK LENGTH a_o (IN)	FAILURE LOAD P (LBF)	K_C KSI$\sqrt{IN}$	K_{app} KSI$\sqrt{IN}$
7075-T651 ALUMINUM								
KC1A	L-T	4.000	0.4933	1.830	1.520	7005	60.5	55.1
KC2A	L-T	4.003	0.4929	1.737	1.480	6620	53.5	49.4
						AVERAGE	57.0	52.3
KC3A	L-T	4.001	0.2520	1.912	1.490	4960	88.9	78.5
4340 STEEL H.T. 180-200 KSI								
KC1S	L-T	4.000	0.4488	2.000	1.460	26250	282.0	240.9
KC2S	L-T	4.001	0.4490	1.974	1.460	26050	275.0	236.5
						AVERAGE	278.5	238.7
KC3S	L-T	4.005	0.2490	1.918	1.480	15600	284.0	249.5

*TEST CONSIDERED INVALID DUE TO EXCESSIVE CRACK LENGTH. $2a_o/W = 0.846$ AND THE THEORETICAL COMPLIANCE EQUATION IS VALID FOR $0.2 < 2a_o/W < 0.8$.

**ADDITIONAL TEST DATA GENERATED USING FAILED CCT SPECIMENS.

included in Table 5-3. These specimens were fabricated from the failed CCT specimens. Using the CT specimens, two tests were conducted for the same thicknesses as the CCT specimens for each material, so that the fracture toughness values can be compared for different specimen configurations. Such a comparison indicates that the fracture toughness values from CT specimen tests are lower for aluminum and higher for steel. Also included in the table are the fracture toughness values from one CT specimen of each material tested with a lower thickness of 0.25 inch. While aluminum shows a significant increase in the fracture toughness value for lower thickness, the steel fracture toughness value shows only a slight increase.

1.4 CRACK GROWTH RATE TESTS

Crack growth rate tests were conducted in a computer-controlled, closed-loop testing machine. EDM slots and fatigue precracking were accomplished as described before. Triplicate tests were performed for two stress ratios, 0.1 and 0.5, for both materials. Four inch wide self-aligning hydraulic grips were used to hold the specimens in the machine, and sinusoidal loading was applied to all specimens at 10 Hz. Reduced data in the form of da/dN versus ΔK relationships for aluminum and steel plates for stress ratios of 0.1 and 0.5 are presented in Figures 5-2 through 5-5. The test data were also analyzed with a least-square method of polynomial fit for use in subsequent analytical-experimental correlation.

2.0 CRACK INITIATION TESTS

Sixteen of the Group I tests were crack initiation tests, which were included to study the natural crack initiation location and growth behavior. The crack initiation tests included aluminum and steel lugs, outer-to-inner radius ratios of 1.5 and 3.0, and two gross section stress levels. All tests were duplicated and were run at a stress ratio of 0.1 with sinusoidal constant-amplitude loading at 10 Hz. Nominal gross section stress levels of 6 ksi and 15 ksi, and 14 ksi and 35 ksi were selected for aluminum and steel lugs, respectively.

These tests were conducted and the results of cycles to failure are given in Table 5-4. The aluminum lug tests were conducted as planned.
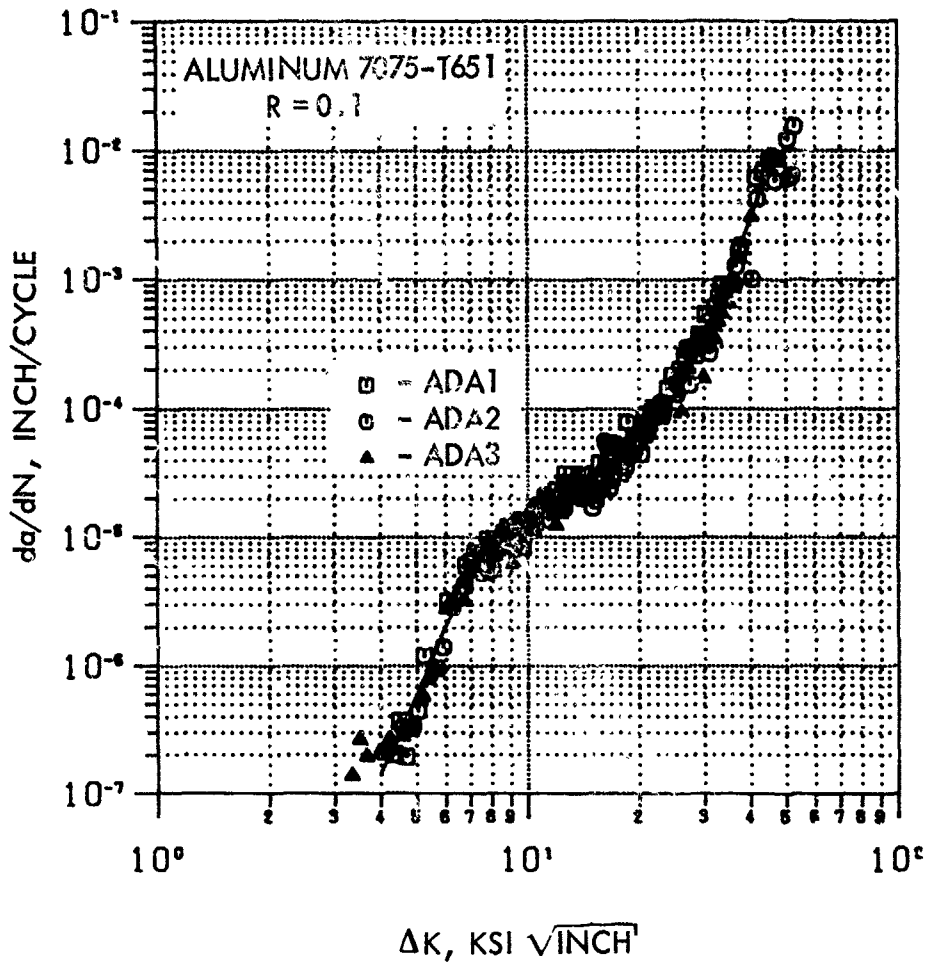
Figure 5-2. Crack Growth Rate Data for Aluminum
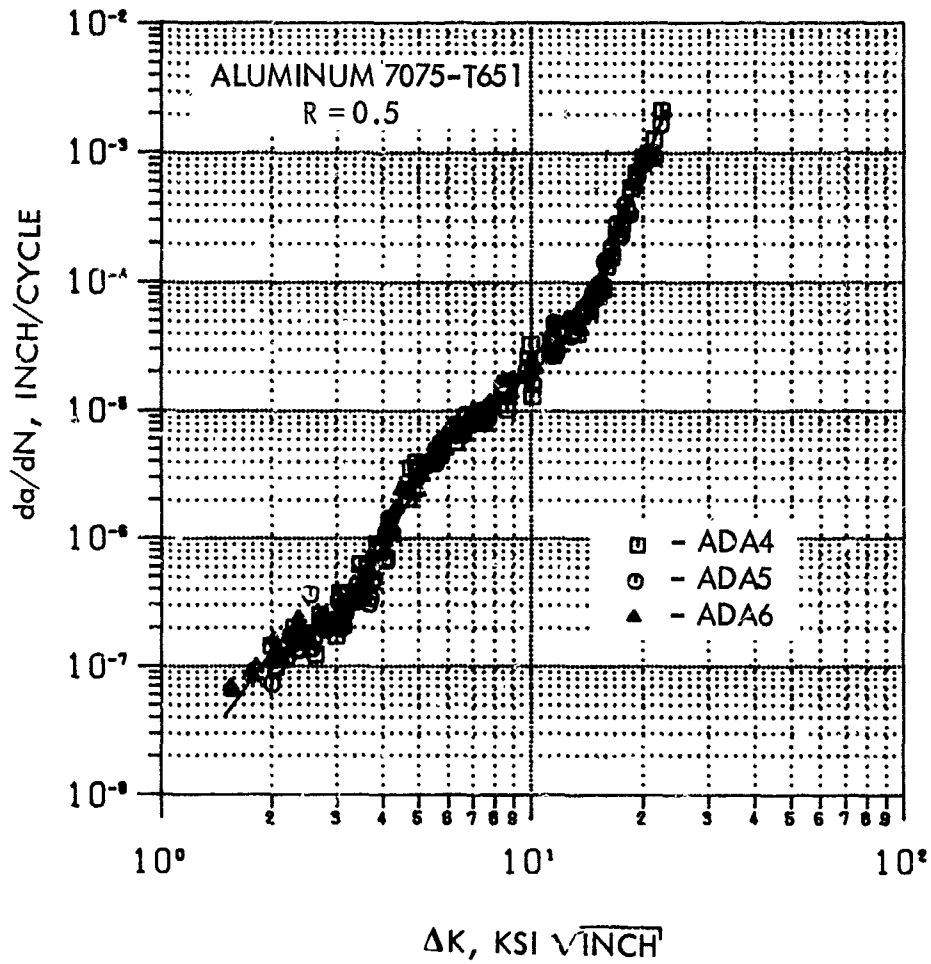Plate for a Stress Ratio of 0.1

106

Figure 5-3. Crack Growth Rate Data for Aluminum
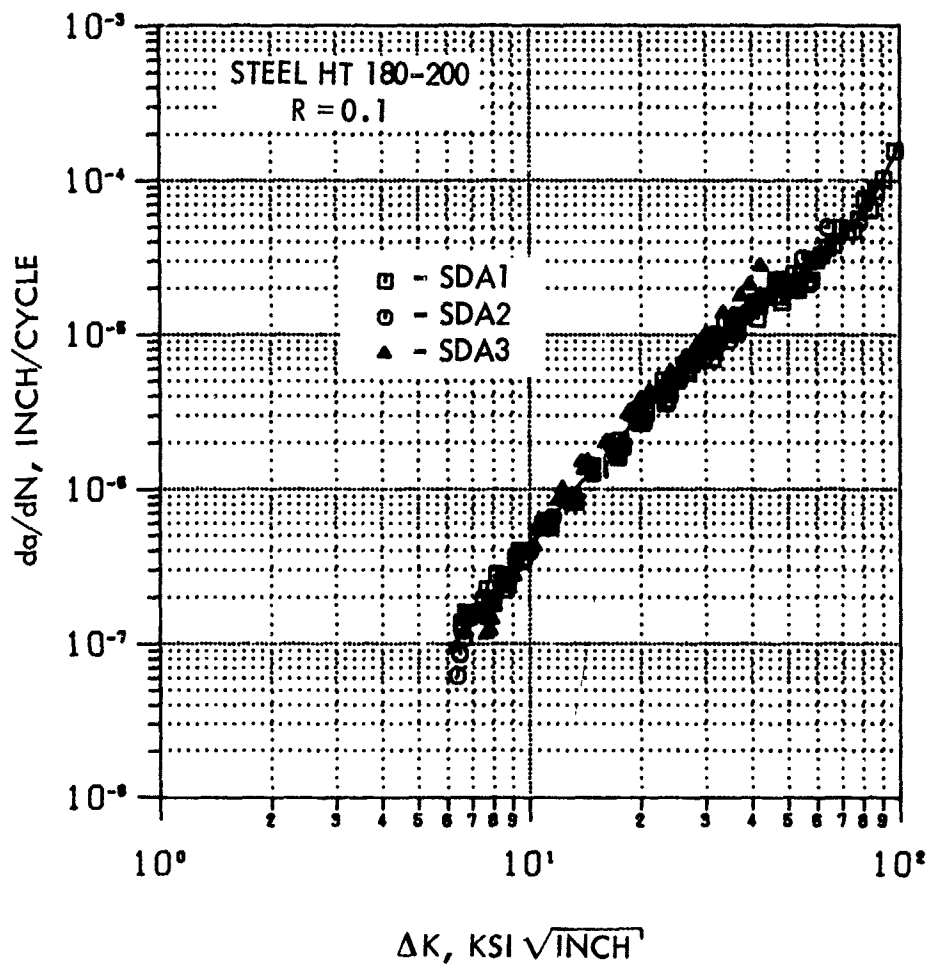Plate for a Stress Ratio of 0.5

Figure 5-4. Crack Growth Rate Data for Steel Plate
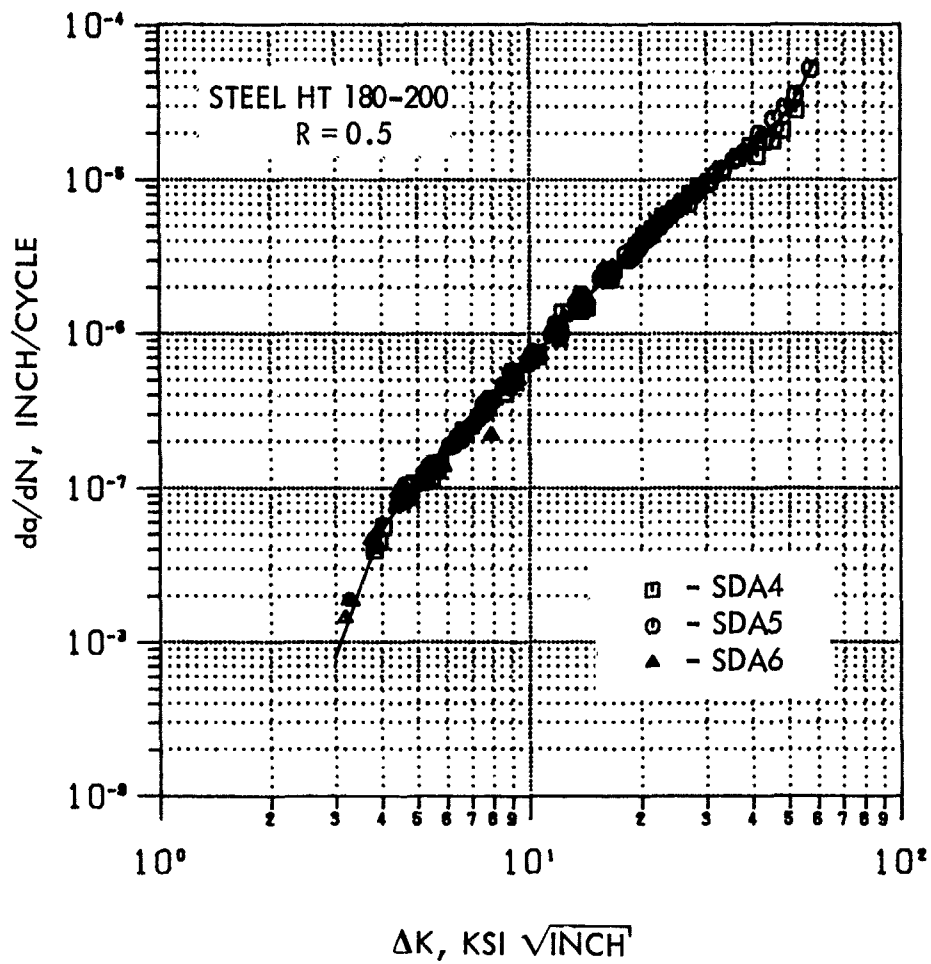for a Stress Ratio of 0.1

Figure 5-5. Crack Growth Rate Data for Steel Plate
for a Stress Ratio of 0.5

TABLE 5-4. CRACK INITIATION TEST RESULTS

SPECIMEN NO.	Ro/Ri	GROSS STRESS (KSI)	2R$_o$ (IN)	THICKNESS (IN)	CYCLES TO FAILURE	ANGLES OF INITIATION[1] (DEGREES)		ANGLE TO FRETTING (DEGREES) θ$_F$ [1]
						θ$_P$	θ$_S$	
7075-T651 ALUMINUM								
ABLI1	3	6	4.504	0.5020	131365	84	282	92
ABLI2			4.505	0.5009	118983	82	288	88
ABLI3	3	15	4.501	0.5000	6124	90	275	87
ABLI4			4.500	0.5024	6555	87	275	91
ABLI9	1.5	6	2.251	0.5044	64975	94	270	93
ABLI10			2.254	0.5000	63590	91	267	93
ABLI11	1.5	15	2.252	0.5006	6147	93	263	95
ABLI12			2.253	0.5022	6324	94	264	95
ABLI99	2.25	6	3.375	0.4988	102770	90	269	93
ABLI100			3.377	0.4892	88210	98	263	85
4340 STEEL H.T. 180-200 KSI								
SBLI1 [2]	3	24	4.506	0.4851	64300	88	(3)	92
SBLI2			4.512	0.4975	83803	73	(3)	90
SBLI3	3	35	4.500	0.4995	15851	85	273	97
SBLI4			4.507	0.5019	24621	85	272	95
SBLI9	1.5	20	2.249	0.5011	91069	89	(3)	94
SBLI10 [2]		24	2.253	0.4993	42581	93	(3)	98
SBLI11	1.5	35	2.254	0.4970	18177	94	271	95
SBLI12			2.247	0.4983	12820	97	263	96

(1) SEE TABLE 5-5 FOR DEFINITIONS OF ANGLES

(2) SEE TABLE 5-5 FOR FURTHER DETAILS ON LOADING HISTORY

(3) NO SECONDARY CRACKING DURING TEST

110

However, the steel lugs subjected to the 14 ksi gross section stress level loading resulted in test-runouts for both the outer-to-inner radius ratios considered. The R_o/R_i = 3.0 steel specimen was then selected for retesting. The stress levels had to be increased four different times before the failure occurred at a gross section stress of 24 ksi. The load history for the test is given in Table 5-5. The R_o/R_i = 1.5 steel specimens were later retested at a gross section stresses of 20 and 24 ksi, as shown in the table.

After failure, the specimens were studied to obtain the angles of crack initiation, primary and secondary, and angles of fretting. The angles are defined in Table 5-5. Angles to crack initiation and angles of fretting are recorded in Table 5-4.

The original test plan was to test lugs with two R_o/R_i ratios of 1.5 and 3.0. However, as there were two spare aluminum lugs with an R_o/R_i ratio of 2.25, they were also tested for crack initiation behavior and the results are included in Table 5-4.

Before the testing, however, an attempt was made to predict the fatigue life of R_o/R_i = 2.25 lugs using the simple S-N curve approximation of

$$KS^b N = 1 \qquad (5-1)$$

where N is the fatigue life in number of cycles, S is the characteristic stress (= stress concentration factor x gross stress), and K and b are material constants. The fatigue life data and stress concentration factors for R_o/R_i = 1.5 and 3.0 lugs were used to calculate the constants K and b. Using these constants, the life of a lug with R_o/R_i = 2.25 was predicted as 114,400 cycles, which correlates well with the experimental average value of 95,490 cycles given in Table 5-4.

3.0 RESIDUAL STRENGTH TESTS

Sixteen of the Group I lug tests were simple residual strength tests which were included to assess the applicability of the fracture toughness concept to attachment lugs. These tests included the following variables:

111

TABLE 5-5.   LOADING HISTORY OF STEEL SPECIMENS NOT RESULTING
            IN FAILURE AND DEFINITIONS OF ANGLES

SPECIMEN NO.[1]	Ro/Ri	GROSS STRESS (KSI)	CYCLES APPLIED
SBLI-1	3	14	4,300,000
	3	16	2,450,000
	3	18	1,040,000
	3	20	93,300
SBLI-10	1.5	14	6,006,000
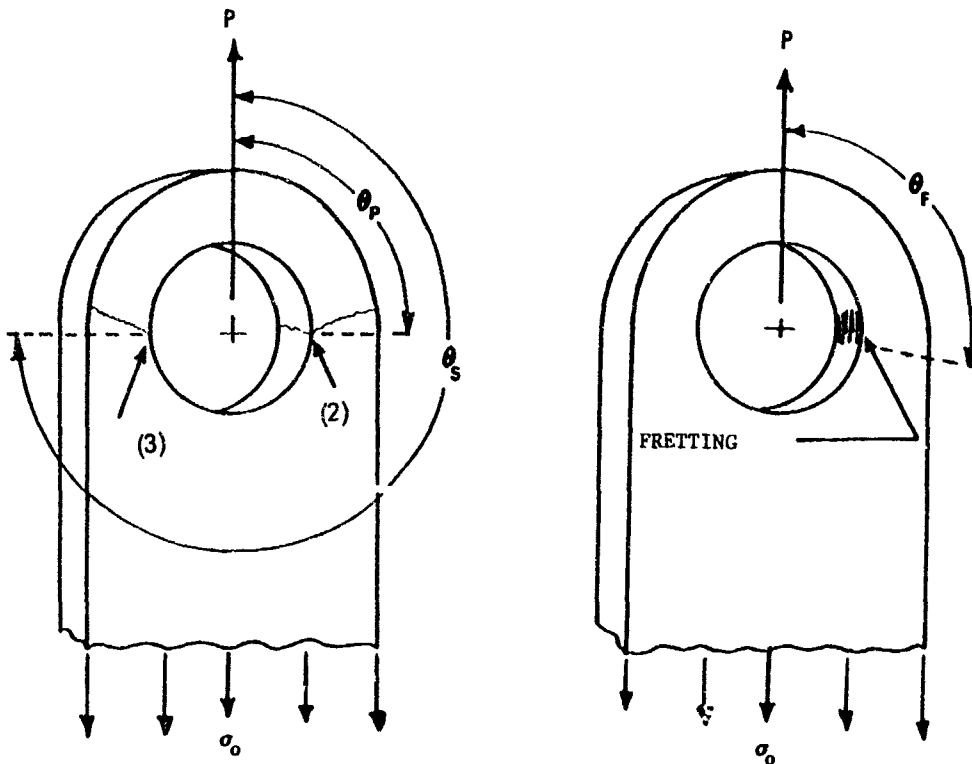
(1) SEE TABLE 5-4 FOR FAILURE DATA AND SPECIMEN DIMENSIONS

(2) PRIMARY INITIATION POINT

(3) SECONDARY INITIATION POINT

two materials-aluminum and steel; two R_o/R_i ratios - 1.5 and 3.0; two crack shapes - single through-the-thickness and single corner; and two crack lengths. Each test was duplicated (except for the experimental scatter of attempting to produce the same crack lengths).

Also, note that the through-the-thickness cracks were tested using larger lugs (R_o/R_i = 3.0) and the corner cracks were tested using smaller lugs (R_o/R_i = 1.50). This selection was based on the initial calculation of load requirements for fracture and the test machine capacity for the crack shapes and lug geometries considered for residual strength tests.

The results of the sixteen residual strength tests are provided in Table 5-6. This table is subdivided into two parts giving the through-the-thickness and the corner crack test results separately. For through-the-thickness cracks, the finite width correction factors, β_T, were calculated using the Green's function method and are included in the table. These factors were calculated using the average (of front and back) crack lengths which are also given in the table. For corner cracks, the Green's function method along with the developed corner crack correction factors were used to calculate the stress intensity factors at two points, C and A, which are the points of intersection of the crack front with the lug front surface and the bore of the lug, respectively. These stress intensity factors were then normalized by $\sigma_o \sqrt{\pi c}$ to obtain the tabulated β_C and β_A correction factors.

Using the above correction factors and the apparent fracture toughness values from Table 5-3, predictions were made for failure stress for all the sixteen tests. While the tabulated β_T values were used for through-the-thickness crack problems, either β_A or β_C, whichever was higher, was used for corner cracks to predict the failure stress. Comparisons of test and analysis results were made using two criteria. The first one was based on the apparent fracture toughness criterion and the results are tabulated in the form of a ratio of the test-to-analysis gross-section stresses. The second criterion was based on the net-section yield. These results are given in the form of a ratio of the test net-section stress to material yield strength. An analysis of the results in Table 5-6 indicates that the lower critical stress from these two criteria will predict failure accurately, depending on the lug geometry, crack shape and crack length.

TABLE 5.6.   RESIDUAL STRENGTH TEST RESULTS

(a) THROUGH-THE-THICKNESS CRACKS

SPECIMEN NO.	MATERIAL	2 Ro (IN.)	THICKNESS B (IN.)	CRACK LENGTH c (IN)	β_T^*	FAILURE STRESS (GROSS) σ_{of} (KSI) TEST	ANALYSIS	$\dfrac{\sigma_{of}\ TEST}{\sigma\ of\ ANA.}$	$\dfrac{\sigma\ NET\text{-}TEST^{**}}{F_{TY}}$
ABLS83		4.501	0.4964	0.405	2.371	22.96	22.77	1.008	0.630
ABLS81	7075-T651 ALUMINUM	4.501	0.5006	0.408	2.364	23.61	22.76	1.037	0.649
ABLS80		4.501	0.5022	0.722	1.886	18.27	20.73	0.881	0.753
ABLS82		4.501	0.5014	0.792	1.878	18.83	20.55	0.916	0.796
SBLS60		4.497	0.4882	0.391	2.408	68.78	83.44	0.824	0.777
SBLS82	4340 STEEL	4.503	0.4853	0.399	2.386	69.83	83.35	0.838	0.794
SBLS57		4.500	0.4948	0.765	1.891	55.42	75.96	0.730	0.945
SBLS8		4.496	0.4941	0.771	1.890	54.91	75.70	0.725	0.946

(b) CORNER CRACKS

SPECIMEN NO.	MATERIAL	2 Ro (IN.)	THICKNESS B (IN)	CRACK LENGTHS (IN.) a	c	β_A^*	β_C	FAILURE STRESS (GROSS) σ_{of} (KSI) TEST	ANALYSIS	$\dfrac{\sigma\ of\ TEST}{\sigma\ of\ ANA}$	$\dfrac{\sigma\ NET\text{-}TEST^{**}}{F_{TY}}$
ABLS13		2.250	0.4996	0.240	0.19	3.859+	3.609	21.17	20.43	1.036	1.049
ABLS16	7075-T651 ALUMINUM	2.255	0.5012	0.300	0.23	3.792+	3.665	17.96	18.90	0.950	1.004
ABLS15		2.251	0.5011	0.390	0.34	3.696	5.038+	12.50	11.70	1.068	1.122
ABLS14		2.253	0.4966	0.400	0.32	3.696	4.472+	13.27	13.58	0.977	1.146
SBLS15		2.250	0.4993	0.295	0.20	3.763+	3.757	47.98	74.65	0.643	1.065
SBLS13	4340 STEEL	2.226	0.4992	0.305	0.20	3.741	3.850+	41.40	72.98	0.567	0.962
SBLS14		2.244	0.4997	0.395	0.25	3.656	3.947+	40.84	63.67	0.641	1.179
SBLS16		2.226	0.5010	0.400	0.30	3.689	4.455+	29.32	51.49	0.569	1.041

* $K_i = \sigma_o \sqrt{\pi c}\ \beta$;   i = T, A OR C   T - THROUGH-THE-THICKNESS, A AND C - LOCATIONS A AND C OF THE CORNER CRACK

** σ NET-TEST = σ of TEST $\dfrac{BR_o}{(BR_o - BR_1 - A_c)}$

A_c = AREA OF CRACK SURFACE

= Bc FOR THROUGH-THE-THICKNESS CRACK

= π ac/4 FOR CORNER CRACK

+ DATA USED FOR PREDICTION OF FAILURE

114

Thus, for attachment lug problems, both the criteria must be considered for prediction of failure of the specimen. Figure 5-6 shows the accuracy of residual strength predictions. In most of the crack propagation tests, where the crack lengths are larger, the critical crack length based on net-section yield criterion was generally the critical parameter that predicted failure.

The equation for calculating the test net-section stress from the test gross-section stress is also given in Table 5-6. This assumes that the loads are evenly divided between the two net sections of the lug. As discussed in Section IV, such an assumption is generally conservative.

4.0 CRACK PROPAGATION TESTS

Group I crack propagation tests consisted of 144 baseline tests and 16 variational tests. The results of analytical-experimental correlations of these crack propagation tests are presented in this subsection by subdividing these tests into the following categories:

(a) Baseline constant amplitude tests - 72 tests

(b) Baseline block spectrum tests - 36 tests

(c) Baseline flight-by-flight spectrum tests - 36 tests

(d) Variational tests - 16 tests

All the crack growth data, except for the 36 baseline block spectrum tests, are presented here for an initial crack size of 0.025 inch. The experimental data were either extrapolated or interpolated to 0.025 inch using the semi-logarithmic linear crack growth behavior discussed in Section III. Such an approximation could not be used for the block spectrum tests due to the following reason. The selected block spectrum does not introduce any retardation effects during its first application. Only the subsequent repetition of the block spectrum loading introduces the retardation effects. The crack growth rates for the first and subsequent applications of the block spectrum loading are significantly different. Thus, use of such a simple approximation would lead to gross errors in extrapolation or interpolation.
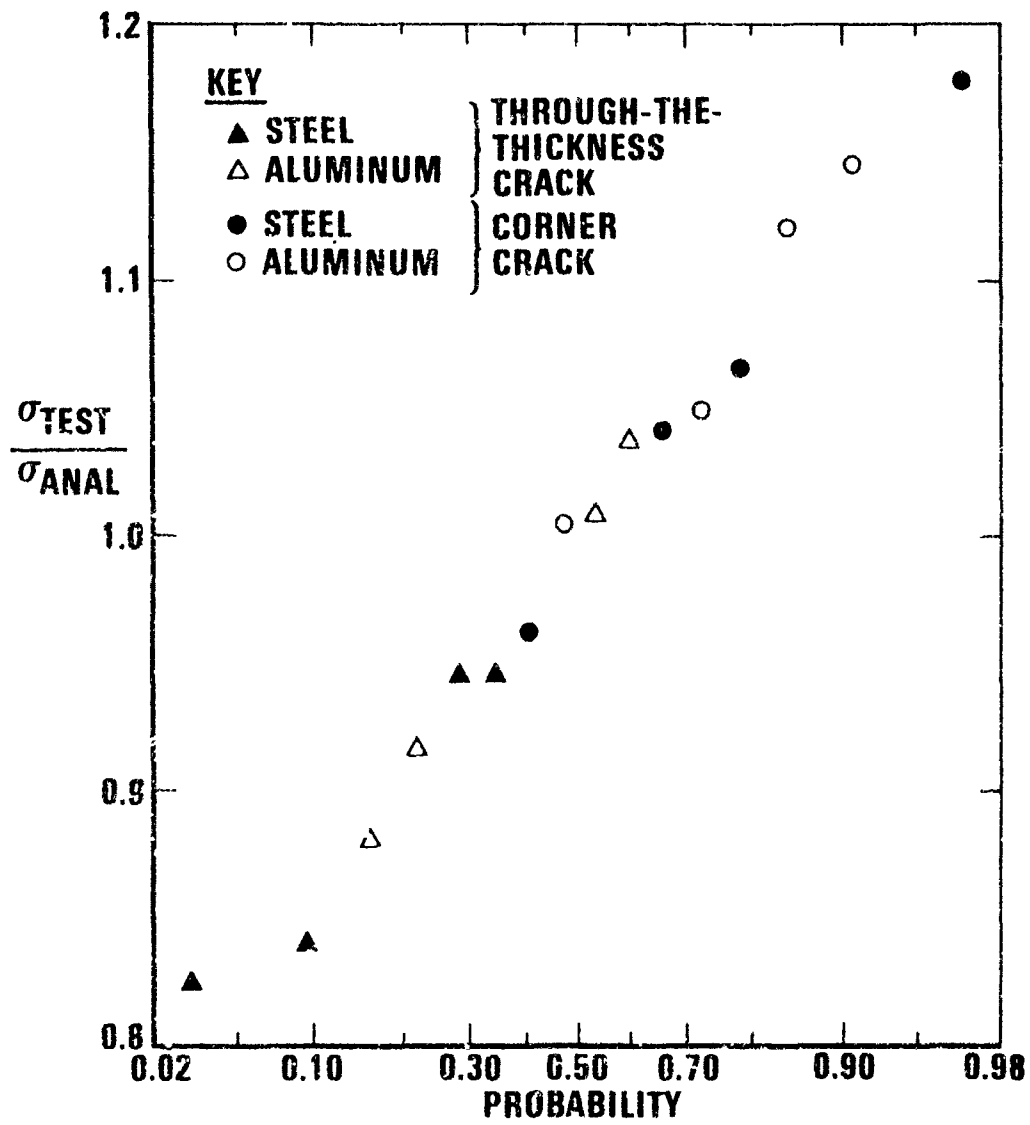
Figure 5-6. Accuracy of Residual Strength Predictions

116

Also, in presenting the crack growth data, marker cycle crack growths were accounted for by using the equivalent test cycle concept discussed in Section III.

4.1 BASELINE CONSTANT AMPLITUDE TESTS

Seventy-two preflawed straight lug specimens, 48 aluminum and 24 steel, were tested using constant-amplitude loading. The gross-section maximum stresses were 6 ksi in half the aluminum specimens and 15 ksi in the other half. All the 24 steel specimens were subjected to a gross-section maximum stress of 14 ksi. Each of the above three groups of 24 tests included 12 specimens with initial through-the-thickness cracks, and 12 with initial corner cracks, covering the following variables: three R_o/R_i ratios (1.5, 2.25 and 3.0), two stress ratios (0.1 and 0.5), and duplicate specimens for each test condition.

4.1.1 Through-the-Thickness Crack Constant-Amplitude Tests

The results of all the initial through-the-thickness crack growth test specimens subjected to constant-amplitude loading are presented in Figures 5-7 through 5-24. The first six figures (Figures 5-7 through 5-12) are for aluminum lugs subjected to a far-field gross maximum stress, σ_o, of 6 ksi, which produces peak stress levels below the yield strength of the material. The next six figures (Figures 5-13 through 5-18) are for steel lugs subjected to $\sigma_o = 14$ ksi, which also produces peak stresses below the yield strength of the material. The next six figures (Figures 5-19 through 5-24) are for aluminum lugs subjected to $\sigma_o = 15$ ksi. For this stress level, the peak stresses in the lugs are above the yield strength of the material. In each of these three sets of six figures, the first three figures correspond to a stress ratio of 0.1 and the next three correspond to a stress ratio of 0.5. These three figures again correspond to R_o/R_i ratios of 1.5, 2.25 and 3.0.

The through-the-thickness crack lengths presented in these figures are the averages of front and back surface crack lengths. Analytical predictions were made using the Green's function and the compounding methods, and
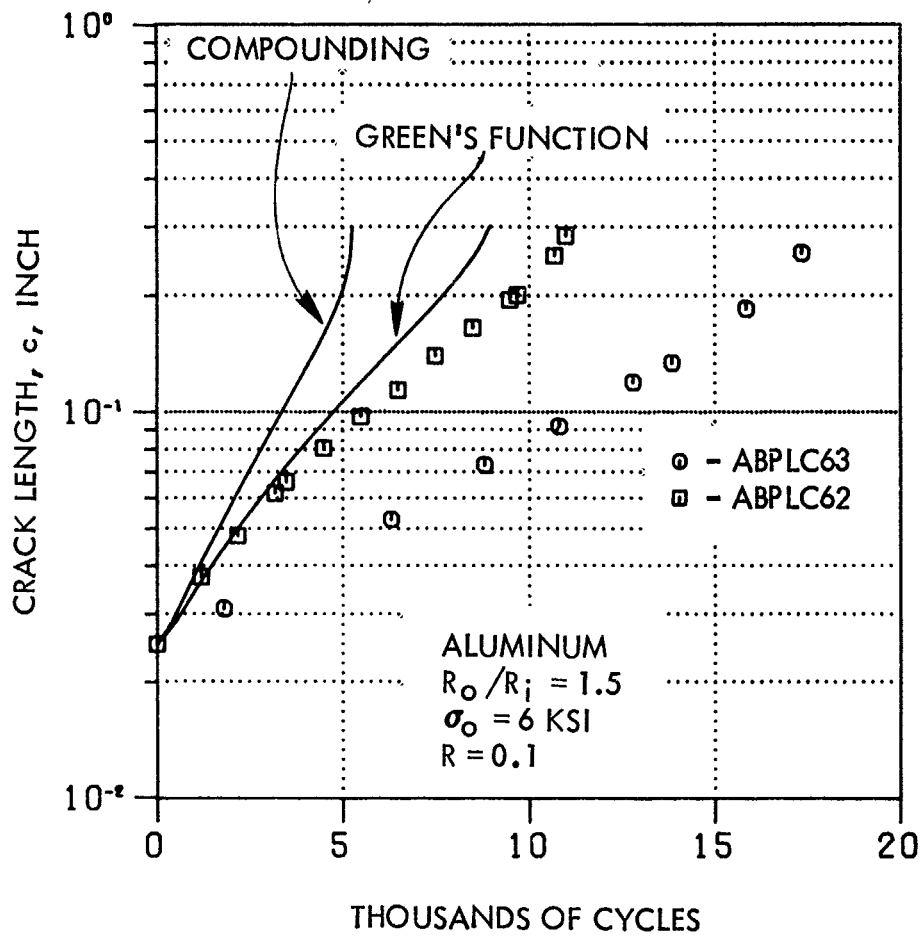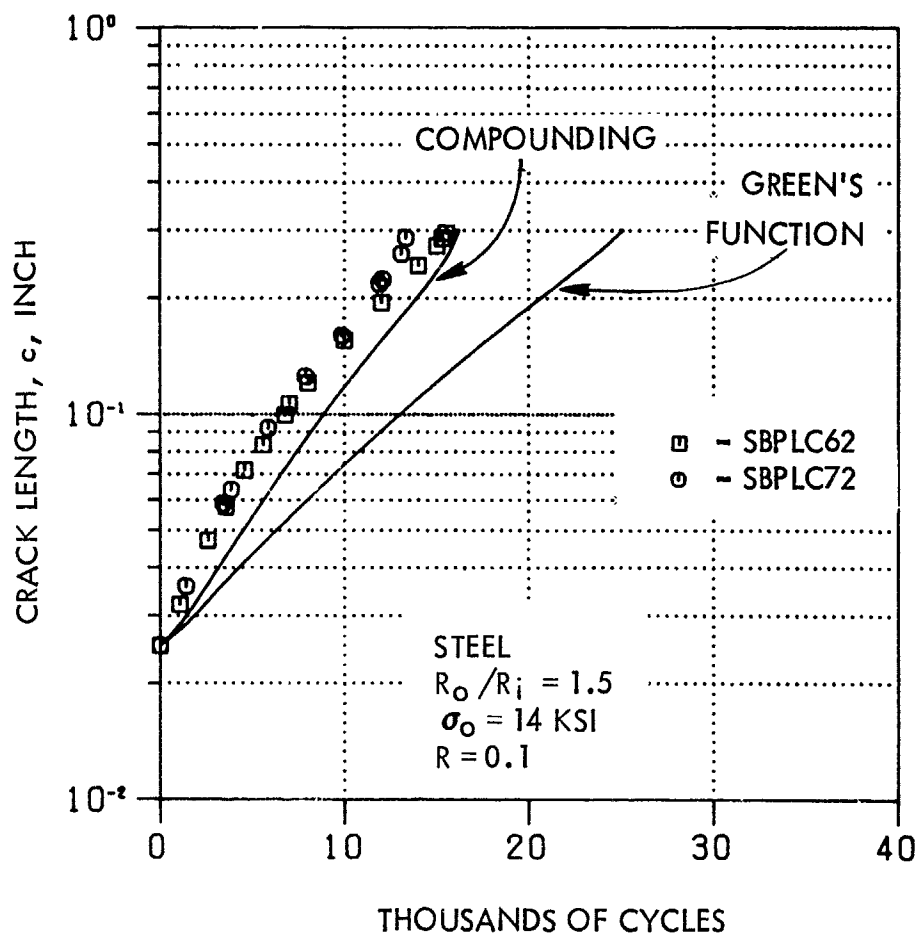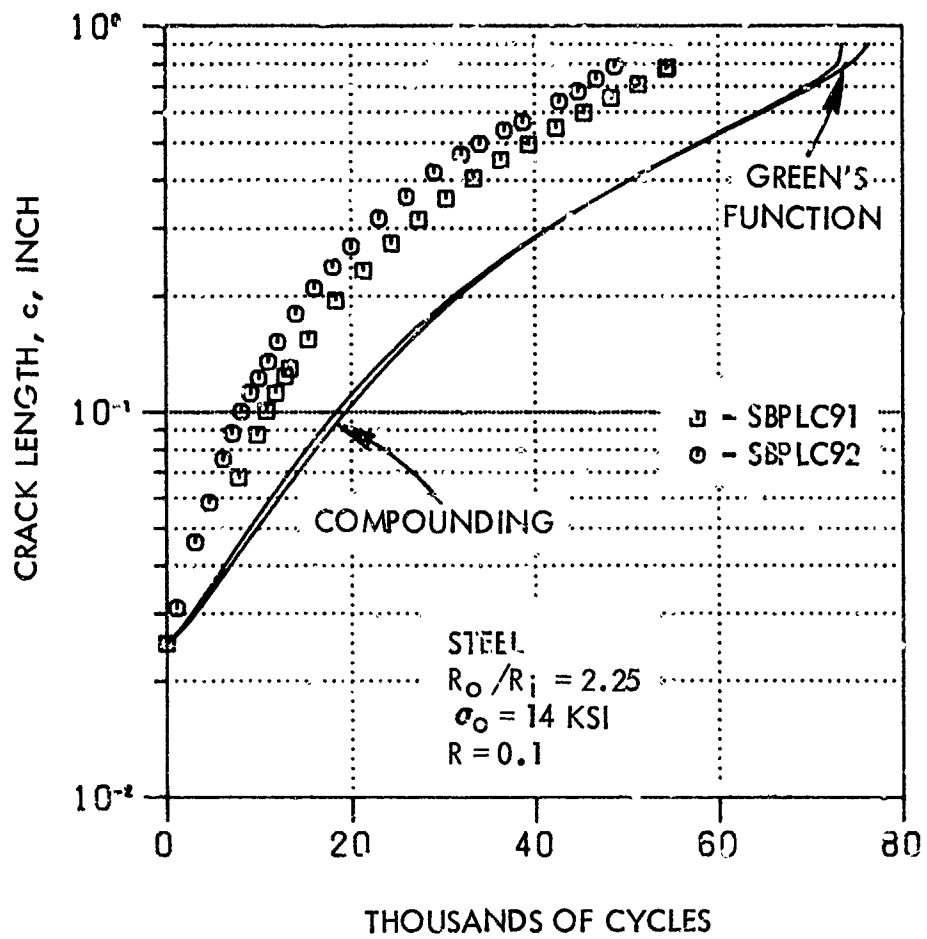
Figure 5-7.   Through-the-Thickness Crack Growth Data and Prediction,
Aluminum Lug, $R_o/R_i = 1.5$, $\sigma_o = 6$ ksi, R=0.1
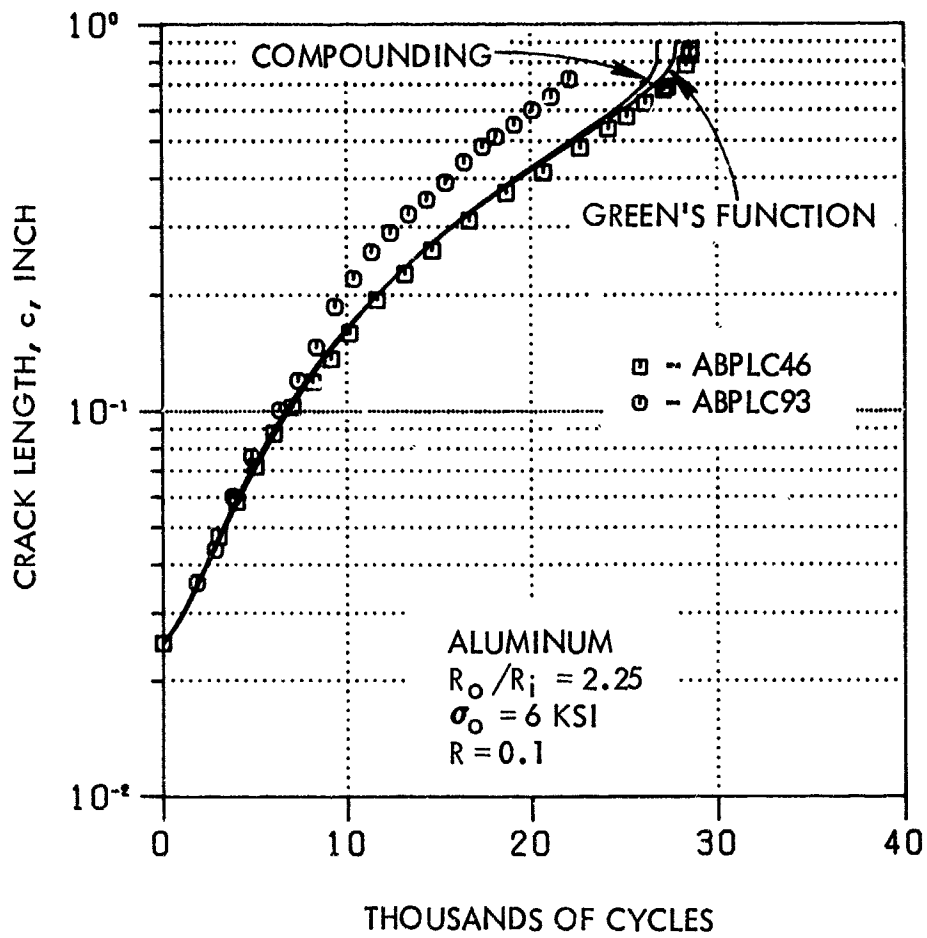
Figure 5-8. Through-the-Thickness Crack Growth Data and Prediction,
Aluminum Lug, R_o/R_i=2.25, σ_o=6 ksi, R=0.1

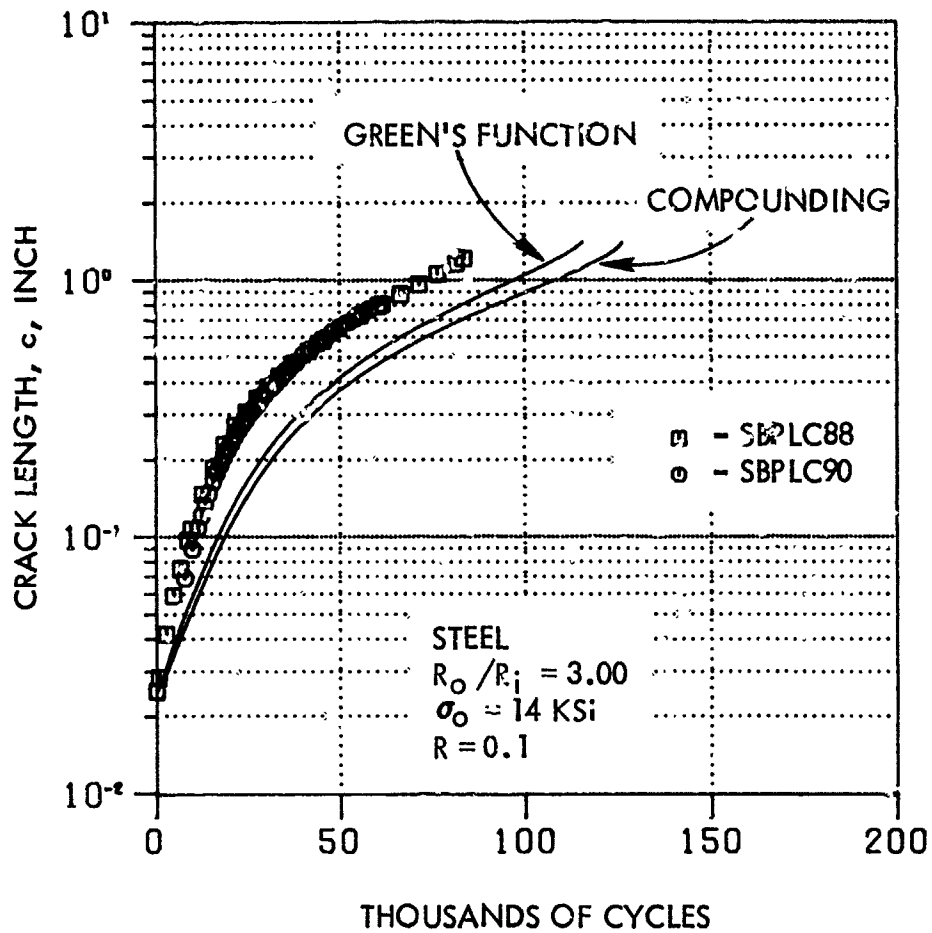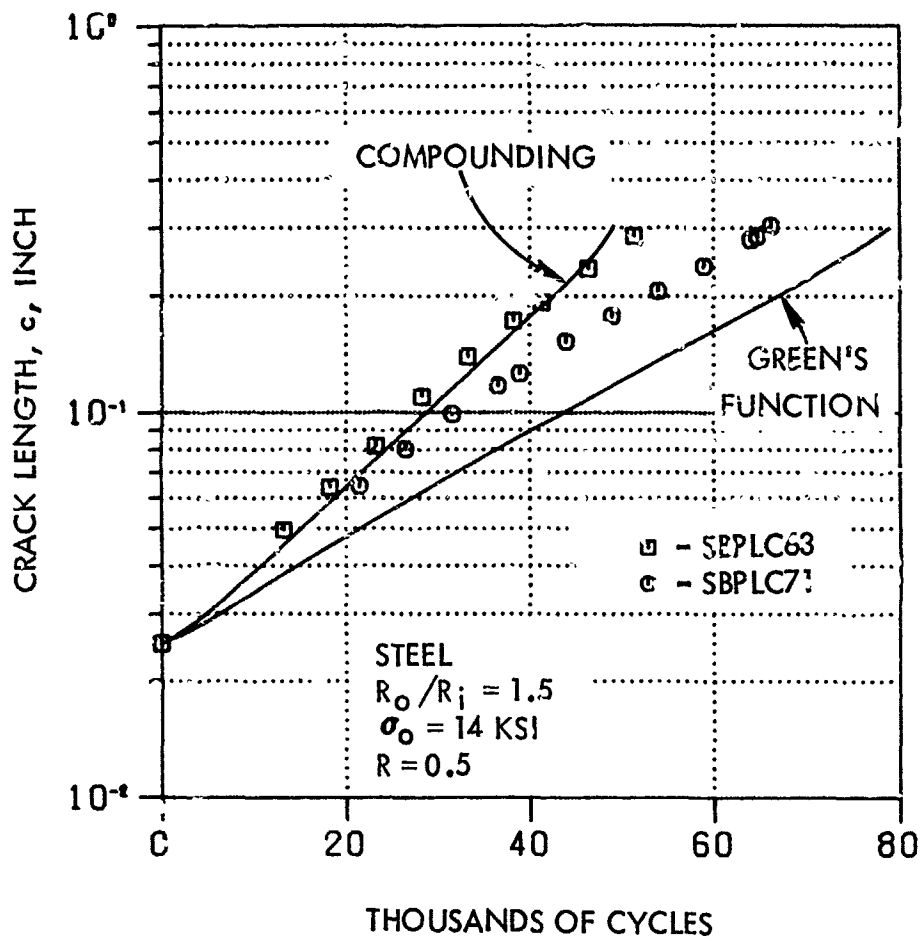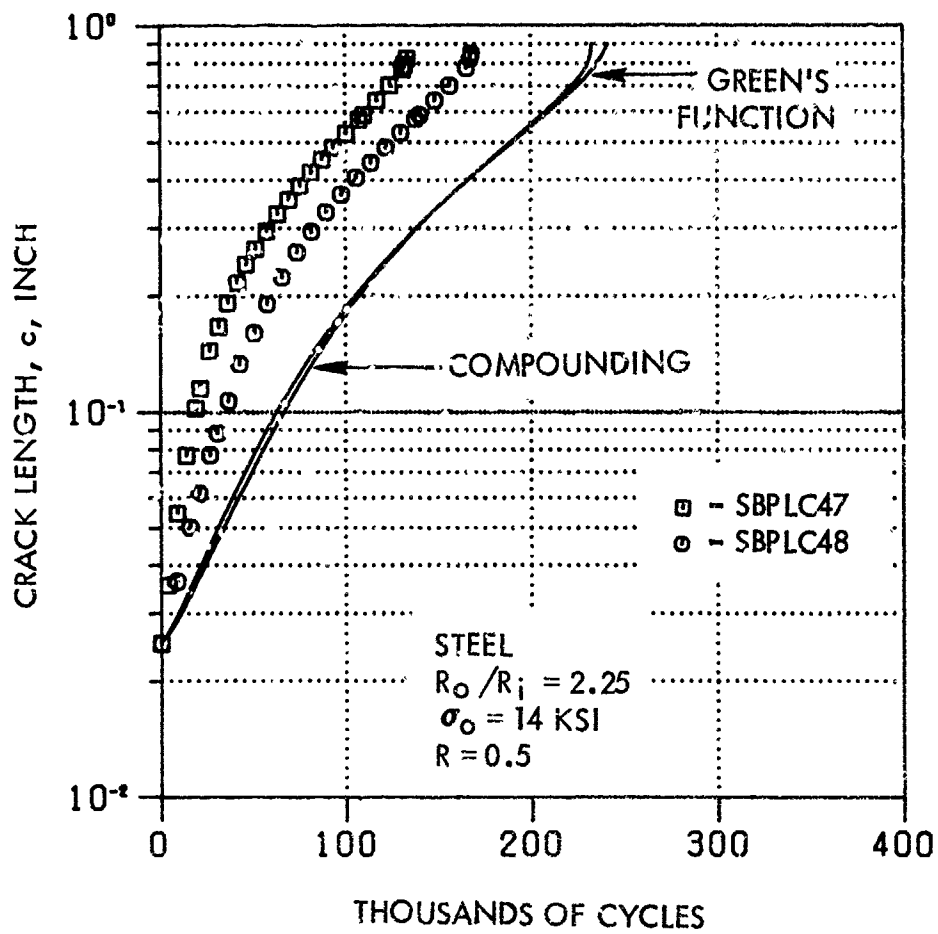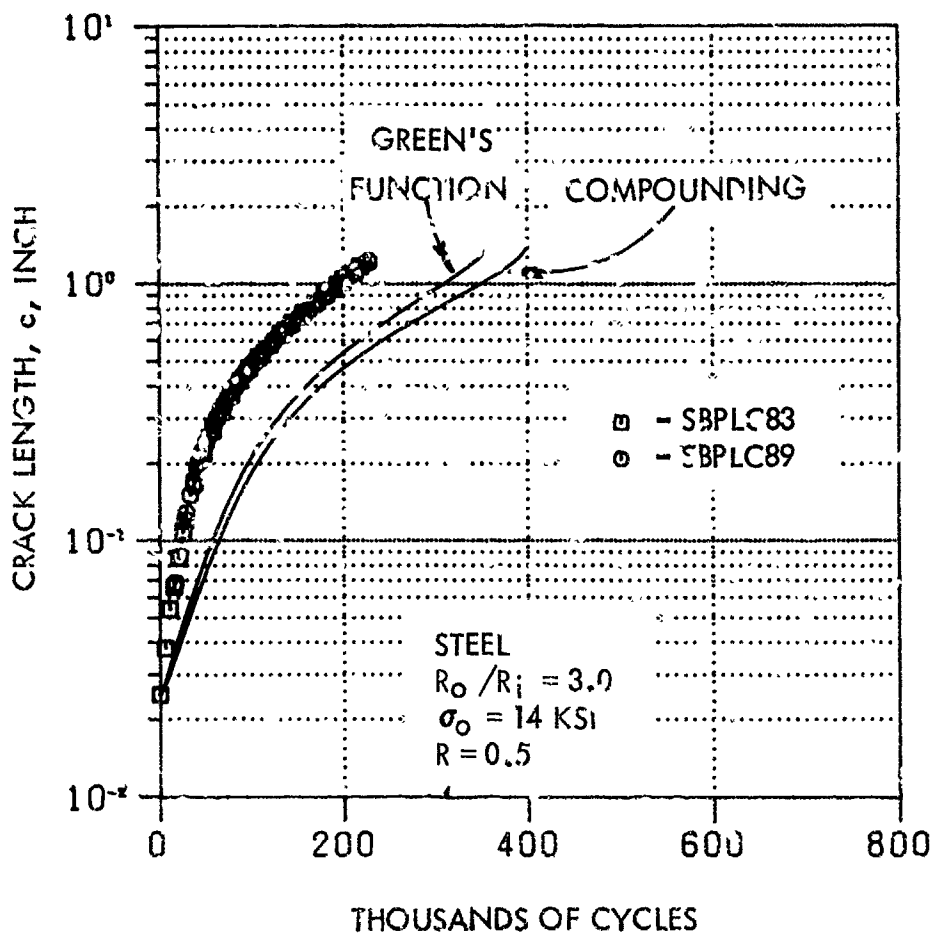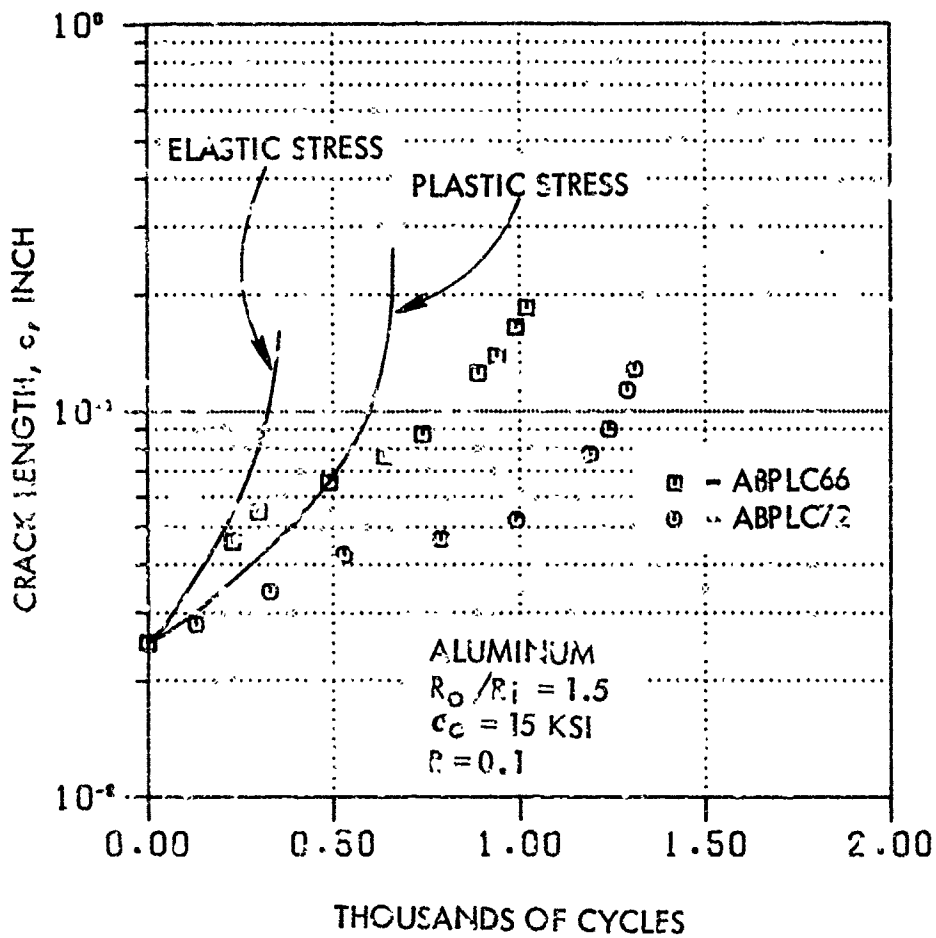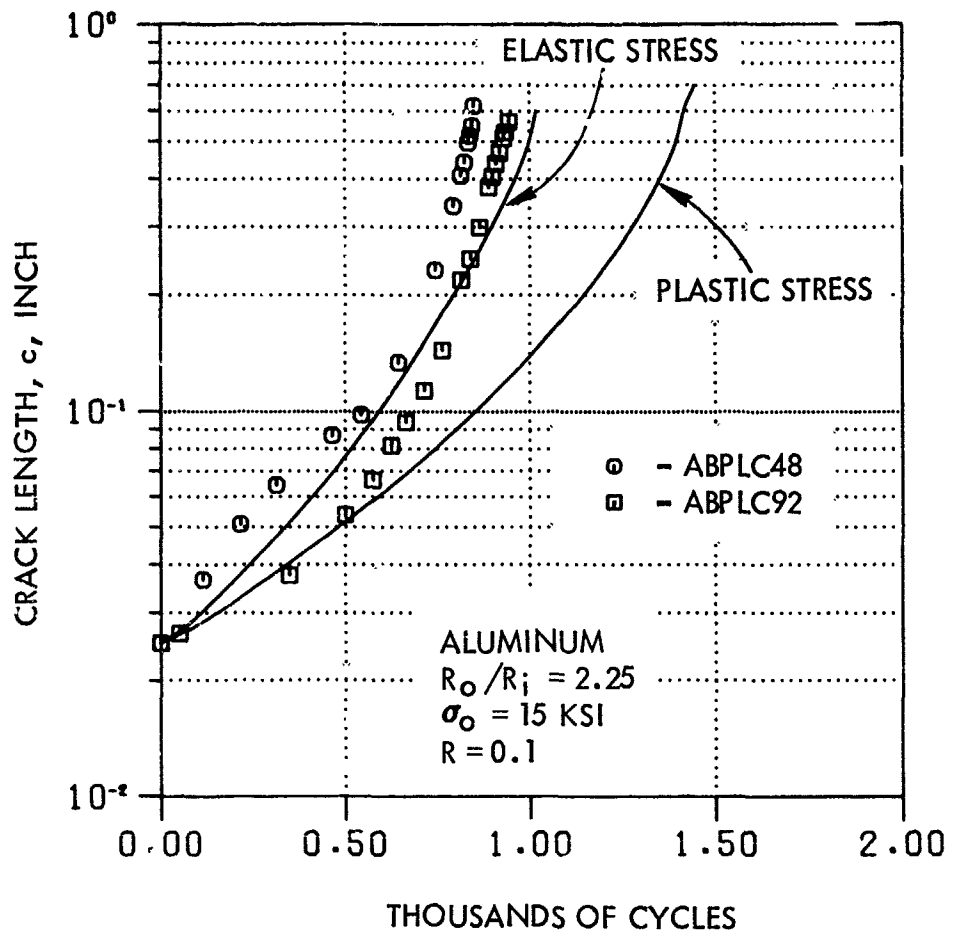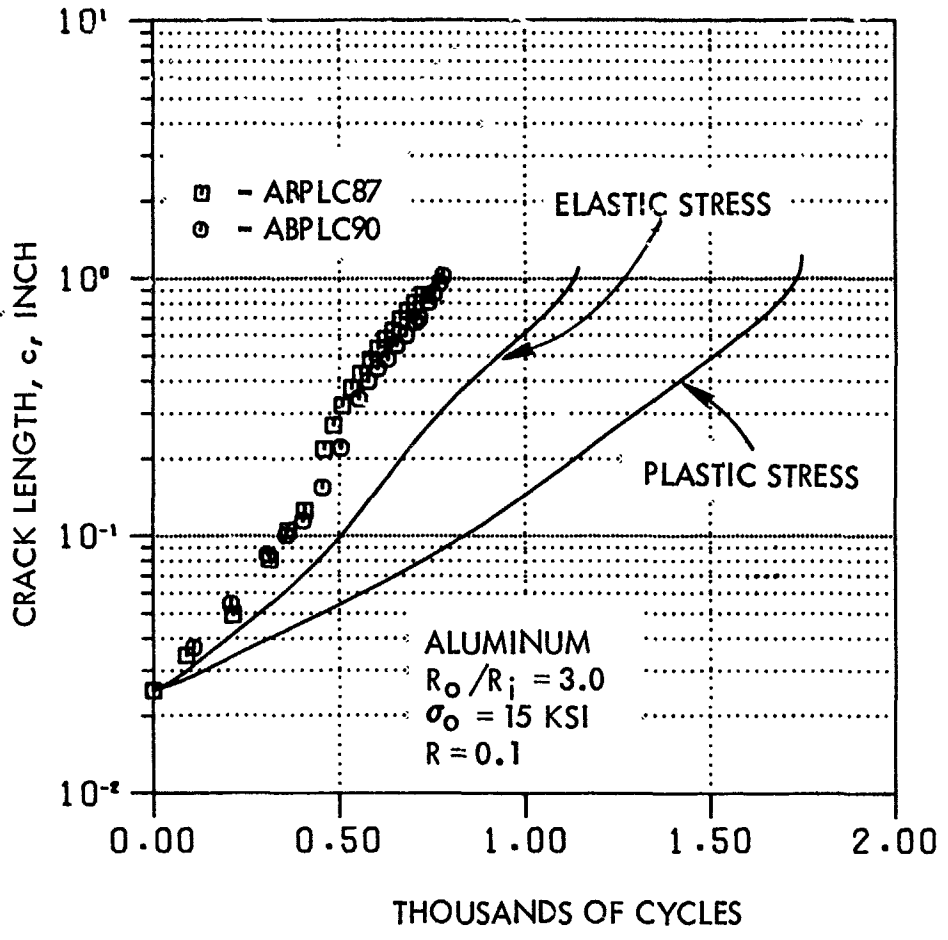Figure 5-9. Through-the-Thickness Crack Growth Data and Prediction, Aluminum Lug, R_o/R_i=3.0, σ_o=6 KSI, R=0.1
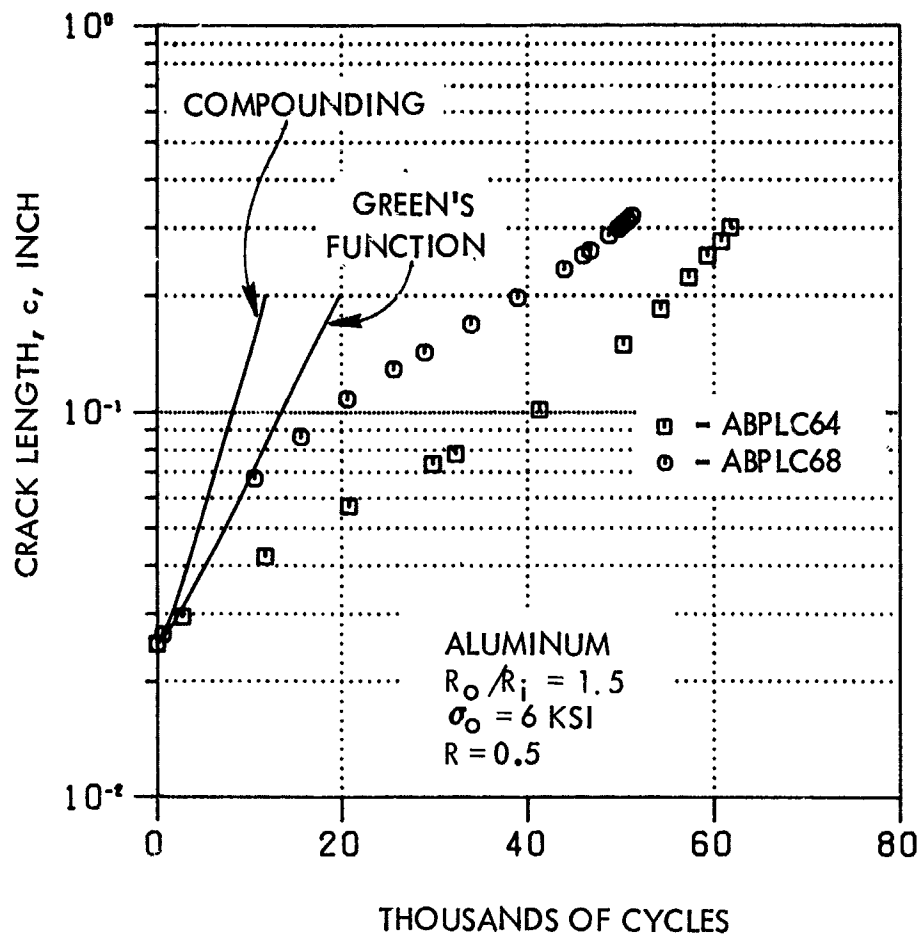
Figure 5-10. Through-the-Thickness Crack Growth Data and Prediction,
Aluminum Lug, R_o/R_i=1.5, σ_o=6 ksi, R=0.5

121
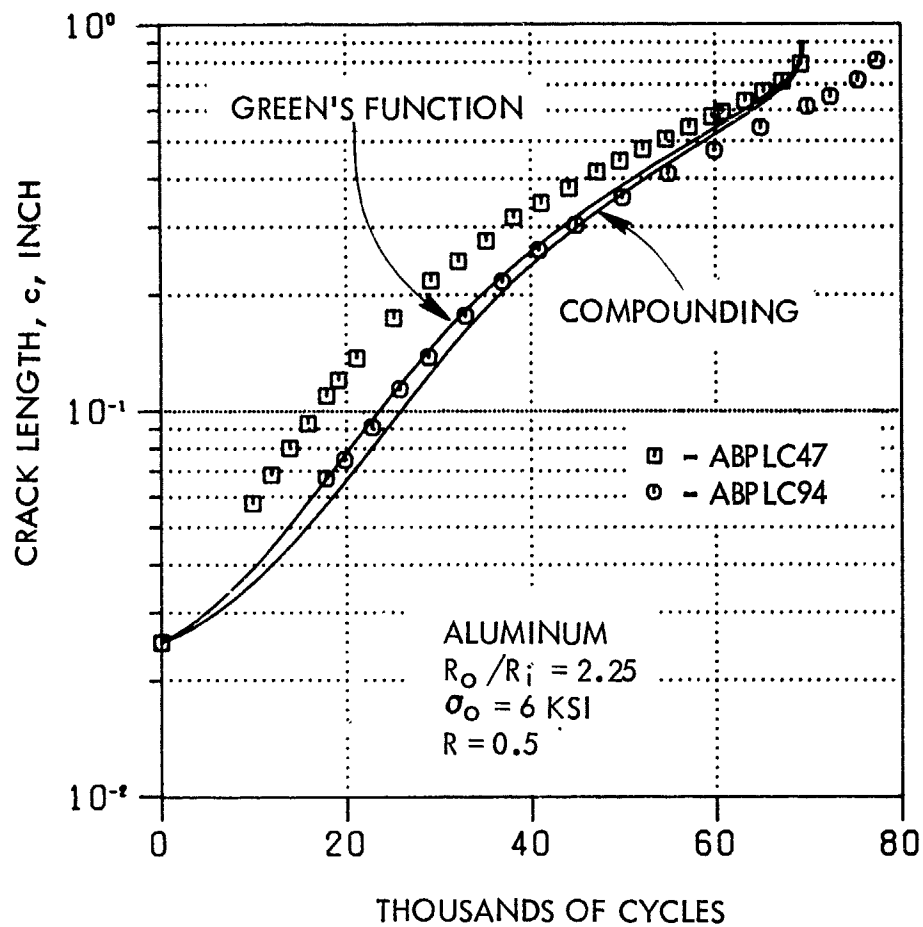
Figure 5-11. Through-the-Thickness Crack Growth Data and Prediction, Aluminum Lug, $R_o/R_i=2.25$, $\sigma_o=6$ ksi, R=0.5
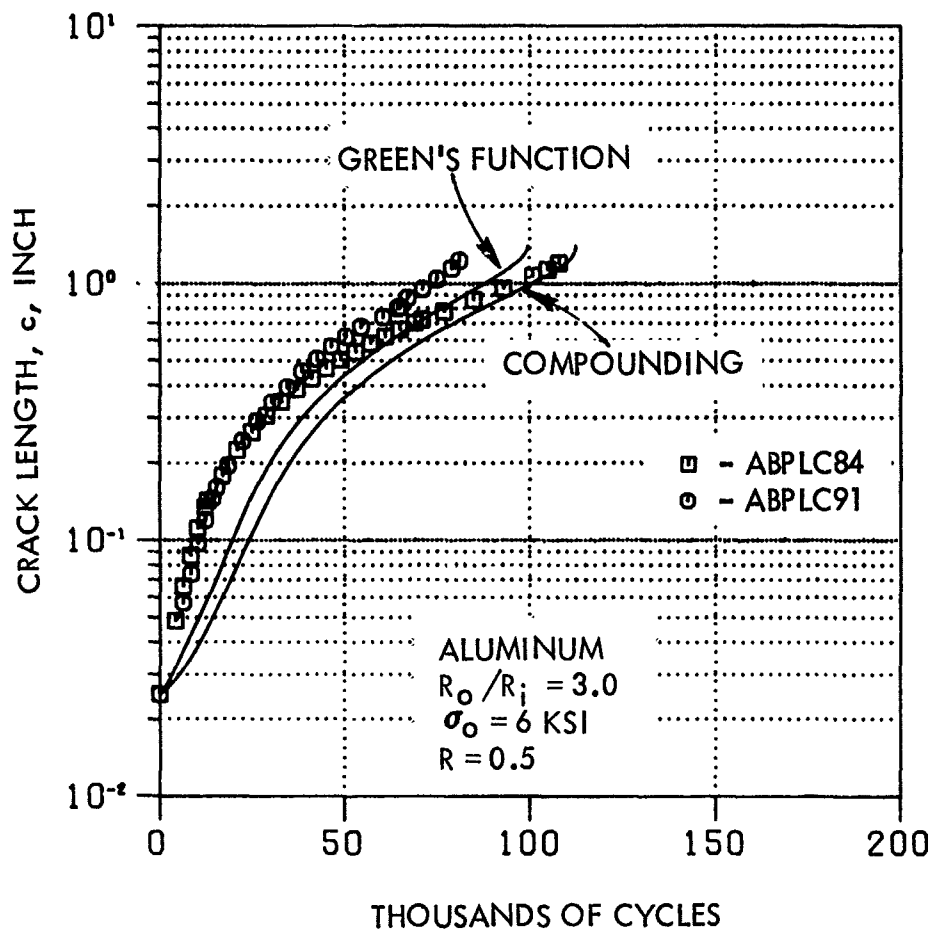
Figure 5-12. Through-the-Thickness Crack Growth Data and Prediction,
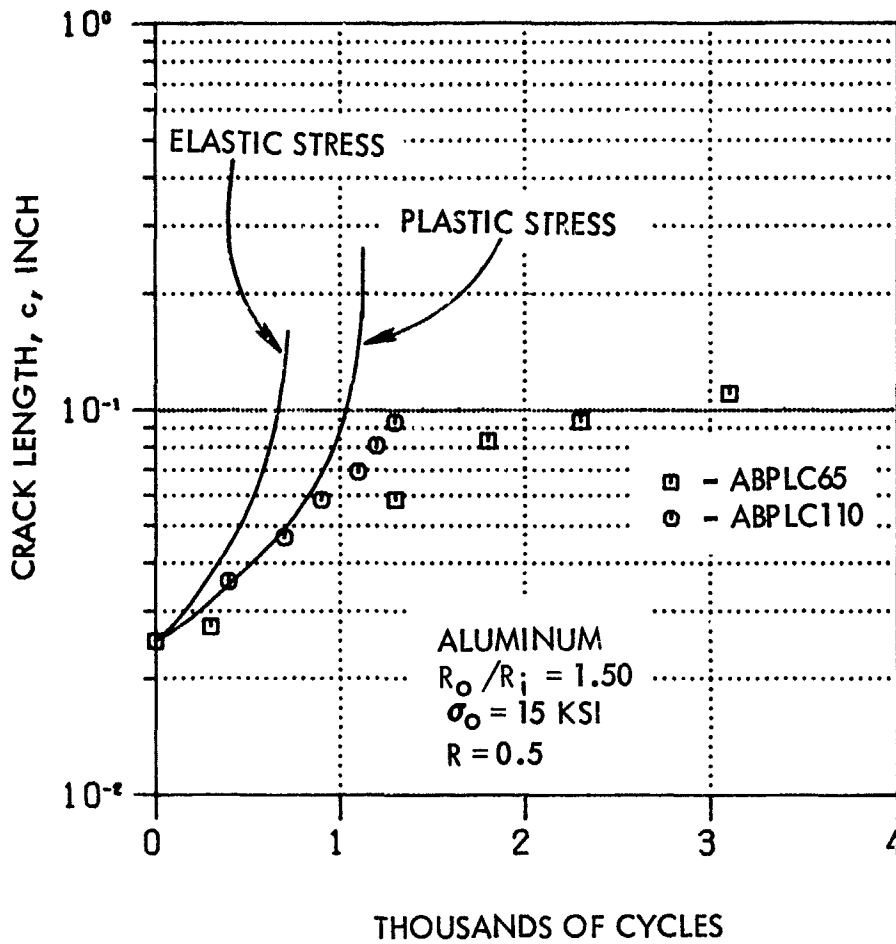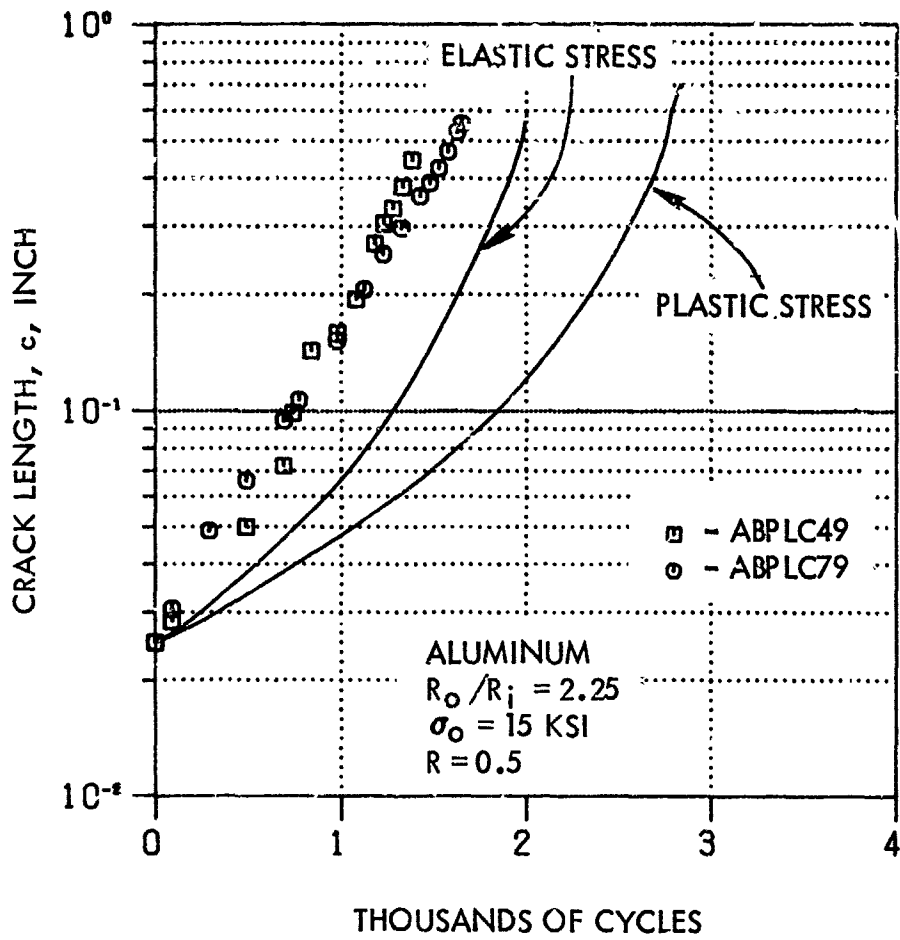Aluminum Lug, R_o/R_i=3.0, σ_o=6 ksi, R=0.5

Figure 5-13. Through-the-Thickness Crack Growth Data and Prediction, Steel Lug, R_o/R_i=1.5, σ_o=14 KSI, R=0.1

124

Figure 5-14. Through-the-Thickness Crack Growth Data and Prediction, Steel Lug, R_o/R_i=2.25, σ_o = 14 ksi, R=0.1

125

Figure 5-15. Through-the-Thickness Crack Growth Data and Prediction, Steel Lug, R_o/R_i=3.0, σ_o = 14 ksi, R=0.1

126

Figure 5-16. Through-the-Thickness Crack Growth Data and Prediction, Steel Lug, $R_o/R_i = 1.5$, $\sigma_o = 14$ ksi, R=0.5

Figure 5-17. Through-the-Thickness Crack Growth Data and Prediction, Steel Lug, $R_o/R_i = 2.25$, $\sigma_o = 14$ ksi, R=0.5
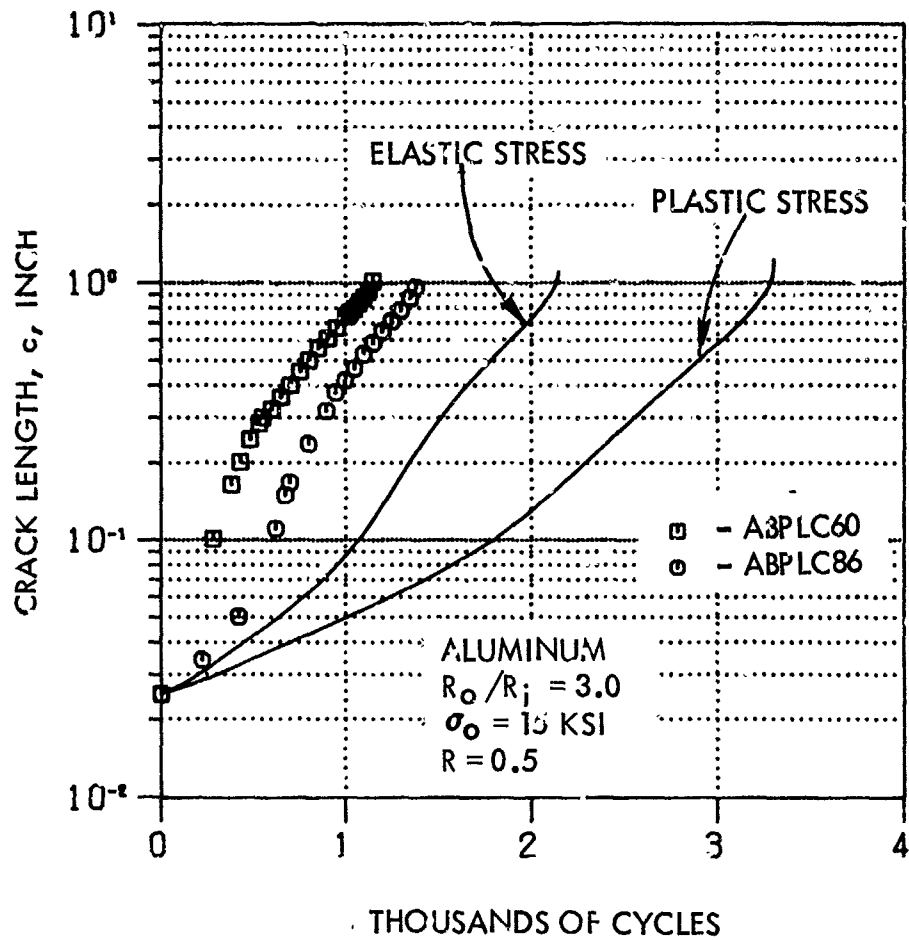
128

Figure 5-18. Through-the-Thickness Crack Growth Data and Prediction,
Steel Lug, $R_o/R_i = 3.0$, $\sigma_o = 14$ ksi, R=0.5

129

Figure 5-19. Through-the-Thickness Crack Growth Data and Prediction,
Aluminum Lug, $R_o/R_i = 1.5$, $\sigma_o = 15$ ksi, R=0.1

130

Figure 5-20. Through-the-Thickness Crack Growth Data and Prediction, Aluminum Lug. $R_o/R_i = 2.25$, $O_o = 15$ ksi, R=0.1

Figure 5–21. Through–the–Thickness Crack Growth Data and Prediction,
Aluminum Lug, R_o/R_i=3.00, σ_o = 15 ksi, R=0.1

132

Figure 5-22. Through-the-Thickness Crack Growth Data and Prediction, Aluminum Lug, $R_o/R_i=1.5$, $\sigma_o = 15$ ksi, R=0.5

Figure 5-23. Through-the-Thickness Crack Growth Data and Prediction, Aluminum Lug, $R_o/R_i=2.25$, $\sigma_o = 15$ ksi, R=0.5

134

Figure 5-24. Through-the-Thickness Crack Growth Data and Prediction, Aluminum Lug, $R_o/R_i = 3.0$, $\sigma_o = 15$ ksi, R=0.5

135

the results are presented in these figures. In the case of aluminum lugs with R_o/R_i = 2.25 and 3.0 and subjected to σ_o = 6 ksi, the analytical predictions are in close agreement with those of the experiments. For aluminum lugs with R_o/R_i = 1.50, the predictions are unconservative by a factor of about 2. These lugs have smaller net-sections, and their flexibility relative to the steel loading pins, may have resulted in large, geometrically nonlinear deformations of the lugs. Such large deformations will result in unconservative life predictions, since linear analysis, in general, will overestimate stresses (and stress intensity factors) when compared with geometric nonlinear analysis. Predictions by the Green's function method and the compounding method are in close agreement for R_o/R_i ratios of 2.25 and 3.0. However, the compounding method differs significantly from that of the Green's function method and predicts conservative results for the lower R_o/R_i ratio of 1.5. Discussion on attempts to improve the compounding method was presented in subsection 3.1.2 of Section IV. In the case of steel lugs subjected to σ_o = 14 ksi, the analytical-experimental correlations are similar to those of aluminum lugs. However, the predictions are slightly unconservative, probably because the effect of loading pin-to-lug rigidity ratio, E_{pin}/E_{lug}, was not represented in the analysis. Limited analysis reported in Reference [2], showed that the steel lug loaded by a steel pin (E_{pin}/E_{lug} = 1.0) experiences slightly higher stresses and stress intensity factors than an aluminum lug loaded by a steel pin (E_{pin}/E_{lug} = 3.0). In all the results presented in this report, stresses and stress intensity factors correspond to an E_{pin}/E_{lug} ratio of 3.0.

The next set of results (Figures 5-19 through 5-24) correspond to aluminum lugs subjected to high far-field gross constant-amplitude stress levels of 15 ksi. Predictions for these cases were made using only the Green's function method, but using two types of stress distributions. First, the stress distributions obtained from the elasto-plastic (labeled "plastic" in figures) stress analysis were used. The stress distributions obtained from elastic analysis were used for the second set of predictions. Plastic stress predictions were conservative for the R_o/R_i ratio of 1.5, and unconservative for R_o/R_i ratios of 2.25 and 3.0. Even the elastic stress predictions, which yielded excellent correlations for low loads (6

ksi), were unconservative for R_o/R_i ratios of 2.25 and 3.0. Note also that the crack growth life increases as the R_o/R_i ratio decreases, contrary to the results at lower load levels. Both the analyses fail to predict this trend.

Thus, both the analyses are inaccurate when the lugs are loaded above the yield strength of the material. The primary reason for this phenomenon may be that the plastic yielding of the crack tip is excessive. To explain the phenomenon and to make better life predictions, one may have to develop and use a special plastic crack-tip finite element embedding the well-known Hutchinson-Rice-Rosengren (HRR) or other similar type singularity. No such effort was made in the present program.

In the elasto-plastic stress analysis, the monotonic stress-strain data obtained from baseline material characterization tests were used. The correlations might have been improved by using cyclic strain-strain data, but none were generated in this program.

Note that the experimental data scatter in the aluminum lugs at both stress levels, 6 and 15 ksi, is very minimal for R_o/R_i ratios of 2.25 and 3.0, but is larger for the R_o/R_i ratio of 1.5. This may be due to the fact that these smaller lugs have high stress concentrations, which may make them very sensitive to parameteric variations; for example, the loading pin-lug clearance.

4.1.2 Corner Crack Constant-Amplitude Tests

Next, the results of all the corner crack growth test specimens subjected to constant-amplitude loading are presented in Figures 5-25 through 5-48. The first four figures (Figures 5-25 through 5-28) are for aluminum lugs subjected to a far-field gross stress, σ_o, of 6 ksi and a stress ratio, R, of 0.1. The next four figures (Figures 5-29 through 5-32) are for σ_o = 6 ksi and R = 0.5. Among the sets of four figures, the first three figures correspond to crack growth data. In the fourth figure, analytically predicted and experimentally observed crack aspect ratios (a/c) are presented as a function of front surface crack length, c, for the preceding three sets of results. Following these eight figures for aluminum lugs with σ_o = 6 ksi are eight similar figures for steel lugs
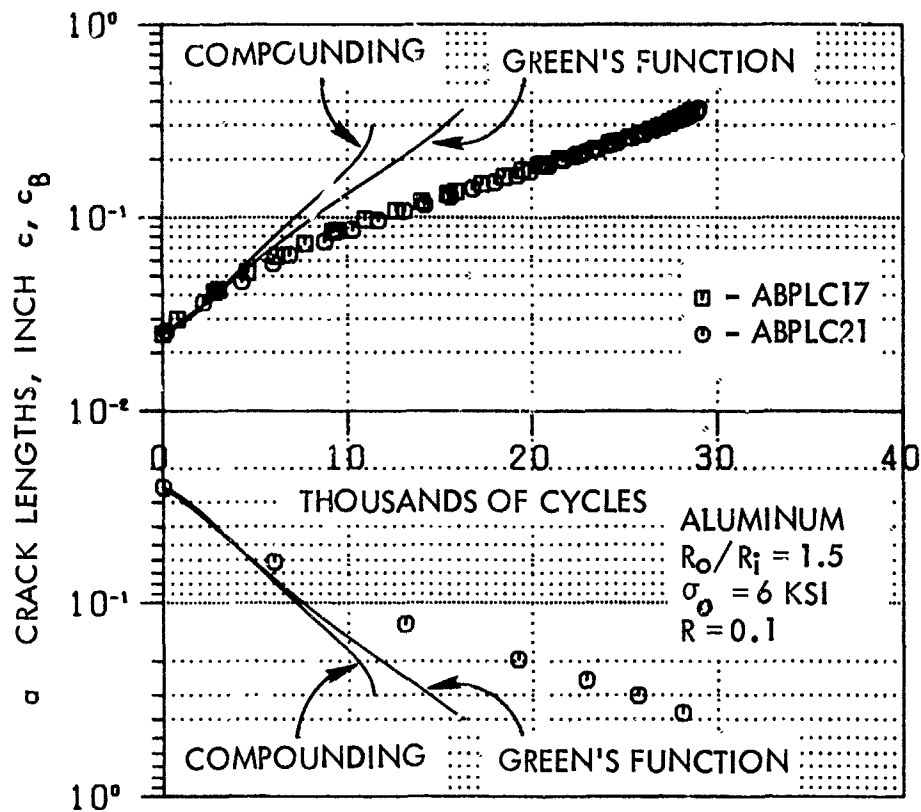
Figure 5-25. Corner Crack Growth Data and Prediction,
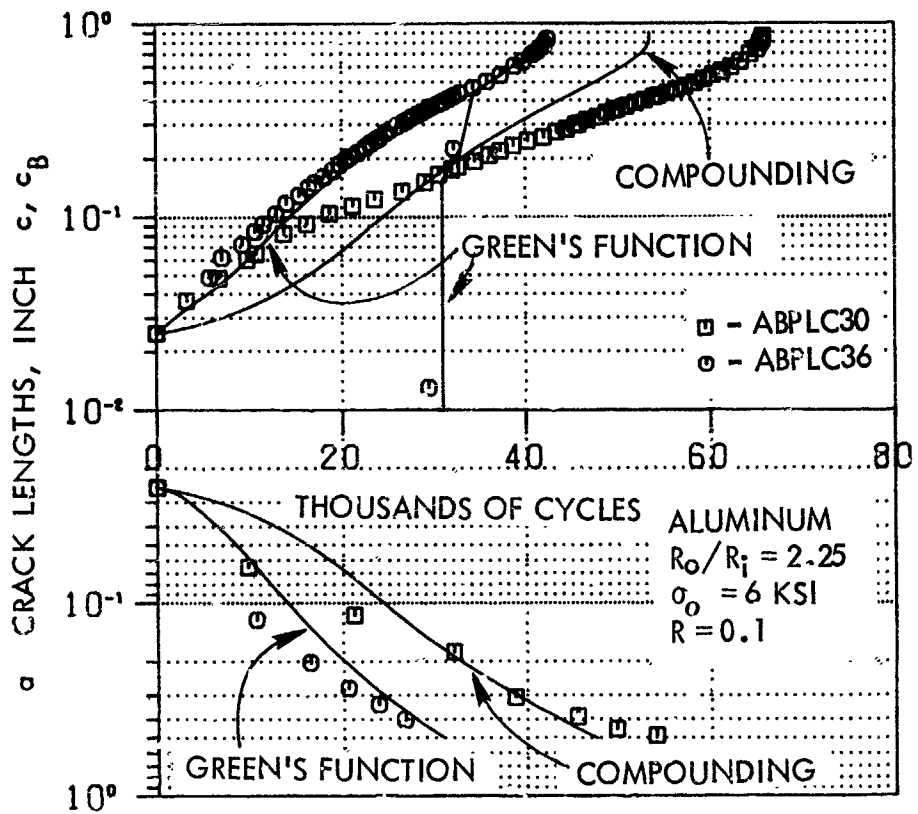Aluminum Lug, R_o/R_i=1.5, σ_o=6 KSI, R=0.1

Figure 5-26. Corner Crack Growth Data and Prediction,
Aluminum Lugs, $k_o/R_i=2.25$, $\sigma_o=6$ KSI, R=0.1

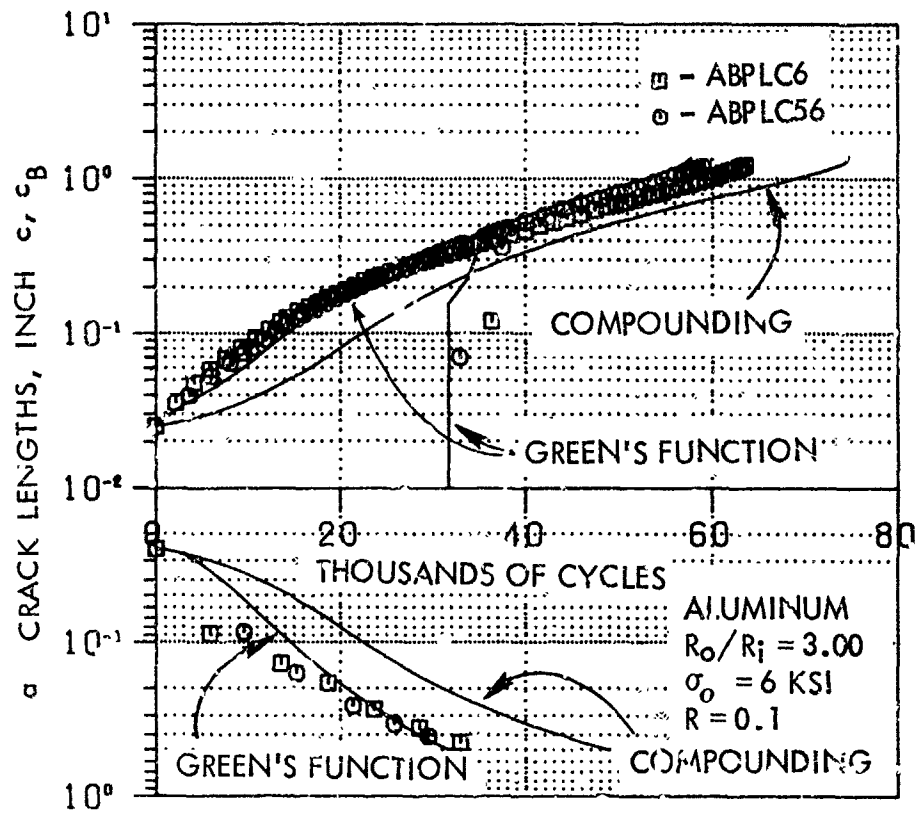Figure 5-27. Corner Crack Growth Data and Prediction,
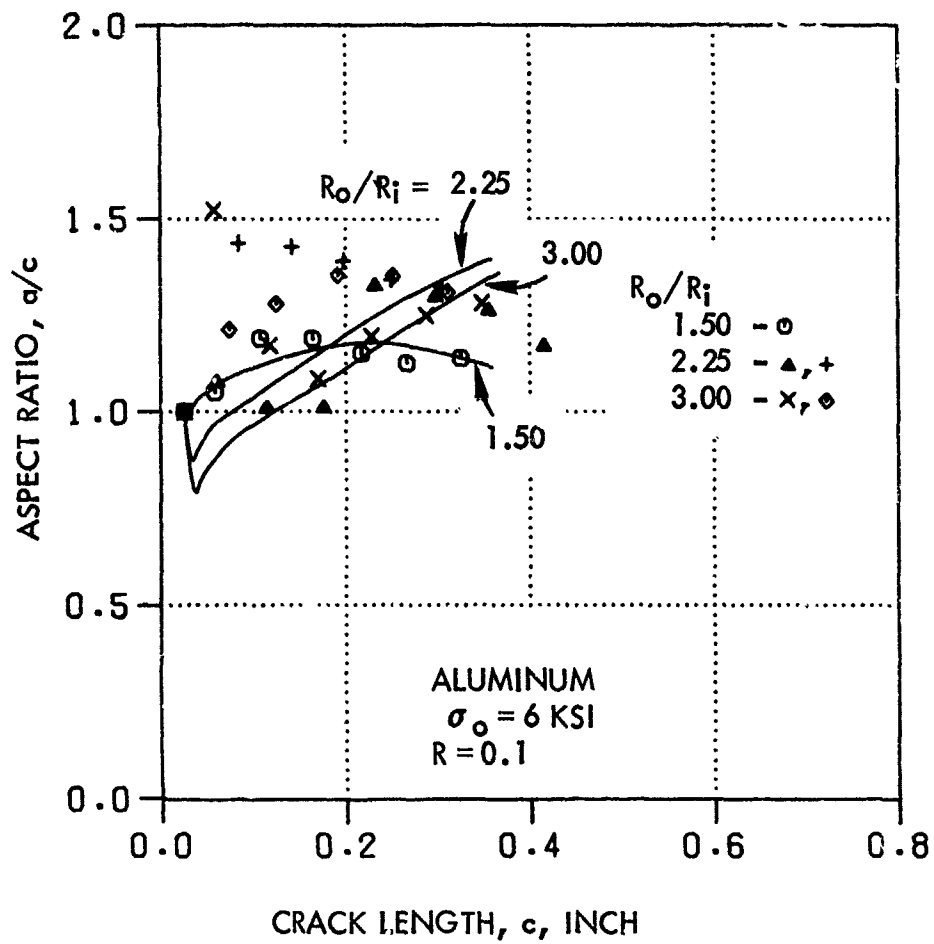Aluminum Lug, $R_o/R_i = 3.0$, $\sigma_o = 6$ KSI, R=0.1

Figure 5-28.   Corner Crack Aspect Ratio Data and Prediction,
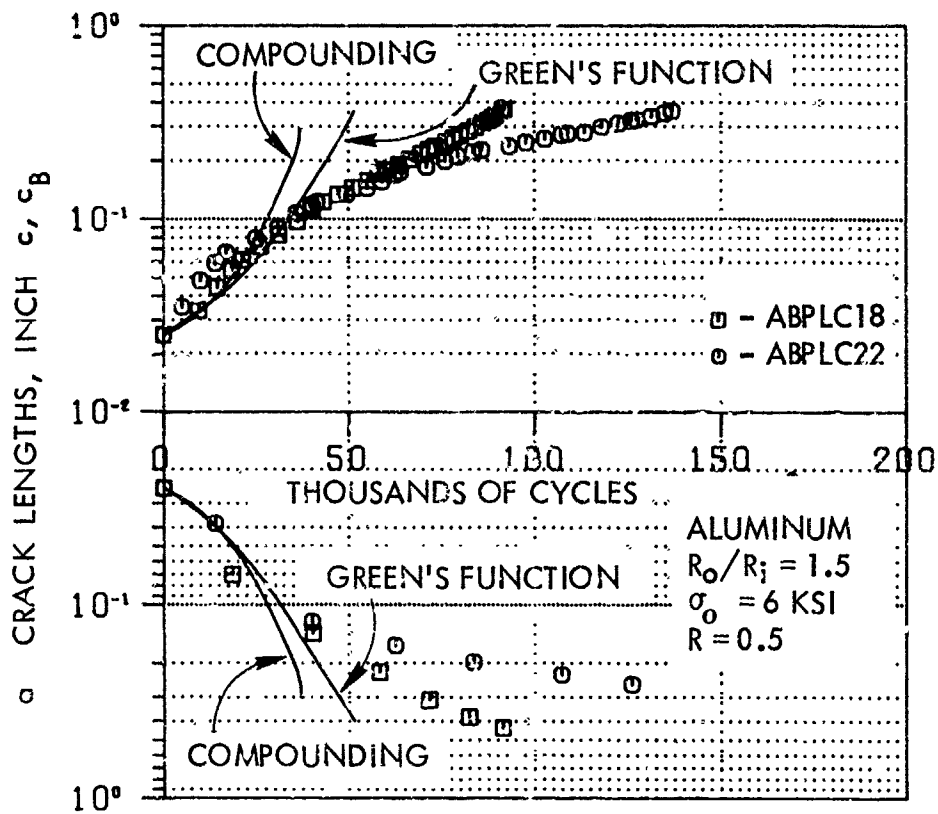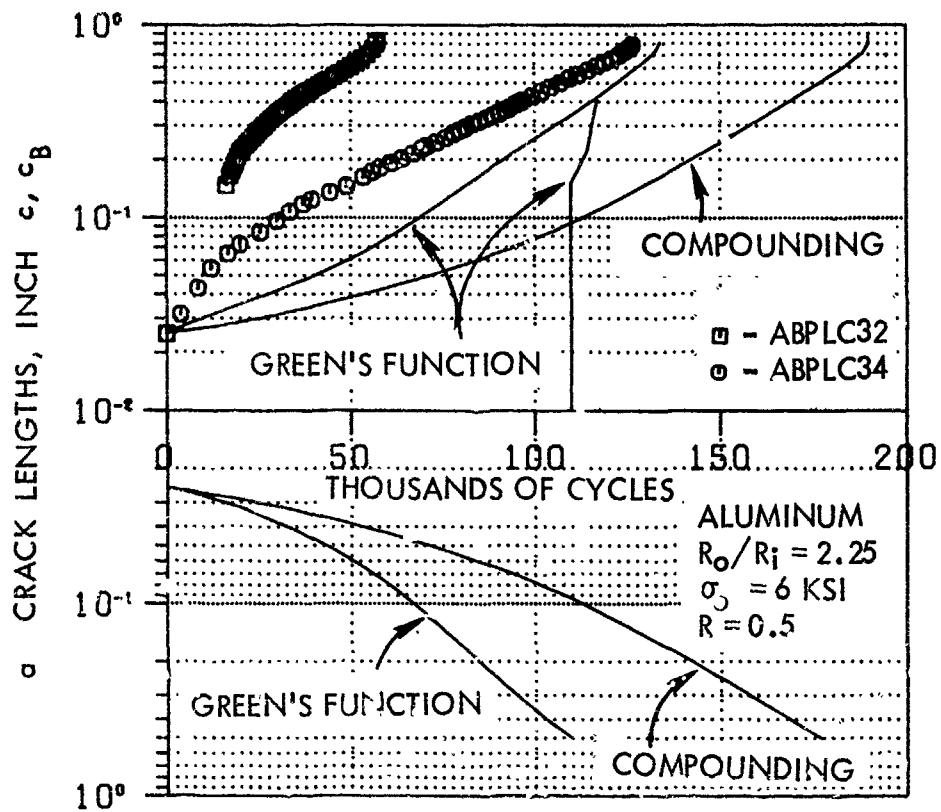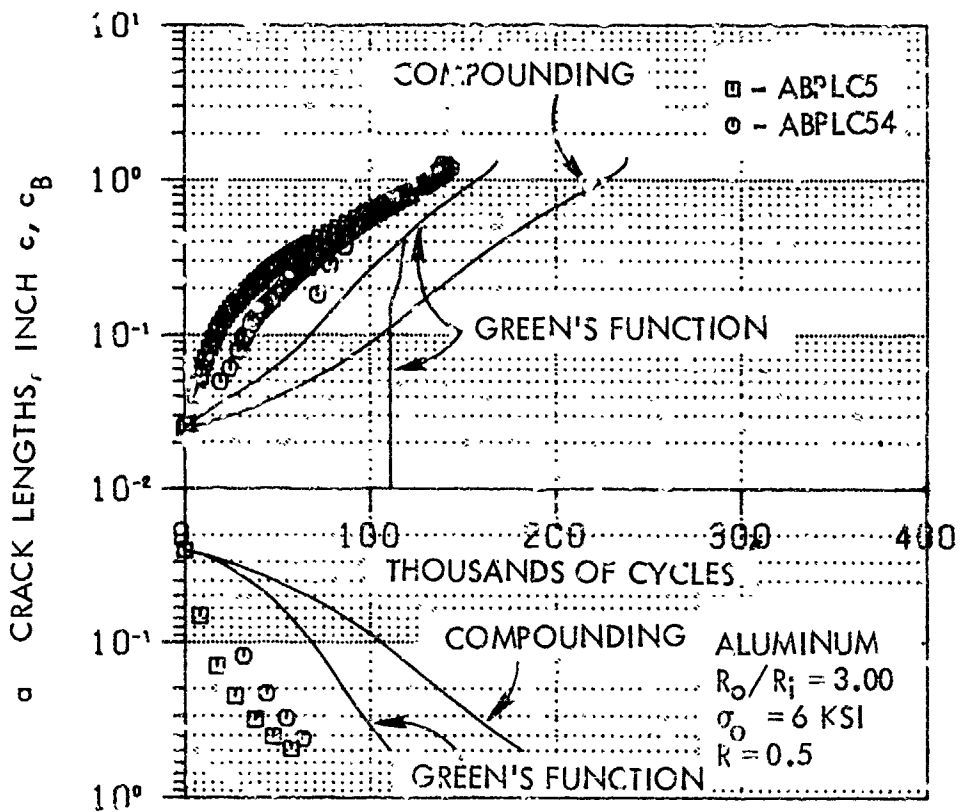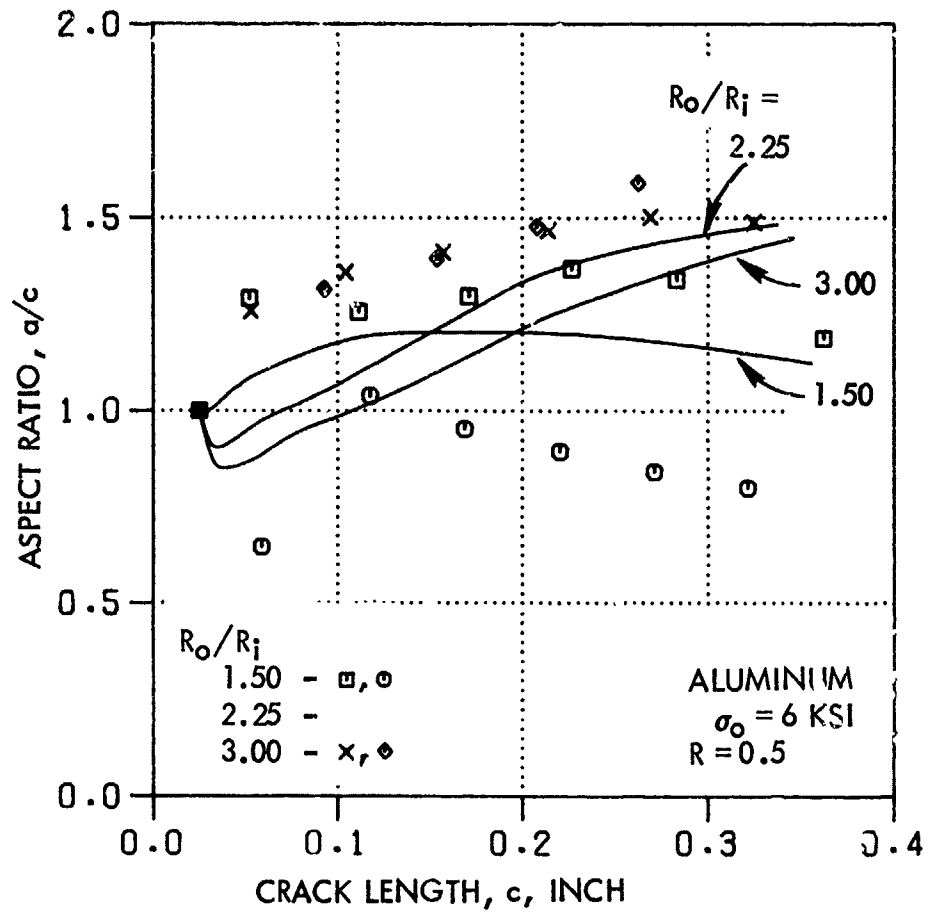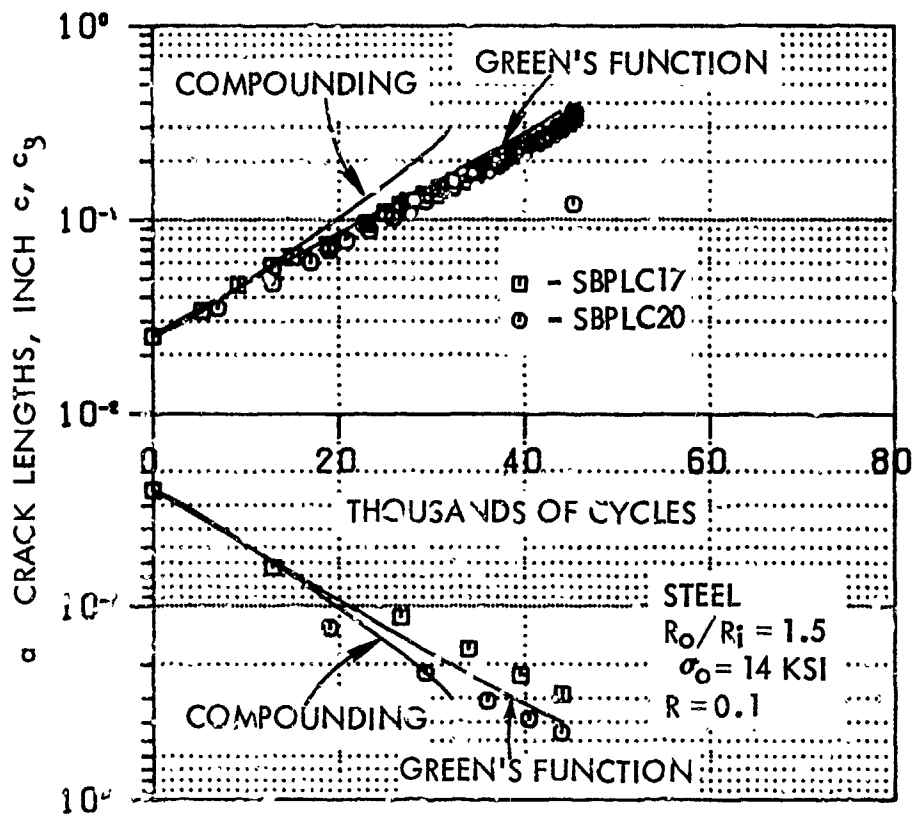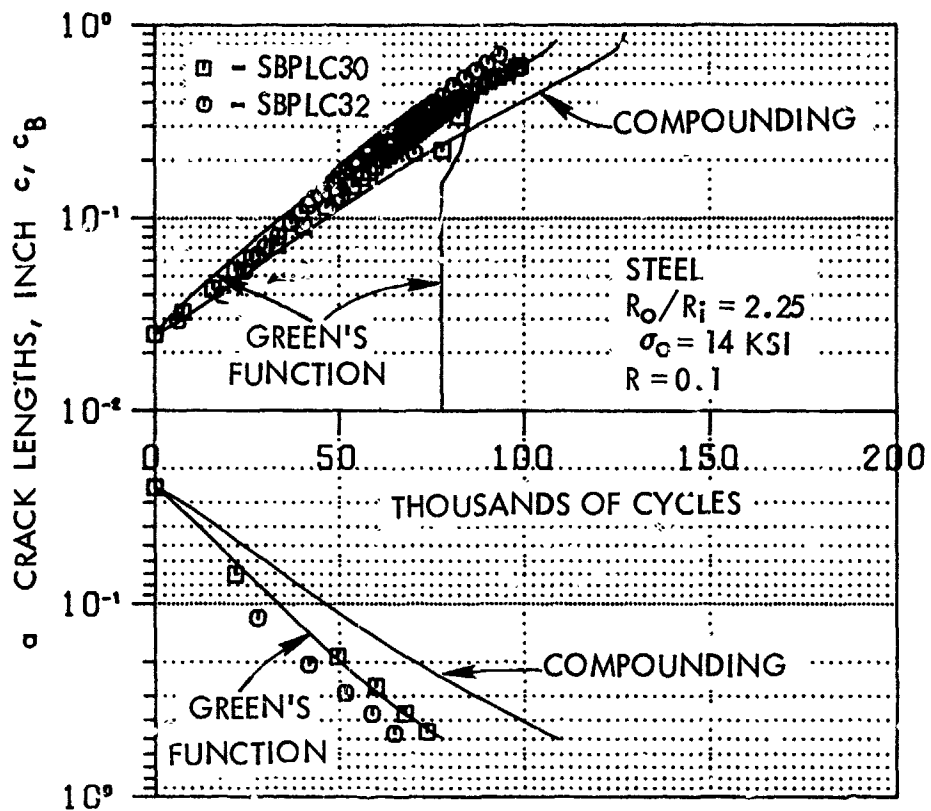Aluminum Lug, σ_o=6 KSI, R=0.1

Figure 5-29. Corner Crack Growth Data and Prediction, Aluminum Lug, $R_o/R_i=1.5$, $\sigma_o=6$ KSI, R=0.5

Figure 5-30. Corner Crack Growth Data and Prediction,
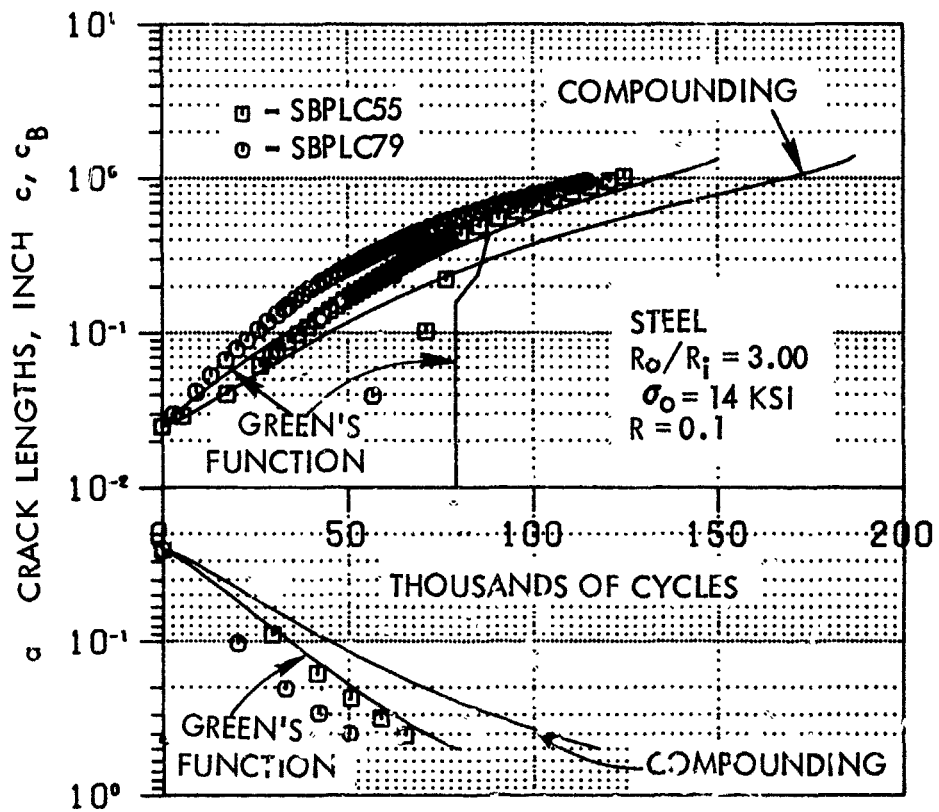Aluminum Lug, R_o/R_i=2.25, σ_o=6 KSI, R=0.5

Figure 5-31. Corner Crack Growth Data and Prediction, Aluminum Lug, $R_o/R_i=3.0$, $\sigma_o=6$ KSI, R=0.5

144
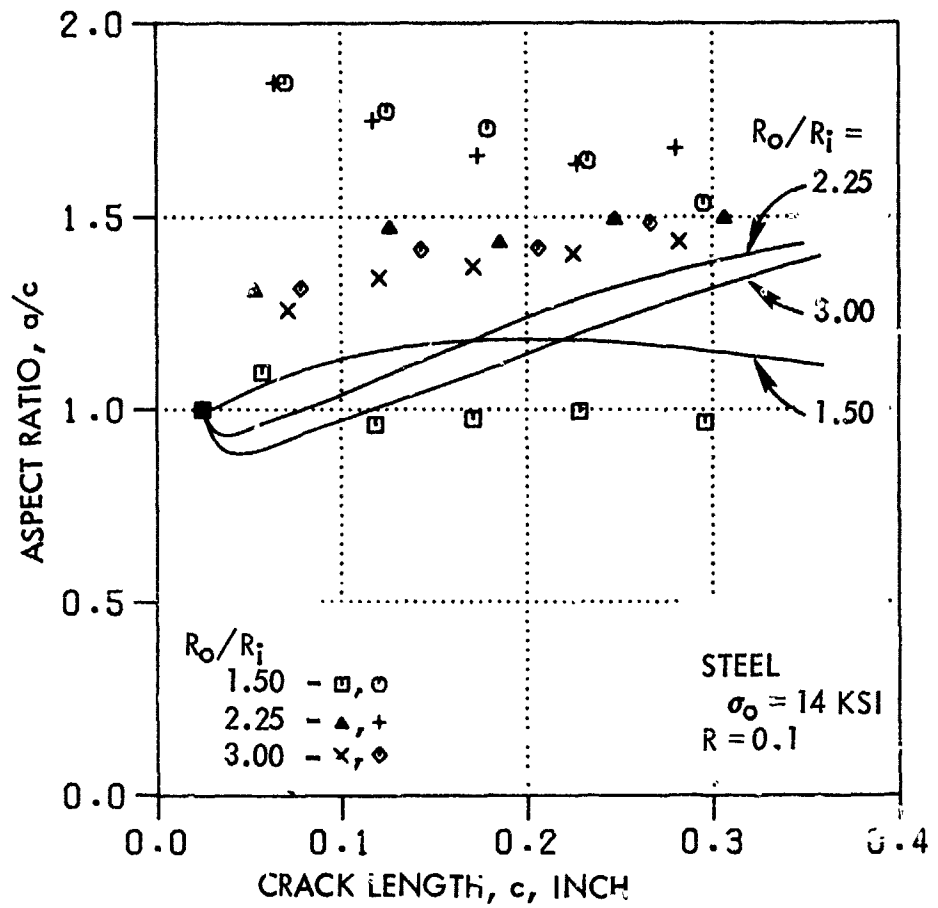
Figure 5-32. Corner Crack Aspect Ratio Data and Prediction,
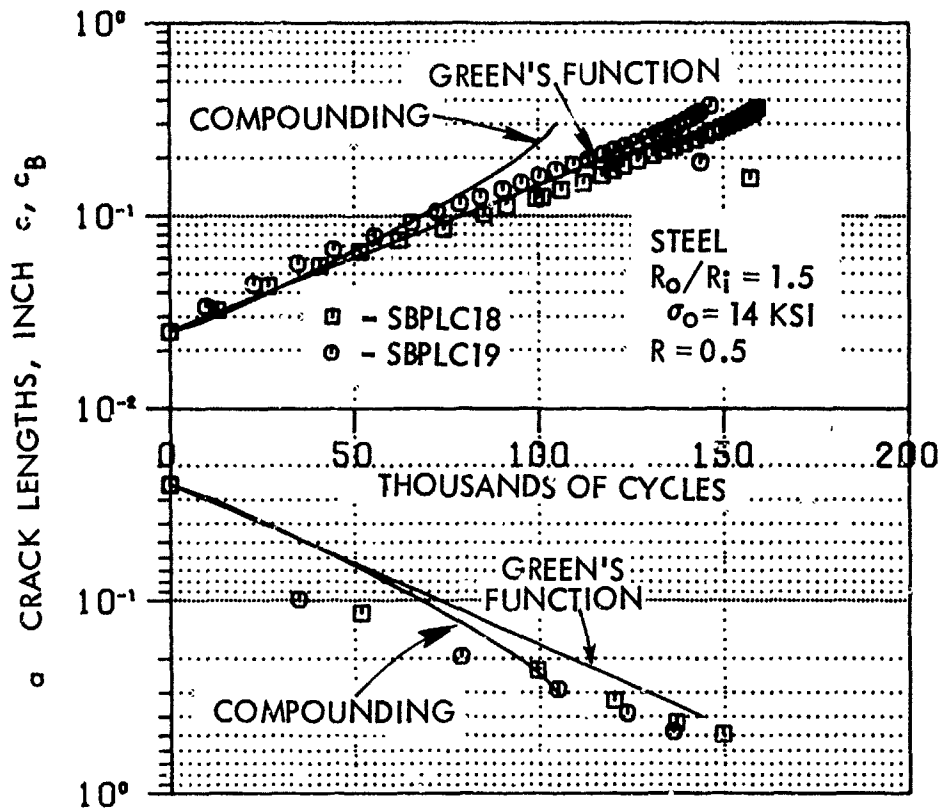Aluminum Lug, σ_o=6 KSI, R=0.5

Figure 5-33. Corner Crack Growth Data and Prediction, Steel Lug, $R_o/R_i = 1.5$, $\sigma_o = 14$ KSI, R=0.1

Figure 5-34. Corner Crack Growth Data arⅆ Prediction,
Steel Lug, $R_o/R_i=2.25$, σ_o ＝14 KSI, R=0.1

Figure 5-35. Corner Crack Growth Data and Prediction,
Steel Lug, R_o/R_i=3.0. σ_o=14 KSI, R=0.1

148

Figure 5-36. Corner Crack Aspect Ratio Data and Prediction,
Steel Lug, σ_o=14 KSI, R=0.1

Figure 5-37. Corner Crack Growth Data and Prediction,
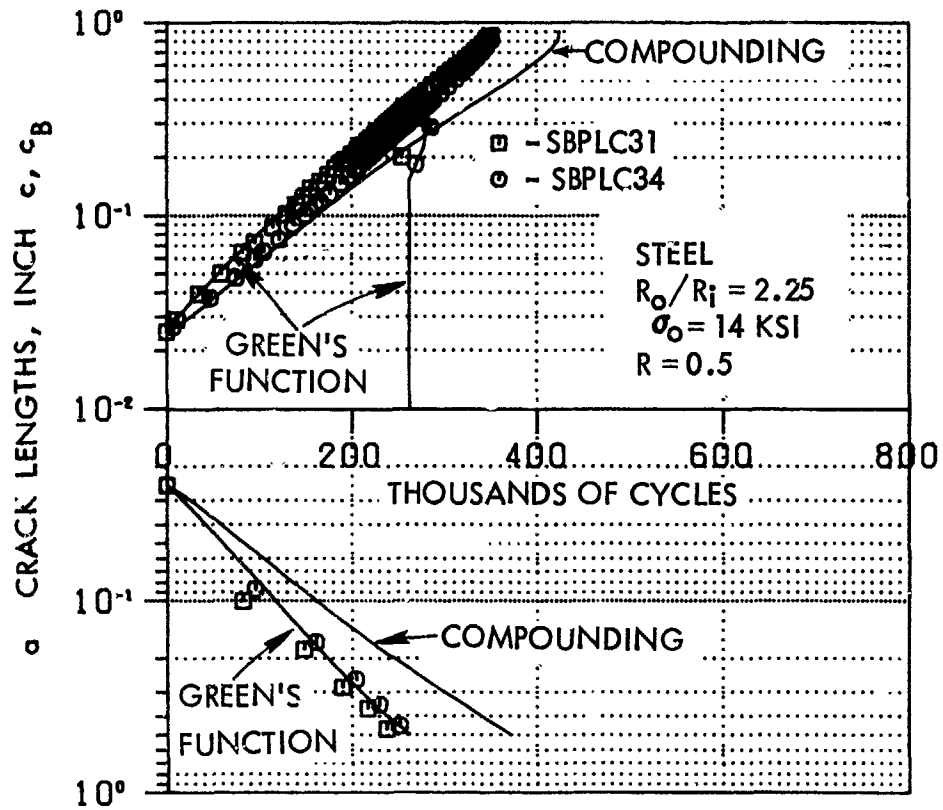Steel Lug, R_o/R_i=1.5, σ_o=14 KSI, R=0.5

150

Figure 5-38.   Corner Crack Growth Data and Prediction,
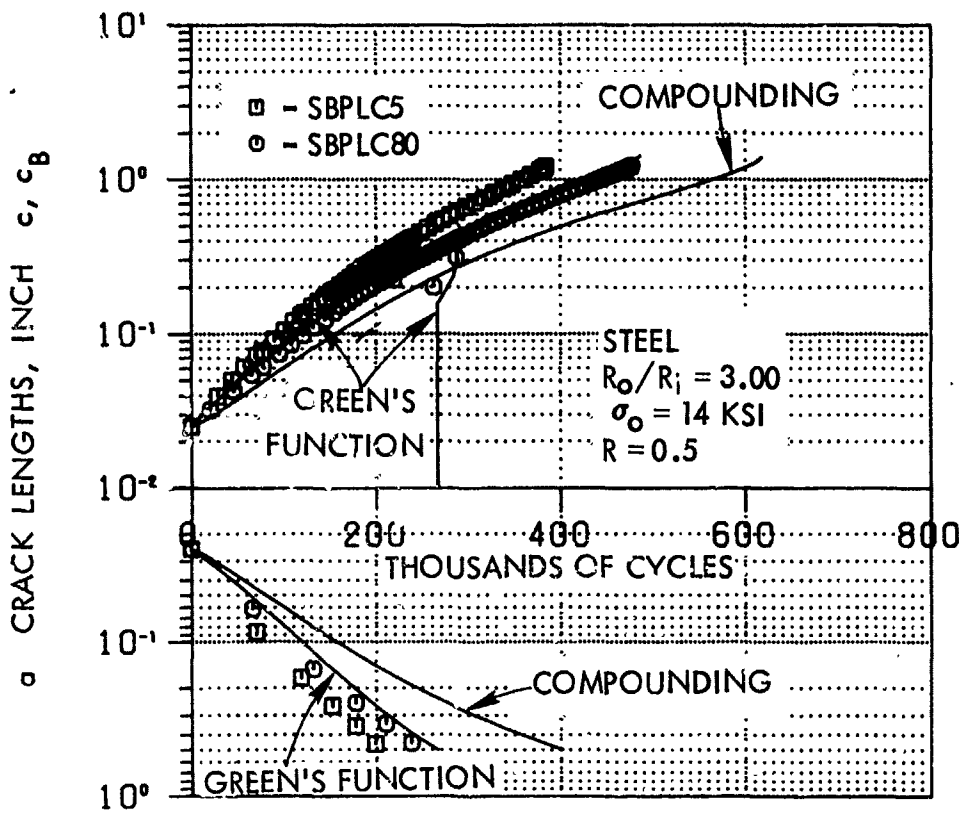Steel Lug, R_o/R_i=2.25, σ_o=14 KSI, R=0.5

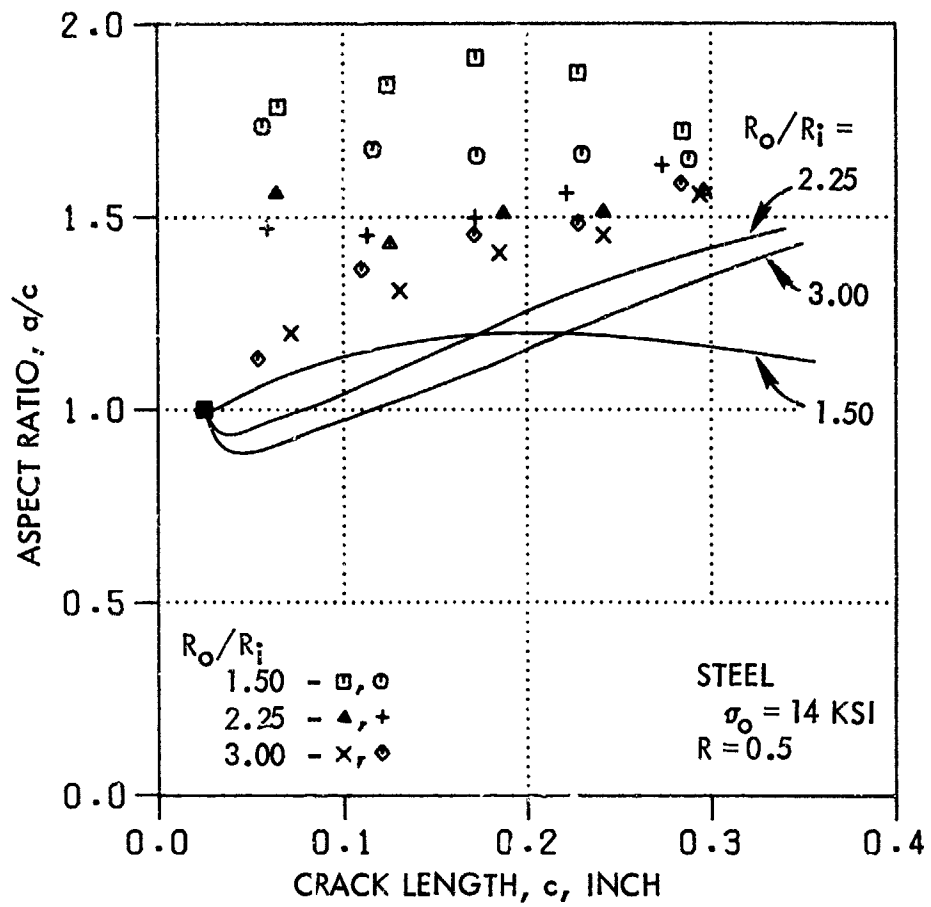Figure 5-39. Corner Crack Growth Data and Prediction, Steel Lug, $R_o/R_i=3.0$, $\sigma_o=14$ KSI, R=0.5

Figure 5-40.   Corner Crack Aspect Ratio Data and Prediction,
Steel Lug, σ_o=14 KSI, R=0.5

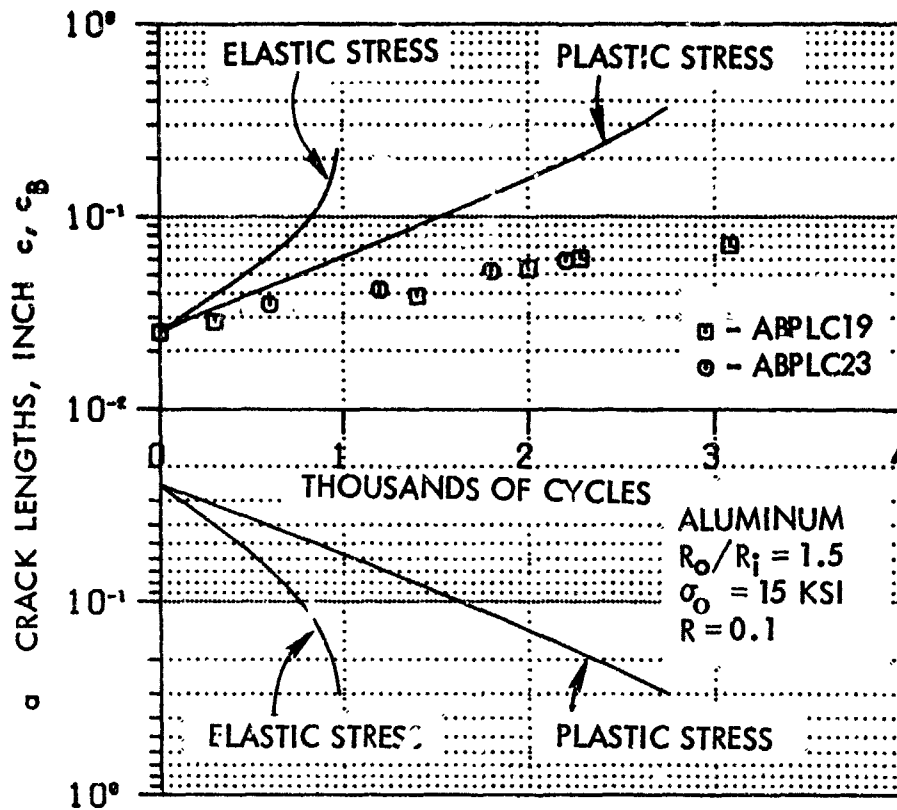Figure 5-41. Corner Crack Growth Data and Prediction,
Aluminum Lug, $R_o/R_i=1.5$, $\sigma_o=15$ KSI, R=0.1

Figure 5-42. Corner Crack Growth Data and Prediction,
Aluminum Lug, R_o/R_i=2.25, σ_o=15 KSI, R=0.1

Figure 5-43.   Corner Crack Growth Data and Prediction,
Aluminum Lug, $R_o/R_i=3.0$, $\sigma_o=15$ KSI, R=0.1

Figure 5-44. Corner Crack Aspect Ratio Data and Prediction,
Aluminum Lug, σ_o=15 KSI, R=0.1

157

Figure 5-45. Corner Crack Growth Data and Prediction,
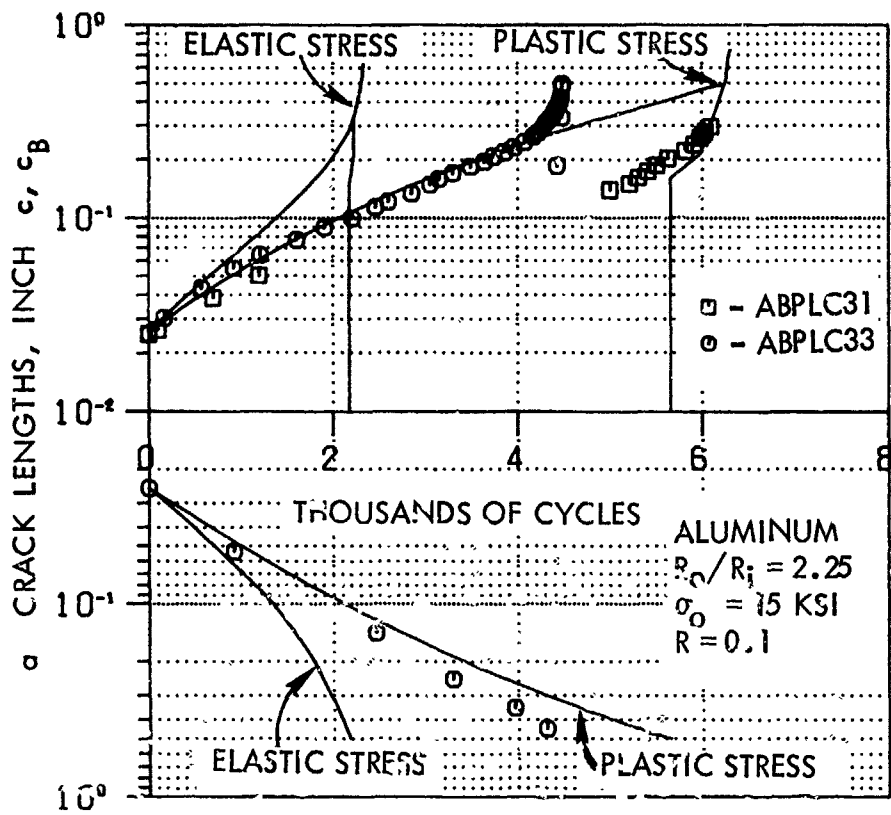Aluminum Lug, $R_o/R_i=1.5$, $\sigma_o=15$ KSI, R=0.5

Figure 5-46. Corner Crack Growth Data and Prediction,
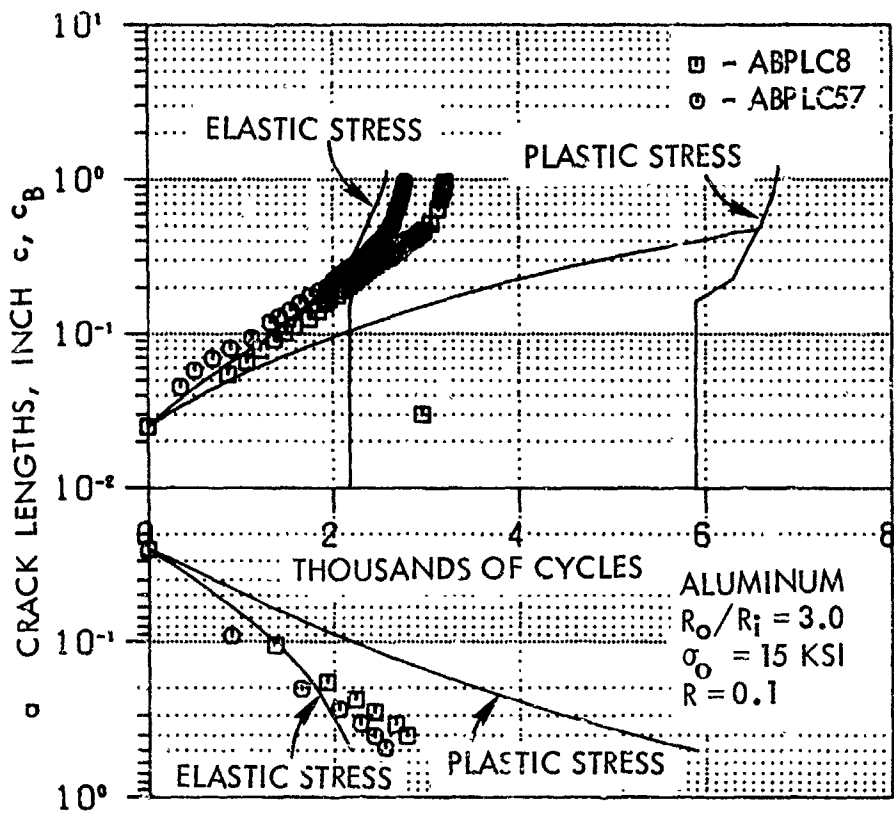Aluminum Lug, $R_o/R_i = 2.25$, $\sigma_o = 15$ KSI, R=0.5

Figure 5-47. Corner Crack Growth Data and Prediction,
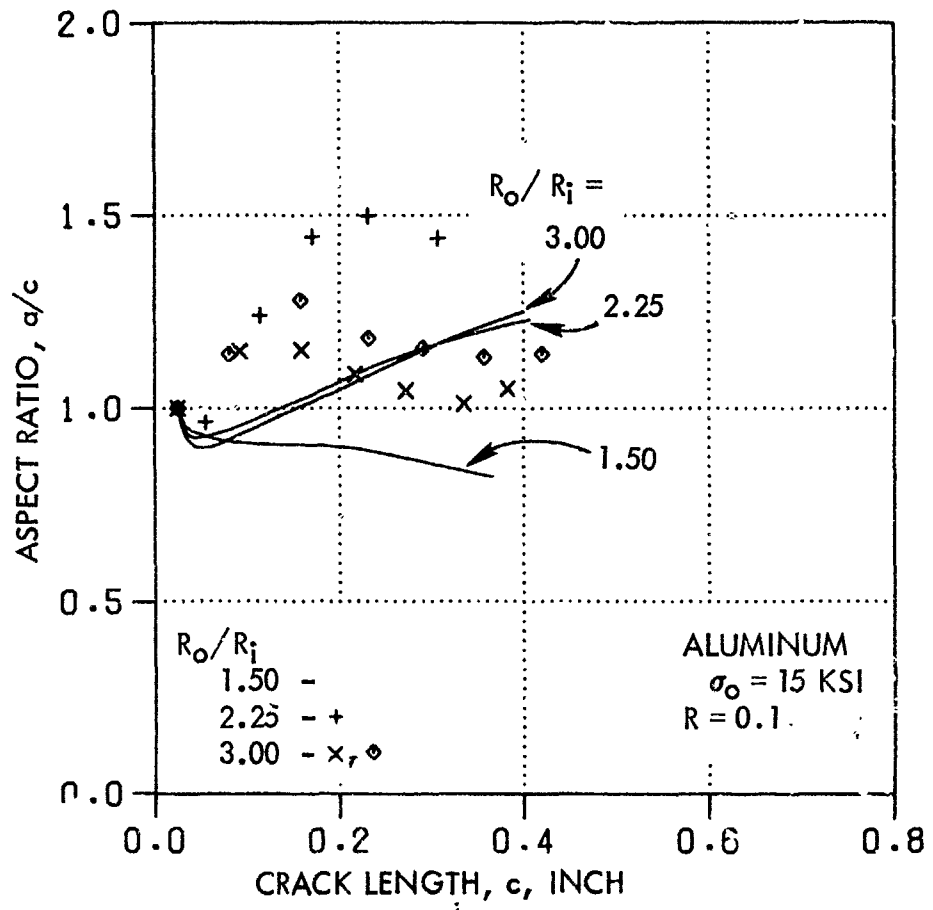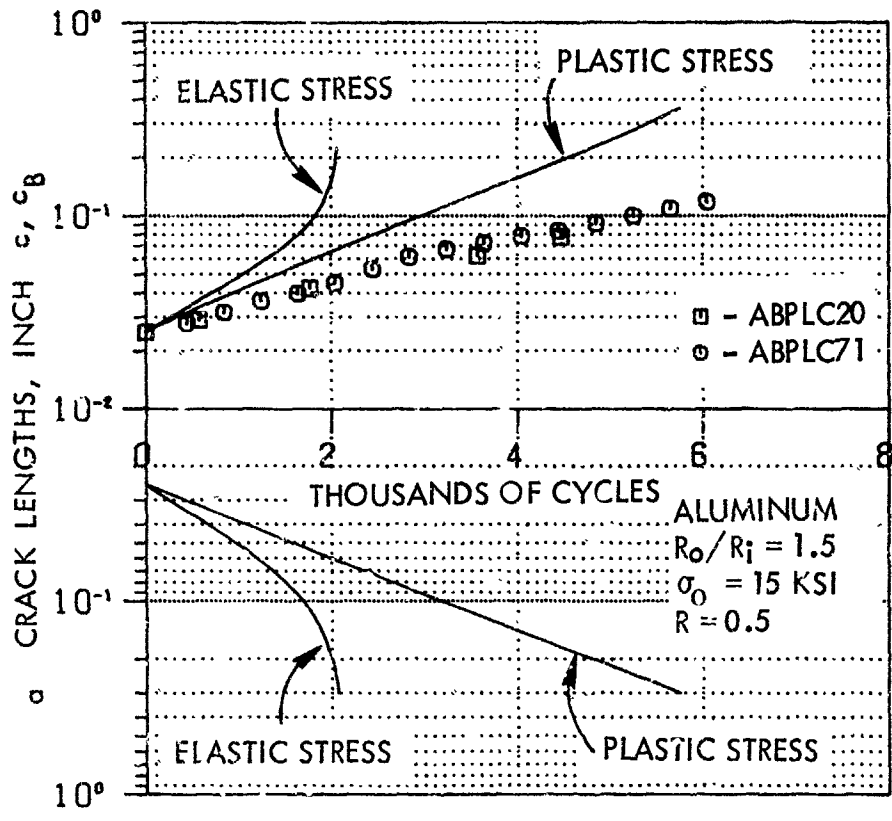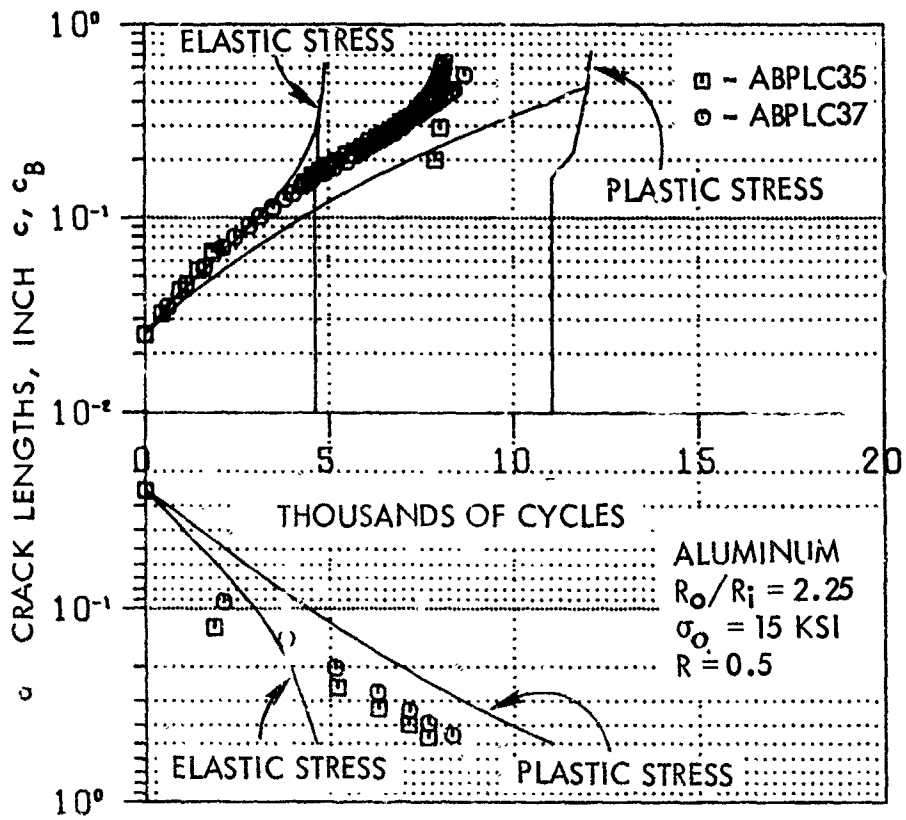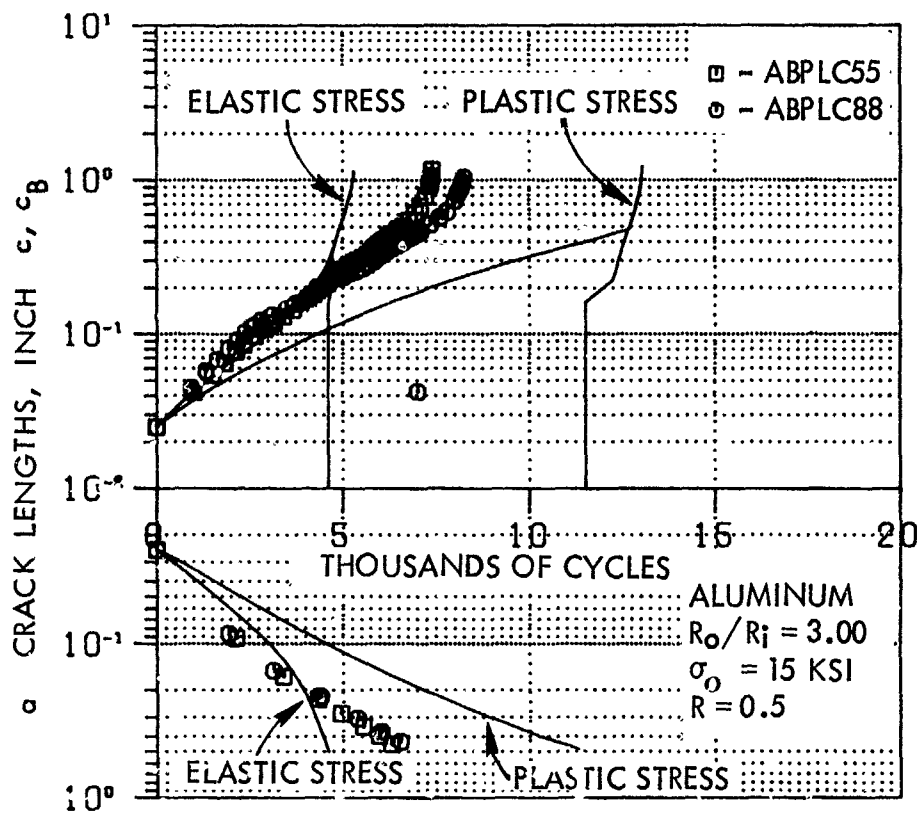Aluminum Lug, R_o/R_i=3.0, σ_o=15 KSI, R=0.5

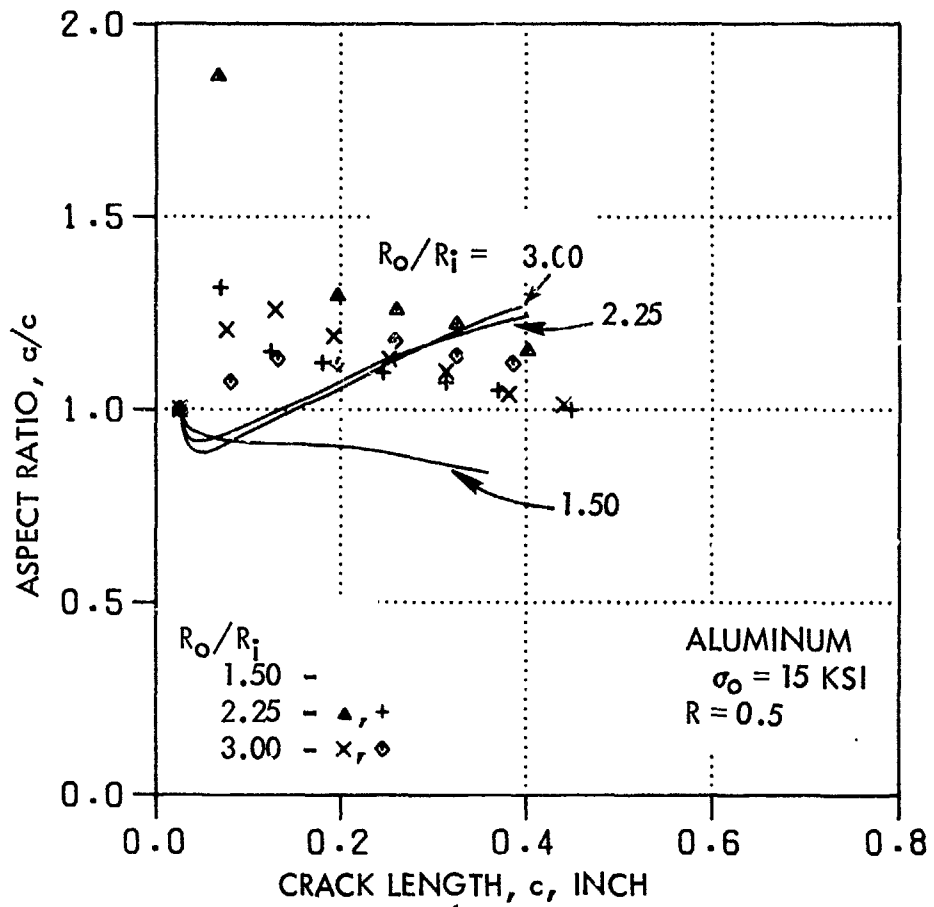Figure 5-48. Corner Crack Aspect Ratio Data and Prediction, Aluminum Lug, σ_o=15 KSI, R=0.5

subjected to a low far-field gross stress of 14 ksi (Figures 5-33 through 5-40) and eight figures for aluminum lugs subjected to a high far-field gross stress of 15 ksi (Figures 5-41 through 5-48). Again, the sets of three figures correspond to increasing R_o/R_i ratios of 1.5, 2.25 and 3.0 with duplicate tests for each test condition.

Once again, the experimental data were extrapolated (or interpolated) to a common initial surface crack length of 0.025 inch for consistency. Also, for corner cracks, the initial shape was assumed to be quarter-circular (a/c = 1.0). The analytical prediction schemes used for corner crack problems were identical to those of the through-the-thickness crack problems: Green's function and compounding methods for lugs subjected to load levels below the yield strength of the materials, and Green's function method with elasto-plastic (labeled "plastic") and elastic stress distributions for lugs subjected to load levels above the yield strength of the materials.

For corner crack problems, three crack lengths are presented in these figures: front surface crack length, c, bore crack length, a, and back surface crack length (after the crack breaks through the thickness), c_B. The crack lengths c and c_B are presented in the upper half and the crack lengths a are presented in the lower half of the figures. For any one specimen, the same symbol was used in these figures for all the three crack lengths, to keep the figures as simple as possible. Thus, at times, it may appear that some of these figures contain some erroneous data points. For example, in Figure 5-27, two data points (one circle and one square) are somewhat remote from the other data points. These are correct data points and are the back surface crack lengths, c_B. The crack lengths a and c_B were obtained from the fractographic examination of marker bands on the fracture surface.

In the analysis, the compounding method assumes that the crack aspect ratio, a/c, remains constant (a/c = 1.0). Thus, this method generates only the front surface crack length, c. The other two crack lengths, a and c_B, can be calculated using the geometry of the crack shape for any given crack length, c. However, only the crack lengths c and a (until a reaches the thickness of the lug) are presented for the compounding method. The Green's function method is used in conjunction with the 2-parameter corner

162

crack correction factor, in which the crack aspect ratio, a/c, is free to vary as the crack grows. The Green's function method also generates the data for transitional crack growth behavior, which are included in these figures. In all the cases of lugs with R_o/R_i = 1.50 (small lugs), the Green's function does not predict any transitional crack growth behavior, since the lugs fail prior to transition. In the other cases (R_o/R_i = 2.25 and 3.0), the Green's function method does predict transition and the data are presented in these figures in terms of the back surface crack length, c_B. After the crack breaks through the thickness, c_B grows very rapidly and catches up with the front surface crack length, c. Thereafter, the crack is analyzed as a through-the-thickness crack.

The Green's function predictions of front surface crack lengths, c, for all the lugs (aluminum and steel) subjected to load levels below the yield strength of the materials (Figures 5-25 through 5-40) show excellent correlation with the test data in terms of growth behavior and life. The only exception is the small (R_o/R_i = 1.5) aluminum lugs where the predictions are conservative by a factor of about 2 to 4. The compounding method, as in the case of through-the-thickness cracks, tends to predict conservative lives for smaller lugs (R_o/R_i = 1.5) and unconservative lives for medium and larger lugs (R_o/R_i = 2.25 and 3.0).

No crack lengths along the bore, a, are presented for Specimen ABPLC17 in Figure 5-25, since the marker bands were not visible for this specimen. Test results corresponding to Specimens ABPLC32 and ABPLC34 (Figure 5-30) are considered invalid because the final failures of these two specimens were due to the presence and growth of natural cracks and not due to the intentional cracks from elox slots.

The analytical-experimental correlation of corner crack growth behavior in aluminum lugs subjected to load levels above the yield strength of the material are presented next in Figures 5-41 through 5-48. As discussed in the through-the-thickness crack problems, neither of the analyses used (Green's functions with elasto-plastic or elastic stress distribution) truly model the actual mechanics of crack growth behavior. Thus, a rigorous correlation analysis cannot be made. It is worthwhile to note, however, that one may use the elastic analysis and make conservative life predictions for all the lug geometries. This applies only to corner crack

problems and not to through-the-thickness crack problems, since even the elastic analysis yielded unconservative lives for through-the-thickness cracks in medium and larger lugs (R_o/R_i = 2.25 and 3.0). It was observed in the through-the-thickness crack problems that the life increased with decreasing R_o/R_i, contrary to prediction. However, in the corner crack problems, such a phenomenon was not observed.

In all the highly loaded small aluminum lug tests (Specimens ABPLC19 and ABPLC23 of Figure 5-41, and Specimens ABPLC20 and ABPLC71 of Figure 5-45), one or more natural cracks were found during testing. The only other specimen in which natural cracks were found during testing was Specimen ABPLC31 of Figure 5-42. These tests are considered to be invalid.

Correlations of analytical-experimental data of corner crack aspect ratio, a/c, for all the above corner crack problems are presented in Figures 5-28, 5-32, 5-36, 5-40, 5-44 and 5-48. These figures show that the analytical predictions of a/c are poor, using the Green's function approach. The analytical predictions are unconservative, in general. Also, there is a large amount of scatter of data for duplicate tests. This scatter hinders any effort to attempt to improve the analytical predictions.

4.2 BASELINE BLOCK SPECTRUM TESTS

Thirty-six preflawed straight lug specimens were tested using block spectrum loading discussed in subsection 6.2 of Section III. Twenty-four of these specimens were aluminum and the remaining 12 specimens were steel. Two spectrum stress magnification factors were used for the 24 aluminum specimens, such that the peak stress in the lug for the maximum spectrum load was below the yield strength of the material in 12 specimens and above the yield strength in the remaining 12 specimens. Corresponding maximum gross-section stresses (σ_{omax}) were 7.5 and 18.75 ksi. All of the 12 steel specimens were subjected to a maximum gross-section stress of 17.5 ksi, which produced peak stress levels below the yield strength of the material. Each group of 12 tests included 6 specimens with through-the-thickness initial cracks and 6 with initial corner cracks, covering three R_o/R_i ratios (1.5, 2.25 and 3.0) and with duplicate specimens for each test condition.

164

4.2.1 Through-the-Thickness Crack Block Spectrum Tests

Analytical-experimental correlation results for all the through-the-thickness crack growth test specimens subjected to block spectrum loading are presented in Figures 5-49 through 5-66. The first six figures (Figures 5-49 through 5-54) are for aluminum lugs subjected to stresses below yield. The next six figures (Figures 5-55 through 5-60) correspond to below-yield loading of steel specimens. The next six figures (Figures 5-61 through 5-66) are for aluminum lugs subjected to above-yield loading. In each of these three sets of six figures, the first two correspond to R_o/R_i of 1.5, the next two correspond to R_o/R_i of 2.25, and the last two correspond to R_o/R_i of 3.00. Duplicate specimens are plotted on separate figures, because the initial crack lengths differed, and because the interpolation/extrapolation procedure used for constant amplitude data to calculate a common initial crack length was judged to be inappropraite for the block spectrum data, as discussed earlier.

The maximum gross stress level for each of the block spectrum tests is provided in each figure. The number of cycles per block of loading for each test can then be obtained from Figure 3-19 and Table 3-17 using the maximum gross stress level and the crack type. The abscissa "PASSES" refers to the number of times the block spectrum was repeated.

For lugs (steel and aluminum) subjected to below-yield loadings, analytical predictions were made using four different retardation models; the Hsu, Generalized Willenborg, Willenborg, and No-Retardation models. The analytical results from these four retardation models have been identified as [A], [B], [C] and [D], respectively, in Figures 5-50 through 5-60. In the Generalized Willenborg model, a value of 0.4 was used for ϕ for both the materials.

The analytical predictions by both the Hsu and Generalized Wilenborg models were generally conservative by about a factor for 2.0 for aluminum lugs (Figures 5-49 through 5-54), whereas for steel lugs (Figures 5-55 through 5-60), the predictions by these two models were unconservative by a factor of about 2.0. However, it was observed in subsection 4.1.1 that even for steel lugs subjected to constant-amplitude loading, the predictions were unconservative by about a factor of 2.0 due in part to the
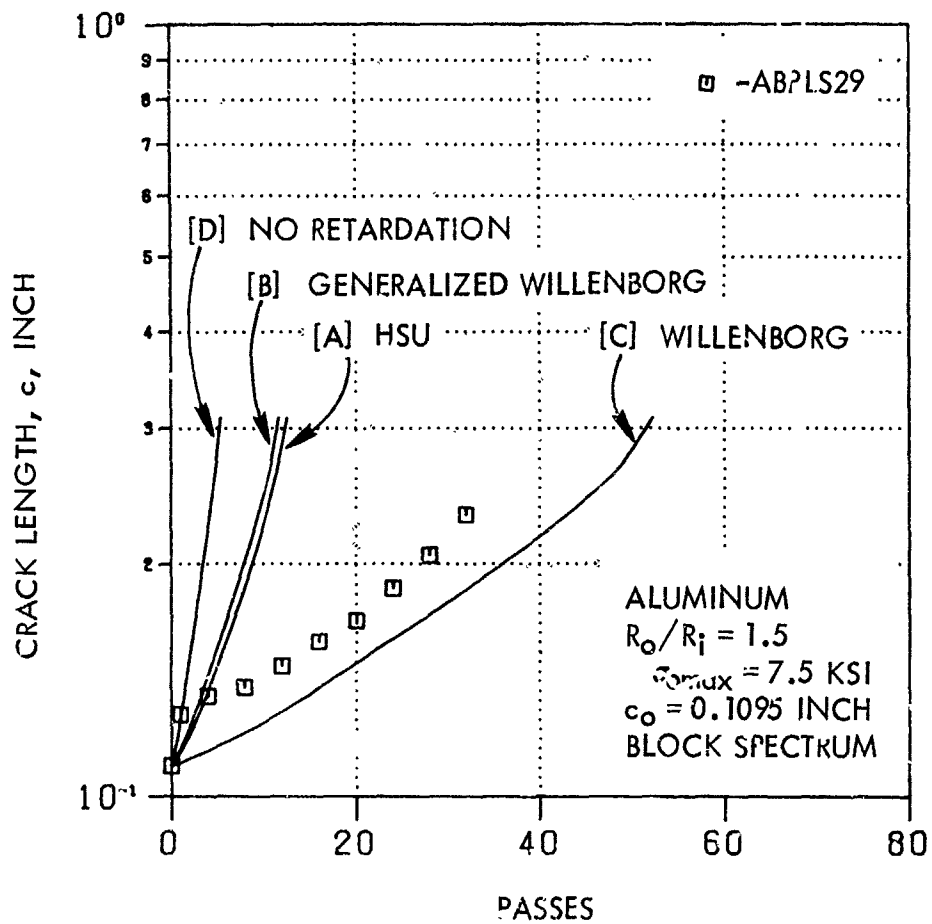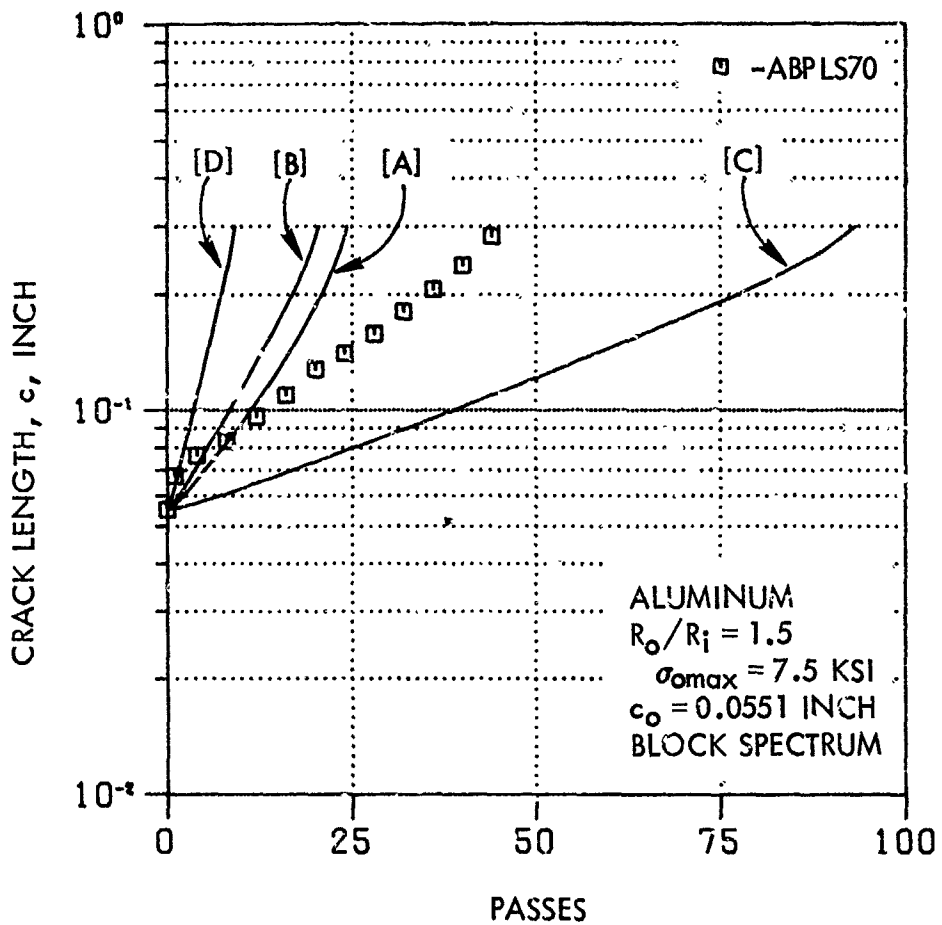
Figure 5-49. Through-the-Thickness Crack Growth Data and Prediction, Aluminum Lug, $R_o/P_i = 1.5$, Block Spectrum Loading, $\sigma_{omax} = 7.5$ KSI
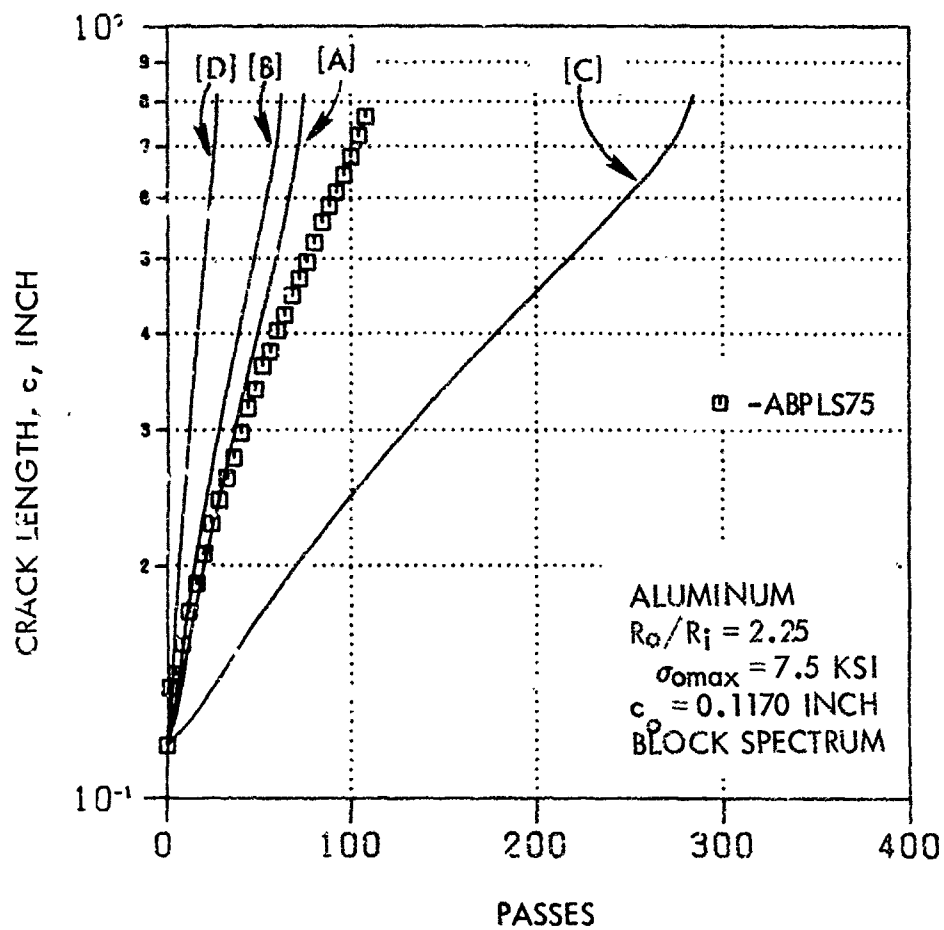
166

Figure 5-50. Through-the-Thickness Crack Growth Data and Prediction, Aluminum Lug, R_o/R_i=1.5, Block Spectrum Loading, σ_{omax} = 7.5 KSI

167

Figure 5-51. Through-the-Thickness Crack Growth Data and Prediction, Aluminum
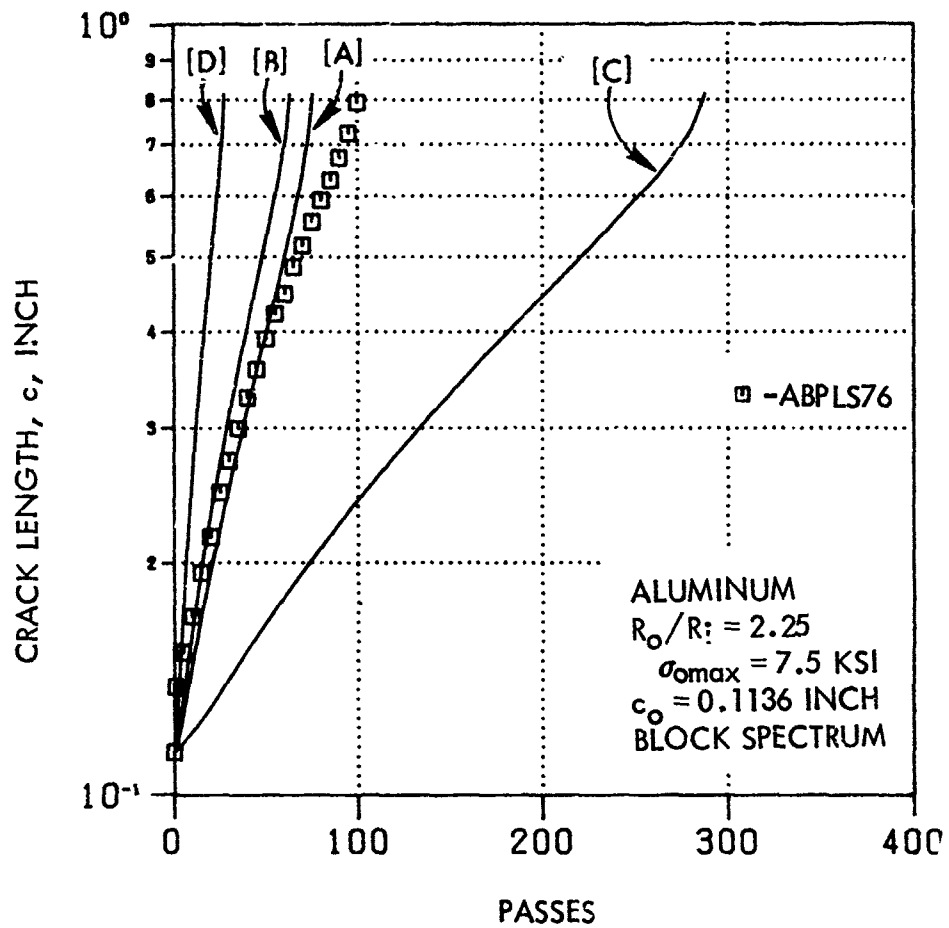L'g, R_o/R_i=2.25, Block Spectrum Loading, σ_{omax} = 7.5 KSI

168

Figure 5-52. Through-the-Thickness Crack Growth Data and Prediction, Aluminum Lug, $R_o/R_i=2.25$, Block Spectrum Loading, $\sigma_{omax} = 7.5$ KSI
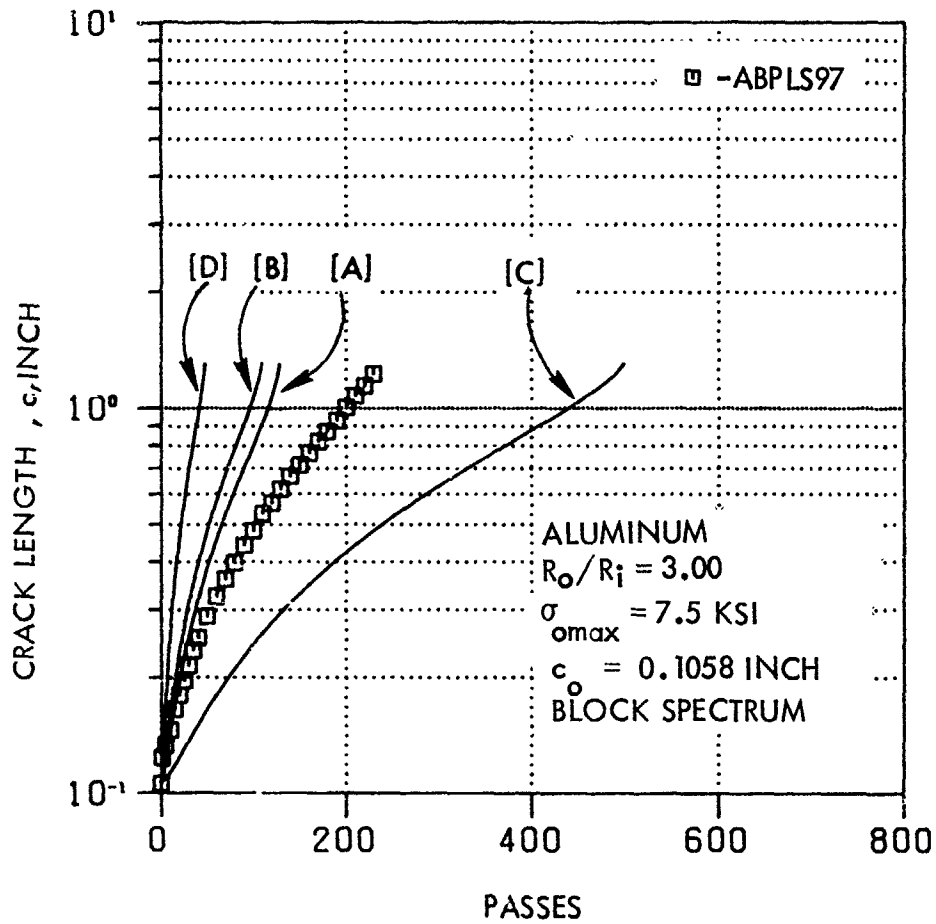
Figure 5-53. Through-the-Thickness Crack Growth Data and Prediction, Aluminum Lug, R_o/R_i=3.0, Block Spectrum Loading, σ_{omax} = 7.5 KSI

Figure 5-54. Through-the-Thickness Crack Growth Data and Prediction, Aluminum Lug, $R_o/R_i=3.0$, Block Spectrum Loading, $\sigma_{omax} = 7.5$ KSI
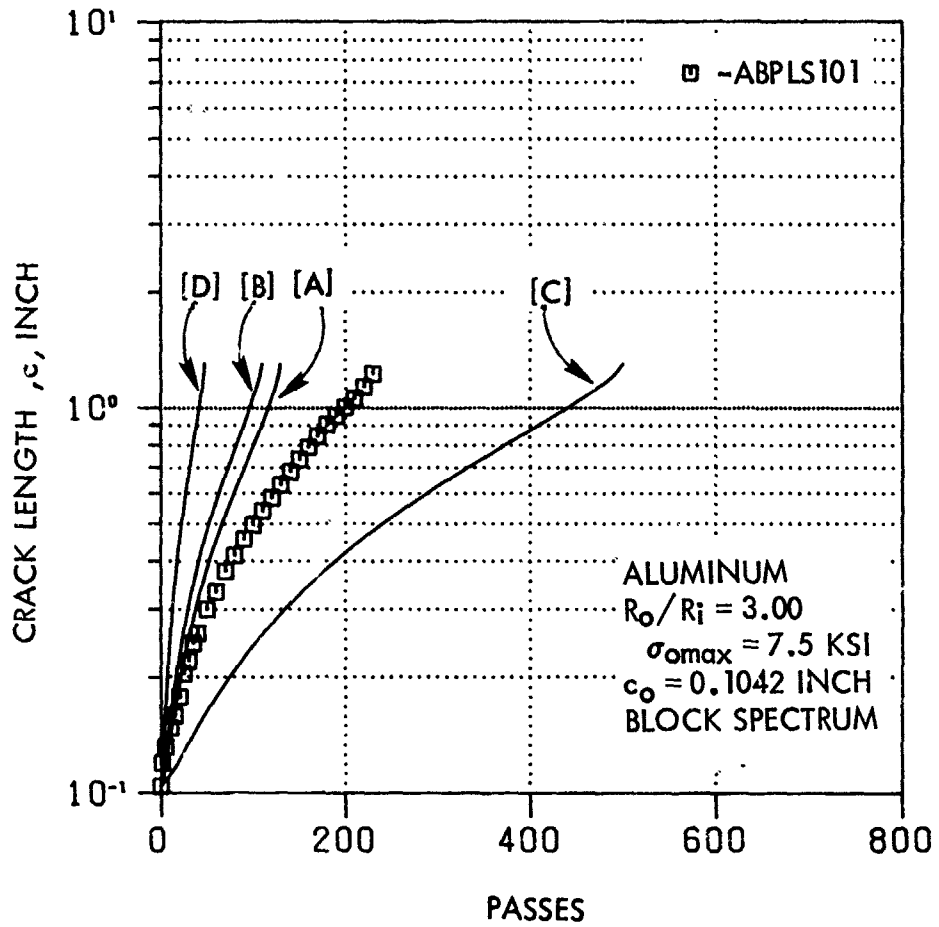
171

Figure 5-55. Through-the-Thickness Crack Growth Data and Prediction, Steel
Lug, $R_o/R_i=1.5$, Block Spectrum Loading, σ_{omax} = 17.5 KSI

172
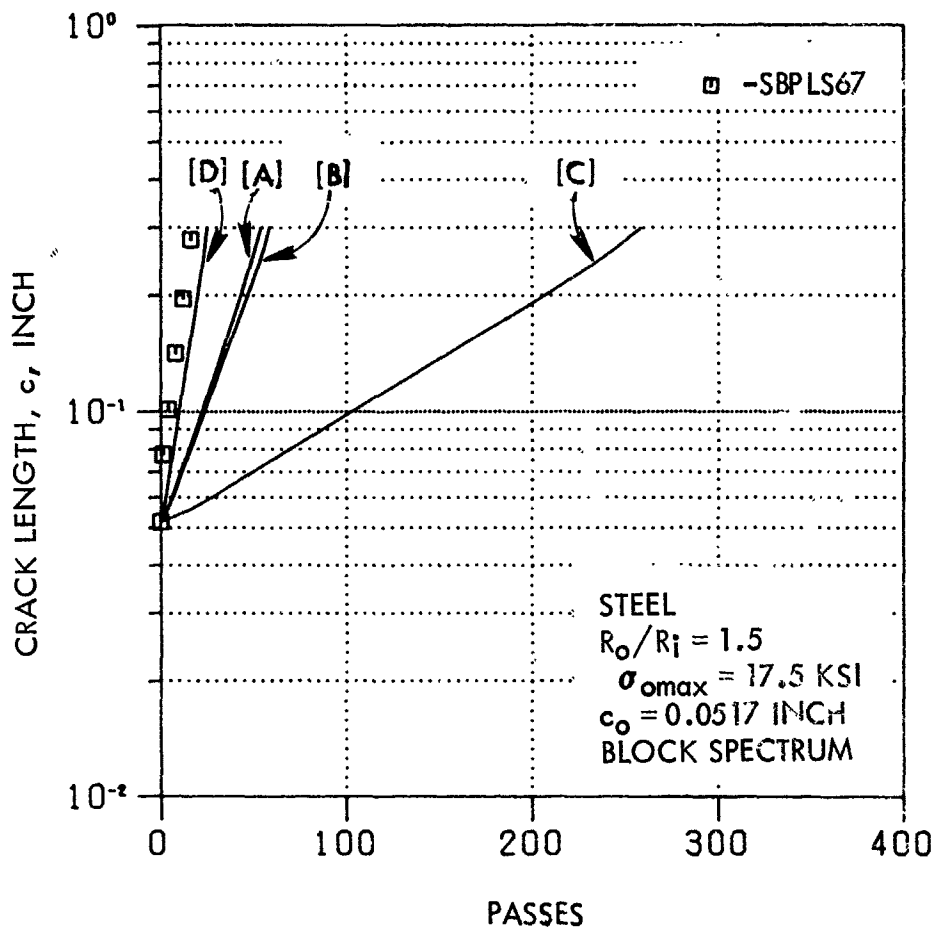
Figure 5-56. Through-the-Thickness Crack Growth Data and Prediction, Steel
Lug, $R_o/R_i = 1.5$, Block Spectrum Loading, $\sigma_{omax} = 17.5$ KSI

Figure 5-57. Through-the-Thickness Crack Growth Data and Prediction, Steel Lug, R_o/R_i=2.25, Block Spectrum Loading, σ_{omax}= 17.5 KSI

174

Figure 5-58. Through-the-Thickness Crack Growth Data and Prediction, Steel Lug, R_o/R_i=2.25, Block Spectrum Loading, σ_{omax} = 17.5 KSI
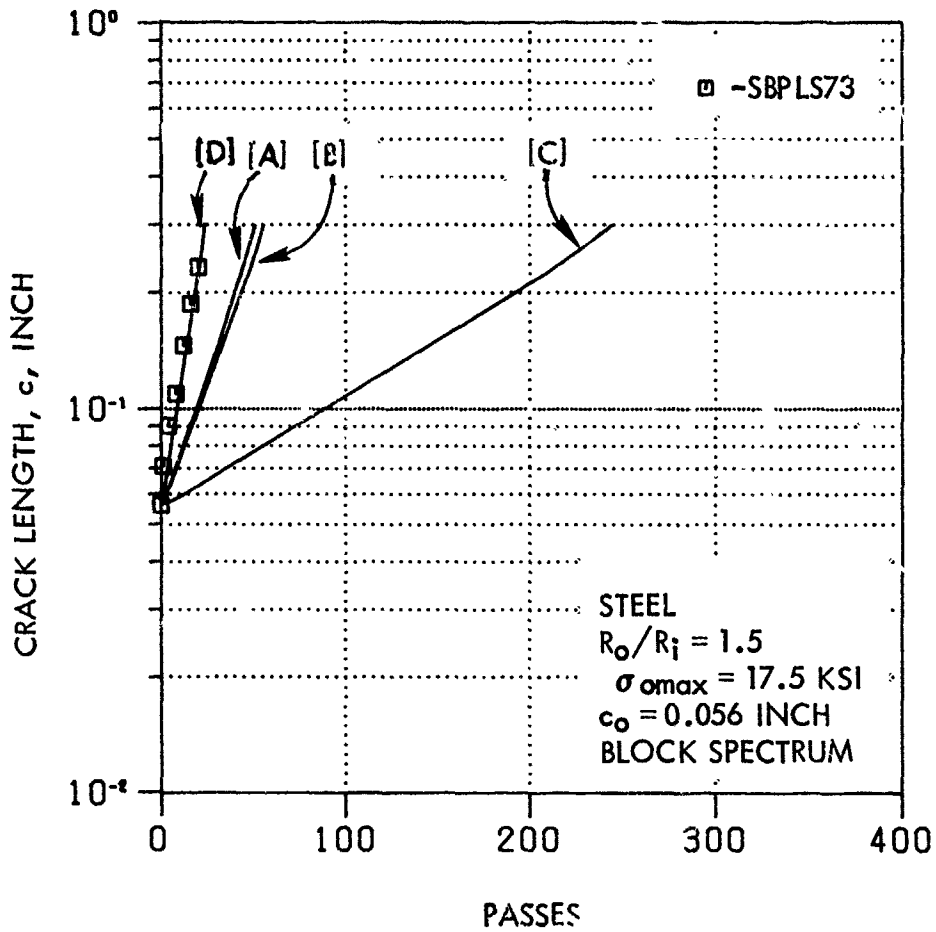
175

Figure 5-59. Through-the-Thickness Crack Growth Data and Prediction, Steel Lug, $R_o/R_i = 3.00$, Block Spectrum Loading, $\sigma_{omax} = 17.5$ KSI

Figure 5-60. Through-the-Thickness Crack Growth Data and Prediction, Steel Lug, $R_o/R_i=3.00$, Block Spectrum Loading, σ_{omax} = 17.5 KSI
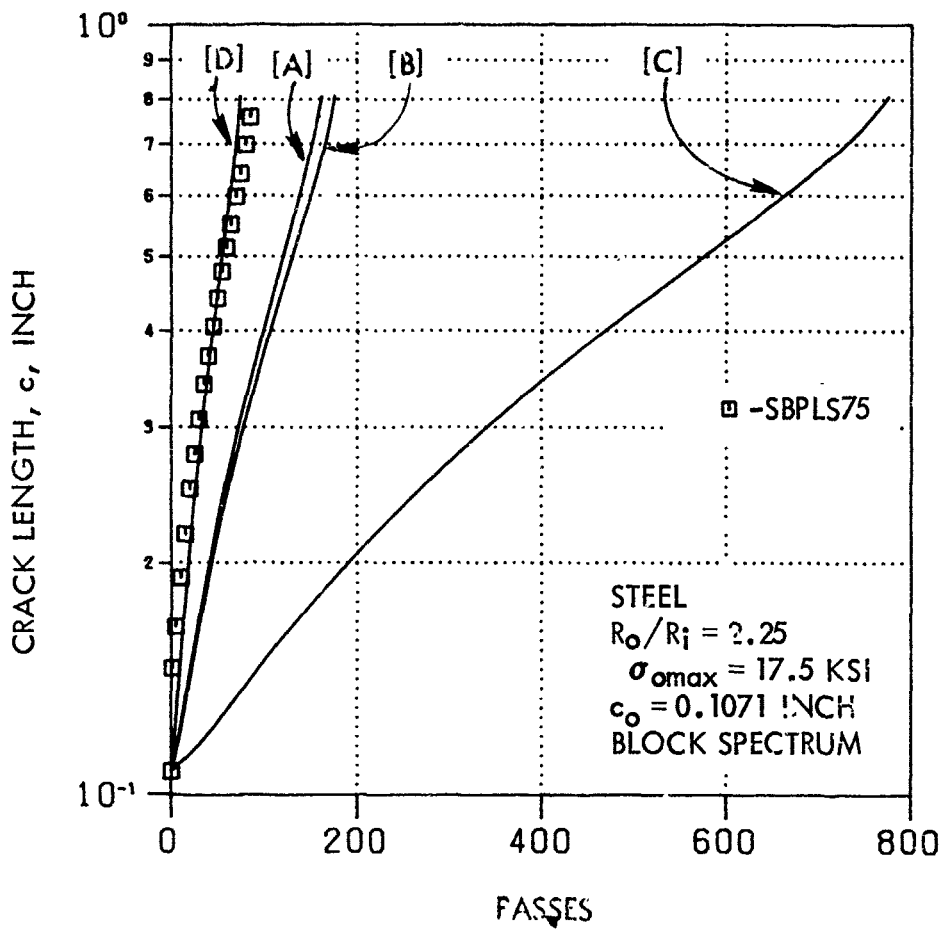
177

Figure 5-61.   Through-the-Thickness Crack Growth Data and Prediction, Aluminum Lug, $R_o/R_i = 1.5$, Block Spectrum Loading, $\sigma_{omax} = 18.75$ KSI

178

Figure 5-62.   Through-the-Thickness Crack Growth Data and Prediction, Aluminum
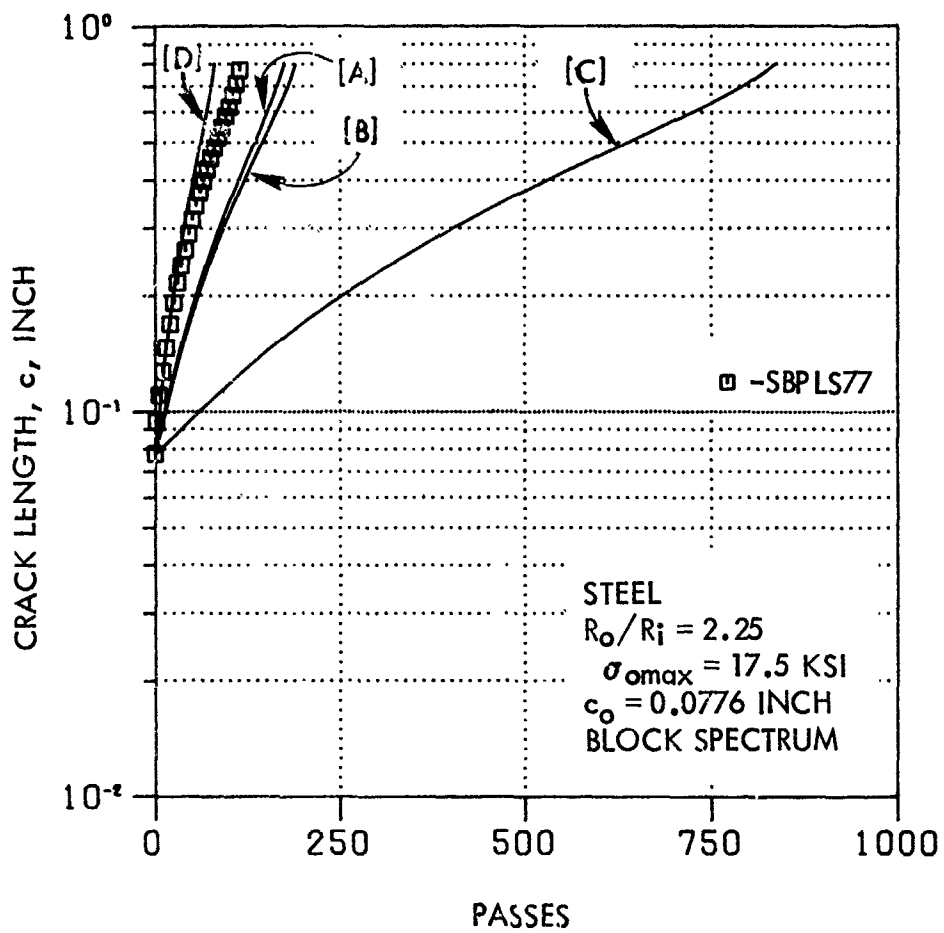Lug, $R_o/R_i = 1.5$, Block Spectrum Loading, σ_{omax} = 18.75 KSI

179

Figure 5-63. Through-the-Thickness Crack Growth Data and Prediction, Aluminum Lug, $R_o/R_i = 2.25$, Block Spectrum Loading, $\sigma_{omax} = 21.0$ KSI

Figure 5-64.   Through-the-Thickness Crack Growth Data and Prediction, Aluminum Lug, R_o/R_i=2.25, Block Spectrum Loading, σ_{omax} = 18.75 KSI
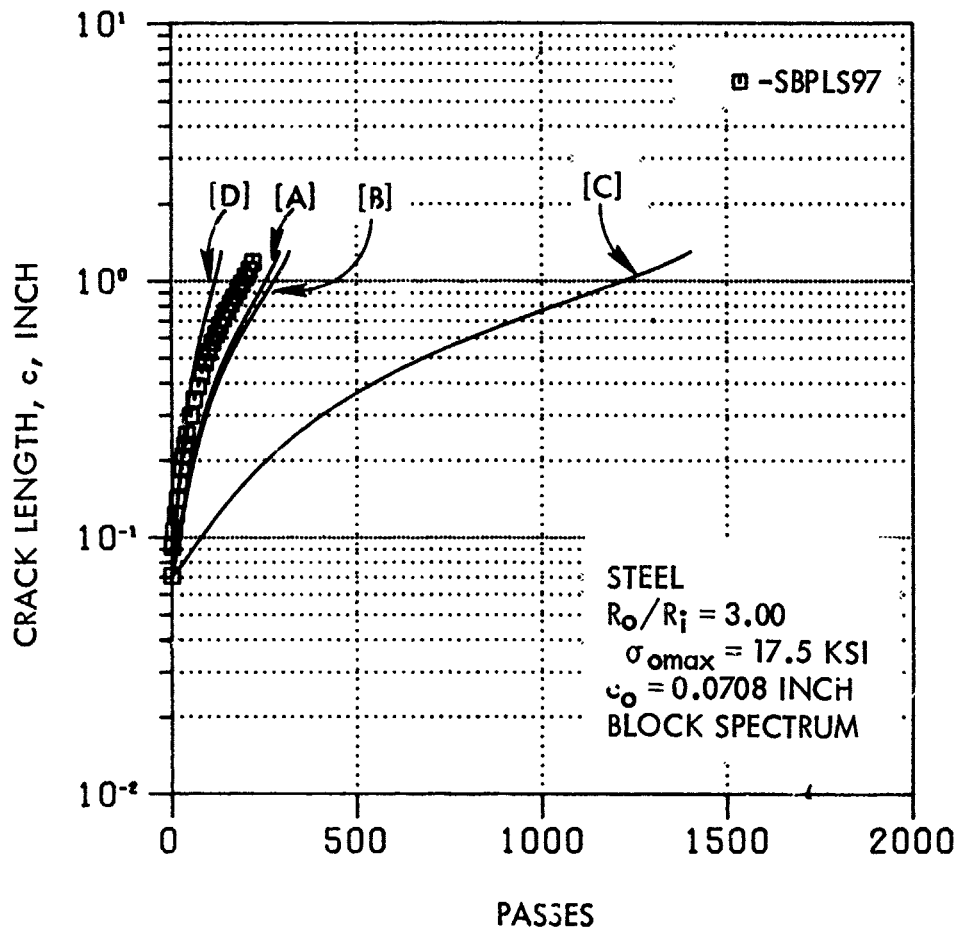
Figure 5-65. Through-the-Thickness Crack Growth Data and Prediction, Aluminum Lug, R_o/R_i=3.0, Block Spectrum Loading, σ_{omax} = 18.75 KSI
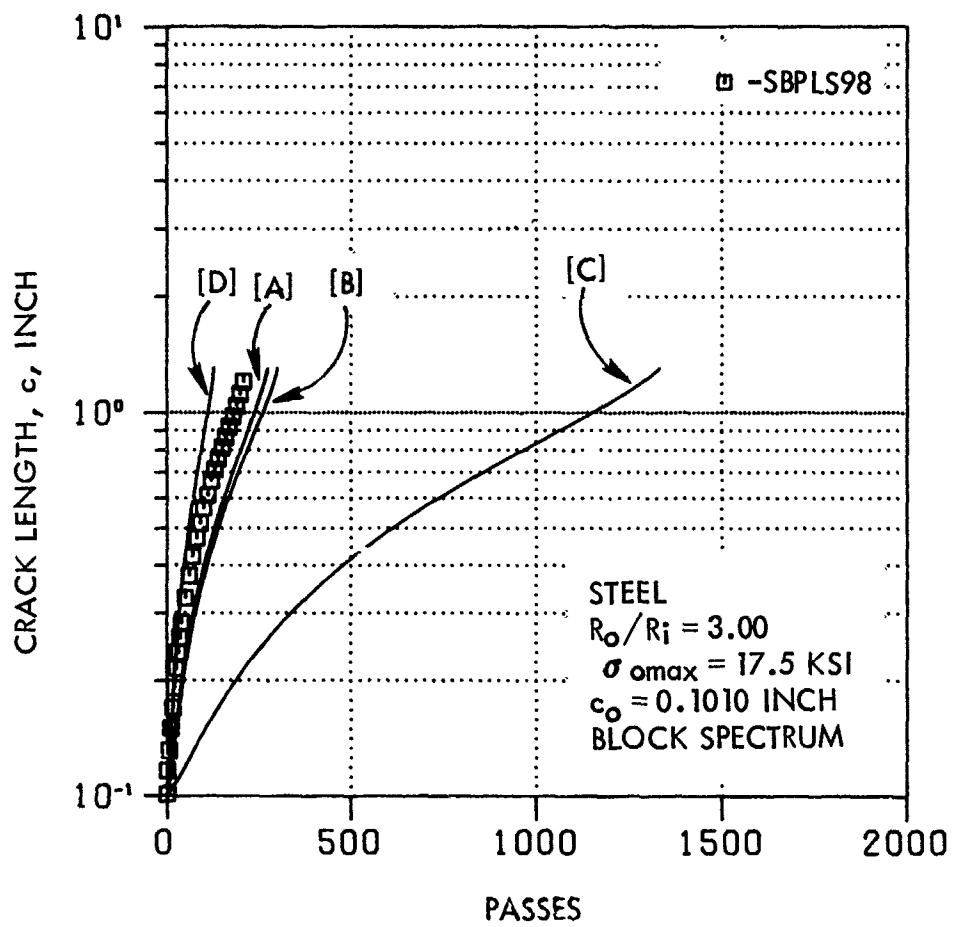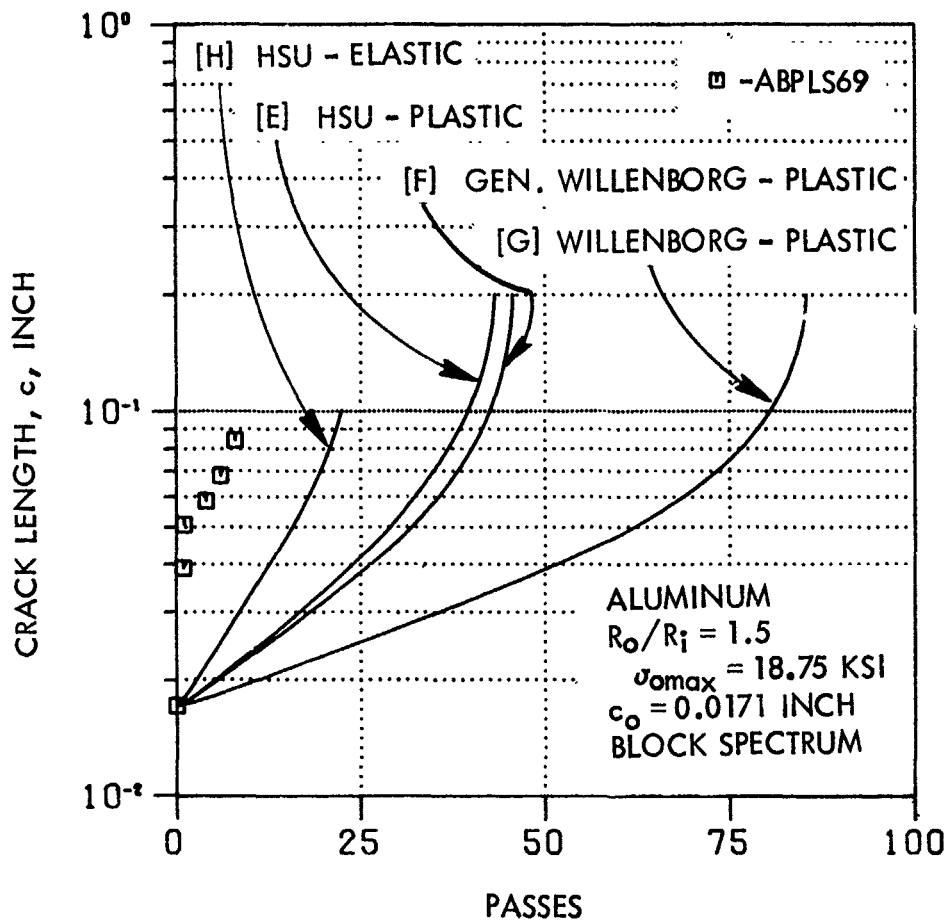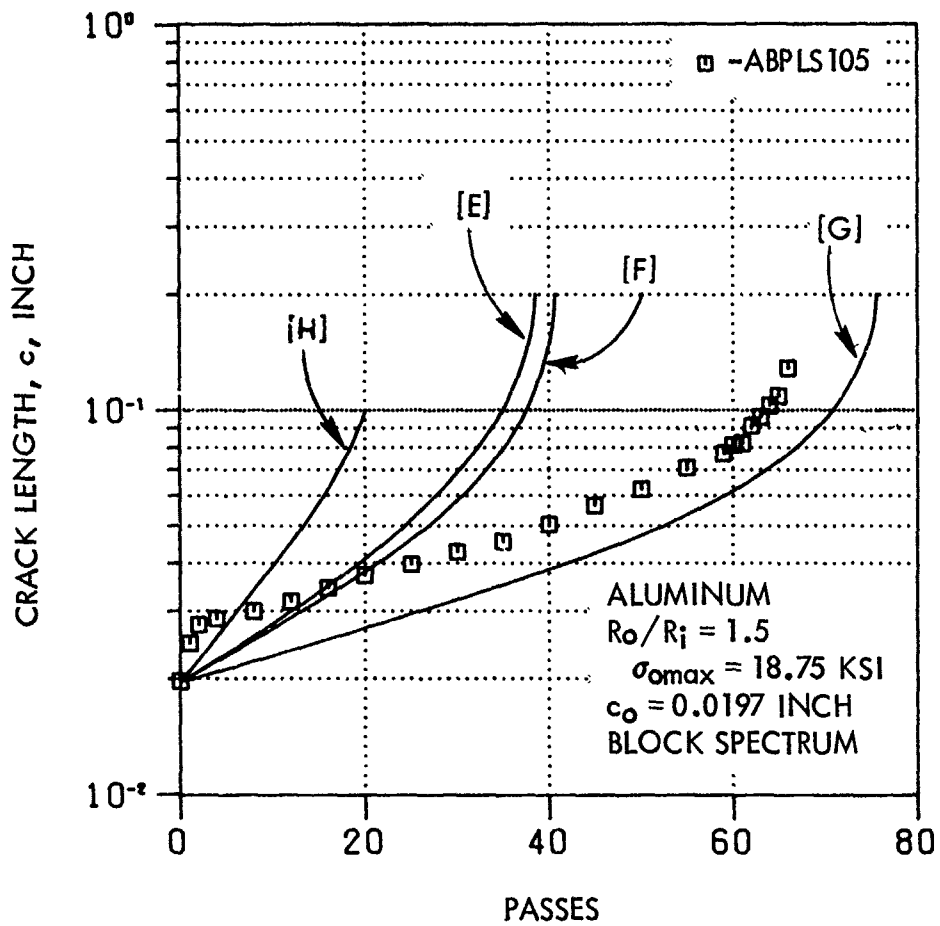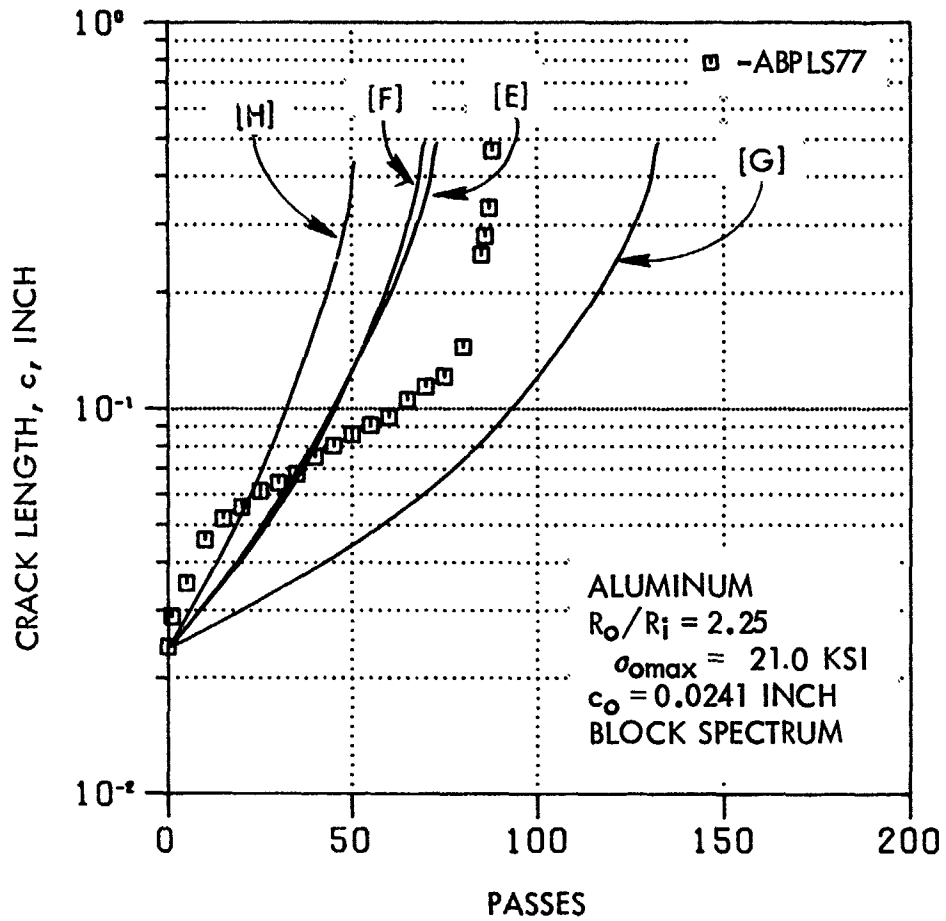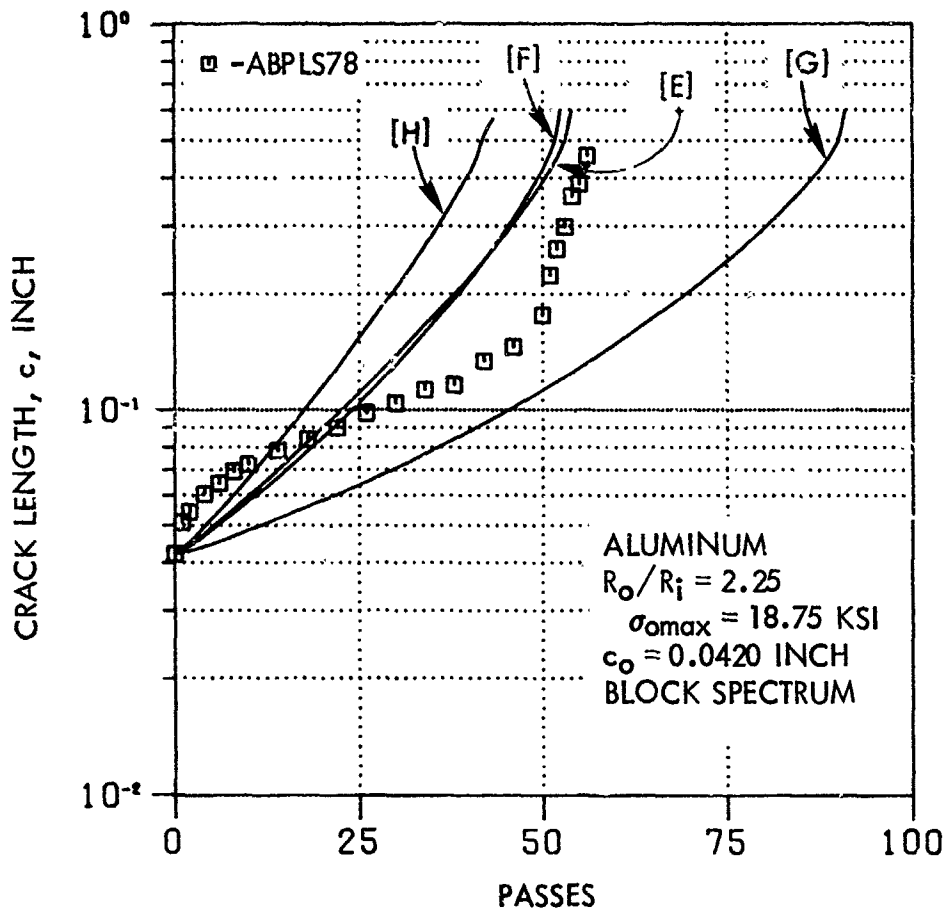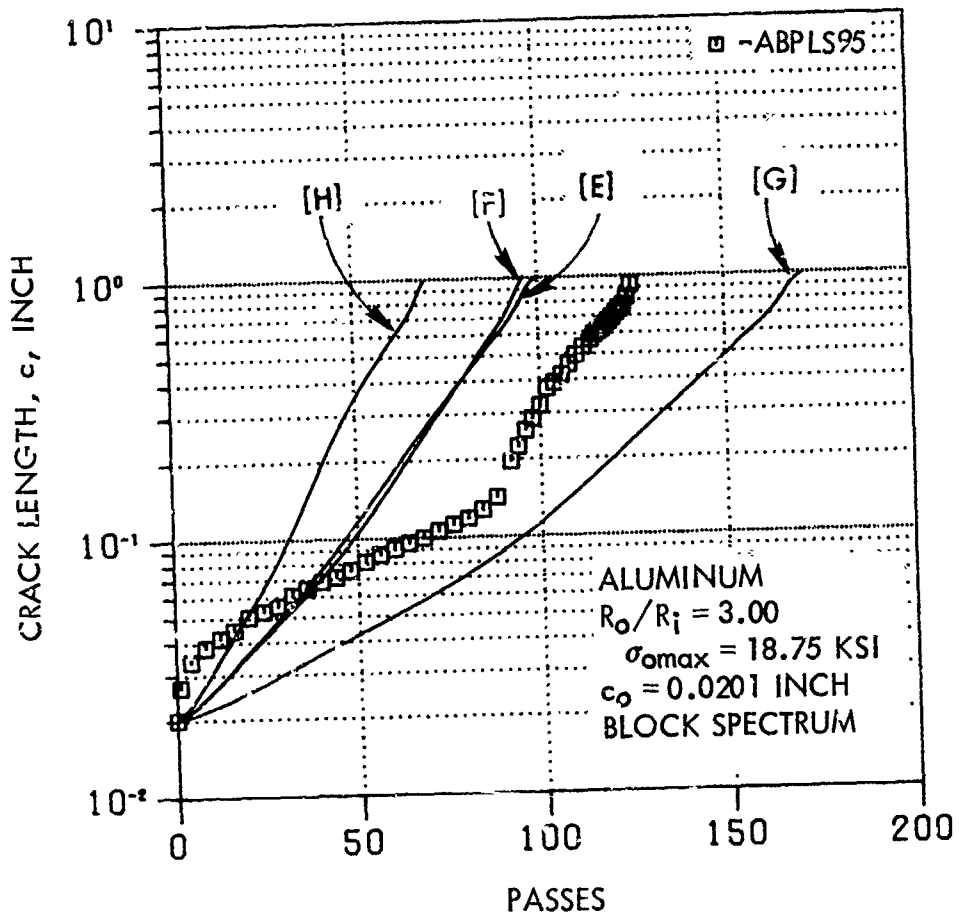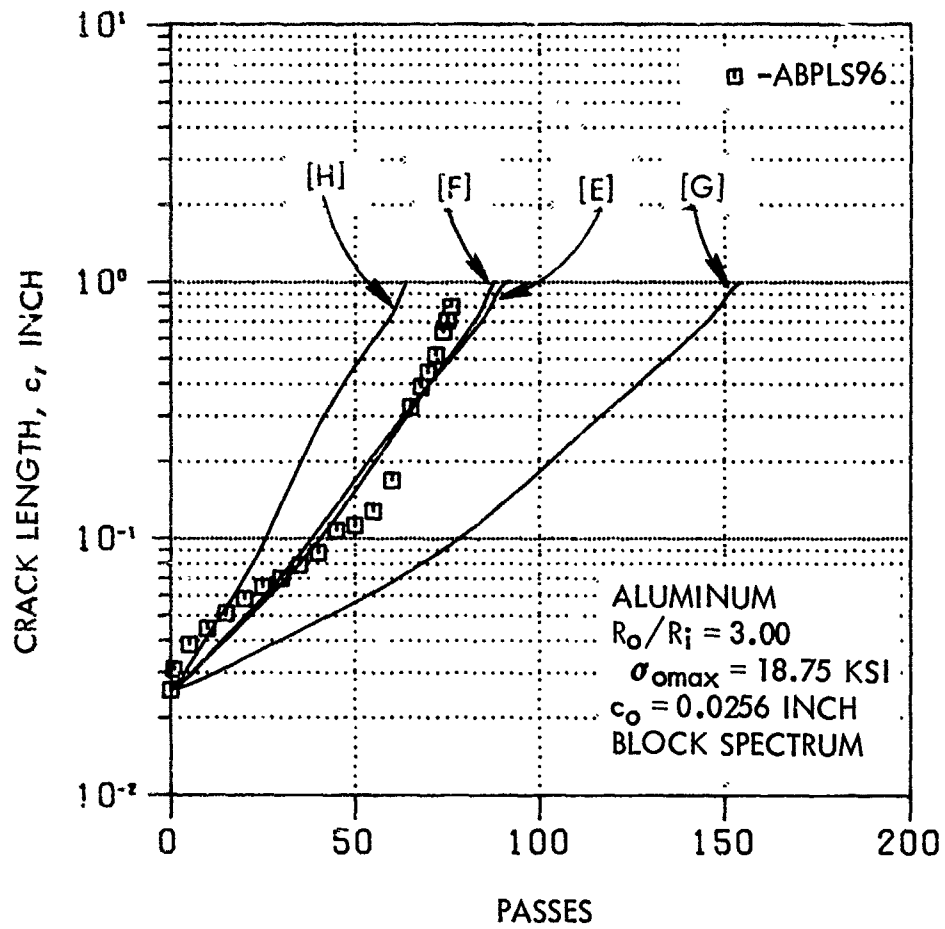
Figure 4-66. Through-the-Thickness Crack Growth Data and Prediction, Aluminum
Lug, R_o/R_i=3.0, Block Spectrum Loading, σ_{omax} = 18.75 KSI

183

change in loading pin-to-lug rigidity ratio (E_{pin}/E_{lug}). If the effect of E_{pin}/E_{lug} is accounted in the analysis, the correlation for steel lugs subjected to block spectrum loading would improve significantly. The analytical results by the Willenborg model and with no-retardation effect ([C] and [D]) are included in these figures only for comparison with other analytical results and not for comparing them with experimental results. Also, note in these results, and in all further results of spectrum loading cases to be presented, the Hsu and the Generalized Willenborg models predict almost the same crack growth behavior and life.

Figures 5-61 through 5-66 present the correlation results of crack growth behavior in aluminum lugs subjected to above-yield block spectrum loading. Four different predictions were made for these cases. The first three are Hsu, Generalized Willenborg and Willenborg models that use the stress distribution from elasto-plastic analysis. The fourth one is the Hsu model using the elastic stress distribution. The results from these models are labelled as [E], [F], [G] and [H], respectively. It was noted in subsection 4.1.1 that neither the elasto-plastic nor elastic solution was able to adequately represent the crack growth mechanism in lugs subjected to above-yield, constant-amplitude loading. The block spectrum loading is much more complex than the constant-amplitude loading since some of the load levels are above the yield level and the remaining below yield level. Thus, none of the analytical results presented are very accurate. The Hsu and Generalized Willenborg models do predict reasonable crack growth behavior and slightly conservative lives. Lower critical crack lengths are predicted by model [H], since it uses the elastic stress distribution.

Note that the test results of Specimen ABPLS69 reported in Figure 5-61 is probably invalid, due to unusually high crack growth rates. Also note that, for Specimen ABPLS77, the σ_{omax} is equal to 21.0 ksi (Figure 5-63) instead of 18.75 ksi, due to a malfunction of the test computer.

4.2.2 Corner Crack Block Spectrum Tests

Similar results of block spectrum tests of lugs with corner cracks instead of through-the-thickness cracks are presented in Figures 5-67

through 5-84. The first six figures (Figures 5-67 through 5-72) are for aluminum lugs subjected to below-yield loading. Figures 5-73 through 5-78 correspond to steel lugs subjected to below-yield loading. The results of aluminum lugs subjected to above-yield loading are presented in Figures 5-79 through 5-84. The maximum far-field gross stresses for the above three cases again were 7.5, 17.5 and 18.75 ksi, respectively. As in the case of through-the-thickness cracks, no extrapolation was made to a common initial crack length, and the results are presented on separate graphs for each specimen.

An extensive effort was made for the corner crack tests to select the block spectrum loadings which produce markings so that the aspect ratio of the corner crack could be obtained using post-failure examination. This effort was not successful due to the number of variables involved and the allotted test period. It was then decided to monitor the back surface crack length, c_B, instead, after the crack breaks through the thickness, in order to extract the maximum amount of data from these tests. Thus, only the crack lengths c and c_B are presented in Figures 5-67 through 5-84.

Prediction schemes were again the same as the through-the-thickness crack problems: Hsu [A], Generalized Willenborg [B], Willenborg [C] and No-Retardation [D] for lugs loaded below yield; and Hsu [E], Generalized Willenborg [F], Willenborg [G] with elasto-plastic stress distribution, and Hsu [H] with elastic stress distribution for lugs loaded above yield.

For aluminum and steel lugs subjected to below-yield loading, the Hsu[A] and the Generalized Willenborg [B] models again predict close and similar crack growth behavior and lives. Also, all the models predict that the smaller lugs (R_o/R_i = 1.5) fail before the corner crack breaks through the thickness. For medium and larger lugs (R_o/R_i = 2.25 and 3.00), transition and through-the-thickness growth behaviors were predicted. For aluminum lugs (Figures 5-67 through 5-72), the predictions were generally conservative by a factor of about 1 to 4. The predictions were either good or slightly unconservative for steel lugs (Figures 5-73 through 5-78). The only odd test in these 12 specimens is that of steel specimen SBPLS61 (Figure 5-78). The block spectrum consisting of 2500 total cycles per block, which corresponds to the through-the-thickness crack block spectrum testing, was used for this specimen instead of 7500 total cycles per block

Figure 5-67. Corner Crack Growth Data and Prediction, Aluminum Lug,
$R_o/R_i = 1.5$, Block Spectrum Loading, $\sigma_{omax} = 7.5$ KSI

186

Figure 5-68. Corner Crack Growth Data and Prediction, Aluminum Lug, R_o/R_i=1.5, Block Spectrum Loading, σ_{omax} = 7.5 KSI

187

Figure 5-69. Corner Crack Growth Data and Prediction, Aluminum Lug, $R_o/R_i = 2.25$, Block Spectrum Loading, $\sigma_{omax} = 7.5$ KSI

Figure 5-70. Corner Crack Growth Data and Prediction, Aluminum Lug,
R_o/R_i=2.25, Block Spectrum Loading, σ_{omax} = 7.5 KSI

189

Figure 5-71. Corner Crack Growth Data and Prediction, Aluminum Lug,
R_o/R_i=3.0, Block Spectrum Loading, σ_{omax} = 7.5 KSI
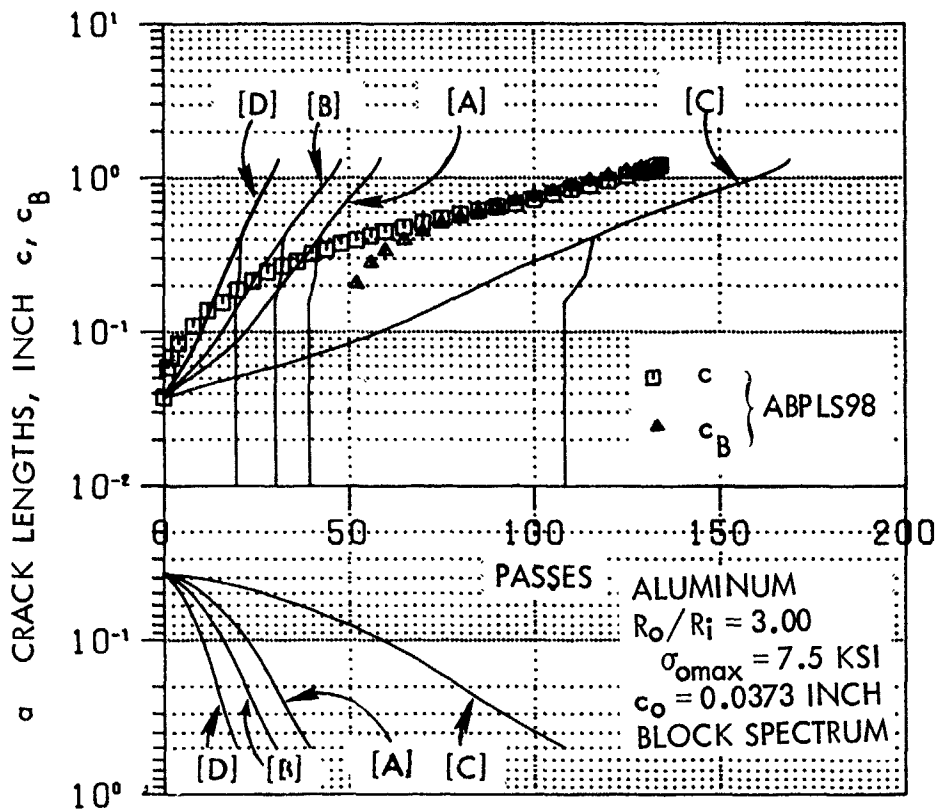
Figure 5-72. Corner Crack Growth Data and Prediction, Aluminum Lug,
$R_o/R_i=3.0$, Block Spectrum Loading, $\sigma_{omax} = 7.5$ KSI

191
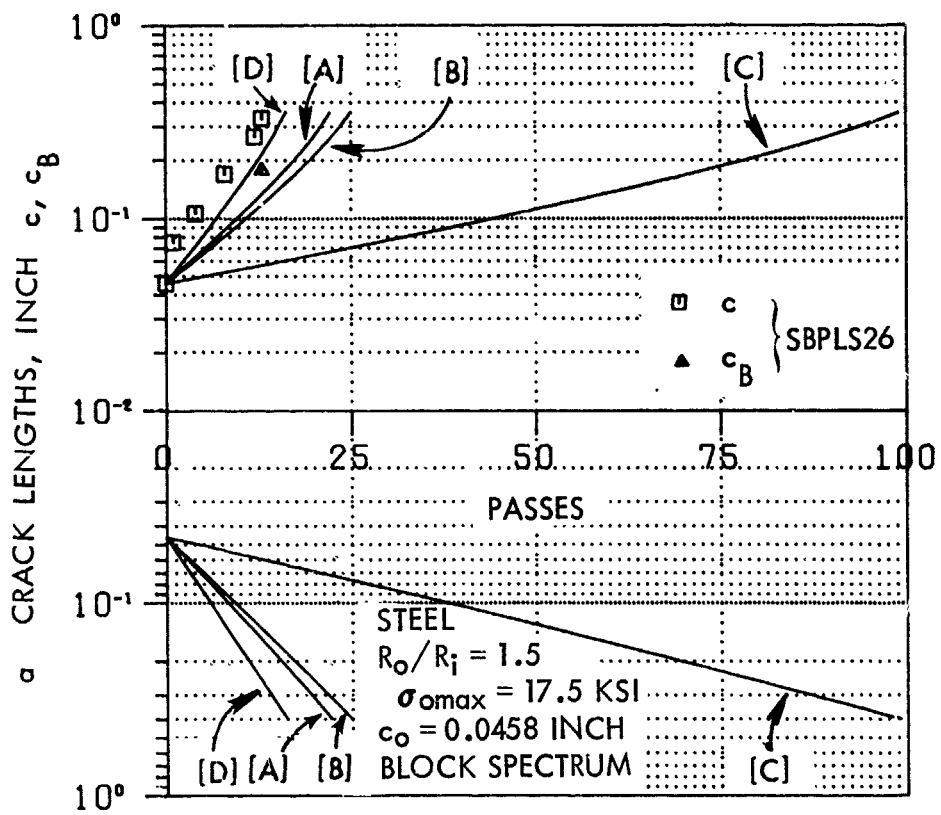
Figure 5-73. Corner Crack Growth Data and Prediction, Steel Lug,
$R_o/R_i = 1.5$, Block Spectrum Loading, $\sigma_{omax} = 17.5$ KSI

192
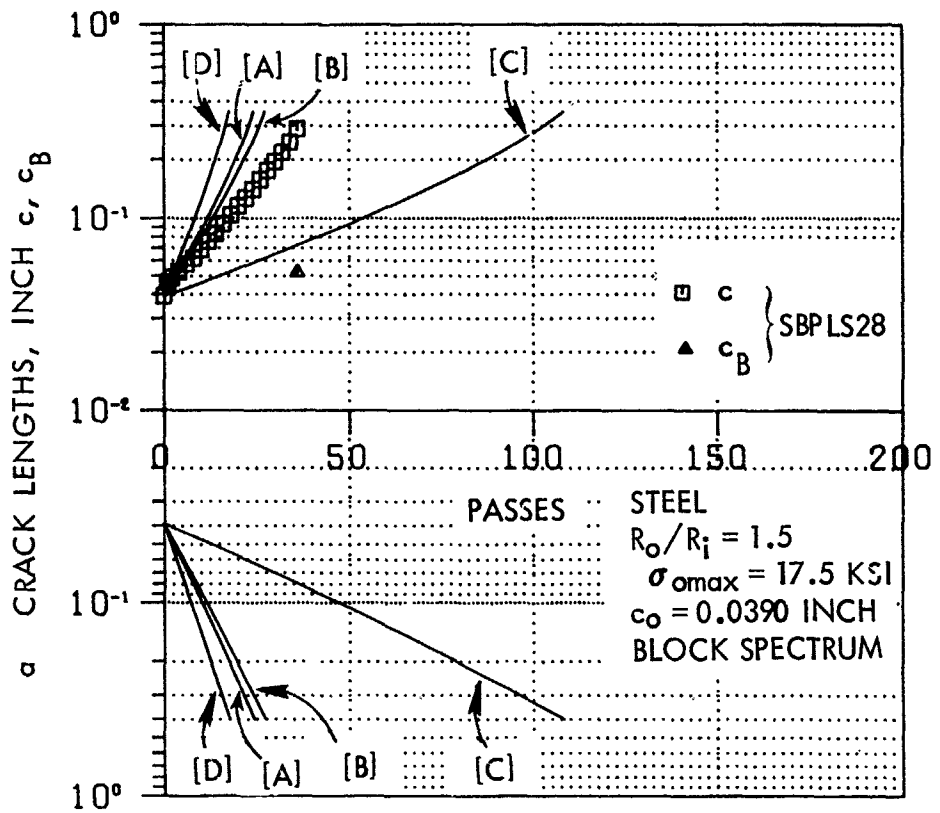
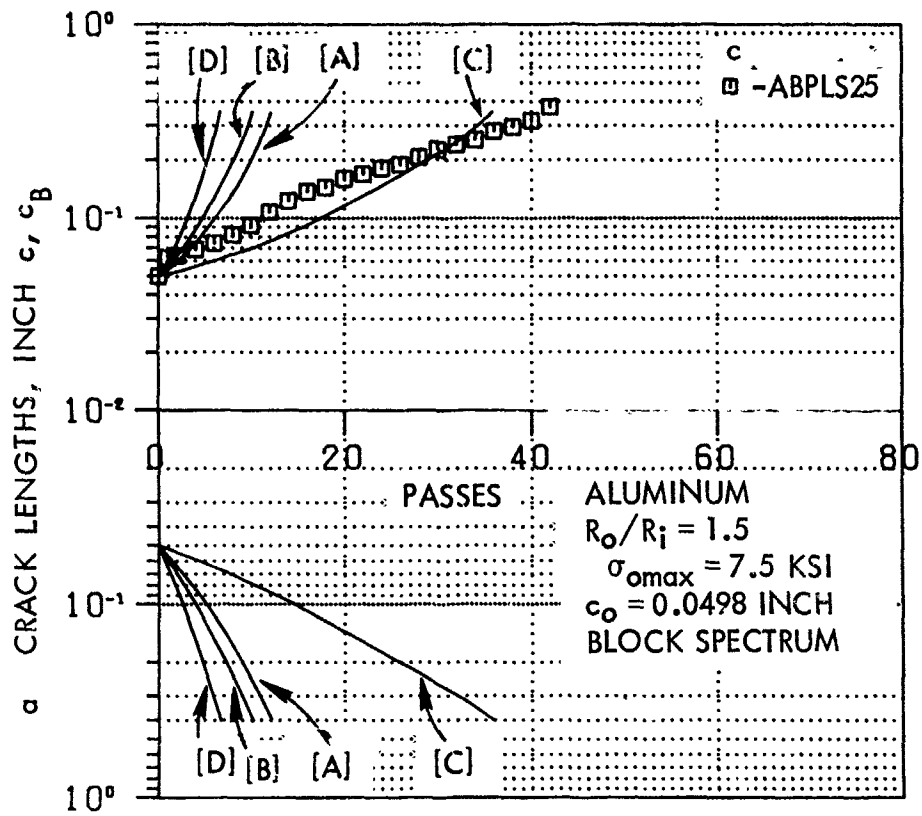Figure 5-74. Corner Crack Growth Data and Prediction, Steel Lug, $R_o/R_i=1.5$, Block Spectrum Loading, $\sigma_{omax} = 17.5$ KSI
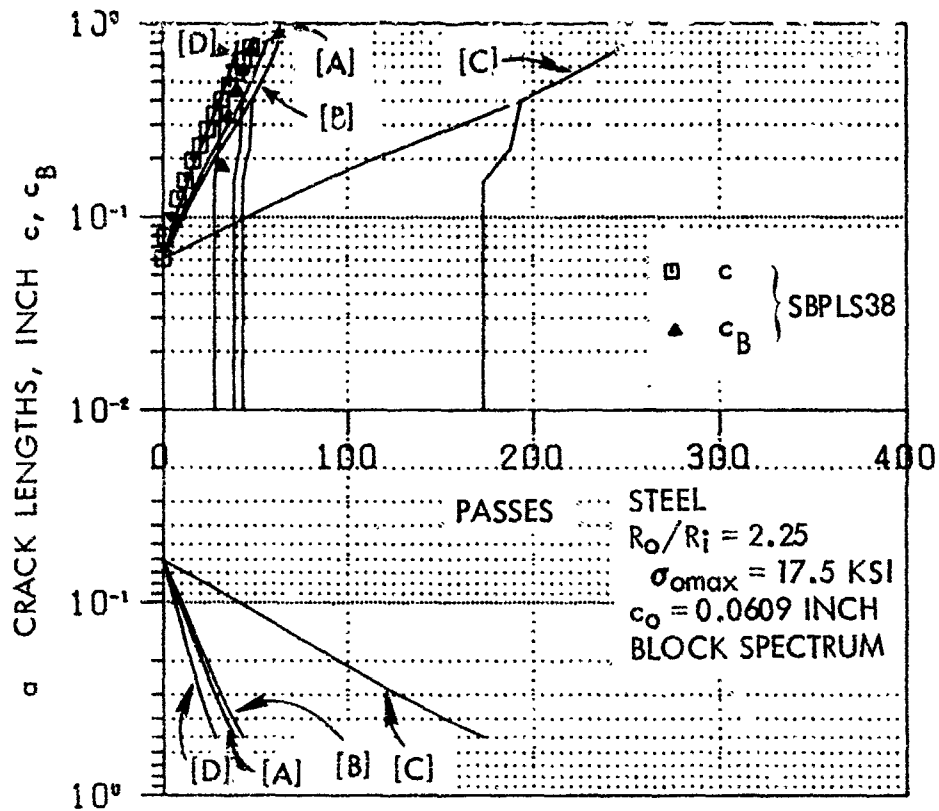
Figure 5-75. Corner Crack Growth Data and Prediction, Steel Lug, $R_o/R_i = 2.25$, Block Spectrum Loading, $\sigma_{omax} = 17.5$ KSI
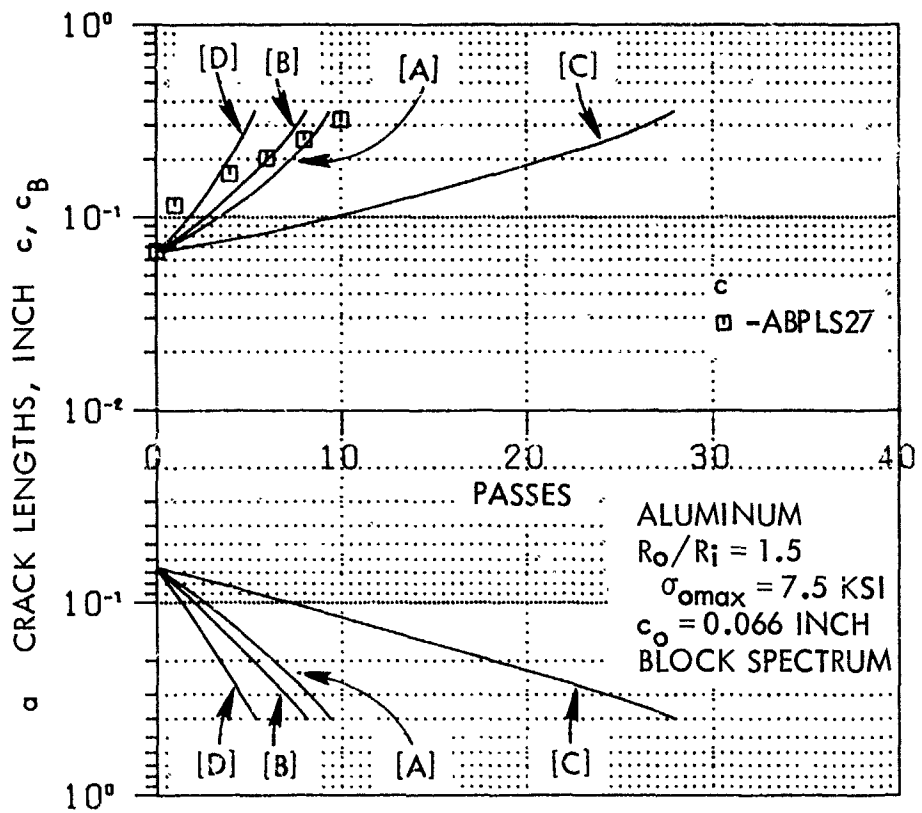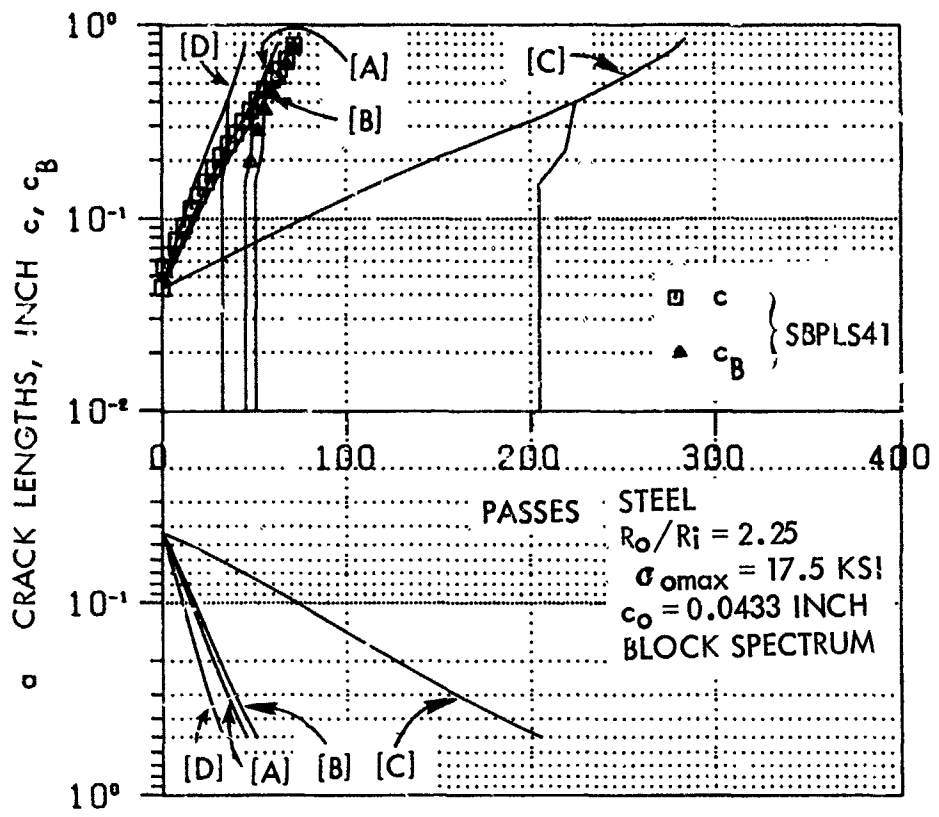
Figure 5-76. Corner Crack Growth Data and Prediction, Steel Lug, $R_o/R_i=2.25$, Block Spectrum Loading, $\sigma_{omax} = 17.5$ KSI
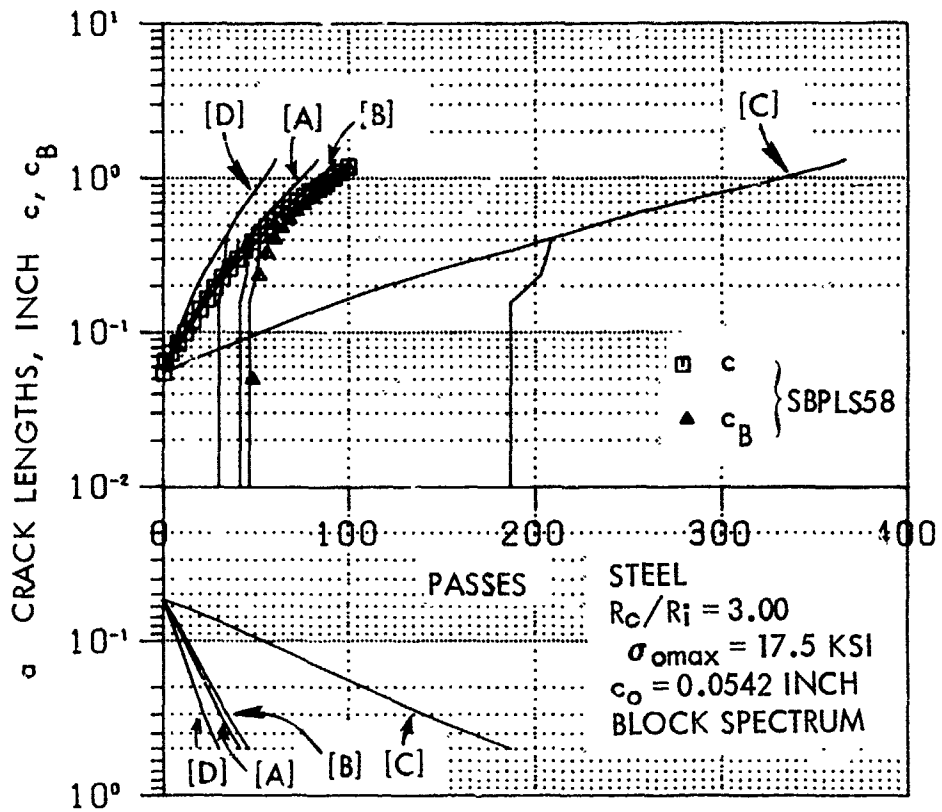
Figure 5-77. Corner Crack Growth Data and Prediction. Steel Lug, $R_o/R_i = 3.0$, Block Spectrum Loading, $\sigma_{omax} = 17.5$ KSI

196
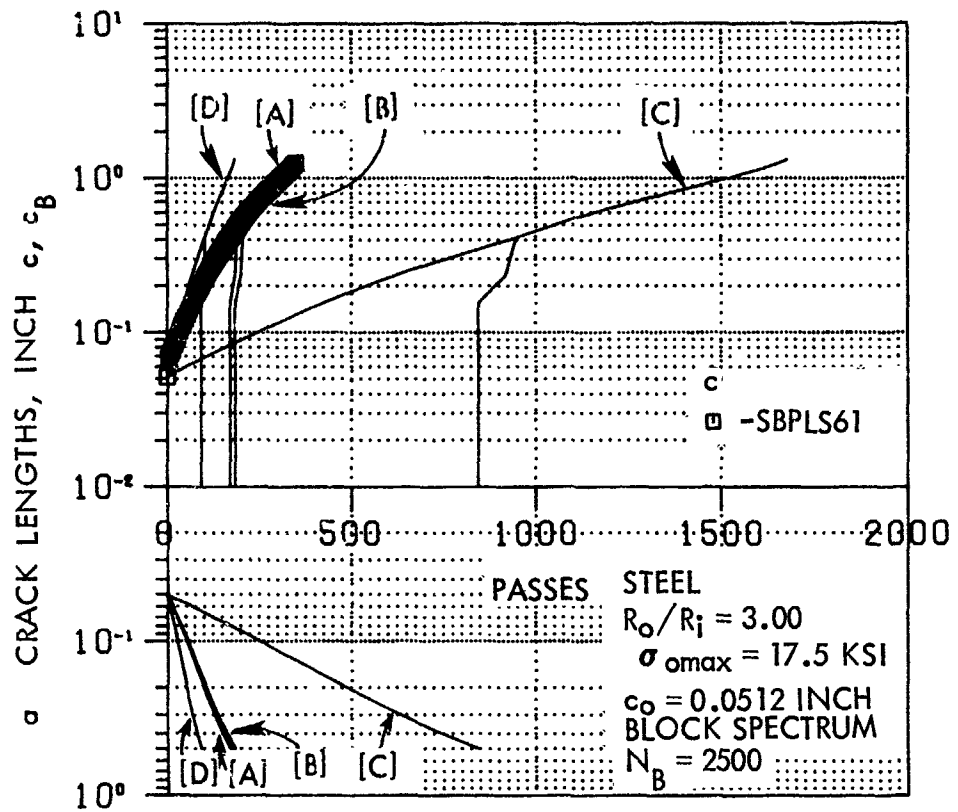
Figure 5-78. Corner Crack Growth Data and Prediction, Steel Lug,
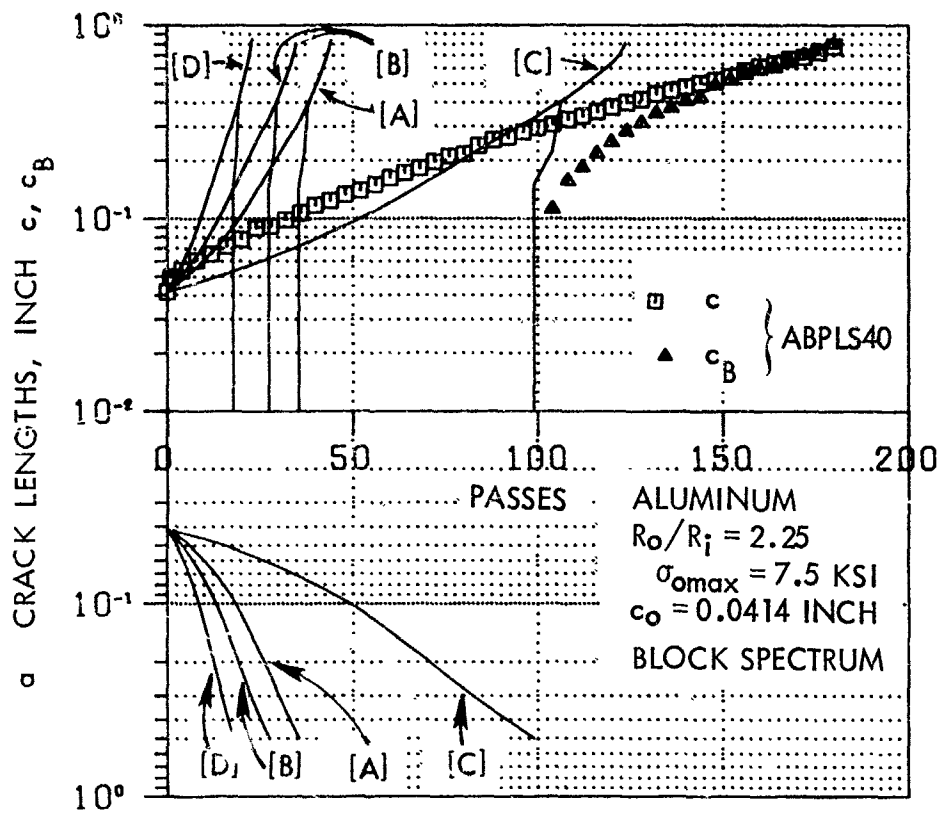R_o/R_i=3.0, Block Spectrum Loading, σ_{omax} = 17.5 KSI
(N_B=2500)
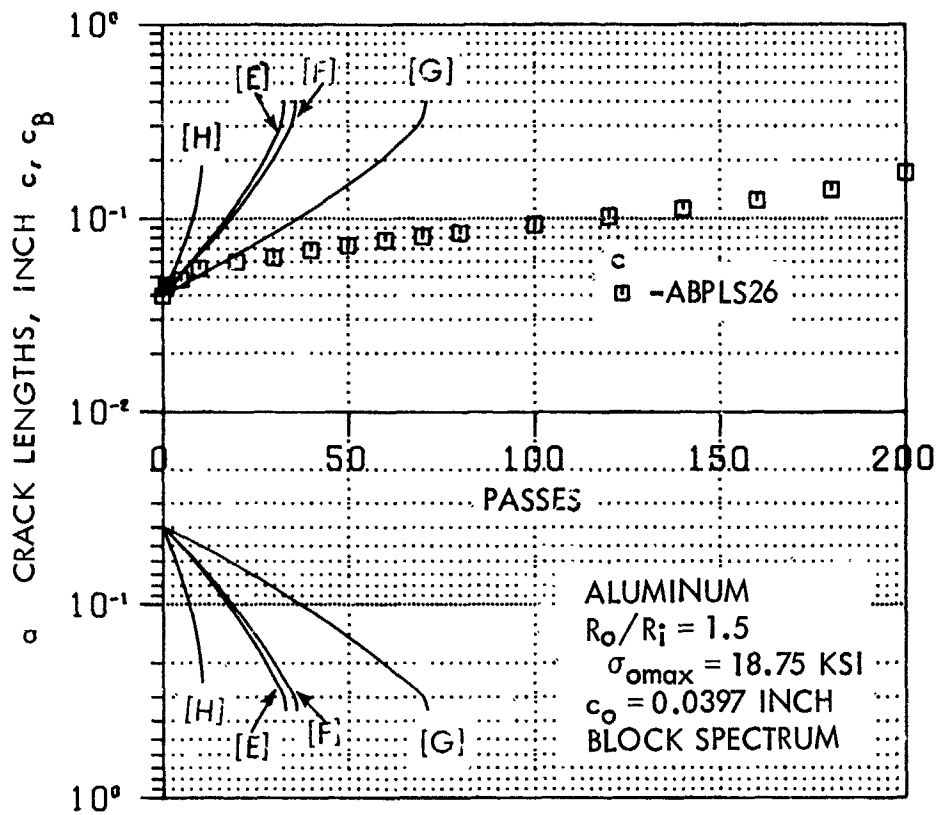
Figure 5-79. Corner Crack Growth Data and Prediction, Aluminum Lug, R_o/R_1=1.5, Block Spectrum Loading, σ_{omax} = 18.75 KSI
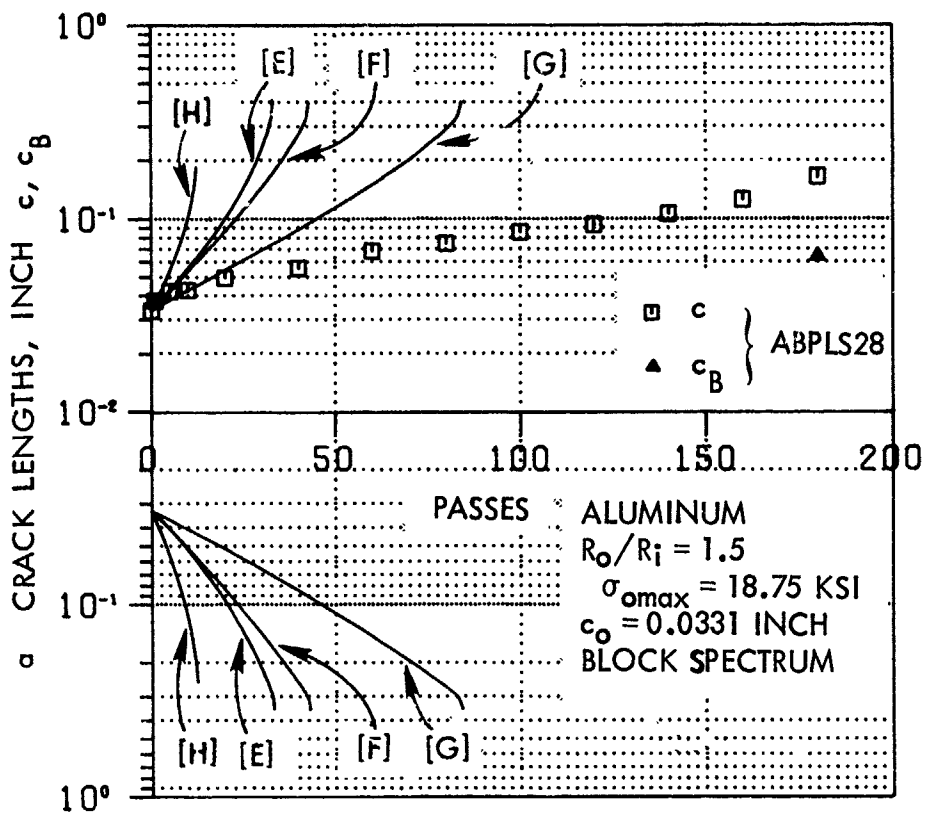
Figure 5-80. Corner Crack Growth Data and Prediction, Aluminum Lug,
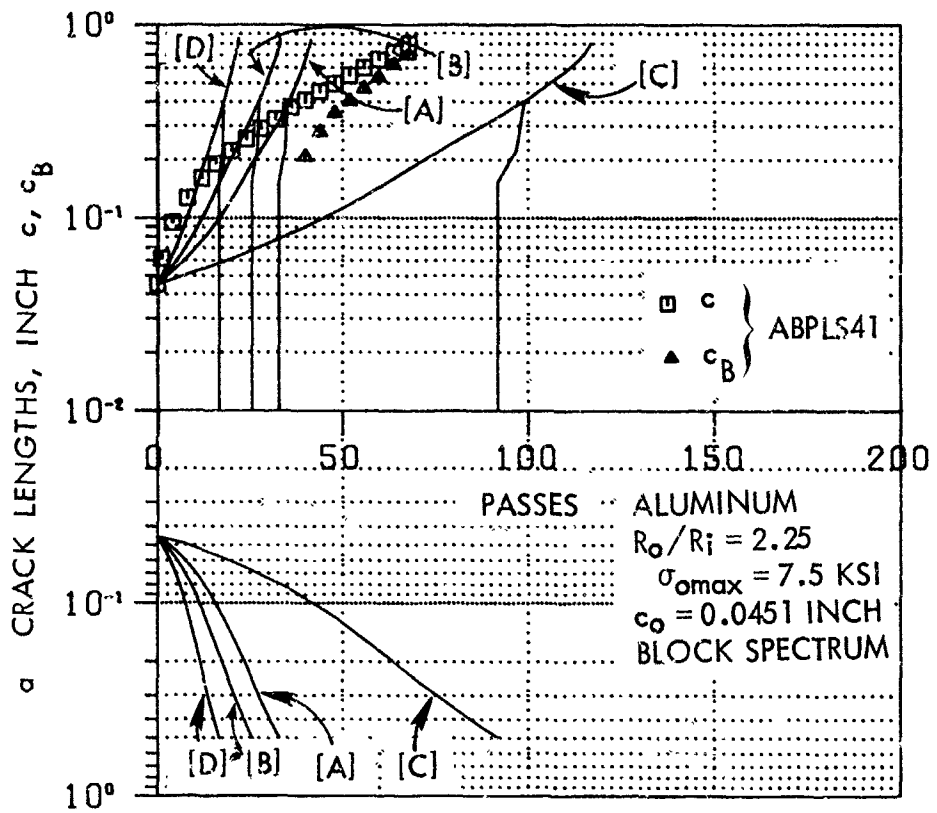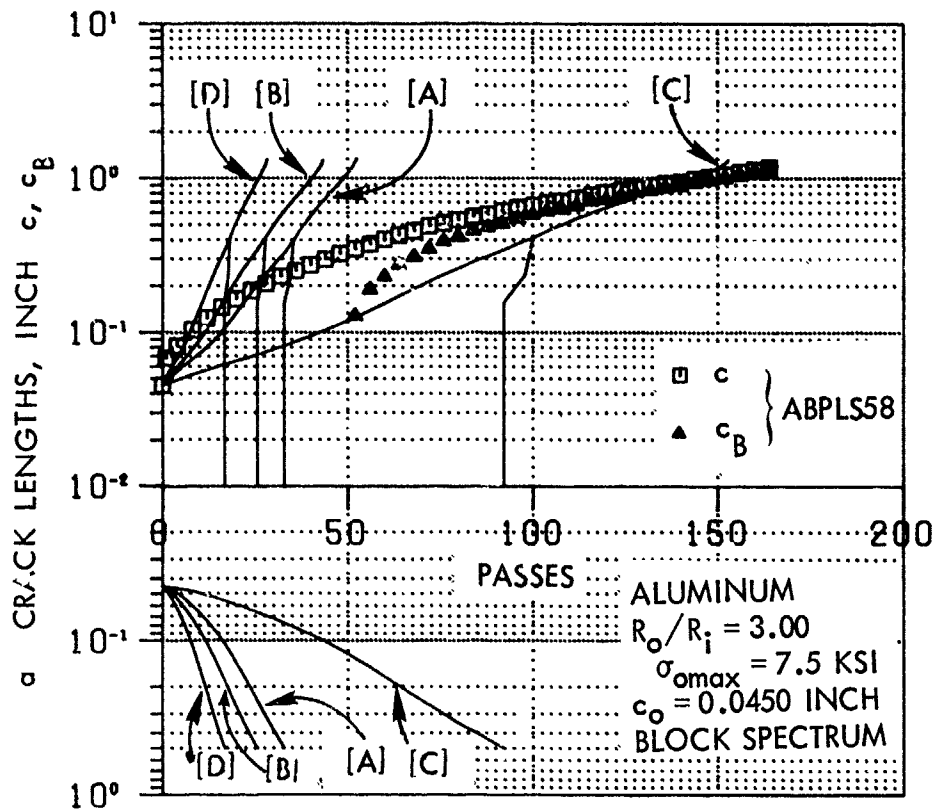R_o/R_i=1.5, Block Spectrum Loading, σ_{omax} = 18.75 KSI

Figure 5-81. Corner Crack Growth Data and Prediction, Aluminum Lug,
$R_o/R_i=2.25$, Block Spectrum Loading, $\sigma_{omax} = 18.75$ KSI
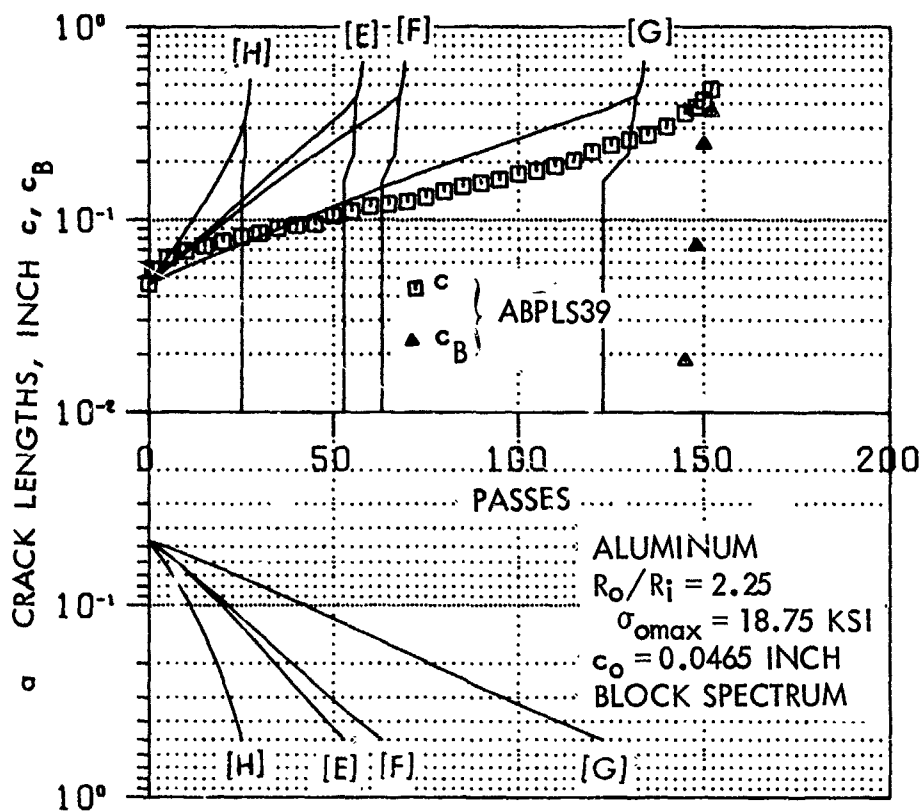
Figure 5-82. Corner Crack Growth Data and Prediction, Aluminum Lug, R_o/R_i=2.25, Block Spectrum Loading, σ_{omax} = 18.75 KSI
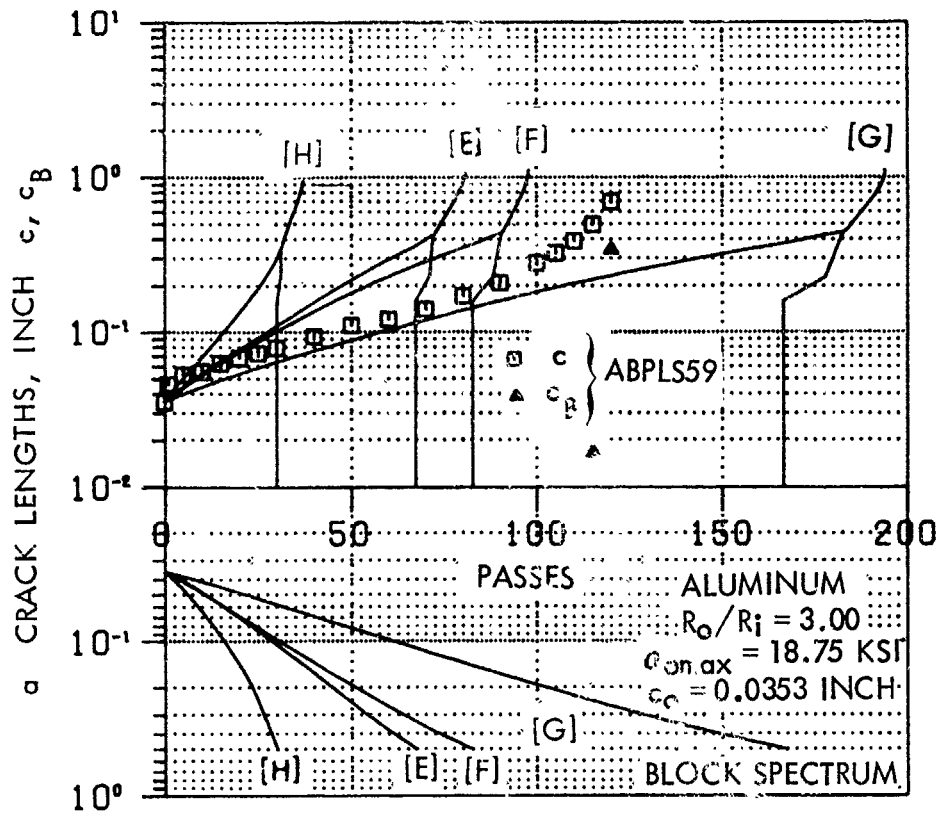
Figure 5-83. Corner Crack Growth Data and Prediction, Aluminum Lug, $R_o/R_i = 3.0$, Block Spectrum Loading, $\sigma_{omax} = 18.75$ KSI
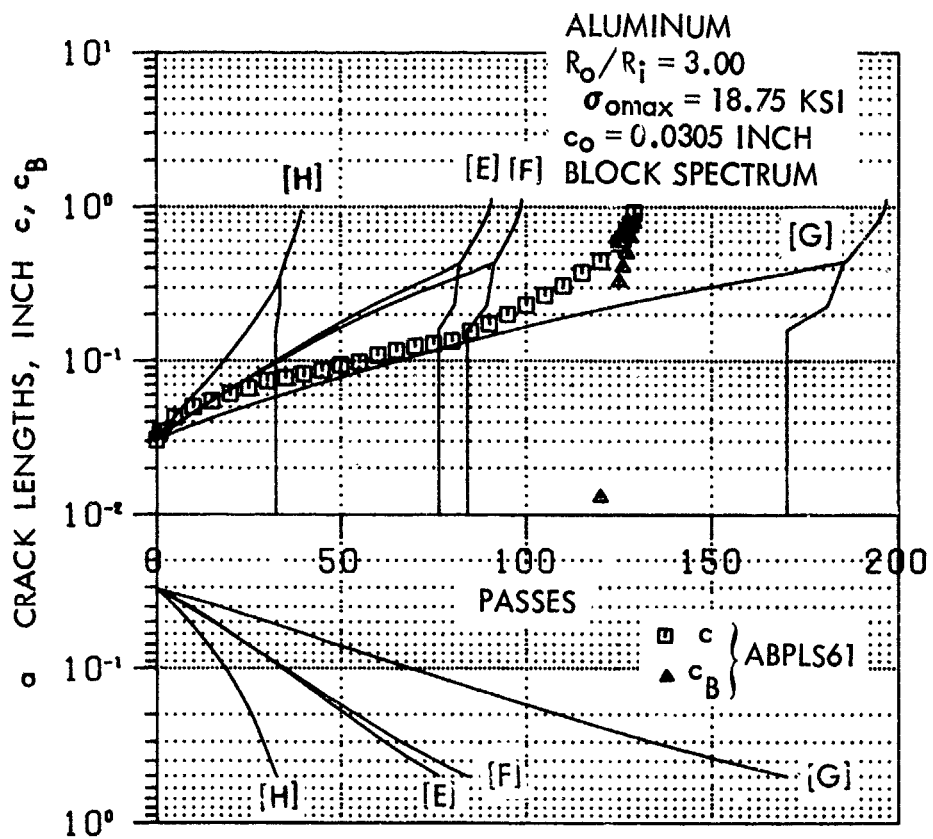
Figure 5-84. Corner Crack Growth Data and Prediction, Aluminum Lug, $R_o/R_i = 3.0$, Block Spectrum Loading, $\sigma_{omax} = 18.75$ KSI
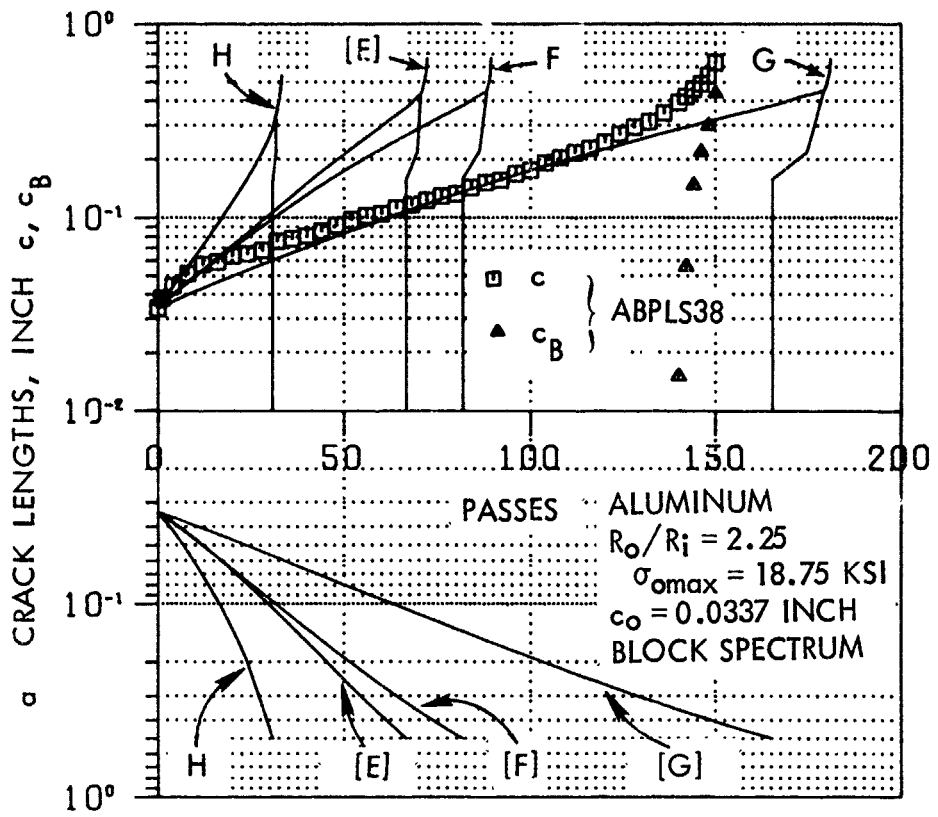
as in the case of duplicate Specimen SBPLS58 (Figure 5-77). This was the first corner crack block spectrum test conducted and the testing period was too long. Thus the block spectrum was modified to 7500 cycles per block and was used in all other cases.

None of the four analytical predictions presented in Figures 5-79 through 5-84 for aluminum lugs subjected to above-yield block spectrum loading are very accurate, for the reasons cited in subsection 4.2.1. However, the Hsu [E] and the Generalized Willenborg [F] models predict consistently conservative lives, as in the case of the through-the-thickness crack cases.

4.3 BASELINE FLIGHT-BY-FLIGHT SPECTRUM TESTS

Thirty-six preflawed straight lug specimens were tested using three different flight-by-flight load spectra: (1) cargo (or transport) spectrum, (2) severe cargo (or transport) spectrum and (3) fighter spectrum. The details of the spectra are provided in subsection 6.2 of Section III and Appendix B. All 36 specimens were steel lugs, 18 with initial through-the-thickness cracks, and 18 with initial corner cracks. Each group of tests covered the 3 different loading spectra and 3 R_o/R_i ratios (1.5, 2.25 and 3.00), with duplicate specimens for each test condition.

4.3.1 Through-the-Thickness Crack Flight-by-Flight Spectrum Tests

Comparison of analytical and experimental results of all the through-the-thickness crack steel specimens subjected to flight-by-flight spectrum loading are presented in Figures 5-85 through 5-93. The first three figures (Figures 5-85 through 5-87) are for the cargo spectrum; the next three (Figures 5-88 through 5-90) are for the severe cargo spectrum; and the last three (Figures 5-91 through 5-93) are for the fighter spectrum. Each set of three figures again corresponds to increasing R_o/R_i ratios of 1.5, 2.25 and 3.00. The results were extrapolated to a common initial crack length of 0.025 inch, and thus the duplicate test results are provided in the same figure for each test condition. The abscissa "PASSES" refers to the number of times the flight-by-flight loading spectrum was repeated. One pass of

204

Figure 5-85. Through-the-Thickness Crack Growth Data and Prediction, Steel Lug, R_o/R_i=1.5, Cargo Spectrum Loading

205

Figure 5-86. Through-the-Thickness Crack Growth Data and Prediction, Steel Lug, R_o/R_i=2.25, Cargo Spectrum Loading

206

Figure 5-87.   Through-the-Thickness Crack Growth Data and Prediction,
Steel Lug, $R_o/R_i = 3.0$, Cargo Spectrum Loading

Figure 5-88. Through-the-Thickness Crack Growth Data and Prediction, Steel Lug, $R_o/R_i=1.5$, Severe Cargo Spectrum Loading

208

Figure 5-89. Through-the-Thickness Crack Growth Data and Prediction, Steel Lug, $R_o/R_i = 2.25$, Severe Cargo Spectrum Loading

Figure 5-90. Through-the-Thickness Crack Growth Data and Prediction, Steel Lug, $R_o/R_i=3.0$, Severe Cargo Spectrum Loading
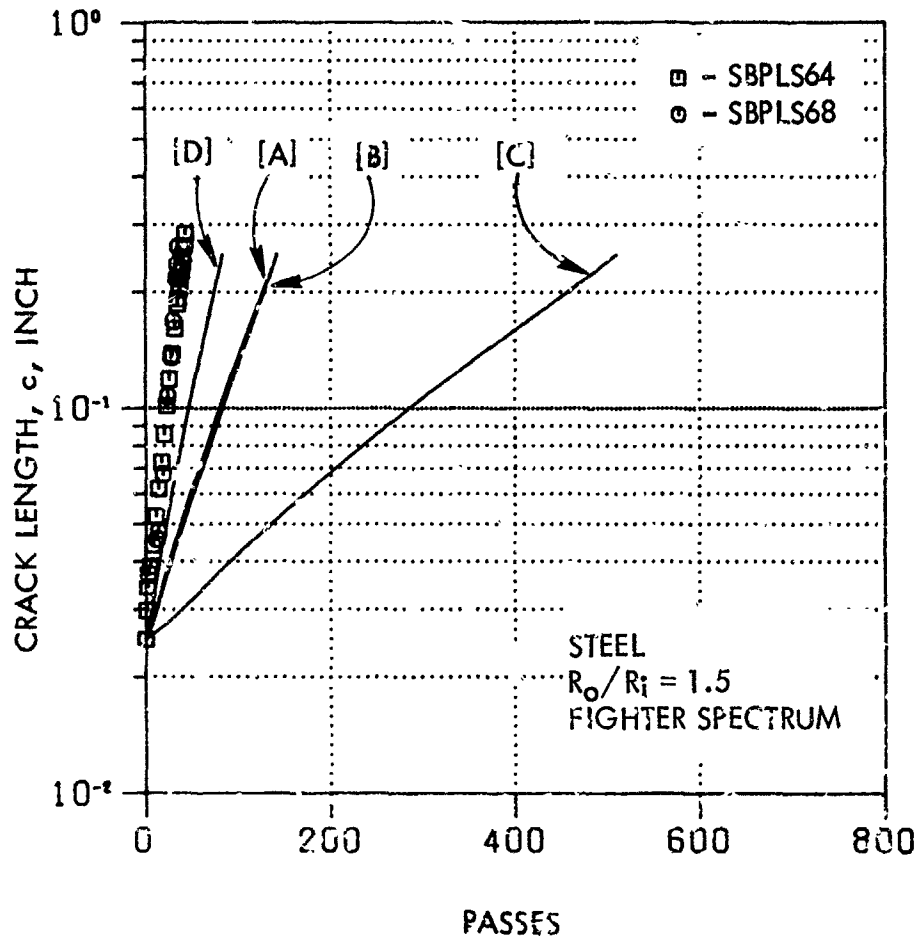
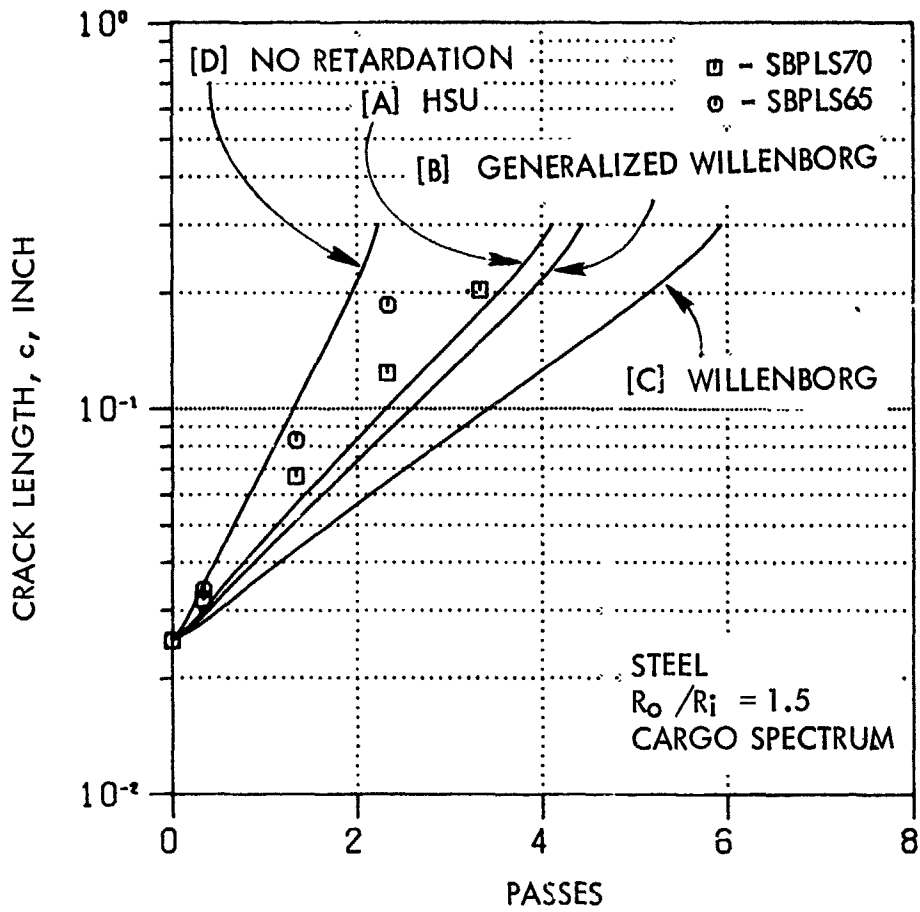Figure 5-91. Through-the-Thickness Crack Growth Data and Prediction, Steel Lug, $R_o/R_i=1.5$, Fighter Spectrum Loading
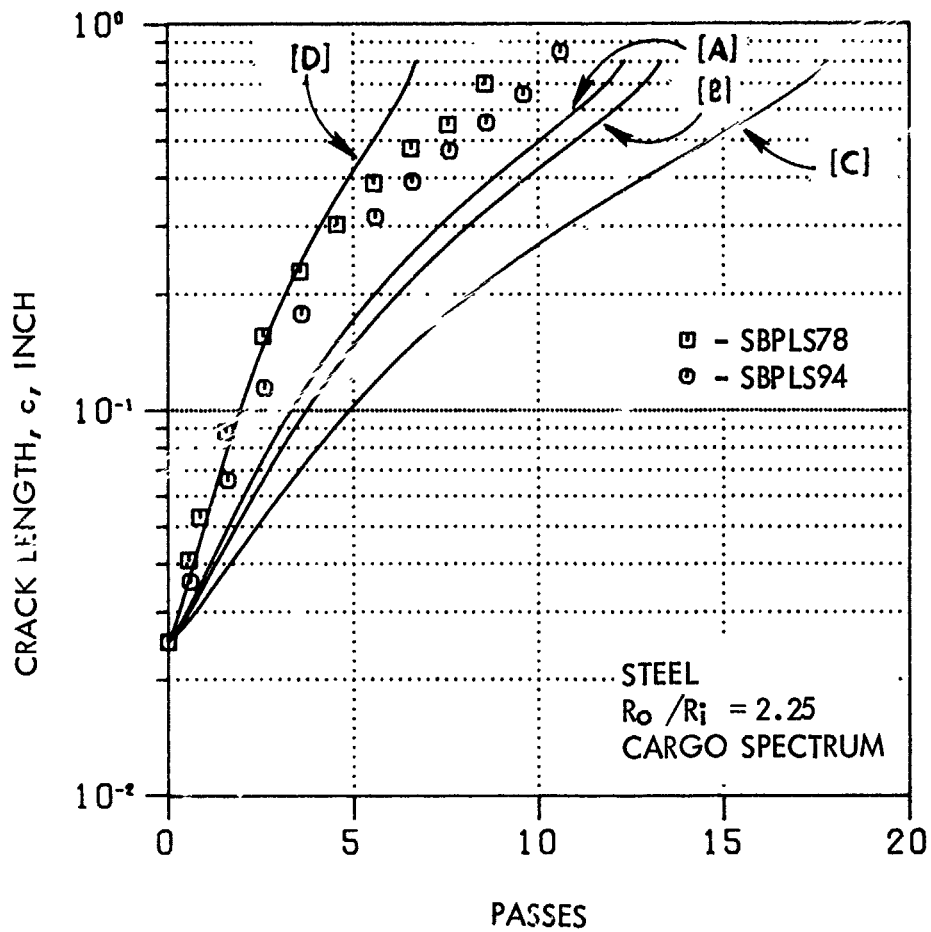
211
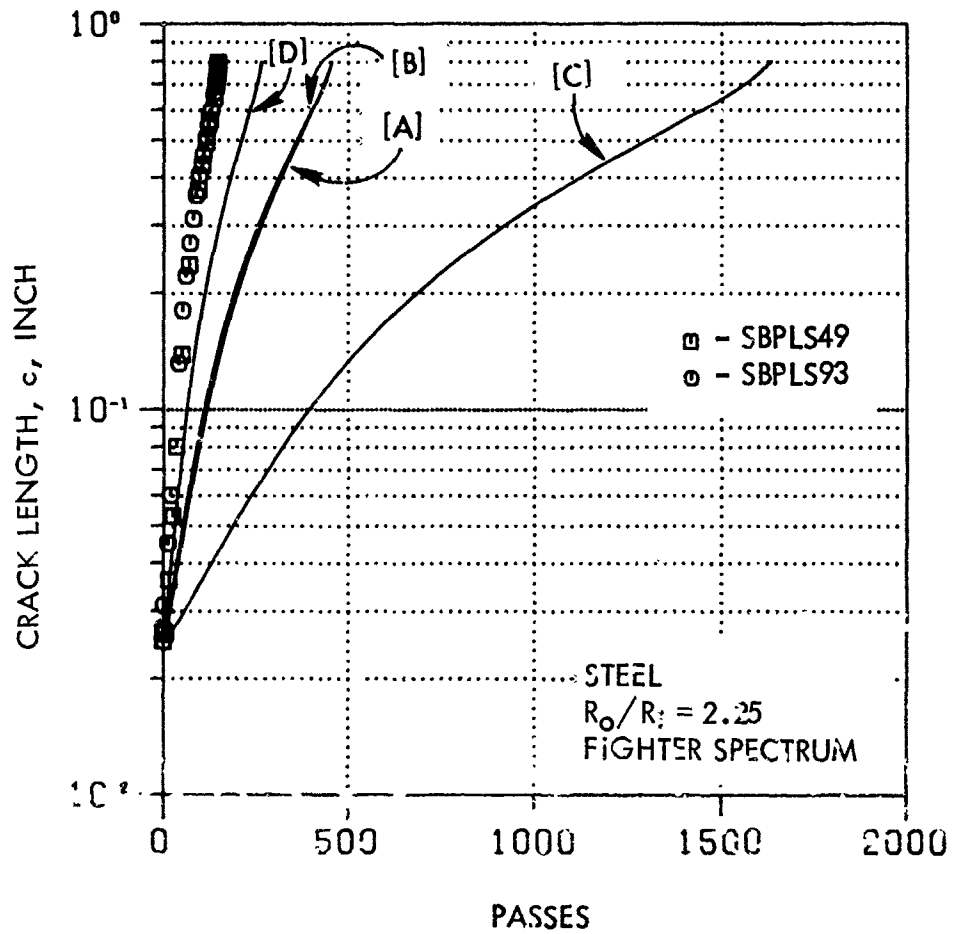
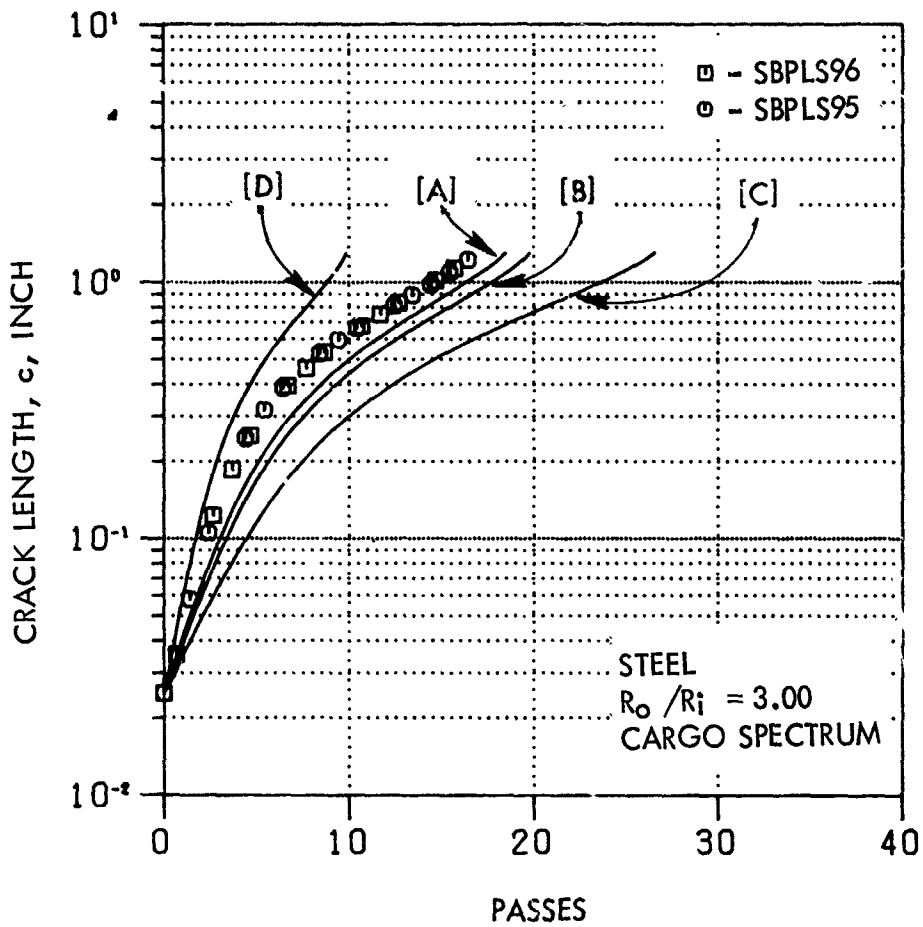Figure 5-92.   Through-the-Thickness Crack Growth Data and Prediction, Steel Lug, $R_o/R_i=2.25$, Fighter Spectrum Loading

212
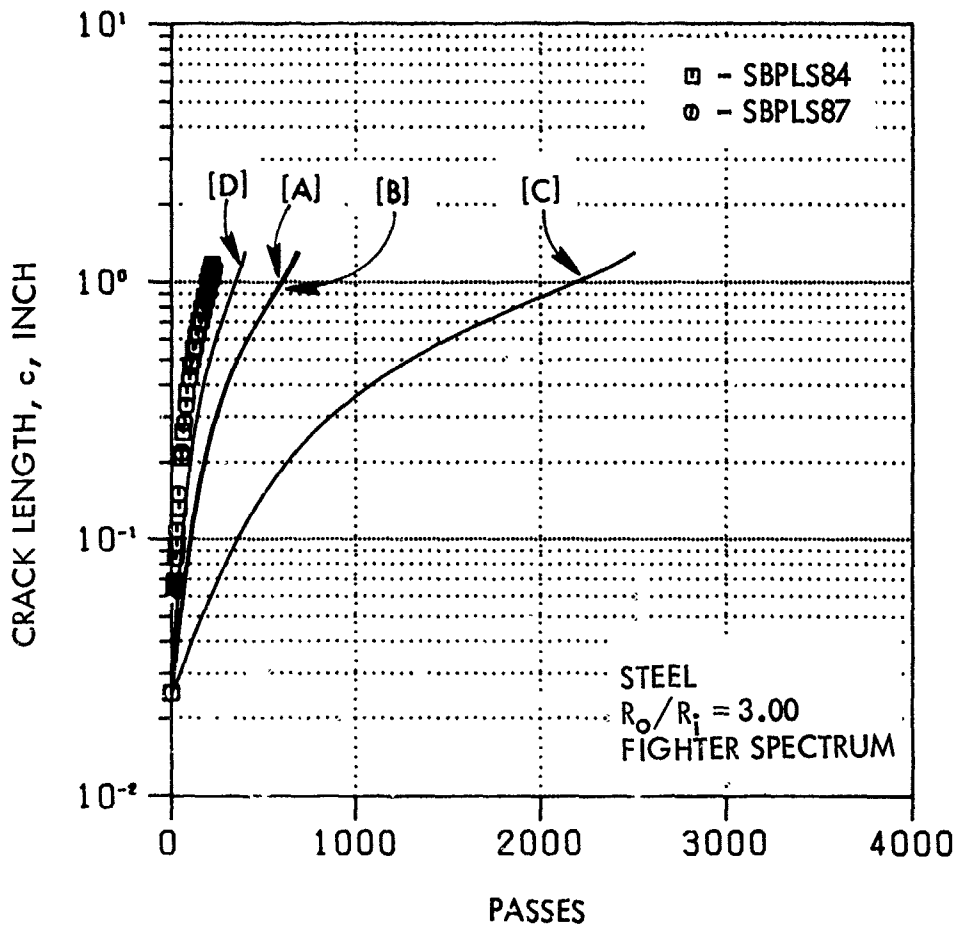
Figure 5-93. Through-the-Thickness Crack Growth Data and Prediction.
Steel Lug, R_o/R_i=3.0, Fighter Spectrum Loading

the cargo and severe cargo spectra conists of 120 flights and the fighter spectrum consists of 80 flights.

Analytical predictions were made using the Hsu [A] and Generalized Willenborg [B] retardation models. A value of $\phi = 0.4$ was used in the Generalized Willenborg model. For reference only, calculations were also made using the Willenborg [C] and No-Retardation [D] models.

Predictions for the cargo and severe cargo spectra were slightly unconservative or in close agreement with the experimental data (Figures 5-85 through 5-90). However for the fighter spectrum results (Figures 5-91 through 5-93), the predictions were consistently unconservative by about a factor of 3 to 4 for all of the R_o/R_i ratios. The experimental lives were even consistently lower than the No-Retardation model prediction. The analytical and experimental data for all the fighter spectrum test cases were thoroughly examined to explain this discrepancy, and no errors or explanations were found. The same fighter spectrum was used for aluminum lug specimens of Group II testing, which are reported in the next section, and good correlations between the predicted and experimental results were observed.

4.3.2 Corner Crack Flight-by-Flight Spectrum Tests

Correlation between the predicted and experimental results of growth behavior of corner cracks in steel lugs subjected to the cargo, severe cargo and fighter flight-by-flight spectra are given in Figures 5-94 through 5-96, 5-97 through 5-99, and 5-100 through 5-102, respectively. The figures are again arranged in increasing order of R_o/R_i ratios of 1.5, 2.25 and 3.0 with duplicate test results presented in each figure.

As in the case of block spectrum loading tests, extensive trial tests were made to select a flight-by-flight spectrum which produces markings on the fracture surface so that the crack aspect ratio, a/c, could be monitored. Such efforts were unfruitful and thus it was decided to monitor the back surface crack length, c_B, to obtain maximum information from these tests.

The same four prediction models were employed. Comparisons of experimental data with either the Hsu [A] or Generalized Willenborg [B]
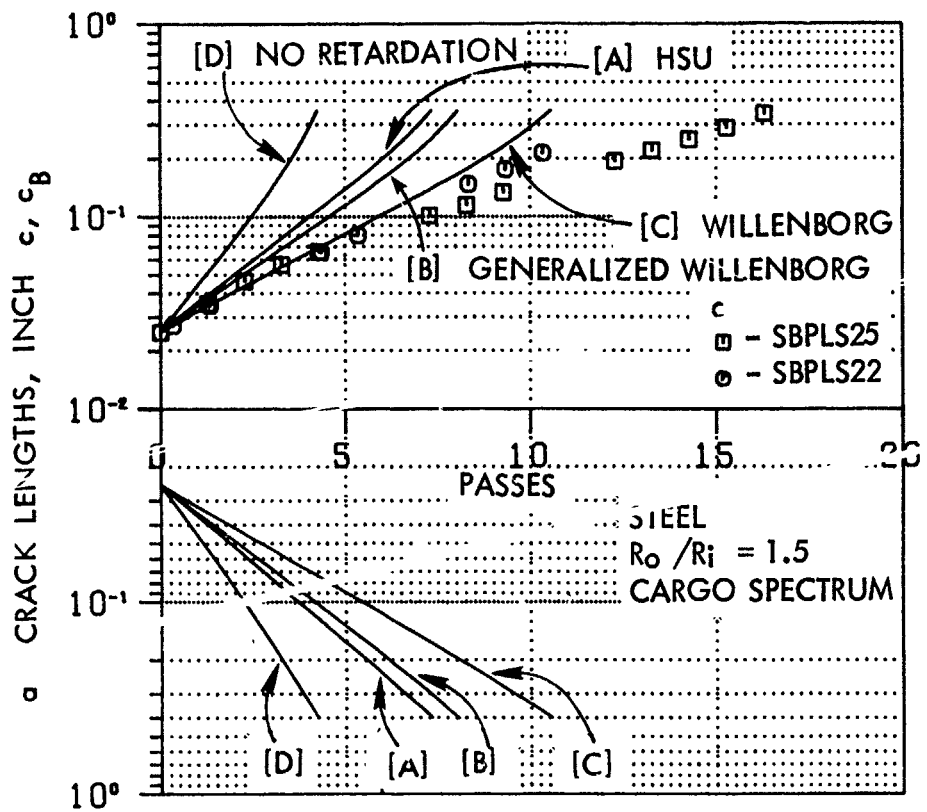
Figure 5-94. Corner Crack Growth Data and Prediction, Steel Lug, $R_o/R_i=1.5$, Cargo Spectrum Loading
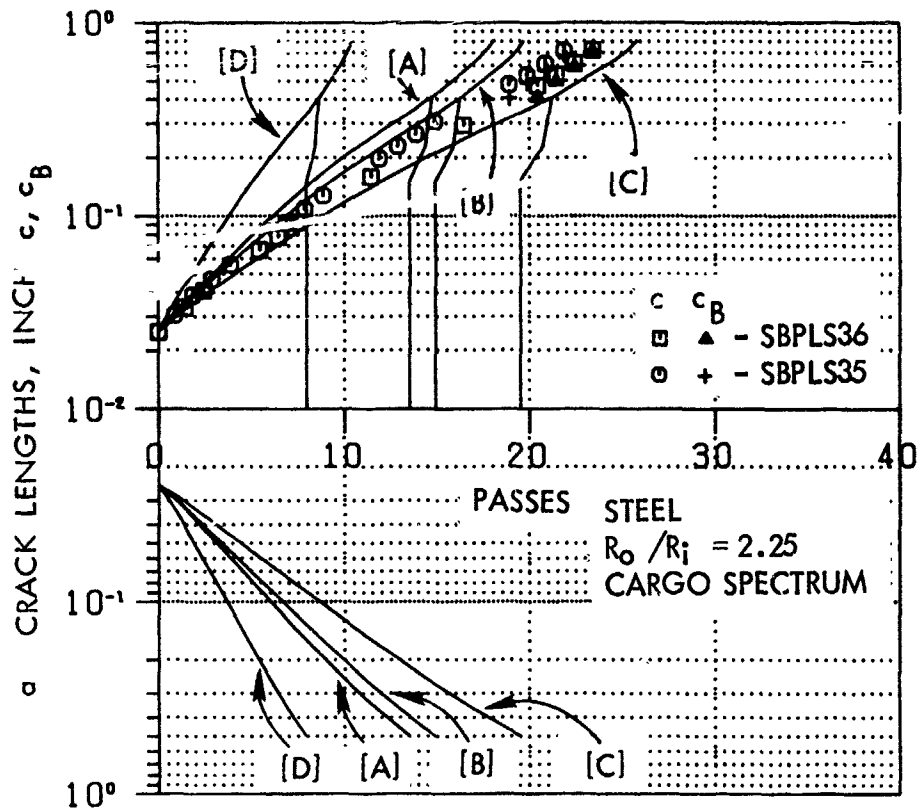
Figure 5-95.   Corner Crack Growth Data and Prediction, Steel Lug,
R_o/R_i=2.25, Cargo Spectrum Loading
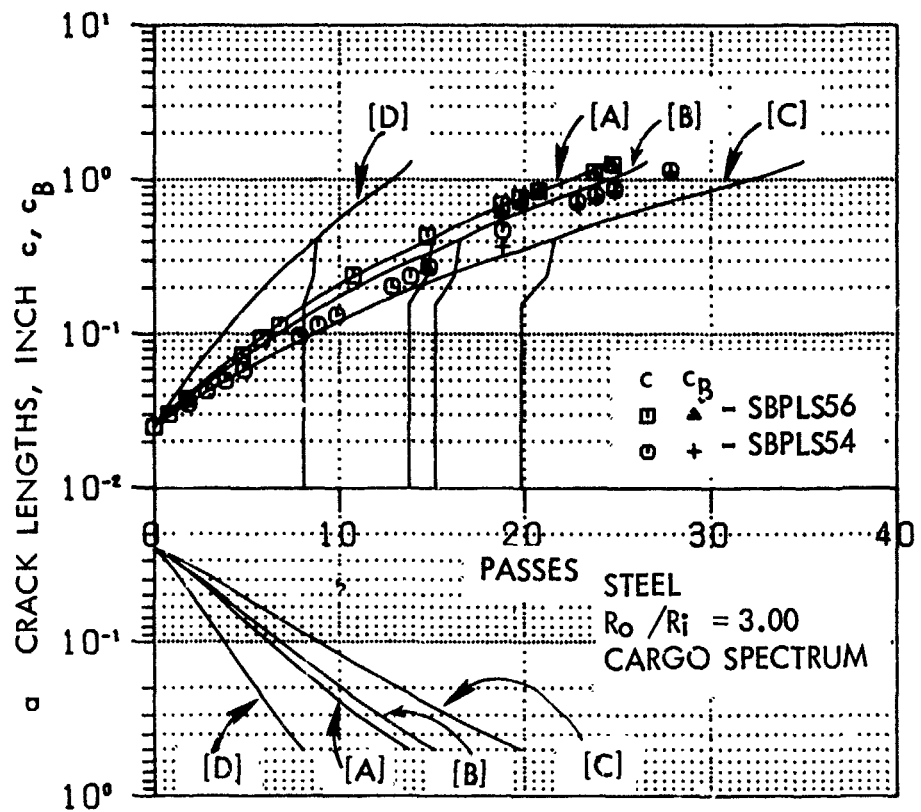
Figure 5-96. Corner Crack Growth Data and Prediction, Steel Lug, R_o/R_i=3.0, Cargo Spectrum Loading
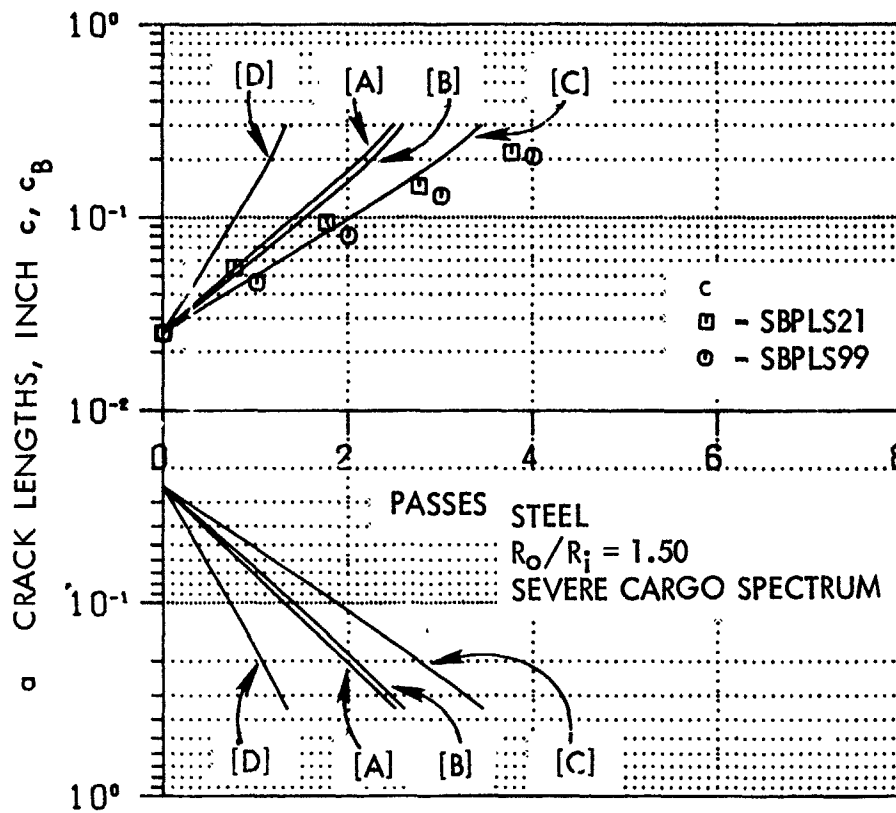
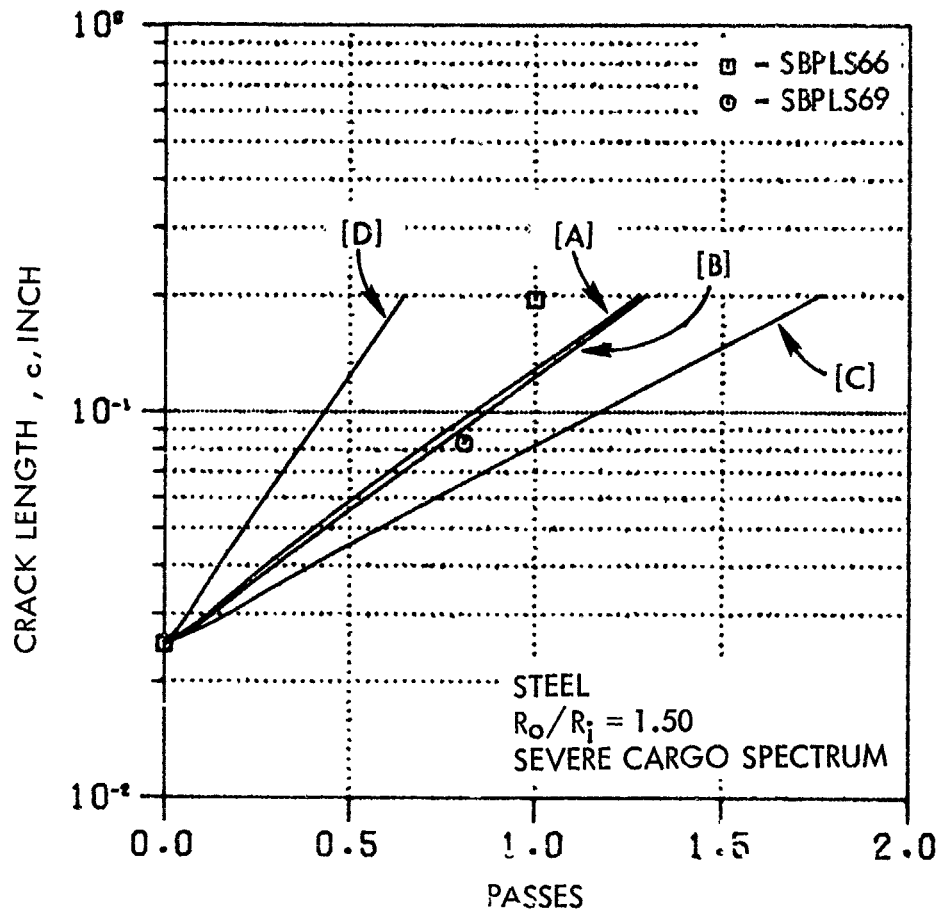Figure 5-97. Corner Crack Growth Data and Prediction, Steel Lug, R_o/R_i=1.5, Severe Cargo Spectrum Loading
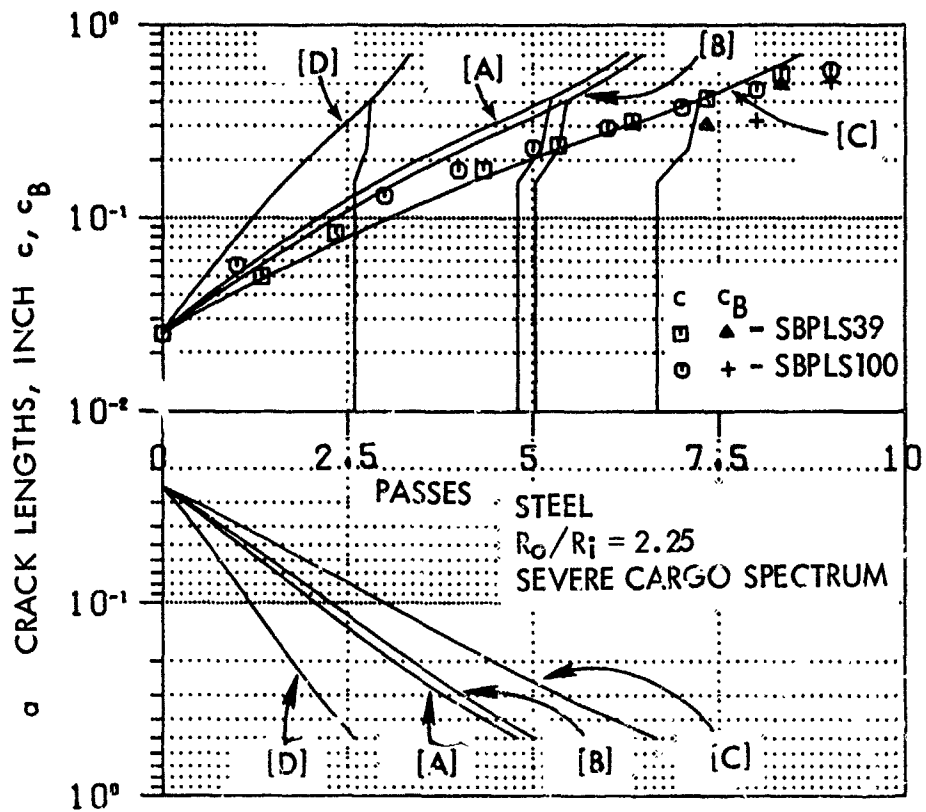
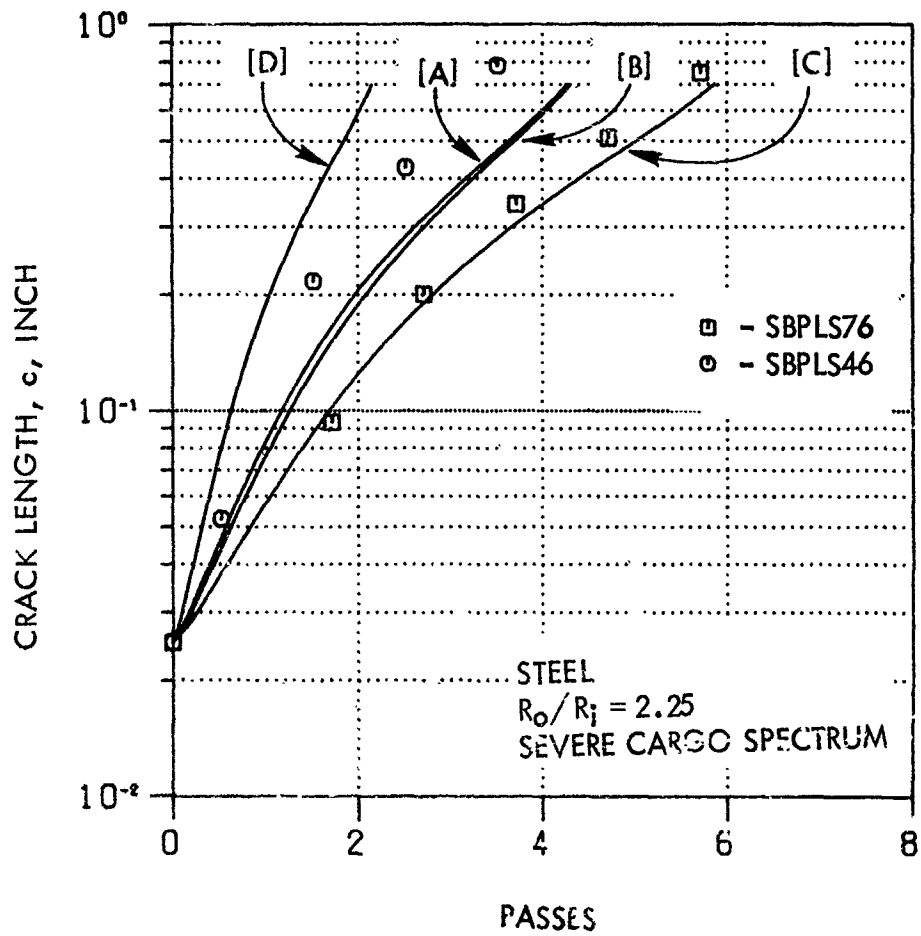Figure 5-98. Corner Crack Growth Data and Prediction, Steel Lug, $R_o/R_i=2.25$, Severe Cargo Spectrum Loading
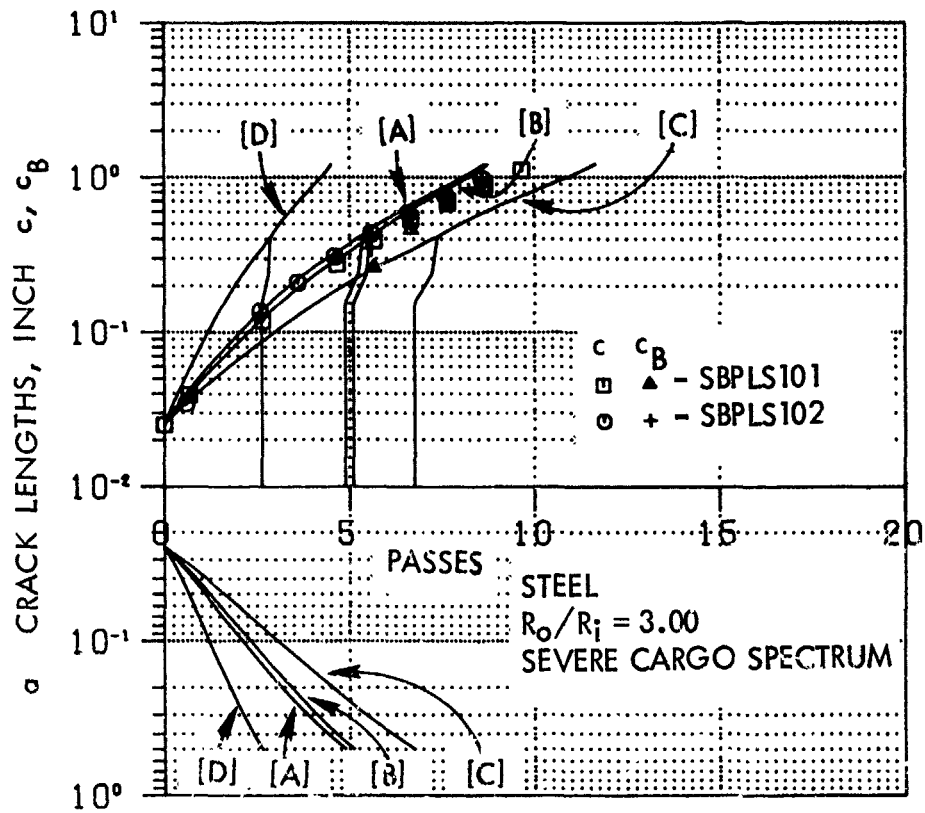
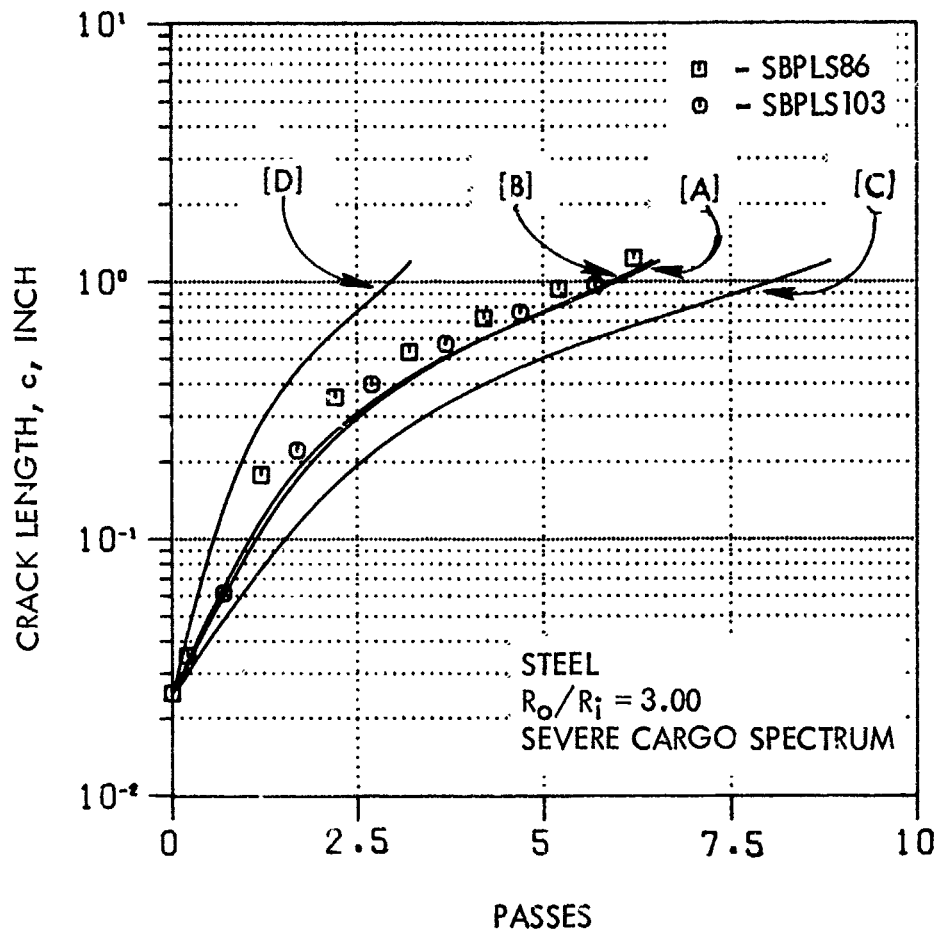Figure 5-99. Corner Crack Growth Data and Prediction, Steel Lug,
$R_o/R_i=3.0$, Severe Cargo Spectrum Loading
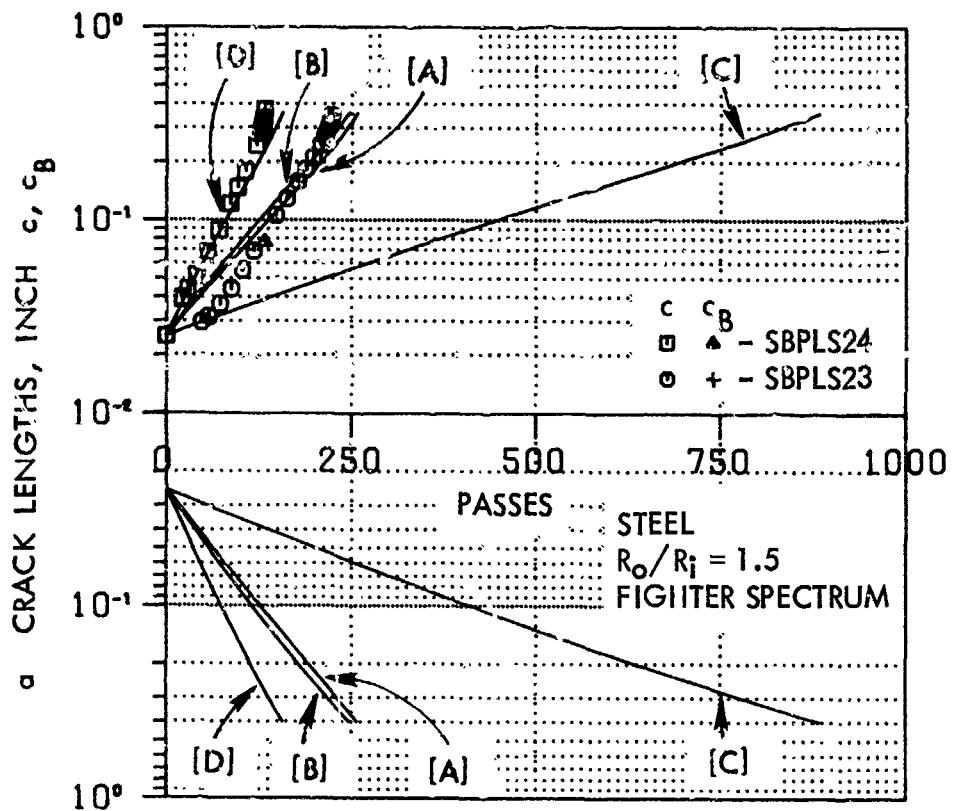
Figure 5-100. Corner Crack Growth Data and Prediction, Steel Lug, R_o/R_i=1.5, Fighter Spectrum Loading

221
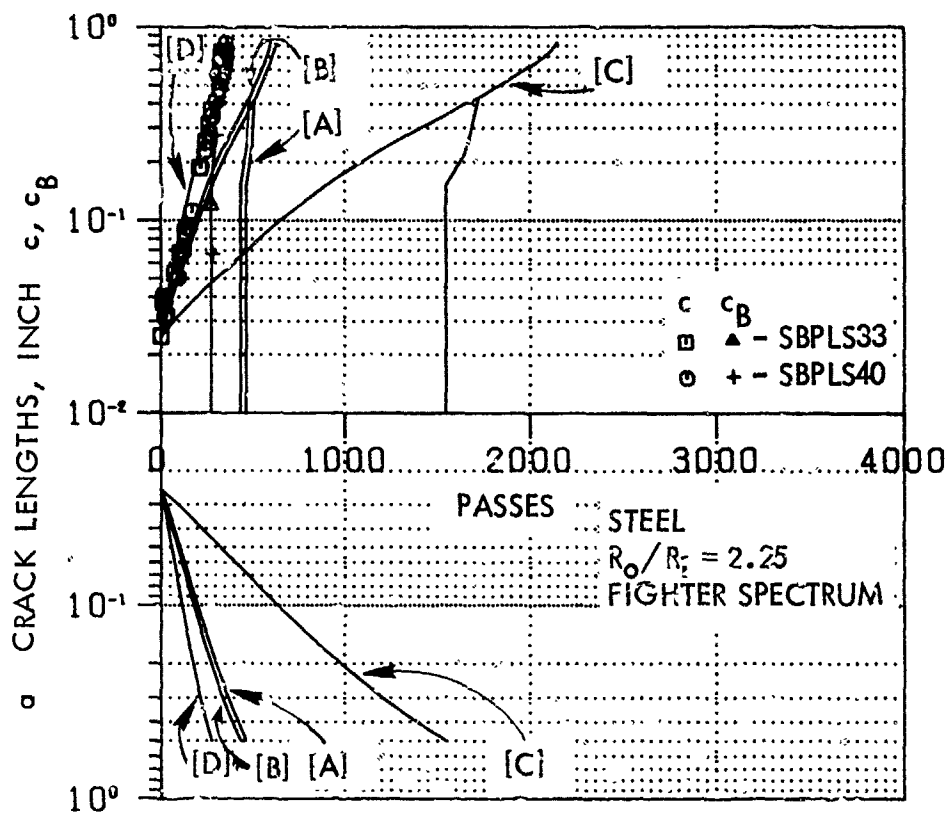
Figure 5-101. Corner Crack Growth Data and Prediction, Steel Lug,
$R_o/R_i=2.25$, Fighter Spectrum Loading
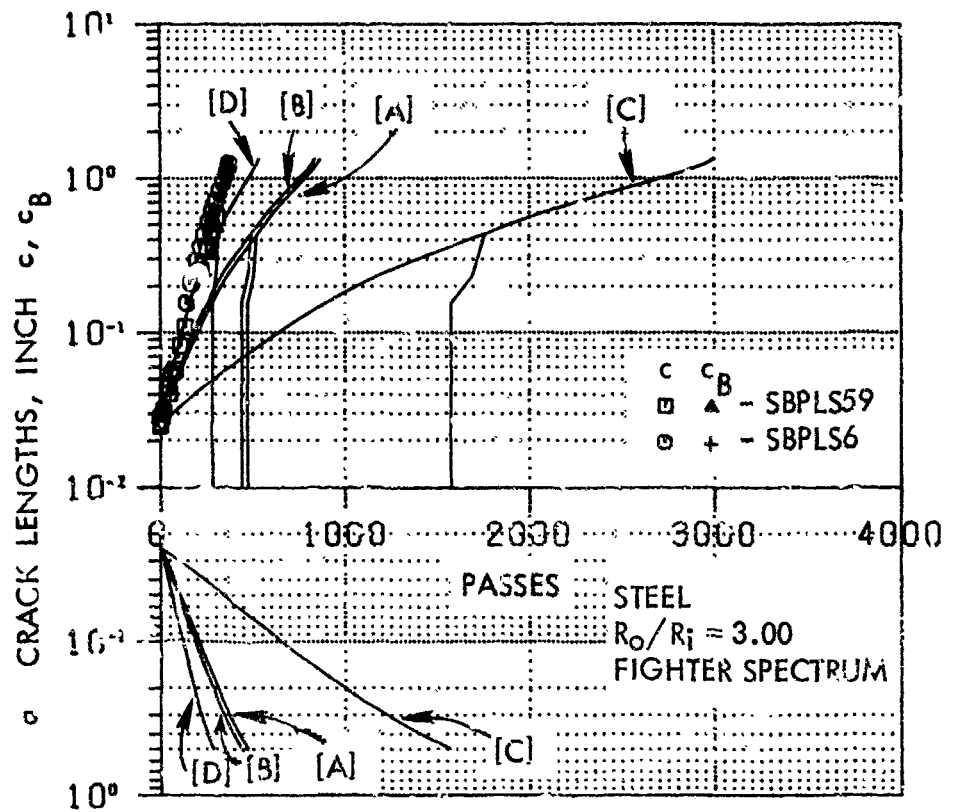
Figure 5-102. Corner Crack Growth Data and Prediction, Steel Lug, $R_o/R_i = 3.0$, Fighter Spectrum Loading

model show good correlations for cargo and severe cargo spectrum loading cases. For fighter spectrum loading cases, the analyses were unconservative, as they were in the case of through-the-thickenss crack problems. All the four models ([A], [B], [C] and [D]) predict failure prior to transition to a through-the-thickness crack for the smaller lugs (R_o/R_i = 1.50), which was the case in most of the experiments. For medium and large lugs during transition, the back surface crack very rapidly catches up with the front surface crack, as predicted by the analyses. This can be observed by noting the back surface crack lengths between two data points where transition takes place. At the first point where the crack has not broken through the thickness yet, c_B is zero. But within the next few passes, where the next data point was taken, the back surface crack length is almost equal to the front surface crack length.

4.4 VARIATIONAL TESTS

In the 16 variational tests of Group I testing, two types of variations from the baseline tests discussed previously were considered. In 8 specimens, residual stresses were introduced in the lug by installing an interference-fit bushing. The nominal thickness of the steel bushings used was 0.09 inch. In the other 8 specimens the thickness of the lug was 0.25 inch instead of 0.5 inch. Only the through-the-thickness initial crack was considered for lug specimens with interference-fit bushings, and only initial corner cracks were considered for the thickness variational tests. In each case, 4 specimens were aluminum lugs and 4 were steel lugs. All were medium lugs with R_o/R_i (R_o/r_i) of 2.25. Other details, such as loading conditions and interference levels, are discussed in the following subsections. All the variational-test experimental data were extrapolated to a common initial crack length of 0.025 inch, so that duplicate results could be presented in the same figure.

4.4.1 Test of Lugs with Interference-Fit Bushings

The results of analytical-experimental correlations of lugs with interference-fit bushings and through-the-thickness initial cracks are

summarized in Figures 5-103 through 5-106. The first two figures (Figures 5-103 and 5-104) correspond to aluminum lugs with steel bushings with a diametral interference level of 0.007 inch. The next two figures (Figures 5-105 and 5-106) correspond to steel lugs with steel bushings with a diametral interference level of 0.008 inch.

Figure 5-103 presents the test data and prediction for bushed aluminum lugs subjected to a far-field constant-amplitude maximum stress of σ_o = 6 ksi and a stress ratio (R) of 0.1. Only the Green's function solution is presented, since the compounding method could not be used for problems with residual stresses. For this case, the Green's function was used in conjunction with the elastic stress distribution along the crack path, since the load level is below the yield strength of the material. The result of the same testing condition except that σ_o = 15 ksi instead of 6 ksi is given in Figure 5-104. The elastic stress distribution was again used with the Green's function method of prediction, rather than the elasto-plastic stress distribution, for this case for the following reason. Though the far-field loading of 15 ksi was high enough to cause yielding in the simple lug (with no bushing), it is not high enough in this case because of the installed steel bushing. A stress analysis showed that both the lug and the bushing are still operating within the linear elastic range. The prediction shows good correlation with the experimental results as shown in Figure 5-104.

Results for steel lugs with steel bushings and σ_o = 14 ksi and R = 0.1 are presented in Figure 5-105. The analytical predictions by the Green's function method with an elastic stress distribution compare very favorably with the experimental results. Figure 5-106 shows the correlation for steel lugs with steel bushings subjected to the severe cargo spectrum loading. Predictions were made using the Hsu [A], Generalized Willenborg [B], Willenborg [C] and No-Retardation [D] models. The predictions by [A] and [B] are conservative by about a factor of 2 to 4. In Figures 5-103 through 5-106, it can be observed that there is a larger amount of scatter of experimental data than observed in previous cases of medium-size steel lugs. Some of this scatter and longer experimental lives might be attributed to the crack-tip blunting caused by the interference-fit bushing installation procedure.

225
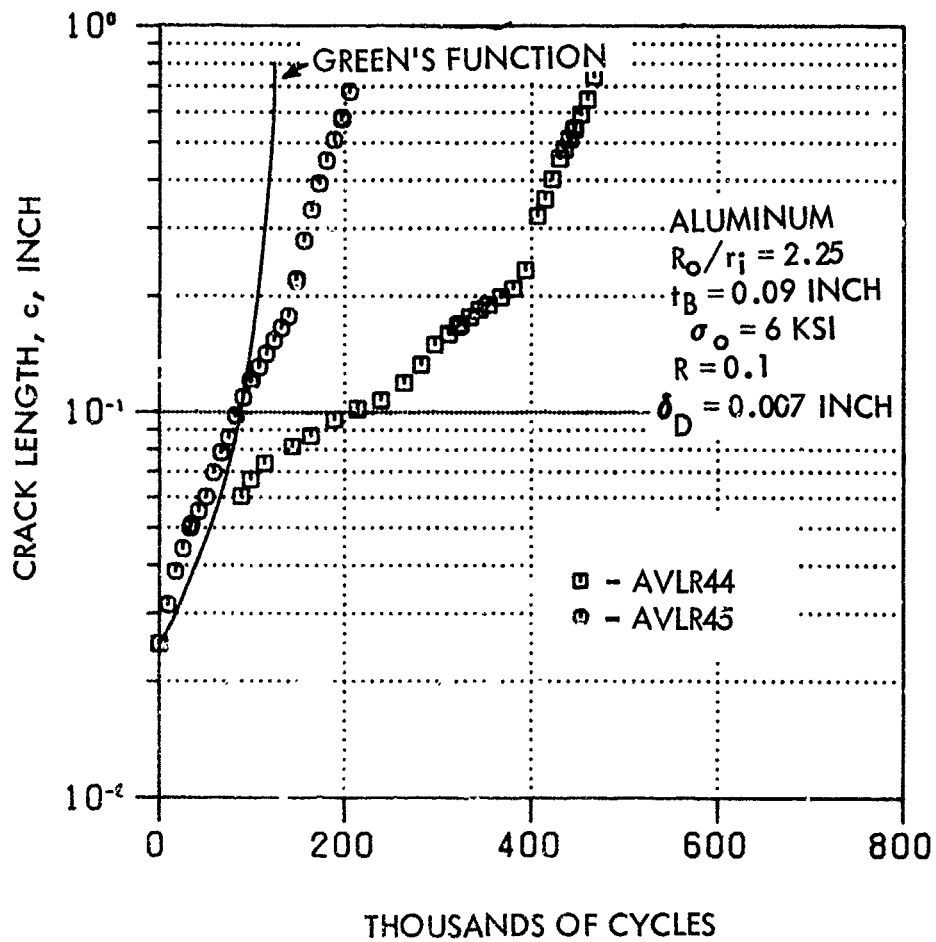
Figure 5-103. Through-the-Thickness Crack Growth Data and Prediction, Aluminum Lug with Steel Bushing, $R_o/r_i = 2.25$, $t_B = 0.09$ Inch, $\sigma_o = 6$ KSI, $R = 0.1$, $\delta_D = .007$ Inch

226
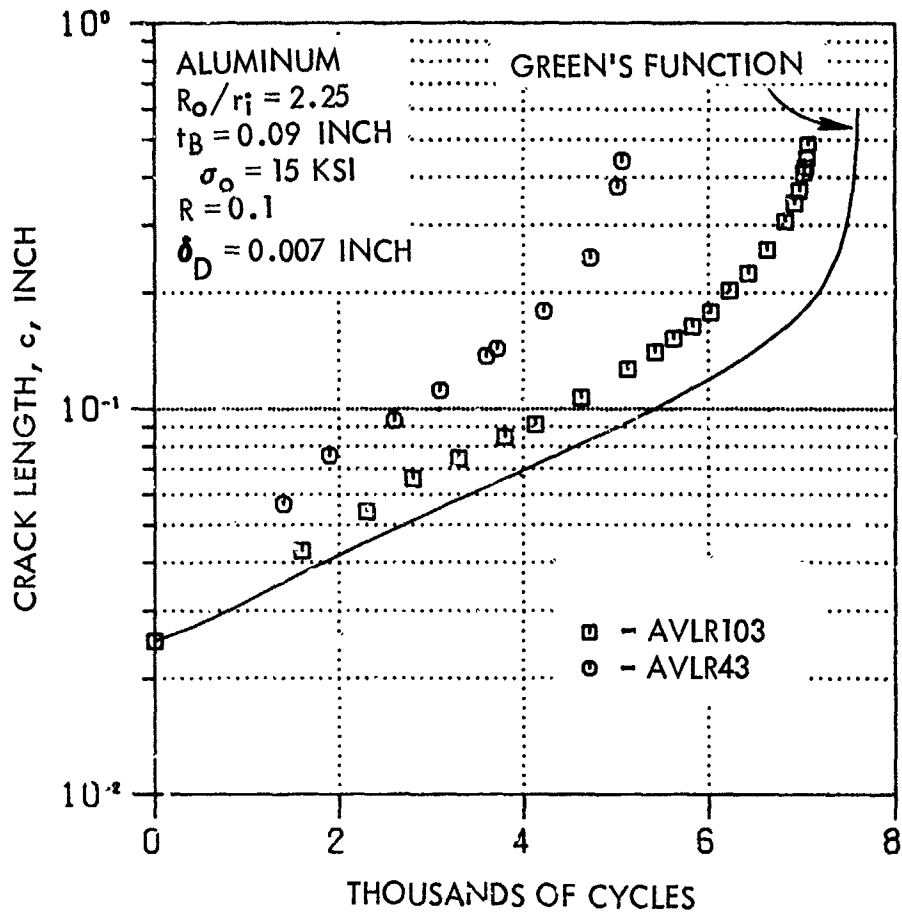
Figure 5-104. Through-the-Thickness Crack Growth Data and Prediction, Aluminum Lug with Steel Bushing, $R_o/r_i=2.25$, $t_B=0.09$ Inch, $\sigma_o=15$ KSI, $R=0.1$, $\delta_D=.007$ Inch
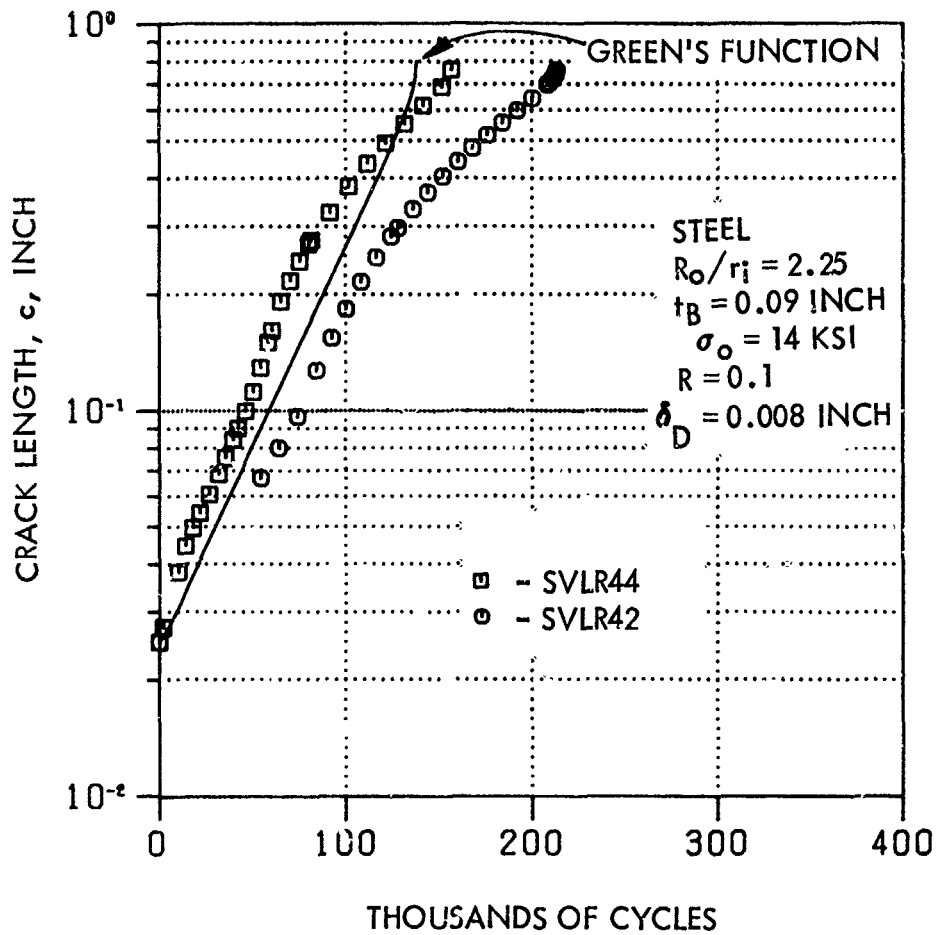
Figure 5-105. Through-the-Thickness Crack Growth Data and Prediction, Steel Lug with Steel Bushing, R_o/r_i=2.25, t_B=0.09 Inch, σ_o=14 KSI, R=0.1, δ_D=.008 Inch

228
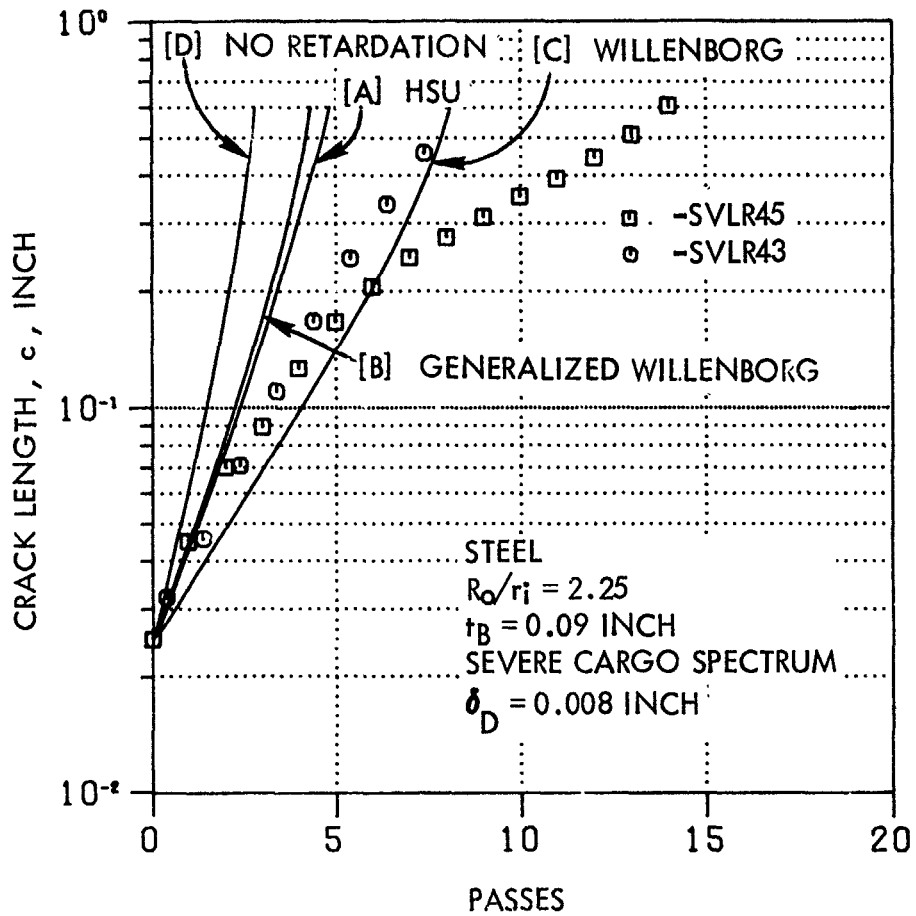
Figure 5-106. Through-the-Thickness Crack Growth Data and Prediction, Steel Lug with Steel Bushing, R_o/r_i=2.25, t_B=0.09 Inch, Severe Cargo Spectrum Loading, δ_D = .008 Inch

4.4.2 Thickness Variational Tests

Analytical-experimental correlation results of thickness variational tests of medium-size lugs (R_o/R_i = 2.25) with initial corner cracks are presented in Figures 5-107 through 5-111. Figures 5-107 and 5-108 correspond to aluminum lugs subjected to far-field constant-amplitude load levels of σ_o = 6 and 15 ksi, respectively, and R = 0.1. These two stress levels again correspond to below and above the yield strength of the lugs. Figure 5-109 presents the constant-amplitude results of steel lugs subjected to σ_o = 14 ksi and R = 0.1. Comparison of analytical and experimental aspect ratios of the crack, a/c, for the above three cases are given in Figure 5-110. The results for steel lugs subjected to severe cargo spectrum loadings are presented in Figure 5-111.

For the cases of lugs loaded below the yield level (Figures 5-107 and 5-109), predictions were made by the Green's function and compounding methods. The Green's function solutions are in close agreement with the experimental data, while the compounding method produced slightly unconservative results. As before, the aspect ratio of the initial crack was assumed as 1.0 in both the methods. In the compounding method, the crack aspect ratio was held constant as 1.0 throughout the crack growth life period.

The Green's function method with elasto-plastic and elastic stress distributions were used for predicting the crack growth behavior and life for the aluminum lugs subjected to the above-yield stress level of 15 ksi, and the results are presented in Figure 5-108. As in the case of the standard-thickness (B = 0.5 inch) lugs, neither of these methods model the actual situation, and the life prediction using the elasto-plastic stress distribution is slightly unconservative.

Analytical and experimental corner crack aspect ratios, a/c, are compared in Figure 5-110 for the above three constant-amplitude thickness variational tests. The analytical data provided in this figure correspond to solutions by the Green's function method with the elastic stress distribution when loaded below yield and with the elasto-plastic stress distribution when loaded above yield.

230
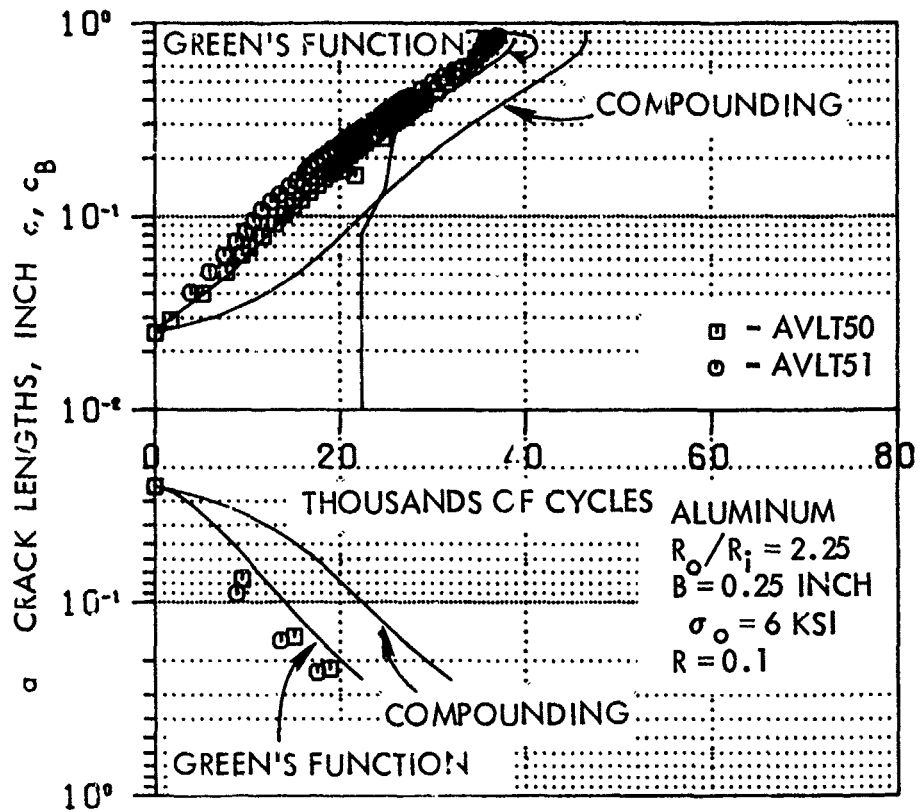
Figure 5-107. Corner Crack Growth Data and Prediction, Aluminum Lug, $R_o/R_i=2.25$, B=0.25 Inch, $\sigma_o=6$ KSI, R=0.1

231
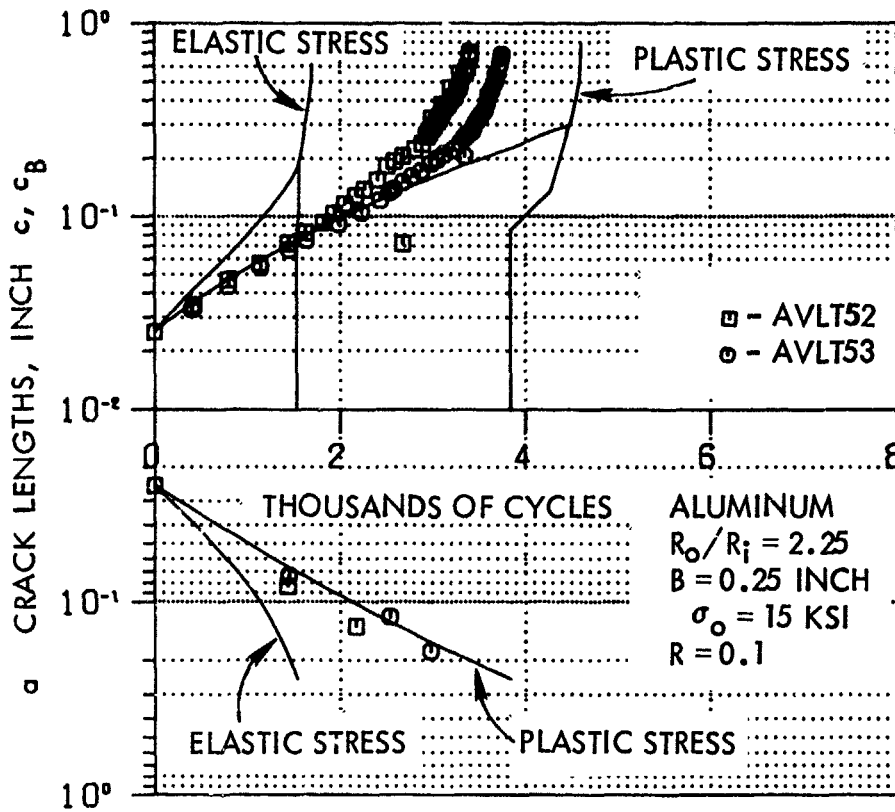
Figure 5-108.   Corner Crack Growth Data and Prediction, Aluminum Lug,
R_o/R_i=2.25, B=0.25 Inch, σ_o=15 KSI, R=0.1
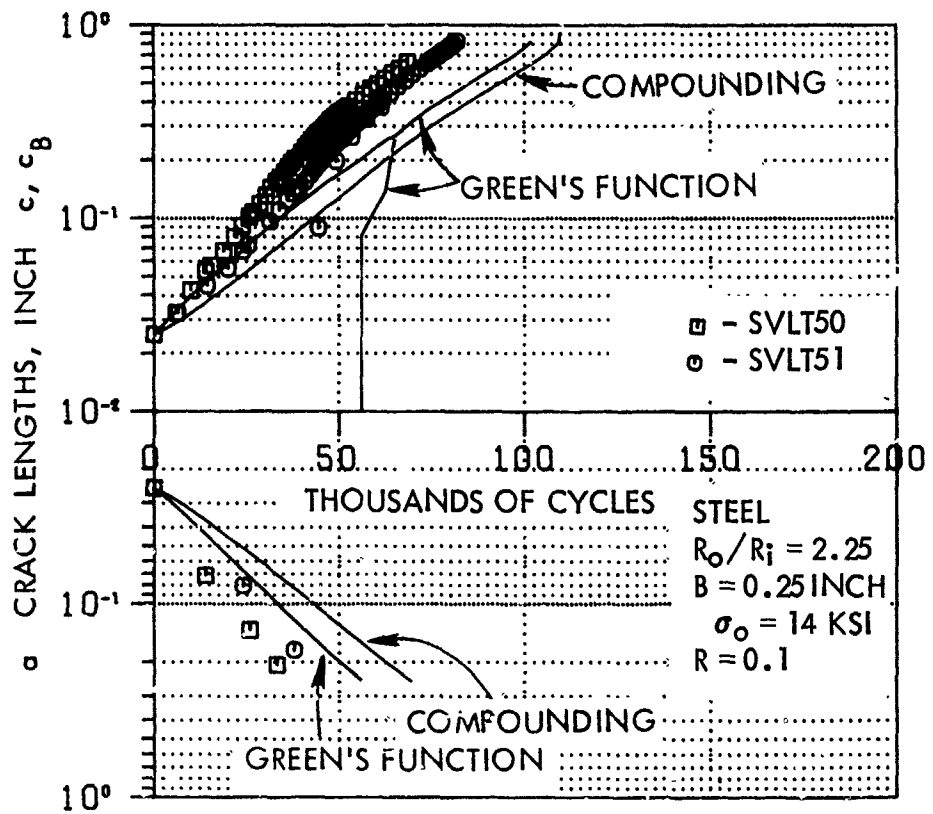
Figure 5-109. Corner Crack Growth Data and Prediction, Steel Lug,
R_o/R_i=2.25, B=0.25 Inch, σ_o=14 KSI, R=0.1
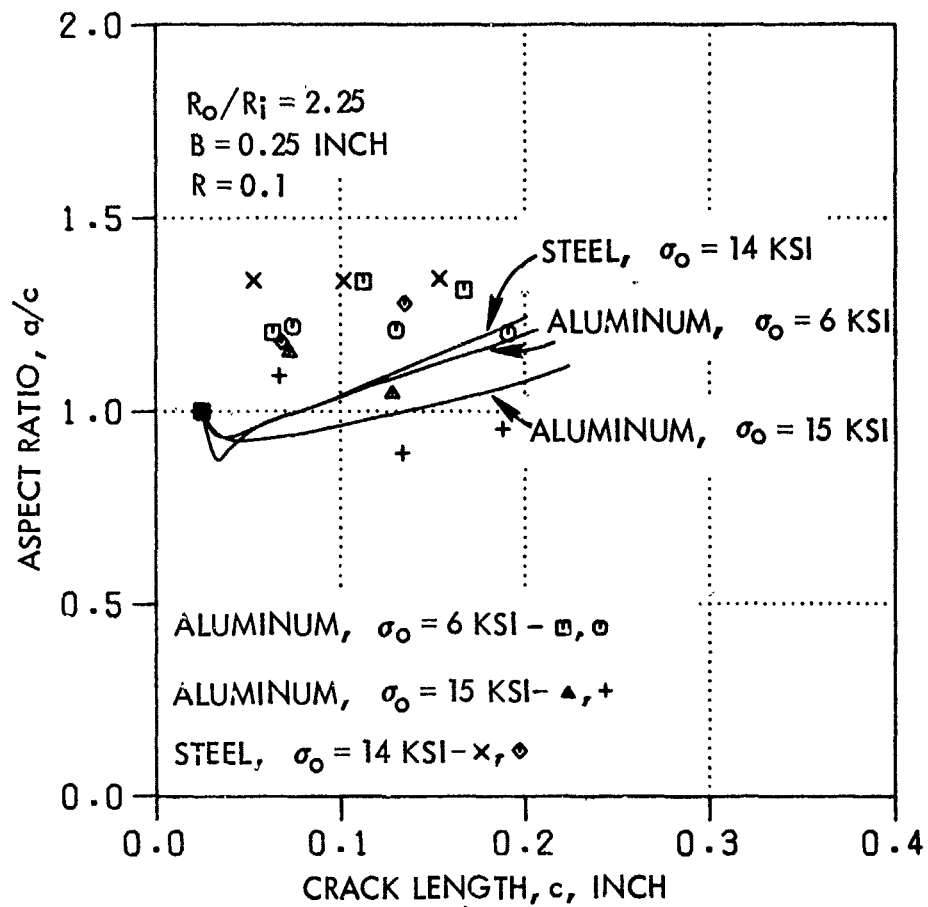
Figure 5-110. Corner Crack Aspect Ratio Data and Prediction, Thickness Variational Tests, R_o/R_i=2.25, B=0.25 Inch, R=0.1
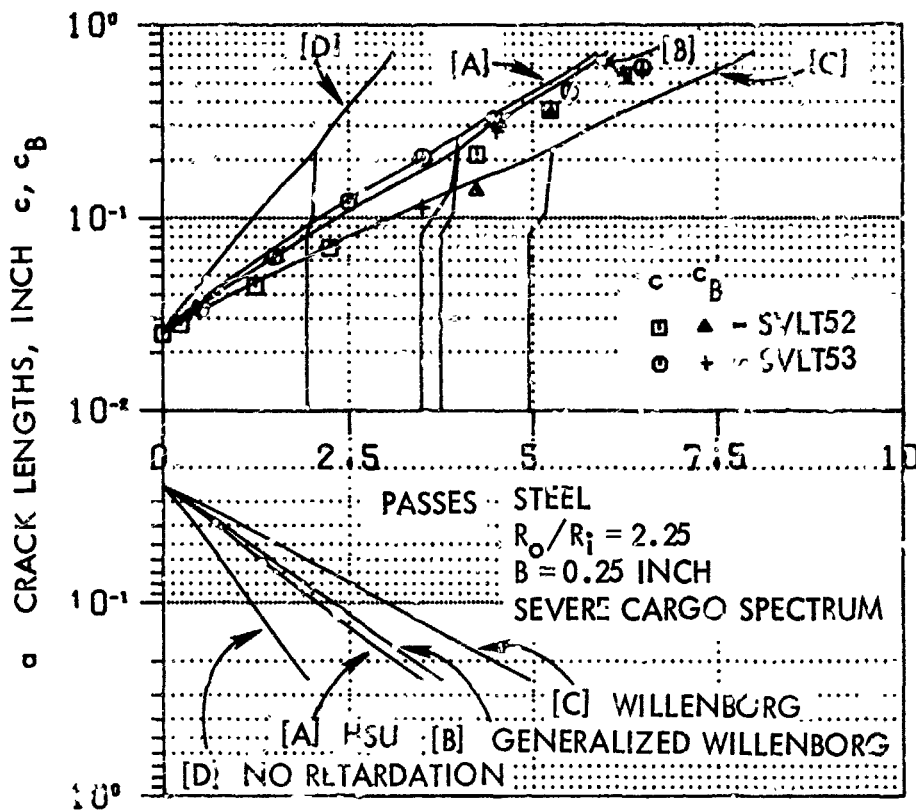
Figure 5-111. Corner Crack Growth Data and Prediction, Steel Lug,
R_o/R_i=2.25, B=0.25 Inch, Severe Cargo Spectrum Loading

The final set of experimental and analytical results of Group I is the thickness variational steel lugs subjected to severe cargo spectrum loading and is presented in Figure 5-111. The predictions were made using Hsu [A], Generalized Willenborg [B], Willenborg [C] and No-Retardation [D] models. The experimental results compare excellently with the analytical predictions by models [A] and [B].

Baseline material property data, such as crack growth rate data and fracture toughness, of standard thickness material were used for the predictions of the above thickness variational cases. Based on the data presented in Figures 5-107 through 5-111, it is evident that such material data were successfully used for lower-thickness lugs. Comparisons of the growth behavior and the accuracy of life predictions for 0.5- and 0.25-inch-thick lugs with identical loading conditions shows that the crack growth rate data of 0.5-inch-thick material can also be used for 0.25-inch-thick lugs. This fact that the crack growth rate does not depend on the material thickness is not a surprising one and has already been established in the open literature. However, one needs to be careful in the use of the fracture toughness value, since it is a strong function of thickness.

4.5 SUMMARY OF ACCURACY OF LIFE PREDICTIONS

Only a simple straight-shank male lug geometry was considered in Group I testing, and this group of tests was designed for analysis development, verification, and refinement. However, several loading complexities, such as loads above yield, block spectrum, flight-by-flight spectrum, and residual stresses due to the installation of interference-fit bushings, were considered in Group I testing. Analytical predictions of crack growth behavior and life were made prior to and for each test using all the appropriate models applicable to that particular test. To evaluate the accuracy and performance of the developed analytical methodology, a comparison of analytical and experimental crack growth lives is made here for all the 160 Group I crack growth tests.

Figure 5-112 presents the comparison of life ratio (test life/predicted life) for the 160 Group I crack growth tests. They are presented in
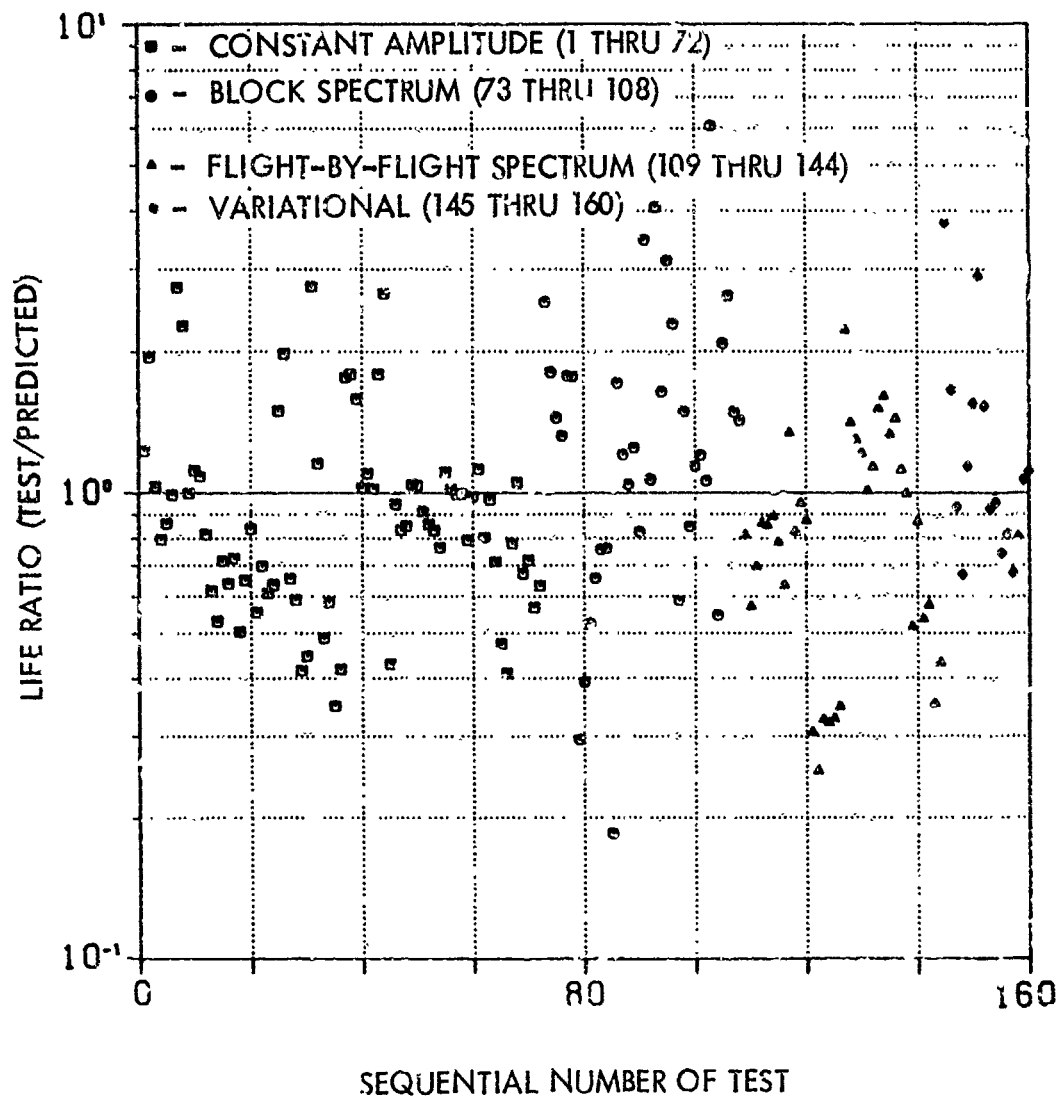
Figure 5-112. Accuracy of Prediction of Total Crack Growth
Life for Group I Tests

the same sequence as they were presented in subsections 4.1 through 4.4. The first 72 data points correspond to constant-amplitude test results, data points 73 through 108 correspond to block spectrum test results, data points 109 through 144 correspond to flight-by-flight spectrum test results, and the last 16 data points correspond to variational tests.

Since several methods or models were used to predict the analytical life for the same test, the following guidelines were used to select an analytical life for use in Figure 5-112:

o   Use only the life predicted by the Green's function method.

o   Use the Green's function method with elasto-plastic stress distribution when the lugs are loaded above yield.

o   Use the Hsu model ([A] or [E]) prediction for spectrum loading cases.

Considering life ratios of 0.5 and 2.0 to be the commonly accepted prediction band due to the scatter of crack growth rate data, the following observations can be made.

One hundred twenty-six of the 160 test results are within this band.

On the unconservative side outside this life prediction band, there are 19 results: 8 constant-amplitude data points, 3 block spectrum data points, and 8 flight-by-flight spectrum data points. All the constant-amplitude data are for lug specimens subjected to load levels above yield for which the developed Green's function method with elasto-plastic stress distributions was found to be inaccurate, or in some cases the test data were invalid. Out of the three block spectrum unconservative data, two are for steel lugs with $R_o/R_i = 1.5$. The unconservative life prediction in these two lugs may have resulted from the effects of large deformation of the lugs and the E_{pin}/E_{lug} ratio and possibly some pin-lug clearance effect. Once these effects are accounted for in the analysis, the life prediction should improve significantly. The third block spectrum data points below the band of 0.5 and 2.0 is that of a prematurely failed aluminum specimen with $R_o/R_i = 1.5$. For the duplicate specimen, the life ratio was 1.711, as opposed to 0.185 for this specimen. The eight flight-

by-flight spectrum data points falling below the band are the fighter spectrum data points. As mentioned in subsection 4.3, no reasonable explanation could be found for this discrepancy.

On the conservative side outside this life prediction band, there are 15 results: 4 constant-amplitude data points, 8 block spectrum data points, 1 flight-by-flight spectrum data point, and 2 variational test data points. Most of the constant-amplitude, block spectrum, and flight-by-flight spectrum data points correspond to lugs with $R_o/R_i = 1.50$, for which large scatter was observed. The other points correspond to block spectrum loading above yield, and only estimates of lives were made with the available methods. The conservatism in the variational tests may sometimes be because of the crack tip blunting effect caused by the bushing installation procedure, since the slow early crack growth rates are primarily responsible for the longer-than-predicted lives.

Figure 5-113 shows the probability plot of the accuracy of crack growth life predictions for all the 160 Group I crack growth specimens. Here each data point is the geometric mean of duplicate test results. This figure indicates that approximately 98 percent of crack growth life predictions for straight lugs would be within a factor of 3.0 of the test results.
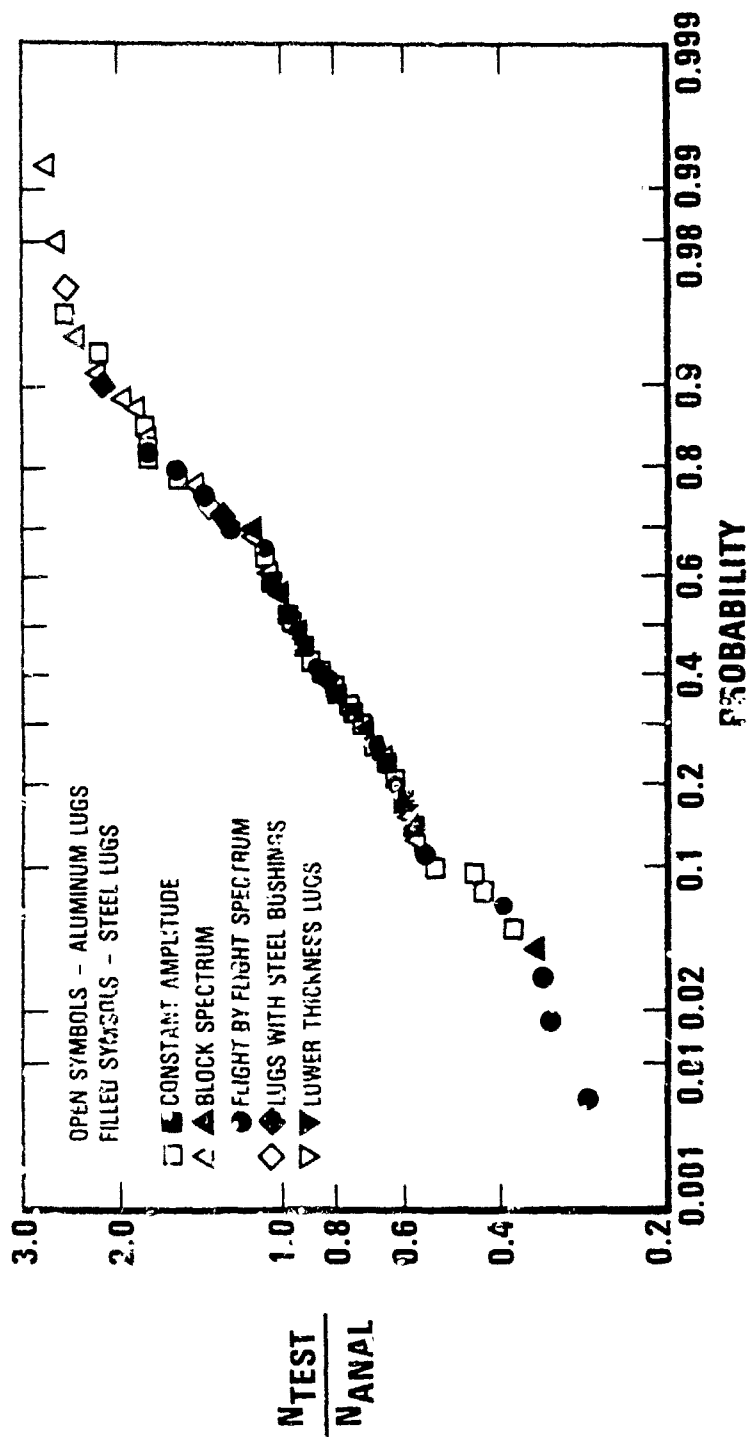
Figure 5-113. Accuracy of Crack Growth Life Predictions for Group I Tests

SECTION VI

GROUP II TEST RESULTS AND CORRELATIONS

The Group II test matrix consisted of 76 crack growth tests of lugs containing corner precracks. Crack growth predictions were carried out prior to each test, by the methods discussed in Reference [1] and Section IV. The purpose of this section is to present the test results and compare them to the analytical predictions.

Verification of material crack growth rate relationships is presented first, in Subsection 1. Then the results of eight fatigue crack initiation tests are discussed in 2. The succeeding four subsections discuss, in order, the results of the four submatrices of tests that were listed in Table 3-11 of Section III, and the corresponding analytical predictions. Test submatrices (a) through (d) address the following variables:

(a) Pin clearance, fabrication and precrack location.

(b) Lug geometry, thickness and use of bushings.

(c) Loading angle, material, bushings and load reversal.

(d) Size effect, spectrum loading, thick lugs, wing-pylon lug.

1.0 VERIFICATION OF MATERIAL CRACK GROWTH RATE RELATIONSHIPS

Baseline crack growth testing was accomplished on compact tension specimens for the purposes discussed in Section III. The results of these tests are discussed in the following two subsections.

1.1 OVERLOAD MARKING SEQUENCES

Baseline crack growth data were obtained for Group II predictions using 0.5-inch thick, 5.0-inch wide aluminum and steel compact tension (CT)

specimens. The aluminum CT specimens were machined from the 1.0 inch and 2.25 inch thick 7075-T651 Aluminum plate stock used in fabrication of the lug specimens. The steel CT specimens were from the 0.625-inch thick 4340 Steel plate stock.

Figure 6-1 shows the crack growth rate data for the aluminum CT specimens. The dark points are for specimens tested at constant amplitude with a stress ratio of R = 0.1. The other points are for specimens tested with a periodic 30-percent overload sequence designed to mark the fracture surface without significantly altering da/dN. The sequence for Specimens CT-A-3, -A-4, and -D-4 consisted of 990 constant-amplitude cycles at R = 0.1, followed by 10 cycles of 30-percent overloads. Better fracture surface markings were then found to be achievable using the altered "final" sequence shown in Figure 6-1, which consisted of 1900 constant amplitude cycles and 100 cycles of 30-percent overloads. Testing of specimens CT-A-5 and -D-5 using this final sequence confirmed that da/dN is virtually the same with and without the overloads.

Figure 6-2 compares the da/dN data for two steel specimens to one another and to the da/dN curve used for Group I predictions. The loads applied in the two tests were identical, except that specimen CT-S-4 was subjected to the sequence of 100 consecutive 30-percent overloads every 2000 cycles, to produce fracture surface markings. The data demonstrate for the steel that the overload sequence had no significant effect on crack growth. In fact, the number of cycles for the crack to grow from the initial length of 1.5 inch to 2.75 inches (when the crack wandered out of plane in Specimen CT-S-4) was nearly the same for the two specimens: 132,000 cycles for CT-S-4 and 122,000 cycles for CT-S-2.

Figure 6-3 shows the fracture surface of specimen CT-S-4. All 66 marks, up to the 2.75-inch crack length, can be seen and counted on the fracture surface. The smallest spacing between marks is 0.010 inch, corresponding to a crack growth rate of 5×10^{-6} inches per cycle.

1.2 CRACK RETARDATION MODELS

Eight of the Group II aluminum lug tests were spectrum tested using the 80-flight fighter/trainer wing lower surface loading sequence discussed
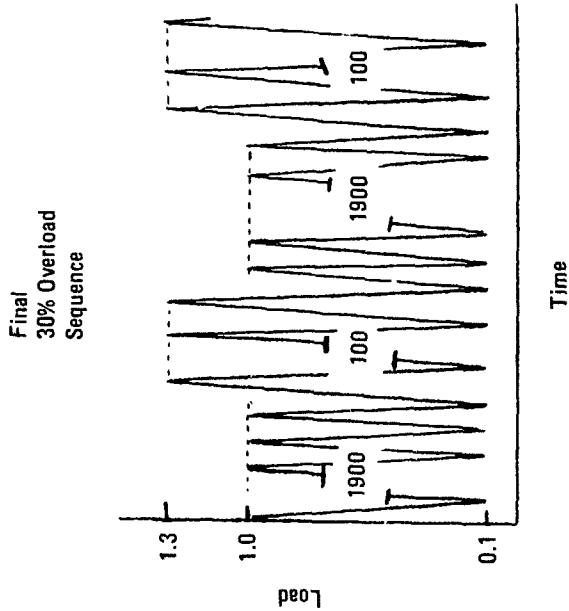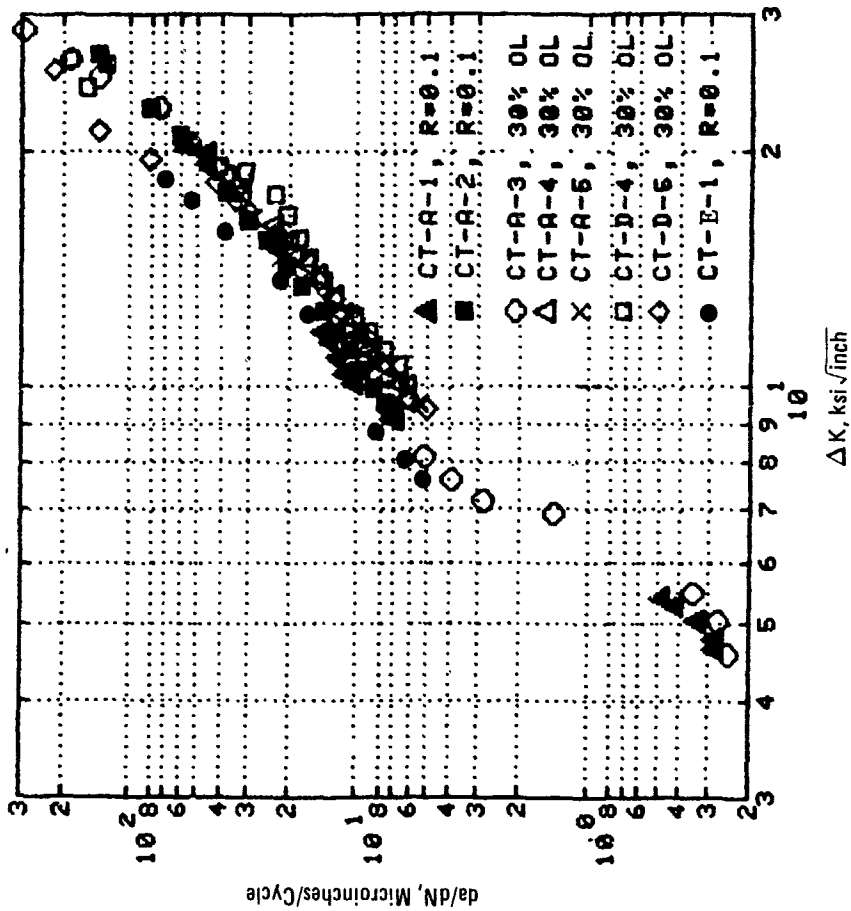
Figure 6-1. Effect of Overload Marking Cycles on da/dN

243
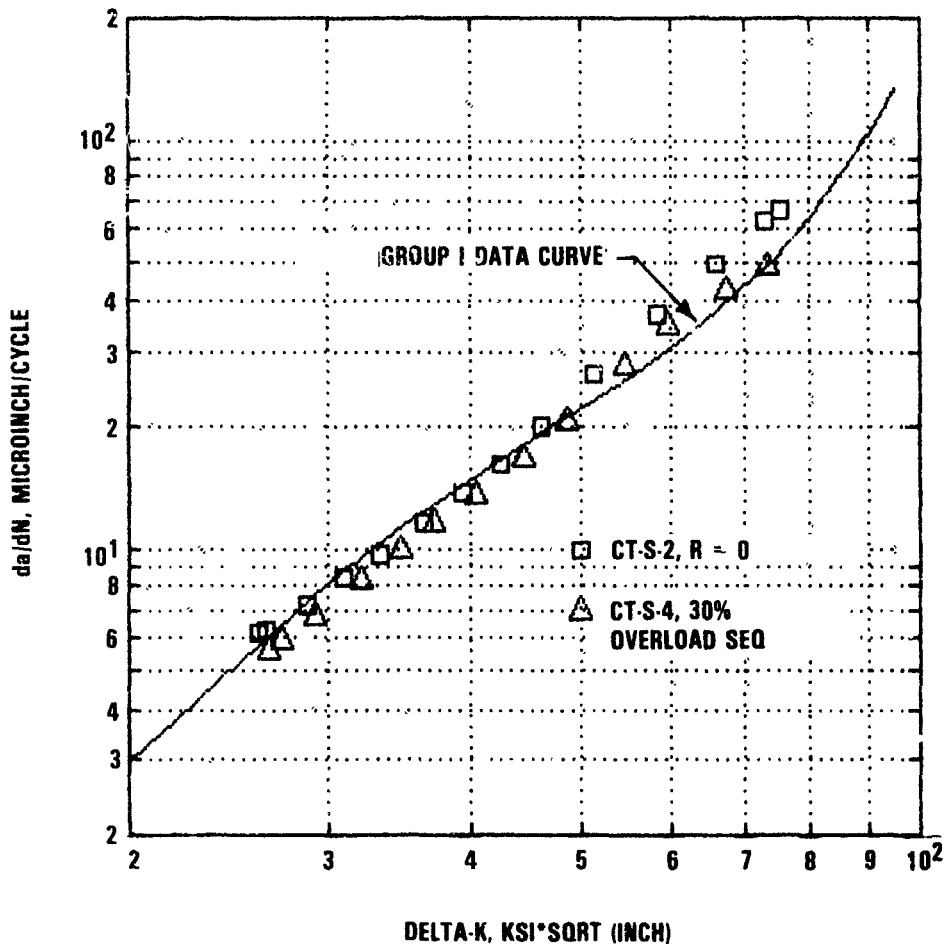
Figure 6-2. Comparison of da/dN Data for 4340 Steel with
and without Periodic 30 Percent Overloads
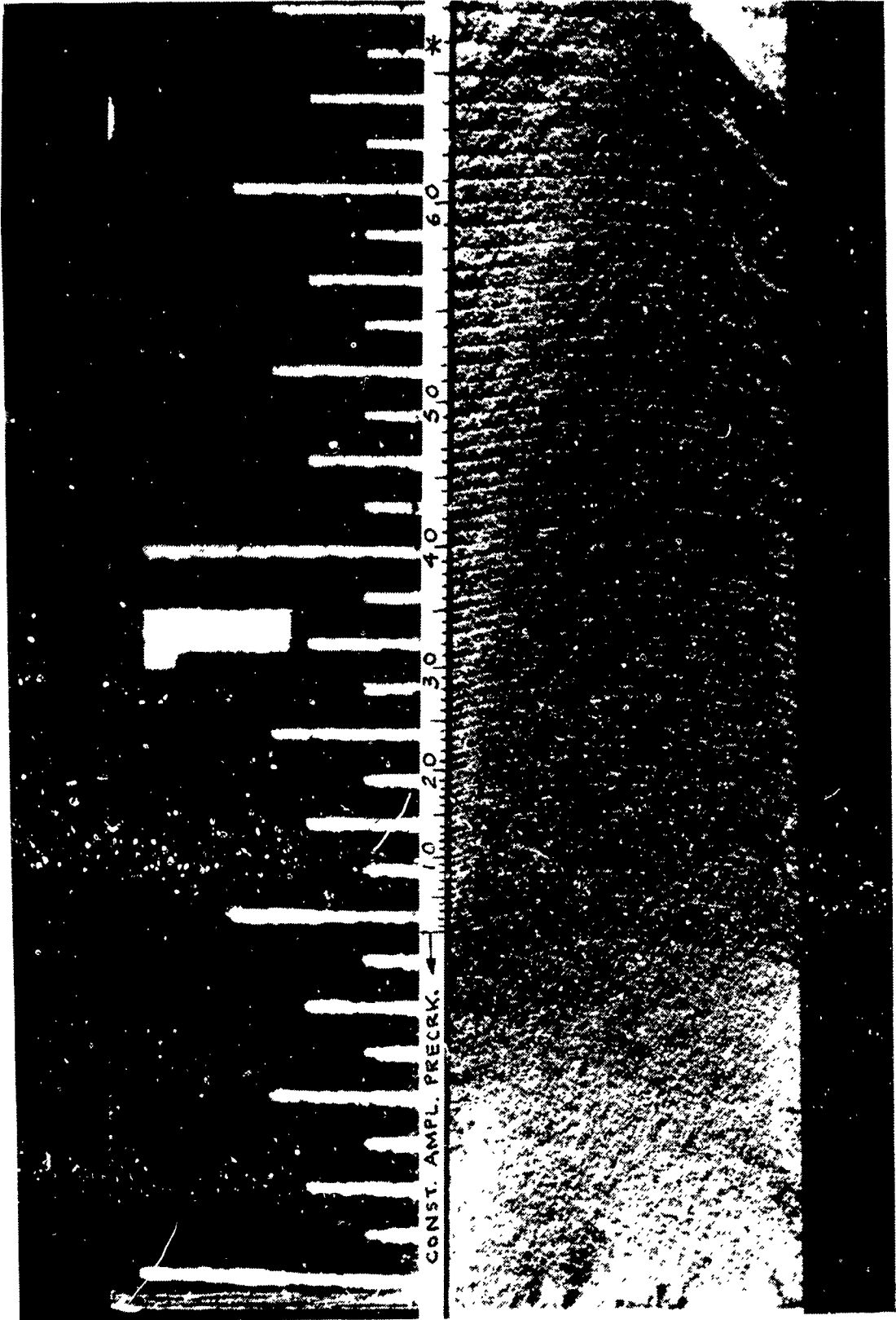
Figure 6-3. Fracture Surface of Steel Specimen CT-S-4. (Asterisk at a = 2.75 inch)

in Subsection 6.2 of Section III and tabulated in Tables B-3 and B-4 of Appendix B. To verify the retardation models as applied to this loading sequence in 7075-T651 Aluminum, a compact tension specimen was analyzed and tested using this loading sequence. The stress intensity factor solution for a CT specimen is of course known very accurately, so the test result was a pure test of the retardation models. As Figure 6-4 shows, the Hsu and Generalized Willenborg Models are both very accurate for this loading sequence and material. The "No Retardation" computation is conservative by a factor of 1.7, and the Willenborg Model (not shown in Figure 6-4) is unconservative by a factor of 3.0.

On this basis the Hsu and Generalized Willenborg models were selected for use in Group II analysis of the 80-flight spectrum tests. In the Generalized Willenborg model, $\Phi = 0.4$ was used.

2.0 CRACK INITIATION TESTS

Eight tapered attachment lugs containing no preflaws were fatigue tested under off-axis loading. Two aluminum and two steel specimens were fatigue loaded in the -45 degree direction with respect to the symmetry axis of the lug, and two of each material were loaded in the -90 degree direction. The primary purpose of the tests was to determine whether the location of initial cracks would correspond to the calculated location of maximum tangential stress.

The locations of the maximum tangential stress had been calculated by finite element analysis. Figure 6-5 is a plot of the tangential stresses around the periphery of the hole, for an applied load of 10 kips at -45 degrees or -90 degrees. For the -90 degree loading, the calculated location of the peak tangential stress was 205 degrees. For the -45 degree loading, essentially equal peak stresses were calculated at 58 and 227 degrees.

As indicated in Figure 6-5, the tests confirmed these to be locations where cracks were most likely to initiate. In all four specimens that were loaded at -90 degrees, the first and primary fatigue crack developed within a few degrees of the 205 degree location. Of the four specimens tested at -45 degrees, two developed first cracks at approximately 58 degrees and two
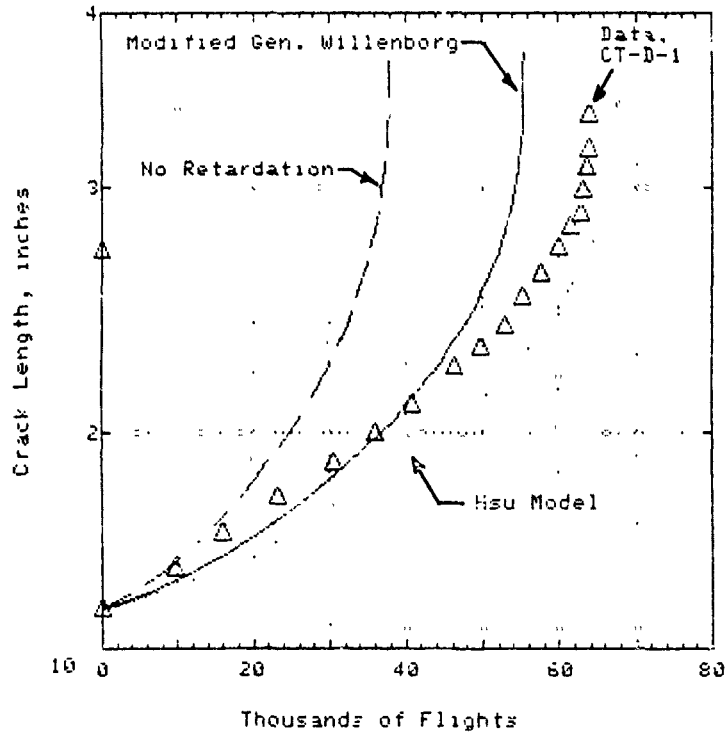
Figure 6-4. Verification of Hsu and Generalized Willenborg
Models for 80-Flight Fighter Spectrum
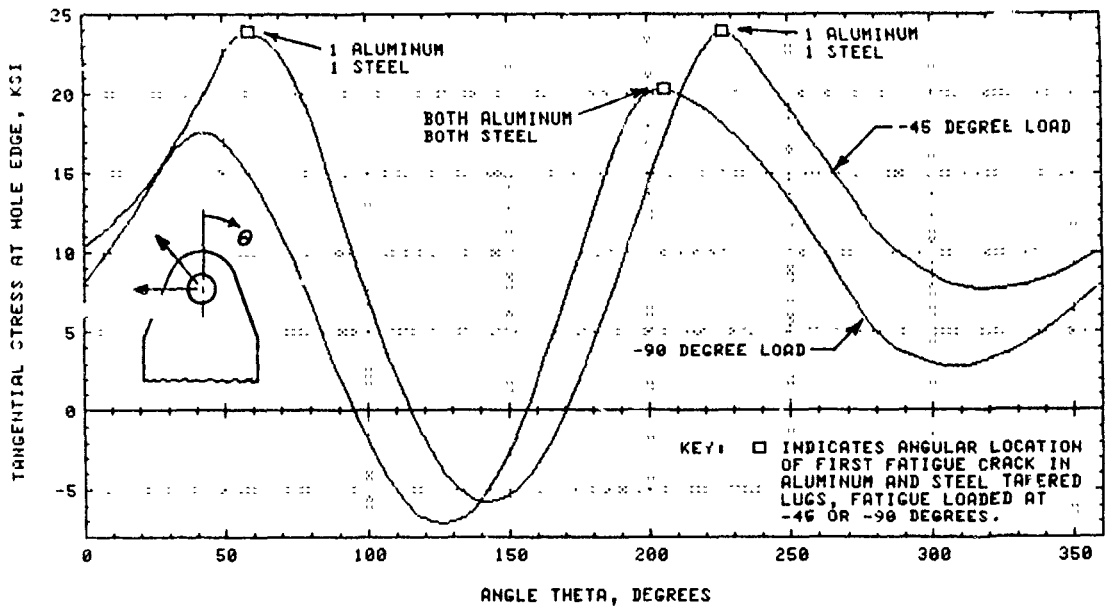
Figure 6-5. Critical Crack Locations for Tapered Lugs Subjected to
Off-Axis Fatigue Loading - Analysis and Test Results

at approximately 227 degrees, confirming that both locations were about equally likely sites for crack initiation.

As a result of these tests and their correlation with the analysis, final selection was made of initial flaw locations in tapered lugs scheduled for off-axis loading. All tapered lug specimens to be loaded at -90 degrees were E.D.M. preflawed at 205 degrees. However, 6 of the first 12 tapered lug specimens to be loaded at -45 degrees were preflawed at 58 degrees and 6 were preflawed at 227 degrees, to compare crack location criticality. The 58 degree location was selected for the remaining specimens scheduled for the -45 degree loading.

3.0 EFFECTS OF PIN CLEARANCE ON CRACK GROWTH

Twenty-four pre-flawed lug specimens were tested in submatrix (a). the primary objective of these tests was to examine the effects of pin clearance. There were also two secondary objectives. In the 12 axial tests of straight lug specimens, the effect of pin lubrication was examined. In the 12 tests of tapered lug specimens loaded at -45 degrees, the criticalities of two initial flaw locations were compared.

In conducting a systematic study of pin clearance effects, dimensional variations larger than ± 0.0001 inch are significant. Therefore, the key to the validity of these tests was extreme care in the fabrication process and careful measurement.

Figures 6-6 and 6-7 show the measured pin clearances in the first 24 Group II specimens. The multiple measurements shown in Figure 6-6 indicate that the requested ± 0.0001 inch accuracy is not always attained. However, it is apparent that the pin clearances are distinctly different for the X, Y and Z-type specimens, so that the study of pin clearance effects was valid.

Figures 6-8 and 6-9 show the effects of pin clearance on total crack growth life in straight axially loaded lugs and in tapered lugs loaded at -45 degrees to the specimen axis. Figure 6-8 clearly shows that the smaller the pin clearance the longer the life, and Figure 6-9 shows a tendency toward the same trend.
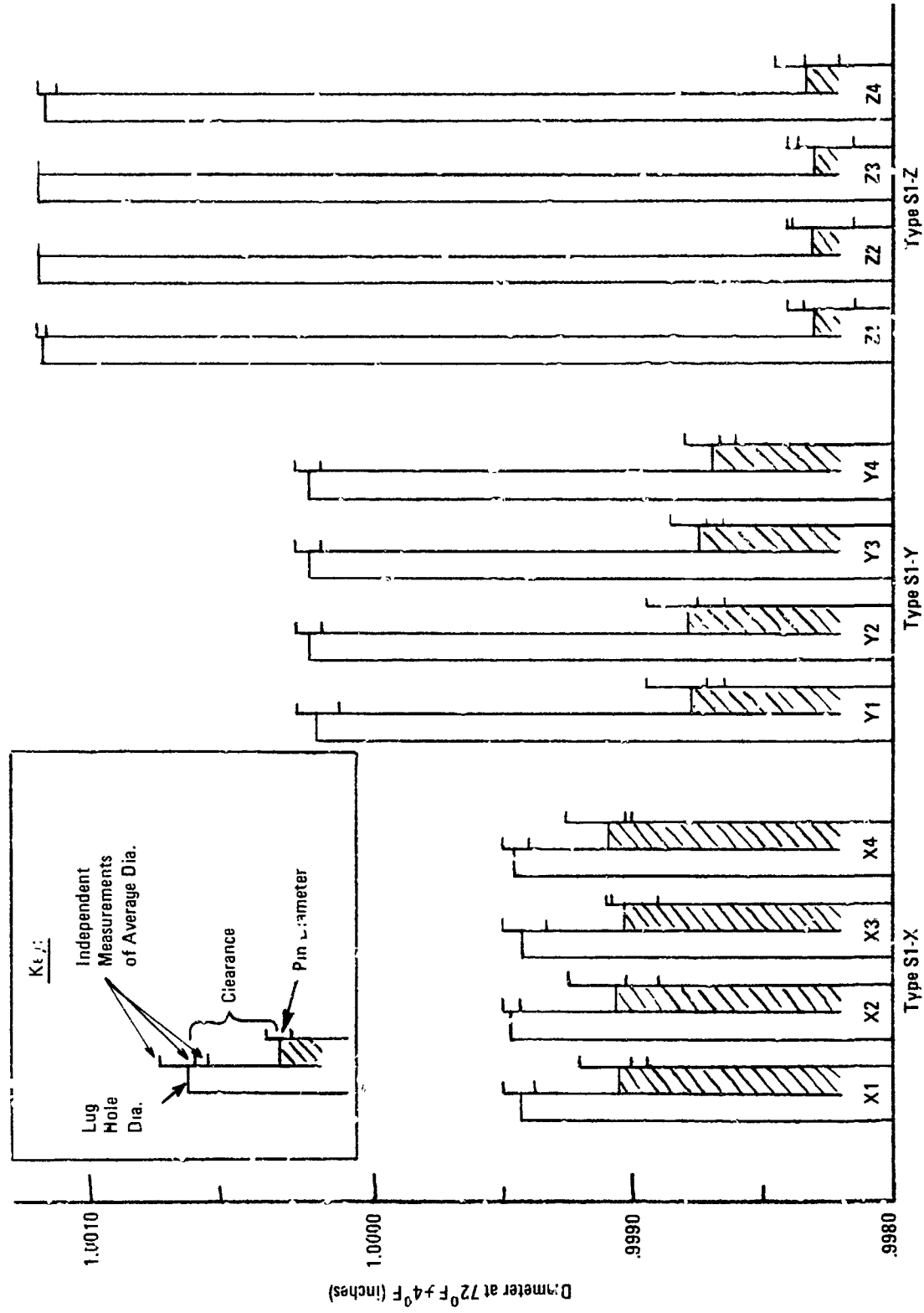
Figure 6-6. Measured Pin Clearance in Twelve Straight Lug Specimens
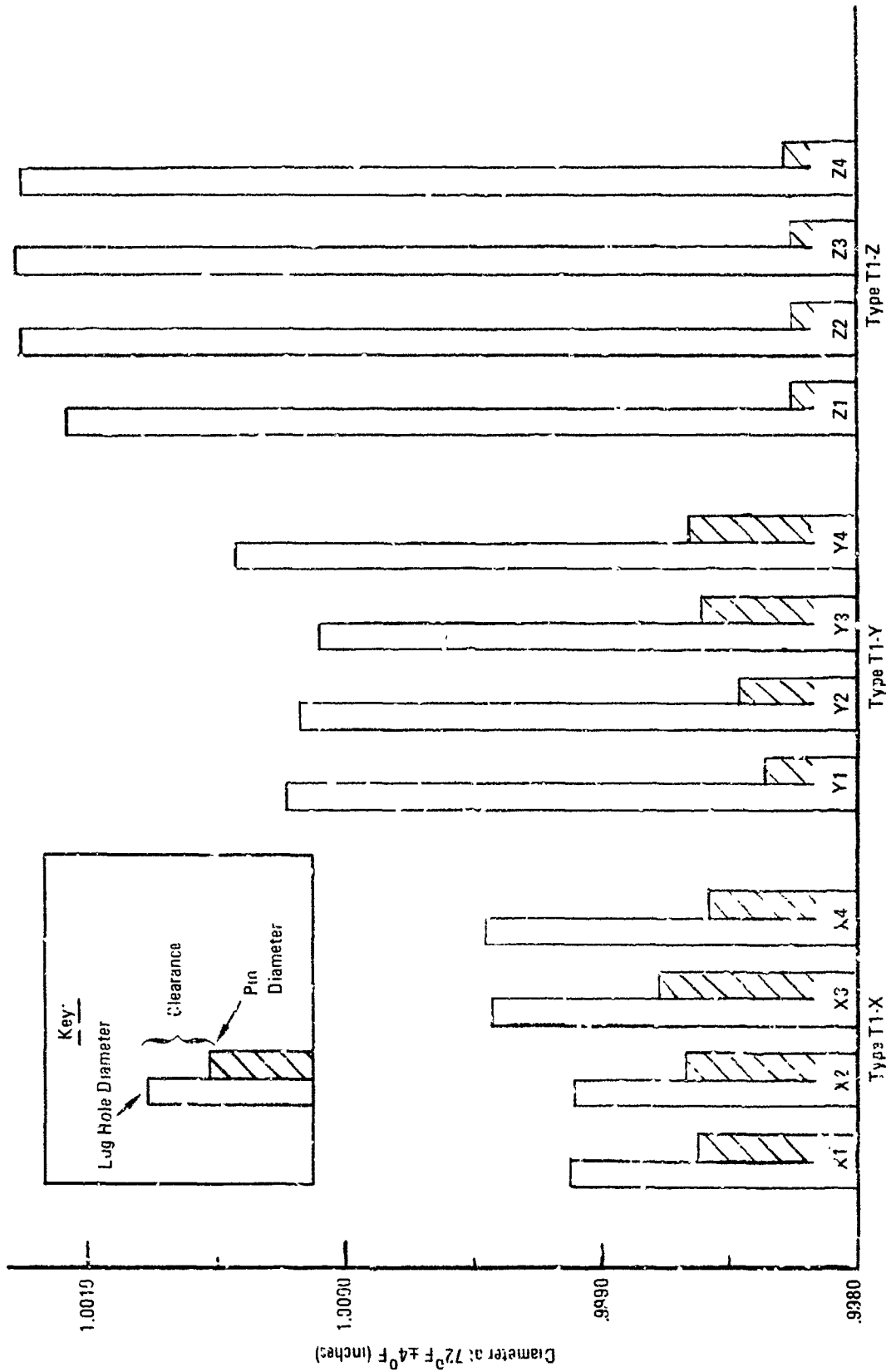
Figure 6-7. Measured Pin Clearances in Twelve Tapered Lug Specimens

251
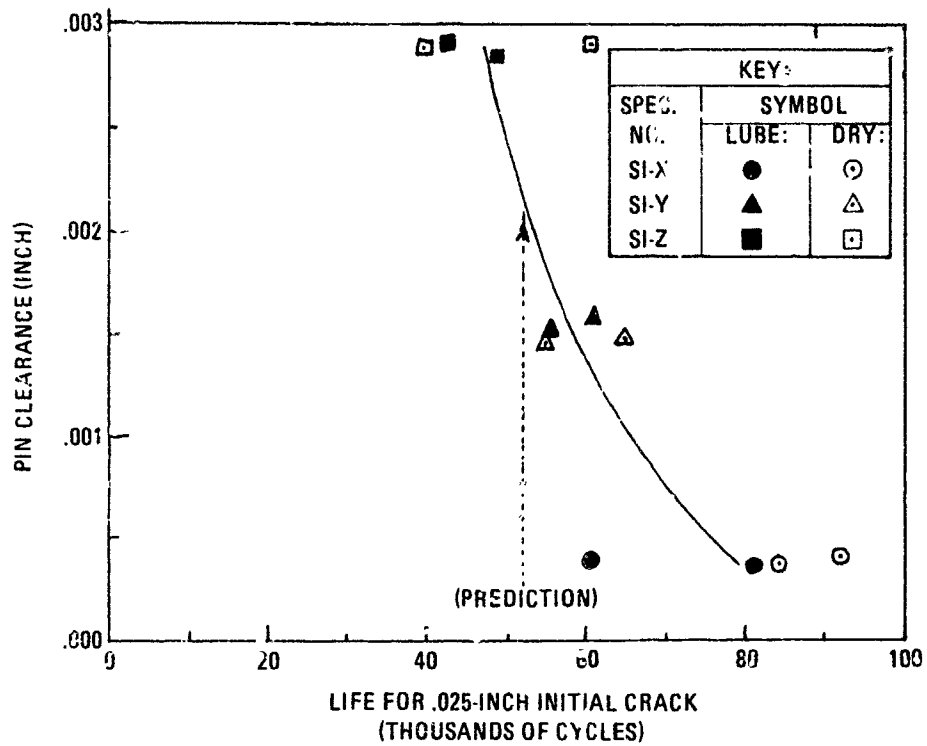
Figure 6-8. Results of Pin-Clearance Study - Axially-Loaded Straight Lugs
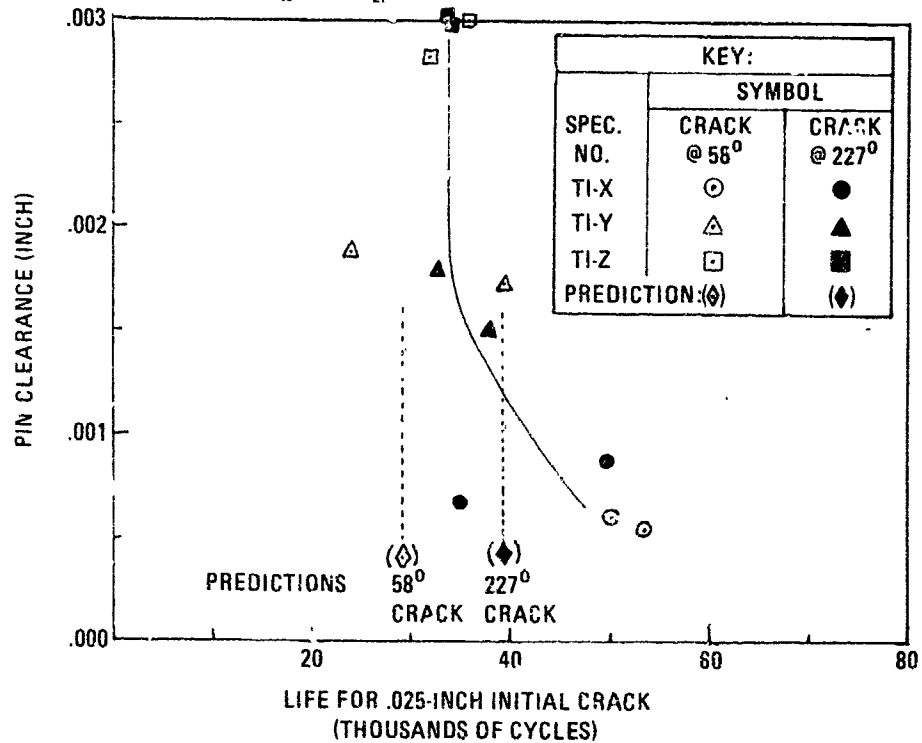
Figure 6-9. Results of Pin-Clearance Study - Tapered Lugs Loaded at -45° Direction

Figures 6-10, 6-11 and 6-12 show crack growth test results for straight lug Specimen types S1-X (low clearance), S1-Y (medium clearance), and S1-Z (large clearance), respectively. The darkened points designate specimens with pin lubrication while the open points designate specimens without pin lubrication. The solid line is the prediction, which is the same for all 12 specimens.

As seen in Figure 6-6 the X, Y and Z specimens had nominal diametrical pin clearances of 0.0005 inch, 0.0015 inch, and 0.0030 inch, respectively. Figures 6-10 through 6-12 clearly show that the closer the fit of the pin the longer the crack growth life.

Comparing the dark points and open points in these figures, no consistent effect of pin lubrication can be seen. This was surprising, since Rooke [12] showed analytically that reduction of frictional shearing forces between the pin and lug will reduce the stress intensity factor of the crack. Apparently, lubricant does not significantly reduce frictional forces; evidences of fretting were comparable on both the lubricated and non-lubricated lugs. Immediately after these tests, the decision was made to use lubricant on the pins in all subsequent Group II tests.

The broken tapered lug specimens in Figure 6-13 show the two initial crack locations and typical crack paths for the -45 degree loading direction used in these 12 tests. The predicted and actual crack growth for these tapered lugs are shown in Figures 6-14 and 6-15. As seen earlier in Figure 6-7, the nominal diametrical pin clearances for types T1-X, T1-Y, and T1-Z are, respectively, 0.0007 inch, 0.00 7 inch, and 0.0029 inch.

In the case of the -58 degree critical crack, the growth for the smallest pin clearance is slower than predicted by a factor of 1.5 (see Figure 6-14(a)). For the two larger pin clearances the prediction is fairly accurate or slightly conservative. The crack shape prediction roughly follows the trend of the data (Figure 6-14(b)).

In the case of the 227° crack, the predicted growth on the lug surface (Figure 5-15(a)) is slightly unconservative for all three levels of pin clearance. However, the predicted flaw depth-to-length ratio (a/c) is significantly higher than the test values, Figure 6-15(b). Therefore, the predicted rate of growth in the depth direction is slightly conservative.
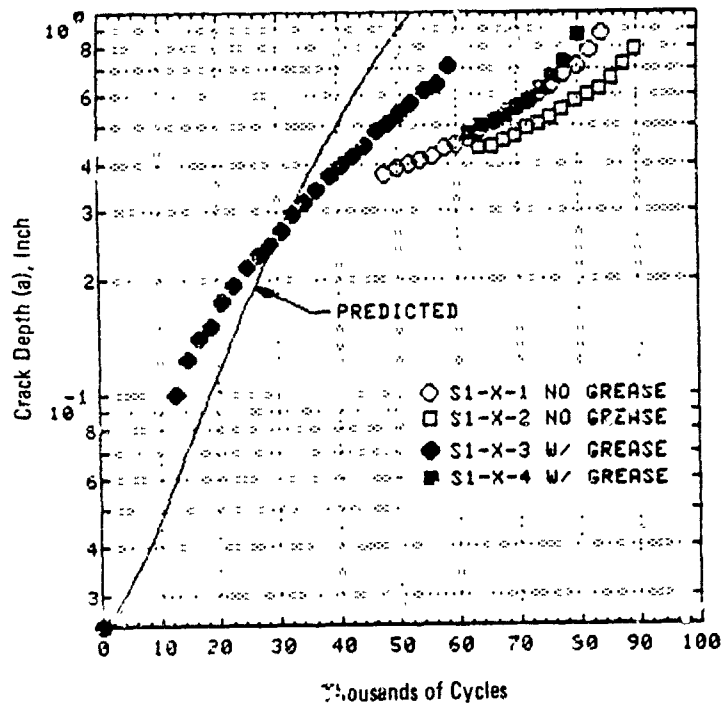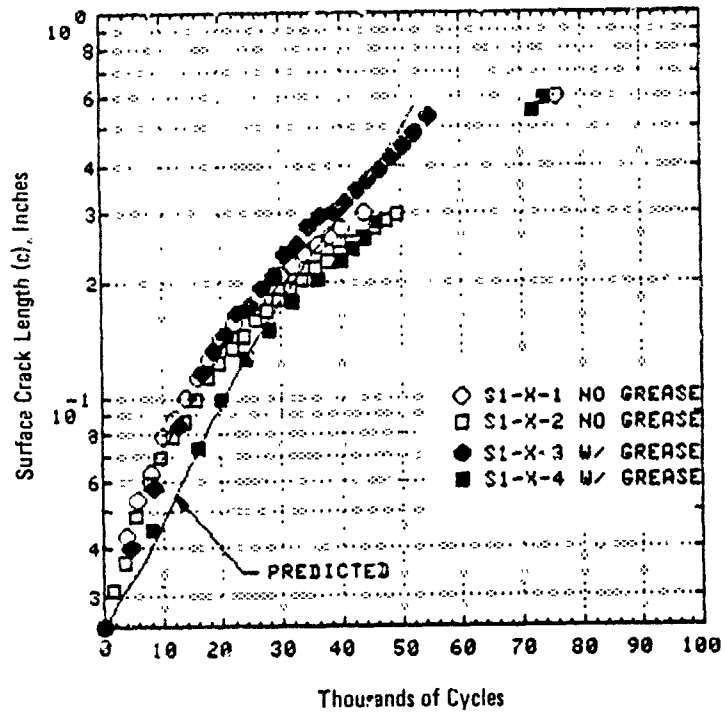
Figure 6-10. Test Results for Specimens S1-X-1 through -4

254
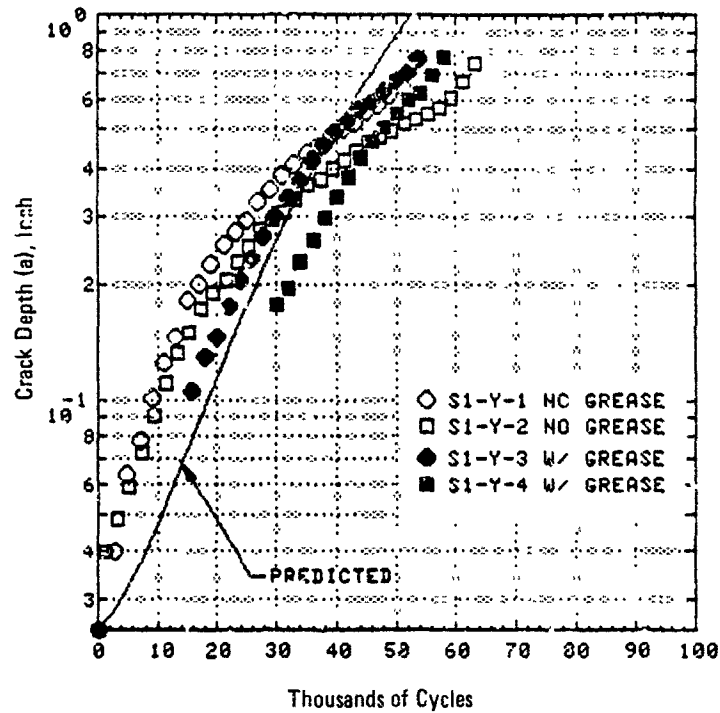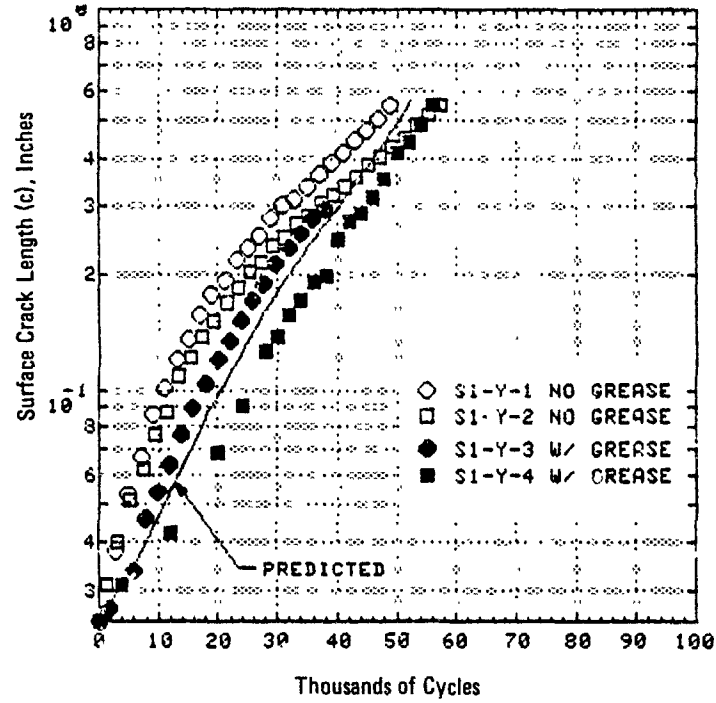
Figure 6-11.   Test Results for Specimens Sl-Y-l through -4
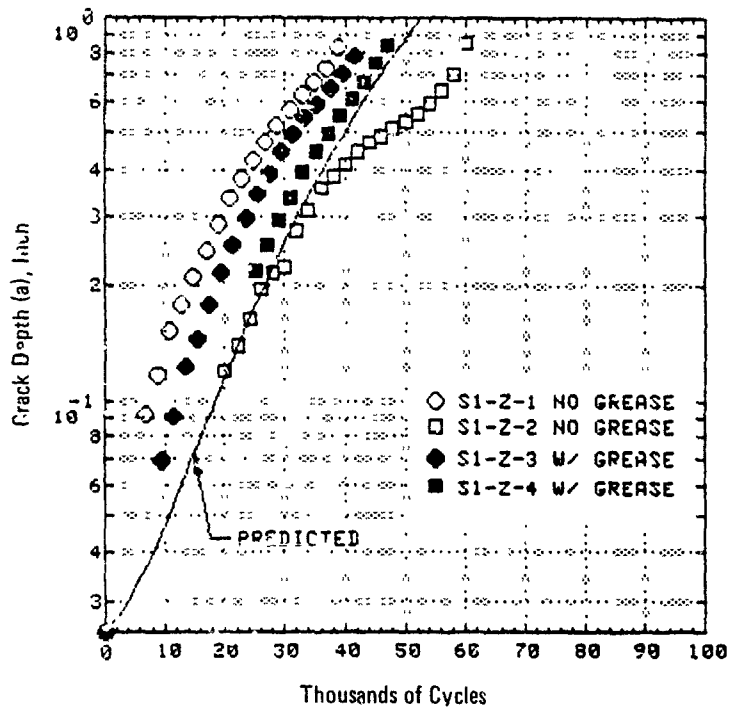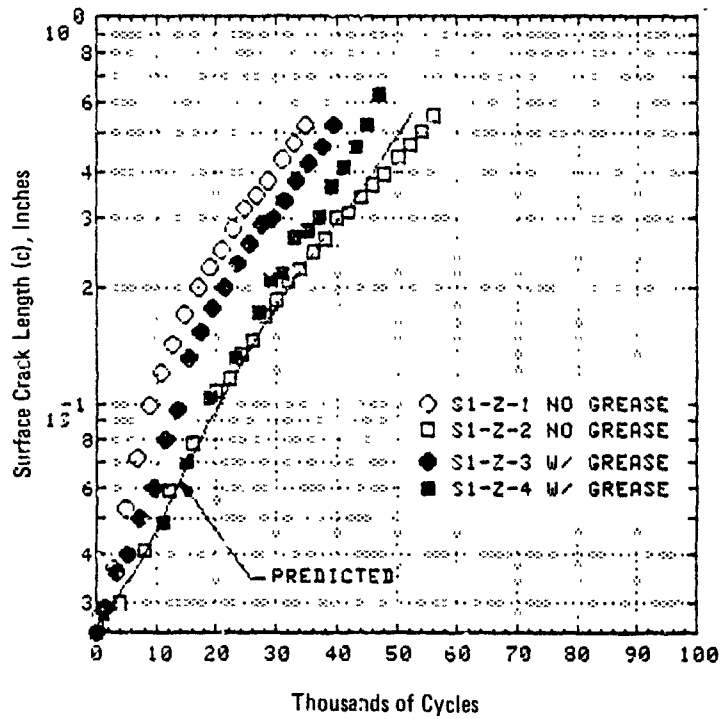
Figure 6-12. Test Results for Specimens S1-Z-1 through -4

256
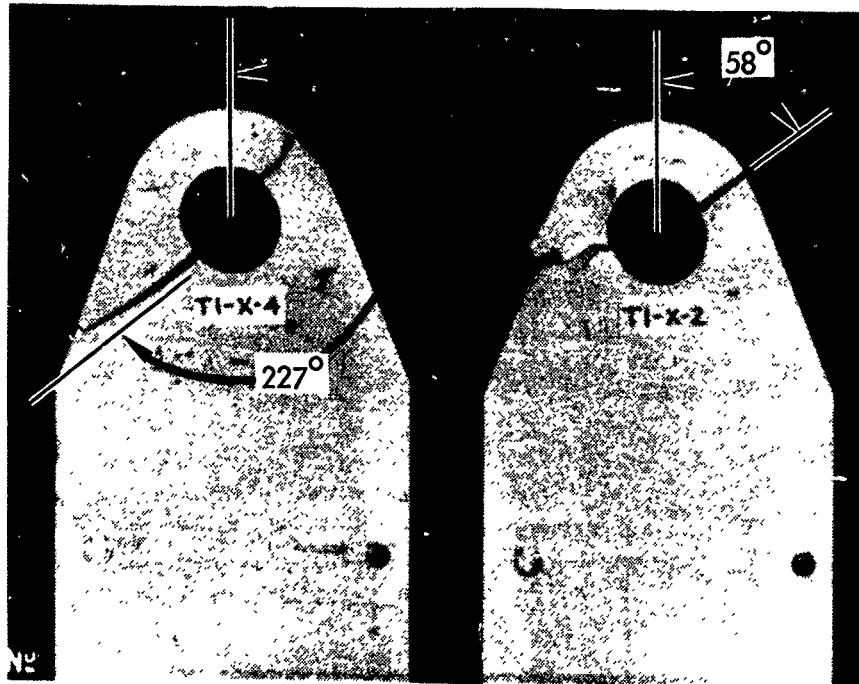
Figure 6-13. Crack Profiles for Tapered Aluminum Lugs, Precracked at 227 Degrees (T1-X-4) and 58 Degrees (T1-X-2) and Fatigue Tested at -45 Degrees
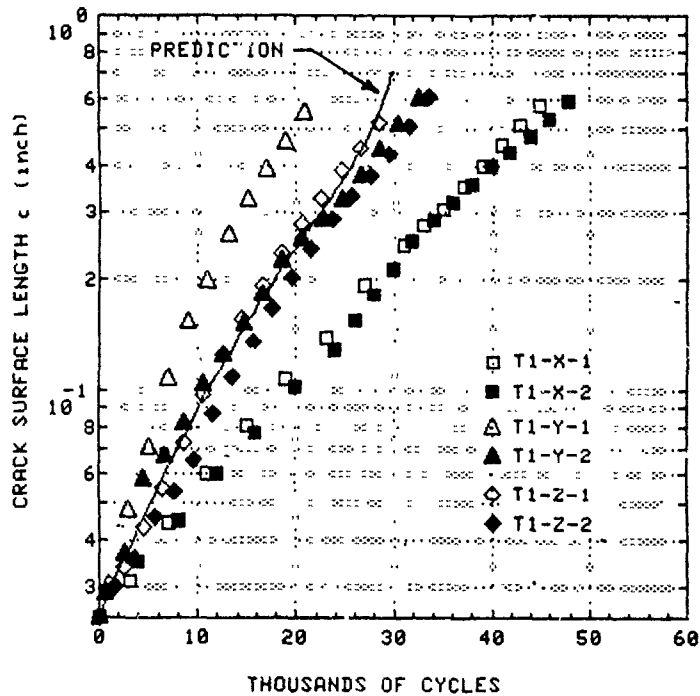
(a)   Crack Growth History
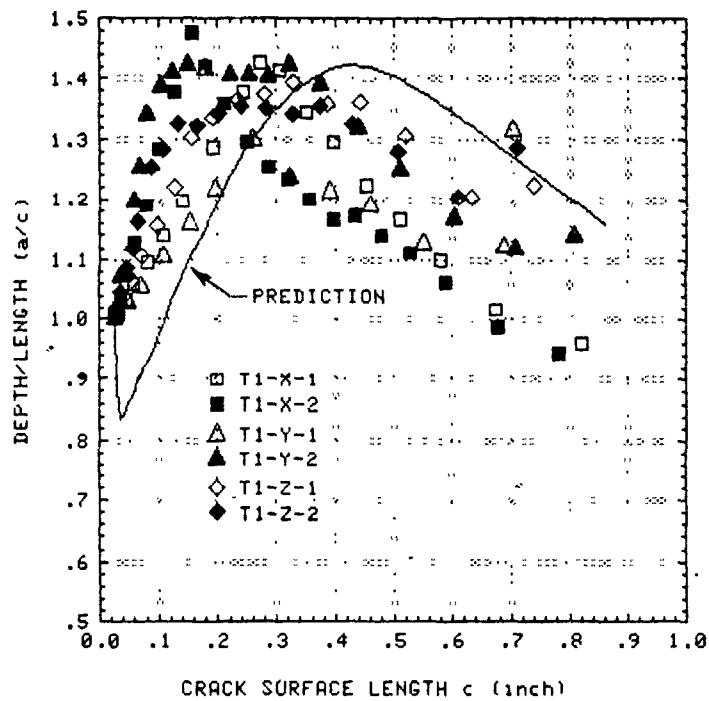
(b)   Crack Aspect Ratio

Figure 6-14.   Data and Prediction, Tapered Lugs with -45° Loading and
+58° Cracks and 3 Pin Clearance Levels
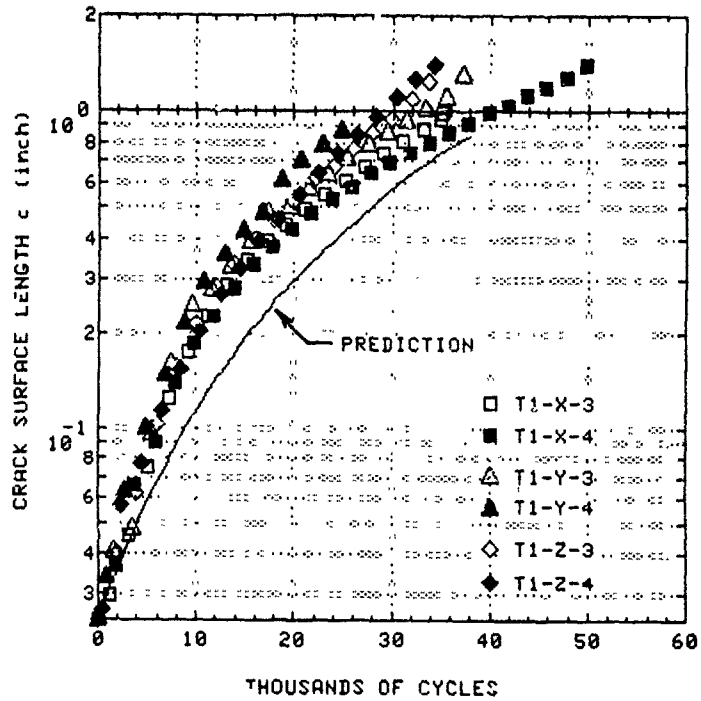
(a) Crack Growth History
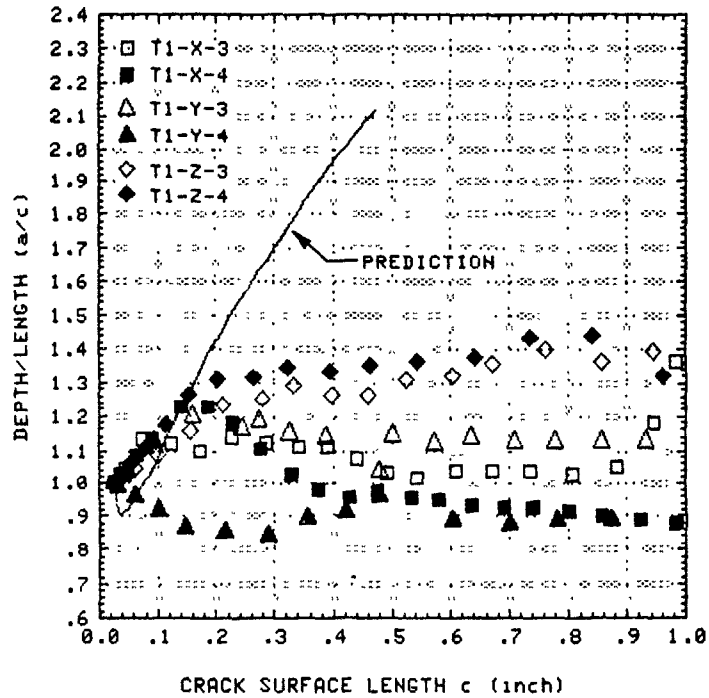
(b) Crack Aspect Ratio

Figure 6-15. Data and Prediction, Tapered Lugs with -45° Loading and
+227° Cracks and 3 Pin Clearance Levels

4.0 EFFECTS OF LUG SHAPE ON CRACK GROWTH

Twenty-two specimens comprising submatrix (b), including two already included in submatrix (a), were fatigue crack growth tested under axial loading. The primary objective of these tests was to determine the effect of the geometric shape of the lug on crack growth. Straight, dogbone-shaped, tapered, and clevis-type lugs were tested. These shape effects were examined at two different thicknesses (0.5 in. and 1.0 in.) and with and without shrink-fit bushings.

The crack growth lives are compared in a bar chart in Figure 6-16. The tapered lug had the longest life in each comparable set, and the life of the dogbone specimen tended to be the shortest. No valid comparison could be made between the lives of specimens with and without bushings, because a higher gross area stress was used for the bushed specimens.

Figures 6-17 through 6-19 compare crack growth predictions to test results for the eight unbushed lugs from this submatrix. The predicted growth at the lug surface is somewhat unconservative for the dogbone-shaped lug (Figure 6-18(a)) but quite accurate for the other three geometries. The experimental depth-to-length ratios tend to be lower than predicted; consequently the predictions of crack depth are slightly more conservative than are the corresponding predictions of surface length.

Figures 6-20 through 6-23 show the extreme unconservatism of the predictions, compared to the test data, for axially-loaded aluminum lugs with shrink-fit steel bushings. As discussed earlier, the predictions were made assuming that the bushing and lug remain in intimate contact throughout the loading cycle. However, for the typical production range of bushing interference and for the loading magnitudes used in these tests, the bushing and lug would separate during the loading, leading to higher lug stresses. As a result, the crack growth predictions are extremely unconservative.

As discussed in Section IV, an improved method was developed to account for bushing interference effects on crack growth. The improved method accounts for the separation and sliding that occur between the lug and bushing during loading, which result in increased stresses and faster crack growth.

260
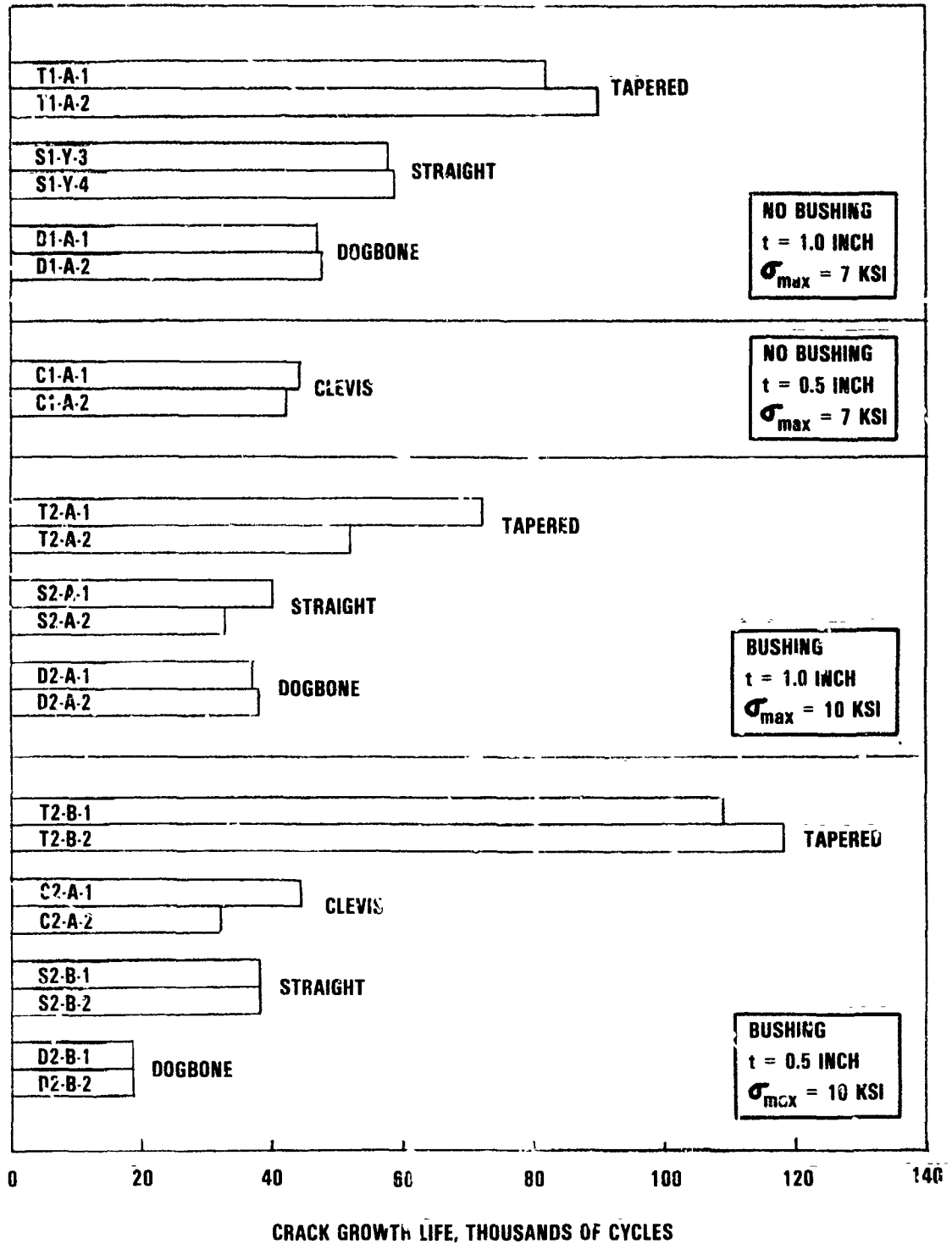
Figure 6-16. Effect of Lug Geometry on Crack Growth Life
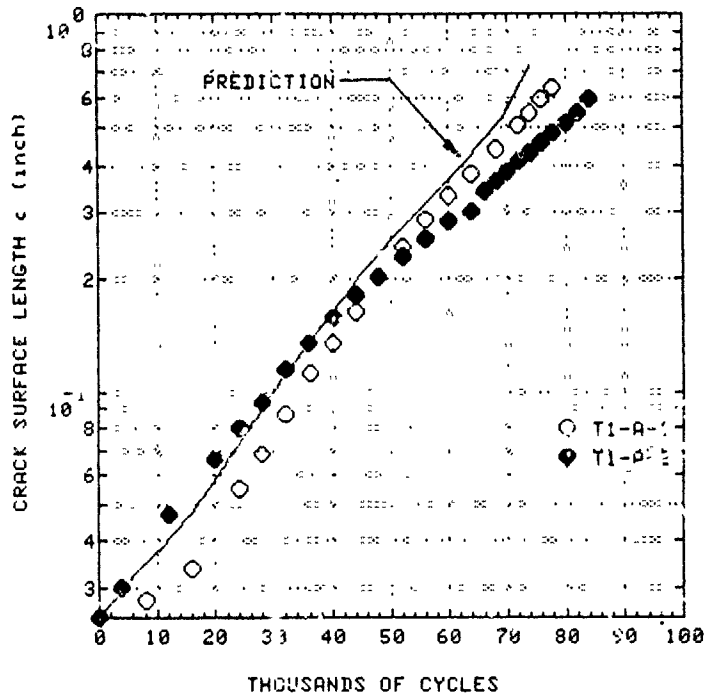
(a) Crack Growth History
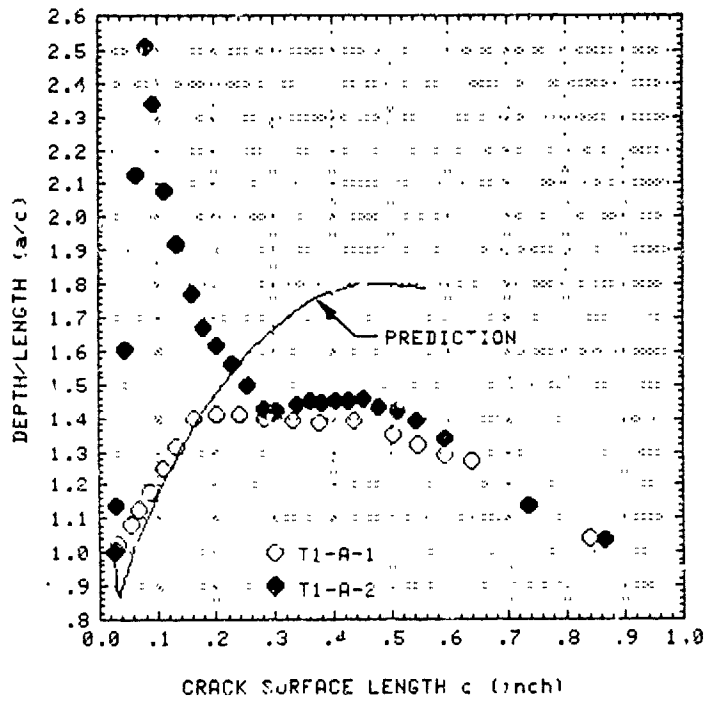
(b) Crack Aspect Ratio

Figure 6-17. Data and Prediction, Tapered Lug, B = 1.0 Inch, Axial
Loading, No Bushing

262
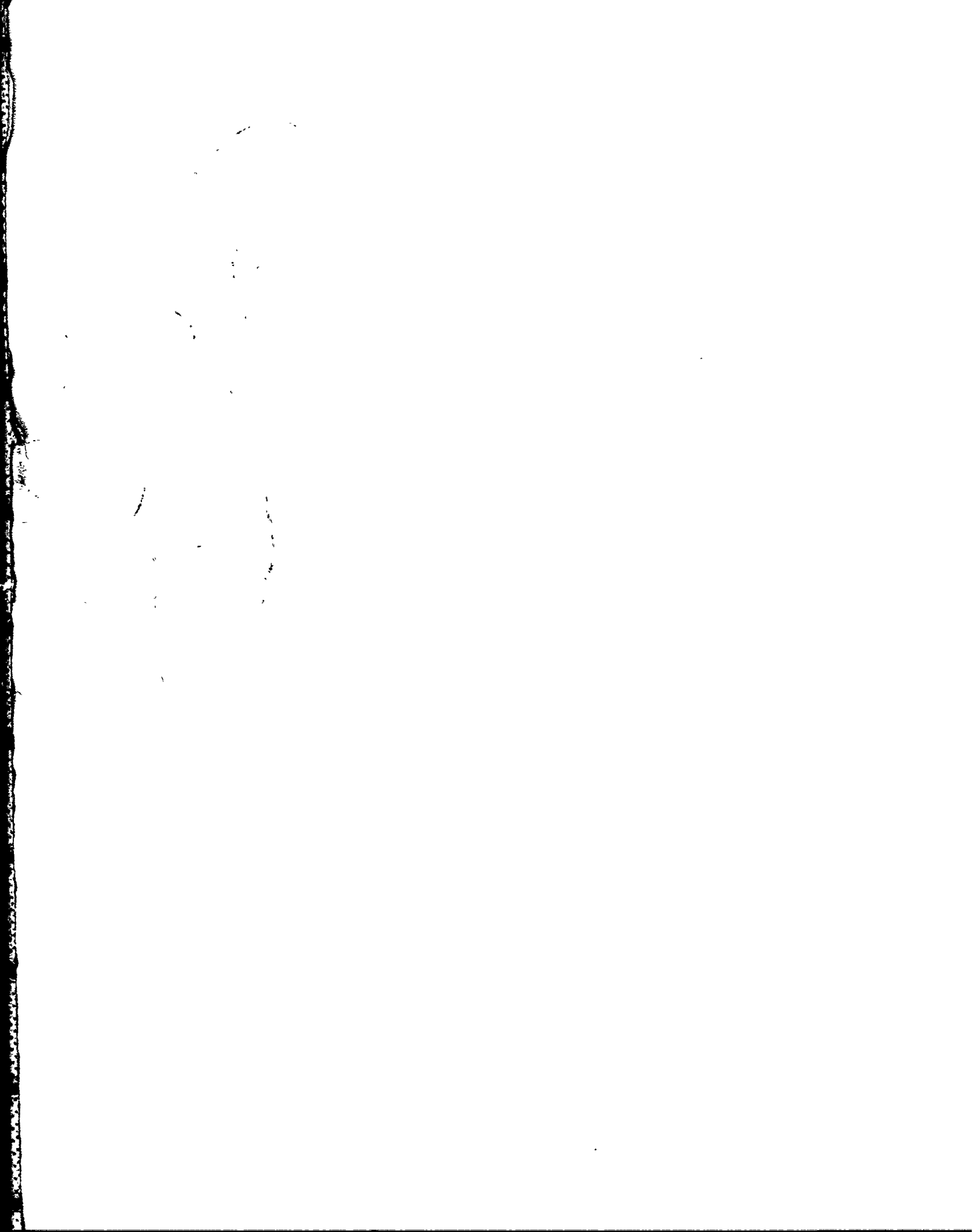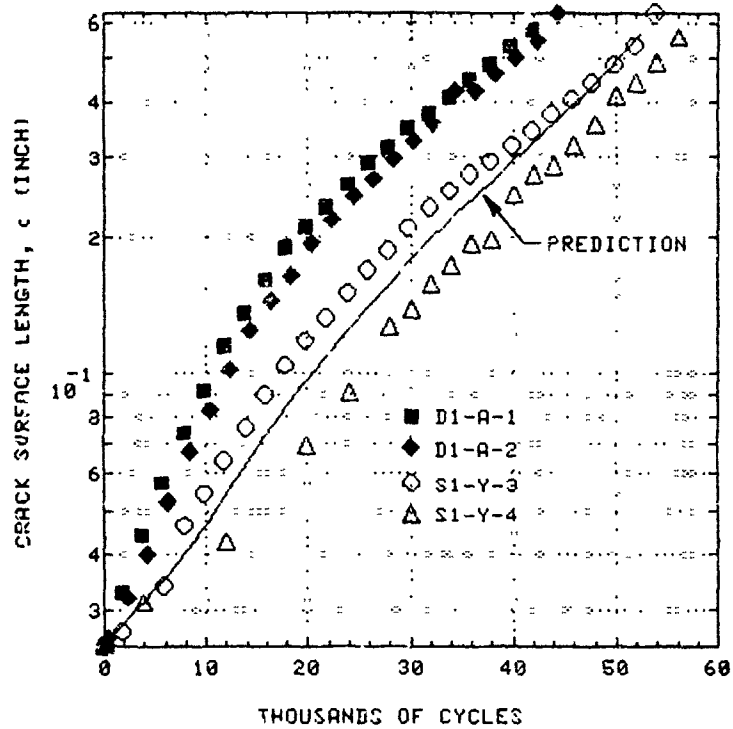
(a) Crack Growth History
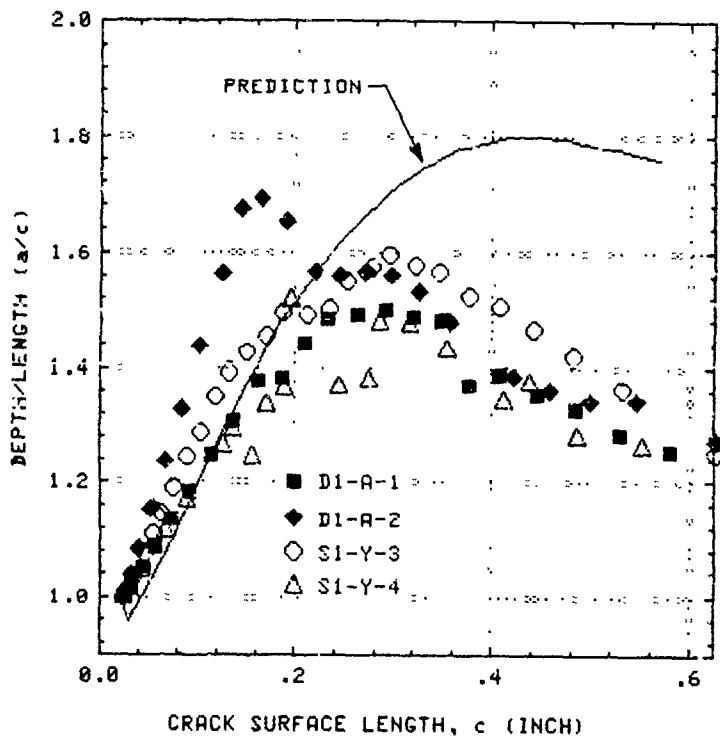
(b) Crack Aspect Ratio

Figure 6-18. Data and Prediction, 1.0-Inch Thick Straight (S1) and Dogbone (D1) Lugs, Axial Loading, No Bushing

263
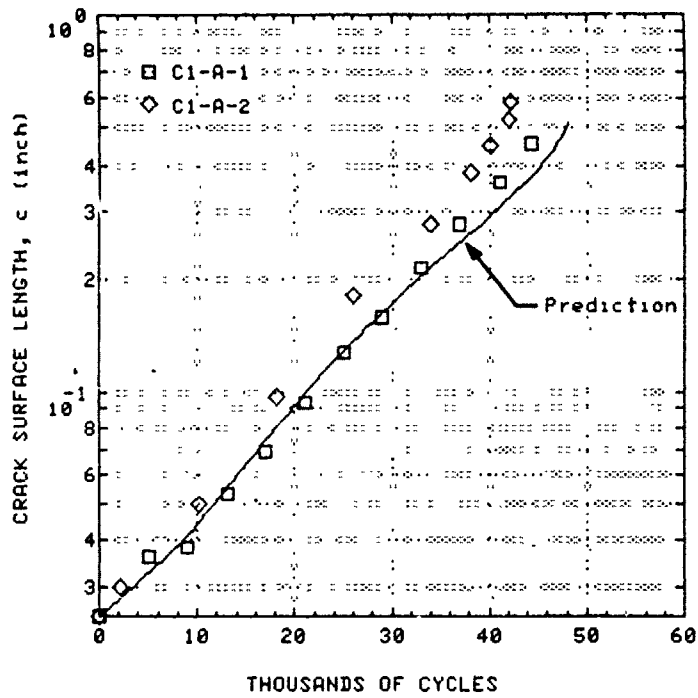
(a) Crack Growth History
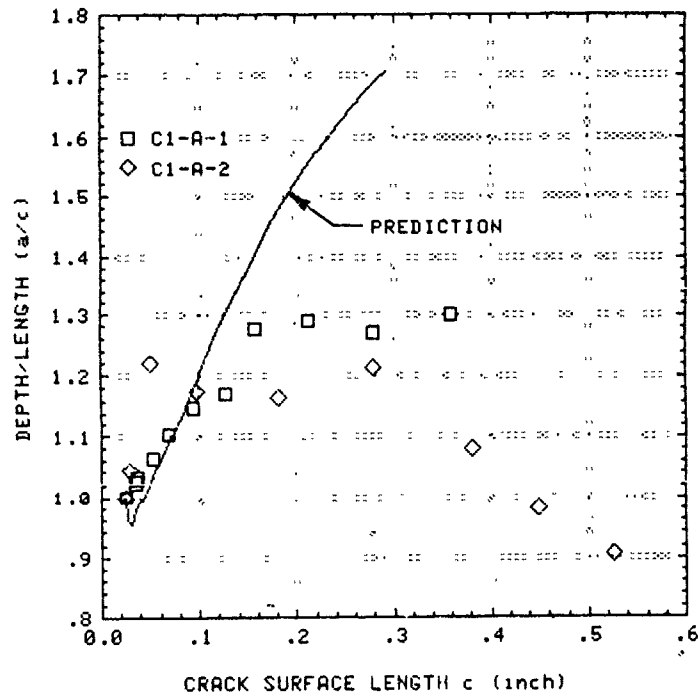
(b) Crack Aspect Ratio

Figure 6-19. Data and Prediction, Clevis, Axial Loading, No Bushing
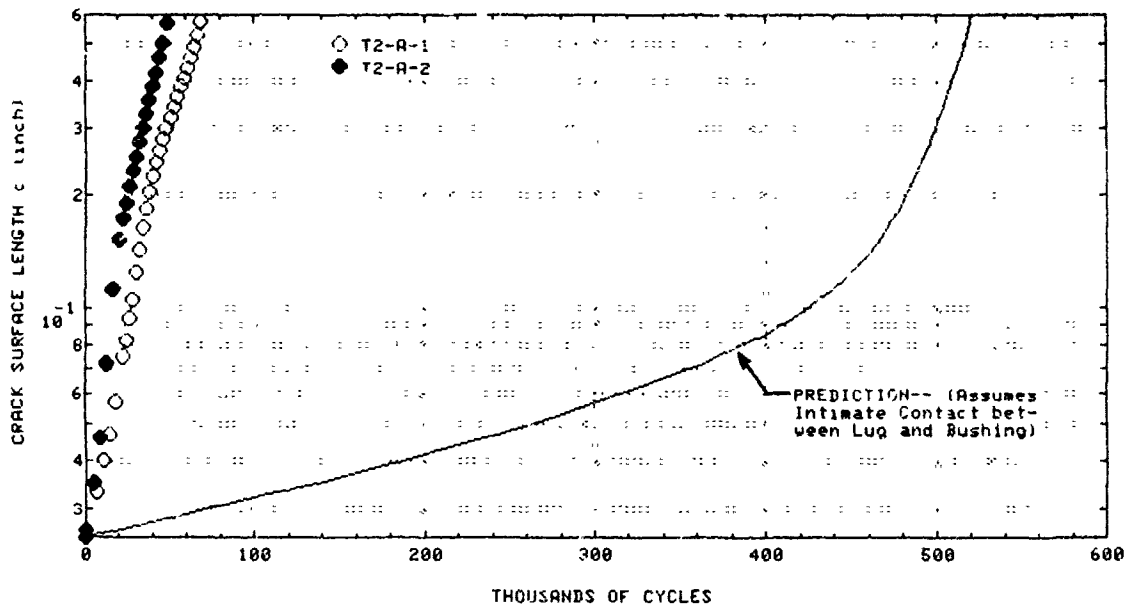
Figure 6-20. Experimental and Predicted Crack Growth History, Axially-Loaded Tapered Lugs, B=1.0 Inch, with Shrink-Fit Bushing
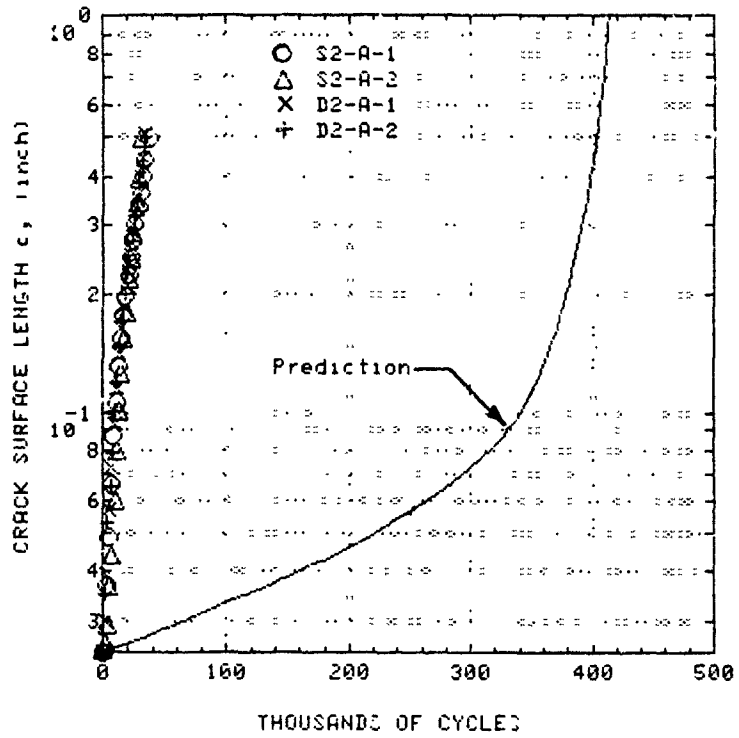
Figure 6-21. Experimental and Predicted Crack Growth History, Straight (S2) and Dogbone (D2) Lugs, B=1.0 Inch, with Shrink-Fit Bushings
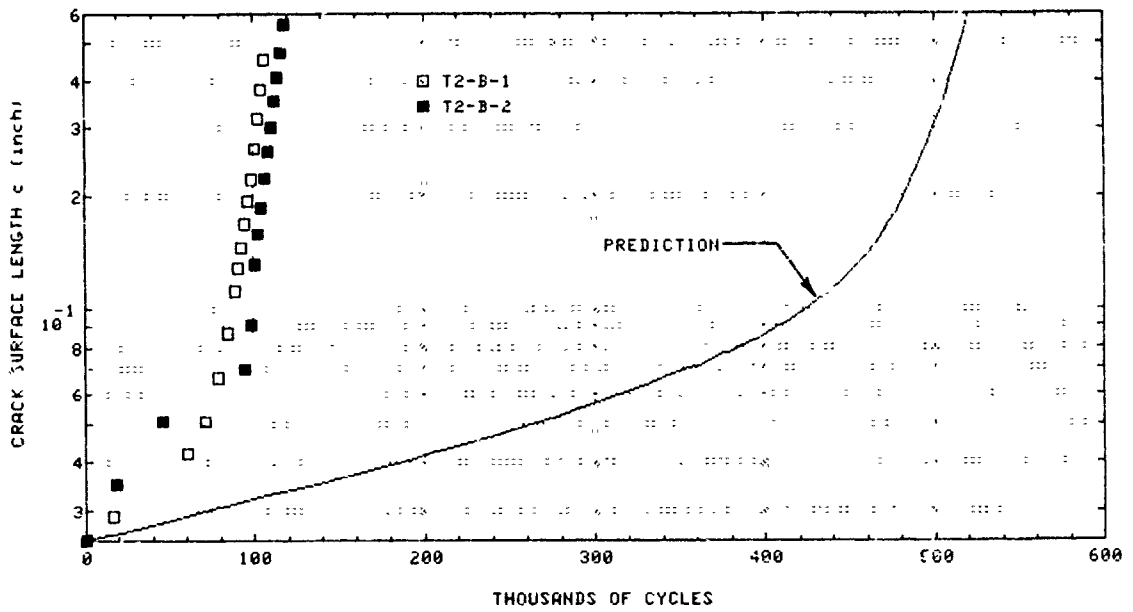
Figure 6-22. Experimental and Predicted Crack Growth History, Axially-Loaded Tapered Lugs, B=0.5 Inch, with Shrink-Fit Bushings
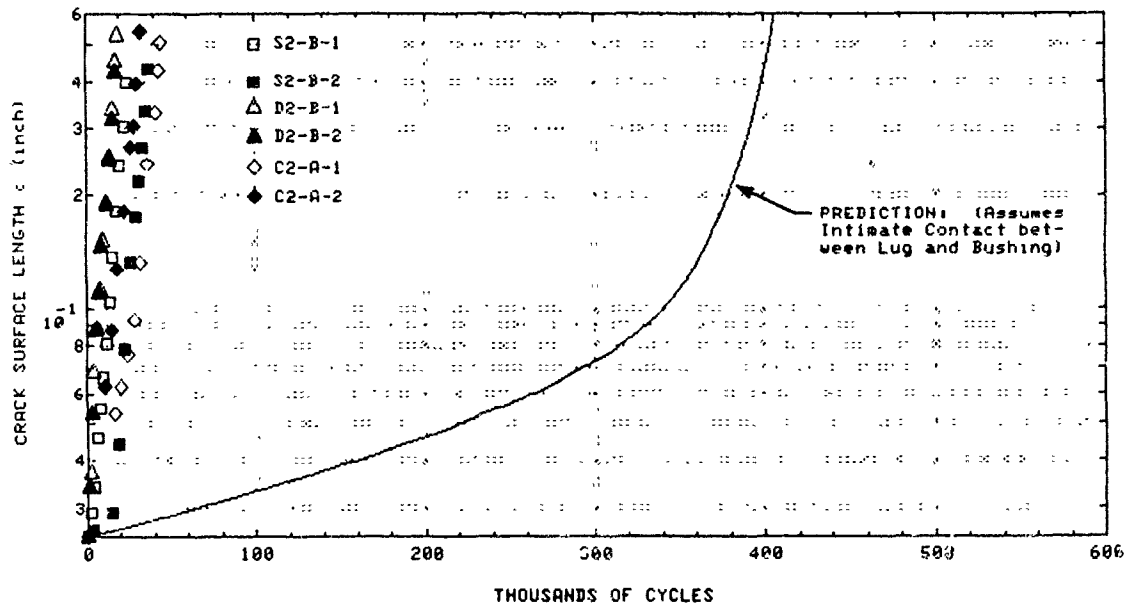
Figure 6-23. Experimental and Predicted Crack Growth History, Axially-Loaded
Straight (S2), Dogbone (D2), and Clevis (C2) Lugs, B=0.5 Inch,
with Shrink-Fit Bushings

Figures 6-24 through 6-26 show the improved predictions that have been obtained for axially-loaded straight, dogbone and clevis-type lugs with shrink-fit steel bushings. As Figure 6-24 shows, the predictions tend to be conservative and significantly more accurate than the large unconservative predictions obtained by the prior method. The error is larger for larger cracks and amounts to a factor of about 1.5 (Figure 6-25(a) and 6-26).

Note in Figure 6-26(a) that the initial crack growth rate of Specimen S2-B-2 was extremely slow, with an abrupt increase in crack growth rate occurring at about c = 0.030 inch. This anomoly was probably caused during bushing installation. The bushing in this specimen (and in no other Group II specimens) had to be forced into place with a heavy press after it fell halfway out at the end of the standard thermal-shrinkage installation. The bushing had not been held in place long enough to adequately expand. Figure 6-26(b) shows the same data/analysis comparison as 6-26(a), except that the initial crack growth data from Specimen S2-B-2 have been appropriately adjusted to eliminate the abrupt slope change.

Predicted and experimental flaw shape histories are shown in Figure 6-27 for four 1-inch thick bushed lugs (straight and dogboned). Both analysis method results are shown. The data scatter makes it impossible to select between the two analysis methods insofar as estimating flaw shape.

5.0 CRACK GROWTH IN OFF-AXIS-LOADED TAPERED LUGS

Eighteen tapered lug specimens comprising submatrix (c), in addition to the 12 already discussed in submatrix (a), were fatigue crack growth tested under off-axis loading. The main objective of these tests was to evaluate the prediction methodology for off-axis loading. Ten aluminum and eight steel lugs were tested. Ten of the specimens contained shrink-fit steel bushings. Six specimens were precracked at 58 degrees to the symmetry axis of the specimen and fatigue loaded at -45 degrees. The other twelve were precracked at 204 degrees and loaded at -90 degrees. Four of the -90-degree-loaded lugs were subjected to load reversal, using a stress ratio of -0.5. A stress ratio of 0.1 was used for the other 14 tests in Submatrix (c).
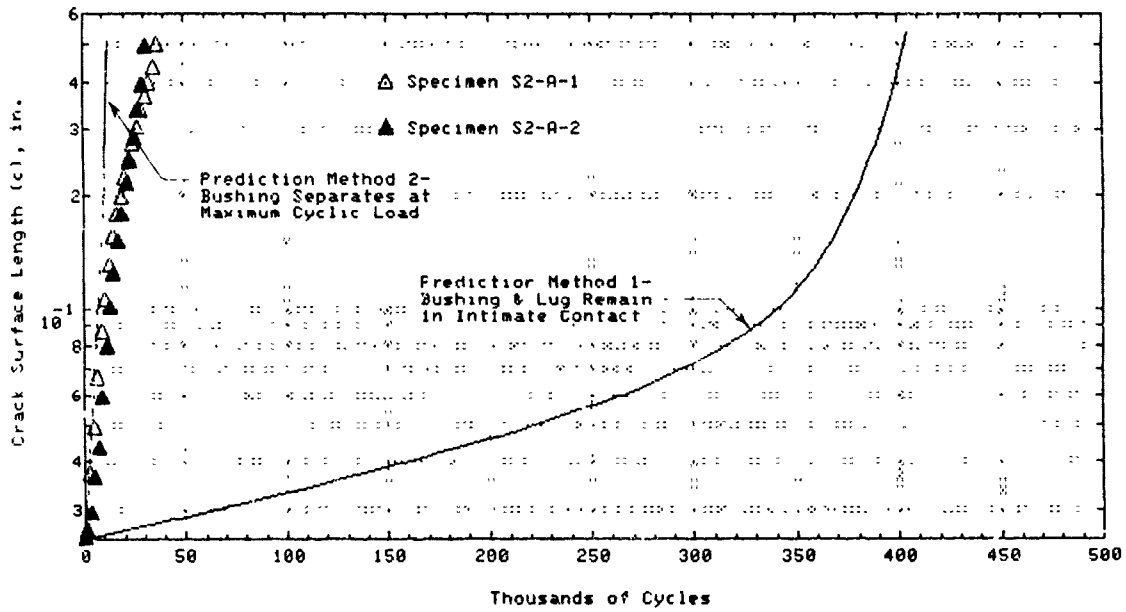
Figure 6-24.   Comparison of Two Analysis Methods for Lugs with Shrink-Fit Bushings

270
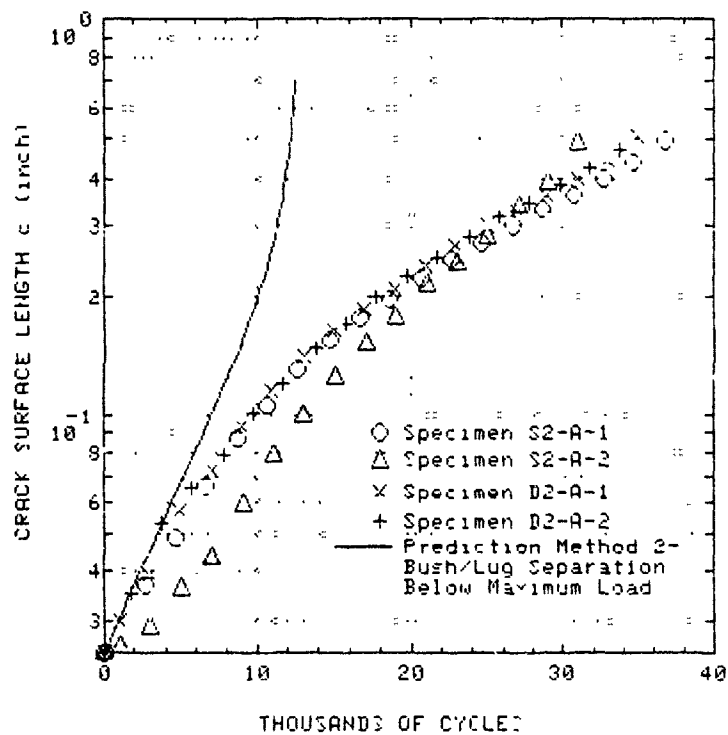
Figure 6-25. Accuracy of Analysis Method 2 (Modeling Bushing-Lug Separation) for Axially-Loaded 1.0-Inch Straight (S2) and Dogbone (D2) Lugs
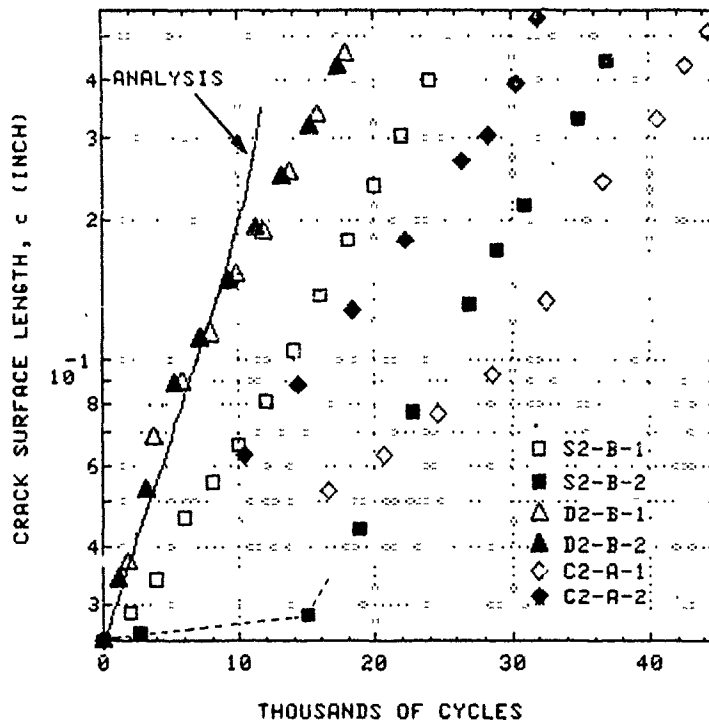
(a) Raw Data (Note Slow Initial Growth in Specimen S2-B-2,
Probably Caused by Bushing Installation Anomaly)
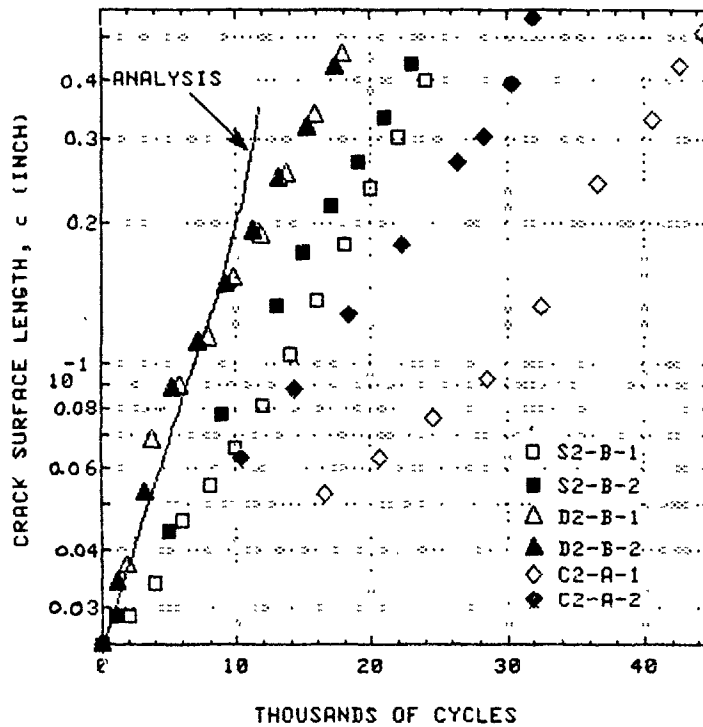
(b) Adjusted Data (Data from Specimen S2-B-2
Shifted to Disregard Slow Initial Crack Growth)

Figure 6-26. Accuracy of Analysis Method 2 (Modeling Bushing-Lug Separation)
for Axially Loaded 0.5-Inch Thick Straight (S2), Dogbone (D2)
and Clevis (C2) Lugs

272
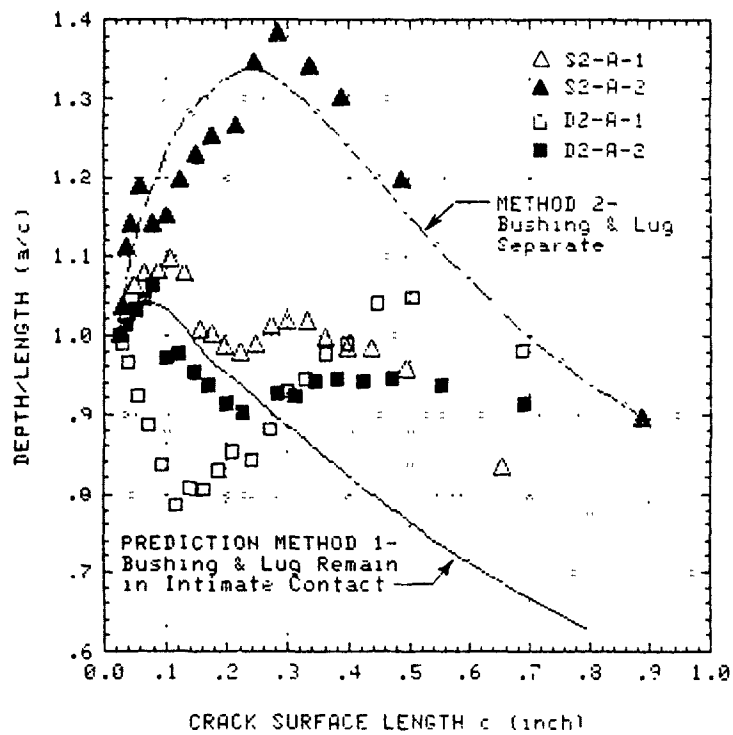
Figure 6-27. Comparison of Crack Shape Prediction by Methods 1 and 2
for Straight (S2) and Dogbone (D2) Lugs with Shrink-Fit Bushings

273

5.1 ALUMINUM TAPERED LUGS

Submatrix (c) includes 10 aluminum tapered lugs subjected to off-axis loading. Two lugs containing shrink-fit steel bushings were precracked at 58 degrees to the symmetry axis of the specimen and loaded in the -45 degree direction. As Figure 6-28 shows, the over-all appearance of the fracture surfaces was similar to the six unbushed lugs with the same precrack location discussed in 3. of Section VI, and to T1-A-U1, an initially-unflawed lug that developed its major fatigue crack at 58 degrees (See 2.0 of Section VI).

In Figure 6-29 the crack growth prediction is compared to the test results for Specimens T2-A-3 and -4. As discussed earlier, the prediction method assumes that the bushing and lug remain in intimate contact throughout the loading cycle. In the aluminum lugs with steel bushings tested in Group II, the nominal diametrical interference level used was only 0.0020 inch, so that the bushing and lug began to separate at a relatively low load level. Consequently, the crack growth life predictions are unconservative by a factor of 15. An alternate prediction method which accounts for separation and corrects this unconservatism was described in Section IV. Unfortunately, the alternate method requires knowledge of the stress distribution along the crack line for an unbushed lug with a pin the size of the bushing outer diameter. This stress distribution was not available for the tapered lugs.

Figure 6-30 shows the crack growth histories for specimens T2-A-3 and -4. The length of the corner crack on the visible face of the lug is plotted in Figure 6-30 (a)*; the crack depth along the bore of the hole, in Figure 6-30(b). Failure occurred in both specimens just after the surface length (c) reached the outer curved surface of the lug.

---

* On this and succeeding graphs, a_B denotes crack depth measured on the outer curved surface; c_B denotes back surface crack length.
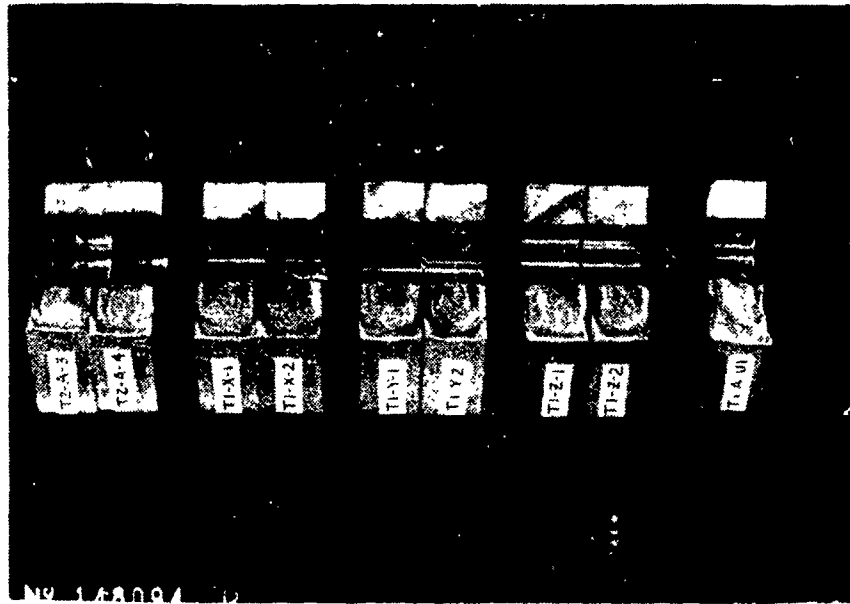
Figure 6-28. Fracture Surfaces for -45 Degree-Loaded Tapered Aluminum Lugs with Primary Fatigue Crack at 58 Degrees

275

Figure 6-29. Data and Prediction, Tapered Aluminum Lugs, B=1.0 Inch, -45 Degree Loading, R=0.1, with Shrink-Fit Steel Bushing

276

(a) Crack Length on Visible Surface

(b) Corner Crack Depth Along Hole Wall

Figure 6-30. Crack Growth Data, Tapered Aluminum Lugs B = 1.0 Inch,
-45 Degree Loading, Shrink-Fit Steel Bushing

Eight precracked tapered aluminum lug specimens were loaded in the -90 degree direction for fatigue crack growth testing. The precrack was located at 205 degrees. Figure 6-31 shows the crack profile on a typical broken specimen. The crack grew down to just below the load reaction point, then turned sharply and went to the free edge. Figure 6-32 shows the similarity of the fracture surfaces of these eight specimens to those of specimens T1-A-U3 and -U4, which were fatigue tested with no initial cracks.

Figures 6-33 and 6-34 show the crack growth data and predictions for unbushed tapered aluminum lugs loaded at -90 degrees. Specimens T1-A-3 and -4 were tested at a stress ratio of R = 0.1, whereas compression-tension loading (R = -0.5) was used for Specimens T1-A-5 and -6. The same value of maximum tension load was used for all 4 specimens. Note that, as predicted, there was little if any effect of the compressive half-cycle, because reversing the external load on a lug does not reverse the internal stresses. The compression half cycle of load caused negligible stresses near the crack.

The stress intensity factors used in the predictions were calculated by finite element analyses using the crack tip element. However, the calculations were only conducted for crack lengths smaller than c = 0.56 inch, so extrapolations were necessary for larger crack lengths. Notice in both Figure 6-33 (a) and 6-34 (a) that approximately half the crack growth life was in the extrapolated region.

Secondly, observe in Figures 6-33 (a) and 6-34 (a) that the critical crack length of approximately 3.2 inches was underestimated by about a factor of 2. Critical crack length was predicted by a plastic hinge criterion explained in Section IV, assuming that the crack would grow radially until the distance (h) from the crack tip to the tapered edge of the lug became too small to react half of the applied load in beam bending. In the tests however, the crack tended to turn away from the tapered edge rather than grow straight radially, as Figure 6-31 shows. This increased the distance h and thereby postponed catastrophic failure until the crack actually passed the load reaction point.

Thirdly, a gap in the data is seen in Figures 6-33 (a) and 6-34 (a) between the last two data points. This reflects the fact that the fracture

Figure 6-32. Comparable Fracture Surfaces for Various
Tapered Aluminum Lugs Loaded at -90 Degrees

Figure 6-31. Typical Crack Profile for
Aluminum Tapered Lugs Loaded
at -90 Degrees
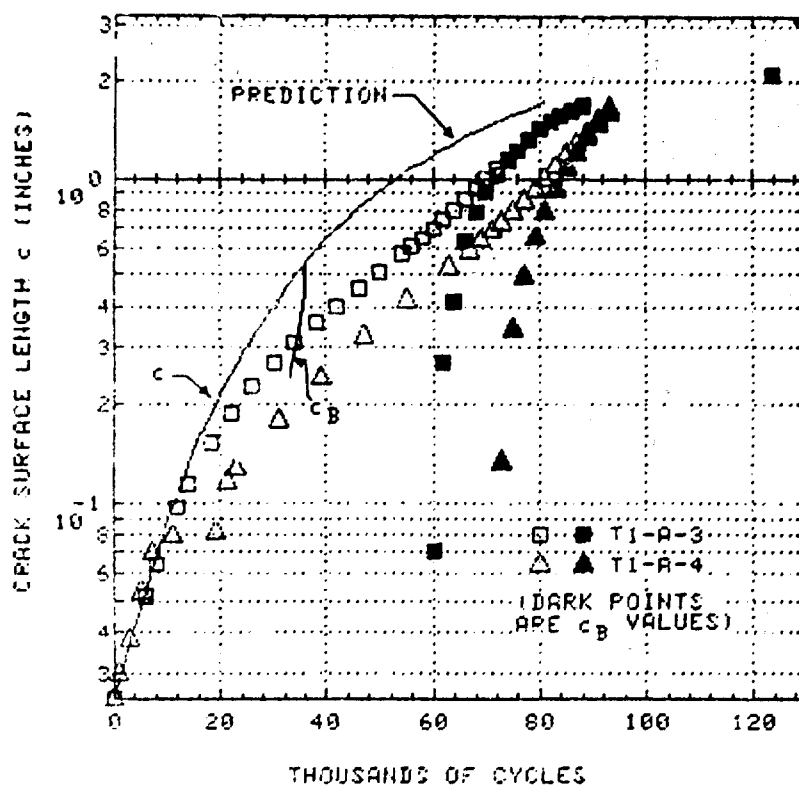
(a) Crack Length on Visible Surface
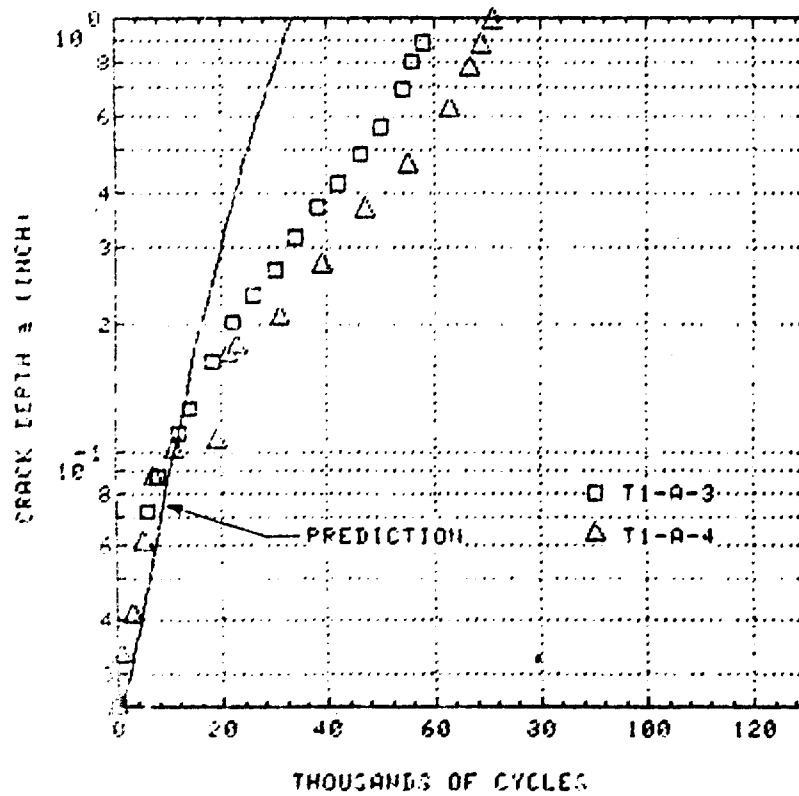
(b) Corner Crack Depth Along Hole Wall

Figure 6-33. Data and Prediction, Tapered Aluminum Lug, B = 1.0 Inch,
-90 Degree Loading, R = 0.1, No Bushing

(a) Crack Length on Visible Surface

(b) Corner Crack Depth Along Hole Wall

Figure 6-34. Data and Prediction, Tapered Aluminum Lug, B = 1.0 Inch, -90 Degree Loading, R = -0.5, No Bushing

281

surface markings cease to be visible for the long crack lengths. No visual data were taken during the tests for long cracks, because it appeared that the fracture surface data would suffice. The data gap was discovered only upon detailed analysis of the fracture surface data.

Fourth, notice in Figure 6-33 that when the corner crack in Specimen T1-A-4 was .08 long and .10 deep, there was an apparent pause in the crack growth. This corresponds to the point when the crack turned temporarily and changed planes, as is seen in Figure 6-35. An immediate change of planes like this was observed to a lesser degree in all four specimens (T1-A-3 through -6). Another way of regarding this behavior is to observe that the initial growth direction is non-radial, and that, briefly at least, the crack starts growing diagonally toward the lug axis of symmetry.

Fifth, in Figure 6-34 (a), crack growth on the front face of Specimen T1-A-5 is observed to arrest at c = 0.77 inch, while on the rear face the crack continued to propagate. The reason for this seemingly strange growth behavior is seen in the photographs in Figure 6-36. At the front face, the crack turned and grew toward the free edge, but eventually this branch stopped growing. Meanwhile, at the back surface, the crack kept growing in the original radial direction, and this turned out to be the primary crack leading to specimen failure. Thus, the fracture surface marks shown in Figure 6-36(b), which are the basis of the data plotted in Figure 6-34 (a), show no front-face growth of the primary crack during the time that the secondary crack was forming.

Figures 6-37 and 6-38 compare the predicted and experimental crack growth behavior for Specimens T2-A-5 through -8, the -90 degree-loaded, aluminum tapered lugs with shrink-fit steel bushings. Once again, the erroneous assumption of intimate contact between the lug and bushing resulted in very unconservative crack growth predictions. To mitigate against the possibility of unreasonably long test lives, the applied loads selected for these 4 tests were 25 percent higher than the loads used for Specimens T1-A-3 through-6, the comparable unbushed specimens. Figures 6-39 and 6-40 show the crack growth data for the four bushed specimens. The well-behaved, repeatable nature of these results is striking.
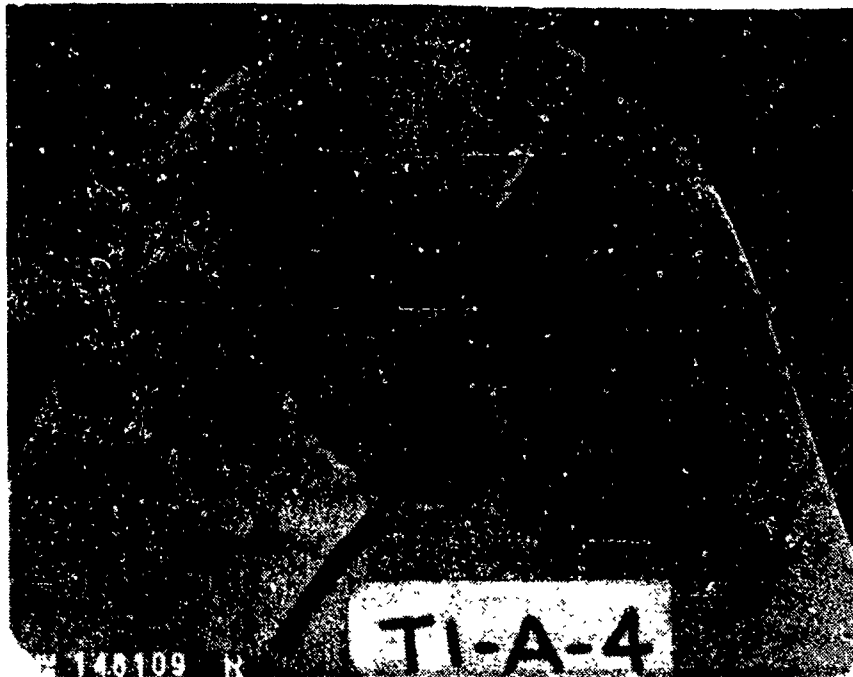
Figure 6-35.   Change of Planes of Initial Corner Crack in
              Specimen T1-A-4
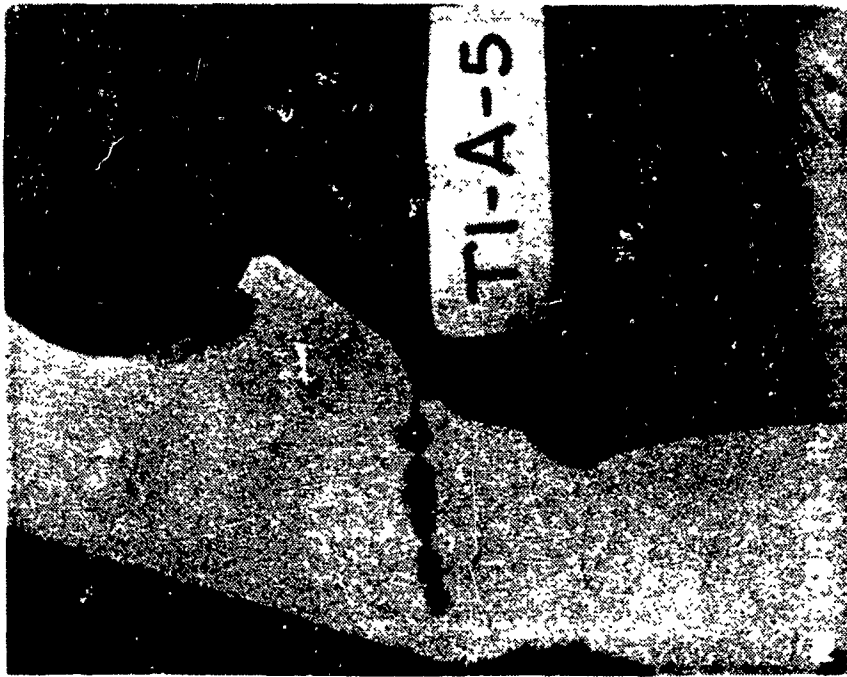
(a) Front Face, Using Dye Penetrant to Show Secondary Crack Branch

(b) Fracture Surface Markings Showing Crack Arrest at Front Face

Figure 6-36. Secondary Cracking in Specimen T1-A-5
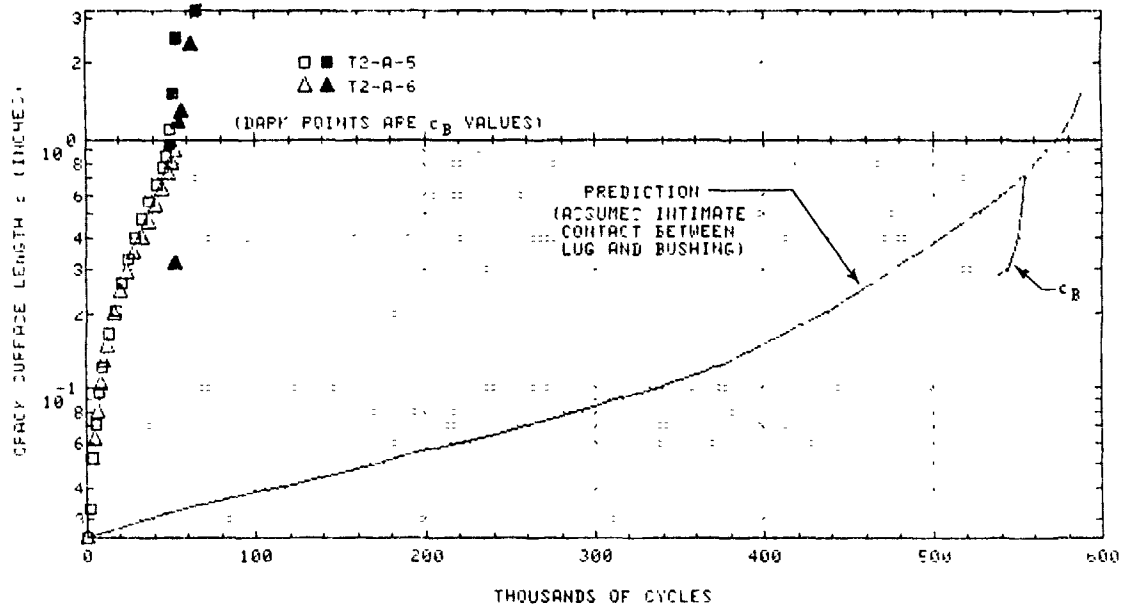
Figure 6-37. Data and Prediction, Tapered Aluminum Lugs, B=1.0 Inch,
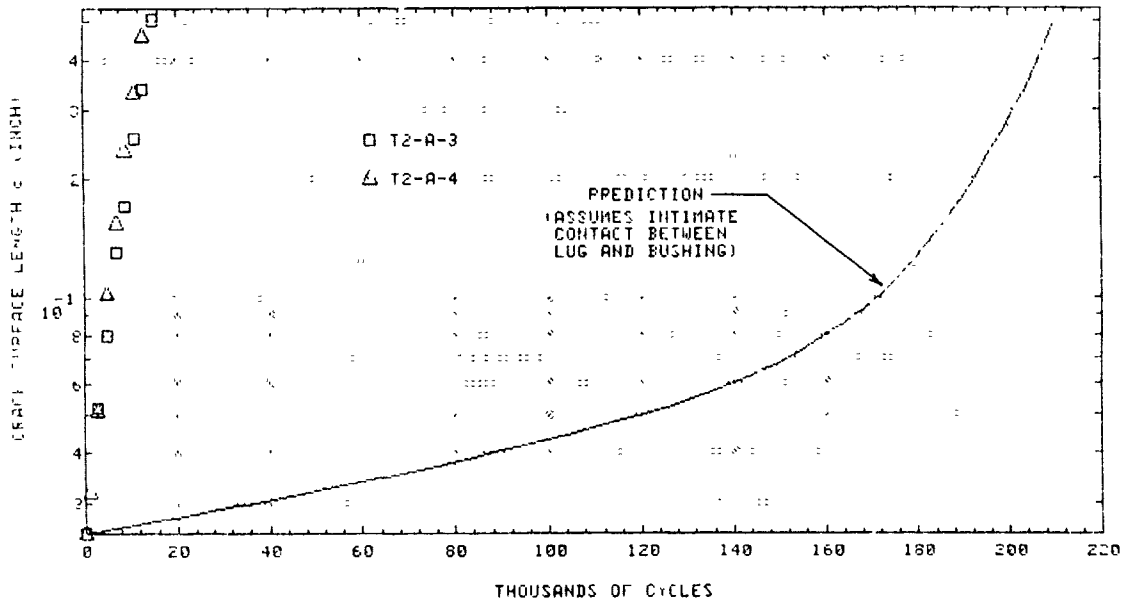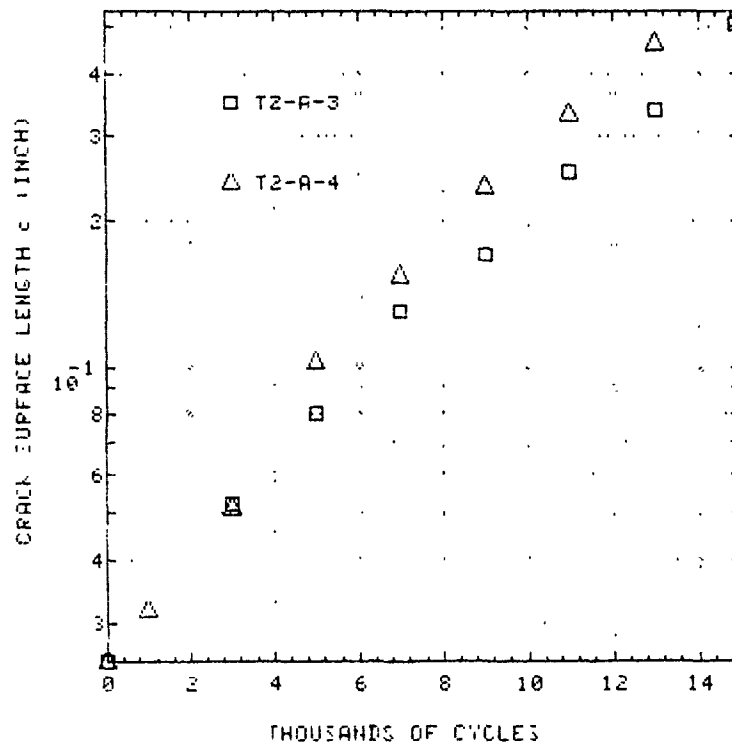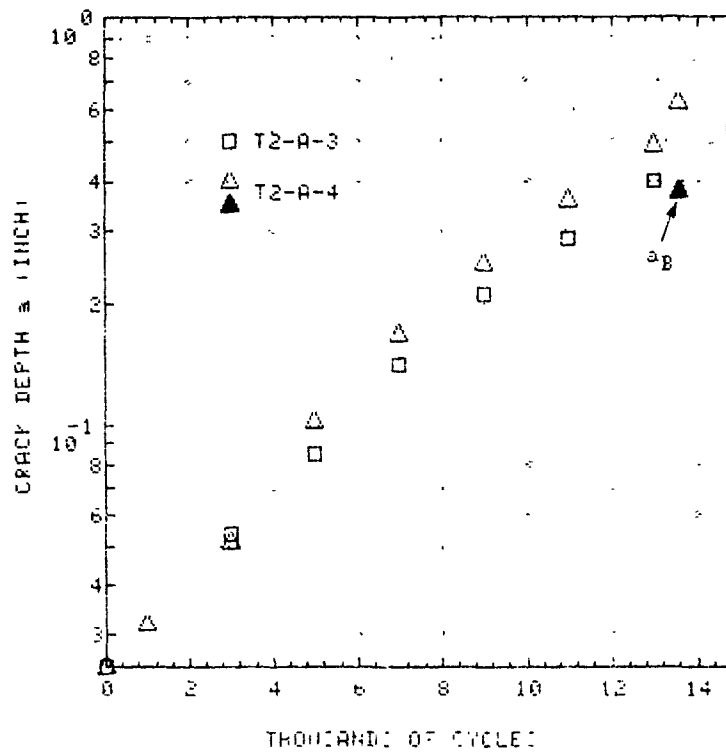-90 Degree Loading, R=0.1, Shrink-Fit Steel Bushing
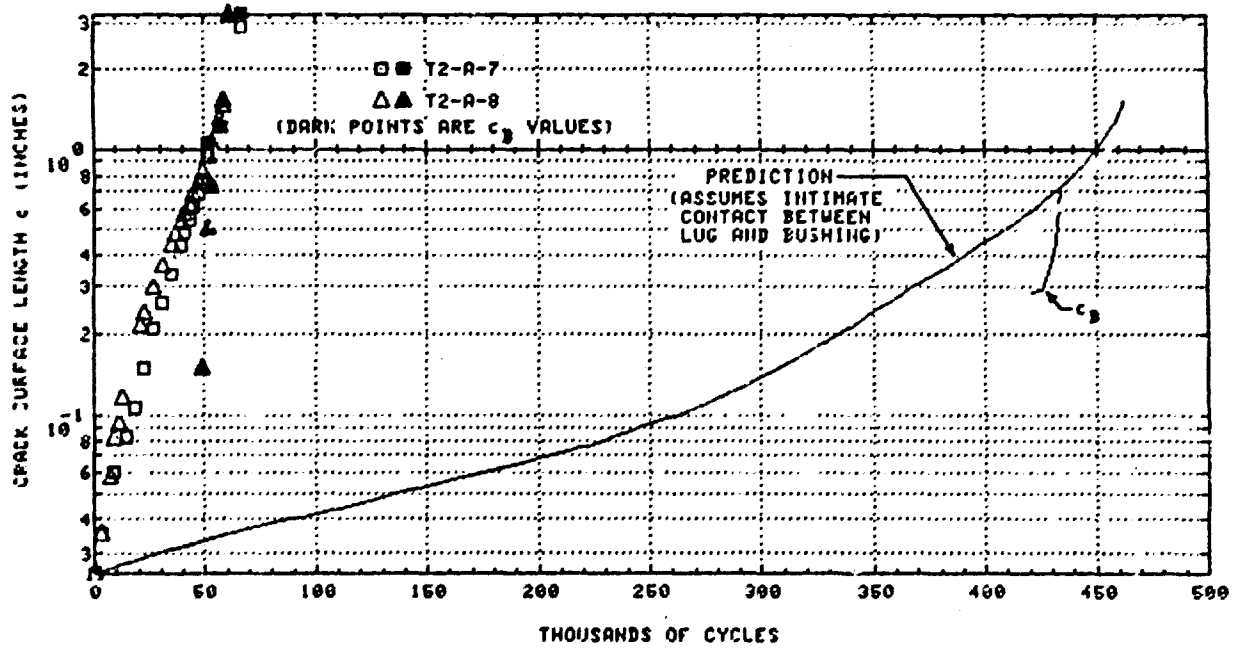
Figure 6-38. Data and Prediction, Tapered Aluminum Lugs, B=1.0 Inch,
-90 Degree Loading, R=-0.5, Shrink-Fit Steel Bushing

286
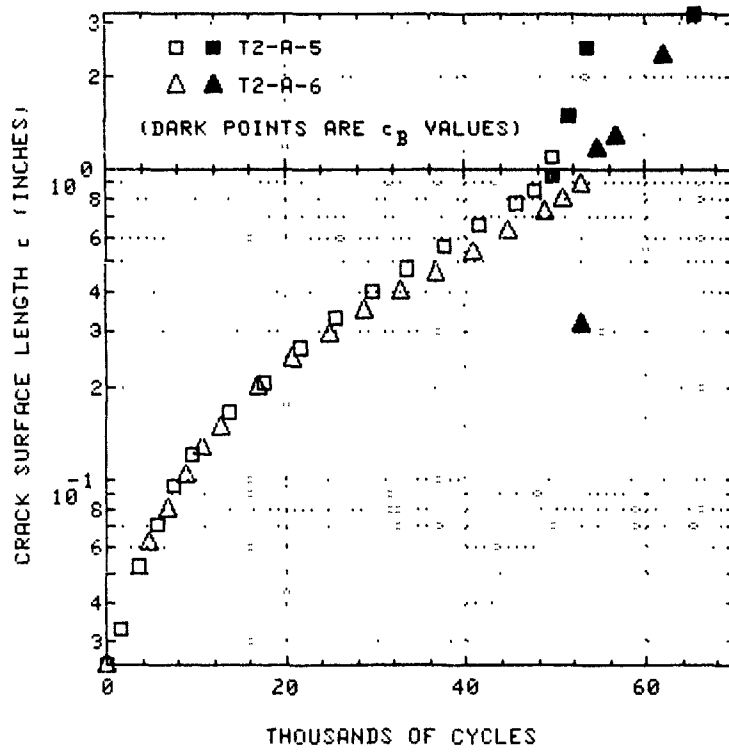
(a) Crack Length on Visible Surface
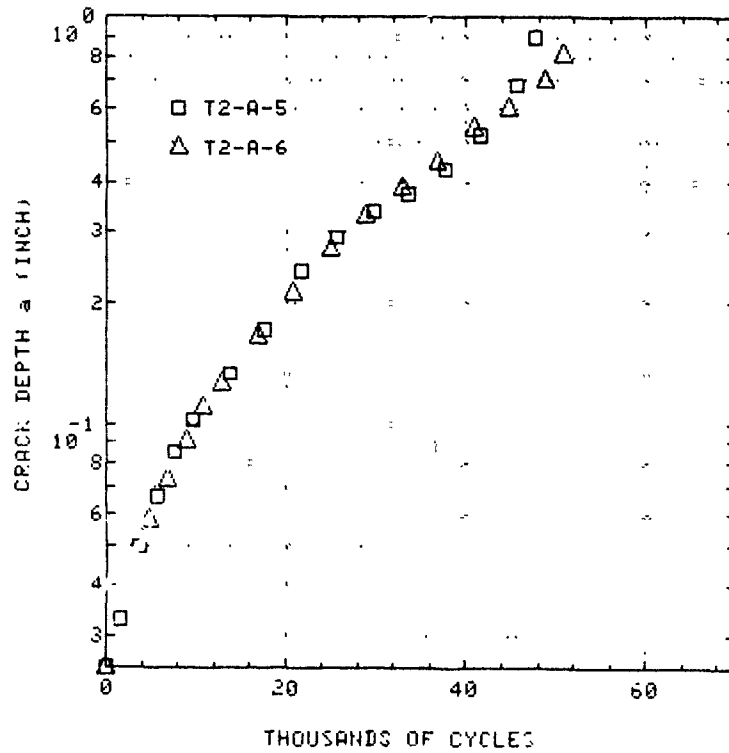
(b) Corner Crack Depth Along Hole Wall

Figure 6-39. Crack Growth Data, Tapered Aluminum Lugs, B = 1.0 Inch, -90 Degree Loading, R = 0.1, Shrink-Fit Steel Bushing

287
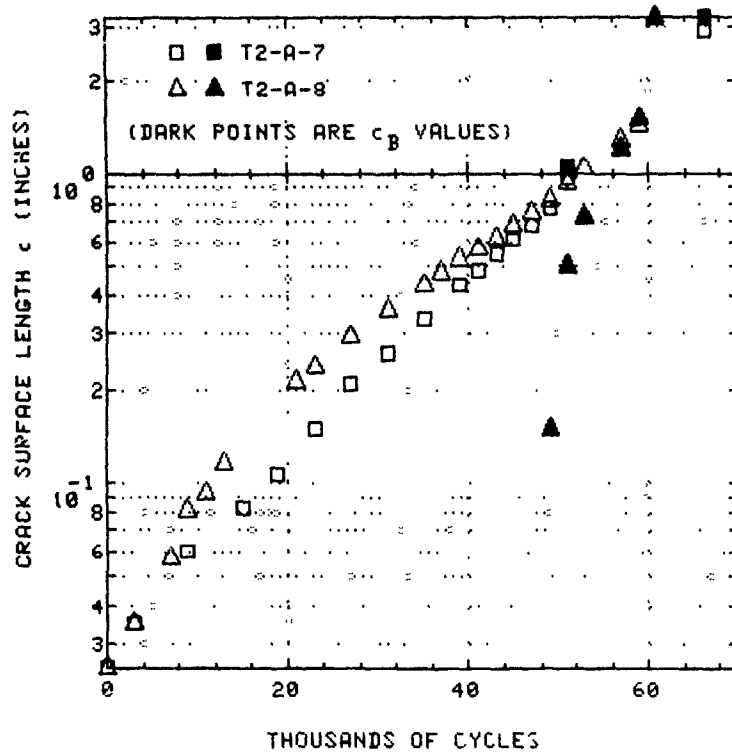
(a) Crack Length on Visible Surface
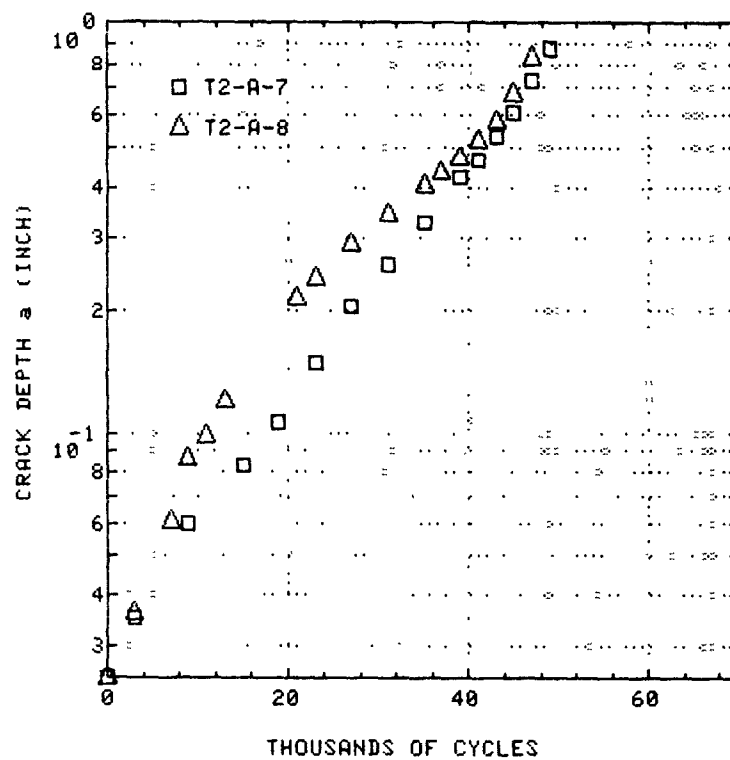
(b) Corner Crack Depth Along Hole Wall

Figure 6-40.   Crack Growth Data, Tapered Aluminum Lugs, B = 1.0 Inch,
-90 Degree Loading, R = -0.5, Shrink-Fit Steel Bushing

288

5.2 STEEL TAPERED LUGS

Eight precracked steel tapered lugs were tested in Group II using off-axis loading. The periodic loading sequence consisted of 1900 cycles at a stress ratio of 0.1, followed by 100 consecutive 30-percent overload cycles for fracture surface marking. Lug thickness was 0.5 inch; outer radius was 1.125 inch; and pin diameter was 1.0 inch. Four specimens were loaded in the -45 degree direction and four in the -90 degree direction. When shrink-fit bushings were used, the nominal diametrical interference level was 0.0021 inch.

Figures 6-41 and 6-42 show comparisons of the test data and predictions for steel lugs loaded at -45 degrees. The prediction was conservative by almost a factor of 2 for the unbushed lugs (Figure 6-41), but by only about 20 percent for the lugs with bushings. Note that for the steel lugs, the assumption of intimate bushing/lug contact did not lead to unconservative predictions.

The applied loads were the same for the bushed and unbushed lugs. Note that the growth rates were virtually the same, whether a bushing was used or not, until the crack broke through the thickness. At that point, the specimens with bushings failed, whereas those without bushings sustained an additional few thousand cycles of growth. Thus, the only effect of the bushing seems to have been a reduced critical crack size due to the reduced net sectional area.

Comparisons between the predicted and actual crack growth in steel lugs loaded in the -90 degree direction are shown in Figures 6-43 and 6-44. For Specimens T1-S-3 and -4 without bushings, the predicted crack growth rates tend to be slightly unconservative, but the predicted final crack size for Specimen T1-S-3 is low by a factor of 2. For specimens T2-S-3 and -4 with bushings, the predicted rate of crack growth is very accurate (especially for surface length c) up to the second-last data point at c = 0.45, but then, despite conservatism of nearly a factor of 3 in the predicted final crack length, the crack growth life prediction is slightly unconservative. Nevertheless, as observed earlier for the other bushed steel specimens, the assumption of intimate bushing/lug contact did not lead to grossly unconservative predictions.
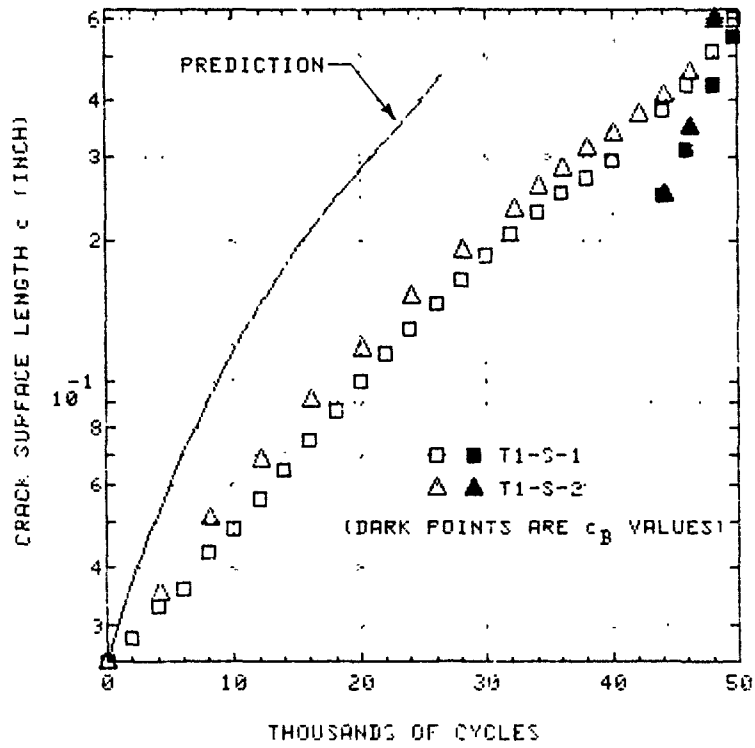
(a) Crack Length on Visible Surface
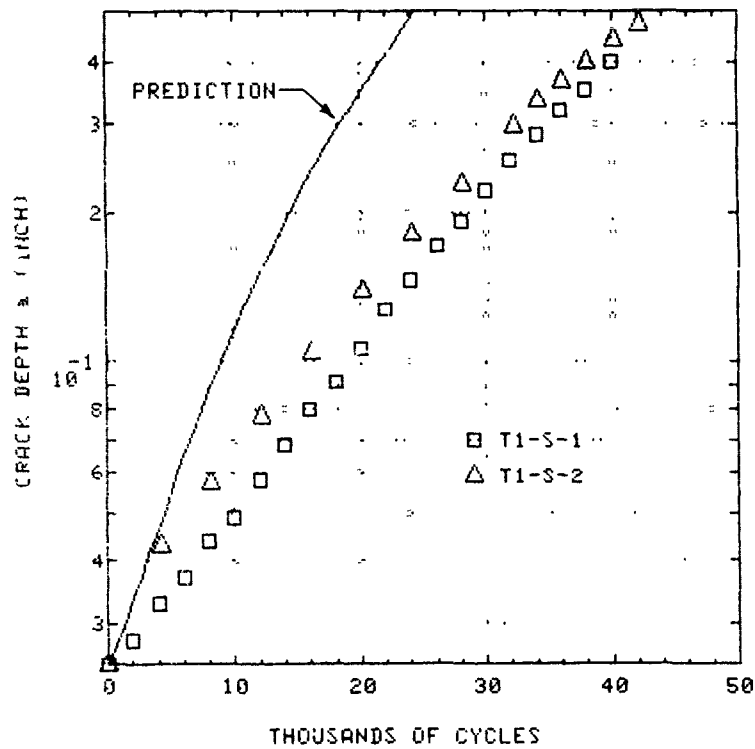
(b) Corner Crack Depth Along Hole Wall

Figure 6-41. Data and Prediction, Steel Tapered Lugs, B = 0.5 Inch, -45 Degree Loading, R = 0.1, No Bushing

290
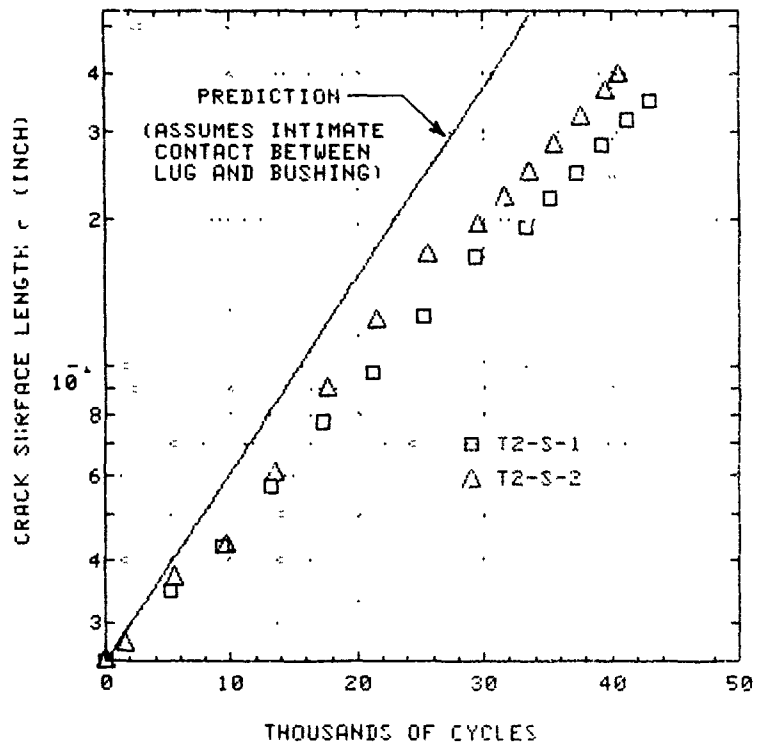
(a) Crack Length on Visible Surface
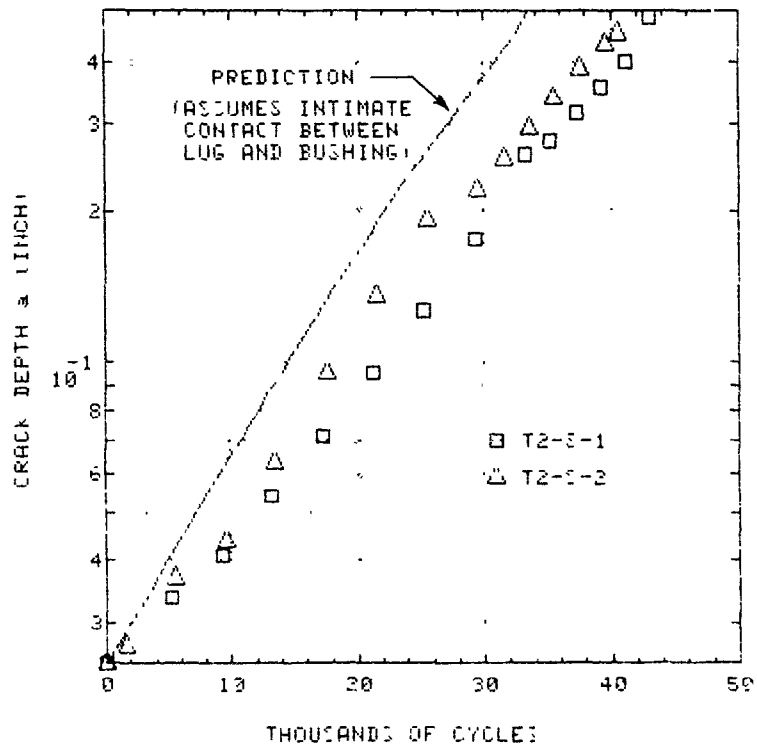
(b) Corner Crack Depth Along Hole Wall

Figure 6-42.   Data and Prediction, Steel Tapered Lugs, B = 0.5 Inch,
-45 Degree Loading, R = 0.1, Shrink-Fit Steel Bushing

291
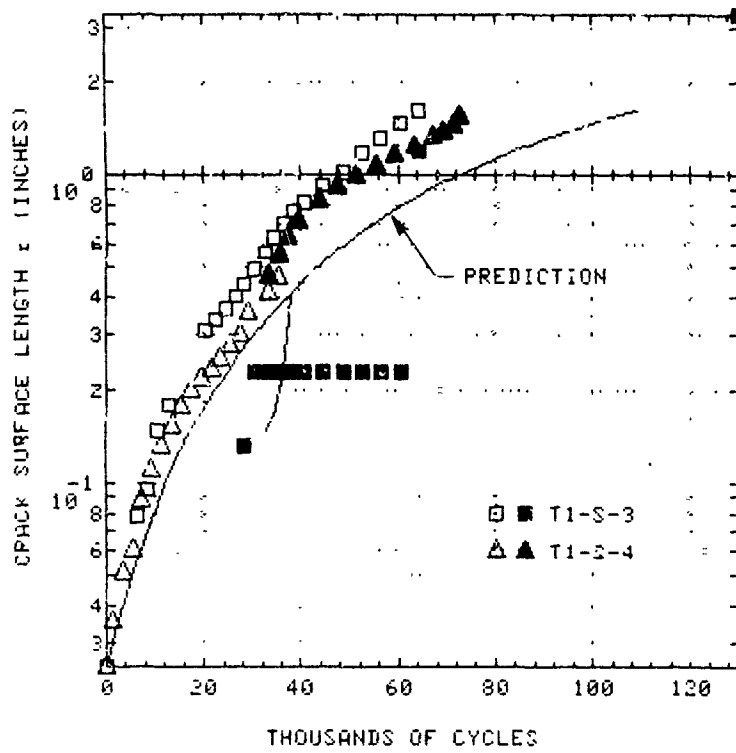
(a) Crack Length on Visible Surface
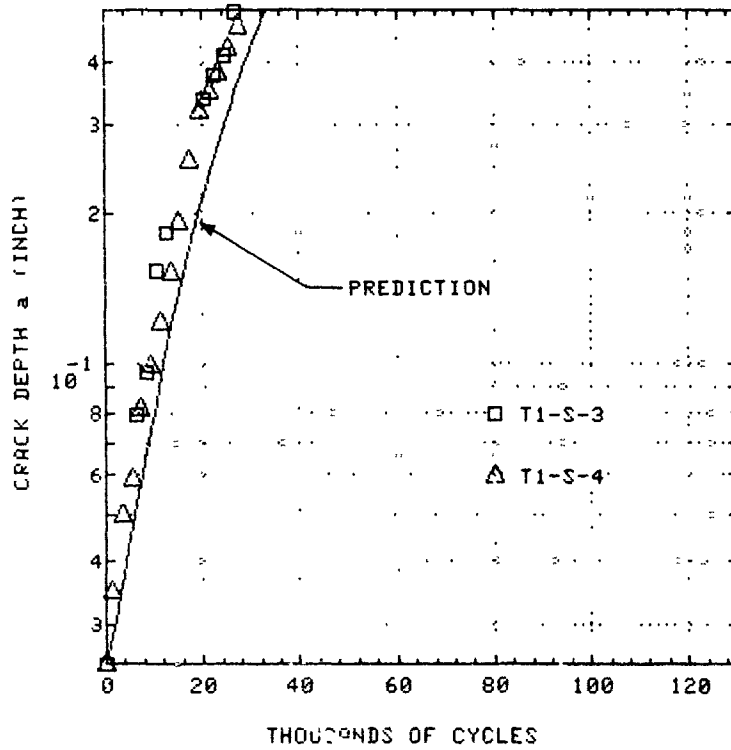
(b) Corner Crack Depth Along Hole Wall

Figure 6-43.   Data and Prediction, Steel Tapered Lugs, B = 0.5 Inch, -90 Degree Loading, R = 0.1, No Bushing
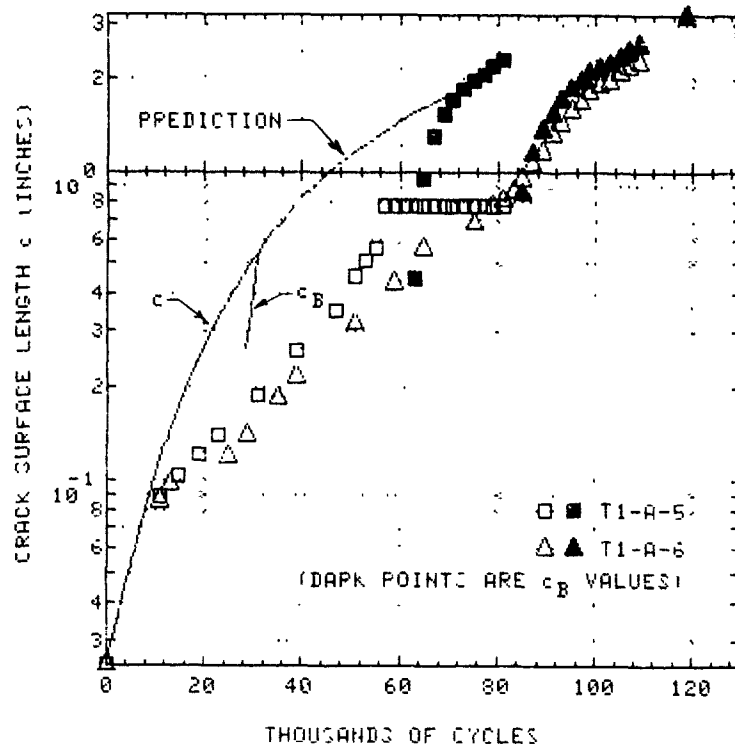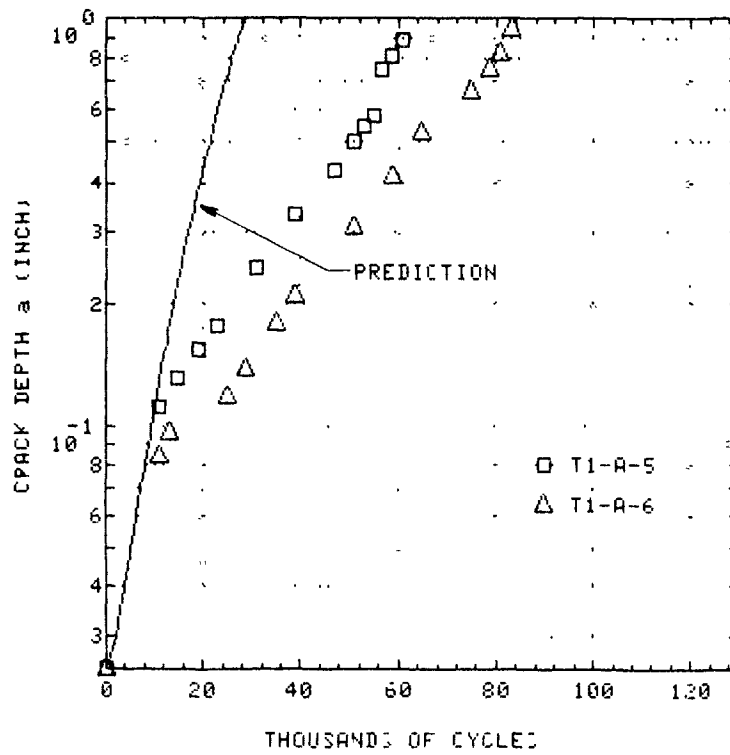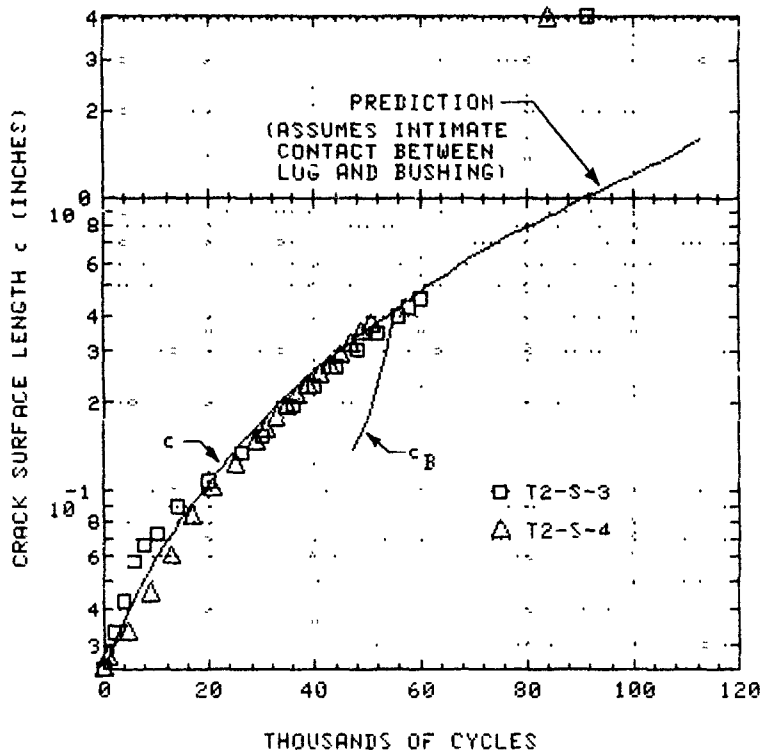
(a) Crack Length on Visible Surface
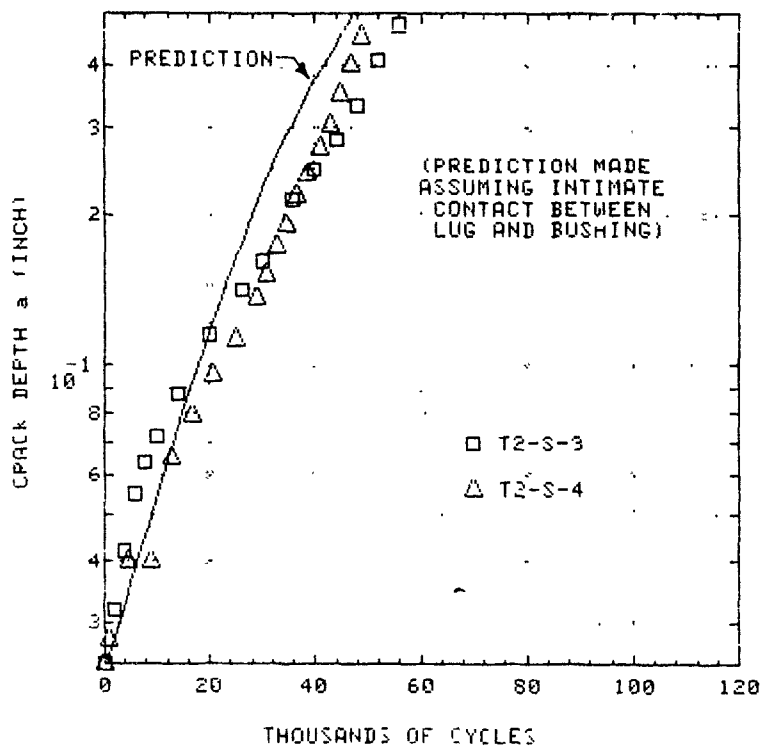
(b) Corner Crack Depth Along Hole Wall

Figure 6-44. Data and Prediction, Steel Tapered Lugs, B = 0.5 Inch,
-90 Degree Loading, R = 0.1, Shrink-Fit Steel Bushing

293

As was the case for the aluminum tapered lugs loaded at -90 degrees, there are a number of complexities in the behavior of these -90 degree-loaded steel lugs that warrant discussion. Each of the following paragraphs corresponds to an observation made in the preceding subsection (5.1) with regard to the aluminum lugs. If anything, these complexities occur to a greater degree in the steel lugs.

First, recall that the stress intensity factor analysis used in the predictions had to be extrapolated for all crack lengths beyond $c = 0.56$ inch for the unbushed specimens and $c = 0.48$ inch for the bushed specimens. Thus, the loss of accuracy for the larger cracks is not surprising.

Secondly, the assumption is made in the analysis that the crack grows radially. Contrast that to the actual crack trajectories shown in Figure 6-45 (Specimens T1-S-U1 and -U2, fatigue tested with no initial crack, were discussed earlier). In three of the four precracked specimens, the crack curved away from the free edge, so that the curved path was approximately tangent to the vertical axis of the specimen. Thus, the distance (h) from the crack tip to the free edge was always much larger than predicted. Since the plastic bending criterion for critical size depends strongly upon h, large errors in predicted critical crack size are not surprising.

Thirdly, there are large gaps in the data between the last two data points in Figures 6-43 (a) and 6-44 (a) for Specimens T1-S-3, T2-S-3, and T2-S-4. This reflects the fact that the fracture surface markings cease to be visible for long crack lengths, and there were no visual measurements of long cracks made during the tests.

Fourth, the initial growth direction in Specimens T1-S-3 and -4 (the unbushed lugs) is non-radial as seen in Figure 6-45. The crack starts out growing diagonally toward the lug axis of symmetry, as it did in the comparable unbushed aluminum lugs. However, in steel Specimen T1-S-3, it kept growing that way.

Fifth, both of the unbushed lugs developed a secondary crack branch that grew normal to the initial crack direction, toward the tapered free edge of the lug. As Figure 6-45 shows, this "secondary" branch became the primary crack resulting in fracture of Specimen T1-S-4. Figure 6-46(a) shows a close-up of the point where crack branching occurred. A large secondary branch, shown in Figure 6-46(b), also developed in Specimen

Figure 6-45. Crack Profiles for Steel Tapered Lugs
Loaded in the -90 Degree Direction

(a) Front Face of T1-S-4, Showing
Where the Crack Turned
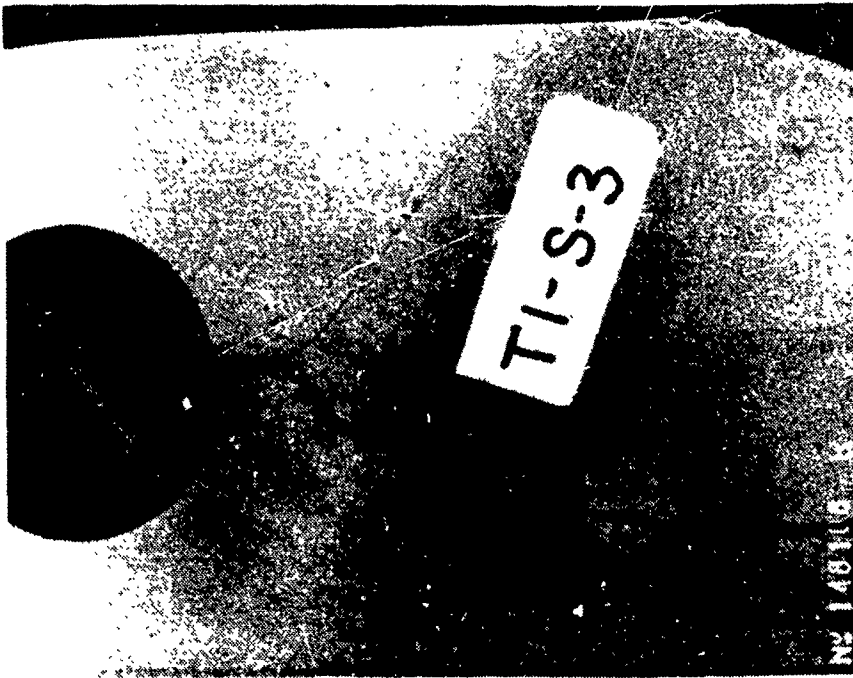
(b) Back Face of Specimen T1-S-3, Showing
a Long Secondary Branch

Figure 6-46. Crack Branching in Unbushed Steel Specimens Loaded at -90 Degrees

T1-S-3, causing the apparent arrest of the back face crack at c_B = 0.22 inch, as plotted in Figure 6-43(a) (The identical phenomenon was discussed in the preceding subsection with regard to Specimen T1-A-5, shown in Figure 6-36).

6.0 CRACK GROWTH IN THICK, STRAIGHT LUGS AND SIMULATED WING-PYLON LUGS

In submatrix (d) of Group II, 12 axially-loaded straight lugs and two complex simulated wing-pylon attack lugs were crack growth tested. The 12 straight lugs were characterized by a high ratio of thickness to pin diameter, which introduced special analysis problems. The two simulated wing-pylon lugs included a number of complexities. The lug shape was non-standard; the stress analysis was dependent on bolt loads, which depended on the stiffness of the support structure; the lug itself was redundant, consisting of 2 angles bolted back-to-back to form a tee; spectrum loadings were applied at an odd angle; and a shrink-fit steel bushing was used. In short, these tests could be viewed as the ultimate attempt to confound the analysis methodology.

6.1 THICK, STRAIGHT ALUMINUM LUGS

Twelve precracked thick, straight aluminum lugs were fatigue crack growth tested in Group II. The lug geometry consisted of a ratio of pin diameter over the thickness of 2/3, and an outer-to-inner radius ratio of 2.0. Three proportional sizes were tested, having pin diameters of 0.625 inch, 1.0 inch, and 1.5 inch. No bushings were used. The loading was axial, and consisted of either the R = 0.1 periodic 30 percent overload sequence or the 80-flight fighter/trainer wing flight-simulation sequence.

Because of the small $(R_o-R_i)/B$ ratio, the corner cracks in these specimens grew across the ligament while the crack depth was still small compared to the lug thickness. Figure 6-47 focuses on the accuracy of the crack growth predictions for the corner cracks. The ordinate is the ratio of the test and predicted loading cycles (or simulated flights) required for the crack surface length c to grow from 0.025 inch to c = R_o-R_i, and the abscissa is R_o-R_i, which indicates the lug size. The test data scatter
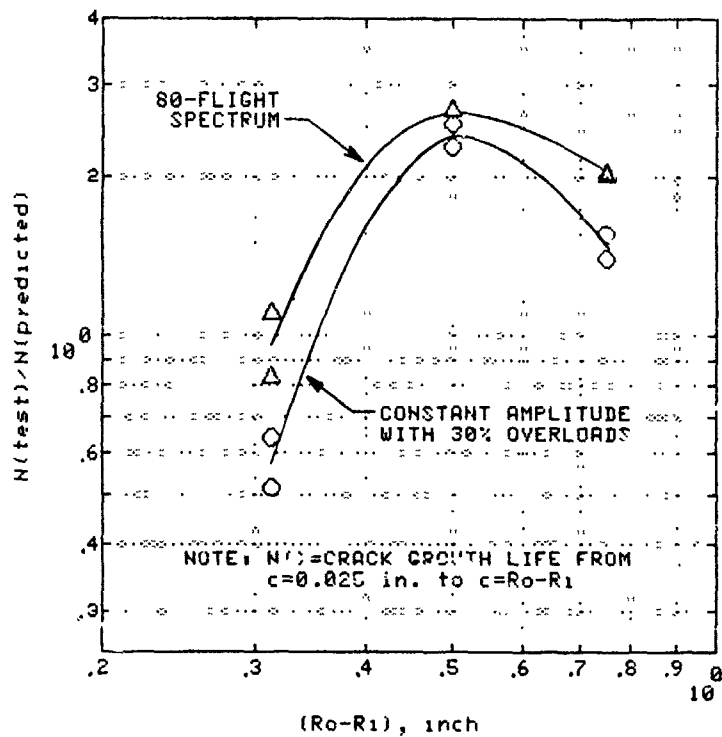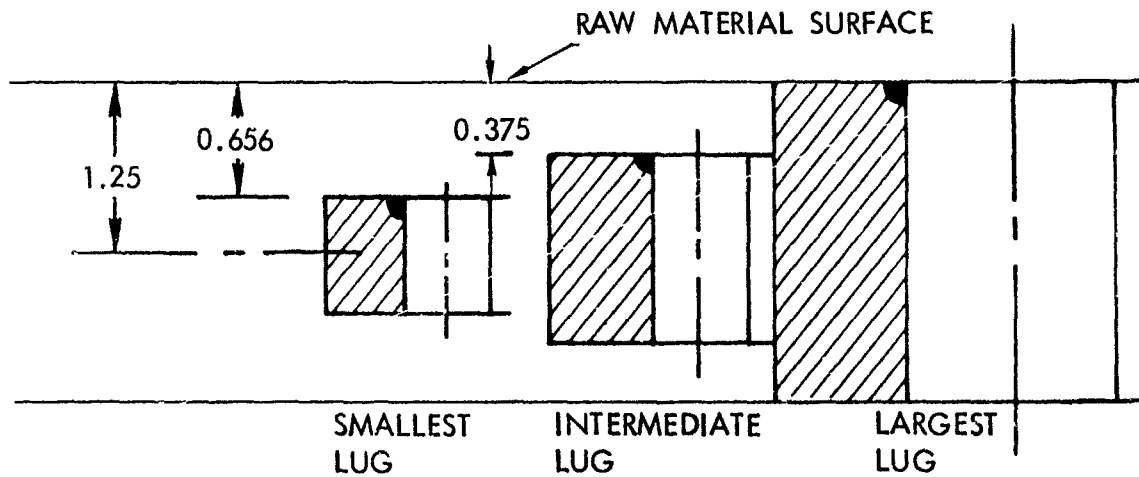
Figure 6-47. Correlation of Test and Predicted Crack Growth Lives
Before Transition for a Corner Crack in Thick Straight Lugs

is low and the trends for the constant amplitude and spectrum loading are similar. However the results vary with lug size, and the variation is not monotonic. The predictions are slightly unconservative for the smallest lug and conservative for the larger two sizes. However, the conservatism is greatest for the intermediate lug size. The dependence of the results on lug size was further investigated and was found that it may have been caused by the manufacturing method of the lugs. All the twelve specimens were fabricated from the same 2.25-inch thick plate. This required machining down equally on both sides of the plate for the smallest and intermediate-sized lugs. Thus the initial crack in the largest lug was at a true surface point of the raw material, but the initial crack in the smallest lug was at a point 0.656 inch below the surface of the raw material as shown in Figure 6-47. Microstructural examination of the 2.25-inch thick plate showed significant difference in the grain sizes through the thickness of the plate, which may result in different crack growth rate properties at the center and surface of the plate. This in turn may have caused the variation (but consistent) of the results with lug size.

The growth of the across-the ligament crack was predicted by extrapolation of the corner crack formulation, and therefore was not expected to be accurate.

Figures 6-48 through 6-50 compare the predictions to the test results for constant amplitude loading with periodic 30 percent overload marking cycles. After the crack length, c, crosses the ligament, $R_o - R_i$, the corner crack undergoes a transition and becomes an across-the-ligament crack, with depth "a" measured along the hole wall and "a_B" measured along the outer surface of the lug. Subsequently, this crack was expected to grow across the lug thickness fairly rapidly, failing the lug. In general, however, such rapid growth did not occur. Examining Figure 6-48(b), for example, the crack dimensions for Specimen S3-A-2 after 27,200 cycles were a = 0.59 inch, a_B = 0.43 inch. Just prior to failure 32,000 cycles later, these dimensions had hardly changed: a = 0.65 inch, a_B = 0.45 inch. Figure 6-51 is a photo showing what was happening during those 32,000 cycles. Instead of going straight across the thickness, the crack rotated and grew toward the rounded top of the lug, then slowed down and stopped.

The turning of the crack toward the top of the lug occurred in most of the thick lug specimens, as seen in Figures 6-52 through 6-54. Figure 6-52 (a) shows that in both Specimens S3-A-1 and -2, the crack turned. Figure 6-52(b) shows that a secondary crack developed in Specimen S3-A-1 at the
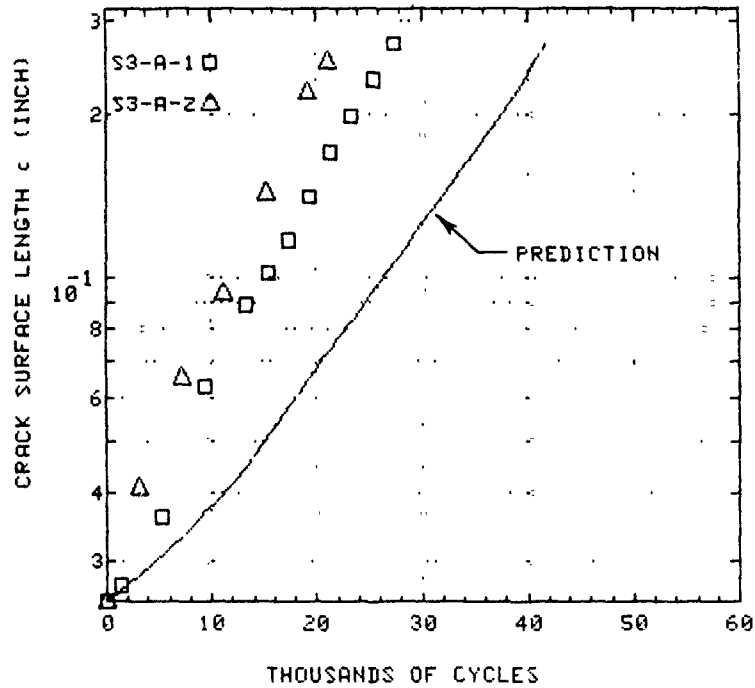
(a) Crack Length on Visible Surface
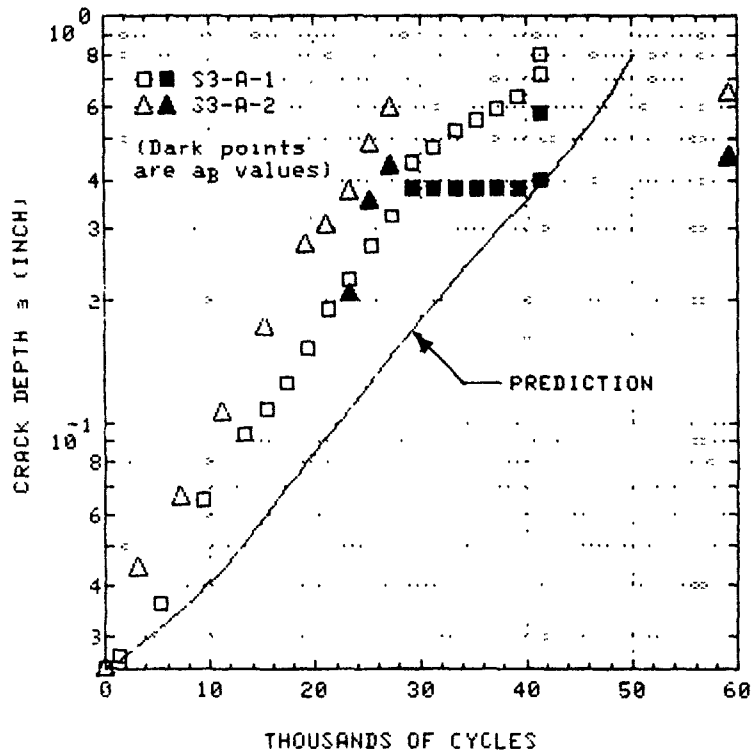
(b) Corner Crack Depth Along Hole Wall

Figure 6-48. Data and Prediction, Straight Thick Aluminum Lugs, $R_i/B = 1/3$, $R_o/R_i = 2.0$, No Bushing, Axial Load, Quasi Constant Amplitude ($R = 0.1$), $R_i = 0.3125$ Inch

300
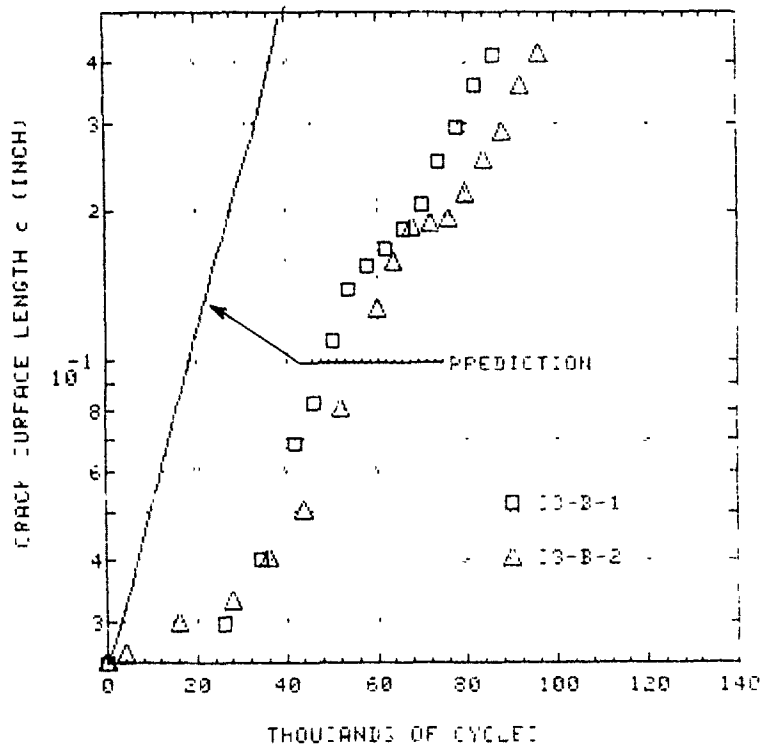
(a) Crack Length on Visible Surface
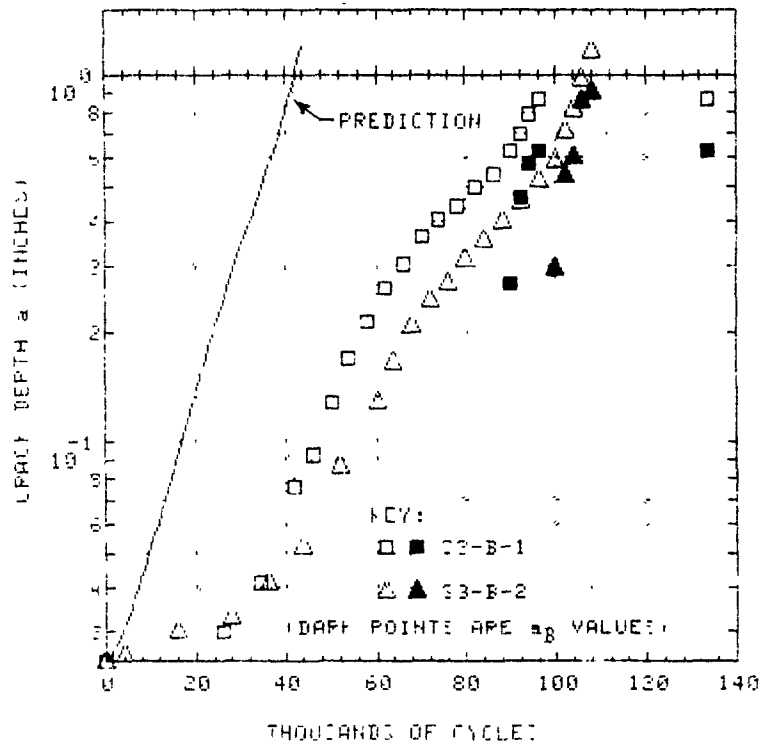
(b) Corner Crack Depth Along Hole Wall

Figure 6-49. Data and Prediction, Straight Thick Aluminum Lugs, $R_i/B = 1/3$, $R_o/R_i = 2.0$, No Bushing, Axial Load, Quasi-Constant Amplitude ($R = 0.1$), $R_i = 0.5$ Inch
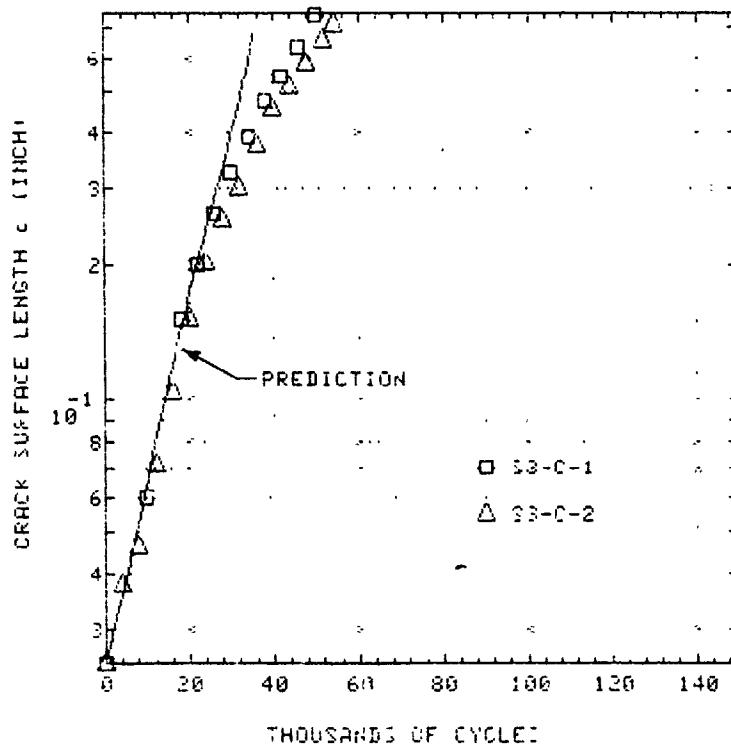
(a) Crack Length on Visible Surface
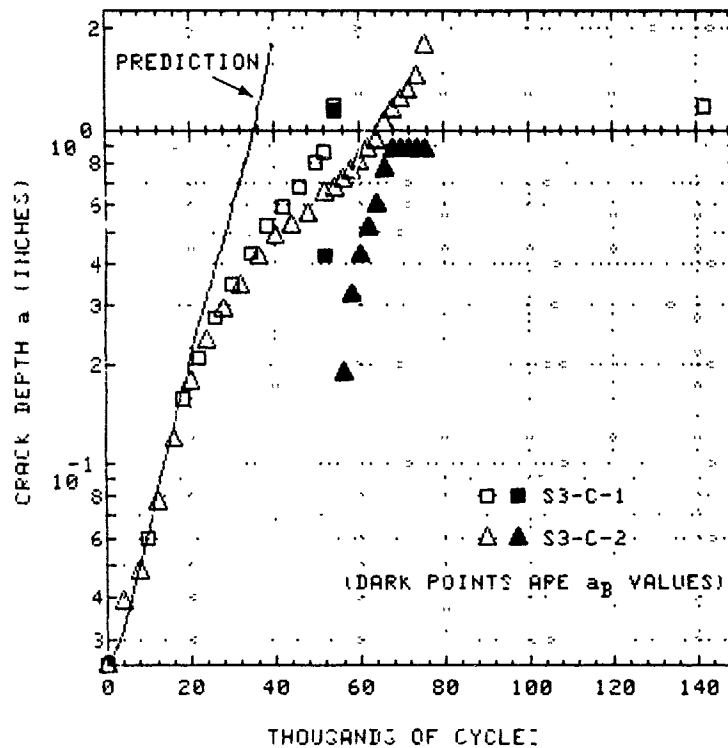
(b) Corner Crack Depth Along Hole Wall

Figure 6-50. Data and Prediction, Straight Thick Aluminum Lugs, $R_i/B = 1/3$, $R_o/R_i = 2.0$, No Bushing, Axial Load, Quasi Constant Amplitude $(R = 0.1)$, $R_i = 0.75$ Inch
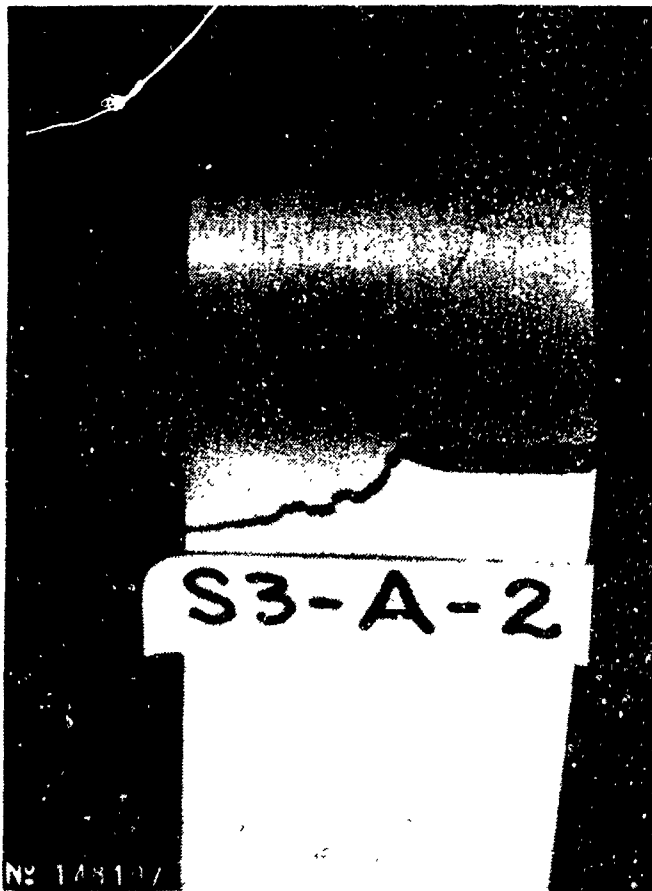
Figure 6-51. Crack Curves Toward Top of Lug and Eventually Stops in Specimen S3-A-2
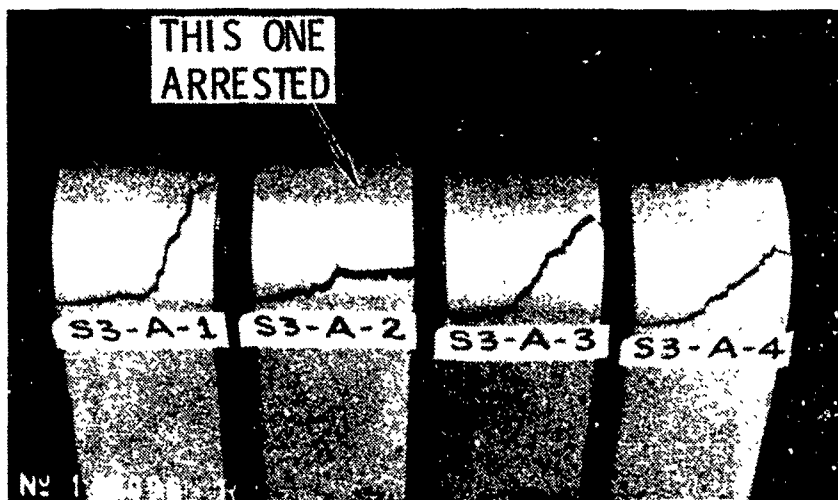
(a)   Curved Crack Paths
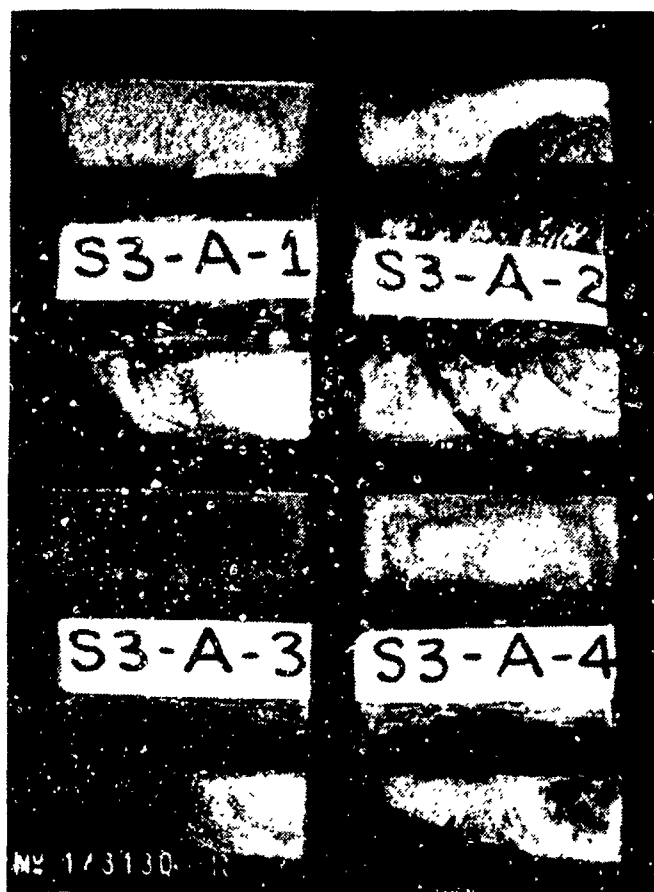
(b)   Fracture Surfaces

Figure 6-52.   Crack Curving and Secondary Cracks in
Specimens S3-A-1 Through -4
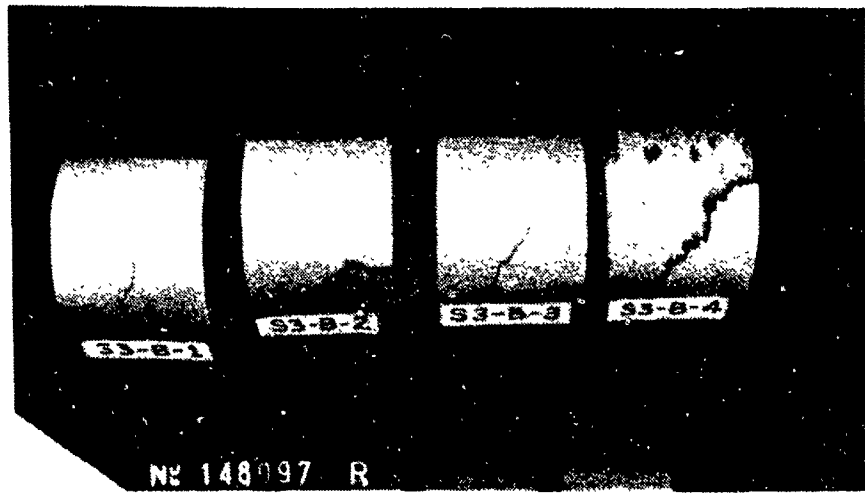
(a) Curved Crack Paths
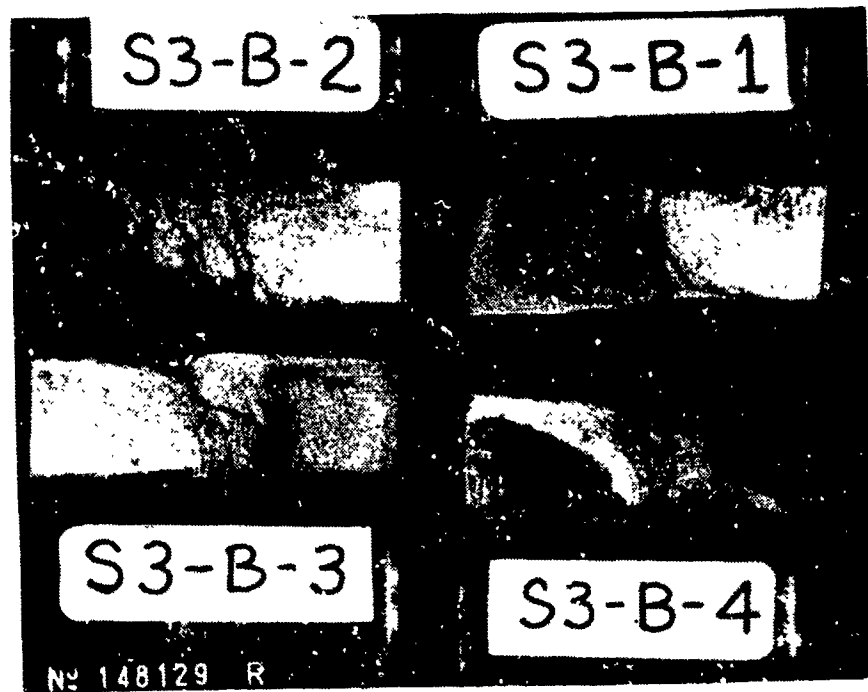
(b) Fracture Surfaces

Figure 6-53. Crack Curving and Secondary Cracks in
Specimens S3-B-1 Through -4
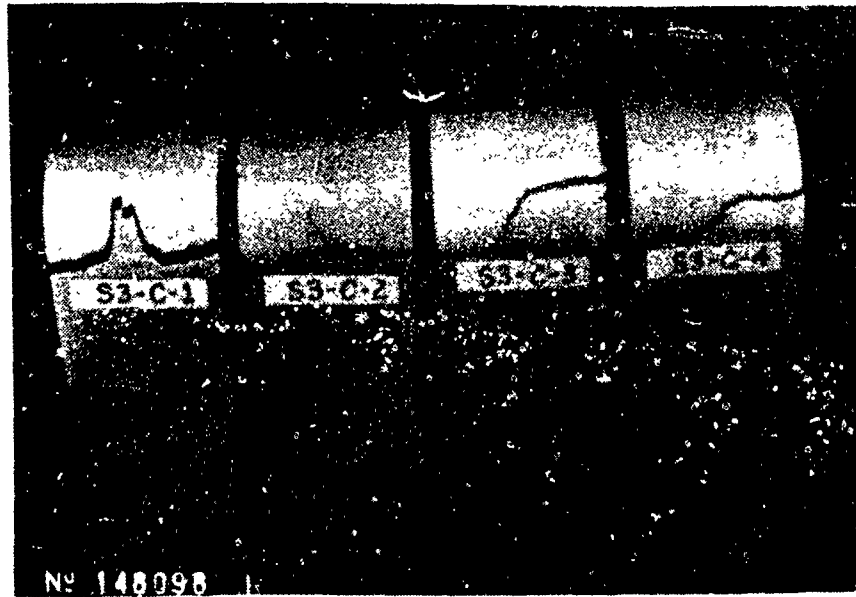
(a) Curved Crack Paths
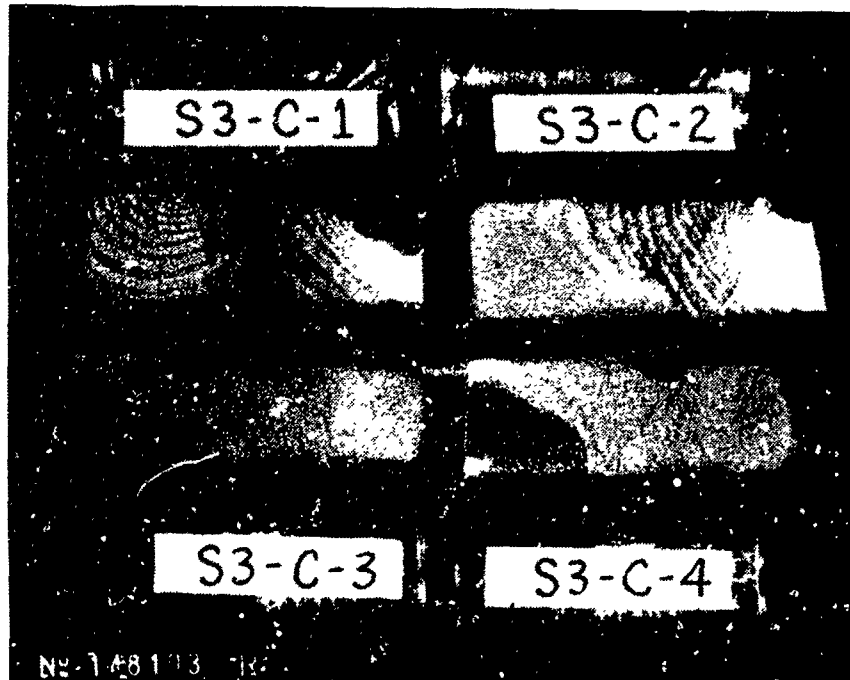
(b) Fracture Surfaces

Figure 6-54. Crack Curving and Secondary Cracks in Specimens S3-C-1 Through -4

midthickness point where the main crack turned. Subsequently both the main (curved) crack and the secondary crack in specimen S3-A-2, seen in Figure 6-52(b), occurred on the opposite side of the hole, weakening the lug for final failure.

Figure 6-53(a) shows that the crack turned and stopped in Specimen S3-B-1, but did not turn in specimen S3-B-2. The crack growth curves (Figure 6-49(b)) show a 37,000-cycle delay in the crack growth across the ligament S3-B-1, but no such delay for Specimen S3-B-2.

Figure 6-54(a) shows that the cracks turned in both Specimens S3-C-1 and -2, but neither progressed very far before crack arrest. The fracture surfaces shown in Figure 6-54(b) indicate evidence that two very different cracking behaviors occur after the crack turned. For Specimen S3-C-1, a secondary surface crack initiated at the hole wall at a location about 70 percent of the way through the thickness. The main crack in Specimen S3-C-2, while turning at the outer surface of the lug, remained straight at the inner surface, and before long, the inner surface growth progressed far enough to precipitate failure. Note in Figure 6-50(b) the large difference in crack growth life between these two specimens. The secondary crack in Specimen S3-C-1 required 88,000 additional cycles to initiate and grow to failure after the complete turning had arrested the main crack. In contrast, the incomplete turning of the main crack in Specimen S3-C-2 permitted failure to occur within 10,000 additional cycles.

The other six thick lug specimens were subjected to flight-simulation spectrum loading using the 80-flight fighter/trainer wing lower surface spectrum. Figures 6-55 through 6-57 show the comparisons of crack growth test results and predictions using the Hsu Retardation Model. The accuracy of the Hsu Model for this spectrum and material was verified by comparison with compact tension crack growth data, as discussed earlier.

Figures 6-55 through 6-57 show that for spectrum loading the cracks barely grew across the ligament before the lug failed. This difference from the quasi-constant amplitude results is not surprising, because the maximum spectrum load was 32 percent higher than the maximum of the overload in the quasi-constant amplitude tests. Note in Figures 6-52 through 6-54 that the crack turned during static failure but did not arrest. The exception is Specimen S3-B-3, wherein the crack progressed far
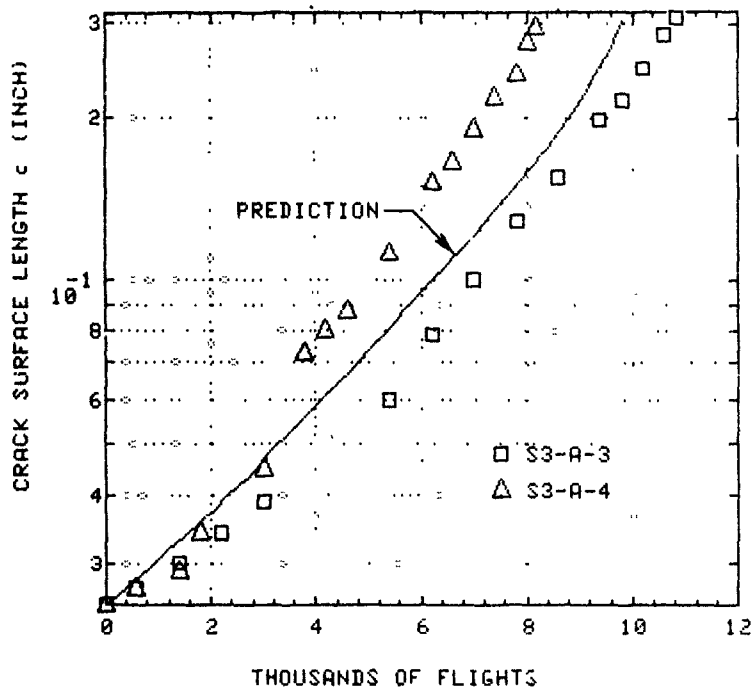
(a) Crack Length on Visible Surface
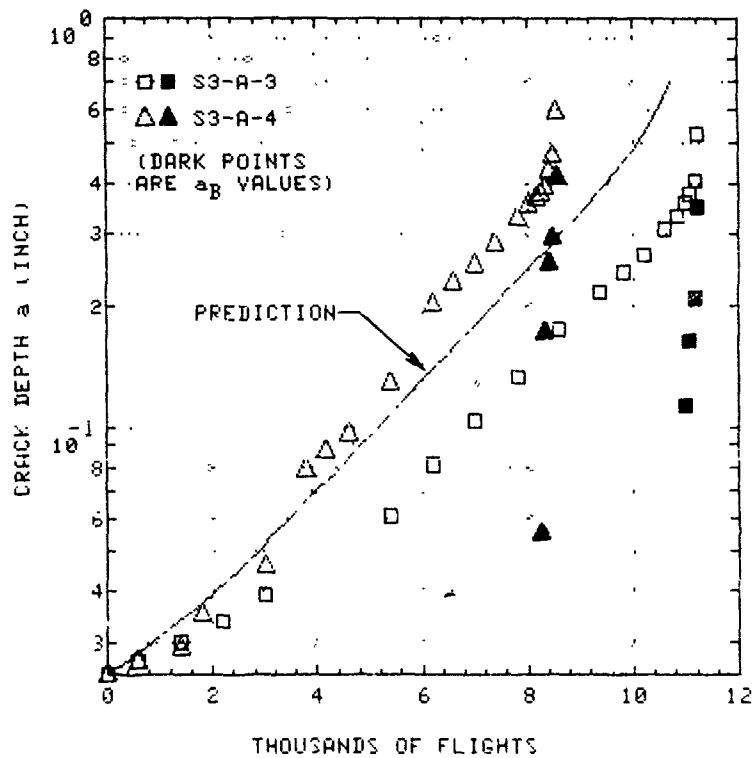
(b) Corner Crack Depth Along Hole Wall

Figure 6-55. Data and Prediction, Straight Thick Aluminum Lugs, $R_i/B = 1/3$, $R_o/R_i = 2.0$, No Bushing, Axial Load, 80-Flt. Spectrum Loading, $R_i = 0.3125$ Inch
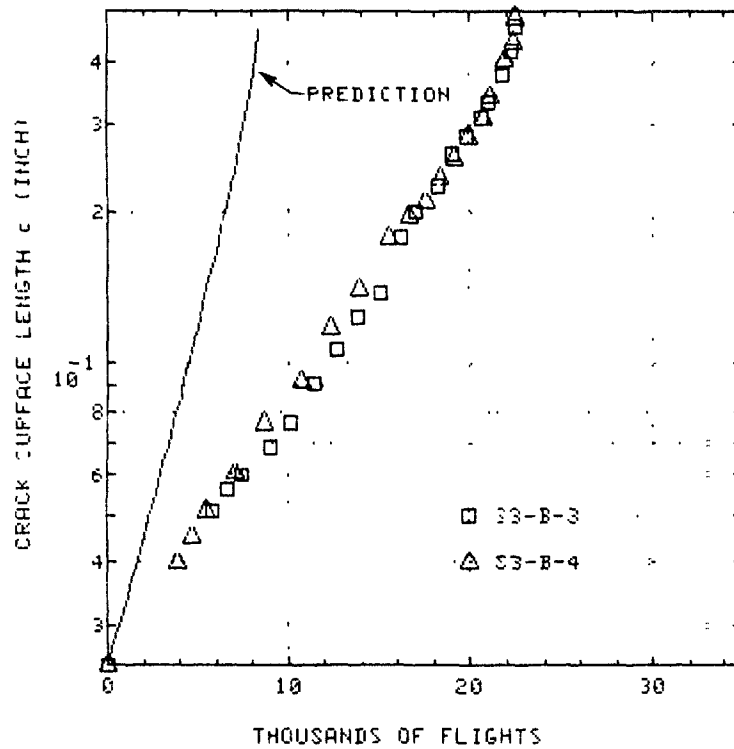
(a) Crack Length on Visible Surface
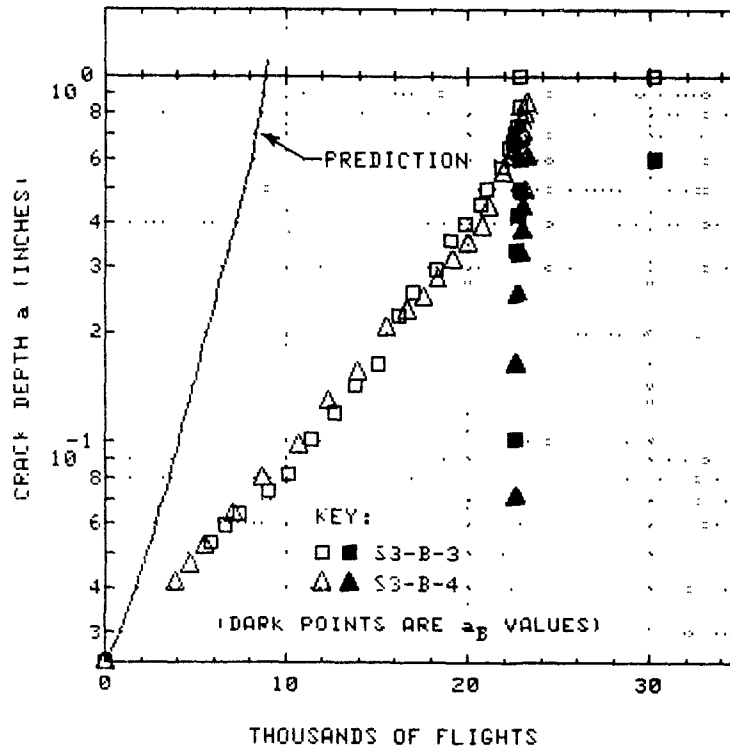
(b) Corner Crack Depth Along Hole Wall

Figure 6-56. Data and Prediction, Straight Thick Aluminum Lugs, $R_i/B = 1/3$, $R_o/R_i = 2.0$, No Bushing, Axial Load, 80-Flt. Spectrum Loading, $R_i = 0.5$ Inch

309
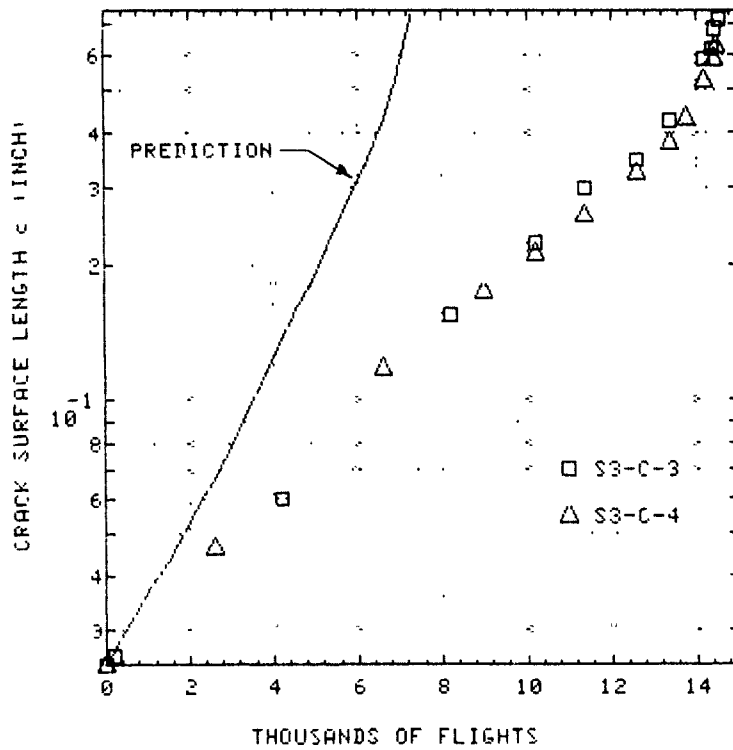
(a) Crack Length on Visible Surface
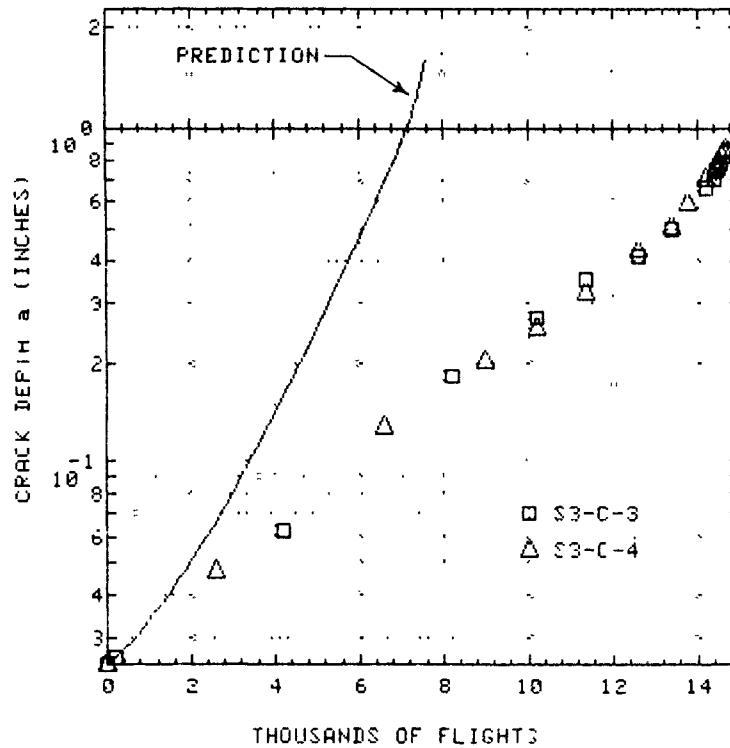
(b) Corner Crack Depth Along Hole Wall

Figure 6-57. Data and Prediction, Straight Thick Aluminum Lugs, $R_i/B = 1/3$, $R_o/R_i = 2.0$, No Bushing, Axial Load, 80-Flt. Spectrum Loading, $R_i = 0.75$ Inch

enough in fatigue to turn and arrest. As Figure 6-56(b) shows, a delay of 7400 simulated flights occurred in this specimen just prior to failure. Nonetheless, the conclusion drawn is that, at the higher stress level, the across-the ligament crack usually will not grow in fatigue long enough to turn, and if it does not turn during fatigue loading, it will not arrest nor extend the life.

6.2 SIMULATED WING-PYLON LUGS

The test setup and testing procedure for the simulated wing-pylon lug was described in Section III. The first of the two such lugs tested is shown in Figure 6-58(a) after removal from test. In the photo it is still bolted to the mounting plate, which simulated the wing skin. Figure 6-58(b) shows a close-up of the bushed loading hole and the final crack. (Failure occurred due to excessive deformation caused by crack opening). The load was applied at 23-degree angle to the plane of the mounting plate, or approximately the 10 o'clock direction in Figure 6-58(b). Note in Figure 6-58(a) that the lug is a redundant design, consisting of two aluminum angles bolted together to form a tee. The initial corner crack was in the "R" piece only, located at the 1 o'clock position in Figure 6-58(b) at the visible edge of the hole.

As discussed in Section IV, finite element modeling of this lug was done two different ways. First, intimate contact was assumed to be maintained between the shrink-fit steel bushing and the aluminum lug. Secondly, a double contact problem was used, solving both the lug-bushing and bushing-pin interfaces as iterative contact problems, and thereby accounting for lug-bushing separation. Two predictions were then made of the growth of the initial crack across the first ligament, in just the one piece. The Hsu Retardation Model was used, since the 60-flight spectrum loading history was applied in the test.

The predictions and test results for the growth of the corner crack to the top edge of the lug are compared in Figure 6-59. As was the case in all the other Group II aluminum lugs with steel bushings, the "intimate contact" prediction was grossly unconservative.
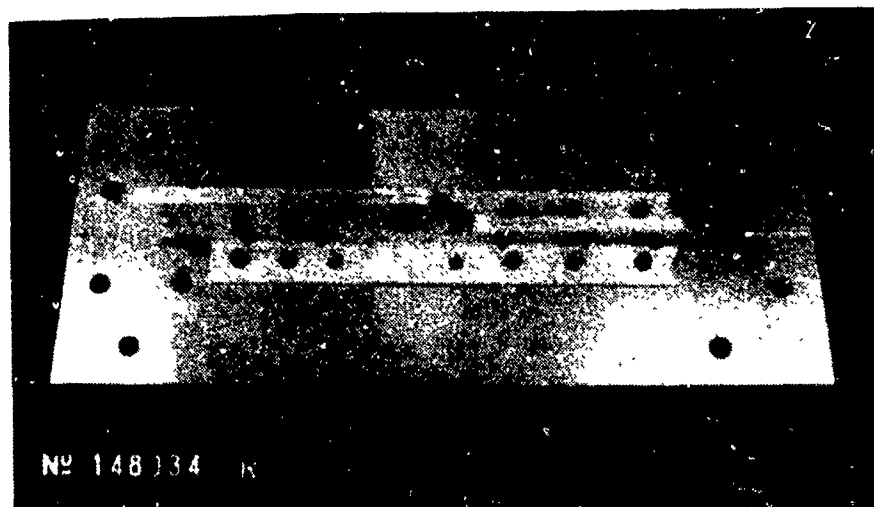
(a) Specimen on Mounting Plate
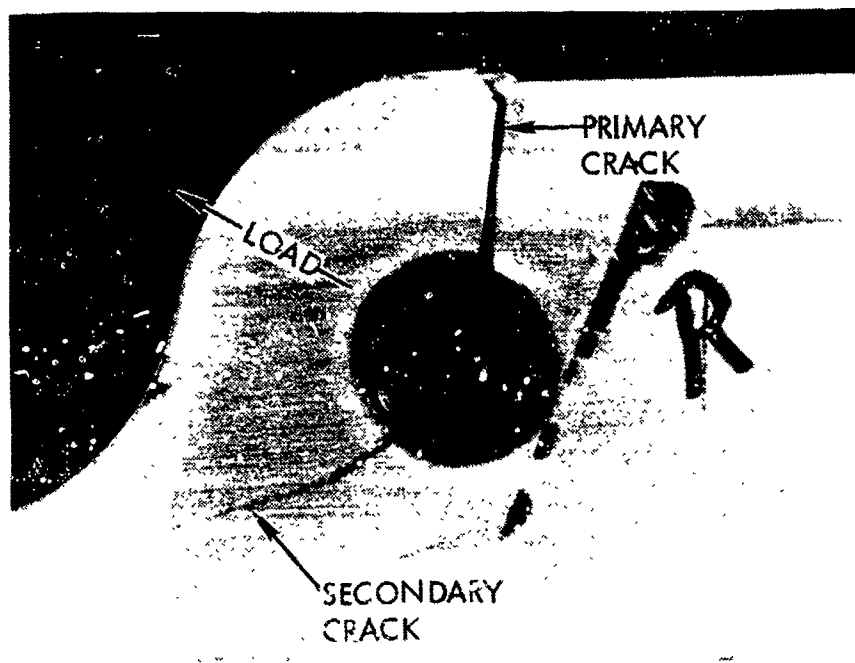
(b) View Showing Primary and Secondary Cracks

Figure 6-58. Simulated Wing/Pylon Lug R2-E-1
After Fatigue Testing

312
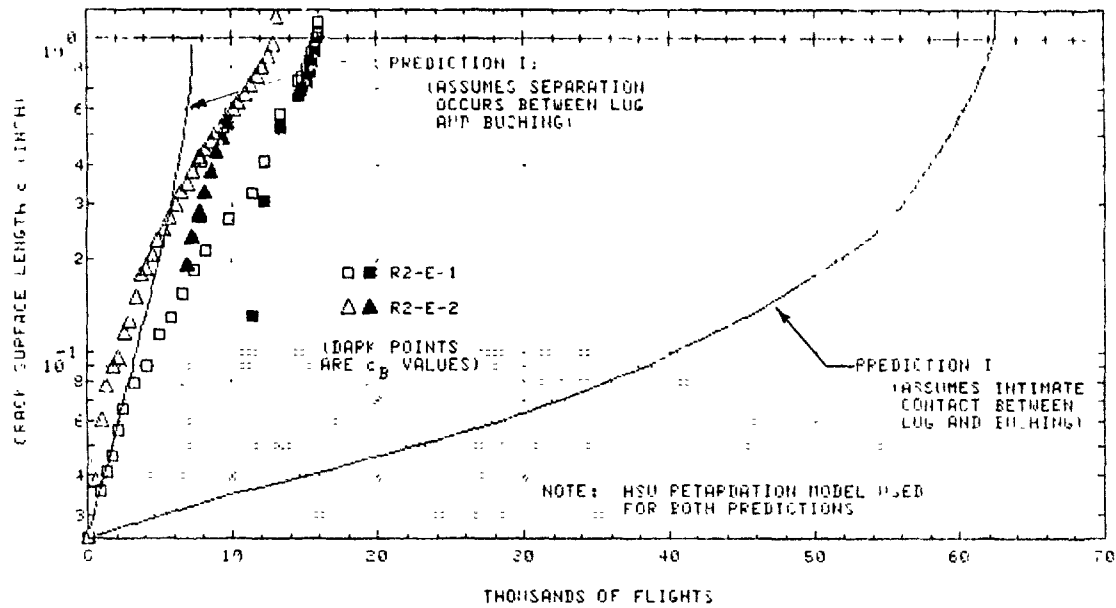
Figure 6-59. Comparisons of Predictions Assuming Intimate Contact of Lug and Bushing and Assuming Separation, and the Test Data for Simulated Wing-Pylon Lugs

313

In Figure 6-60 a detailed comparison can be made between the test data and the predictions assuming lug/bushing separation. Predictions by both the Hsu and the Generalized Willenborg Retardation Models are shown. The predictions tend to be accurate for small cracks, but as the crack becomes longer, the rate predictions become quite conservative.

Complete history of the simulated wing-pylon lug tests is shown in figure 6-61, since Figure 6-60 does not show all the crack growth data for these simulated wing-pylon lugs. These redundant lugs did not fail when the crack had traversed across the top ligament of the precracked half. On the contrary, the number of simulated flights until failure of the first ligament was significantly less than half of the total flights to failure in both lug tests. The fracture surfaces of the two specimens are shown in Figures 6-62 and 6-63. These figures describe an annotated record of the failure sequence, showing the initial crack location (I.C.), and sequence of events (failure or crack initiation) with encircled numbers along with corresponding flight numbers or locations of crack fronts.

As Figure 6-62 shows, the first ligament of the precracked piece in Specimen R2-E-1 failed after 15,960 simulated flights. Fatigue testing was continued, and at the end of 33,760 simulated flights, no further cracking had occurred. The loads were uniformly increased by 16 percent and testing was continued. At 34,470 and 34,870 flights, cracks of approximately .05 inch were present in the initially uncracked angle adjacent to the precrack (lower right in Figure 6-62), and in the precracked angle diametrically opposite the initial crack (upper left in Figure 6-62), respectively. At 36,695 flights the test ended with both of the top ligaments broken and a lower crack of more than 2 inches in both members.

Similarly, as shown in Figure 6-63, the first ligament of the precracked angle in Specimen R2-E-2 failed after 12,959 simulated flights. No further cracking occurred until 28,760 flights, when a .088 inch quarter-circular corner crack appeared in the initially-cracked angle diametrically opposite from the main crack (upper left in Figure 6-63). At 31,640 flights this crack was 1.36 inches long, and its growth rate was beginning to slow down, when a 0.035-inch crack appeared in the other angle adjacent to the growing secondary crack (lower left, Figure 6-63). At 32,840 flights, a quarter-circular corner crack occurred at the hole, in
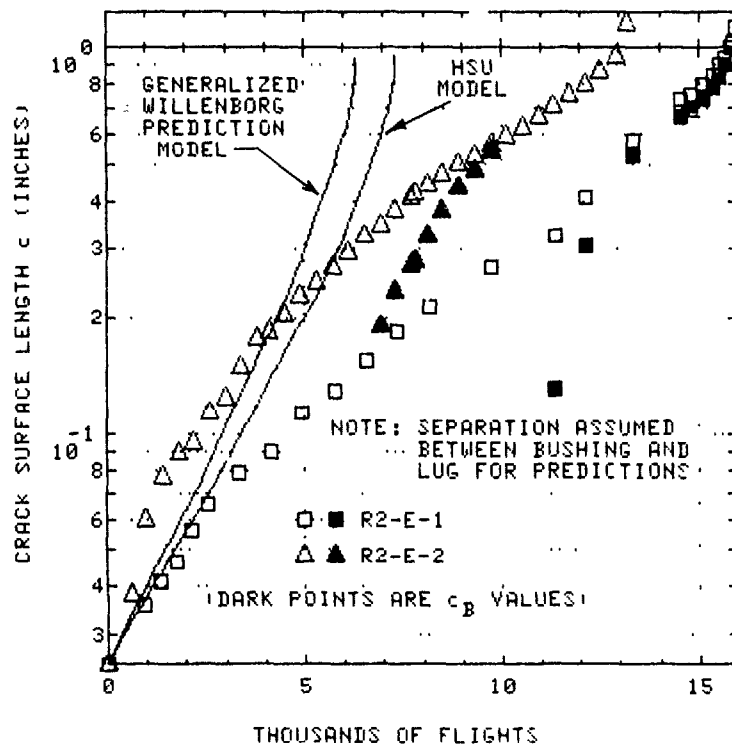
(a) Crack Length on Visible Surface
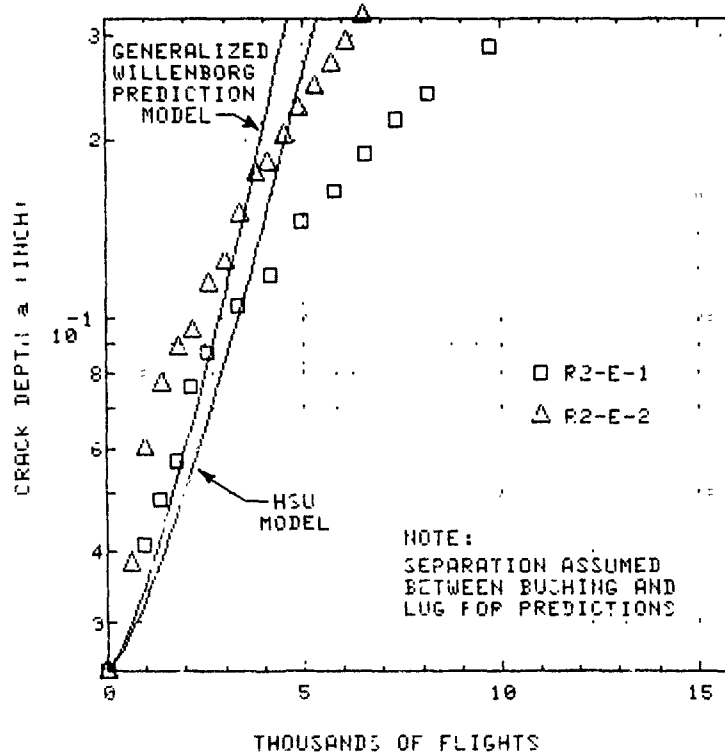
(b) Corner Crack Depth Along Hole Wall

Figure 6-60. Data and Prediction, Simulated Wing-Pylon Lug. (Predictions
Model the Separation at the Lug-Bushing Interface During
Loading.)

315
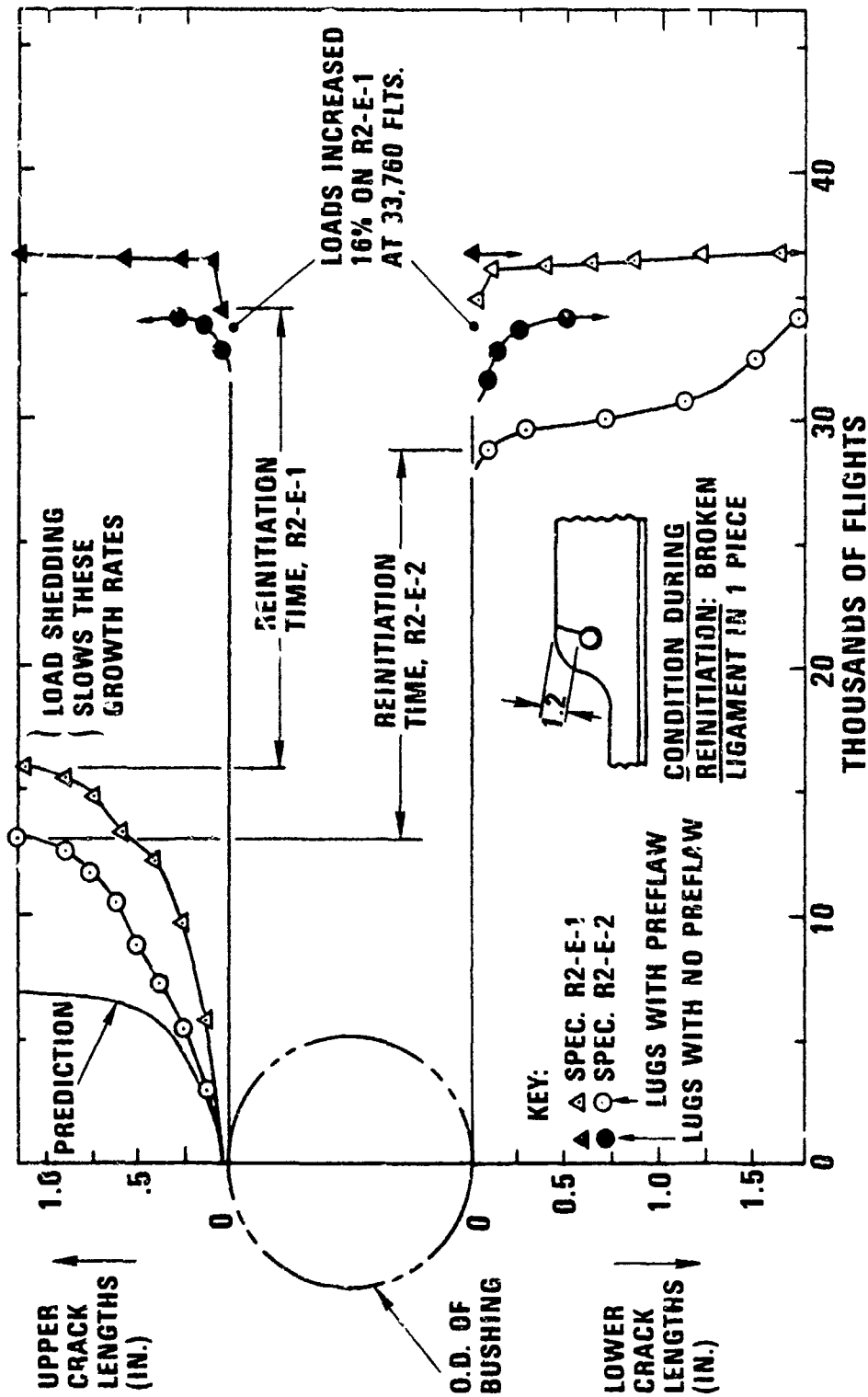
Figure 6-6. Crack Growth in Simulated Wing-Pylon Specimens R2-E-1 and R2-E-2
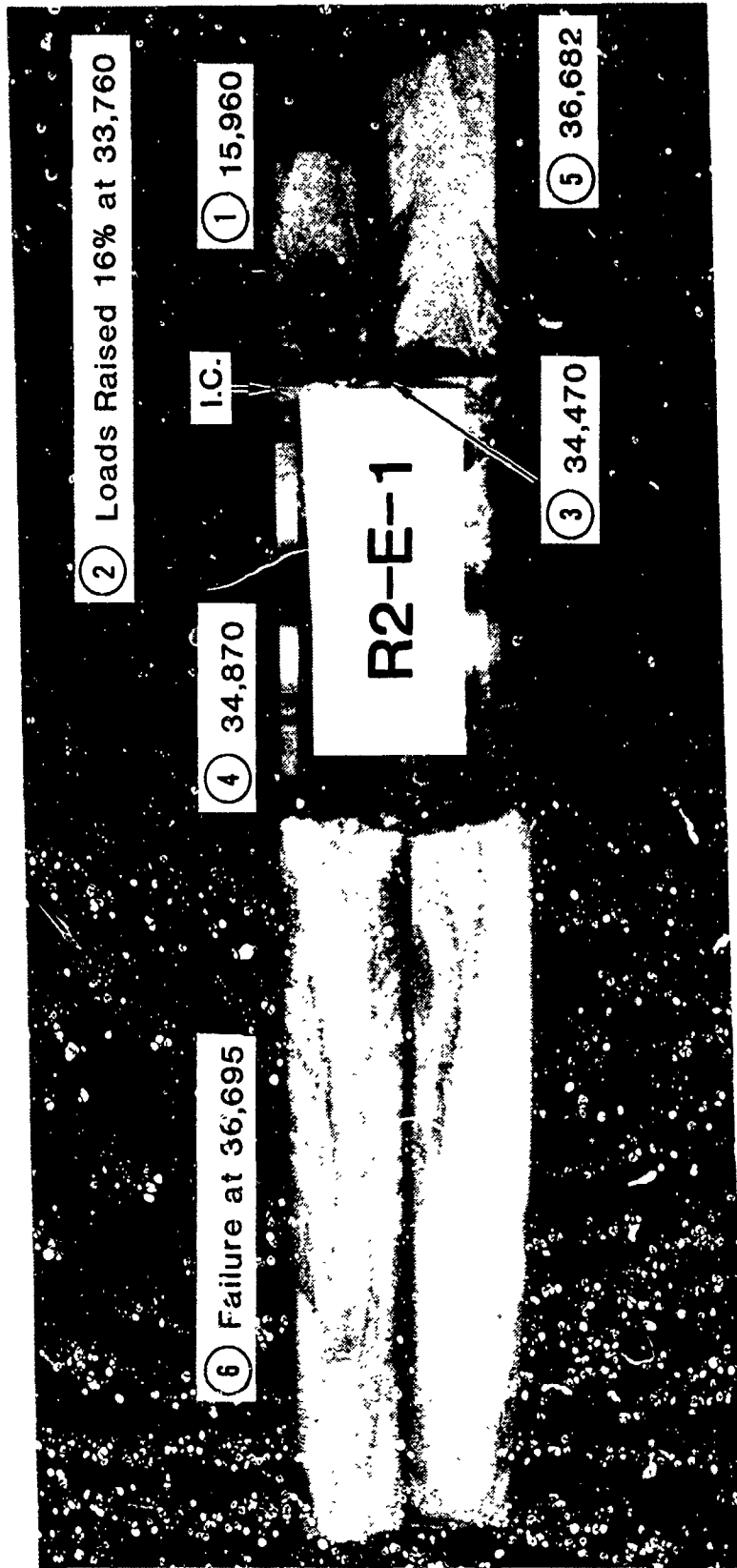
Figure 6-62. Fracture Surface of Simulated Wing-Pylon Lug, Specimen R2-E-1
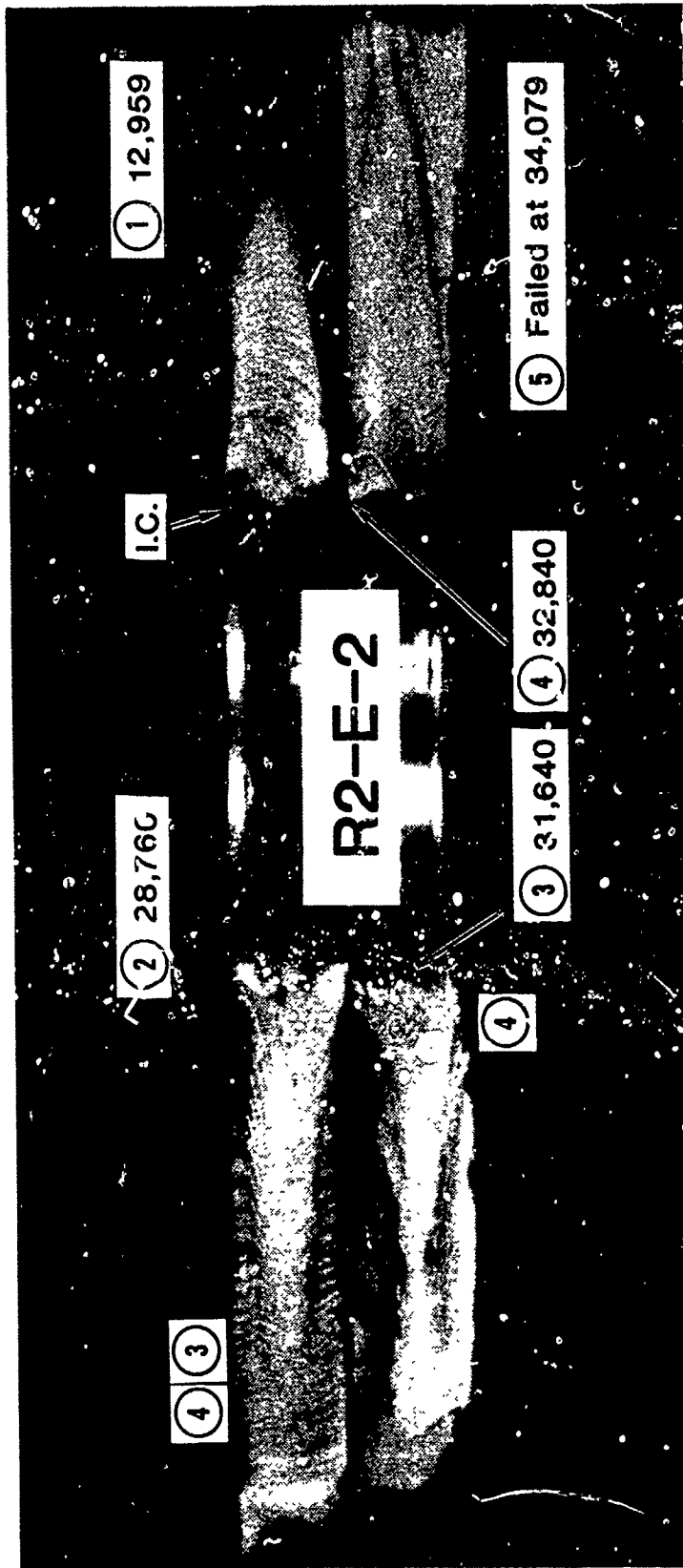
Figure 6-63. Fracture Surface of Simulated Wing-Pylon Lug Specimen R2-E-2

the top ligament of the initially-undamaged angle (lower right, Figure 6-63). At that time the other two cracks were 1.565 in. and 0.141 in. long, respectively. Failure of the lug occurred at 34,079 flights.

Two benefits of redundant lug design were pointed out in Reference [13]:

o The initial crack grows more slowly, due to load shedding to the uncracked adjacent member.

o After the first crack breaks through to the edge, there can be a very long delay time before initiation of the next crack. During this entire time, the crack is fairly evident for visual inspection.

These tests of the simulated wing-pylon lugs bear out both of these advantages. The conservatism in the prediction shown in Figure 6-60 for the cracks above 0.2 inch probably reflects the benefits of load-shedding. Even more dramatically, the 16,000 to 19,000-flight delay periods between the fracture of the first ligament and the initiation of a secondary crack would in service provide a very inspectable damage for a very lengthy time interval, greatly enhancing safety. Presumably, this is descriptive of the characteristics of the C-5 wing-pylon lugs, used as a basis for this specimen geometry.

7.0 SUMMARY OF ACCURACY OF LIFE PREDICTIONS

A variety of lug geometries and test conditions were covered in Group II testing. Before each test the analysis methods of [2] were utilized to obtain crack growth predictions. By comparing the predicted and actual crack growth lives for all Group II tests, it is possible to concisely evaluate the prediction methodology.

The experimental crack growth lives for an initial crack size of 0.025 inch are compared to the corresponding predictions in Figure 6-64. The ordinate is a logarithmic scale showing the ratio of test life to predicted life. Thus for conservative predictions this ratio is above 1.0, and for unconservative predictions the ratio is below 1.0. The different types of points indicate the different types of tests. The asterisks (*) indicate
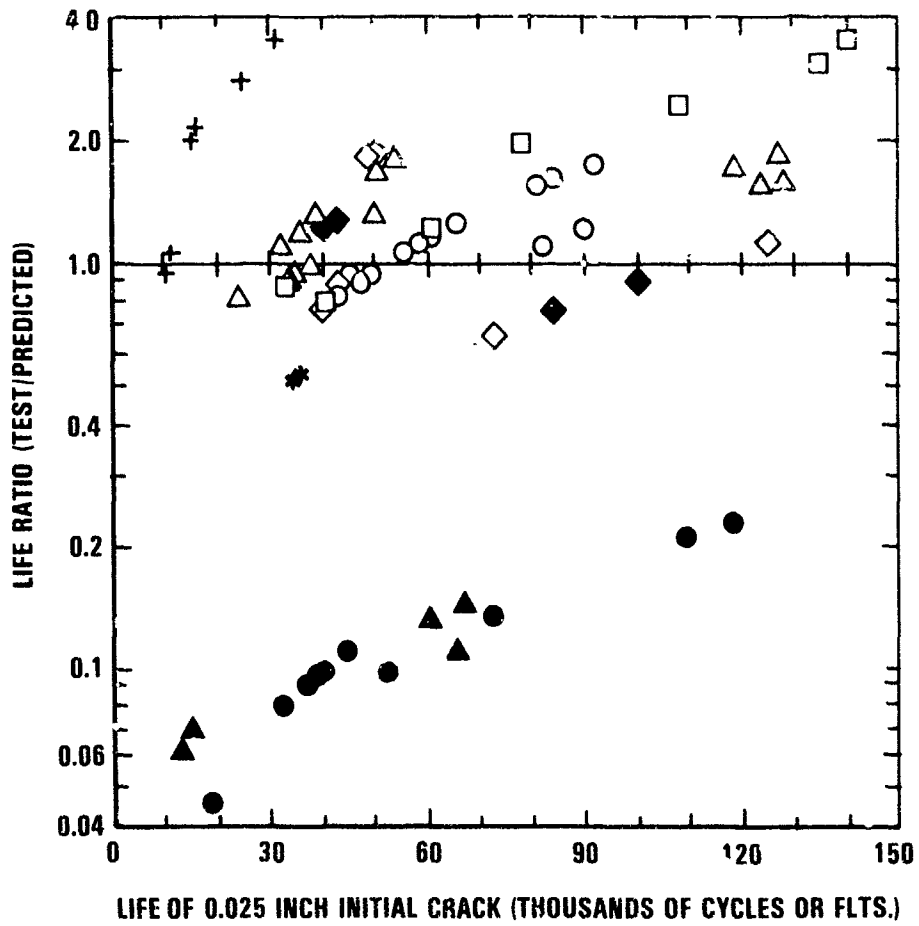
Figure 6-64.   Accuracy of Prediction of Total Crack
Growth Life for Group II Tests

the two redundant wing-pylon lugs. The other symbols in Figure 6-64 have the following meanings:

o Plus (+) points are spectrum tests; all others are constant amplitude (with 30% overloads for marking the fracture surface).

o Dark points are lugs with shrink-fit steel bushings; all others have no bushings.

o Diamonds ($\diamondsuit$, $\blacklozenge$) are steel lugs; all others are aluminum.

o Diamonds and triangles ($\diamondsuit$, Δ) indicate off-axis loading; all others are axially-loaded.

o Squares and pluses ($\square$, +) have $R_o/R_i = 2.0$ and $B/2R_i = 1.50$; all others have $R_o/R_i = 2.25$ and $B/2R_i = 0.5$ or 1.0.

The first observation from Figure 6-64 is that the predictions for aluminum lugs with shrink-fit bushings were consistently unconservative, because the prediction method used did not take into account the increased stresses resulting from separation between the bushing and lug. The predictions overestimated the life by factors of 4.4 to 22 for all aluminum lugs with bushings, except the two redundant wing-pylon lugs. For those two lugs the total error was smaller, because of the compensating effect of failing to include in the analysis the benefits of redundancy.

The second observation from Figure 6-64 is that the eight most conservative predictions are for eight of the twelve very thick ($B/2R_i = 1.50$) specimens. A contributing factor to this error was the unanticipated tendency of the crack, after becoming an across-the-ligament crack, to grow toward the top of the lug and then stop.

Figure 6-65 incorporates revised predictions for the 22 aluminum lugs with bushings to account for lug-bushing separation, using the method recommended in Section IV. Additional analysis, not discussed above, was required to obtain these revised predictions for the tapered lugs and the simulated wing-pylon lug. For the tapered lugs, the Green's function calculation method could not be used to model bushing-lug separation until appropriate stress distributions were estimated along the line of cracking. Stress distributions were estimated for an R_o/R_i ratio of 1.894 by interpolation of the results given in Reference 2. For the simulated
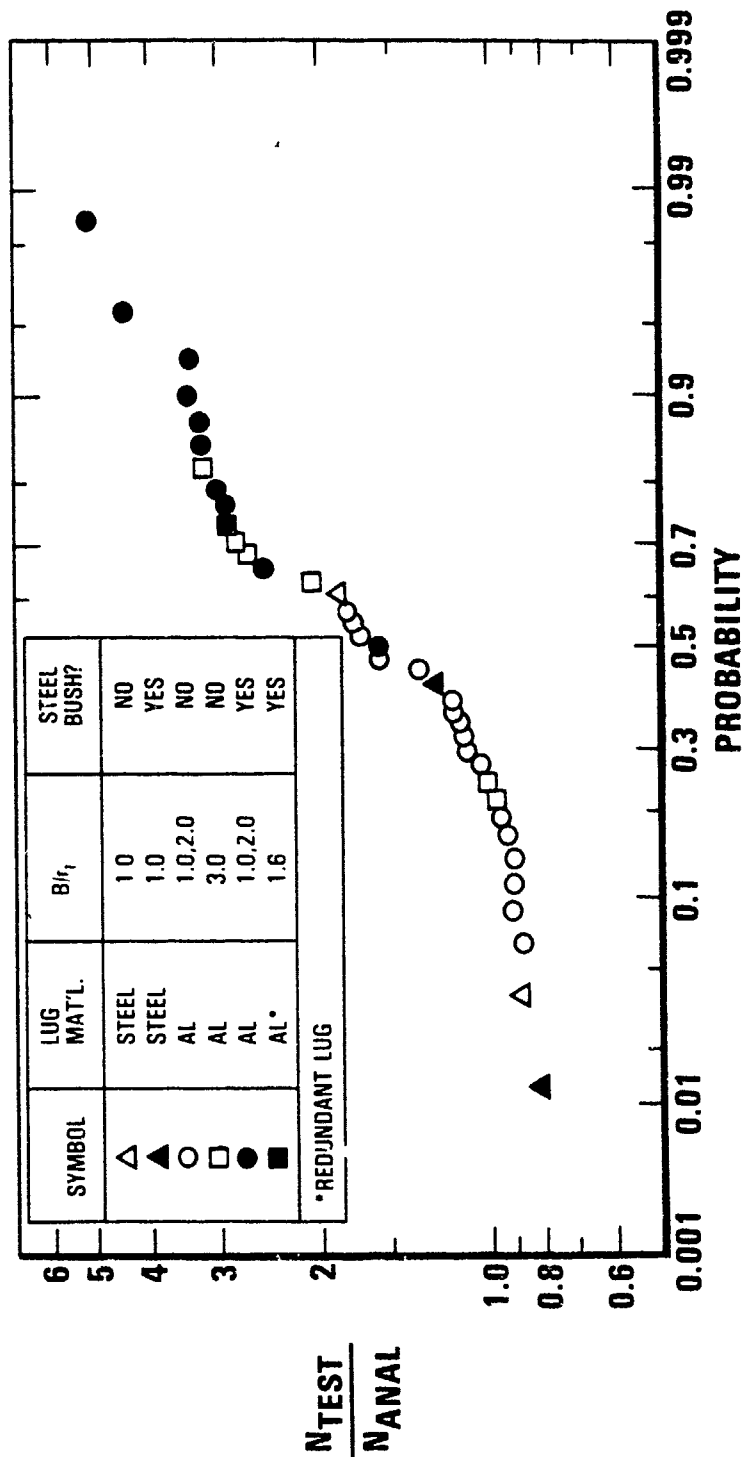
Figure 6-65. Accuracy of Crack Growth Life Predictions for Group II Tests (Considering Pin-Bushing Separation in Bushed Lugs)

wing-pylon lug, a simple fatigue analysis was employed to predict a delay period of 5670 flights, which was added to crack growth Prediction II shown in Figure 6-59 to provide an estimate of total life for Figure 6-65.

By accounting for separation of the bushing and lug in the Group II specimens with bushings, accurate or conservative analysis results are obtained for all 76 Group II crack propagation test cases, as shown in Figure 6-65.

SECTION VII

SUMMARY AND CONCLUSIONS

1.0 CONCLUSIONS FROM GROUP I TESTING

All the aluminum lugs with no preflaws subjected to fatigue crack initiation tests had both primary and secondary flaws and failures. For steel lug crack initiaton tests, some specimens did not have any secondary origins. The fatigue threshold of steel lugs was above 14 ksi, and thus the stress levels were increased to conduct the crack initiation tests.

In residual strength tests, failures of all the corner crack and some through-the-thickness crack specimens were due to net section yielding rather than the exceedance of the critical stress intensity values.

Final failure of lugs following fatigue crack growth testing also tended to be by a net section yielding phenomenon rather than by exceedance of a critical stress intensity factor value for most of the specimens. The exceptions are the specimens loaded such that the peak stress at the lug hole was above the yield strength of the material.

For through-the-thickness cracks, the 2-D finite element method and Green's function method are found to be reliable and versatile. The compounding method also performed excellently, especially in the context of the simplicity of the method. The compounding method predicted conservative lives for $R_o/R_i = 1.5$ and unconservative lives for $R_o/R_i = 2.25$ and 3.0 when compared with the Green's function method. Efforts to improve the compounding method were unsuccessful. However, one can use the compounding method with reasonable confidence to predict life, at least as a first approximation when no other solutions are available. This program recommends, however, the use of the Green's function method for more accurate predictions of crack growth behavior and life.

For corner crack problems, the 2-parameter corner crack correction factors modifying the through-the-thickness crack solution are found to make excellent predictions for the crack growth behavior and life. The predictions of crack aspect ratio, a/c, can be considered only satisfactory. The actual a/c ratios were slightly higher than predicted.

The one-parameter corner crack approach also yielded reasonable crack growth and life predictions, but is also only approximate since the experimental aspect ratios were not constant as is assumed in the one-parameter approach.

The experimental data scatter in the aluminum lugs at both stress levels, 6 and 15 ksi, is very minimal for R_o/R_i ratios of 2.25 and 3.0, but is larger for the R_o/R_i ratio of 1.5. The authors believe that this may be due to the fact that these smaller lugs have high stress concentrations, which may make them very sensitive to parametric variations, for example the loading pin-lug clearance.

The authors also believe that the pin-to-lug rigidity ratio, E_{pin}/E_{lug}, and large deformation of the lug due to pin loading may have influenced the crack growth behavior and life. However, such effects were predominant only in small lugs with $R_o/R_i = 1.5$ and diminished as the R_o/R_i ratio was increased.

Failure of corner crack specimens was predicted prior to transition for $R_o/R_i = 1.5$, but transitional and subsequent through-the-thickness crack growth behaviors were predicted for $R_o/R_i = 2.25$ and 3.0. In almost all cases this agreed with the experimental results.

In the cases of lug specimens subjected to load levels that induced peak local stresses above the yield strength of the material, there were many difficulties in conducting these tests including premature failure and the presence of a large number of natural cracks. The analysis procedure developed using the Green's function and the elasto-plastic stress distribuiton was also found to be inaccurate. For example, the analysis predicted increasing life as R_o/R_i increases, whereas the experimental data for initial through-the-thickness cracks (but not for initial corner cracks) show the opposite trend of increasing life as R_o/R_i decreases. The correlation could have been improved further by the use of cyclic stress-strain data instead of the monotonic stress-strain data used in the analysis. Even such an improvement may not have been sufficient to explain the above phenomenon and one may have to resort to the use of special plastic crack tip elements embedding the HRR (Hutchinson-Rice-Rosengren) type singularity.

In all the spectrum loading cases, the Hsu and the Generalized Willenborg retardation models predicted nearly identical crack growth behavior and lives. These models predicted solutions which were in excellent agreement with experimental data for most of the cases. The solutions were unconservative only for steel specimens subjected to fighter spectrum loading and no reasonable explanation could be found for this discrepancy. The Willenborg model results were unconservative by a factor of about 2 to 5 when compared with the Hsu or the Generalized Willenborg model. The no-retardation model predicted lives which were about half of the lives predicted by the Hsu or the Generalized Willenborg model.

The bushing installation procedure introduced some blunting of the crack tip due to the high interference levels. This in turn sometimes retarded the initial crack growth and resulted in conservative life predictions.

Extensive experimentation was made to select block and flight-by-flight spectra which would introduce markings on the fracture surface so that the corner crack aspect ratio could be monitored. Such efforts were unsuccessful due to the constraints imposed by the present program. However, maximum information was extracted from these tests by monitoring the back surface crack lengths after the crack had broken through the thickness.

Of the total of 160 Group I crack growth tests, the test-to-analytical life ratio of 126 tests fall within the band of 0.5 and 2.0. Giving allowance for some of the analytical and/or experimental difficulties cited above, a very satisfactory performance of all the analytical methods developed in this program is indicated by this correlation.

2.0 SUMMARY OF NEW ANALYSIS METHODS

Two method improvements were attempted after completing [2]. The first was the incorporation of net section yielding as an alternative failure criterion for a lug; equations for critical crack size based on net section yielding have been given for the example configurations shown in Figure 4-1. The second was an unsuccessful attempt to improve the compounding method solution presented in [2].

New finite element solutions were obtained for tapered lugs with steel bushings and the simulated wing-pylon attach lug. The "unflawed stress distribution" results for tapered lugs are given in Tables 4-1 and 4-2, and for the wing-pylon lug in Figure 4-5.

A new analytical method was developed to account for separation between a lug and bushing during loading. First, the finite element model for the wing-pylon lug was revised to model lug-bushing separation with an unknown region of radial contact. Figure 4-7 shows the increase in stresses at a given load, compared to assuming intimate contact between the bushing and lug. Used with the Green's function, these increased stresses result in increased values of stress intensity factor, correcting a source of unconservatism in the former analysis method. Secondly, the approximate method was proposed to estimate the stresses by assuming that the bushing and pin act together as a larger pin.

3.0 CONCLUSIONS FROM GROUP II TESTING

Crack growth life of a lug is longer if the pin clearance is smaller, based on tests of lugs with nominal diametrical pin clearances of 0.0005 inch, 0.0015 inch and 0.0030 inch.

Lubricant applied to the pin before testing failed to have the expected beneficial effect. Apparently, judging from fretting evidence, the lubricant did not significantly reduce the frictional shear stresses at the pin-lug interface.

For the same magnitude of axial load and the same R_o/R_i ratio, the crack growth life of the tapered lug is longer than that of a straight lug, but the straight lug analysis can be used as an approximation.

A steel shrink-fit bushing in an aluminum lug, with typical production interference of $\Delta r/r = .0020$, will tend to separate from the lug under load. If this separation is not accounted for in the analysis, crack growth life can be overestimated by a large factor (7 to 20 in these tests). Separation can be conservatively represented by modeling the pin and bushing together as a larger (frictionless) pin.

Stress intensity factors obtained from crack-tip finite element analysis of off-axis-loaded tapered lugs were available for $c/(R_o-R_i)$

≤ 0.95. Within this range, crack growth predictions tended to be mildly conservative.

Crack growth in off-axis-loaded tapered lugs was complicated by the following phenomena:

o   The cracks grew to lengths far beyond the range covered by FEM analysis, necessitating major extrapolation of the K vs. c relationship.

o   Crack growth was non-radial and non-coplanar, especially in steel (but in aluminum also).

o   There was a tendency for the crack to branch in an alternative direction. Usually the secondary crack would cease propagating, prolonging the growth life of the primary crack. However, in one steel specimen the growth of the secondary crack eventually caused specimen failure.

Despite these complexities the life predictions for these specimens were normally within a factor of 2 of the test results and tended to be conservative. Predictions for the steel lugs were especially accurate.

The shrink-fit steel bushings in the off-axis loaded steel tapered lugs had a very small effect on crack growth. Although bushing-lug separation may have occurred, it did not strongly affect either predicted or test life like it did in aluminum lugs with steel bushings (wherein the bushing-to-lug modulus ratio was 3:1).

In thick, axially loaded straight lugs the crack tended to turn out of plane shortly after the corner crack had become an across-the-ligament crack. Subsequently the turned crack tended to slow down and stop, necessitating the initiation of a second crack to bring about lug failure. This added test life contributed to the conservatism of the analysis of these specimens.

Even while the crack was a corner crack, the crack growth predictions for the thick straight lug specimens were somewhat inaccurate. The magnitudes of the errors in prediction were similar for spectrum loading and constant amplitude loading, but differed for different lug sizes.

The redundant wing-pylon lug analysis required special finite element modeling to account for the lug shape, effects of fasteners and structural supports, and effect of a shrink-fit bushing including separation at the

329

lug-bushing interface. The Green's function for an axially loaded straight lug had to be used for this complex geometry without correction. Spectrum loading was applied, requiring use of the Hsu Retardation Model. No account was taken for redundancy of the lug or load transfer between the cracked and uncracked member. In light of these complexities it is a pleasant surprise that the analytical prediction of failure time for the first ligament was within a factor of 2.0 of the average test result and was conservative.

There can be a dramatic damage tolerance advantage to redundant design of a lug if the initial crack occurs in only one member. In the simulated wing-pylon lug tested, the following advantages were noted:

o   The remaining life after failure of the initial ligament exceeded the crack growth life prior to ligament failure, because of a very long crack reinitiation period

o   The damage condition throughout this reinitiation period was a broken 1.2 inch ligament, which would be highly inspectable.

o   The crack growth rate prior to ligament failure was reduced due to load shedding to the neighboring member.

It is apparent that these advantages would disappear in the event of a compound misfortune in which both members in the redundant lug were preflawed equally.

Crack growth life predictions for bushed monolithic aluminum lugs were unconservative by factors of 1.4 to 22, because of the failure of the analysis to consider separation between the bushing and lug. Smaller total errors for the bushed redundant lugs resulted from a partially compensating failure to include redundancy effects in the analysis. If lug-bushing separation is considered as described in Section IV, the analytical crack growth life results for Group II specimens range from accurate to conservative.

REFERENCES

1. Anon., "Damage Tolerance Design Requirements," Military Specification MIL-A-83444 (USAF), Air Force Aeronautical Systems Division, March 1973.

2. K. Kathiresan, T. M Hsu and T. R. Brussat, "Advanced Life Analysis Methods - Crack Growth Analysis Methods for Attachment Lugs," AFWAL-TR-84-3080, Vol. II, Air Force Wright Aeronautical Laboratories, September 1984.

3. T. R. Brussat, K. Kathiresan and T. M. Hsu, "Advanced life Analysis Methods - Cracking Data Survey and NDI Assessment for Attachment Lugs," AFWAL-TR-84-3080, Vol. I, Air Force Wright Aeronautical Laboratories, September 1984.

4. J. Schijve and A. H. W. Hoeymakers, "Fatigue Crack Growth in Lugs," Fatigue of Engrg Mat'l, and Struct., Vol. 1, No. 2, 1979, pp. 185-201.

5. T. D. Gray, "An Equivalent Initial Flaw Analysis of the A-7A Wing Fatigue Tests," Report No. 2-53410/ASIP/5DIR-10, LTV Aerospace Corporation, May 1975.

6. T. R. Brussat, S. T. Chiu and M. Creager, "Flaw Growth in Complex Structure," AFFDL-TR-77-79, Vol. I, Air Force Flight Dynamics Laboratory, December 1977.

7. H. D. Dill and J. M. Potter, "Effects of Fighter Attack Spectrum on Crack Growth," AFFDL-TR-76-112, Air Force Flight Dynamics Laboratory, 1976.

8. G. S. Johnson, "F-16 Durability and Damage Tolerance Load Spectra," Proc. AF/Industry Workshop on Fatigue Spectra Development for Aircraft, AFWAL-TM-81-61-FIBE, Air Force Wright Aeronautical Laboratories, December 1980, pp. 187-218.

9. D. J. White, "Summary of Flight Spectra Development for Fighter Aircraft," Proc. AF/Industry Workshop on Fatigue Spectra Development for Aircraft, AFWAL-TM-81-61-FIBE, Air Force Wright Aeronautical Laboratories, December 1980, pp 323-348.

10. K. Kathiresan and T. R. Brussat, "Advanced Life Analysis Methods - User's Manual for "LUGRO" Computer Program to Predict Crack Growth in Attachment Lugs," AFWAL-TR-84-3080, Vol. VI, Air Force Wright Aeronautical Laboratories, September 1984.

11. H. C. Harris and I. U. Ojalvo, "Simplified Three-Dimensional Analysis of Mechanically Fastened Joints," Proc. Army Symp. on Solid Mechs 1974: The Role of Mechanics in Design - Structural Joints, AMMRC-MS 74-8, Army Mat'ls. and Mechs. Res. Center, Watertown, Mass., September 1974, pp. 177-192.

12. D. P. Rooke, "Fracture Mechanics Analysis of Short Cracks at Loaded Holes," Behavior of Short Cracks in Airframe Components, AGARD-CP-328, NATO Advisory Group for Aerospace Research and Development, April 1983, pp 8.1-8.6.

13. R. J. H. Wanhill, A. A. Jongebreur, E. Morgan and E. J. Moolhuijsen, "Flight Simulation Fatigue Crack Propagation in Single and Double Element Lugs," NLR-MP-80023U, Nat. Aero. Lab., Amsterdam, The Netherlands, March 1981.

APPENDIX A
SPECIMEN MANUFACTURING DRAWINGS

This appendix contains the dimensioned drawings that were used to machine the lug test specimens for the test program.

Figure A-1.   Group I Lug Specimens, R_o/R_i = 1.50 and 2.25

The figure contains the following annotations:

1.500 $^{+.001}_{-.000}$

RADIUS = W/2 $^{\pm.015}$ CONCENTRIC TO HOLE WITHIN ±.010

$\cancel{C}$ SYM

AVOID MISMATCH, NO SHARP CORNER (TYP)

±.002 MISMATCH (TYP.)

2W

GRAIN

4.0

W

$\cancel{C}$ SYM

B $^{\pm.005}$

/40 (TYP)

1.0 R

t
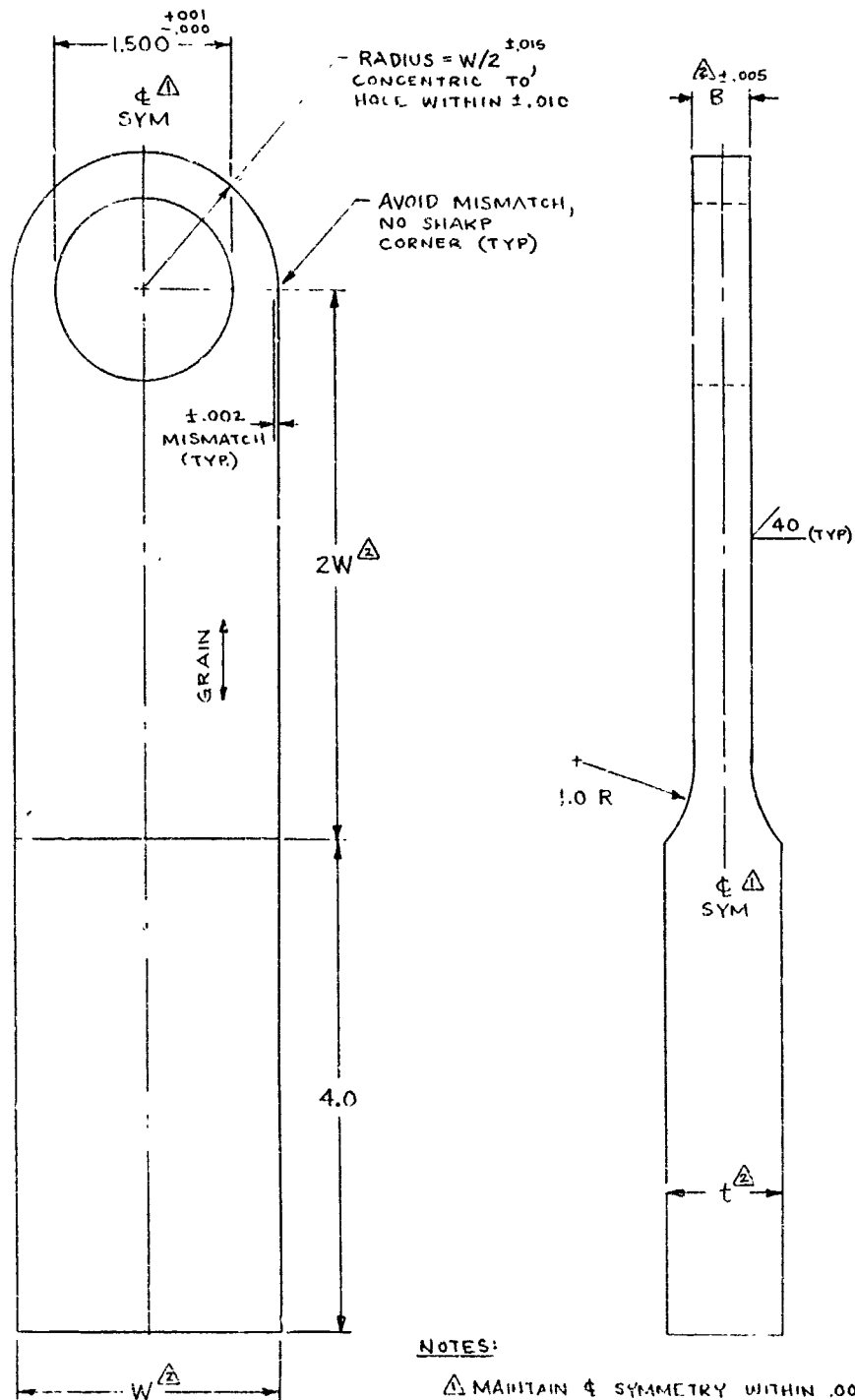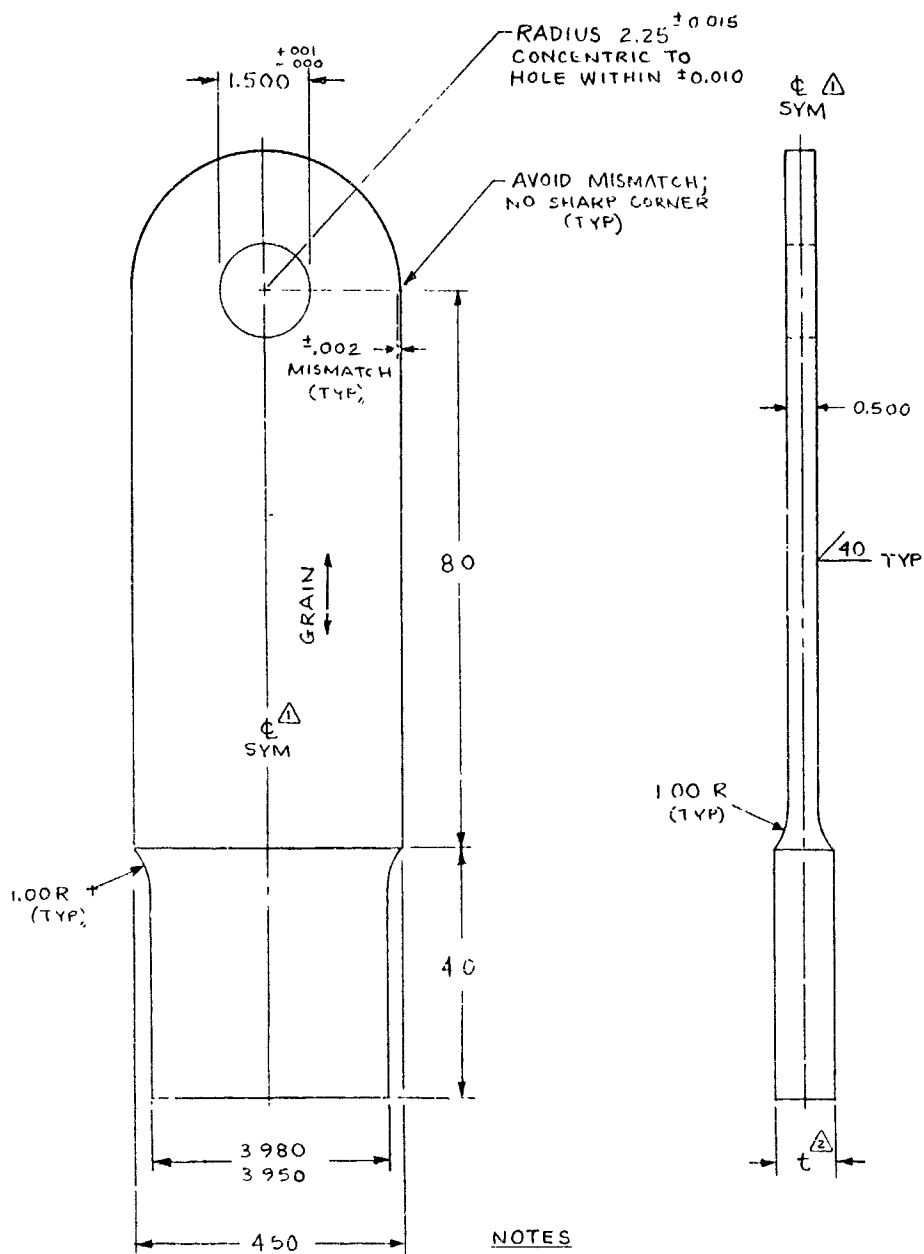
NOTES:

1. MAINTAIN $\cancel{C}$ SYMMETRY WITHIN .005

2. SPECIMENS REQUIRED:

MATERIAL	t	B	W	NO. REQ'D
4340 STEEL (180-200 KSI)	0.55	0.50	2.25	32
			3.375	28
		0.25	3.375	4
7075-T651 ALUMINUM	1.00	0.50	2.25	32
			3.375	28
		0.25	3.375	4

334

Figure A-2. Group I Lug Specimens, $R_o/R_i = 3.00$

RADIUS = 1.125 ±.010, CONCENTRIC TO HOLE WITHIN .007 INCH T.I.R.

AVOID MISMATCH; SMOOTH TRANSITION (TYP)

D $\triangle{1}$ $^{+.0009}_{-.0000}$

€ SYM

GRAIN

$\triangle{5}$

7.8 ±.05

B $\triangle{3}$

LEAVE SHARP EDGE, BOTH SIDES ON SPECIMEN TYPE S1 DO NOT DEBURR $\triangle{4}$

32
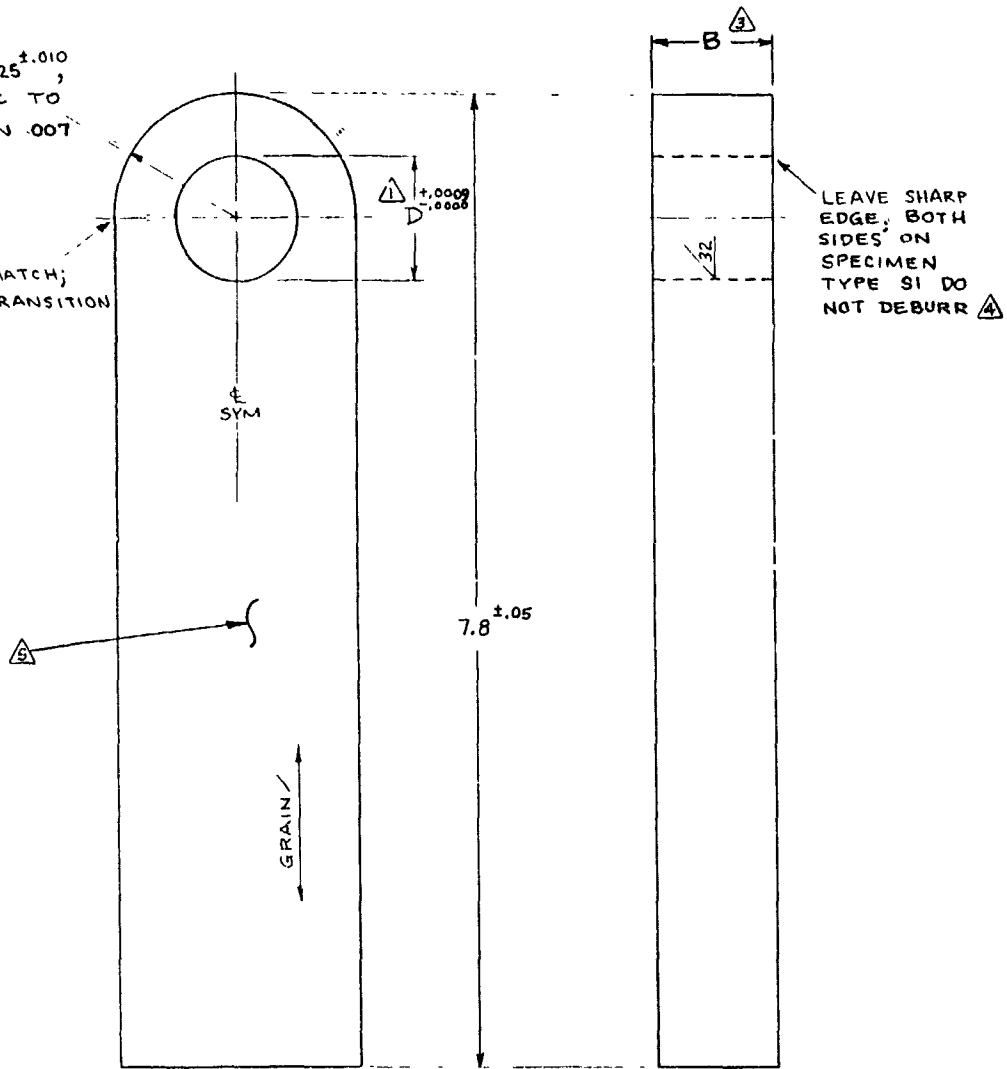
STAMP ID NUMBER ON BUTT END $\triangle{2}$

TABLE S1 SPECIMEN TYPES AND DIMENSIONS

SPECIMEN TYPE	D (INCH)	B (INCH)
S1 – X –	0.9990	1.0 REF
S1 – Y –	1.0000	1.0 REF
S1 – Z –	1.0010	1.0 REF
S2 – A –	1.1875	1.0 REF
S2 – B –	1.1875	0.50 ±.02

NOTES

$\triangle{1}$ MACHINE HOLE IN LUG TO DIAMETER "D" GIVEN IN TABLE S1, USING JIG BORE. MEASURE EXACT DIA. WITHIN ±.0001 INCH AT 72°F ±4°F AND RECORD WITH SPECIMEN I.D. NO. ON INSPECTION DATA SHEET.

$\triangle{2}$ SEE TABLE S1 AND TABLE 3-12 FOR SPECIMEN TYPES AND I.D. NUMBERS.

$\triangle{3}$ MACHINE FROM 10-INCH 7075-T651 ALUMINUM PLATE. SEE TABLE S1 FOR FINAL THICKNESS "B". REMOVE EQUAL AMOUNT FROM EACH FACE.

$\triangle{4}$ NO CHAMFER ON SPECIMEN TYPE S1. CHAMFER REQUIRED ON SPECIMEN TYPE S2, AS FOLLOWS:

.050 ±.010 × 45° ±5° CHAMFER, ONE SIDE ONLY

LEAVE SHARP EDGE, DO NOT DEBURR

1.1875 $^{+.0009}_{-.0000}$

32
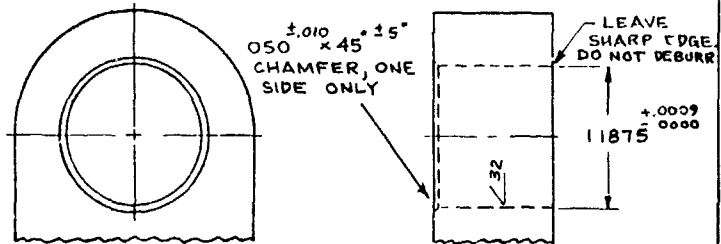
$\triangle{5}$ 125 RHR; DO NOT HAND-WORK.

Figure A-3. Basic Straight Lug Specimens–Type S1 and S2

336

RADIUS = 1125 ±.010 CONCENTRIC TO HOLE WITHIN .007 INCH T.I.R.

AVOID MISMATCH; MAKE SMOOTH TRANSITION (TYP)

MAINTAIN & SYMMETRY WITHIN .007 INCH T I R.

GRAIN

SYM

D +.0009 -.0000

2.80 ±.010

1175 ±.05

152 ±.007

1.75 ±.05

3.82 ±.02

B

LEAVE SHARP CORNER, BOTH SIDES ON SPECIMEN TYPE T1. DO NOT DEBURR. 4

BREAK EDGE, BOTH SIDES

STAMP I.D NO ON BUTT END 2
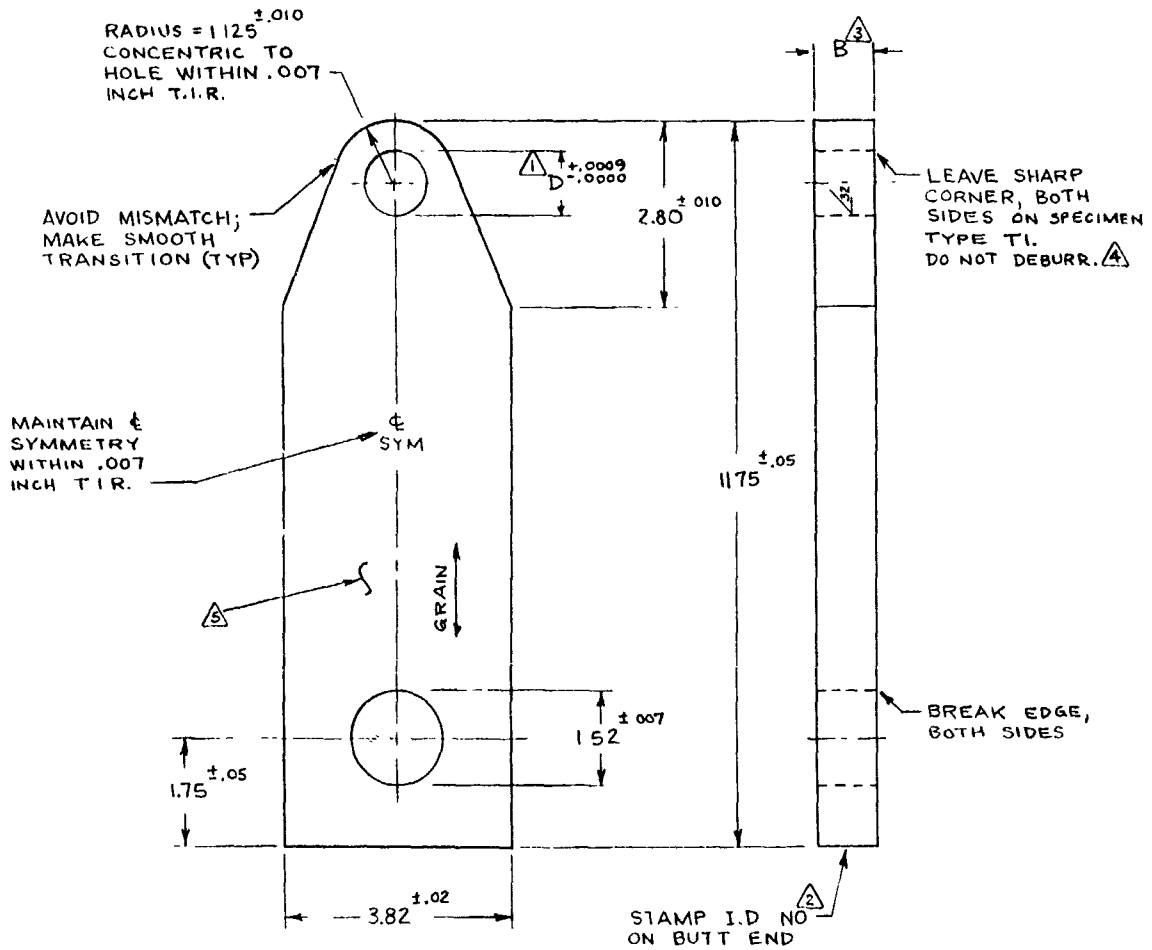
TABLE T1 SPECIMEN TYPES AND DIMENSIONS

SPECIMEN TYPE	D (INCH)	B (INCH)	MATERIAL
T1-X-	0.9990	1.0 REF	7075-T651
T1-Y-	1.0000	1.0 REF	
T1-Z-	1.0010	1.0 REF	
T1-A-	1.0000	1.0 REF	
			7075-T651
T1-S-	1.0000	0.50 REF	4340
T2-A-	1.1875	1.0 REF	7075-T651
T2-B-	1.1875	0.50 ±.02	7075-T651
T2-S-	1.1875	0.50 REF	4340

NOTES

1. MACHINE HOLE IN LUG TO DIAMETER "D" GIVEN IN TABLE T1. USE JIG BORE. MEASURE EXACT DIA WITHIN ±.0001 IN. AT 72°F ±4°F AND RECORD WITH SPECIMEN I.D. NO. ON INSPECTION DATA SHEET.

2. SEE TABLE T1 AND TABLE 3-12 FOR SPECIMEN TYPES AND I D NUMBERS.

3. MACHINE FROM 1.0-INCH 7075-T651 ALUMINUM PLATE OR 5.0×3.9×11.9-INCH 4340 STEEL PLATE (180-200 KSI); SEE TABLE T1 FOR MATERIAL AND FINAL THICKNESS "B".

4. ONLY ON SPECIMEN TYPE T2: CHAMFER ONE SIDE ONLY OF 1.200 - IN. HOLE WITH .050 ±.010 × 45° ±5° CHAMFER

11875 +.0009 -.0000

.050 ±.010 × 45° ±5° CHAMFER, ONE SIDE ONLY

LEAVE SHARP EDGE. DO NOT DEBURR
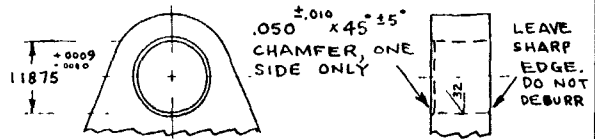
5. REDUCE THICKNESS FOR SPECIMENS TYPE T1-B AND T2-B AS FOLLOWS:
   • REMOVE EQUAL AMOUNT FROM EACH FACE.
   • GRIND PARALELL TO GRAIN DIRECTION
   • FINISH 125 RHR (ALUMINUM).

Figure A-4. Basic Tapered Lug Specimens – Type T1 and T2

RADIUS = .625 $\pm.010$; CONCENTRIC TO HOLE WITHIN .007 INCH T.I.R.

AVOID MISMATCH, MAKE SMOOTH TRANSITION (TYP)

MAINTAIN ₵ SYM. WITHIN .007 IN. T.I R.

₵ SYM

GRAIN

$.625^{+.0009}_{-.0000}$

7.90 $^{\pm.05}$

STAMP I.D. NO ⚠ ON BUTT END

⚠ $\pm.015$
.938

LEAVE SHARP CORNER, BOTH SIDES
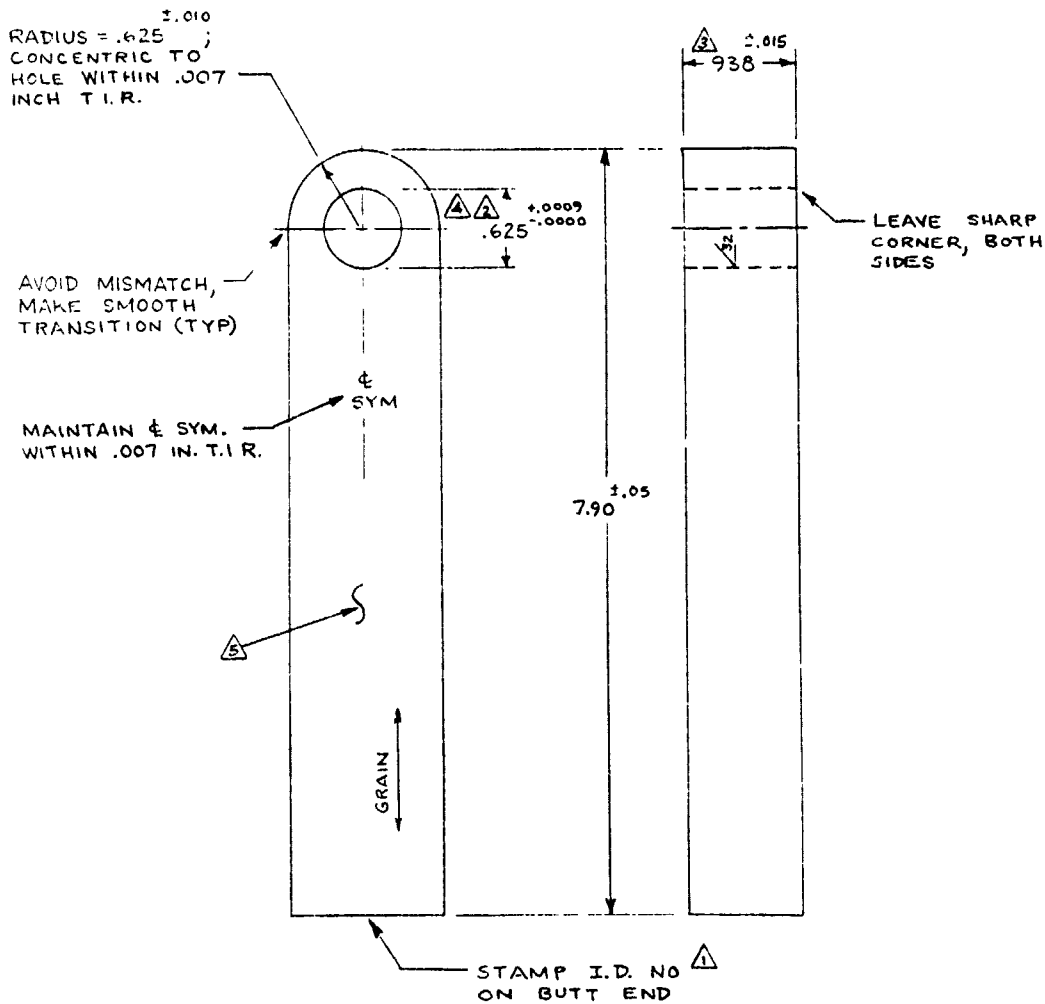
NOTES

⚠ USE THE FOLLOWING I.D. NUMBERS:

S3-A-1
S3-A-2
S3-A-3
S3-A-4

⚠ MEASURE EXACT HOLE DIA. WITHIN ±.0001 IN. AT 72°F ±4°F AND RECORD ON INSPECTION DATA SHEET.

⚠ MACHINE FROM 2.25-IN 7075-T651 PLATE. REMOVE EQUAL AMOUNT FROM EACH FACE.

⚠ USE JIG BORE FOR "TRUE" HOLE

⚠ 125 RHR FINISH; GRIND PARALLEL TO GRAIN DIRECTION ONLY. DO NOT HAND-WORK.

Figure A-5. Straight Lug Specimen Type S3-A

338

Figure A-6.   Straight Lug Specimen Type S3-B

RADIUS = 1.00 ±.010; CONCENTRIC TO HOLE WITHIN .007 INCH T.I.R.

AVOID MISMATCH, SMOOTH TRANSITION (TYP)

MAINTAIN ℄ SYMMETRY WITHIN .007 INCH T.I.R.

℄ SYM

GRAIN

1.000 +.0009 -.0000 △2 △4

5.0 ±.05

8.75 ±.05

1.0 RADIUS ±.05 TYP

1.52 ±.007

175 ±.05

2.80 ±.05

1.50 △3 ±.015

LEAVE SHARP CORNER, BOTH SIDES. DO NOT DEBURR

BREAK SHARP CORNER, BOTH SIDES

STAMP I.D NO ON BUTT END △1

NOTES

△1 USE THE FOLLOWING SPECIMEN I.D. NO.'S:
S3-B-1   S3-B-3
S3-B-2   S3-B-4

△2 MEASURE EXACT HOLE DIA WITHIN ±.0001 IN AT 72°F ±4°F AND RECORD ON INSPECTION DATA SHEET

△3 MACHINE FROM 2.25-IN. 7075-T651 PLATE. REMOVE EQUAL AMOUNT FROM EACH FACE.

△4 USE JIG BORE FOR 1-INCH HOLE

△5 125 RHR FINISH. GRIND PARALLEL TO GRAIN ONLY. DO NOT HAND WORK

339

RADIUS 1.50 $\pm$.010; CONCENTRIC TO HOLE WITHIN .007 INCH T.I.R.

AVOID MISMATCH; SMOOTH TRANSITION (TYP)

MAINTAIN & SYMMETRY WITHIN .007 INCH T.I.R.

₵ SYM

GRAIN

1.5 RAD. (TYP) $\pm$.05

2.25 (REF) △3

LEAVE SHARP CORNER, BOTH SIDES DO NOT DEBURR.

1.500 $^{+.0010}_{-.0000}$ △2 △4

7.50 $\pm$.05

13.2 $\pm$.05

2.02 $\pm$.007

2.50 $\pm$.05

4.20 $\pm$.05

BREAK SHARP CORNER; BOTH SIDES

STAMP I.D NUMBER ON BUTT END △1

NOTES

△1 USE THE FOLLOWING I D NUMBERS

S3-C-1
S3-C-2
S3-C-3
S3-C-4

△2 MEASURE EXACT DIA. OF 1.5-INCH DIA. HOLE WITHIN $\pm$.0001 INCH AT 72°F $\pm$4°F AND RECORD ON INSPECTION DATA SHEET

△3 MACHINE FROM 2.25-IN 7075-T651 PLATE.

△4 USE JIG BORE FOR 1.5-INCH HOLE.

△5 125 RHR FINISH, DO NOT HAND WORK.

Figure A-7. Straight Lug Specimen Type S3-C

340

NOTES:

△1 USE THE FOLLOWING I.D. NUMBERS:

    C1-A-1
    C1-A-2

△2 MEASURE EXACT DIA. OF 1-INCH HOLES WITHIN ±.0001 INCH AT 72°F ±4°F AND RECORD ON INSPECTION DATA SHEET.

△3 MACHINE FROM 2.25-INCH 7075-T651 ALUMINUM PLATE.

△4 USE JIG BORE FOR 1-INCH HOLES.

△5 125 RHR DO NOT HAND-WORK.

△6 LEAVE SHARP CORNERS, BOTH SIDES. DO NOT DEBURR

Figure A-8. Clevis Lug Specimen Type C1

341

Figure A-9. Clevis Lug Specimen Type C2
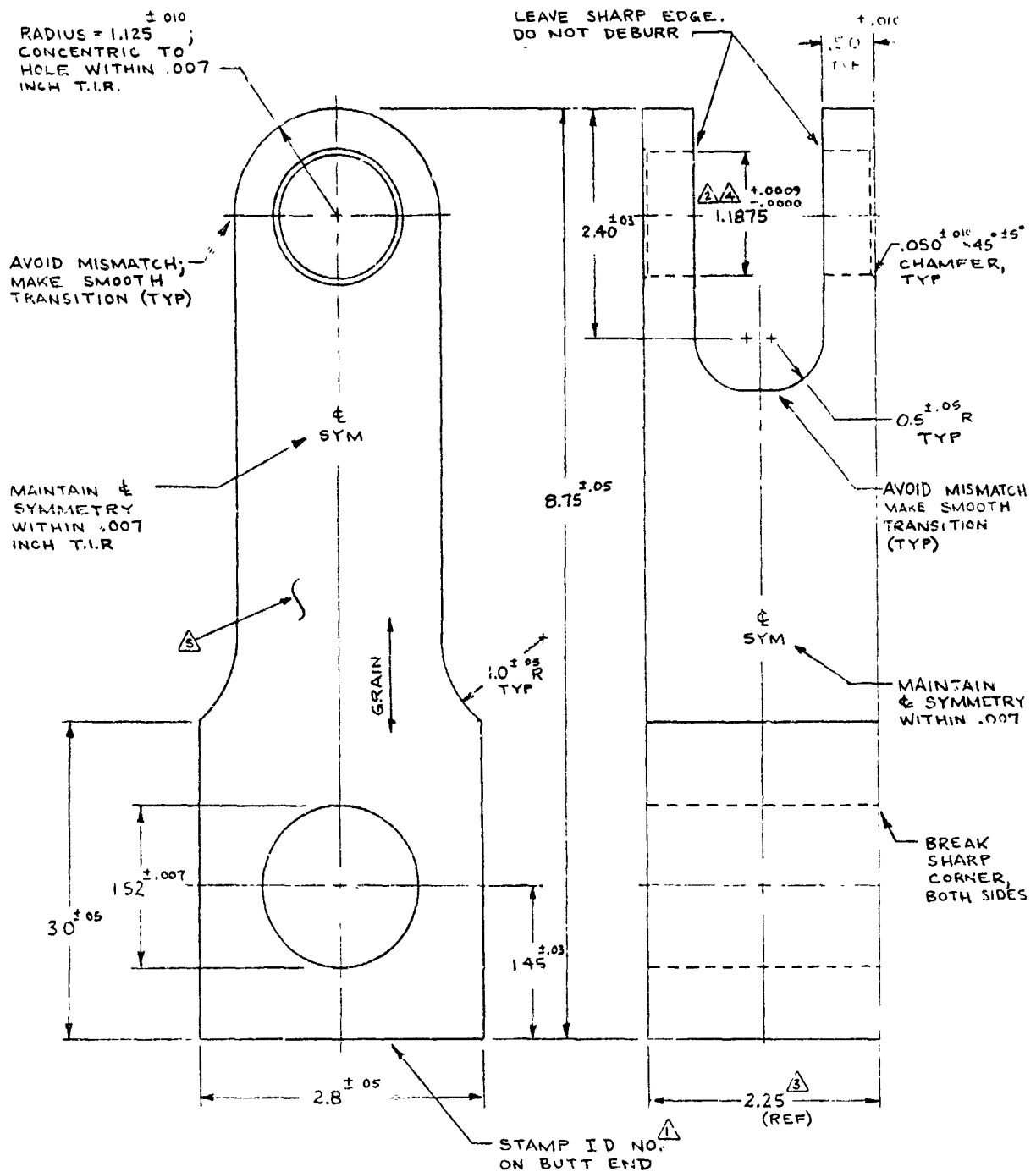
NOTES:

△1 USE THE FOLLOWING I D. NUMBERS:

    C2-A-1
    C2-A-2

△2 MEASURE EXACT DIA. OF 1.2-INCH HOLES WITHIN ±.0001 INCH AT 72°F ±4°F AND RECORD ON INSPECTION DATA SHEET.

△3 MACHINE FROM 2.25-INCH 7075-T651 ALUMINUM PLATE.

△4 USE JIG BORE FOR 1.1875-IN. HOLES

△5 125 RHR FINISH. DO NOT HAND-WORK.

342

RADIUS = 1.125$^{+.010}$,
CONCENTRIC TO
HOLE WITHIN .007
INCH T.I.R.

3△ 4△ $1.000^{+.0009}_{-.0000}$

LEAVE SHARP
EDGE, BOTH
SIDES. DO NOT
DEBURR.

AVOID MISMATCH,
MAKE SMOOTH
TRANSITIONS (TYP)

B

1.5 R
TYP

1.5 R
TYP

7.8 $^{±.05}$

MAINTAIN ₵
SYMMETRY
WITHIN .007
INCH T.I.R

₵
SYM

5△

GRAIN

3.0 $^{±.05}$

1.4 $^{±.02}$

2.25 $^{±.05}$

STAMP I.D NO
ON BUTT END 2△

TABLE D1. LUG THICKNESSES
AND I.D. NUMBERS

LUG I D NO.	THICKNESS B (INCH)
D1-A-1 D1-A-2	1.00 (REF.)

NOTES.

1△ MACHINE FROM 1.0-IN. 7075-T651
ALUMINUM PLATE. SEE TABLE D1
FOR FINAL THICKNESS, B.

2△ SEE TABLE D1 FOR I.D. NUMBERS.

3△ MEASURE EXACT HOLE DIA. WITHIN ±.0001 IN.
AT 72°F ±4°F AND RECORD ON
INSPECTION DATA SHEET.

4△ USE JIG BORE FOR 1.0-INCH HOLE.

Figure A-10. Dogbone Lug Specimen Type D1

343

RADIUS = 1.125 ±.010
CONCENTRIC TO,
HOLE WITHIN .007
INCH T.I.R.

LEAVE SHARP EDGE,
ONE SIDE ONLY

B

.050 ±.010 × 45° ±5°
CHAMFER, ONE
SIDE ONLY

3 4 1.1875 +.0009 −.0000

1.5 R TYP

AVOID MISMATCH;
MAKE SMOOTH
TRANSITION (TYP)

7.8 ±.05

15 R TYP

5

MAINTAIN ¢
SYMMETRY
WITHIN .007
INCH T.I.R.

¢ SYM

GRAIN

3.0 ±.05

1.40 ±.02

2.25 ±.05

STAMP I.D. NO.
ON BUTT END

2
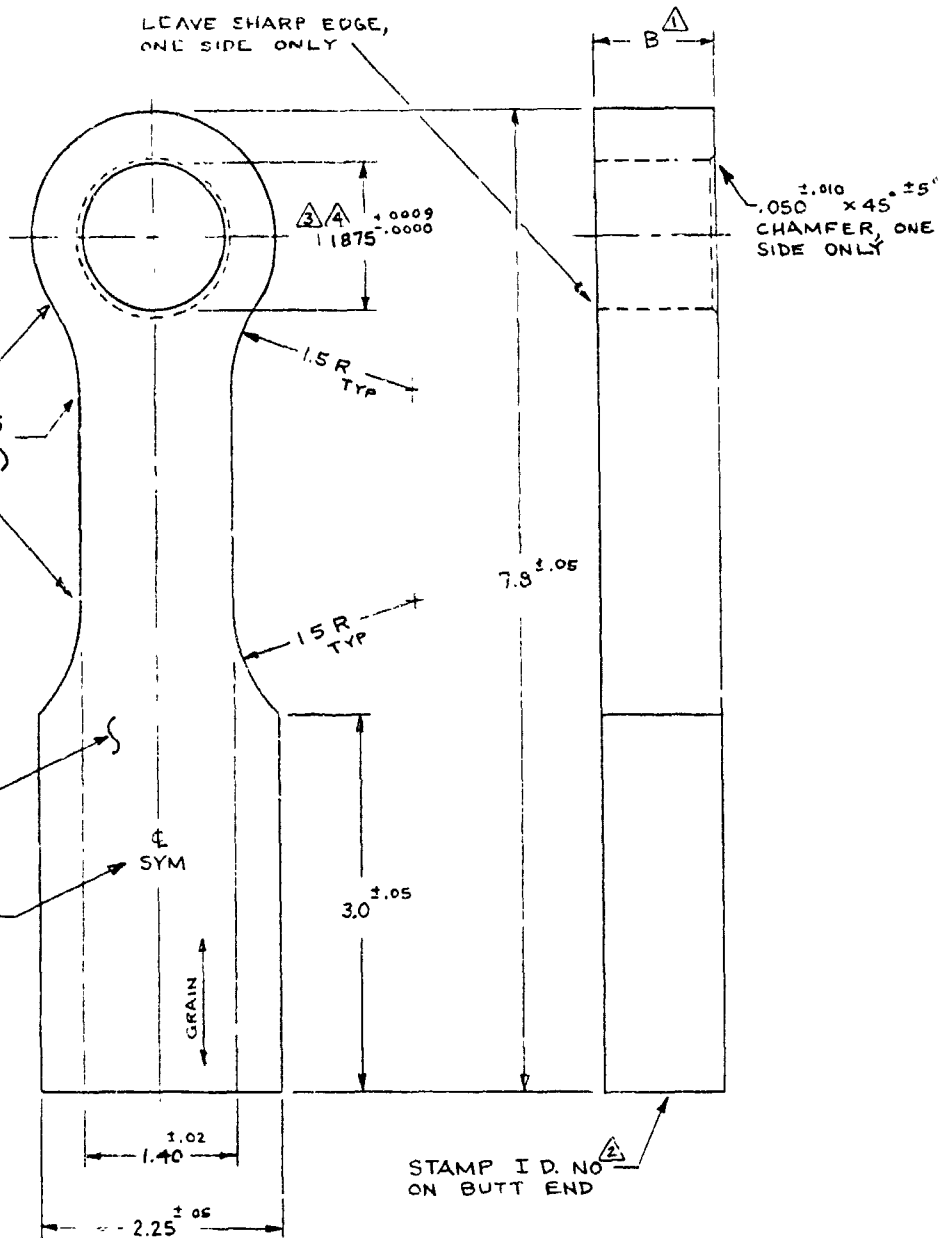
TABLE D2. LUG THICKNESSES
AND I.D. NUMBERS

LUG I.D. NO.	THICKNESS B (INCH)
D2-A-1 D2-A-2	1.00 (REF.)
D2-B-1 D2-B-2	0.50 ±.010 5

NOTES

1 MACHINE FROM 1.0-IN. 7075-T651
ALUMINUM PLATE. SEE TABLE D2
FOR FINAL THICKNESS, B.

2 SEE TABLE D2 FOR I.D. NUMBERS

3 MEASURE EXACT HOLE DIA. WITHIN ±.0001 IN. AT
72°F ±4°F AND RECORD ON
INSPECTION DATA SHEET.

4 USE JIG BORE FOR 1.1875-IN. HOLE.

5 REDUCE THICKNESS ON LUG-TYPE D2-B AS FOLLOWS:
 • REMOVE EQUAL AMOUNT FROM EACH FACE.
 • MACHINE PARALLEL TO GRAIN DIRECTION ONLY.
 • 125 RHR FINISH.
 • DO NOT HAND WORK.

Figure A-11. Dogbone Lug Specimen Type D2

344
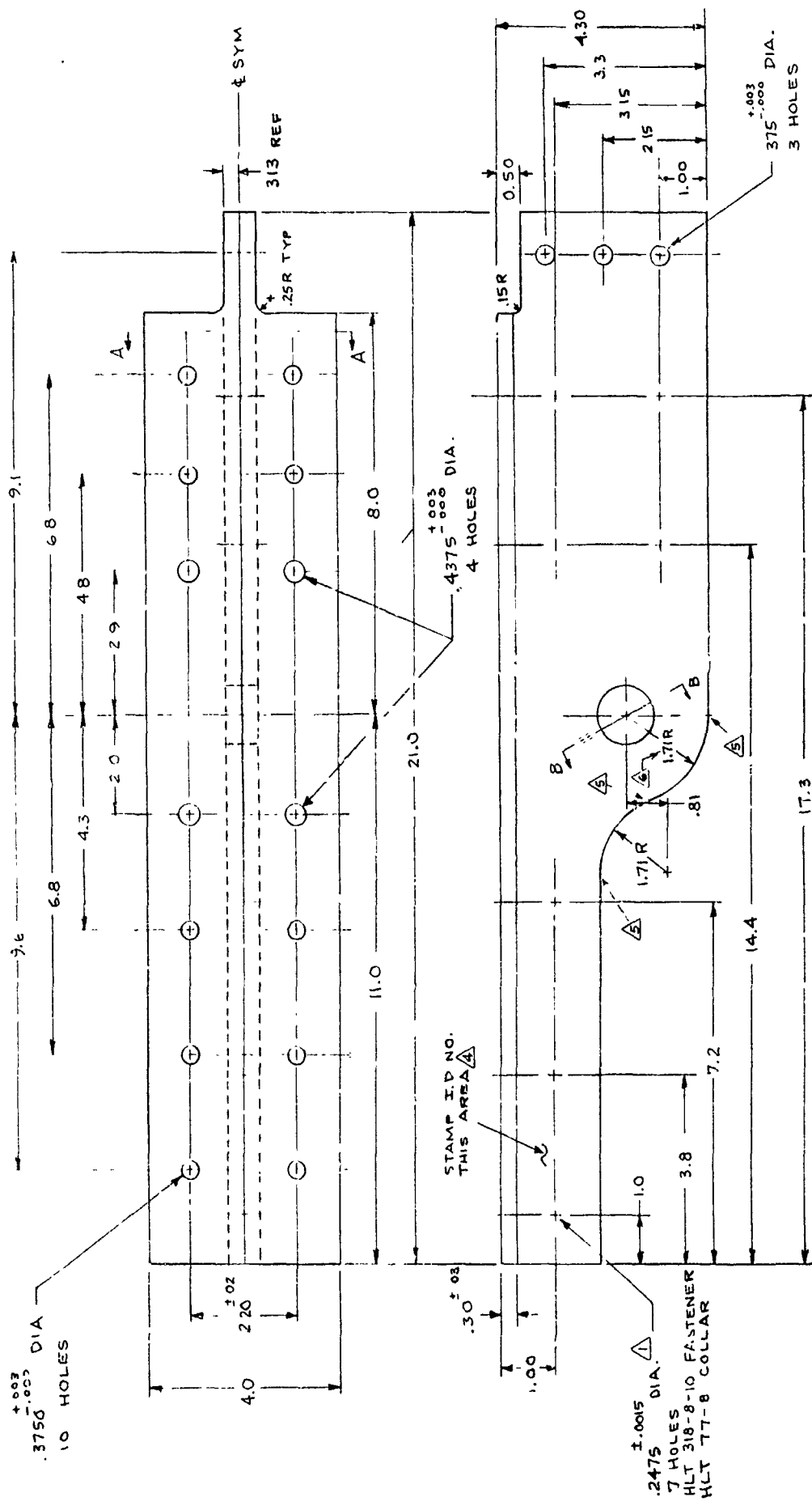
Figure A-12. Typical Wing-Pylon Attach Lug for Transport Aircraft; Specimen Type R2 (Sheet 1 of 2)

NOTES

△1 MACHINE FROM 7075-T6511 ALUMINUM EXTRUSION, FIGURE A-13. NOTE THAT THICKNESS OF EXTRUSION IS CORRECT.

USE THE FOLLOWING FABRICATION SEQUENCE:

° FASTEN 2 EXTRUSION PIECES TOGETHER AS SHOWN IN VIEW A-A, WITH 7 FASTENERS

° COMPLETE ALL OTHER MACHINING

△2 DIMENSIONAL TOLERANCES ±.05 IF NOT SPECIFIED

△3 USE JIG BORE FOR 1.1875 - IN. HOLE. MEASURE EXACT HOLE DIA. WITHIN ±.0001 IN. AT 70°F ±4°F AND RECORD ON INSPECTION DATA SHEET.

△4 USE THE FOLLOWING SPECIMEN I D NUMBERS
R2-E-1
R2-E-2

△5 AVOID MISMATCH, MAKE SMOOTH TRANSITIONS

△6 1.71 RADIUS CONCENTRIC TO HOLE WITHIN .007 IN. T.I.R

LONG FLANGE

HI-LIT 318 FASTENERS 7 HOLES △1

VIEW A-A

.313 REF

VIEW B-B (FULL SCALE)

1.1875 DIA +.0009/-.0000 △3

LEAVE SHARP CORNER, ONE SIDE ONLY

.050 +.010/-.000 × 45° ±5° CHAMFER, ONE SIDE ONLY
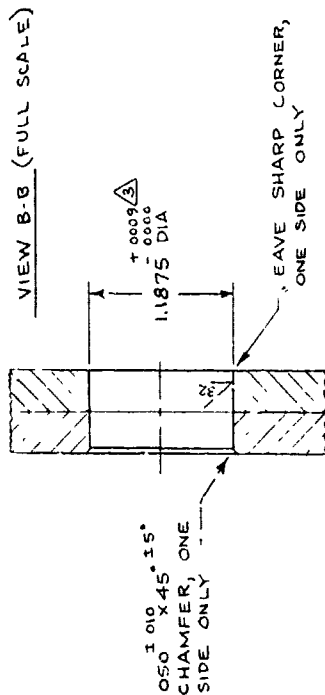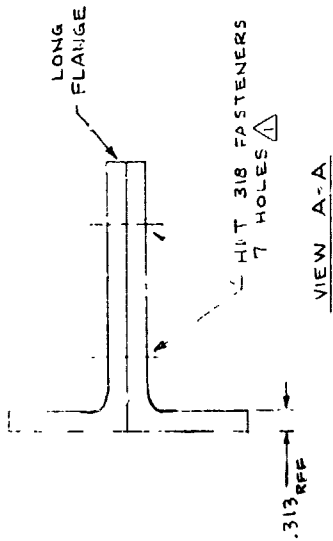
Figure A-12. Typical Wing-Pylon Attach Lug for Transport Aircraft; Specimen Type R2 (Sheet 2 of 2)

346
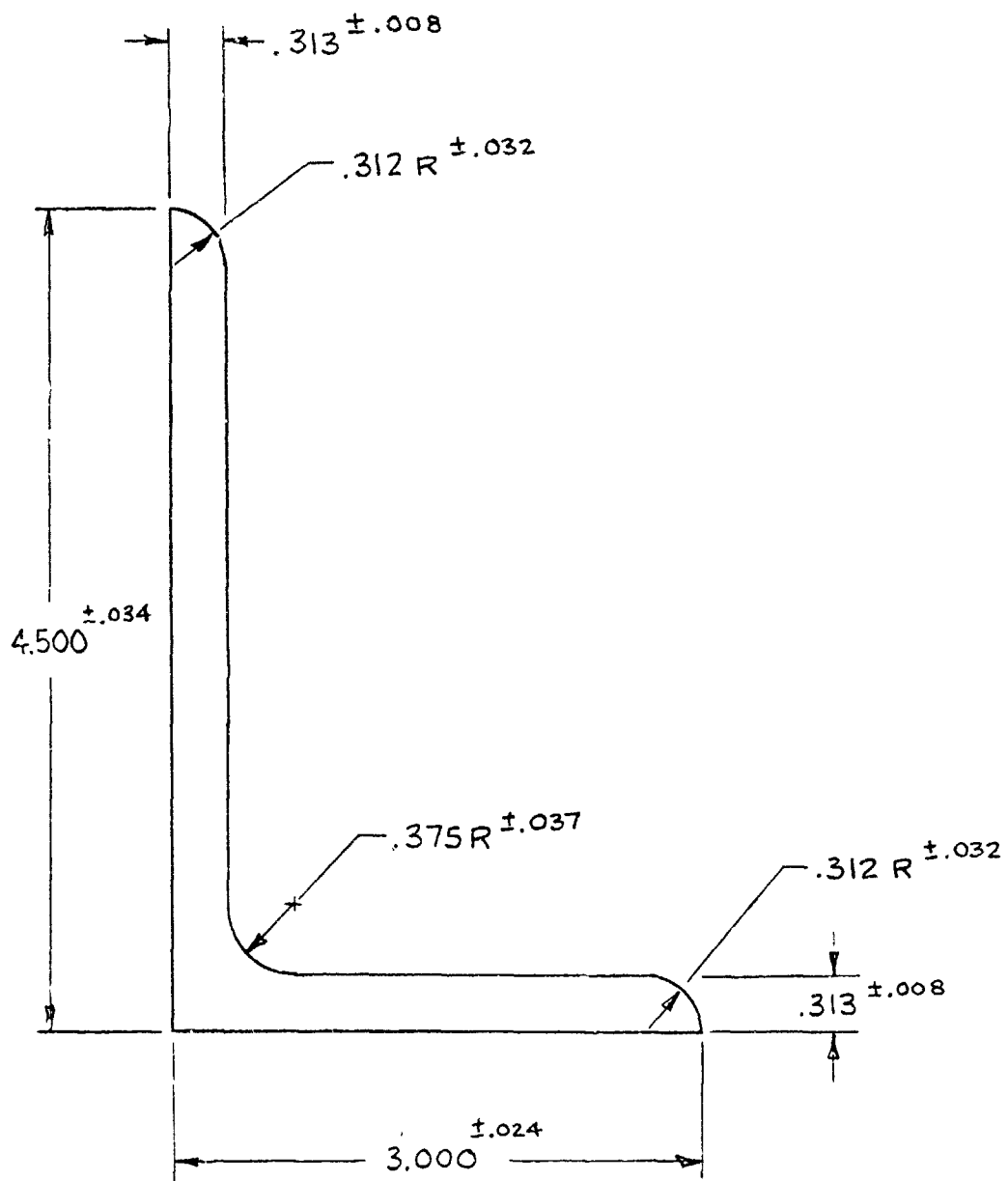
Figure A-13. 7075-T6511 Aluminum Extrusion for Specimen Type R2.

APPENDIX B
TEST SPECTRA
FOR
FLIGHT-BY-FLIGHT LOADING

This appendix contains the tables that fully describe the two flight-by-flight spectrum loading sequences used in the test program.

	MAX STRESS KSI	MIN STRESS KSI	N/FLT
MIS 0			
	19.108	-1.184	1.00
MIS 1			
	18.083	-1.808	1.00
	4.423	2.423	1993.00
	13.492	9.49_	193.00
	15.106	9.106	24.00
	15.863	7.863	4.00
	16.909	5.572	1.00
	18.083	2.602	.10 *
MIS 2			
	17.987	-1.799	1.00
	5.080	3.080	2273.00
	13.824	9.824	204.00
	15.189	9.189	25.00
	15.908	7.908	5.00
	16.899	5.494	1.00
	17.987	2.384	.10
MIS 3			
	16.751	-1.675	1.00
	4.888	2.888	2891.00
	14.139	10.139	227.00
	15.304	9.304	25.00
	15.918	7.918	4.00
	16.751	5.302	1.00
MIS 4			
	16.695	-1.669	1.00
	6.157	4.157	2827.00
	14.755	10.755	209.00
	15.562	9.562	23.00
	16.065	8.065	4.00
	16.695	5.536	1.00
MIS 5			
	17.952	-1.795	1.00
	4.737	2.737	2099.00
	14.329	10.329	175.00
	15.420	9.420	21.00
	16.101	8.101	4.00
	16.936	5.964	1.00
	17.952	2.888	.10

* N/FLT = 0.1–Means the application of this load once in ten occurrences
of this mission (refer to sequence of missions table).

	MAX STRESS KSI	MIN STRESS KSI	N/FLT
MIS 6			
	16.778	-1.678	1.00
	6.313	4.313	3082.00
	15.372	11.372	204.00
	15.904	9.904	21.00
	16.321	8.321	3.00
	16.778	6.050	1.00
MIS 7			
	17.861	-1.786	1.00
	5.628	3.628	2100.00
	14.634	10.634	164.00
	15.592	9.592	19.00
	16.232	8.232	3.00
	16.916	6.358	1.00
	17.861	3.335	.10
MIS 8			
	17.518	-1.752	1.00
	6.414	4.414	2714.00
	15.401	11.401	187.00
	15.941	9.941	19.00
	16.373	8.373	3.00
	16.820	6.253	1.00
	17.518	2.991	.10
MIS 9			
	17.761	-1.776	1.00
	6.544	4.544	2260.00
	15.197	11.197	161.00
	15.853	9.858	17.00
	16.406	8.406	2.00
	16.913	6.694	1.00
	17.761	3.686	.10
MIS 10			
	17.001	-1.700	1.00
	6.806	4.806	1989.00
	15.273	11.273	151.00
	15.918	9.918	18.00
	16.475	8.475	2.00
	17.001	6.760	1.00

TABLE B-1. MISSIONS DEFINITION FOR CARGO SPECTRUM (CONTINUED)

	MAX STRESS KSI	MIN STRESS KSI	N/FLT
MIS 11			
	14.546	-1.808	1.00
	15.523	.000	1.00
	15.523	.000	1.00
	15.523	.000	1.00
	18.083	.000	1.00
	15.523	.000	1.00
	15.523	.000	1.00
	15.523	.000	1.00
	16.191	.000	1.00
	16.191	.000	1.00
	3.774	1.774	5418.00
	12.842	8.842	419.00
	14.546	8.546	51.00
	15.523	7.523	9.00
	16.191	6.191	2.00
	16.913	4.425	1.00
	18.083	1.151	.10
MIS 12			
	15.650	-1.849	1.00
	15.650	.000	1.00
	15.650	.000	1.00
	15.650	.000	1.00
	18.487	-1.849	1.00
	15.650	.000	1.00
	16.323	.000	1.00
	16.323	.000	1.00
	16.323	.000	1.00
	3.848	1.848	6512.00
	13.112	9.112	556.00
	14.771	8.771	69.00
	15.650	7.650	12.00
	16.323	6.323	5.00
	17.267	4.096	1.00
	18.487	.919	.10

6

TABLE B-2. ONE PASS OF SEQUENCE OF MISSIONS OF CARGO SPECTRUM

SEQUENCE NO.	MISSION NO.	SEQUENCE NO.	MISSION NO.	SEQUENCE NO.	MISSION NO.
1	7	41	2	81	7
2	8	42	5	82	12
3	1	43	12	83	11
4	2	44	7	84	9
5	12*	45	2*	85	7
6	7	46	8	86	8*
7	5	47	1	87	2
8	11	48	9	88	5
9	8	49	4	89	1
10	9	50	7	90	12
11	7	51	12	91	7
12	1	52	8	92	10
13	12	53	11	93	8
14	2	54	5	94	11
15	7*	55	7*	95	3
16	8	56	1	96	7*
17	11	57	2	97	2
18	5	58	12	98	1
19	1	59	8	99	12
20	7	60	7	100	5
21	12	61	0	101	7
22	4	62	3	102	8
23	2	63	5	103	9
24	7	64	1	104	2
25	8*	65	7	105	7
26	6	66	12*	106	11*
27	11	67	8	107	12
28	1	68	2	108	1
29	12	69	11	109	8
30	7	70	9	110	5
31	8	71	7	111	7
32	2	72	1	112	2
33	5	73	12	113	12
34	7	74	8	114	8
35	1*	75	7	115	7
36	9	76	5*	116	9*
37	12	77	2	117	1
38	8	78	4	118	11
39	11	79	1	119	4
40	7	80	8	120	12

*Missions with application of once in ten occurrances loads (i.e., loads with N/FLT = 0.1)

TABLE B-3. STRESSES AND FREQUENCES FOR 80-FLIGHT FIGHTER SPECTRUM

LOAD NO.	MAX. STRESS, KSI	MIN. STRESS, KSI	NO. PER 80 FLIGHTS	FREQUENCY Hz	
1	20.000	2.778	1	1.0	
2	18.611	2.778	1	1.0	
3	18.056	2.778	1	1.5	
4	17.722	2.778	1	1.5	
5	17.333	2.778	2	1.5	
6	16.944	2.778	2	2.0	
7	16.611	2.778	3	2.0	LOADS FOR 40 SEVERE FLIGHTS
8	16.167	2.778	4	2.0	
9	15.722	2.778	6	3.0	
10	15.278	2.778	10	3.0	
11	14.722	2.778	16	3.0	
12	14.167	2.778	25	4.0	
13	13.472	2.778	30	4.0	
14	12.778	2.778	40	4.0	
15	12.028	2.778	58	4.0	
16	11.333	2.778	80	5.0	
17	10.361	2.778	120	6.0	
18	9.389	2.778	170	7.0	
19	8.333	2.778	230	8.0	
20	18.889	2.778	1	1.0	
21	17.222	2.778	1	1.5	
22	16.417	2.778	1	2.0	
23	15.889	2.778	1	2.0	
24	15.333	2.778	2	3.0	
25	14.861	2.778	2	3.0	
26	14.444	2.778	3	3.0	LOADS FOR 40 TYPICAL FLIGHTS
27	13.889	2.778	4	4.0	
28	13.278	2.778	6	4.0	
29	12.556	2.778	10	4.0	
30	11.806	2.778	16	4.0	
31	10.889	2.778	25	5.0	
32	10.083	2.778	30	6.0	
33	9.361	2.778	40	7.0	
34	8.750	2.778	58	8.0	
35	8.111	2.778	80	8.0	

TABLE B-4. LOADING SEQUENCE OF 80-FLIGHT FIGHTER SPECTRUM

LOAD NUMBERS

FLIGHT NO.	NO. OF CYCLES																						
1	20	19	14	18	18	18	19	16	19	18	19	16	17	18	17	19	19	18	18	18	19	19
2	20	10	19	6	18	18	19	35	14	19	17	19	18	9	17	11	16	18	18	17	18	18
3	7	34	31	35	31	35	32	35														
4	7	35	32	31	31	35	32	29														
5	7	32	34	33	34	35	35	34														
6	7	29	32	34	33	33	35	31														
7	7	35	33	35	35	35	33	35														
8	20	7	19	18	15	18	16	13	12	17	19	19	17	15	18	11	18	18	17	17	
9	20	15	18	18	19	15	19	19	17	19	9	29	2	17	12	15	17	18	9	14	19
10	20	18	19	13	16	18	18	19	13	19	19	19	14	17	11	11	15	11	11	13	
11	7	32	28	30	35	34	35	34														
12	20	17	18	19	18	14	12	17	19	19	19	19	12	19	19	18	18	18	8		
13	20	17	19	17	18	16	18	9	5	17	12	2	17	17	12	19	14	19	18		
14	20	19	18	15	19	16	14	18	18	19	16	19	12	18	19	16	17	19	8		
15	20	13	15	16	15	16	18	12	19	19	16	18	16	18	19	19	19	16	19		
16	20	18	19	17	19	16	19	12	12	19	14	19	14	19	11	18	11	18	17		
17	7	34	35	35	33	33	33	34														
18	20	19	10	19	7	15	14	18	9	19	16	17	16	17	15	16	17	14	15		
19	20	15	19	18	19	16	13	19	17	18	16	13	16	18	13	13	18	19	13		
20	7	32	32	35	33	34	34	32														
21	20	17	19	18	19	17	17	17	12	11	19	14	19	19	19	14	18				
22	7	35	35	25	31	31	34	35														
23	20	19	19	19	19	17	18	18	14	14	16	16	18	19	12	19	12	12	17		

TABLE B-4. LOADING SEQUENCE OF 80-FLIGHT FIGHTER SPECTRUM (CONTINUED)

LOAD NUMBERS

FLIGHT NO.	NO. OF CYCLES	LOAD NUMBERS
24	7	21 34 34 34 34 24 26 32
25	20	15 19 15 16 19 18 18 15 19 17 15 18 17 19 16 17 18 19 17 18 19
26	7	34 35 34 35 31 33 24
27	20	18 18 16 19 18 18 18 19 17 17 13 17 19 16 19 18 14 17 14 19
28	7	30 34 32 35 35 32 33
29	20	17 14 14 19 17 18 16 10 18 18 17 19 18 19 18 18 14 12 11
30	20	18 19 15 17 16 18 18 18 19 15 16 15 18 19 9 17 18
31	20	19 19 16 18 17 19 11 18 16 18 16 9 18 18 18 15 16
32	7	34 35 33 30 34 31 35
33	7	35 32 31 35 32 35 34
34	20	14 16 14 13 19 12 18 17 16 19 19 13 19 10 16 15 13 8 19
35	20	18 13 15 18 13 19 16 19 16 18 15 11 17 14 13 19 17 19 19
36	7	23 35 35 35 34 27 35
37	7	33 29 33 35 35 34 34
38	7	31 30 31 33 32 29 35
39	20	19 19 17 19 19 17 18 11 18 18 19 14 18 17 1 18 19 14 18 16
40	7	34 34 33 35 34 31 34
41	7	33 31 34 34 33 34 31
42	20	17 19 17 19 19 18 16 19 17 10 19 17 19 17 17 17 18 19
43	7	34 34 33 28 35 35 33
44	20	16 19 18 5 18 18 18 17 19 10 19 19 15 19 16 18 17 16
45	7	35 33 33 34 35 26 30
46	20	18 17 18 18 17 15 18 15 18 16 19 13 19 19 19 19 18 19

TABLE B-4. LOADING SEQUENCE OF 80-FLIGHT FIGHTER SPECTRUM (CONTINUED)

LOAD NUMBERS

FLIGHT NO.	NO. OF CYCLES	LOAD NUMBERS
47	7	25 35 35 35 32 34 33
48	7	32 35 34 32 31 34 35
49	7	34 33 34 35 35 32 28
50	7	35 35 35 34 30 32 31
51	7	29 34 33 33 20 33 32
52	20	17 19 15 17 18 18 14 19 18 17 18 13 15 10 18 14 16 17 19
53	20	18 17 15 17 16 15 15 18 17 19 16 17 16 18 17 15 17 11
54	20	18 16 15 17 13 16 6 19 18 15 19 10 16 17 16 19 13 14 17
55	7	33 34 35 34 34 34 31
56	7	35 26 33 32 31 35 32
57	20	15 16 19 18 14 16 17 18 17 17 18 17 17 16 12 17 11 17 17
58	20	16 18 17 16 18 12 15 13 18 15 16 18 16 18 18 18 19 18
59	20	19 18 16 18 15 19 18 18 12 17 17 12 15 19 19 17 19 19
60	20	18 19 13 18 19 19 15 18 17 16 19 16 9 19 14 17 15 19
61	20	17 16 18 14 13 17 15 19 18 17 17 16 19 17 14 14 19 19
62	20	16 17 18 18 17 18 17 18 19 19 18 15 17 17 18 16 17 10
63	20	19 16 19 7 19 19 19 19 18 19 18 16 19 18 19 16 18 19
64	20	19 17 19 15 17 19 18 16 15 18 14 12 18 19 19 19 14 19
65	7	35 28 30 33 34 34 35
66	7	35 34 30 34 33 27 30
67	20	12 19 17 19 17 13 14 18 19 12 18 18 19 18 18 10 16 18
68	7	34 34 35 34 34 30 31
69	7	29 35 35 32 34 27 33

TABLE B-4. LOADING SEQUENCE OF 80-FLIGHT FIGHTER SPECTRUM (CONTINUED)

LOAD NUMBERS

FLIGHT NO.	NO. OF CYCLES																					
70	20	16	12	18	14	18	17	19	19	11	13	15	19	19	19	19	18	18	16	18	17
71	20	19	18	19	19	15	18	14	19	:7	19	14	19	15	15	19	18	16	16	19	12
72	7	35	30	35	31	29	30	31													
73	7	35	35	35	29	31	35	35													
74	7	35	35	34	32	35	29	31													
75	7	33	35	33	34	33	35	32													
76	7	32	3ᴗ	30	30	35	35	34													
77	7	34	35	32	33	35	ᵌ3	34													
78	20	19	17	19	18	17	19	17	16	16	19	18	15	19	18	17	16	19	19		
79	7	33	34	22	35	24	28	27													
80	7	33	30	32	30	35	32	33													